ECOLE DES MINES
DE PARIS

Collège doctoral

N° attribué par la bibliothèque
/_/_/_/_/_/_/_/_/_/_/

THESE

pour obtenir le grade de
Docteur de l'Ecole Nationale Supérieure des Mines de Paris
Spécialité Sciences et Génie des Matériaux

présentée et soutenue publiquement par

Stéphanie GRAFF

le 13 Octobre 2006

Viscoplastic behavior of zirconium alloys in the temperatures range $20°C$–$400°C$: characterization and modeling of strain ageing phenomena

Directeurs de thèse : ***Samuel FOREST***
Jean–Loup STRUDEL

Jury

M. Bouaziz	Rapporteur	Arcelor research
M. Lemaignan	Rapporteur	CEA
M. Benallal	Examinateur	Ecole Normale Supérieure de Cachan
M. Béchade	Examinateur	CEA
M. Neuhäuser	Examinateur	University of Braunschweig
M. Forest	Examinateur	Ecole des Mines de Paris
M. Prioul	Invité	Ecole Centrale de Paris
M. Strudel	Invité	Ecole des Mines de Paris

Centre des Matériaux P.M. FOURT de l'Ecole des Mines de Paris,
B.P. 87, 91003 EVRY Cedex

”L’important est de ne jamais désespérer”

Alan Parker: Midnight Express

Acknowledgements

This thesis, which would not be possible without the financial support from the SMIRN (Simulation des Métaux et Installations des Réacteurs Nucléaires) owes its existence to the help, support and inspiration of many people. In the first place, I would like to express my sincere appreciation and heartily gratitude to my main thesis supervisor, Professor Samuel Forest for initiating me to finite element method, for his guidance and encouragement during the more than three years of this thesis's work and for his endless availability for any question I felt the need to discuss with him. His uncompromising quest for excellence significantly shapes everyone at Centre des Matériaux. I would like also to address my thanks to Claude Prioul for his endless support, Jean-Luc Béchade for welcoming me into the "zirconium world" and Jean-Loup Strudel for his fruitful discussions on dislocations. I am also honoured to thank to the jury members of this thesis: Oliver Bouaziz, Clément Lemaignan, Ahmed Benallal, Jean-Luc Béchade, Harmut Neuhäuser, Samuel Forest, Claude Prioul and Jean-Loup Strudel for the examination of this dissertation.

The discussions and cooperation with all of my colleagues have contributed substantially to this work: Sandrine Pallu for her valuable advices on relaxation tests, Hanno Dierke and Professor Neuhäuser for their kindly collaboration in the frame of the European project EU-RTN-DEFINO (University of Kaiserslautern Germany 24/11/2004–26/11/2004), Franck N'Guyen for his help during calculations and Odile Adam for his advices and support on the bibliography part. I am as well very grateful to all members of the "Salle de Calcul" at Centre des Matériaux for the cooperative spirit and the excellent working atmosphere, especially to Grégory Sainte Luce for helping me with my computational problems. I also extend my appreciation to all staff members of the "Atelier" at Centre des Matériaux for their support.

Finally, I owe special gratitude to my family, especially my mother and my father for continuous and unconditional encouragement during all the time and my best friends Mylène Canivet and Caroline Gourdin. The warmest thanks also go to Franck Bluzat for his neverending enthusiasm during this work and his kindness...

Abstract

The anomalous strain rate sensitivity of zirconium alloys over the temperatures range $20°C$–$600°C$ has been widely reported in the literature. This unconventional behavior is related to the existence of strain ageing phenomenon which results from the combined action of thermally activated diffusion of foreign atoms to and along dislocation cores and the long range of dislocations interactions. The important role of interstitial and substitutional atoms in zirconium alloys, responsible for strain ageing and the lack of information about the domain where strain ageing is active have not been yet adequately characterized because of the multiplicity of alloying elements and chemical impurities.
The aim of this work is to characterize experimentally the range of temperatures and strain rates where strain ageing is active on the macroscopic and mesoscopic scales. We propose also a predictive approach of the strain ageing effects, using the macroscopic strain ageing model suggested by McCormick (McCormick, 1988; Zhang et al., 2000).
Specific zirconium alloys were elaborated starting from a crystal bar of zirconium with 2.2 wt% hafnium and very low oxygen content (80 wt ppm), called ZrHf. Another substitutional atom was added to the solid solution under the form of 1 wt% niobium. Some zirconium alloys were doped with oxygen, others were not. All of them were characterized by various mechanical tests (standard tensile tests, tensile tests with strain rate changes, relaxation tests with unloading). The experimental results were compared with those for the standard oxygen doped zirconium alloy (1300 wt ppm) studied by Pujol (Pujol, 1994) and called Zr702. The following experimental evidences of the age–hardening phenomena were collected and then modeled:

- low and/or negative strain rate sensitivity around $200°C$–$300°C$,
- creep arrest at $200°C$,
- relaxation arrest at $200°C$ and $300°C$,
- plastic strain heterogeneities observed in laser extensometry on the millimeter scale.

Relaxation experiments give information about deformation mechanisms. At lower plastic strain rates, the macroscopic response is associated with the dragging mode (higher temperatures) and at higher plastic strain rates, the macroscopic response is associated with the friction mode (lower temperatures). Between these two limiting modes, the behavior is unstable. For Zr702, the change in the deformation mechanism was observed between $200°C$ and $400°C$. The apparent activation volumes associated with friction and dragging modes are almost the same for Zr702, close to 0.7 $nm^3.atom^{-1}$. By reconstruction of the entire relaxation curve at the temperature peak of $300°C$ for strain ageing, an estimated "drag stress" of about 250 MPa was determined for Zr702 (1300 wt ppm oxygen). For ZrHf, the dragging mechanism was observed for lower temperatures close to $300°C$. The apparent activation volumes are close to 2 $nm^3.atom^{-1}$ for the friction mode and 1 $nm^3.atom^{-1}$ for the dragging mode. For this alloy which contains only about 80 wt ppm of oxygen, the "drag stress" was estimated at about 130 MPa. These relaxation tests provided also evidence that strong internal stresses develop in the tested specimens for both alloys.
The macroscopic strain ageing model was implemented in a finite element code. An internal variable, characterizing a global ageing time of the material and associated with a non–linearity of the constitutive equations allows to simulate plastic strain (rate) localization under the form of bands extending across the width of the sample. The material parameters were identified for Zr702. A reliable prediction of the strain ageing phenomena observed experimentally can be ensured with this model. The development of strain heterogeneous fields observed by laser scanning extensometry may be also predicted by the model.

Contents

General introduction

In the core of a nuclear reactor, the cladding tubes retain the fissile material. They prevent nuclear material from leaking into the coolant as the first safety wall of a nuclear fuel of the Pressurized Water Reactors (PWR) in France. Zirconium alloys such as Zircaloy have been used since the 1960's as the material because they meet the criteria of the resistance to an irradiation and corrosion in the reactor core system and have a small cross section for neutron absorption. The current challenge in the French industry of nuclear energy is to increase PWR fuel performance at burn-ups beyond 65 GWd/t in a more demanding operating environment. In this scope, a program was performed to develop superior cladding and guide–tube materials. New zirconium alloys were produced by AREVA NP and its partners: quaternary materials (Zr, Sn, Fe and V), (Zr, Sn, Fe and Nb) and ternary materials (Zr, Nb, O).
The viscosity of nuclear zirconium alloys such as Zircaloy–4 evolves in an "unconventional" way within the temperatures range $20°C$–$600°C$, covering the operating temperatures in PWR. Especially the outer temperature of the fuel rod is about $350°C$. Moreover, such effects can be observed under certain conditions of strain rate (time) and chemical composition of the zirconium alloys (microstructure). Various studies in the 1970's years suggested that this "anomalous" behavior is related to microscopic strain ageing phenomena. The basic mechanisms of deformation are the coupling between diffusive processes of solute atoms and moving dislocations, and the long range dislocation interactions.
In dilute zirconium alloys, the most famous macroscopic effects due to strain ageing, reported in the literature are:

- Static Strain Ageing (SSA), corresponding to the existence of a "stress peak" and/or a Lüders plateau on the macroscopic tensile curve,
- Dynamic Strain Ageing (DSA), which is associated with the decrease of the Strain Rate Sensitivity (SRS) parameter which can tend to zero and/or negative values.

In particular, low and/or negative strain rate sensitivity can have a major impact on the mechanical properties such as the loss of ductility and elongation. Strain ageing can also induce strong effects on creep behavior. Drastic changes in creep properties such as sudden decrease in creep rate for temperatures covering the operating temperatures of PWR were observed by Pujol in transverse type 702 zirconium alloy, Zr702 (Pujol, 1994).
Consequently, the objectives of nuclear industry are on the one hand to better understand the microscopic strain ageing phenomena observed in various industrial zirconium alloys such as Zircaloy–4 and on the other hand to predict the macroscopic behavior of these alloys.
That is why, the present study was proposed in the framework of "Contrat de Programme de Recherche CEA–CNRS–EDF" called "Simulation des Métaux des Installations et Réacteurs Nucléaires" (CPR SMIRN), based on the viscoplastic behavior of zirconium alloys in the temperatures range $20°C$–$400°C$. One problem in materials mechanics is to use an appropriate scale: macroscopic, mesoscopic or microscopic. The main objective of this thesis is to take a phenomenological approach based on experiments and modeling of strain ageing in dilute zirconium alloys. We chose to describe plasticity not on the microscopic scale but examining the results of macroscopic mechanical tests and field measurements (millimeter scale), in order to suggest constitutive laws taking strain ageing phenomena into account. Anomalous behavior observed in the studied zirconium alloys can also be described by these laws. The manuscript is divided into four parts, which are introduced as follows.

Part A introduces the most reliable findings of the current state of knowledge about microscopic strain ageing phenomena and their macroscopic effects observed in various dilute zirconium alloys. The bibliography review is used to specify the experimental and numerical aspects of this research work. The existence of strain ageing phenomena has not been yet adequately characterized because of the multiplicity of alloying elements and chemical compositions in zirconium alloys. Furthermore, a lack of information about creep and relaxation behavior was evidenced, for instance while during operating conditions in PWR, the fuel rod is kept under creep conditions at about $350°C$. Besides, no constitutive modeling of strain ageing effects in zirconium alloys has been proposed, although various models taking the physical mechanisms of strain ageing phenomena into account have been suggested in the bibliography for other materials such as aluminium alloys. Indeed, the Portevin–Le Chatelier (PLC) effect and the negative strain rate sensitivity can be simulated in aluminium alloys using either the Kubin–Estrin's model (Kubin and Estrin, 1985) or the McCormick's model (McCormick, 1988).

In part B, we show experimental evidence of strain ageing phenomena in the chosen zirconium alloys for various loading conditions. The major aim of this part is to better characterize the range of temperatures and strain rates where strain ageing phenomena are active on the macroscopic scale. The mechanical tests were carried out at Centre des Matériaux/Ecole Nationale Supérieure des Mines de Paris (ENSMP), in addition to microstructural characterization of the materials at "Service des Recherches Métallurgiques Appliquées" at CEA Saclay. In particular, this part focuses on two main points. First, the impact of interstitial and substitutional atoms on strain ageing effects is studied by comparing specific zirconium alloys. For this, five zirconium alloys were elaborated starting from a zirconium crystal bar with 2.2 wt% hafnium and very low oxygen content (80 wt ppm), called ZrHf. Another substitutional atom was added to the solid solution under the form of 1 wt% niobium. One set of zirconium alloys was doped with oxygen, the other one was not. These zirconium alloys were compared to a standard zirconium alloy, Zr702, studied by Pujol (Pujol, 1994). Secondly, many mechanical experiments permitted to better characterize these five zirconium alloys. Tensile tests were carried out at various applied strain rates and temperatures. From tensile tests carried out with strain rate changes, the values of SRS at various temperatures between $20°C$ and $400°C$ can be measured. However, both mechanical tests are limited. Indeed they do not show experimental evidence of deformation mechanisms because the investigated strain rates range is too narrow. Two alternative strengthening mechanisms are possible in a material exhibiting strain ageing effects: hardening by solute drag force exerted on moving dislocations and the usual strain hardening mechanism associated with an increase in the dislocation density. That is why, repeated relaxation tests at constant temperature, including unloading sequences before reloading were carried out in order to investigate wide ranges of strain rates in the entire temperatures domain explored. The main deformation mechanisms for Zr702 and ZrHf are identified. The interpretation is mainly based on the determination of the apparent activation volumes detected at constant temperature and constant microstructure. Each well–defined activation volume is associated with one deformation mechanism. The evolution of these deformation mechanisms is then studied as a function of temperature, stress and strain rate for both zirconium alloys.

The basic mechanisms of deformation associated with strain ageing phenomena lead to spatio–temporal plastic instabilities. In the literature review, two main types of plastic instabilities are extensively recalled. The Lüders phenomenon is characterized by a continuous propagation of a strain band front moving along the entire specimen only once and at a nearly constant velocity. This macroscopic effect can be mainly observed in mild steels (Lomer, 1952; Butler, 1962). The other plastic instability is the Portevin–Le Chatelier (PLC) effect which is characterized by plastic strain heterogeneity concentrated within a spatially limited region denoted as the PLC bands. Such bands can nucleate and vanish periodically or erratically and sweep across the same region of the sample several times. Three different types of band propagation were studied in particular in aluminium alloys (Estrin and Kubin, 1989; Klose et al., 2003a), labelled types A, B and C. Consequently, in part C, we checked whether strain ageing phenomena lead to strain heterogeneities on the mesoscopic scale in Zr702 and ZrHf. We chose the experimental method of laser scanning extensometry which seems to be an appropriate method, permitting to detect and characterize strain heterogeneities on the millimeter scale such as the Lüders bands and the PLC effect (Casarotto et al., 2003). These experiments were carried out at the University of Braunschweig in the European network of DEFINO RTN (DEformation and Fracture Instabilities in NOvel materials Research Training Network). After validating the experimental set up by testing standard alloys such as a mild steel and aluminium alloys, fields of local strain were measured for both zirconium alloys at various temperatures $20°C$, $100°C$ and $250°C$. Then, the type of strain heterogeneities detected in zirconium alloys were compared to the case of the more standard alloys.

Finally, the aim of part D is to present a predictive approach of the strain ageing effects observed in dilute zirconium alloys in the temperatures range $20°C$–$400°C$, using a macroscopic model based on negative strain rate sensitivity. For this purpose, we compared various constitutive models taking PLC effect into account, suggested in the literature. We retained two main models. The phenomenological constitutive model suggested by Penning and improved by Kubin–Estrin (Penning, 1972; Kubin and Estrin, 1985) which introduces the evolutionary behavior of the coupled densities of mobile and forest dislocations. The second model is a constitutive model suggested by McCormick (McCormick, 1988) which introduces a local solute concentration at moving dislocations temporarily arrested by forest dislocations. We chose to use the macroscopic strain ageing model suggested by McCormick (McCormick, 1988) and used by Zhang and McCormick (Zhang et al., 2000) in finite elements simulations. Before applying this model to zirconium alloys, we tested the possibilities and limitations of this model, based on a parametric study. Then we simulated the deformation of notched and CT specimens in tension. Specific sets of parameters were determined for standard alloys such as a mild steel and aluminium alloys. This study is based on the finite element code ZEBULON, developed by ENSMP. Experiments carried out especially at Ecole Centrale de Paris and simulations were compared. Then we present a predictive approach of the strain ageing effects observed in zirconium alloys especially in Zr702, based on low and/or negative strain rate sensitivity, creep arrest and other macroscopic effects observed during our experiments. For this purpose, the parameters of the model were identified using the parametric study and the experimental characterization in the temperatures range $100°C$–$300°C$ and strain rates range $10^{-5}s^{-1}$–$10^{-3}s^{-1}$ where strain ageing is active. Afterwards, comparisons between simulations of a flat tensile specimen and experiments were presented, based on the development of heterogeneous plastic strain fields.

Chemical compositions of various zirconium alloys used in nuclear industry

Name	Zircaloy-2	Zircaloy-4	Zr–Nb	M5	Zr–1%Nb	Zr702
Reference					1	2
Alloying elements (%wt)						
Sn	1.2–1.7	1.2–1.7				0.2280
Fe	0.07–0.02	0.18–0.24				0.076
Cr	0.05–0.15	0.07–0.13				0.024
Ni	0.03–0.08					0.005
Nb			2.4–2.8	0.81–1.2		
O	0.011–0.14	0.011–0.14	0.09–0.93	0.09–0.149	1.07	0.13
Impurities (ppm max)						
Al	75	75	75		30	
B	0.5	0.5	0.5			
Cd	0.5	0.5	0.5			
C	270	270	270			58
Cr			200		80	
Co	20	20	20		19	
Cu	50	50	50		32	
Hf	100	100	100		400	
Hf	25	25	25			
Fe			1500		360	760
Mg	20	20	20			
Mn	50	50	50		23	
Mo	50	50	50		56	
Ni		70	70		30	50
N	65	65	65		12	33
Si	120	120	120		51	
Sn			50		8	
Ti	50	50	50		26	
U	3.5	3.5	3.5			
W	100	100	100		25	

1 : (Thorpe and Smith, 1978b)
2 : (Pujol, 1994)

Part A

Review of strain ageing phenomena in dilute zirconium alloys

Chapter -I-

Introduction

Abstract: The aim of this bibliography part is to give a synthetic view of the various strain ageing phenomena observed in dilute zirconium alloys in order to direct the experimental and numerical aspects of this work over the temperatures range $20°C$–$400°C$. Attention is focused on the main points:

- the important role of interstitial and substitutional atoms,
- the appropriate parameters relative to strain ageing phenomena,
- the lack of information about creep and relaxation behavior.

In dilute zirconium alloys, "anomalous" mechanical behavior over the temperatures range $20°C$–$600°C$ has been reported in the literature. Two main effects can be directly observed, the Static Strain Ageing (SSA) and the Dynamic Strain Ageing (DSA).

- The SSA behavior corresponds to the existence of a "stress peak" and/or a Lüders extension on the macroscopic tensile stress versus strain curve. We call "stress peak", the existence of a maximum stress followed by a sharp softening, which is a characteristic of the Lüders behavior. The value of the stress peak is denoted $\Delta\sigma$. The SSA mechanical test consists in straining the specimen into the plastic region at constant strain rate, then interrupting the loading experience at the prescribed stress level or plastic strain level, waiting for a given interval of time (called τ_s), and at the end reloading. After yielding, the work–hardening of the specimen is observed. This cycle is repeated at different increasing plastic strain levels. The SSA effect is measured by the parameter $\Delta\sigma$ at constant temperature, applied strain rate and microstructure. Consequently, this type of effect appears after an initial plastic deformation and is observed when the material is aged and deformed again.

- The DSA behavior is associated with the decrease of the Strain Rate Sensitivity parameter (SRS) which can tend to zero and/or negative values. Tensile tests carried out at different applied strain rates or strain rate jumps at constant temperature and constant microstructure allow to obtain the SRS parameter, defined as follows:

$$SRS = \left(\frac{\partial\sigma}{\partial \log \dot{\varepsilon}_p}\right)_{T,\varepsilon_p} = \frac{k_B T}{V_a} \tag{I.1}$$

where V_a is the apparent activation volume. A negative strain rate sensitivity leads to the Portevin–Le Chatelier (PLC) effect which can be observed by the presence of stress drops, called also serrations on the macroscopic stress versus strain curve during plastic deformation. Consequently, this type of effect is observed during plastic deformation.

SSA and DSA effects are linked, observed under certain conditions of temperature, strain rate (time) and chemical composition of the tested materials. The basic mechanism of deformation is the coupling between diffusive processes of solute atoms and moving dislocation, and long range dislocation interactions. This microscopic phenomenon is also commonly called "strain ageing". The SSA behavior is attributed to the pinning of mobile dislocations, created during previous straining into the plastic region, by diffusion of some solute atoms during the ageing time, τ_s. The DSA effects are connected with dynamic interactions between mobile dislocations during on–going plastic deformation.
The relationship between SSA and DSA is a consequence of the time/temperature equivalence associated with the thermally activated processes. Consequently, these mechanisms are linked to laws of solute atoms diffusion, described by the Arrhenius equation. For SSA, the deformed material exhibits some initial concentration of solute atoms. The ageing time, τ_s or the dislocation pinning is generally so long that unpinning of dislocation is irreversible on the time scale of tensile test (the impurities can diffuse around dislocations, leading to their anchoring). The fact that dislocations can move during the next straining is perturbed by this anchoring, thus leading to the changes of mechanical properties and plastic deformation such as the Lüders extension. This phenomenon can be observed at lower temperatures than for DSA for which the strain rate or the stress rate is imposed. That is why the observation of DSA effects is on the one hand reduced to a limited temperatures range and on the other hand to a limited strain rates range, depending on the mobility of diffusive solute atoms during straining. The perturbations are due to the fact that the diffusion rate of solute atoms is in the same range than this of the glide dislocations. The competition of the mobilities between dislocations and solute atoms leads to successive anchoring–unanchoring of dislocations, associated with some changes of mechanical properties and plastic deformation, called the PLC effect. Note that in the literature, this effect is observed in some ranges of temperatures and strain rates for which negative strain rate sensitivity is observed. Consequently the coupling between strain ageing and plastic deformation depends on plastic strain (the microstructure), strain rate and temperature. Moreover, a material can be sensitive to DSA without exhibiting PLC effect.

These microscopic effects occur at intermediate temperatures (0.3 T_f) in the b.c.c. and c.f.c. metals but also in the h.c.p. metals, strengthened by interstitial and substitutional atoms in solid solution. They are also connected to dislocations core spreading of screw dislocations in b.c.c. and h.c.p. metals.
In dilute zirconium alloys, strain ageing phenomena lead to various "unconventional" macroscopic stress–strain behaviors, for instance:

- Lüders phenomenon,
- plateau or maximum in the flow stress versus temperature diagram,
- minimum in the strain rate sensitivity versus temperature diagram,
- maximum in the apparent activation volume versus temperature diagram,
- minimum in ductility and elongation for increasing temperature.

Strain ageing phenomena can also induce strong effects on creep and relaxation behavior. These main points are developed in the following chapters of part A.

Chapter -II-

From microscopic mechanisms to macroscopic plastic instabilities in strain ageing alloys

Contents

Abstract: In this chapter, we first explain the general basic mechanisms of deformation associated with strain ageing phenomena, leading to spatio–temporal plastic instabilities. Then, we present some macroscopic features observed in typical strain ageing materials such as $Al - Mg$ alloys.

II.1 Microscopic mechanisms in strain ageing alloys

The motion of dislocations is inherently inhomogeneous in space and discontinuous in time, due to various local stresses along dislocation lines and thermally activated break away from different extrinsic obstacles. These obstacles can be the Peierls stress itself, the mutual intersection of dislocations on various glide planes (the interaction with immobile dislocations, for instance forest dislocations, and impurity atoms or their clusters). Even though the motion of single dislocations is locally inhomogeneous and discontinuous in time, macroscopic deformation, especially for pure metals develops homogeneously and stably except if observed

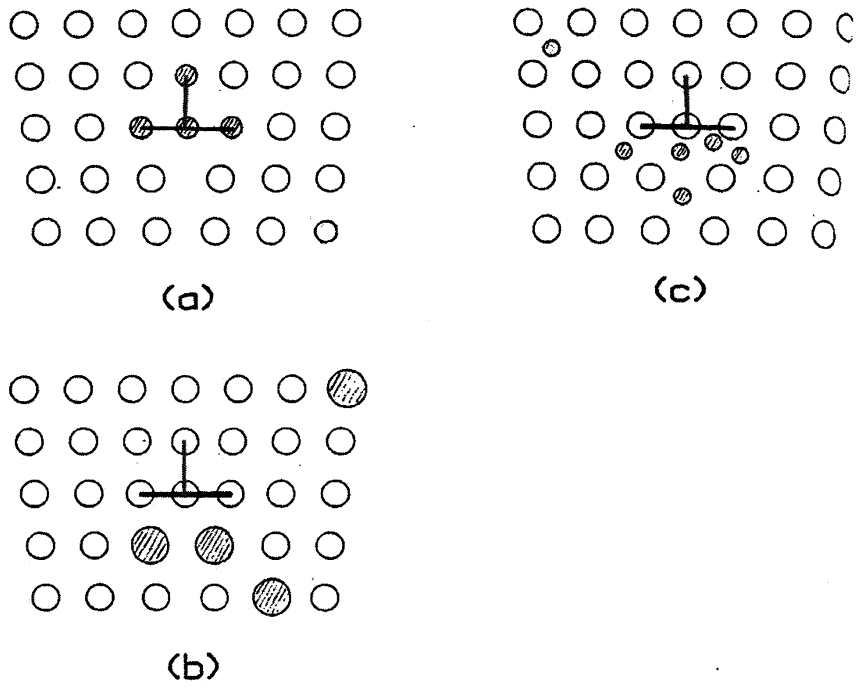

Figure II.1 : Cottrell cloud around a edge dislocation (Cottrell and Bilby, 1949).

with acuracy like strain field measurements (Neuhäuser, 1983) or infrared pyrometry (Ranc and Wagner, 2005). The most famous unstable behavior is the PLC effect, discovered in the 20^{th} century. For a comprehensive description of the PLC effect in metals, it is necessary to start with the basics of plastic deformation. The literature is extensive (Friedel, 1964; Schoeck, 1980; Hirth and Lothe, 1982; Haasen, 1983; Hull and Bacon, 1984). It is generally accepted that the existence of strain ageing is one of the necessary conditions for the occurrence of certain type of plastic instabilities which appears in macroscopic measurements. According to Cottrell, strain ageing results from the interaction between the viscous glide of dislocations and foreign atoms with a drift velocity of the order of magnitude of the dislocations velocity (Cottrell, 1948; Cottrell and Bilby, 1949; Cottrell, 1953; Nabarro, 1947). The idea of strain ageing was further developed in (Louat, 1956; Sleeswyk, 1958; Friedel, 1964; McCormick, 1972; van den Beukel, 1975a; Mulford and Kocks, 1979; van den Beukel, 1980; Louat, 1981; Schwarz, 1982; Schwarz, 1974; Schwarz, 1985b; Schwarz, 1985a; McCormick, 1986; McCormick, 1988; Estrin et al., 1993; Springer, 1998). Note that the list of references is not exhaustive, that is why in chapter VIII, we discuss more precisely about the microscopic mechanisms of strain ageing. This classical theory of DSA due to interstitial atoms and dislocations interactions depends on long range diffusion of solute atoms towards dislocations. Generally, one calls the "Cottrell cloud", the development by bulk diffusion of solute atoms around edge dislocations. This organization is non local. Consequently, the local concentration of solute atoms around dislocations increases as shown in figure II.1. Interstitial and substitutional atoms can diffuse in volume around the edge dislocations. The solute atoms having a size inferior to those of the lattice can diffuse to the compressive part of the stress field of dislocations (see figure II.1 (a)). The substitutional atoms with diameter superior to those of the lattice can diffuse to the tensile zone of the stress field of dislocations (see figure II.1 (b)). This is also the case for interstitial atoms (see figure II.1 (c)).

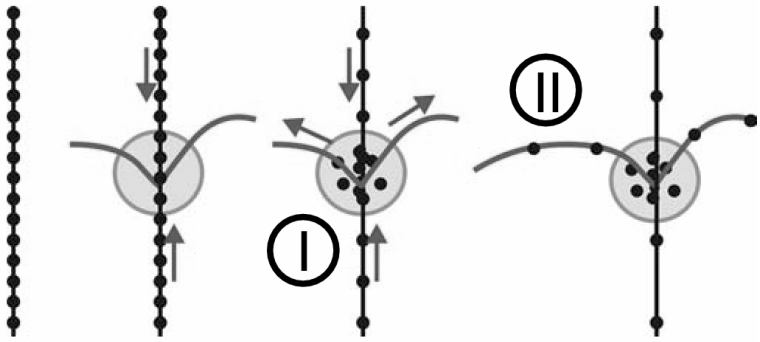

Figure II.2 : Scheme of the diffusion processes within the scope of strain ageing illustrating the intersection strengthening (I) (Mulford and Kocks, 1979) and the line strengthening (II) mechanism (van den Beukel, 1980) respectively. The straight lines represent immobile dislocations (for instance forest dislocations) intersected by a bowed mobile dislocation (Klose et al., 2003a).

Contrary to the Cottrell's view, the motion of dislocations is basically discontinuous even in the absence of strain ageing. Tabata et al. (Tabata et al., 1980) observed this discontinuous motion of dislocations by Transmission Electron Microscopy (TEM) during in situ deformation of $Al - Mg$ single crystals. It must be noted that on the microscopic scale of single dislocations, most of the strain ageing phenomena occur as static strain ageing of stationary dislocations. The influence of strain ageing leads to a preferential activation of slightly "aged dislocations" that mainly carry the plastic strain rate. In today's view, strain ageing is a necessary but not sufficient condition to observe "non conventional" macroscopic behavior. Indeed a synchronization of dislocations is required. They "communicate" with each other by means of their long range stress fields. The result is a correlated motion and generation of dislocation avalanches (Korbel et al., 1976; Hähner, 1993; Hähner, 1996a; Hähner, 1996b; Hähner, 1996c; Hähner, 1997). Contrary to the classical Cottrell's theory, this mechanism of fast dislocations locking depends on short range diffusion, associated with high diffusion coefficients of solute atoms to dislocations. Two interpretations were suggested:

- the first interpretation suggested by Sleeswijk (Sleeswyk, 1958), then by Cuddy and Leslie (Cuddy and Leslie, 1972) and Mulford and Kocks (Mulford and Kocks, 1979) is based on the enhanced diffusion of foreign atoms along the distorted lattice around the dislocation lines and cores. This type of diffusion is called the "pipe diffusion" mechanism. Two ageing mechanisms have to be distinguished: (I) an intersection strengthening mechanism at lower temperatures and higher stresses (Mulford and Kocks, 1979), (II) a line strengthening mechanism at higher temperatures (van den Beukel, 1975a). Figure II.2 shows these two different diffusion processes within the scope of strain ageing. Hence the exhaustion of mechanism (I) is enhanced when foreign atoms migrate from the intersection points along the dislocation lines. Mechanism (II) becomes sufficiently dominant only at elevated temperatures,

- the second interpretation suggested by Schoeck and Seeger (Schoeck, 1956; Schoeck and Seeger, 1959) is based on the Snoek ordering (Snoek, 1941) of interstitial solute atom pairs in the stress field of dislocations as shown in figure II.3.

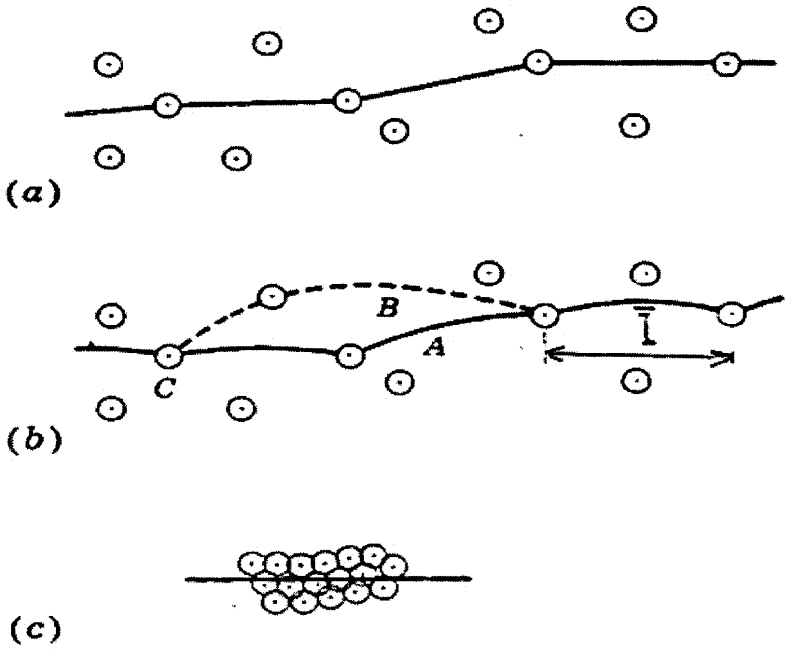

Figure II.3 : Interaction dislocation–solute atom: (a) diffusion of solute atoms atmosphere without applied stress, (b) diffusion of solute atoms atmosphere with applied stress, (c) concentration of solute atoms without applied stress (Snoek, 1941).

The Snoek's mechanism (Snoek, 1941) can explain the anelastic phenomena observed in the α iron–carbon solid solution. For instance, a single well defined internal friction peak, called the "Snoek peak", is observed due to the stress induced ordering of nitrogen and carbon interstitial atoms, occupying the octahedral interstices in b.c.c. α iron lattice. Snoek considered that without an applied force, the interstitial atoms fill the octahedral sites of the iron lattice at random (i.e. the centers of the faces and the edges of the b.c.c. lattice). As these sites are asymmetric, the interstitial atoms distort the lattice in an asymmetric manner. The application of a stress, parallel to one crystalline axis decreases the distorsion in this direction and favours also the jumps in the interstitial sites to other sites. Then Schoeck and Seeger developed the idea that an internal stress field associated with dislocations can also order the interstitial atoms. The new organization, decreasing the free enthalpy of the crystal leads to more stable dislocations. Consequently, the organization is local and the concentration of solute atoms around the dislocations does not increase as in the case of the Cottrell's model. The Snoek's mechanism is the base of the microscopic Friedel's model (Friedel, 1964). Thus, these dislocations are released from the solute atoms interaction. That is why, a stress peak can be observed on the macroscopic curve of a SSA mechanical tensile test.

To conclude, the strain ageing phenomena are the combined action of the thermally activated diffusion of foreign atoms ("Cottrell clouds" of mobile solute atoms) to and along the dislocation cores and the long range dislocations interactions. The result is an additional anchoring of the mobile dislocations when they are arrested during "ageing time".

Regarding the bibliography, we can define two types of ageing time, (1) the "macroscopic ageing time", related to the collective behavior of dislocations and microstructure changes and (2) the "microscopic ageing time", usually shorter than the macroscopic ageing time because the cell size is superior to the cell of all the structure:

- the "macroscopic ageing time" is the interval of time of a tensile test carried out at constant strain rate and constant temperature with interrupted loading, waiting for during a given interval of time and then reloading. Due to the external load, that enforces the multiplication and the motion of dislocations, strain ageing leads to stress peaks on the macroscopic stress versus strain curve after ageing times and reloading,
- the "microscopic ageing time" is the time that a dislocation spends at extrinsic obstacles such as the forest dislocations. Strain ageing phenomena leads to their repeated break away from mobile solute atoms. This physical model is introduced by isolated dislocations.

II.2 Macroscopic features of spatio–temporal plastic instabilities

II.2.1 Some generalities

Two types of instabilities are associated with strain ageing phenomena: the Lüders front and the PLC effect. Lüders front and PLC effect were observed in a variety of f.c.c. and b.c.c. substitutional and interstitial alloys in particular ranges of temperatures and strain rates, as well as in non–metal matrix such as silicon (Mahajan et al., 1979). Recently, PLC effect was observed in ordered intermetallics (Brzeski et al., 1993).

The Lüders front, in a tensile specimen, is a delineation between plastically deformed and undeformed material (Lomer, 1952). It appears at one end of the specimen and propagates with typically constant velocity, if the cross–head velocity is kept constant, towards the other end (Butler, 1962). The nominal stress versus strain curve appears flat during the propagation. However, the localization is preceded by yield point behavior. After reaching a peak, the flow stress quickly drops to a lower value. This effect was initially observed by Piobert (Piobert, 1842) in iron. Then in 1860, Lüders described this deformation bands, bended to about 45° of the tensile axis at the surface of middle steel specimen.
PLC effect denominates spatio–temporal instabilities during plastic deformation of solid solutions in a certain range of deformation rates, temperatures and predeformations. Initially in 1909, Le Chatelier (Chatelier, 1909) was the first to show this type of effect in middle steel between $80°C$ and $250°C$. Then Portevin and Le Chatelier studied the discontinuous plastic flow in tension of $Al - 4.8\%Cu$ at room temperature, between 1920 and 1923 (Portevin and Chatelier, 1923). Especially, spatial inhomogeneities denote localized rapid deformation in a limited part of the specimen's gauge length called the "PLC bands", while the bulk of the specimen is deforming very slowly. Indeed, a sequence of shear bands appearing sequentially with sometimes regular spacing, or a set of propagating bands with a source at one end of the specimen were observed (Chihab et al., 1987). Temporal instabilities occur as a succession of stress drops on the stress versus strain curve in strain rate controlled tests [1]. In stress rate controlled tests [2], the temporal instabilities arise as repeated strain bursts after an almost

[1] $\dot{\varepsilon} = constant$. The experimental condition is usually applied as a constant cross head velocity $\dot{l} = constant$ of the tensile or compression test machine.
[2] $\dot{\sigma} = constant$. This mode of deformation is usually applied through as a constant force rate.

elastic increase of stress (at lower temperatures and smaller stress rates). Hence a staircase like stress versus strain curve is obtained (Caisso, 1959). Two examples for the $Al-3\%Mg$ alloy at $20°C$, at strain and stress rate controlled deformation respectively at $\dot{\varepsilon} = 10^{-4}\ s^{-1}$ and $\dot{\sigma} = 0.2\ MPa^{-1}$ are given in figures II.4 (a), (b) (Dierke, 2005). Although the stiff machine used here is able to change its speed by a factor of 100 within about 50 ms, this is not sufficient to impose a perfectly constant stress rate control condition in the present case of plastic PLC instabilities. This can be recognized in the resulting staircase stress versus strain curve of figure II.4 (b). Apart from the serrated or the stepped shape, the work hardening is effectively compensating for the absence of drag stress in the active PLC bands. An other example of staircase stress versus strain curve is given in figure II.5 for the 316 type stainless steel steel at various temperatures.

Transition from Lüders front to PLC response, while changing temperature or strain rate was observed (Cottrell, 1953; Nadai, 1950; Brindley et al., 1962; Sleeswyk, 1958). At the beginning of the macroscopic stress versus strain curves obtained at constant strain rate, the plastic deformation often (for small grain sizes) starts with the Lüders band (see figure II.4 (a)). The stress drop at the beginning of plasticity corresponds to the initiation of the deformation band. Then the plateau is associated with the progressive propagation of the band in the whole specimen. Note that the tensile curve can exhibit an abrupt drop of stress, called the upper upper yield point, which is followed by an extended deformation at constant stress, called the lower yield point. This plateau shows some successive stress drops and corresponds to the Lüders band in the sample.

Regarding tensile tests carried out at constant strain rate, the PLC strain heterogeneity is concentrated within a spatially limited region denoted as the PLC band with the band width w_b. This band, mostly inclined at an angle of about 45° from the tensile axis according to the direction of maximum shear stress propagates along the specimen axis with the band velocity v_b. PLC effect has been investigated most extensively using strain rate controlled tensile tests. Three different types of deformation mode can characterize PLC effect. They are labeled type A, B and C bands (Brindley and Worthington, 1970; Wijler and van Westrum, 1971; Cuddy and Leslie, 1972; Pink and Grinberg, 1982; McCormick, 1986; Chihab, 1987). These various types of plastic heterogeneities are given as follows (see figure II.6):

- type A bands correspond to a continuous propagation of bands which usually nucleate near one of the specimen's grip and propagate with a nearly constant velocity and band width to the other end of the specimen. These bands sweep across the gauge length periodically. Such a plastic instability can mathematically be described as a solitary wave. The increase in strain is quite slow, and the fluctuations of load are moderate during propagation. Sometimes the nucleation starts within the specimen length, preferentially within the first stage of deformation. The external applied strain (rate) is mainly concentrated within the active width of the PLC band. The continuously moving type A bands are associated with a smooth rise of the local strain, resulting in a smooth global strain curve for each PLC band,

- type B PLC bands propagate discontinuously along the specimen, or more precisely, small strain bands nucleate in the nearest surroundings of the former band. The average velocity is significantly reduced in comparison with type A bands. After nearly elastic loading, the stress abruptly drops down due to a very rapid local plastic deformation ($\dot{\varepsilon}_{loc} > \dot{\varepsilon}_{ext}$). The associated saw–tooth like load serrations become more and more periodic with increasing strain (Schwarz, 1985b),

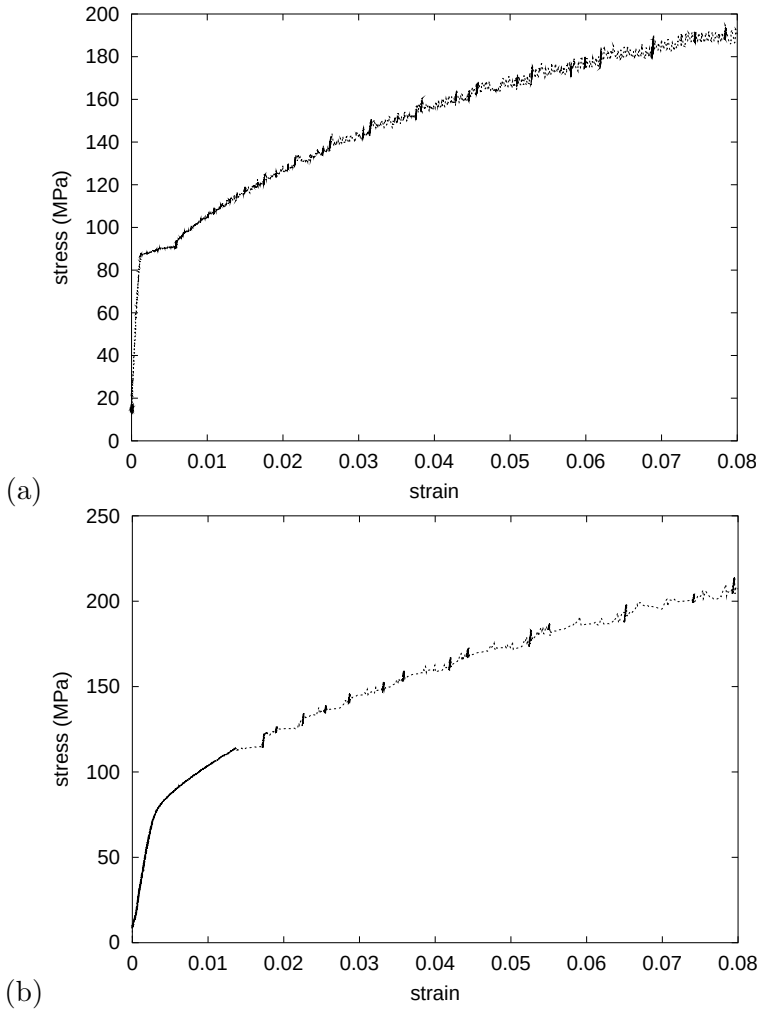

Figure II.4 : Macroscopic stress versus strain curves for the deformation of $Al-3\%Mg$ alloy at $20°C$ in (a) a strain rate controlled mode with $\dot{\varepsilon} = 10^{-4}\ s^{-1}$ and (b) a stress rate controlled mode with $\dot{\sigma} = 0.2\ MPa^{-1}$. The serrated yielding in the strain rate controlled mode is replaced by strain bursts in a staircase shaped deformation curve in stress rate controlled mode (long term elastic loading periods without plastic deformation are interrupted by sudden strain bursts, the "PLC events") (Dierke, 2005).

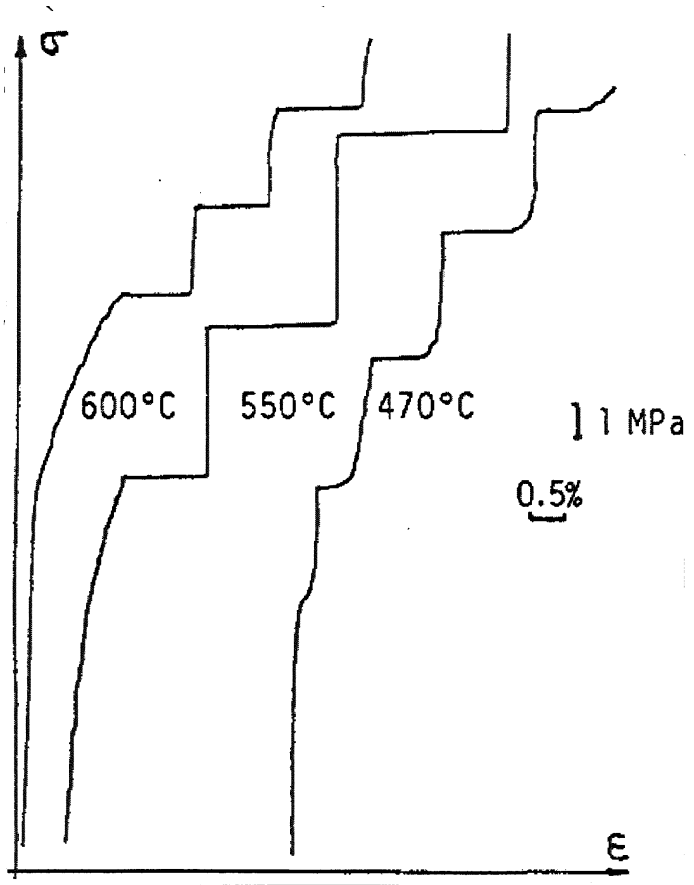

Figure II.5 : Stress versus strain curves on a soft tensile machine again the PLC region for 316 type stainless steel (Blanc, 1987).

- type C bands are characterized by a spatially random nucleation of bands with limited subsequent propagation accompanied by strong, high frequency and chaotic load drops. The load frequently drops from the upper level of flow stress reached at the onset of the stress versus strain curve.

Figure II.6 (a) shows the serrations of type A, B, C (Lacombe, 1985). Figure II.6 (b) displays various serrations, observed for a Cu–In alloy as a function of temperature (Lacombe, 1985).

Strain ageing phenomena may affect manufacturing processes, as well as the fracture properties of a material. Delafosse (Delafosse et al., 1993) found that DSA affects the fracture resistance of Al–Li alloy. Their tests, in the range of temperatures and strain rates where DSA is active, showed localization in the form of PLC bands near the crack tip, high temperatures and loading rate dependence of the tearing modulus.

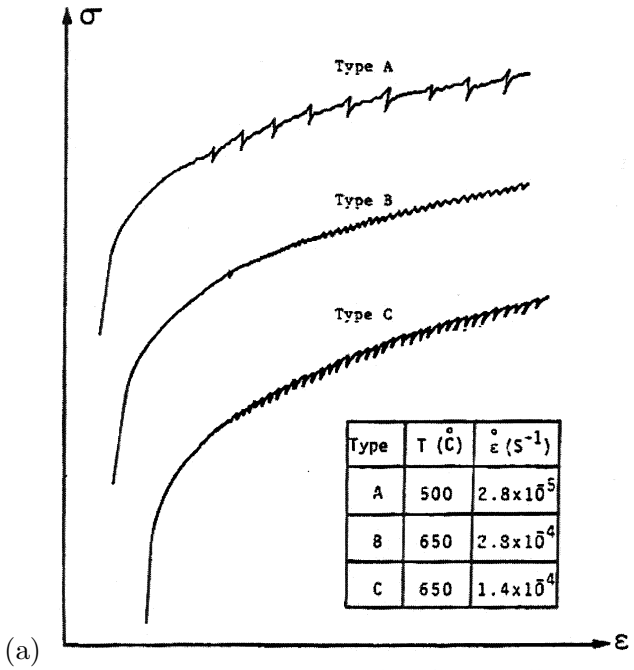

(a)

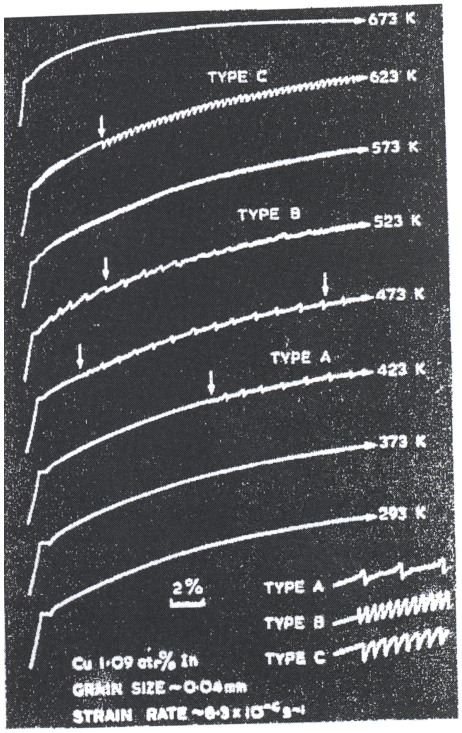

(b)

Figure II.6 : (a) Serrations of type A, B, C in the stress versus strain diagram for the 316L steel (Karimi, 1981); (b) Various serrations, observed for a Cu–In alloy as a function of temperature (Lacombe, 1985).

II.2.2 Comparison between Portevin–Le Chatelier effect and Lüders phenomenon

These types of spatio–temporal plastic instability can be distinguished, based on a temporal criterion (Estrin and Kubin, 1995) and a spatial criterion (Rauch and G'sell, 1989). The homogeneous plastic strain becomes unstable in some parts of the sample and the strain gradient increases in one direction of the band as the following conditions:

- $h < \sigma$ and $SRS > 0$, the instability is type h, associated with Lüders phenomenon,
- $h > \sigma$ and $SRS < 0$, the instability is type S, associated with PLC effect,

where h is the hardening rate and SRS is the Strain Rate Sensitivity parameter, defined by:

$$h = (\frac{\Delta\sigma}{\Delta\varepsilon_p})_{T,\dot{\varepsilon}_p} \qquad ; \qquad SRS = (\frac{\Delta\sigma}{\Delta \log \dot{\varepsilon}_p})_{T,\varepsilon_p} \tag{II.1}$$

According to Ziegenbein et al. (Ziegenbein, 2000), the propagation velocity of the Lüders band is significantly smaller than that of the PLC bands because of the high strain concentration within the Lüders band.
The PLC effect is thermally activated. This effect depends on the type of the tensile machine, temperature, chemical composition, microstructure and strain level. The Lüders behavior is not thermally activated but depends on the grain size.
PLC effect is due to the propagation of successive bands which can spread in the whole specimen, being able to reflect themselves at the ends of the sample. The Lüders bands can initiate at any point of the sample, often in many points. They cross over the whole sample just one time. Lüders bands belong to a strain softening phenomena, contrary to the strain rate softening type of PLC bands (Kubin and Estrin, 1984).
With a soft machine, the flow stress is constant during the propagation of the Lüders band. However, the flow stress increases during PLC deformation.

In mild steels, PLC effect appears at high temperature, and it is not obvious to observe these localized bands because of the furnace. Contrary to PLC effect, at room temperature it is easier to observe the Lüders band, by using a low–angled light. Some techniques are used to observe both phenomena, but it is not so easy when the experimental set up is used at high temperatures. For instance, extensometric micro–grids were carried out on sample in Al–Li alloy by Delafosse (Delafosse et al., 1993). A network of parallel lines by lithography was put on the sample. Tests were carried out in–situ in order to follow the evolution of the grids by microscopy. An other technique is the infrared pyrometry. The overheating associated with the plastic deformation was observed by Ranc in Al–Cu alloy (Ranc and Wagner, 2005; Louche and Chrysochoos, 2001). Especially, the front of PLC bands and their displacement were observed when the variations of temperature were reproduced, as shown in figure II.7.

(a)

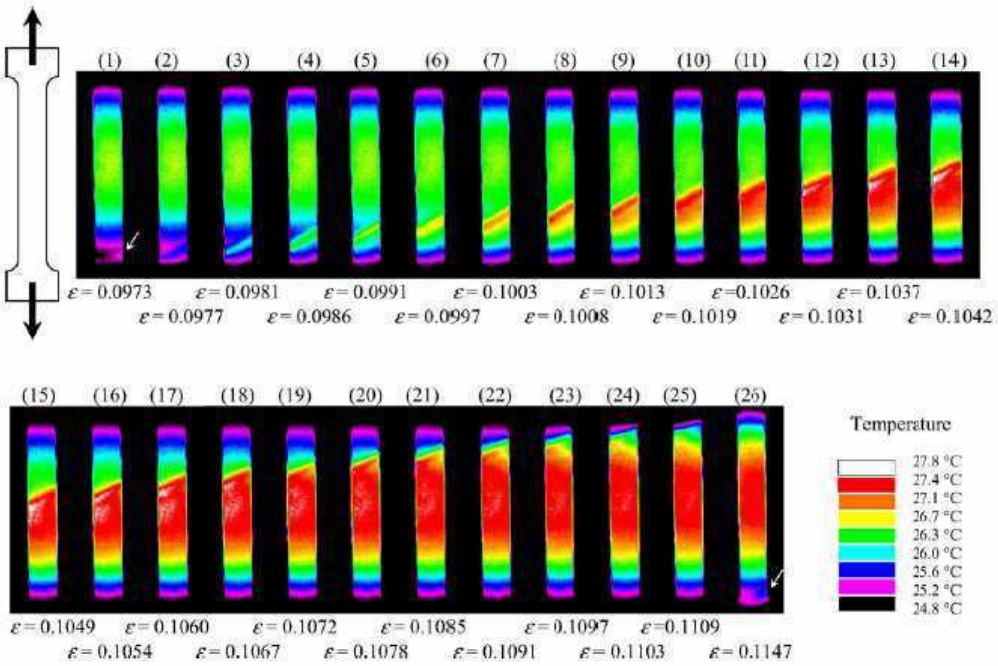

(b)

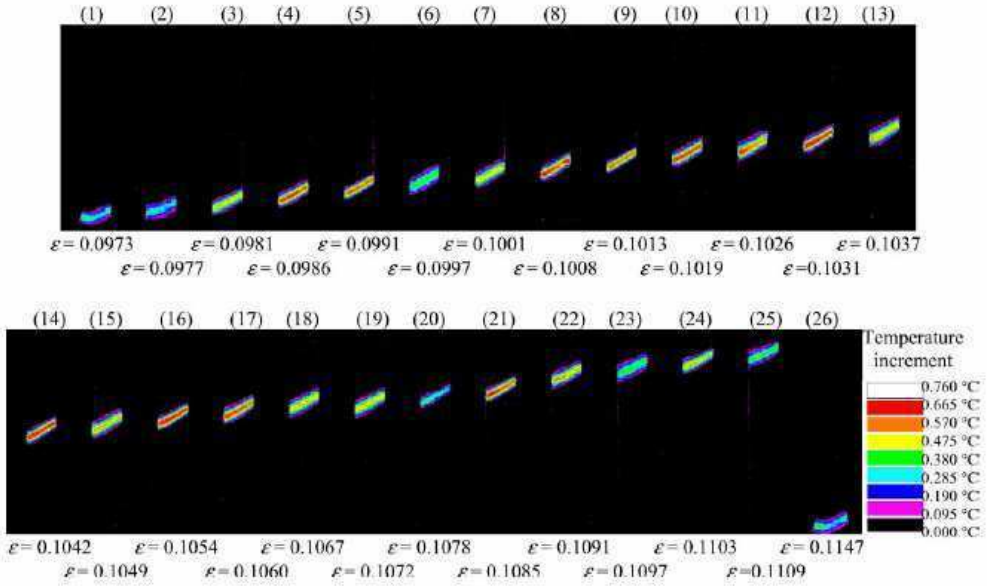

Figure II.7 : Observation of the PLC bands by infrared pyrometry in 4% copper–aluminium alloy : (a) thermographs of tensile specimen, (b) temperature increment during the occurrence of PLC bands (Ranc and Wagner, 2005).

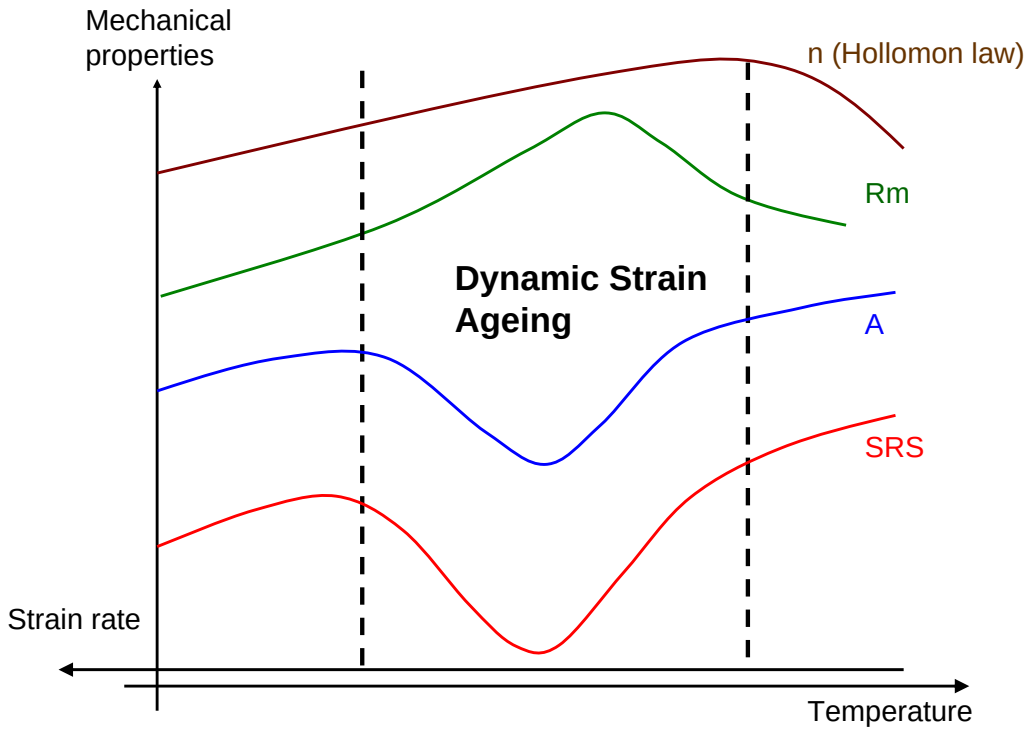

Figure II.8 : Schematic evolution of the tensile mechanical properties due to dynamic strain ageing.

II.2.3 Consequences on mechanical properties

In addition to plastic strain heterogeneities, strain ageing phenomena lead to various changes of mechanical properties in tension. The influence of DSA on the tensile mechanical properties is shown in a synthetic view in figure II.8. When the temperature increases, these effects are characterized by:

- the increase of yield stress (σ_0 and $\sigma_{0.2\%}$ and the mechanical strength R_m),
- the increase of yielding rate (the parameter n of the Hollomon law $\sigma = K\varepsilon^n$),
- the decrease of SRS,
- the decrease of ductility (A), and necking parameter (Z).

When referring to simple models describing the local modes of plasticity versus strain rate as nonlinear, some authors suggested (Estrin and Kubin, 1988; Kubin and Estrin, 1989a) to plot the various means of the existence of the DSA phenomena in a temperature versus strain rate diagram (see figure II.9). Stress peak for instance can be observed in the largest domain described in figure II.9 in connection with SRS values going down to a minimum in the center of the domain. Crossing this domain at constant temperature (2 in figure II.9) or constant strain rate (4 in figure II.9), the minimum value of SRS will remain positive. On the other hand, in a restricted domain located at the center of the previous one (1 and 3 in figure II.9), the SRS curves will go through negative values around their minimal values. A purely theoretical approach will lead to conclude that PLC serrations can only be observed under the condition that SRS is negative (Kubin and Estrin, 1991b).

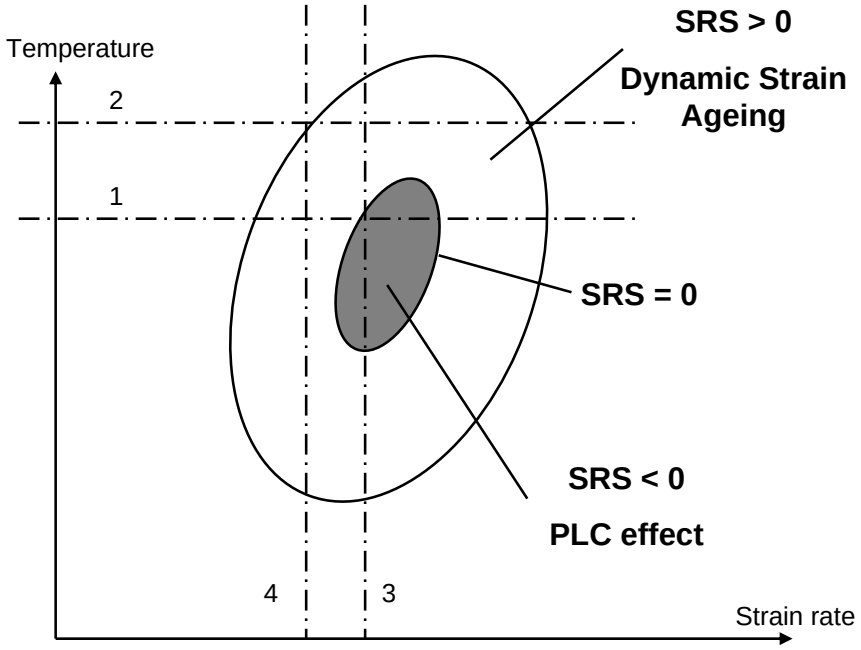

Figure II.9 : Dynamic strain ageing (DSA) and Portevin–Le Chatelier (PLC) domains associated with the strain rate sensitivity (SRS).

Experimentally, it was reported in the literature that the PLC domain is probably wider, since the so–called instantaneous strain rate sensitivity must be distinguished from the relaxed strain rate sensitivity as pointed out by McCormick (McCormick, 1988). Similar observations were reported by Blanc (Blanc, 1987) in 316 stainless steel around $600°C$ (low positive values of the strain rate sensitivity associated with PLC serrations on the macroscopic curve) and by Korbel (Korbel et al., 1976; Korbel et al., 1979) in Cu–Zn alloys. This point which relates to the internal microstructure of the specimen and the change of scale from microplasticity to macroplasticity will be further explored and discussed in this work.

II.3 Dislocation cores and yield stress anomalies

The dislocation cores were mainly studied by Hirth and Lothe (Hirth and Lothe, 1968). In addition, yield stress anomalies were found in numerous intermetallic alloys with many different crystallographic structures as well as in some pure metals and disordered alloys. They occurred with many different glide systems and their amplitude could for instance be small, forming a plateau–like stress versus temperature curve, or large, leading to an increase of yield stress by a factor 10. Three types of explanation were thus suggested to explain yield stress anomalies in these different cases (Caillard and Couret, 1991):

- diffusion controlled frictional forces,
- Peierls type frictional forces,
- cross slip leading to non planar antiphase boundaries.

These three various microscopic mechanisms are summarized as follows.

II.3.1 Stress anomalies in case of diffusion controlled frictional forces

Dislocations are assumed to be slowed down by diffusion controlled mechanisms, such as climb dissociation and core interaction with solute atoms. Such effects are observed in Al_3Ti, steel... An equilibrium configuration is progressively reached after some temperature dependent relaxation time. It is important to note that many dislocation characters are related to these mechanisms, which results in an isotropic dislocation substructure. Three domains can be defined:

- high dislocation velocities, low temperatures: diffusion is too slow to contribute the structure of mobile dislocations, and the temperature dependence of the flow stress is negative,
- low dislocation velocities, high temperatures: diffusion is so fast that even mobile dislocations reach their equilibrium configurations almost instantly. The temperature dependence of the flow stress is also negative,
- intermediate dislocation velocities and temperatures: the speed of diffusion is comparable to the velocity of dislocations, in such a way that dislocations move easier at a higher velocity, thus inducing negative stress–velocity dependence. At a given strain rate, only a very low density of dislocations is gliding very rapidly at the same time, which leads in some cases to the so–called "jerky flow" or PLC effect.

II.3.2 Yield stress anomalies in case of Peierls type frictional forces

The materials which are subjected to this effect are: Be (dislocations in pure metals), TiAl (ordinary dislocations), Fe_3Al (superdislocations with planar antiphase boundaries)... Since dislocation substructures have a tendency to lie along crystallographic directions, it can be concluded that dislocations have a minimum velocity in these directions (the strain rate is controlled by the mobility of these dislocation segments which are subjected to Peierls frictional stresses). Peierls forces are expected to originate from a non planar core structure. Régnier and Dupouy (Régnier and Dupouy, 1970) were the first to apply the case of Peierls type frictional forces for dilute alloys (f.c.c. streel and h.c.p. titanium). Stress anomalies were observed in stainless steel in the temperatures range $200°C$–$600°C$ (Barnby, 1965), associated with a "jerky flow" or PLC effect. According to these authors, the origin of these anomalies is that screw dislocations may have two possible configurations, corresponding to dissociations in the basal and the prismatic planes, and that the energy barrier to the prismatic–basal cross slip is lower than that to the reverse process. It is noted that this prediction is in agreement with calculations of Legrand (Legrand, 1984) which indicate the possibility of dislocation spreading in prismatic planes with high stacking–fault energy. The deformation mechanism corresponding to the jerky movement of dislocations is a series of locking and unlocking processes by double cross slip between basal and prismatic planes, with activation energies of G_L (prismatic–basal) and G_{UL} (basal–prismatic respectively, as shown in figure II.10). It is based on the assumption already made by Régnier that screw dislocations can have two different core structures, extended in the basal and the prismatic planes respectively.

This locking–unlocking mechanism is not fundamentally different from the Peierls mechanism, since the Peierls mechanism is a limiting case of the locking–unlocking mechanism when the jump distance between locked positions decreases and scales with interatomic distances (Caillard et al., 1991; Couret and Caillard, 1991). The locking–unlocking mechanisms were evidenced in several h.c.p. metals with either normal or "anomalous" stress–temperature relationship (Couret and Caillard, 1991; Couret et al., 1991). The transition

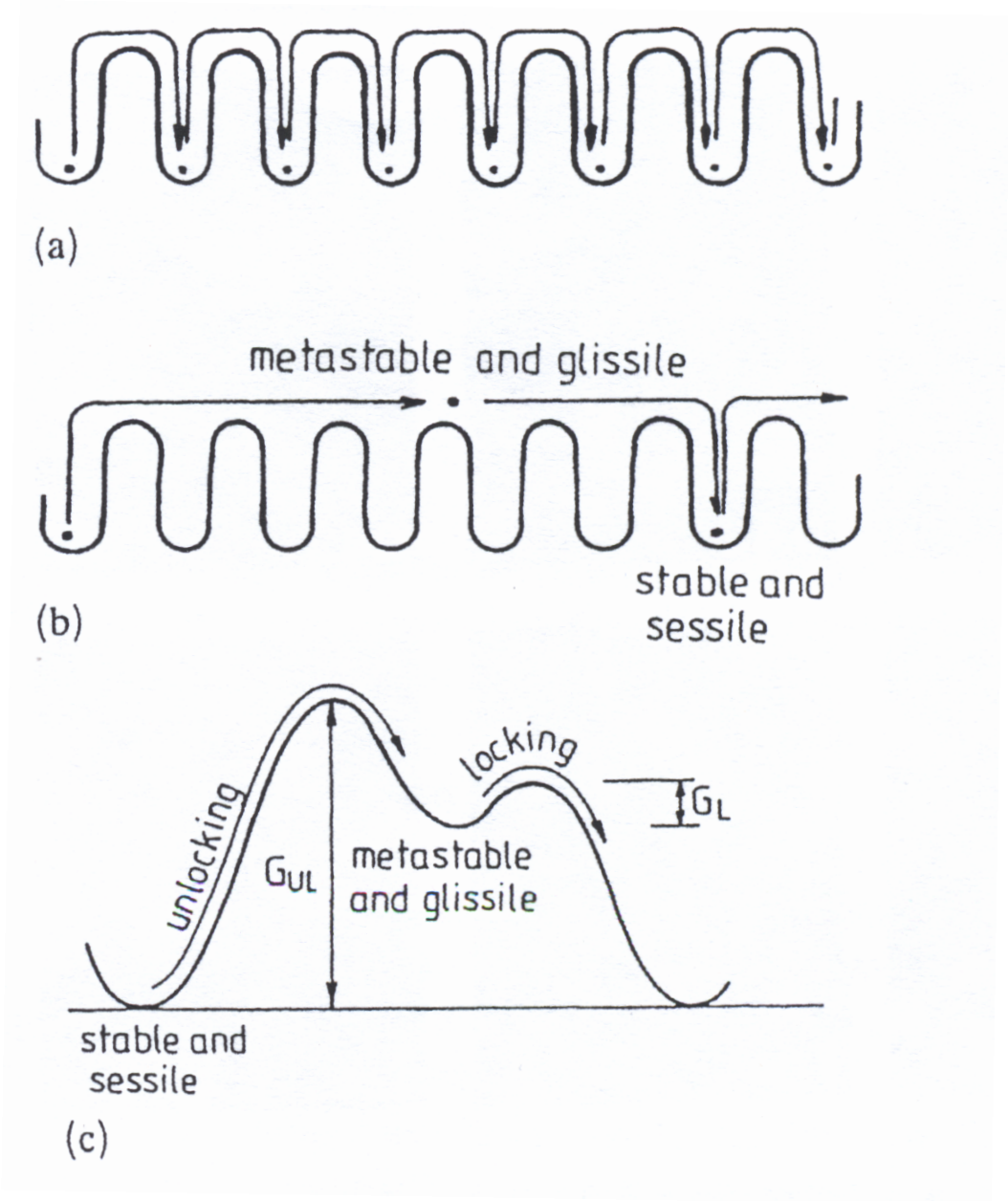

Figure II.10 : Peierls type frictional forces in metals and alloy: (a) and (b) Peierls and locking–unlocking (double cross slip) mechanisms; (c) energy diagram of the locking–unlocking mechanism (Caillard et al., 1991).

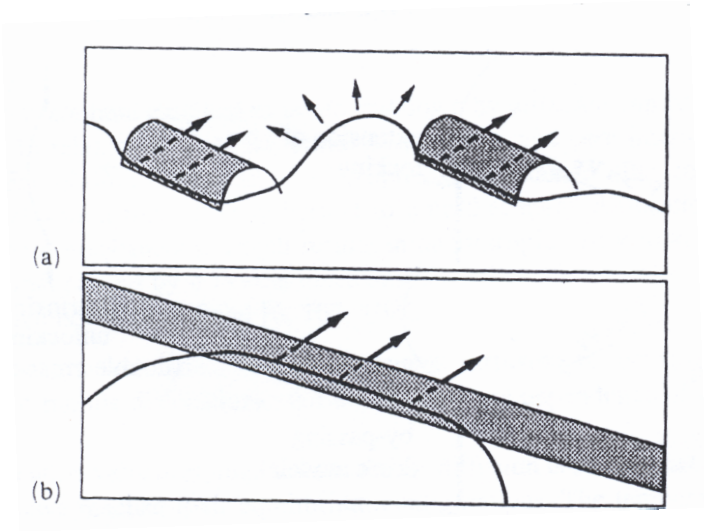

Figure II.11 : Two possible topologies of dislocation–obstacle interactions: (a) by passing and cutting; (b) by cutting (Caillard et al., 1993).

between locking–unlocking and Peierls mechanisms was studied in titanium (Farenc et al., 1995). The Peierls stresses are very sensitive to material purity. Note that all dislocation characters are concerned with such a diffusion process. Thus, the Peierls stresses which control prismatic slip in titanium are much higher when oxygen content is higher (Farenc, 1992; Naka et al., 1988). It is also possible that the Peierls stresses are increased by the chemical interaction between dislocation cores and diffusing solute atoms or impurities, at increasing temperatures. Such a behavior corresponds to an evolution of the dislocation core structure with temperature in basal and/or prismatic planes. Assuming dislocations in basal planes are split into two Shockley partials separated by a stacking fault, this evolution can be described by a decrease in the stacking fault energy with increasing temperature.

II.3.3 Stress anomalies in case of antiphase boundary cross slip

The materials which display antiphase boundary cross slip are the following: Ni_3Al, $TiAl$, Fe_3Al... The hypothesis is based on the thermally activated locking of superdislocations by cross slip from the primary plane, leading to an antiphase boundary partly or completely out of the primary plane. For instance in Ni_3Al, the type of dislocation–obstacle interaction depends only on the respective velocities of free dislocation segments and glissile–sessile transitions along screw dislocations. Analogies can also be found between screw dislocations blocked by cross slip leading to a non planar antiphase boundary and dislocations blocked in Peierls valleys. In both cases, dislocations have a non planar structure, and superdislocations with their antiphase boundary out of the glide plane can be considered as lying in a peculiar type of Peierls valley. Accordingly, glide mechanisms may have the same origin, based either on by passing or cutting processes, as shown in figure II.11.

In conclusion, the Snoek's mechanism, the Cottrell cloud and the dislocation cores diffusion have the same effect. The individual behavior of a dislocation is not sufficient and the collective behavior of dislocations has to be taken into account.

Chapter -III-

Microscopic mechanisms in zirconium alloys

Contents

Abstract: Anomalous macroscopic behavior was observed in dilute zirconium alloys over the temperatures range $200°C$–$600°C$ in the past fifty years. Many of these macroscopic effects were related to some forms of strain ageing phenomena and a variety of microscopic mechanisms were proposed in the literature, which revealed many inconsistencies. The purpose of this chapter is to present some reliable findings about microscopic mechanisms in dilute zirconium alloys, especially the anelastic relaxation phenomena associated with oxygen diffusion and strain ageing measurements.

III.1 Theory of mechanical relaxation modes of paired point defects in h.c.p. crystals

In the past fifty years, large attention were paid to study the impurities and lattice defects in crystals. The awareness of a large amount of information was obtained through the study of the anelastic behavior of solids (Nowick and Heller, 1963). Several anelastic phenomena observed in crystals can be associated with the stress induced ordering of paired point defects (the internal friction due to interstitial atom pairs or the Zener relaxation effect in alloys) (Berry, 1965). In general, paired point defects induce an ellipsoidal stress field around them whereas an isolated defect produces a spherical distortion of the lattice. An external stress applied to the crystal interacts with the elastic field of the pair, which rotates in order to minimize the free energy of the system. This relaxation phenomenon may result in a dissipative process. In this interpretation, one of the defects in the pair is assumed to remain fixed and the other can occupy any of the neighbouring positions. Three types of nearest

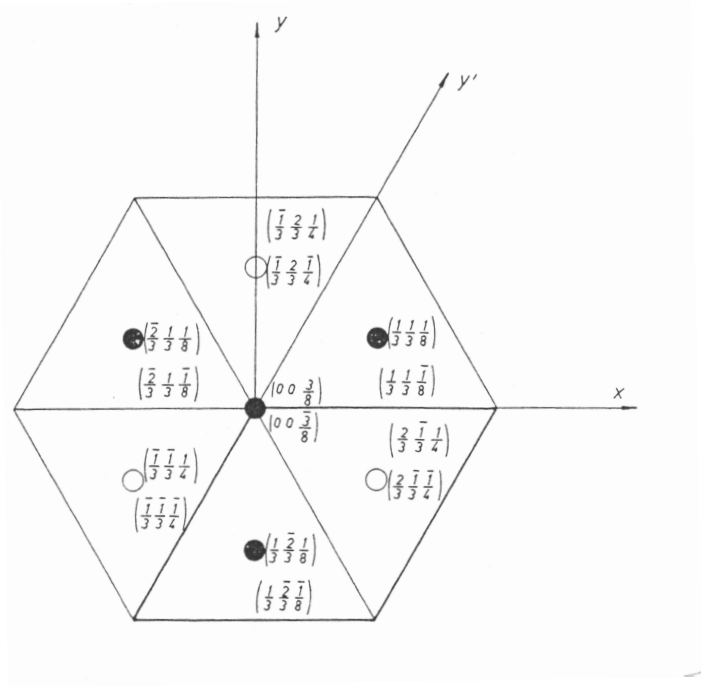

Figure III.1 : Coordinates of the two kinds of interstitial sites in the h.c.p. lattice: octahedral (white points) and tetrahedral (black points) sites (Povolo and Bisogni, 1966).

neighbours have to be considered: the first (nn) , second (nnn) and third nearest (tnn) neighbours. The mechanical relaxation modes are studied for the pairs s–i, i–i, s–s and v–v where s denotes a substitutional atom, i an interstitial atom and v a vacancy in the h.c.p. lattice. Since in the h.c.p. lattice there are two kinds of interstitial sites, the octahedral being about twice as large as the tetrahedral (Azaroff, 1960), the main configuration for the s–i pair is the occupancy of the octahedral sites. The coordinates of all the sites are shown in figure III.1. There are two tetrahedral sites (nn) with coordinates (0, 0, $\frac{3}{8}$) and located at a distance $\pm c/2$ in the <c> direction, six (nnn) with coordinates ($\frac{1}{3}$, $\frac{1}{3}$, $\frac{1}{8}$) and six octahedral sites (tnn) in positions ($\frac{2}{3}$, $\frac{1}{3}$, $\frac{1}{4}$), located at a distance $\pm a$ along the three main directions in the basal plan (see appendix I giving some generalities about the crystalline structure of h.c.p. zirconium alloys).

The literature reveals that there is evidence of anelastic effects which are attributed to the stress induced ordering of i–i atom pairs (Wu and Wang, 1958) and s–i atom pairs (Kê and Tsien, 1956), which should possess the required anisotropic stress fields in h.c.p. alloys. Consequently, the distortion introduced by such defects is anisotropic and the Snoek's mechanism is possible with only certain jump frequencies between the different sites. That is why, internal friction studies should be able to provide measurements of the jump frequency of interstitial atom if it is assumed that the substitutional atom is fixed and the reorientation for the s–i pairs occurs by jumps of the more mobile interstitial. Two distinct types of jumps can lead to the reorientation for the s–i pairs when dissociation of this pair is excluded. As shown in figure III.2, the first jump denoted W_1 is parallel to the basal plane, while the second jump denoted W_2 is perpendicular to the basal plane.

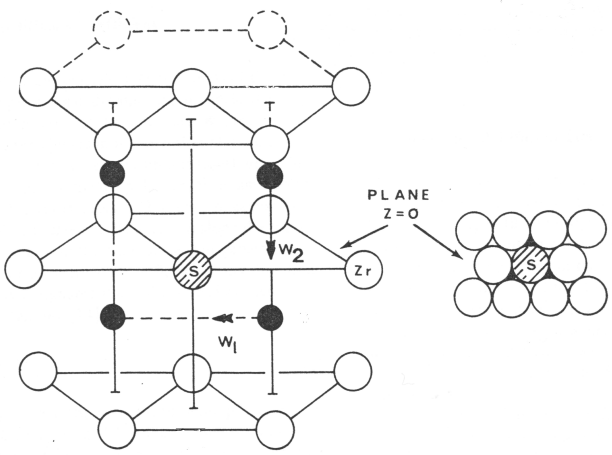

Figure III.2 : Illustration of the two types of interstitial jumps which produce reorientation of the nearest–neighbour substitutional–interstitial pair in zirconium. The jump rate W_1 is parallel to the basal plane, while that of W_2 is parallel to the <c> awis. Note that only four of the six equivalent s–i orientations are shown in this diagram while in the basal plane projection three of the interstitial sites are at $z = \pm c/4$ and the other three immediately below at $z = -c/4$ (Nowick and Heller, 1963).

III.2 Internal friction and anelastic diffusion coefficient of oxygen

It is now fairly well established that the internal friction peaks associated with impurities exist in "hard" h.c.p. metals which have a ratio c/a less than the ideal. The internal friction spectrum of α zirconium–hafnium type Van Arkel, containing oxygen in solid solution exhibits an anelastic relaxation peak at about $420°C$ (Gacougnolle et al., 1970). However there are conflicting experimental evidences concerning the identity of the anelastic dipole responsible for this peak. Mishra and Asundi (Mishra and Asundi, 1971; Mishra and Asundi, 1972) argued that the peak is due to the reorientation of the s–i pairs, while Browne (Browne, 1971) suggested that the i–i pairs are also involved.

Gacougnolle et al. (Gacougnolle et al., 1970) showed that both s–i and i–i reorientations can give rise to internal friction peaks. But the internal friction peak due to the stress induced reorientations of the s–i pairs predominates at low oxygen concentrations (<3%at.). These authors observed that the height of the peak is a function of the oxygen content and is due to the Hf–O pairs in α zirconium. For hafnium contents superior to 1%at., the temperature of the appearance of the peak is independent of the oxygen content. However for hafnium content inferior to 350.10^{-6}at., the temperature of the occurrence of the peak increases linearly with oxygen content. The height of the peak for a constant oxygen content is very sensitive for low hafnium content, contrary to high hafnium content. The oxygen atoms located on the octahedral sites jump from the compressive sites to the tension sites due to the applied stress and the substitutional atoms. Consequently, there is a maximum threshold of substitutional content from which the lattice is distorded on the whole. All the sites are affected by the applied stress and then contribute to relaxation. This effect can explain the influence of oxygen and hafnium atoms on the height of the peak for low hafnium content.

Mishra and Asundi (Mishra and Asundi, 1972) also found that for each particular substitutional solute species, oxygen interstitial impurity gives two internal friction peaks. Their relative intensities depend upon the concentration of oxygen. They suggested that when plotting the logarithm of the oxygen content versus the logarithm of the intensity of the internal friction, the slope of the straight line indicates the type of mechanism probably operating. When the slope is unity a single oxygen jump is associated with the relaxation process, when it is two, a pair mechanism is operative. This technique is used for explaining the three oxygen atoms jump mechanism observed at high temperature for zirconium–niobium with low oxygen content. These authors showed that substitutional atoms whose atomic diameters are larger than zirconium (for instance tin) or smaller than zirconium (for instance iron, niobium, hafnium) show the following features:

- an oxygen–substitutional interaction peak called P1 occurs at high temperatures ($>450°C$) when the oxygen content is low (<0.1%at.). This peak is associated with s–oxygen–oxygen–oxygen complex,

- an oxygen–substitutional interaction peak called P2 occurs at low temperatures ($<550°C$) when the oxygen content is moderately high (>2%at.). This peak is associated with s–oxygen complex.

Tables III.1 and III.2 summarize the results of the internal friction measurements found by Mishra and Asundi (Mishra and Asundi, 1972) for respectively the peaks P1 and P2.

Table III.1 : Characteristics of the internal friction peak P1 associated with s–O–O–O complex: high temperature and low oxygen content (Mishra and Asundi, 1972).

Element	Amount (%at.)	Size factor with respect to Zr (%)	Peak temperature ($°C$)	Oxygen content (%at.)
Fe	0.03	- 22	425	0.3
Fe	0.8	- 22	425	0.3
Nb	0.25	- 8.75	540	0.22
Nb	0.5	- 8.75	550	0.22
Ti	1	- 8.12	520	0.22
Hf	0.3	- 1.2	645	0.22
Sn	0.5	+ 1.25	645	0.22

Then Ritchie et al. (Ritchie et al., 1976) presented strong evidence from low frequency internal friction experiment on single crystals of zirconium–oxygen alloys with 5000 wt ppm oxygen that the atomic jump rate for jumps parallel to the basal plane W_1 is responsible for the observed internal friction peak. The authors found a relaxation frequency factor of $\tau^{-1} = 3W_1$. In figure III.3, the dominant jump frequency is around $450°C$ and the small broadening of the peak can be attributed to various contributions:

- a small contribution from the reorientation of the i–i pairs,

- the probability that more than one type of substitutional impurity (for example Hf) contributes to the peak,

Table III.2 : Characteristics of the internal friction peak P2 associated with s–O complex: low temperature and high oxygen content (Mishra and Asundi, 1972).

Element	Amount (%at.)	Size factor with respect to Zr (%)	Peak temperature ($°C$)	Oxygen content (%at.)
Fe	0.03	- 22	350	3
Fe	0.8	- 22	350	3
Nb	0.25	- 8.75	480	1
Nb	0.5	- 8.75	475	1
Ti	1	- 8.12	430	4
Hf	0.3	- 1.2	570	2
Sn	0.5	+ 1.25	630	1

- the probability that some larger complexes such as i–s–i or i–i–i triplets also contribute to the measured peak.

Browne et al. (Browne, 1971) were the first to discuss the relationship between anelastic relaxations and diffusion of oxygen in h.c.p. metals. But these workers assumed that W_2 is the rate controlling jump. Ritchie et al. (Ritchie et al., 1976) re–examined the results of these authors taking W_1 as the rate controlling jump. For interstitial diffusion in h.c.p. lattice where the diffusion occurs in the basal plane (Manning, 1968), following Browne (Browne, 1972), the equation for the mean diffusivity D is:

$$D = a^2 W_1 \tag{III.1}$$

Ritchie (Ritchie et al., 1976) found also experimentally:

$$D = 0.58 exp(-\frac{46000}{RT}) \tag{III.2}$$

with RT is in $J.mol^{-1}$. This diffusion equation is in excellent agreement with the diffusion equations found by Béranger and Lacombe (Béranger and Lacombe, 1965) for the bulk diffusion of oxygen in α zirconium in the temperatures range of $650°C$–$850°C$:

$$D^{\Delta} = 0.22 exp(-\frac{47000}{RT}) \quad ; \quad D^{m} = 0.50 exp(-\frac{46800}{RT}) \tag{III.3}$$

From the studies of the dissolved oxygen concentration gradient beneath an oxide layer, D^{Δ} refers to results obtained from microhardness measurements of oxygen concentration, while D^m refers to results obtained from measurements of the mass of diffused oxygen. Consequently, the good agreement between equations (III.2), (III.3) may be taken as further evidence that jumps of type W_1 is the rate controlling phenomenon in the diffusion of oxygen in α zirconium. Moreover, the activation energy of the peak is equal to 192 $kJ.mol^{-1}$, which is in good agreement with the value of 197 $kJ.mol^{-1}$ found by Béranger and Lacombe (Béranger and Lacombe, 1965) for the diffusion of oxygen in α zirconium in the temperatures range $650°C$–$850°C$.

De Paula E Silva et al. (Silva et al., 1971; Tyson, 1967) seem to be the first authors to discuss the kinetics of static strain ageing in terms of the anisotropy of oxygen diffusion

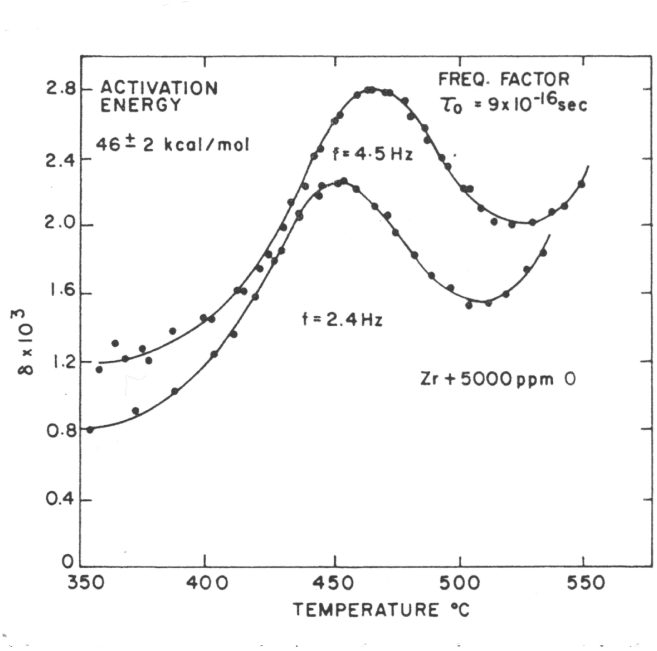

Figure III.3 : Oxygen friction peak at two frequencies measured in the single crystal zirconium–oxygen alloys with 5000 wt ppm oxygen tested in flexure (Ritchie et al., 1976).

in α zirconium. Although de Paula E Silva et al. assumed that W_2 is the rate controlling jump as Browne did, they established the interval of time τ_s for which the amplitude of the stress peak $\Delta\sigma$ did not increase for different temperatures. Table III.3 gives the values of the distance covered by oxygen interstitial atoms during τ_s at various temperatures (Shewmon, 1963). These values are obtained with the following diffusion equation:

$$x = 2\sqrt{D^{\Delta}t} \tag{III.4}$$

where x is the distance covered by the interstitial atoms during τ_s.

Table III.3 : Summary of the results of de Paula E Silva about kinetics of SSA in terms of the anisotropy of oxygen diffusion in α zirconium where RT is in $J.mol^{-1}$ (Silva et al., 1971).

Temperature ($^\circ C$)	x (Å)	D^{Δ} ($cm^2.s^{-1}$)	τ_s (s)	$\tau = 9.10^{-16} exp(\frac{46000}{RT})$ (s)
290	2.1	1.6 10^{-19}	660	663
330	2.3	2.8 10^{-19}	50	43
350	2.8	9.3 10^{-18}	22	13

Table III.3 shows also that the distances covered by oxygen atoms and deduced from τ_s exclude long range diffusion phenomena. That is why De Paula E Silva suggested a Snoek ordering diffusion to explain static strain ageing effects. The value of τ_s measured in strain ageing experiments are compared with the relaxation time for s–i reorientation τ. As it can be seen from table III.3, the good agreement between the values obtained from τ_s and τ suggest that a reorientation of s–i pairs is responsible for the observed strain ageing in α zirconium.

Many workers investigated the diffusion of oxygen in α zirconium according to various techniques (internal friction, conventional strain ageing, microhardness profile...). Ritchie et al. (Ritchie et al., 1976) gave a compilation and an analysis of data related to oxygen diffusion in α zirconium taking two assumptions into account:

- basal plane oxygen jumps which effectively produce reorientation of the s–i pairs are not significantly perturbed by the presence of the substitutional impurity and can therefore be directly compared to the free migration jumps of single oxygen interstitial atoms,
- basal jumps which are rate controlling in the reorientation of the s–i pairs at temperature around $400°C$ are also rate controlling in the free migration of interstitial atoms at similar temperatures.

They showed that for temperatures ranging from $290°C$ to $650°C$, the bulk diffusion coefficient of oxygen in α zirconium (in $cm^2.s^{-1}$) is given by:

$$D = 0.661 exp(-\frac{44000}{RT}) \tag{III.5}$$

It is attributed to the jumps of oxygen intertitials in the basal plane. They showed also that for temperatures ranging from $650°C$ to $1500°C$, the bulk diffusion coefficient of oxygen in α zirconium (in $cm^2.s^{-1}$) is given by:

$$D = 16.5 exp(-\frac{54700}{RT}) \tag{III.6}$$

It is suggested that in this temperatures range, jumps of oxygen interstitial atoms in the <c> direction are rate controlling.

III.3 Effect of substitutional–interstitial interaction on static strain ageing behavior

In the previous section, internal friction measurements with different oxygen contents and various types of substitutional impurities lead to various internal friction responses (for instance the temperature of its occurrence or the height of the peak). Consequently the oxygen content and the nature of the substitutional atom must play an important role on static strain ageing behavior. Thirty years ago, a substantial amount of work was published on the strain ageing characteristics of zirconium–oxygen alloys (Silva et al., 1971; Kelly and Smith, 1973), Zircaloy–2 (Veevers and Rotsey, 1968; Veevers et al., 1969; Veevers and Snowden, 1973), Zircaloy–4 (Silva et al., 1971), zirconium solid solutions (Veevers, 1975) and Zr–2.5 wt%Nb (Sinha and Asundi, 1977b).

Figure III.4 illustrates the role of oxygen content by comparing the temperature dependence of the stress peak, measured by $\Delta\sigma$ for zirconium alloyed with various amounts of oxygen (Kelly and Smith, 1973). For 430 wt ppm oxygen, $\Delta\sigma$ shows a single peak at $295°C$. Its height is lower than the peak for 1000 wt ppm oxygen at $325°C$. The strain ageing parameter increases with increasing oxygen content. This effect was also observed by Kelly (Kelly and Smith, 1973) by comparing the strain ageing response for zirconium–oxygen alloys with various oxygen contents at $325°C$ as shown in figure III.5.

The argument that substitutional atoms may play an important part in strain ageing response is supported by the fact that Veevers showed that the temperature dependence of $\Delta\sigma$ is strongly affected by substitutional alloying elements (Veevers, 1975). The main feature of the figure III.6 is that zirconium–iron alloys show a peak at $450°C$, whereas zirconium–tin, zirconium–chromium, zirconium–nickel alloys exhibit a peak in the temperatures range of

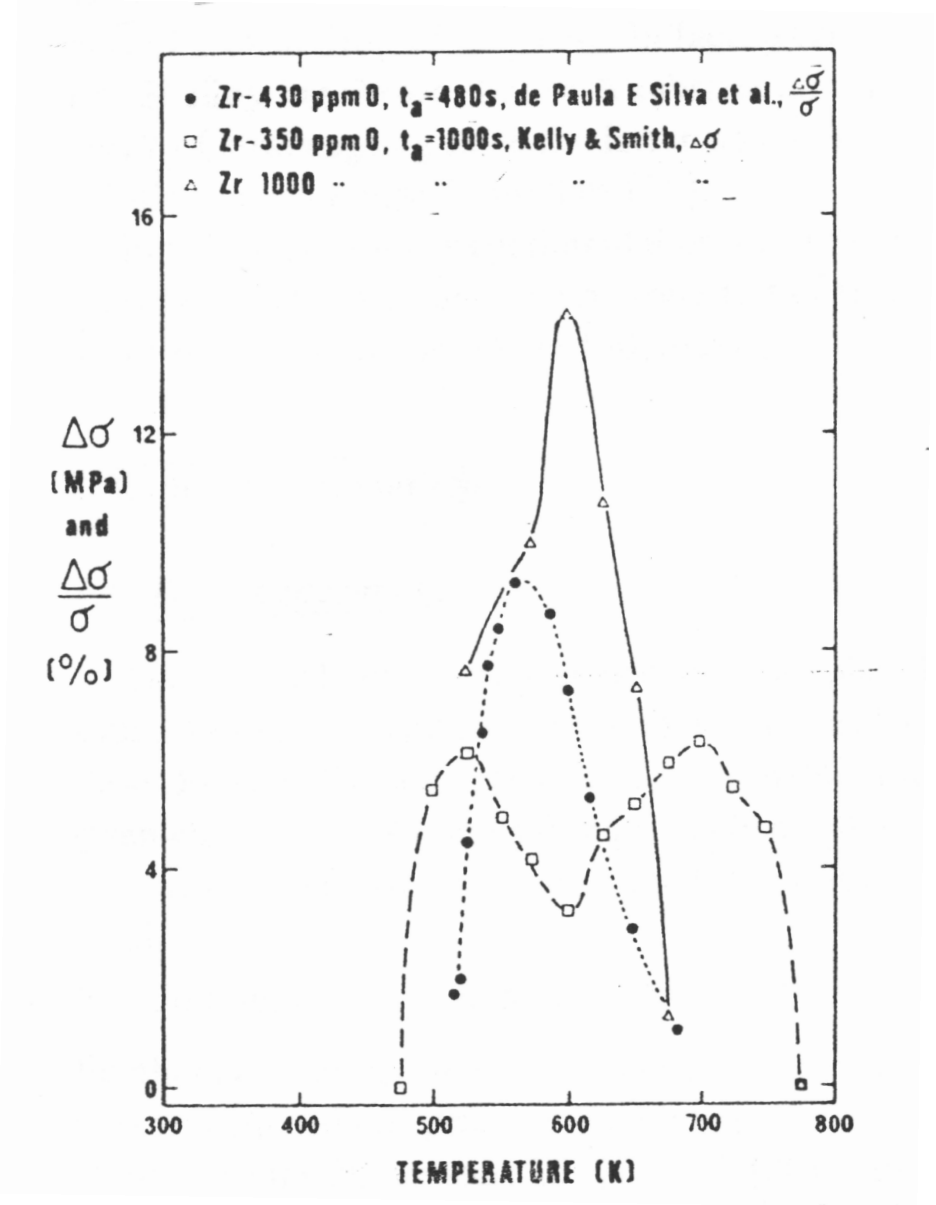

Figure III.4 : Variation of the temperature dependence of strain ageing parameters in zirconium–oxygen alloys with two oxygen concentrations and between alloys with similar oxygen content but possibly different substitutional impurities (Silva et al., 1971; Kelly and Smith, 1973).

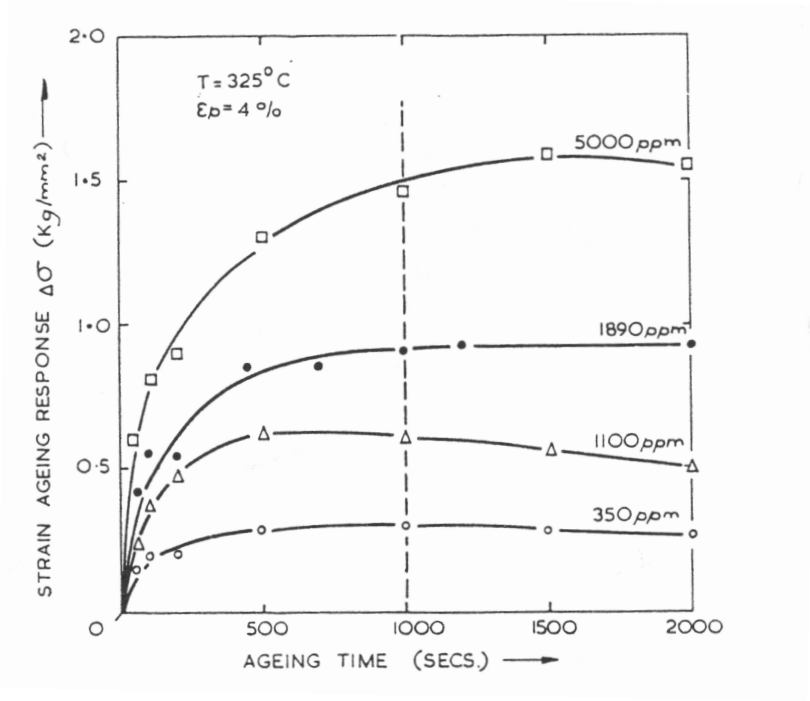

Figure III.5 : Variation of the strain ageing parameter $\Delta\sigma$ as a function of ageing time after 4% pre–strain at $325°C$ for zirconium–oxygen alloys with various oxygen contents (Kelly and Smith, 1973).

$275°C$–$325°C$. Note that the high peak of $\Delta\sigma$ for zirconium–tin alloy is due to the amount of the alloying element which is about an order of magnitude greater than in the other alloys. Figure III.6 can give an explanation for the fact that in figure III.4, for 350 wt ppm oxygen, $\Delta\sigma$ exhibits two peaks at $250°C$ and $425°C$ while at 1000 wt ppm oxygen, there is a single peak at $325°C$. This can be explained by the fact that at low oxygen levels (350 wt ppm), the high temperature peak is caused by an interaction between iron and dislocations.

Veevers and Snowden (Veevers and Snowden, 1973) compared the behavior of annealed and quenched Zircaloy–2 to study the role of the s–i pairs on strain ageing response. They showed that quenching from $750°C$ enhances the strain ageing parameter by a factor of about 2 at $300°C$ and reduced by a factor of about 4 at $425°C$ as compared with the behavior of annealed Zircaloy–2. This effect is shown in figure III.7. The increased amount of strain ageing in quenched Zircaloy–2 at $300°C$ can also be readily explained by a Snoek's interaction between glide dislocations and an increased concentration of the s–i atom pairs frozen in by the quenching treatment. Many evidences in the literature indicate that quenching retains oxygen interstitial atoms in solution with the result that higher yield points are usually observed on the strain ageing response. This result was also found by Keh and Leslie on iron–carbon alloys (Keh and Leslie, 1963). The absence of strain ageing at $425°C$ in quenched Zircaloy–2 is thought to be due to the trapping of iron by quenched–in defects so that the residual concentration of iron atoms is not sufficient to cause significant interaction with glide dislocations.

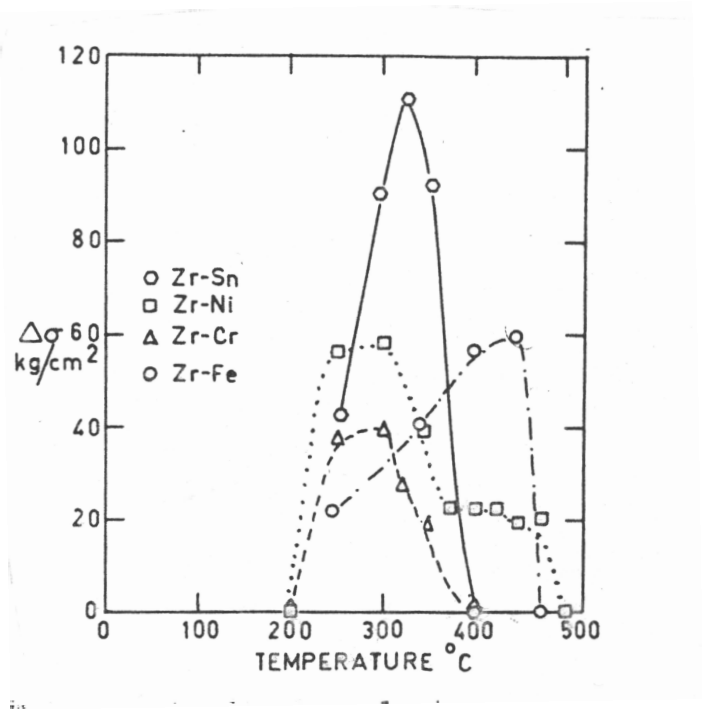

Figure III.6 : $\Delta\sigma$ versus temperature for various zirconium alloys (Veevers, 1975).

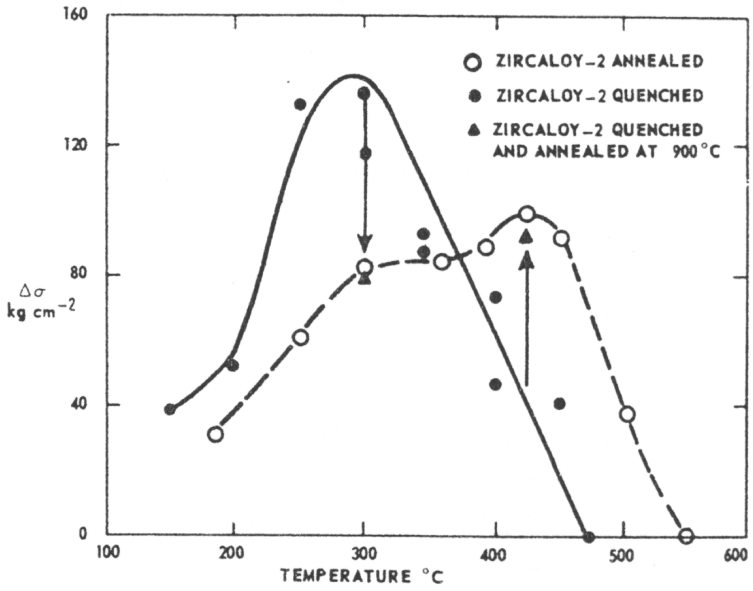

Figure III.7 : $\Delta\sigma$ versus temperature for annealed Zircaloy–2 at $750°C$ and quenched from $750°C$ Zircaloy–2 (Veevers and Snowden, 1973).

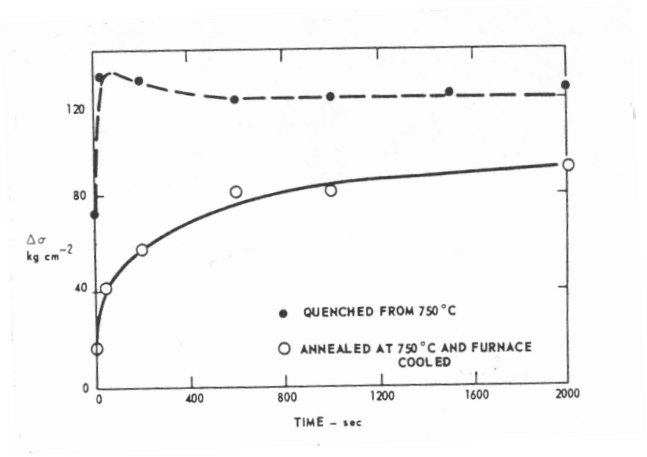

Figure III.8 : $\Delta\sigma$ versus ageing time for annealed Zircaloy–2 at $750°C$ and quenched from $750°C$ Zircaloy–2 (Veevers and Snowden, 1973).

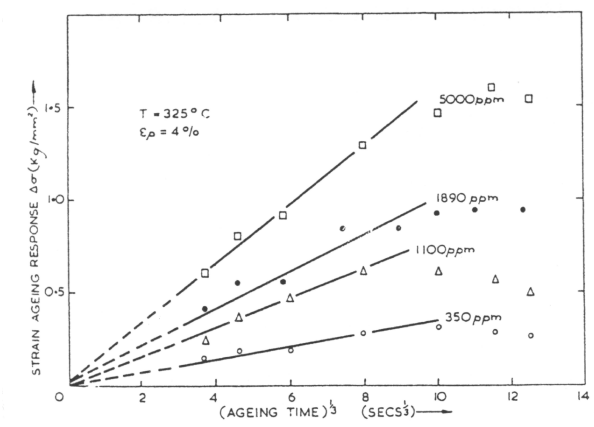

Figure III.9 : Strain ageing response at $325°C$ for zirconium–oxygen alloys with various oxygen contents versus $(\text{time})^{1/3}$ showing the linear relation during the initial stages of ageing (Kelly and Smith, 1973).

In figure III.8, maximum strain ageing occurs after about 40 seconds. Strain ageing increases rapidly with ageing time. However for ageing periods beyond about 1000 seconds, it occurs to level off. That is why, the value of 1000 seconds is selected as the standard ageing time (see also figure III.5). Moreover the initial stages of ageing followed a $(\text{time})^{1/3}$ relationship rather than a $(\text{time})^{2/3}$ relationship suggested by Cottrell and Bilby as shown in figure III.9. Likewise $(\text{time})^{1/3}$ kinetics were reported in the literature for zirconium–oxygen alloys (Kelly and Smith, 1973), Zircaloy–4 (Rheem and Park, 1976) and iron–carbon alloys (Imanaka and Fujimoto, 1968), but no theoretical basis was proposed.

Chapter -IV-

Anomalous macroscopic behavior in zirconium alloys

Contents

Abstract: The purpose of this chapter is to give the main results related in the literature, regarding the macroscopic point of view. We call "anomalous" or "unconventional" behavior, any macroscopic manifestation of strain ageing phenomena that are not observed in pure metals. First, yielding and tensile properties are discussed. We focus our attention on the following unconventional features of macroscopic behavior:

- Lüders phenomenon,
- plateau or maximum in the flow stress versus temperature diagram,
- minimum in the strain rate sensitivity versus temperature diagram,
- maximum in the apparent activation volume versus temperature diagram,
- minimum in ductility and elongation for increasing temperature.

Then, the effect of strain ageing phenomena on creep and relaxation behavior is discussed. Note that ten years ago Prioul (Prioul, 1995) proposed a review of strain ageing phenomena observed in dilute zirconium alloys and their consequences on mechanical properties.

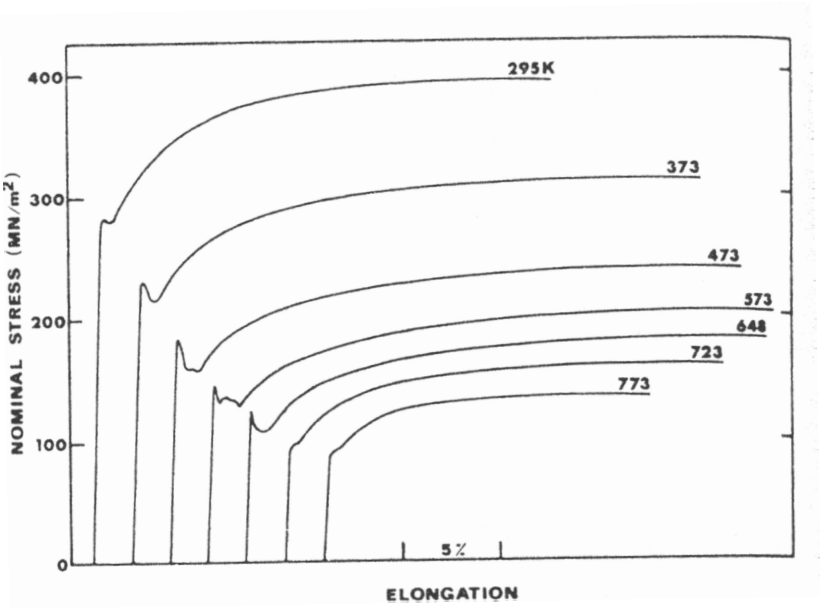

Figure IV.1 : Nominal stress versus elongation curves for Zr–1 wt%Nb alloy at a nominal strain rate of 3.5 10^{-4} s^{-1} for various temperatures (Thorpe and Smith, 1978b).

IV.1 From tensile yielding to fracture

IV.1.1 Lüders phenomenon

Figure IV.1 shows the Lüders phenomenon for annealed Zr–1 wt%Nb by plotting the nominal stress versus elongation curve at a strain rate of 3.5 10^{-4} s^{-1} for various temperatures in the range $20°C$–$500°C$. Note that this is the only example of the Lüders phenomenon observed in a dilute zirconium alloy mentioned in the literature. A maximum Lüders elongation of about 1.5% occurs at $300°C$ as compared to about 0.5% at $20°C$. The Lüders elongation is a function of the testing temperatures and ranges from 14% to 28% as shown in figure IV.1.

Outside the Lüders plateau, the behavior can be described by the Hollomon relationship:

$$\sigma = K(\varepsilon - \varepsilon_{plateau})^n \tag{IV.1}$$

It offers an accurate description of the data (Hollomon, 1945). Here K is the strength coefficient and n is the strain hardening exponent.

A plot of the strain hardening exponent n versus temperature is presented in figure IV.2. From $20°C$ to $300°C$, n rises continuously with temperature to a maximum value, whereupon it decreases with increasing temperature. The temperature corresponding to the maximum value of n decreases with decreasing strain rate while concurrently the maximum value of n increases. An apparent activation energy of 213 $kJ.mol^{-1}$ is determined for this process. This value is in agreement with the activation energy for bulk diffusion of oxygen in α zirconium found by Ritchie (Ritchie et al., 1976) and Béranger and Lacombe (Béranger and Lacombe, 1965).

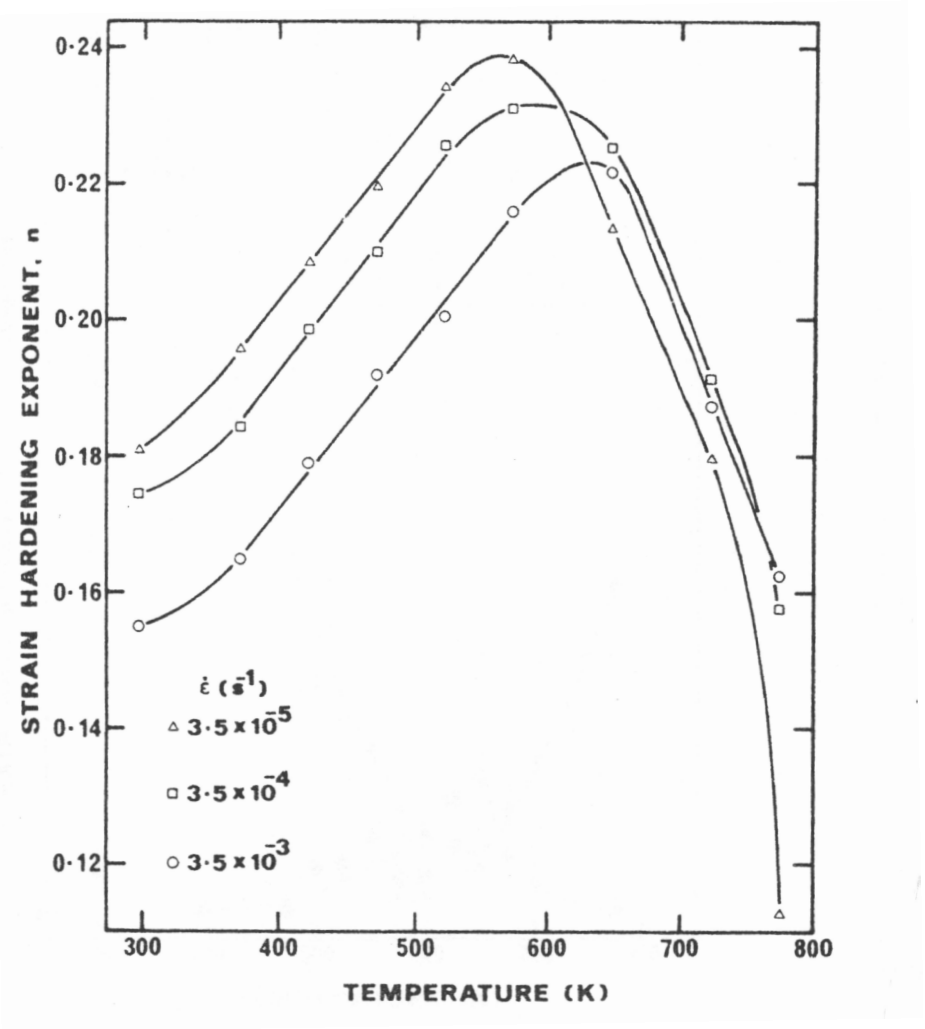

Figure IV.2 : Temperature dependence of the strain hardening exponent for Zr–1 wt%Nb alloy at various strain rates (Thorpe and Smith, 1978b).

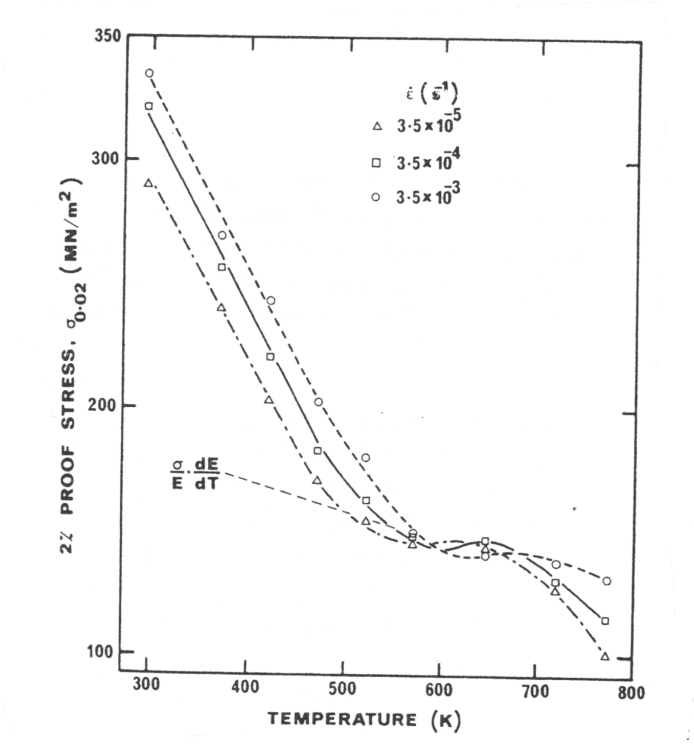

Figure IV.3 : Temperature dependence of yield stress of Zr–1 wt%Nb alloy for various strain rates (Thorpe and Smith, 1978b).

IV.1.2 Plateau or maximum in the yield stress versus temperature diagram

In figure IV.3, yield stress is plotted as a function of temperature at various strain rates for Zr–1 wt%Nb alloy. Yield stress generally decreases with increasing temperature in the temperatures range of thermally assisted deformation. However, a plateau region can be observed in the temperatures range between $280°C$ and $400°C$, depending on strain rate. Especially, the yield stress versus temperature plots exhibit a local maximum in flow stress with increasing temperature. Such a region is commonly labeled in the literature as the "athermal region". Similar behaviors are observed in Zircaloy–4 (Yi et al., 1992; Lee et al., 2001), zirconium–nitrogen–oxygen alloys (Tyson, 1967; Kelly and Smith, 1973) and zirconium alloys doped with niobium, tin and iron as shown in figure IV.4 (Kapoor et al., 2002). Figure IV.4 shows the stress divided by the shear modulus versus temperature plots at various strains. For each strain level, the stress decreases with increasing temperature up to about $300°C$. At high temperatures, a slight increase with increasing temperature is observed.

The effect of oxygen on the yield stress versus temperature plot is given in figure IV.5 for zirconium–oxygen alloys with various oxygen contents. The low temperature strength of zirconium–oxygen supports the idea that the rate controlling process in the deformation of α zirconium below $300°C$ is the interstitial strengthening by oxygen atoms. However above $300°C$, the yield stress versus temperature plots are almost independent of the oxygen content.

Thorpe et al. (Thorpe and Smith, 1978b) pointed out that strain ageing is associated with the increase of yield stress with increasing temperature. In strain ageing, the local maximum in the yield stress versus temperature curve is a function of strain rate. Thus, the activation energy of strain ageing can be obtained from a shift of this local maximum change with strain

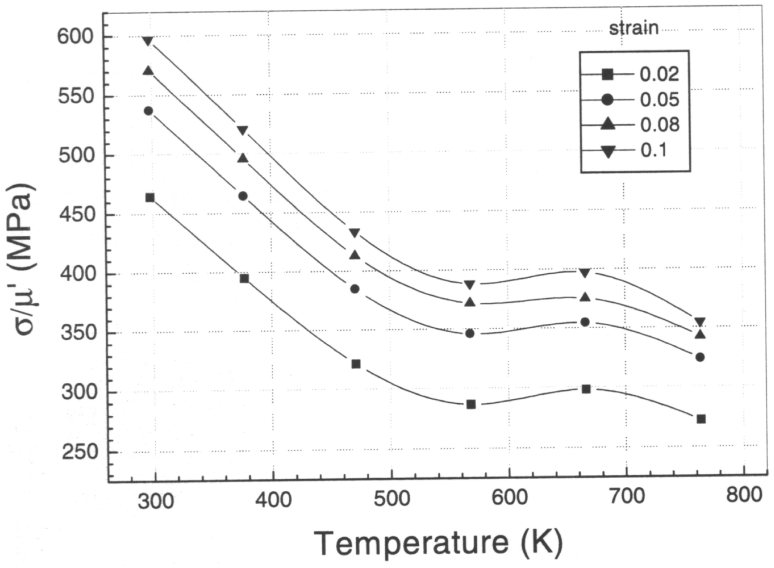

Figure IV.4 : Normalized stress as a function of temperature at different strains (Kapoor et al., 2002).

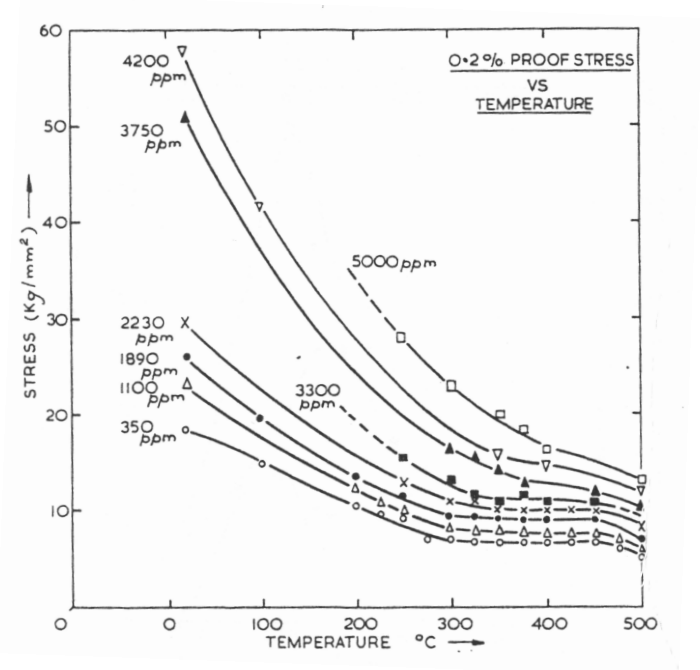

Figure IV.5 : Variation of yield stress with temperature for zirconium–oxygen alloys with different oxygen contents (Kelly and Smith, 1973).

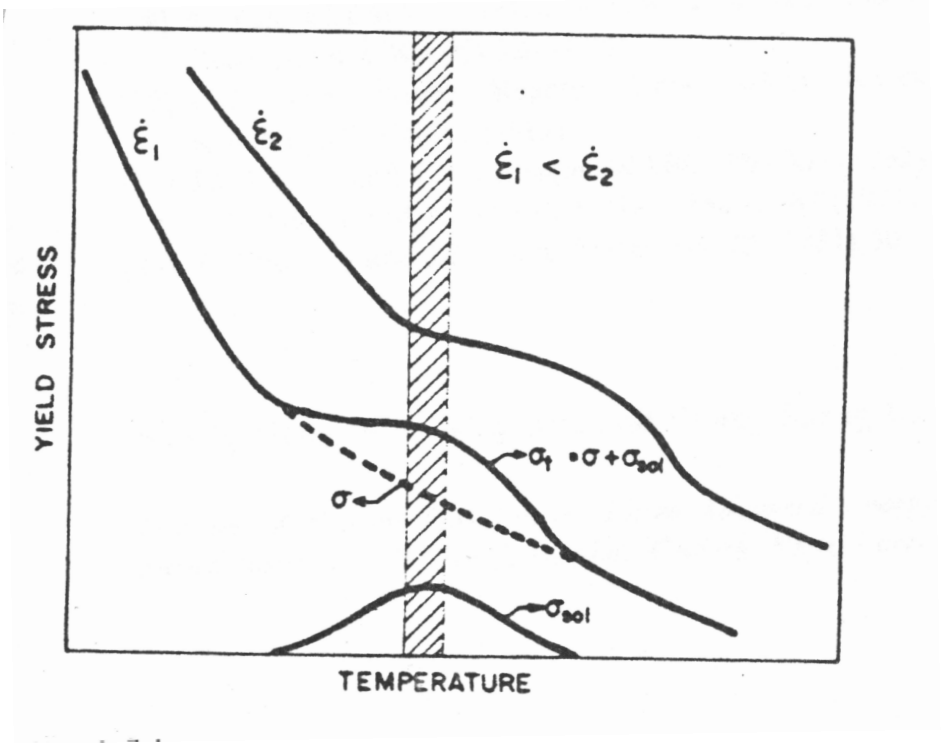

Figure IV.6 : Superimposition of σ_{sol}, the solute strengthening term of strain ageing due to the Snoek's ordering peak and the flow stress σ, characteristic of a single rate controlling process in the absence of strain ageing. The total flow stress σ_t is the addition of these two separable terms and is plotted as a function of temperature. The region of the low strain rate sensitivity is shaded with SRS>0 (Hong et al., 1983).

rate. The Arrhenius plot of strain rate versus the inverse of the local maximum temperature deduced from the yield stress versus temperature curve is obtained by the following equation:

$$\dot{\varepsilon} = Aexp(-\frac{Q}{RT}) \tag{IV.2}$$

where A is a constant and Q is the activation energy of DSA. Yi (Yi et al., 1992) found that the activation energy Q for Zircaloy–4 (Yi et al., 1992) is equal to 228 $kJ.mol^{-1}$. This value corresponds to the activation energy for bulk diffusion of oxygen in α zirconium.

The athermal region can be rationalized in terms of the superposition of two mechanisms:

- the strain ageing due to Snoek's ordering of the s–i pairs,
- the thermally activated overcoming of the oxygen atom clusters.

The effects of Snoek's ordering and of the thermally activated cutting of oxygen atom clusters on the yield stress versus temperature curve is illustrated in figure IV.6. The athermal region produced by the Snoek's peak is similar to that observed in α zirconium alloys.

To conclude this section, table IV.1 gives a comparison between the values of maximum in the flow stress versus temperature plot, obtained by various authors.

Table IV.1 : Comparison between maximum in the flow stress versus temperature plot, obtained by various authors.

Materials	Temperature ($^\circ C$)	Strain rate (s^{-1})	Authors
Zircaloy–4	300	$1.2\ 10^{-7}$	(Yi et al., 1992)
Zircaloy–4	350	$2.\ 10^{-6}$	(Yi et al., 1992)
Zircaloy–4	400	$3.2\ 10^{-5}$	(Yi et al., 1992)
zirconium	300	$1.\ 10^{-3}$	(Ramachandran and Reed-Hill, 1970)
Zircaloy–4	420	$3.3\ 10^{-5}$	(Derep et al., 1980)
Zircaloy–4	417	$1.33\ 10^{-4}$	(Hong et al., 1983)
zirconium–niobium	377	$1.33\ 10^{-4}$	(Thorpe and Smith, 1978c)
zirconium–niobium	325	$9.8\ 10^{-4}$	(Rheem and Park, 1976)

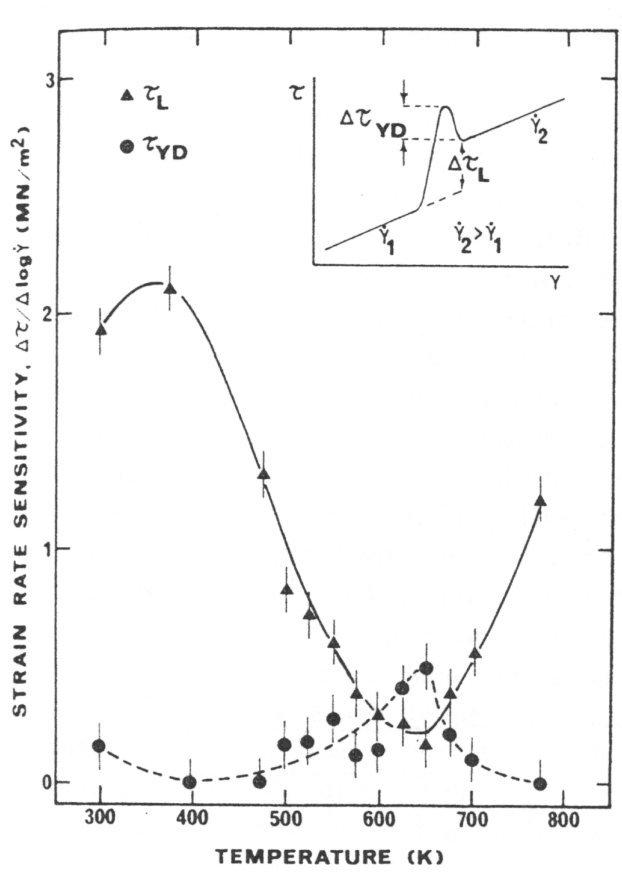

Figure IV.7 : Temperature dependence of the strain rate sensitivity parameter, $\Delta\tau_L/\Delta log\dot{\gamma}$ and $\Delta\tau_{YD}/\Delta log\dot{\gamma}$ from $\times$ 3 strain rate change experiments at a initial nominal tensile strain rate of 3.5 10^{-4} s^{-1} for Zr–1 wt%Nb alloy. The inset shows a typical transient in the shear stress versus shear strain curve observed after a change in strain rate (Thorpe and Smith, 1978b).

IV.1.3 Minimum in the strain rate sensitivity versus temperature diagram

Figure IV.7 shows SRS (or often labeled $m = SRS/\sigma$ in the literature) as a function of temperature for Zr–1 wt%Nb alloy (Thorpe and Smith, 1978b). A typical transient accompanying a strain rate change is also shown in the inset of figure IV.7. The strain sate sensitivity parameter is defined as the increase in stress needed to cause a certain increase in plastic strain rate at a given level of plastic strain and at constant temperature. This parameter is defined by:

$$SRS = (\frac{\Delta\sigma}{\Delta log\dot{\varepsilon}_p})_{T,\varepsilon_p} \tag{IV.3}$$

Generally, SRS tends to increase more or less linearly with temperature in "standard" materials.

Experimentally, two measurements of SRS, $\Delta\tau_L/\Delta log\dot{\gamma}$ and $\Delta\tau_{YD}/\Delta log\dot{\gamma}$ are presented in figure IV.7 as a function of temperature, for tensile tests at an initial strain rate of 3.5 10^{-4} s^{-1}. The definitions of τ_L and τ_{YD} are given in figure IV.7. Following Tyson (Tyson, 1967), the shear stress τ is taken to be half of the tensile stress σ. The SRS of Zr–1 wt%Nb alloy does not increase monotonically with temperatue as it is the case for a simple thermally activated process. But SRS ($\Delta\tau_L/\Delta log\dot{\gamma}$) decreases over a broad temperatures

range $100°C$–$400°C$, reaching a minimum value over this temperatures range. The minimum SRS ($\Delta\tau_L/\Delta log\dot{\gamma}$) occurs at $380°C$. The shape of the SRS ($\Delta\tau_L/\Delta log\dot{\gamma}$) versus temperature plot is similar to that obtained by Ramachandran and Reed–Hill (Ramachandran and Reed-Hill, 1970) in α zirconium and by Lee (Lee et al., 2001) in Zircaloy–4. Note that the SRS is close to zero around $380°C$. This low value of SRS can be explained in terms of DSA. Indeed, the temperature corresponding to the maximum stress peak after a strain rate increment is the same as that of the maximum in the yield stress versus temperature plot (see figure IV.3). This suggests that the stress peak may also be partly due to strain ageing and not only to the variations of mobile dislocations density. It is likely that the increase in mobile dislocation density which is thought to accompany an increase in strain rate could be initially inhibited by strain ageing, resulting in a momentary raising of the flow stress followed by a stress drop.

Note that the inverse SRS in the temperatures range $300°C$–$400°C$ shown in figure IV.2 for Zr–1 wt%Nb alloy is not detected by strain rate change experiments although SRS does approach zero at $370°C$. This is possibly due to a greater change in substructure after strain rate jumps in the case of the flow stress versus temperature measurements.

IV.1.4 Maximum in the apparent activation volume versus temperature diagram

From strain rate change tests, the apparent activation volume for plastic flow can be determined, using the following classical equation (Conrad, 1964):

$$V_a = k_B T(\frac{\Delta log\dot{\varepsilon}_p}{\Delta\sigma})_{T,\varepsilon_p} = \frac{k_B T}{SRS} \tag{IV.4}$$

The apparent activation volume and its strain dependence give information about the rate controlling mechanism of plastic flow. Note that if SRS tends to zero, V_a tends to infinity. Consequently, the physical meaning of undefined apparent activation volume determined under this condition is questionable. Figure IV.8 shows the evolution of the apparent activation volume as a function of temperature for Zircaloy–4 at a plastic strain of 0.02. The values of the apparent activation volume as a function of temperature vary between about $50b^3$ and $200b^3$ in air and vacuum where b is about 10^{-10} m. As shown in figure IV.8, a maximum in air is observed at $350°C$ and a minimum is observed at $410°C$. Note that Yi et al. (Yi et al., 1992) found that the temperatures range $350°C$–$410°C$ coincided with that of the maximum of yield stress and the SRS minimum. This suggests that these anomalous behaviors are closely associated with strain ageing by solid solution strengthening.

Moreover, Sinha (Sinha and Asundi, 1977b) showed also that the values of the apparent activation volume for Zr–2.5 wt%Nb alloy are independent of strain. They vary from $20b^3$ at $25°C$ to $110b^3$ at $290°C$. These values have a comparable magnitude to those found for sponge zirconium (Gupta and Arunachalam, 1968) and Zircaloy–4 (Coleman et al., 1972). These materials have almost the same interstitial content, which suggests that the rate–controlling mechanism of plastic flow is the same in all these materials. This mechanism is associated with the thermally activated overcoming of interstitial solutes by dislocations.

IV.1.5 Minimum in ductility and elongation for increasing temperatures

For Zircaloy–4, the plot of fracture strain (ε_t) and necking strain (ε_n) with respect to the test temperature shows that ε_t and ε_n decrease with temperature between $250°C$ and $400°C$ as shown in figure IV.9. These behaviors are anomalous since for most metals, the values of ε_t and ε_n increase with temperature. Such anomalous effects are also observed in Zr–2.5 wt%Nb for which the ductility is found to decrease with increasing temperature. However, they are

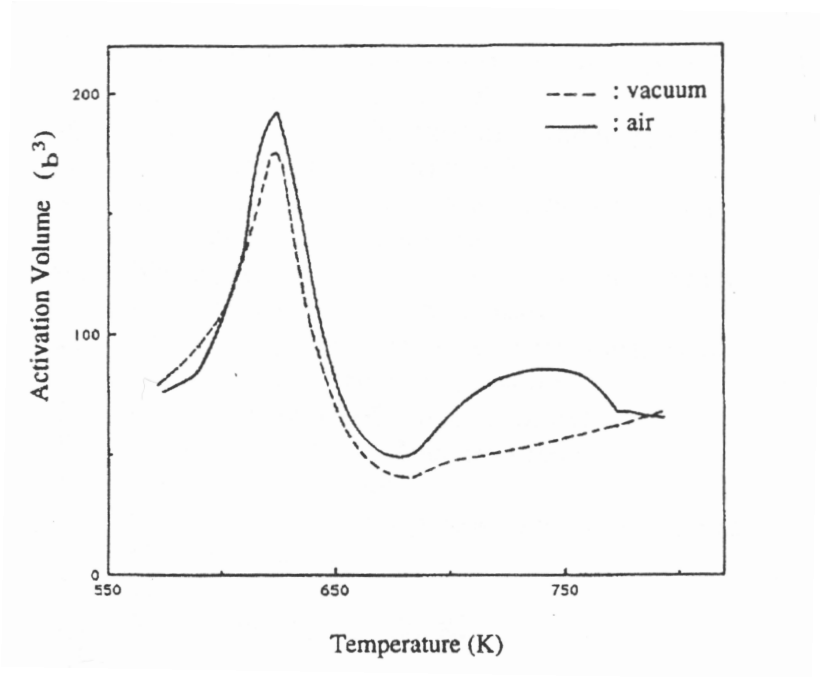

Figure IV.8 : Apparent activation volume versus temperature for Zircaloy–4 (Yi et al., 1992).

almost insensitive to strain rate changes (Sinha and Asundi, 1977a). The total elongation value is minimum at $290°C$.

Ahn et al. (Ahn and Nam, 1990) showed that the maximum uniform strain (ε_u) is obtained in the same temperatures range where the minimum values of ε_t and ε_n are observed. The strain rate dependence of the maximum value in ε_u is also the same as those of the minimum values in ε_t and ε_n. The strain rate for which ε_u is maximum versus temperature plots lead to determine the activation energy of this process, equal to 195 $kJ.mol^{-1}$. This value is very close to the values reported for the oxygen diffusion energy in α zirconium. All the results introduced above strongly indicate that the anomalous behavior of the uniform strain and necking strain is controlled by the strain ageing of oxygen atoms at the moving dislocations.

In figure IV.10, the fracture elongation of Zircaloy–4 is plotted as a function of temperature. A minimum in ductility is observed at each strain rates. The minimum is shifted to higher temperature with increasing strain rate. The type of fracture in the temperatures region of the elongation minimum is typically of a ductile nature (Hong et al., 1983) in Zircaloy–4. In this material, low SRS concentrates the deformation resulting in a low ductility.

The minimum elongation can be related to the minimum of strain rate sensitivity. When a neck forms, the strain rate in the necked region increases. If SRS is high, the increase of strain rate in the necked region may increase the resistance to flow sufficiently so that deformation tends to occur above and below the neck. In contrast, low value of SRS promotes strain localization in the neck, once a neck is formed, resulting in low ductility. Therefore we can conclude that the activation energy obtained from the shift of the elongation minimum temperature with the change in strain rate is close to that of strain ageing. The Arrhenius plot of strain rate versus the inverse of the elongation minimum temperature leads to an activation energy of 205 $kJ.mol^{-1}$ for Zircaloy–4. This value corresponds to the activation energy for oxygen diffusion in α zirconium.

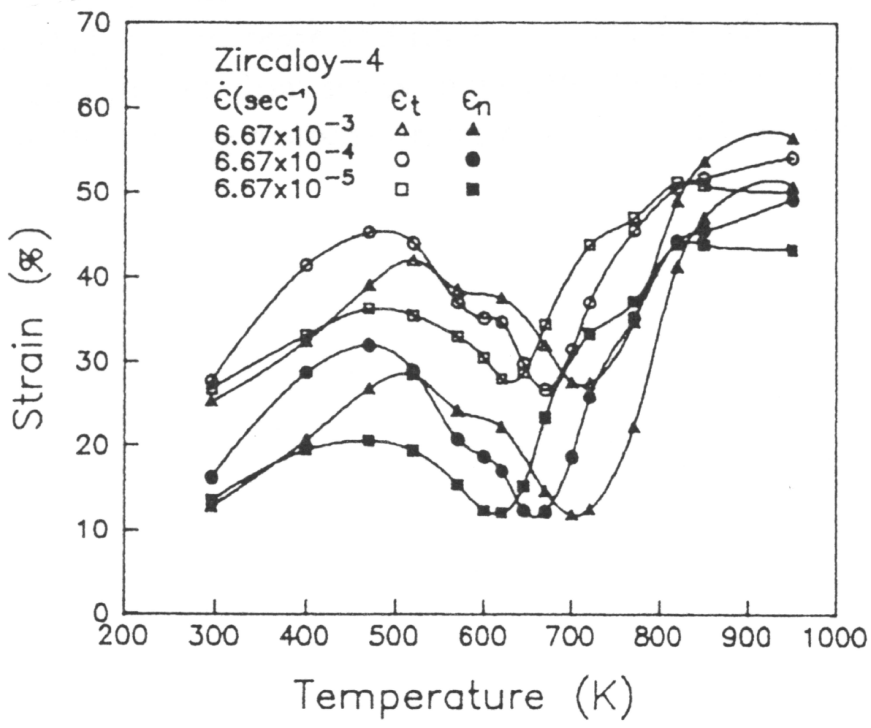

Figure IV.9 : Total and necking strain (ε_t and ε_n) of Zircaloy–4 versus temperature for three strain rates (Ahn and Nam, 1990).

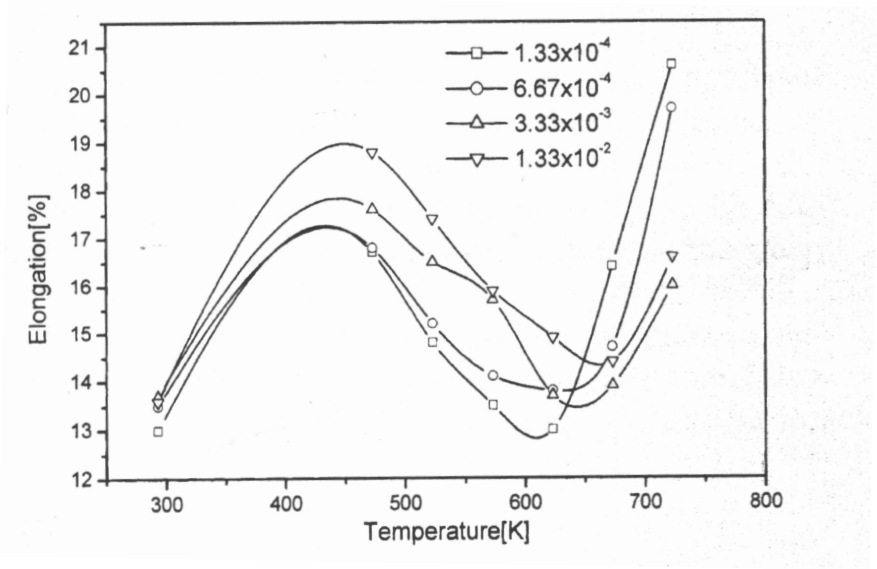

Figure IV.10 : Variation of elongation of Zircaloy–4 as a function of temperature and strain rate (Lee et al., 2001).

As a conclusion of this section, table IV.2 gives a comparison between some values of the activation energy for bulk diffusion of oxygen in various zirconium alloys according to different experimental methods and authors.

Table IV.2 : Values of the activation energy for oxygen bulk diffusion in different zirconium alloys according to various experimental methods and authors.

Activation energy for oxygen diffusion ($kJ.mol^{-1}$)	Materials	Experimental methods and authors
228	Zircaloy–4	expanding copper mandrel test (Yi et al., 1992)
205	Zircaloy–4	tensile test (Ahn and Nam, 1990) (Lee et al., 2001)
207	α zirconium	static strain ageing test (Veevers, 1975)
213	α zirconium	static strain ageing test (Ritchie and Atrens, 1977)
184	α zirconium	tensile test (Ahn and Nam, 1990)
220	Zircaloy–2	tensile test (Choubey and Jonas, 1981)

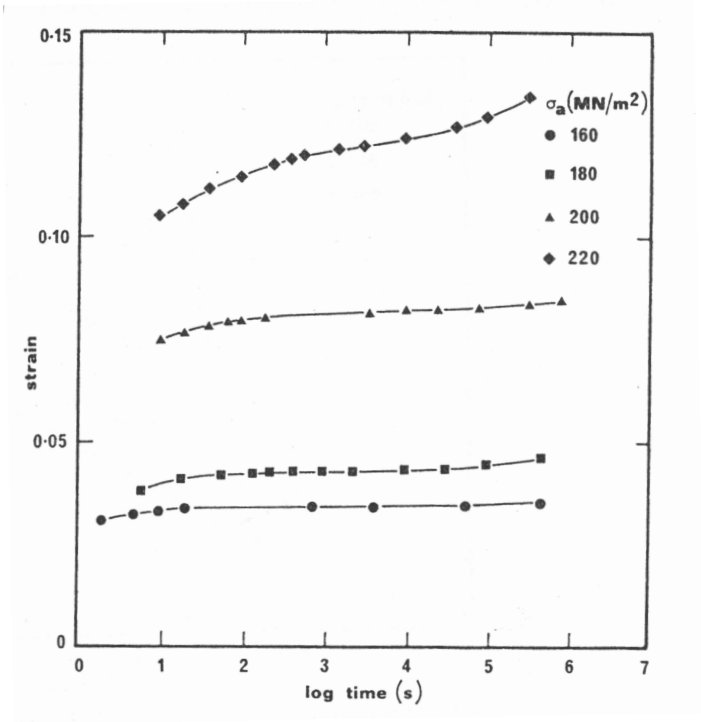

Figure IV.11 : Creep curves for Zr–1 wt%Nb alloy at 300°C plotted as strain against log time (Thorpe and Smith, 1978a).

IV.2 Effect of strain ageing on creep behavior

The review of the literature on the creep of α zirconium and Zircaloy–2 shows that it is not possible to define unambiguously the rate controlling mechanisms. Various conclusions were drawn by different authors, which is also the case regarding to the tensile properties of these alloys. Knorr and Notis (Knorr and Notis, 1975) tried to clarify the matter by constructing deformation mechanism maps (Ashby, 1972) for α zirconium and Zircaloy–2. These maps were constructed by selecting the appropriate parameters from the literature. However the drastic changes in creep properties due to strain ageing phenomena (Snowden, 1970) were not taken into account.

Such an anomalous change in creep properties was observed by Thorpe (Thorpe and Smith, 1978a) for Zr–1 wt%Nb alloy at 300°C. The strain as a function of the logarithm of time is shown in figure IV.11 for various applied stresses. A transition from hyperbolic to parabolic creep is observed where the curves exhibit an inflexion point. For many metals, creep transient undergoes the transition from hyperbolic form. With increasing temperature, the creep transient changes to logarithmic to parabolic form (Cottrell, 1953).

The effect of temperature on the strain rate is shown in figure IV.12. The strain rate decreases very rapidly typically by three orders of magnitude when temperature increases up to 275°C. However, the decrease of the creep rate is less drastic at longer times and higher stresses as shown in figure IV.11. Then, a rapid increase in creep rate with temperature is observed in the vicinity of 350°C. This minimum in the creep rate versus temperature diagram can be related to strain ageing. Possibly, the strain ageing process in this zirconium alloy causes an exhaustion of mobile dislocations by locking sources. The minimum of creep rate can be attributed to strengthening effect due to strain ageing.

The sudden decrease in creep rate with temperature implies a ”negative apparent

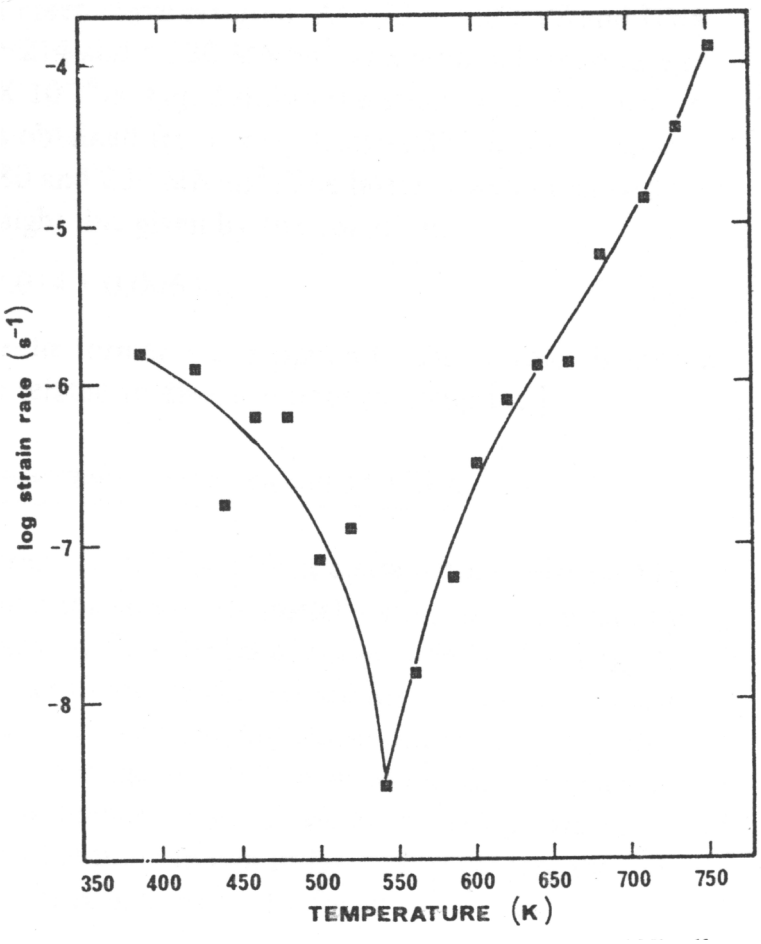

Figure IV.12 : Effect of temperature on creep rate of Zr–1 wt%Nb alloy at an applied stress level of 180 MPa (Thorpe and Smith, 1978a).

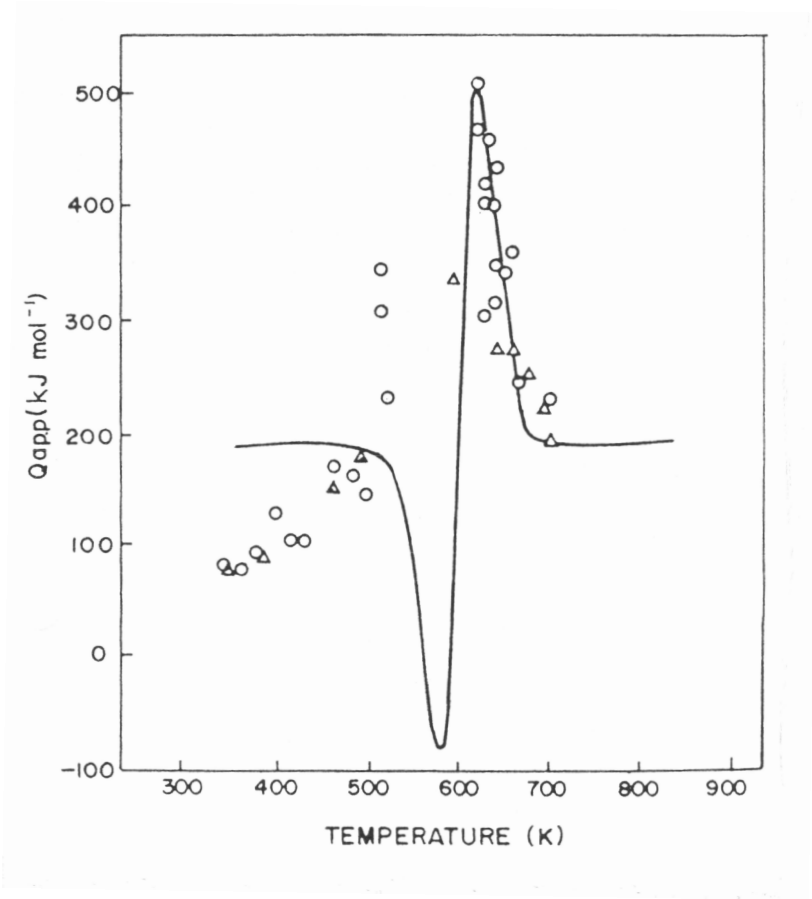

Figure IV.13 : Variation in activation energy for creep of Zircaloy–2 with temperature at 138 MPa. In straight line, the predicted values, by rounds the values of Zircaloy–2 taking in transverse direction, by triangle the values of Zircaloy–2 loading in longitudinal direction (Hong, 1984).

activation energy" and the rapid increase in creep rate with temperature implies a high activation energy. These effects were observed by Hong (Hong, 1984) for Zircaloy–2 as shown in figure IV.13. Negative activation energies for creep were also reported for Zr–2.5 wt%Nb alloy. Usually high activation energies for creep were observed for $Al - 3\%Mg$ alloys (Borch et al., 1960) in the temperatures range in which strain ageing phenomena are active. So the physical meaning of activation energy determined under these conditions is questionable. It is suggested that the high creep apparent activation energy and the negative apparent activation energy are caused by solute strengthening term due to strain ageing phenomena.

The equations suggested by Hong (Hong, 1984) are useful to simulate the maximum of yield stress and the negative activation energy but also to simulate the minimum SRS. Note that according to the direction of material loading (in the transverse or longitudinal rolling directions), the macroscopic behavior is different linked to crystallographic texture.

More recently, Pujol (Pujol, 1994) studied the creep behavior of α type 702 zirconium, called Zr702 and showed that there are two domains of stress labeled D1 and D2 for which the deformation mechanisms are different. According to the applied stress level, D1 is the domain where a saturation of deformation is reached and D2 is the domain where the creep behavior is more classical. Figure IV.14 shows these two domains at $150°C$.

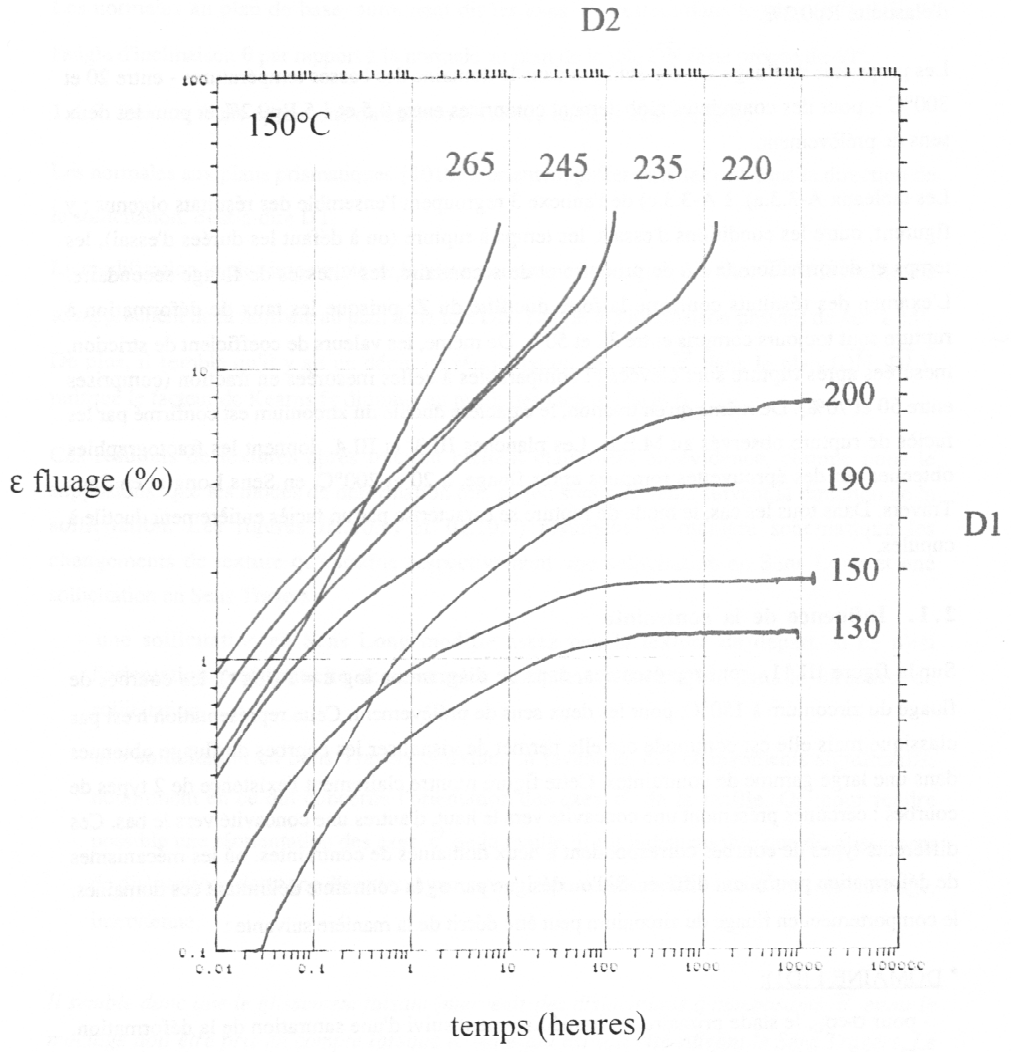

Figure IV.14 : Creep behavior of Zr702, for loading at various stresses (MPa) in the transverse rolling direction at 150°C. The logarithm of creep strain is plotted as a function of time (Pujol, 1994).

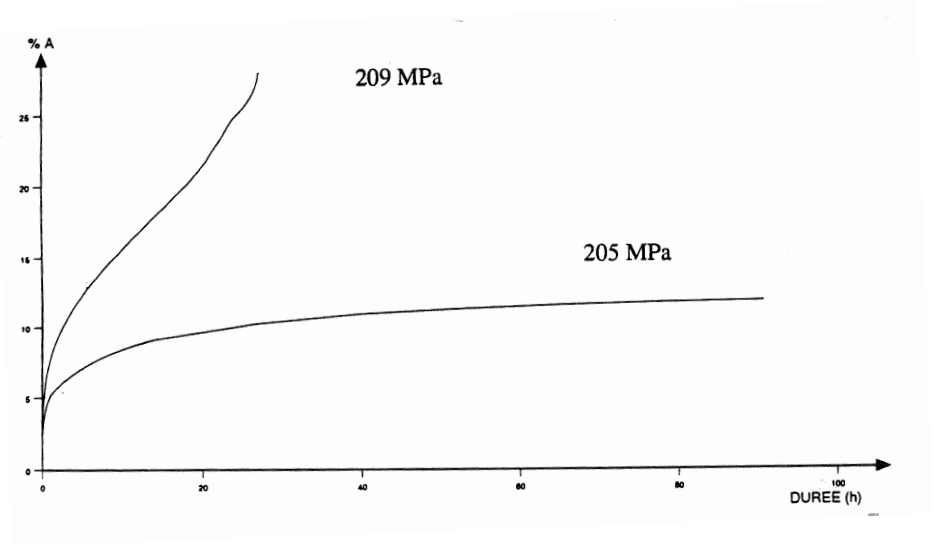

Figure IV.15 : Creep behavior of Zr702 in longitudinal direction of rolling at $200°C$ in the strain–time space (Pujol, 1994).

The limit between the domains D1 and D2 is particularly sharp. That is why the stress defining the two domains is labeled the critical stress σ_c. Table IV.3 gives the values of the critical stress for the two directions, transverse and longitudinal as a function of temperature. "Creep arrest" is observed for loading both in the transverse and longitudinal directions.

Table IV.3 : Critical stress (σ_c) between the creep domains D1 and D2 as function of temperature (Pujol, 1994).

Temperature ($°C$)	σ_c Longitudinal direction (MPa)	σ_c Transversal direction (MPa)
100	200–240	200–240
150	200–220	190–220
200	205–209	190–195

The creep arrest is observed at $150°C$ and $200°C$, but it is less evident at $100°C$ and $20°C$ for which one expects to wait for larger creep times than those studied by Pujol. The author showed a strong stress sensitivity at $200°C$. Figure IV.15 shows that when applied stress is increased by 4 MPa, the experiment test leads to fracture for Zr702 loaded in longitudinal direction.

Especially, in the domain D1 (for $\sigma < \sigma_c$), the stage I is followed by saturation of deformation. This phenomenon implies a creep rate nearly equal to zero (smaller than $10^{-9}s^{-1}$). Although the applied stress is near or larger than the yield stress, the creep times are very important (larger than to 10000 hours). Thus creep is logarithmic at $150°C$ for an applied stress of 200 MPa. The author showed that the time for creep arrest is lower for higher temperatures. The phenomenon responsible for the saturation of deformation is thermally activated. The activation energy determined is about 1.76 eV ($170\ kJ.mol^{-1}$). Figure IV.16 shows the thermal activation of the phenomenon for the transverse direction.

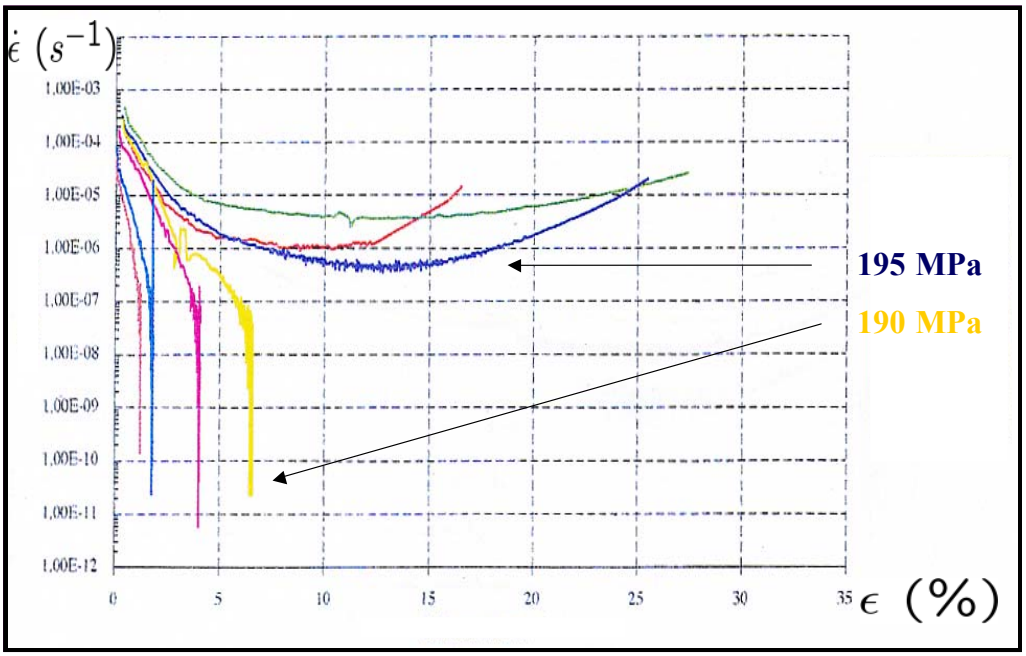

Figure IV.16 : Creep behavior at $200°C$ for Zr702, taken in transverse direction of rolling in the logarithm of creep rate versus strain curve (Pujol, 1994).

The maximum value of the saturation deformation obtained in the domain D1 at $200°C$ is about 15% for Zr702, taken in the longitudinal direction and about 7% for Zr702, taken in the transverse direction.

In the domain D2 ($\sigma > \sigma_c$), the curves are classical. During the stage I, the creep rate decreases. During the stage II, the creep rate is constant. Then during the stage III, the creep rate increases faster up to the fracture of the sample. In this domain, the stress sensitivity is defined by these two parameters:

$$-[\frac{\partial log(t_R)}{\partial log\sigma}]_T \quad ; \quad [\frac{\partial log(\dot{\varepsilon}_s)}{\partial log\sigma}]_T \tag{IV.5}$$

where t_R is the fracture time and $\dot{\varepsilon}_s$ is the secondary creep rate. The activation energy found for these two parameters is about 1 eV (96.6 $kJ.mol^{-1}$).

Graff (Graff and Béchade, 2001) studied the creep behavior under internal pressure of Zircaloy–4 in stress relieved state in the temperatures range $20°C$–$380°C$. They distinguished two domains of temperatures. Between $20°C$ and $300°C$, the creep is called "intermediate", with mainly stage II for applied stresses between 327 MPa and 825 MPa. For some temperature, as $150°C$, the creep arrest is observed. Within this domain, two sub–domains of temperatures can be defined:

- from $20°C$ to $150°C$, the creep rates are very low, close to 10^{-10}–10^{-9} s^{-1}. The stress sensitivity parameter defined by $m = \dfrac{\partial \log \dot{\varepsilon}_p}{\partial \sigma}$ is high, between 8 and 11.

The activation energy is also very low, inferior to 40 $kJ.mol^{-1}$,

- from 150°C to 300°C, the creep kinetics are modified. This effect is explained by strain ageing. The stress sensitivity parameter is equal to 5 and the activation energy is stable around 40 $kJ.mol^{-1}$.

Between 300°C and 380°C, the creep is mainly stage II for stresses between 101 MPa and 434 MPa. The creep rates are high, between 10^{-8}–10^{-6} s^{-1}. The stress sensitivity is between 7 and 3. The activation energy increases strongly when decreasing the temperature, to reach 150 $kJ.mol^{-1}$. Consequently, the mechanisms controlling the creep kinetic are not the same according to the ranges of temperatures and stresses.

IV.3 Effect of strain ageing on relaxation behavior

Kapoor (Kapoor et al., 2002) studied the relaxation phenomenon of zirconium alloys doped with niobium, tin and iron. In the strain rates range 10^{-4} s^{-1}–10^{-6} s^{-1} and in the temperatures range 20°C–500°C, the activation parameters are studied as a function of strain using the stress–plastic strain rate and stress–temperature relationships. The stress versus strain rate diagram is obtained using the stress relaxation technique. In general during stress relaxation, stress as well as the absolute value of stress rate both decrease with time. The yield stress can be separated in two components, on the one hand a thermal stress (also called viscous stress) depending only on the instantaneous strain rate and temperature and on the other hand an athermal stress depending only on deformation. During a relaxation test, plastic strain rate is continuously decreasing with time, thus activation volume varies with both stress and strain rates. The apparent activation volume versus the thermal stress, σ^* plot at 10^{-4} s^{-1} is shown in figure IV.17, where b is the Burgers vector taken as $b = 3.2\ 10^{-10}$ m. The activation volume increases with decreasing thermal stress. It is unaffected by strain up to 0.09 strain level. The activation enthalpy, ΔH versus σ^* is also shown in figure IV.17 on the second y axis. ΔH increases with decreasing thermal stress. Kapoor (Kapoor et al., 2002), Lee (Lee, 1972) and Conrad (Conrad, 1964) on the basis of stress relaxation experiments, concluded that substitutional solutes, niobium and aluminium contribute only to the athermal component of the flow stress in zirconium–niobium and Ti–Al alloys respectively.

Pujol (Pujol, 1994) studied the relaxation behavior, especially the influence of temperature, the value of the initial plastic strain and the applied strain rate during loading for Zr702, along the transverse direction. The author observed that there are differences between the macroscopic behavior at 20°C and 200°C. Up to about 100 hours, the relaxation is always effective at 20°C contrary to 200°C at which the stress relaxation is significantly smaller. Consequently, at this temperature, a threshold stress σ_s exists upon which the stress relaxation is stopped. This effect is called the "relaxation arrest". At 200°C, σ_s is about 250 MPa. One can argue that there is an interaction between dislocations and solute atoms to explain this threshold stress at 200°C. The diffusion of solute atoms being faster at 200°C than at 20°C, the solute atoms can pin the dislocations, thus limiting their moving.

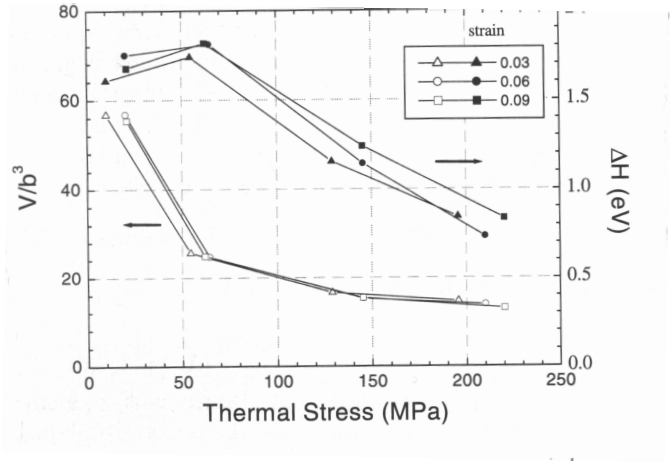

Figure IV.17 : Experimental activation volume and activation enthalpy versus thermal stress at a strain rate of $10^{-4}\ s^{-1}$ (Kapoor et al., 2002).

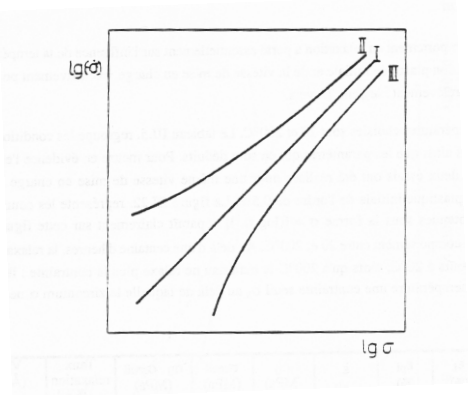

Figure IV.18 : Various type of relaxation curves in $log(-\dot{\sigma})$ versus $log(\sigma)$ plot (Hamersky and Trojanova, 1985).

Hamersky and Trojanova (Hamersky and Trojanova, 1985) showed that whatever the plastic strain, the activation volumes are larger at $200°C$ (1000 Å$.atom^{-1}$) than at $20°C$ (300 Å$.atom^{-1}$). Dislocation glide is controlled by the crossing of localized obstacles. The activation volume is an indication for the extension of considered obstacles. The values suggest that the crossing of these obstacles requires more energy at $200°C$ than at $20°C$. Moreover, these authors showed also three types of relaxation curves in $log(-\dot{\sigma})$ versus $log(\sigma)$ plot. Figure IV.18 shows these three types:

- type I: the dependence is linear,
- type II: the concavity is turned towards the top,
- type III: the concavity is turned towards the bottom.

For zirconium alloys, they showed that, at room temperature, the dependence is linear. They linked this type of variation with a thermally dislocation glide process without diffusion. In the case of variation of type III, they suggested that two mechanisms are superimposed (but they were not identified) or there existed one mechanism with a threshold stress.

Chapter -V-

Conclusion

The bibliography study is a synthesis of the current state of knowledge, regarding especially strain ageing phenomena in zirconium alloys. This review permits to define more clearly the context of our study, entitled: "Viscosity behavior of zirconium alloys in the temperatures range $20°C$–$400°C$: characterization and modeling of strain ageing phenomena". Complex strain ageing phenomena were observed in various zirconium alloys according to different experimental methods and authors. However, these manifestations of strain ageing have not yet been adequately characterized because of the multiplicity of alloying elements and chemical impurities. The phenomena of SSA and DSA, associated sometimes with PLC effect reach a maximum around $200°C$–$400°C$ in zirconium alloys. The points which are interesting for us are the following:

- the relaxation modes theory of paired point defects in h.c.p. crystals and internal friction measurements reveal that anelastic effects, attributed to the stress induced ordering of s–i atom pairs in zirconium alloys are responsible for jumps of oxygen interstitial atoms, parallel to the basal plane. The three phenomena, SSA, DSA and PLC effect have the same physical origin: the interaction between oxygen atoms (interstitial elements) interacting at short range distance with substitutional elements and moving dislocations,
- the oxygen content and the nature of substitutional atoms may play an important role on strain ageing behavior. The temperature dependence of the stress peak, associated with SSA is strongly affected by substitutional alloying elements and the height of this peak depends on oxygen content,
- the activation energy for bulk diffusion of oxygen established according to different experimental methods and various zirconium alloys lies between 184 $kJ.mol^{-1}$ to 228 $kJ.mol^{-1}$,
- even for oxygen content inferior to 100 wt ppm, this element is responsible for a fast anchoring of dislocations, which leads to important effects on the macroscopic behavior. For instance, anomalous behaviors are observed during yielding including: Lüders phenomenon, plateau or maximum in the flow stress versus temperature diagram, minimum in the SRS versus temperature plot, minimum in the apparent activation volume versus temperature diagram and minimum in ductility and elongation for increasing temperature. However, the effect of strain ageing phenomena on the toughness of zirconium alloys is not well documented and characterized,

- strain ageing exerts also a strong effect on creep and relaxation behavior. Drastic changes in creep properties such as a sudden decrease in creep rate for temperatures where strain ageing is active are observed. The relaxation can be stopped at some temperatures, due to the existence of a threshold stress. We have called these effects, the creep arrest and the relaxation arrest.

This bibliography review was used to direct the experimental and numerical aspects of this thesis introduced in the next chapters. The main points are the following.
The impact of interstitial and substitutional elements on strain ageing effects is studied by comparing the strain rate sensitivity of various zirconium alloys, whose chemical compositions were precisely chosen.
The important role of strain ageing phenomena on tensile yielding and relaxation behavior is studied in the temperatures range $100°C$–$400°C$. Especially, the influence of plastic strain (rate) localization phenomena is studied according to both scales, macroscopic and mesoscopic in the domain of temperatures and strain rates where strain ageing is active.
A modeling of strain ageing effects, observed experimentally in dilute zirconium alloys is suggested, using a macroscopic strain ageing model. In the literature, various constitutive models, taking the physical mechanisms of strain ageing into account were suggested. These models are able to simulate the negative strain rate sensitivity, taking the Lüders phenomenon and PLC effect into account. The model that we chose for our study is this suggested by McCormick (McCormick, 1988) and used in finite element simulation by Zhang and McCormick (Zhang et al., 2000).

Part B

Experimental study of strain ageing phenomena in dilute zirconium alloys in the temperatures range $20°C$–$400°C$

Chapter -VI-

Materials and mechanical testing

Contents

Abstract: The aim of this chapter is to introduce the various zirconium alloys and the experimental techniques. Our attention is focused on:

- the various chemical compositions of the five zirconium alloys with the main alloying elements (oxygen, niobium, tin),
- the mechanical test procedures of the three experiments (strain rate controlled tensile tests, tensile tests with strain rate changes and relaxation tests with unloading).

VI.1 Introduction

Many of macroscopic strain ageing effects, observed in dilute zirconium alloys have been related to various forms of strain ageing. However, these phenomena have not yet been adequately characterized because of the multiplicity of alloying elements and chemical impurities, although a variety of mechanisms have been suggested. In the bibliography part A, the important role of substitutional atoms on strain ageing is evidenced. That is why, in order to better understand the elasto–viscoplastic behavior of zirconium alloys in the temperatures range $20°C$–$400°C$, especially the strain ageing phenomena, new zirconium alloys were specially processed within the framework of "Contrat de Programme de Recherche

CEA–CNRS–EDF" called "Simulation des Métaux des Installations et Réacteurs Nucléaires" (CPR SMIRN). The fabrication route was investigated at CEA/Saclay, thanks to "Direction de la Recherche Technologique" tools at "Laboratoire Technologies des Milieux Extrêmes" (LTMEx), starting from a bar of zirconium with 2.2 wt% hafnium and low oxygen content (about 80 wt ppm). Then the influence of the nature of substitutional atoms were tested, elaborating other compositions with niobium content (1 wt%). Moreover to better characterize the effect of interstitial atoms (oxygen atoms), various compositions, especially with different oxygen contents (from 80 wt ppm to 1200 wt ppm) were elaborated (Béchade, 2004). Thus, the various zirconium alloys studied are the following:

- zirconium with 2.2 wt% hafnium, labeled ZrHf,
- ZrHf with 1 wt% nobium added, labeled ZrHf-Nb,
- ZrHf with 1100 wt ppm oxygen added, labeled ZrHf–O,
- ZrHf with 1 wt% nobium and 1100 wt ppm oxygen added, labeled ZrHf–Nb–O.

All of our investigations were performed in the temperatures range $20°C$–$400°C$. More precisely, the temperatures around $200°C$–$400°C$, which are known to be those where strain ageing phenomena are active in zirconium alloys were aimed. These four zirconium alloys were compared to one reference material, the type 702 zirconium, labeled Zr702 (VI.1). This alloy is mainly used in chemical engineering applications (Miquet, 1982), but also in nuclear industry for applications involving severe combinations of temperature and reactive environment, especially for the reprocessing of used fuel. This material was studied by Pujol (Pujol, 1994). However, this material has not been adequately characterized in the temperatures range $200°C$–$400°C$.

For each temperature, the experimental techniques were based on:

- standard tensile tests at various applied strain rates to observe plateau or peak in the flow stress versus temperature diagram,
- tensile tests with strain rate changes to obtain the values of the SRS parameter,
- repeated relaxation tests, including an unloading sequence before reloading in order to evaluate internal stresses and to obtain information about deformation mechanisms in the tested zirconium alloys.

The main objective of these mechanical experiments is to better characterize:

- the effect of strain ageing on tensile properties (application to Zr702),
- the impact of interstitial and substitutional elements on strain ageing effects by studying the evolution of SRS as a function of temperature (comparisons between Zr702, ZrHf, ZrHf–Nb, ZrHf–O, ZrHf–Nb–O),
- the effect of strain ageing on relaxation behavior (comparison between Zr702 and ZrHf).

This chapter is divided into two main sections. First, the microstructural characterization of all these zirconium alloys is presented. Then, we introduce the experimental techniques.

Table VI.1 : Chemical composition of Zr702 (Zr balance).

Element	C	H	O	N	Cr	Fe	Ni	Sn
(wt%)	0.0058	0.0004	0.1300	0.0033	0.0240	0.0760	0.0050	0.2230

VI.2 Microstructural characterization of the zirconium alloys

VI.2.1 Chemical composition

The standard composition for Zr702 is given in table VI.1.
The initial product, zirconium crystal bar refined by the Van Arkel–De Boer iodide decomposition process, consists in several rods (25 mm diameter) with large grains of high purity alloy containing 2.2 wt% hafnium content (ZrHf) as found in the nature (material for non nuclear applications). In order to obtain a final product with small grains and an homogeneous microstructure, the processing of the crystal bar was performed at LTMEx (CEA at Saclay). Specific fabrication route (hot rolling at $760°C$; $\varepsilon = 25\%$ and cold rolling; $\varepsilon = 33\%$ and final heat treatment under vacuum; $700°C$ 2 hours) was followed to obtain plates, about 8 mm thickness in recrystallized metallurgical state. Various chemical compositions were obtained, starting from ZrHf in order to quantify the effect of alloying elements (oxygen and niobium) on plastic mechanism compared to the initial composition with very low oxygen content, about 80 wt ppm (interstitial element in octahedral position) and no substitutional element except hafnium:

- the first one with niobium addition (1 wt%), ZrHf–Nb,
- the second one with oxygen addition (0.11 wt% fixed but heterogenous distribution was found after processing, in the range 0.02%–0.2% due to high difficulties during melting process), ZrHf–O,
- the third one with niobium and oxygen additions (O: 0.12 wt% and Nb:1 wt%), ZrHf–Nb–O.

The content for the others elements was controlled after manufacturing in order to verify that no pollution occurred during melting process. The chemical compositions of the various zirconium alloys, based on ZrHf are given in table VI.2. The main features of the five zirconium alloys are the following.
For Zr702, the main substitutional atom is tin (Sn: 2230 wt ppm, high content) and the main interstitial atom is oxygen (O: 1300 wt ppm, high content).
For ZrHf, the main substitutional atom is hafnium (Hf: 2.2 wt%, high content) and the interstitial atom is oxygen (O: 84 wt ppm, low content).
For ZrHf–Nb, the main substitutional atoms are hafnium and niobium (Hf: 2.2 wt%, high content; Nb: 1 wt%, high content) and the interstitial atom is oxygen (O: 84 wt ppm, low content).
For ZrHf–O, the main substitutional atom is hafnium (Hf: 2.2 wt%, high content) and the main interstitial atom is oxygen (O: 1100 wt ppm, high content).
For ZrHf–Nb–O, the main substitutional atoms are hafnium and niobium (Hf: 2.2 wt%, high content; Nb: 1 wt%, high content) and the main interstitial atom is oxygen (O: 1200 wt ppm, high content).

Table VI.2 : Chemical composition of ZrHf, ZrHf–Nb, ZrHf–O, ZrHf–Nb–O (Zr balance).

Materials / Elements (wt%)	C	S	O	N	H	Fe	Si	Hf	Nb
ZrHf	0.008	0.001	0.0084	0.0007	0.00033	0.05	< 0.01	2.2	-
ZrHf–Nb	0.008	0.001	0.0084	0.0007	0.00033	0.05	< 0.01	2.2	1.0
ZrHf–O	0.008	0.001	0.1100	0.0007	0.00033	0.05	< 0.01	2.2	-
ZrHf–Nb–O	0.008	0.001	0.1200	0.0007	0.00033	0.05	< 0.01	2.2	1.0

VI.2.2 Microstructure

The polycrystalline Zr702, taken as reference alloy (8 mm sheet) exhibits equiaxed grains with average grain size of 15 μm–30 μm. The micrograph of Zr702 is shown in figure VI.1 (a). Typical recrystallized microstructure was found in this case.
ZrHf has similar microstructure compared to Zr702, with grain size in the range of 5 μm–30 μm. ZrHf with oxygen and/or niobium alloying elements present more heterogeneous microstructure especially in the case of oxygen additions. Through thickness analysis showed that, in few cases, strong heterogeneities with well recrystallized areas (with grain size in the range of 10 μm–30 μm) and non recrystallized ones with deformation bands (with elongated grains) were observed. In order to eliminate these areas, additional heat treatments were performed for ZrHf with oxygen and/or niobium alloying elements (two hours at $700°C$). The micrographs for ZrHf, ZrHf–Nb, ZrHf–O and ZrHf–Nb–O are shown in figure VI.1.

VI.2.3 Crystallographic texture

Global crystallographic textures were determined through the measurements of pole figures ((10.0), (00.2), (10.1), (10.2) and (11.0)) with x–ray diffraction techniques using a SIEMENS texture goniometer with copper radiation in reflexion up to 75° tilt angle. The pole figures are shown in figure VI.2 for the five zirconium alloys.

Previously, samples were polished and chemically etched in order to observe the specimen on a depth of 0.2 mm. Parallelepiped samples were cut from the initial plates, defined by three initial directions: RD, the rolling direction, TD, the transverse direction and ND, the normal direction. The three dimensional Orientation Distribution Function (ODF) analysis was applied for quantitative evaluation, using spherical harmonics algorithm.

Classical texture for cold rolled plates were found for Zr702 even for ZrHf and the other zirconium alloys with oxygen and/or niobium alloying elements. For Zr702, the <c> axis are mainly concentrated in the transverse/normal plane at approximatively 30°–40° from the normal direction and between 0° to 30° from the rolling direction. Consequently, the texture is not characteristic of a fully recrystallized material (Béchade, 1995). Kearns anisotropic factors, given in table VI.3, which are proportional to the volume fraction of basal planes oriented relative to the sample reference axis (fN along DN, fT along DT and fL along RD) were calculated from (00.2) pole figures, obtained after ODF analysis (Kearns, 1965). The analysis of these three factors shows the similarity between the different plates obtained from a texture point of view. The <c> axis (normal to the basal plane) are mainly oriented along the normal direction with a spread toward the transverse direction.

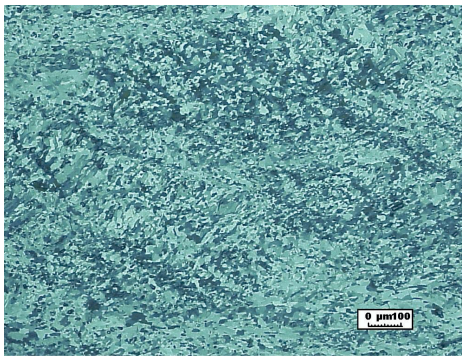

(a) Zr702

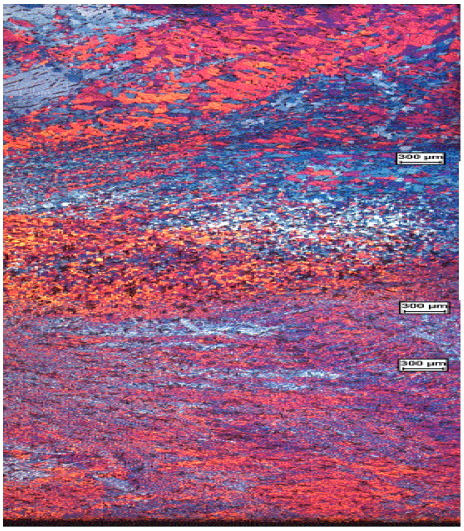

(b) ZrHf

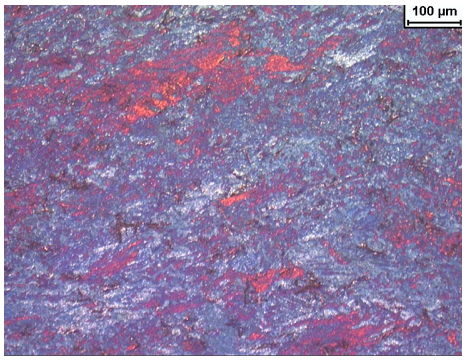

(c) ZrHf–Nb

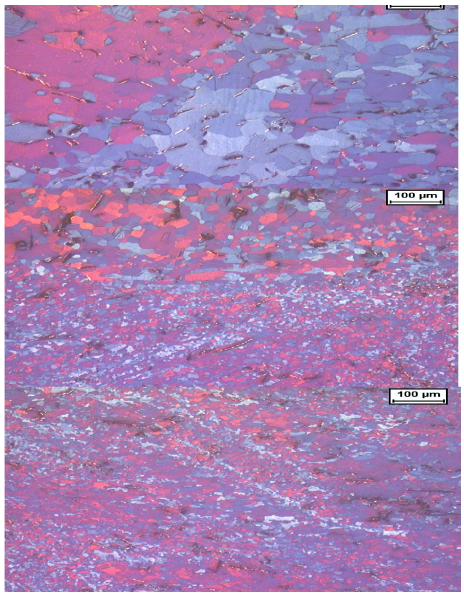

(d) ZrHf–O

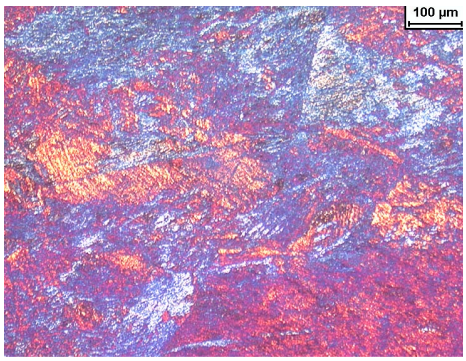

(e) ZrHf–Nb–O

Figure VI.1 : Micrographs of the five zirconium alloys.

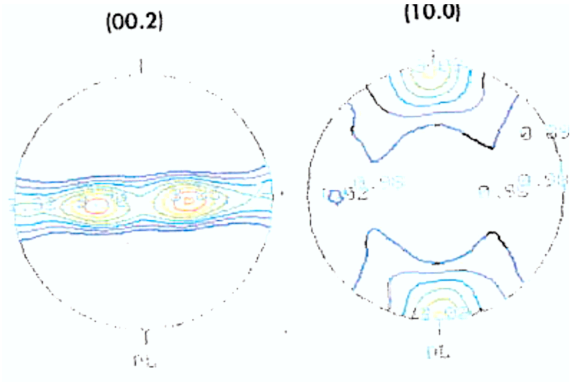

(a) Zr702

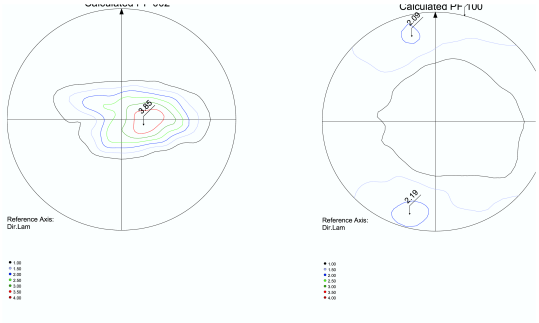

(b) ZrHf

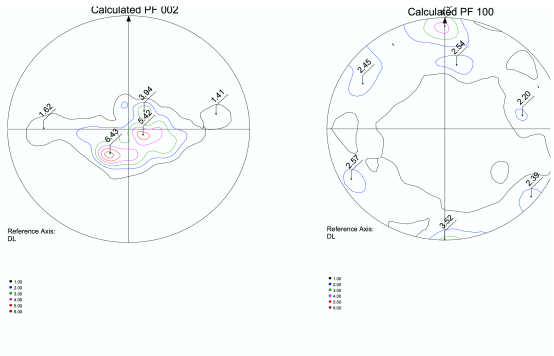

(c) ZrHf–Nb

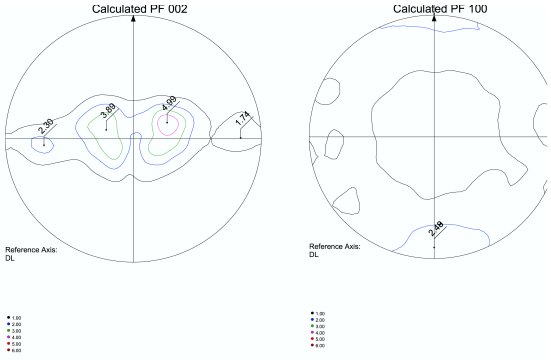

(d) ZrHf–O

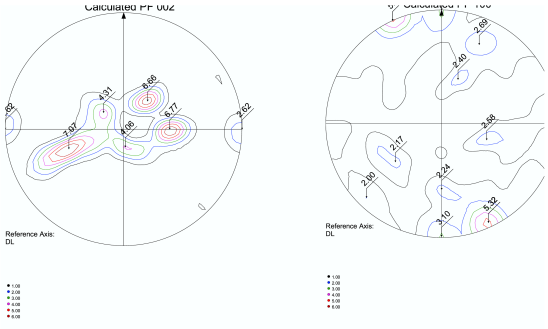

(e) ZrHf–Nb–O

Figure VI.2 : (00.2) and (10.0) pole figures for the five zirconium alloys.

Table VI.3 : Kearns factors.

Materials	fN	fT	fL
Zr702	0.578	0.273	0.150
ZrHf	0.583	0.285	0.132
ZrHf–Nb	0.610	0.244	0.146
ZrHf–O	0.601	0.282	0.117
ZrHf–Nb–O	0.549	0.332	0.119

VI.3 Mechanical testing: specimen geometry, experimental devices and test procedures

For temperatures between 20° to 400°C, the experimental techniques were based on standard tensile tests controlled at constant strain rates, tensile tests with strain rate changes and relaxation experiments with unloading.

VI.3.1 Strain rate controlled tensile tests

The material Zr702 is given in the form of a rolled sheet metal. Flat samples of Zr702 with gauge length of 55 mm, width of 4 mm and thickness of 1.4 mm were loaded in tension at various nominal strain rates of $10^{-3}s^{-1}$, $10^{-4}s^{-1}$, $10^{-5}s^{-1}$. Three directions are defined, compared to the sheet metal: RD, TD and ND. The taking directions are the following:

- when the direction of the applied stress is parallel to RD, the material is constrained in the longitudinal direction,
- when the direction of the applied stress is parallel to TD, the material is constrained in the transverse direction.

Figure VI.3 shows the plan of the tensile specimen. The experiments were carried out in a computer controlled screw driven Zwick testing machine. A computer was used online both for controlling the machine functions and for data acquisition. Note that no extensometer was used. A three zone resistance heating furnace was used. About 1 hour was necessary to heat the sample from room temperature to the prescribed temperature. The temperatures tested were 20°C, 100°C, 200°C, 300°C. The experimental data such as load and specimen cross section and length were used for calculating the values of the nominal stress σ and the nominal strain ε. The load cell had a ±10000 daN span. The strain accumulated during tension was determined from the cross head displacement.
The accuracy of the measurements during tensile test on flat specimens is the following:

- $\frac{\Delta\sigma}{\sigma} = \pm 3.4\ 10^{-2}$
- $\frac{\Delta\varepsilon}{\varepsilon} = \pm 6\ 10^{-3}$
- $\Delta T = \pm 10°C$

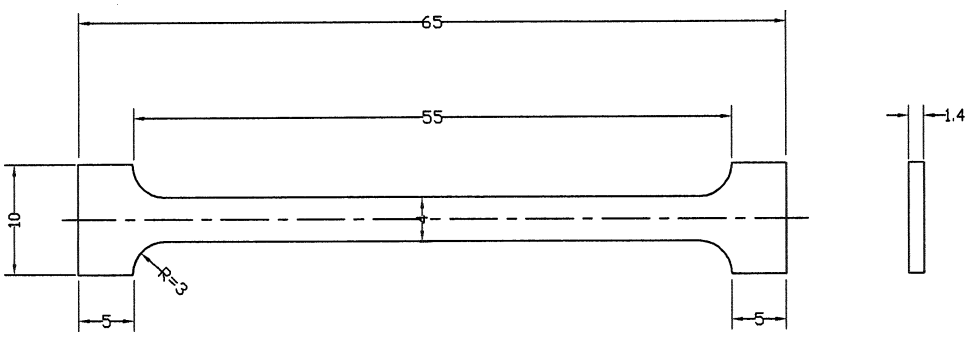

Figure VI.3 : Plan of the flat specimen of tensile tests.

VI.3.2 Tensile tests with strain rate changes

Tensile tests with strain rate changes were carried out on cylindrical samples with gauge length of 22 mm, diameter of 2.5 mm, initially elaborated for relaxation experiments. Figure VI.4 shows the plan of the specimen for tensile tests with strain rate changes.

These tests were realized on the machine used for the relaxation tests in order to not take the stiffness of the machine into account. Figure VI.5 shows the principle of the relaxation machine used for strain rate changes and relaxation tests. The tests were conducted on an ADAMEL T.R. creep machine, modified to be used for relaxation tests. The system of loading was made with an electric jack, equipped with a motor of low inertness continuous power, leading to the displacement of a steel wire fixed to one extremity of the control lever hand and the machine. A spring was placed between the load sensor and the wire in order to adjust the compliance of the machine and the gain in close loop of the regulation system in strain and/or stress. A resistance furnace surrounded the specimen with the extensometer. The temperature of the specimen during testing was controlled to within $\pm 0.2°C$. The temperature gradient along the gauge length was maintained at less than $2°C$. One hour was usually required to reach thermal equilibrium after an initial heat up period of approximately 15 min. The load cell range was 0–100 kN. The elongation value was measured using an extensometer, fixed on the ruffs of the specimen. The displacement was recorded by two L.V.D.T sensors with a stroke of 2 mm.

The loading was conducted at total constant strain rate. The specimens were subjected to strain rate change tests with a ten fold change. Both the load cell and the L.V.D.T. signals were first amplified and filtered. Load and elongation data were converted to nominal stress and nominal strain by the usual method using a computerised routine.
The accuracy of the measurements during tensile test on cylindrical specimen is the following:

- $\Delta\sigma = \pm 0.5 MPa$
- $\Delta L = \pm 0.5 \mu m$
- $\Delta\varepsilon = \pm 1.7\ 10^{-5}$
- $\Delta T = \pm 1°C$

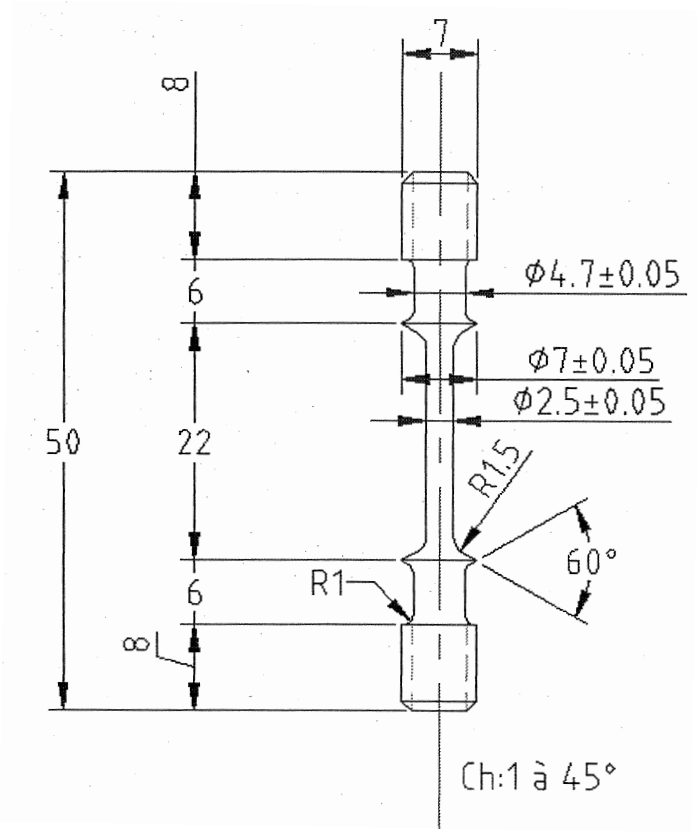

Figure VI.4 : Plan of the specimen of tensile tests with strain rate changes and relaxation tests.

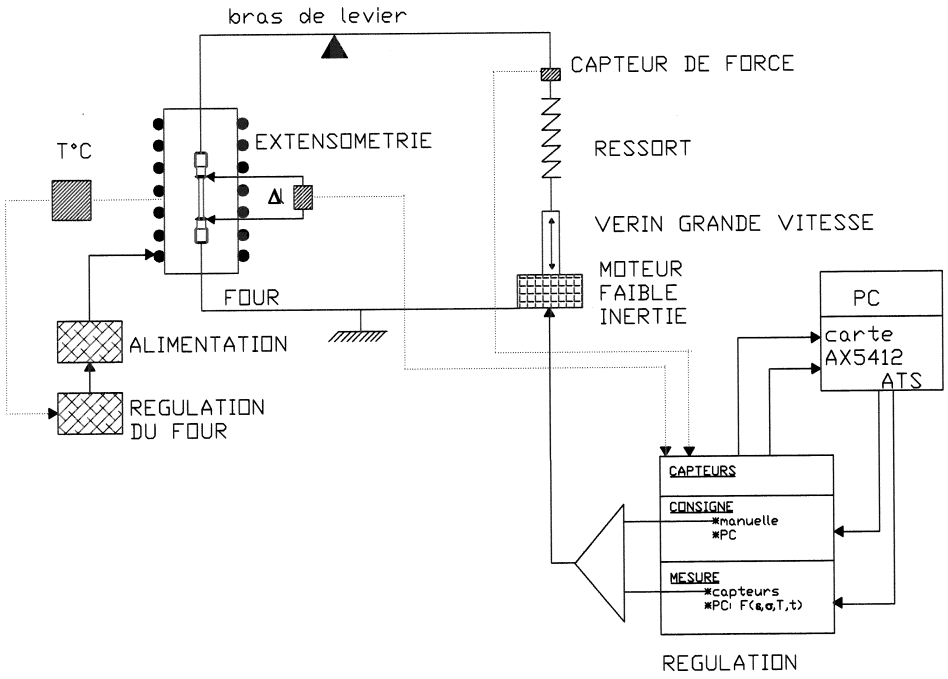

Figure VI.5 : Principle of the relaxation machine used for strain rate changes and relaxation tests.

VI.3.3 Relaxation tests with repeated loading and unloading

The main advantage of stress relaxation experiments is to describe the viscoplastic behavior of materials on a large interval of strain rates ($10^{-3}s^{-1}$–$10^{-9}s^{-1}$), contrary to creep tests which give only the strain response of materials at a given stress. These experiments are used for evaluating the constitutive relaxation governing the inelastic behavior of materials.
The general stress relaxation test was performed by isothermally loading a specimen to a fixed value of constraint. The constraint was maintained constant and the constraining force was determinate as a function of time. The major problem in the stress relaxation test was that constant constraint is virtually impossible to maintain. The effects on test results were very significant and considerable attention must be taken to minimize the constraint variation. This test can be divided into two steps.

1. **The loading**, the total strain is the sum of the elastic strain and plastic strain:

$$\varepsilon_{tot} = \varepsilon_e + \varepsilon_p \qquad ; \qquad \varepsilon_e = \frac{\sigma}{E} \tag{VI.1}$$

   where E is Young's modulus. When the sample was deformed at a given strain level, the loading was stopped and the relaxation phenomenon can begin.

2. **The relaxation**, the total strain obtained at the end of the loading was imposed constant $\varepsilon_{tot} = constant$. During the test, the decrease of stress with time was recorded. Deriving equation (VI.1) gives:

$$\dot{\varepsilon}_{tot} = \dot{\varepsilon}_e + \dot{\varepsilon}_p = 0 \qquad ; \qquad \dot{\varepsilon}_p = -\frac{\dot{\sigma}}{E} \tag{VI.2}$$

   where $\dot{\varepsilon}_{tot}$ is the total strain rate and $\dot{\varepsilon}_p$ is the plastic strain rate. Consequently, stress relaxation is a time dependent decrease of stress in a solid due to the conversion of elastic strain into inelastic strain.

Some definitions can be given as follows.
The initial stress, labeled σ_0 is the stress applied to the specimen by imposing the given constraint conditions before that stress relaxation begins.
The zero time, labeled t_0 is the time when the given loading or constraint conditions are initially obtained in a stress relaxation test.
The remaining stress, labeled σ is the stress remaining at a given time.
The relaxed stress, labeled $\sigma_0 - \sigma$ is the initial stress minus the remaining stress at a given time.
The stress relaxation curve is the plot of the remaining or relaxed stress as a function of time.
The relaxation ratio, labeled $\dfrac{|\sigma_0 - \sigma|}{\sigma_0}$ is the relative difference of stresses along the relaxation curve at a given time.
The plastic strain is $\varepsilon_p = \dfrac{\sigma_0 - \sigma(t)}{E}$.

Especially, in our relaxation tests, unloadings were performed between $100°C$ and $400°C$ on cylindrical specimens, taken in transverse direction. Thus, we call a "relaxation cycle", a stress relaxation test with unloading as shown in figure VI.6. A relaxation cycle is divided into four sequences as follows.

1. During the loading sequence, the specimens were deformed in tension under constant strain rate up to a given plastic strain level. In chapter A, we showed the effect of strain rate on the specimen loading (tensile tests with various strain rate changes, between $10^{-3}s^{-1}$, $10^{-4}s^{-1}$, $10^{-5}s^{-1}$). For the loading of specimen, we chose a strain rate equal to $10^{-4}s^{-1}$, because it was easier to control this strain rate with our testing machine.

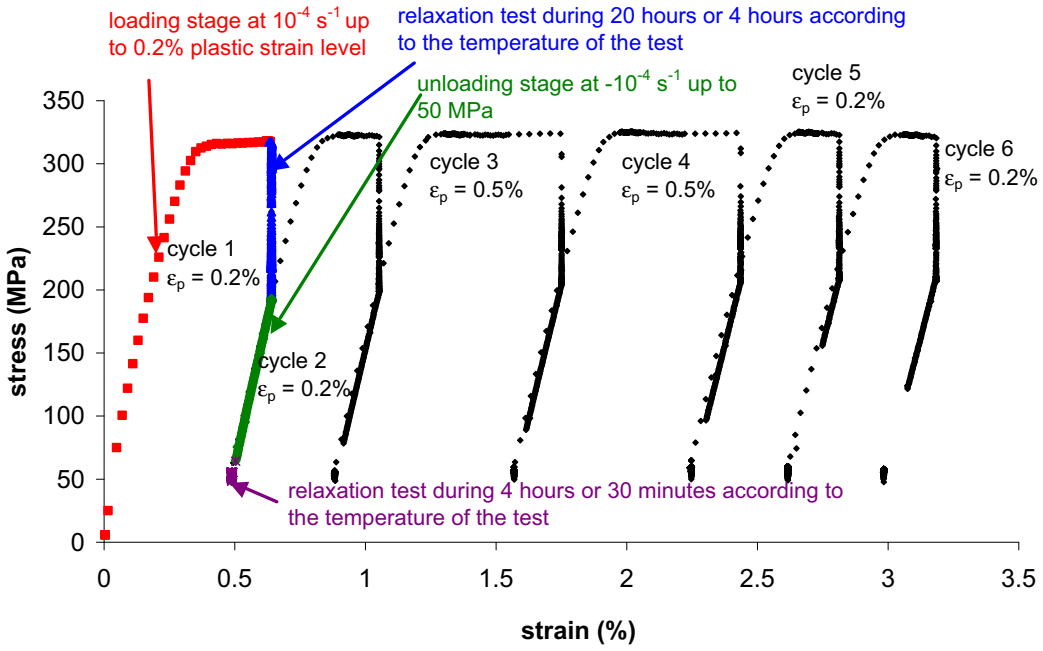

Figure VI.6 : Principle of the relaxation test with unloading, divided into six relaxation cycles in the true stress versus true strain diagram.

2. After loading the specimen up to the prescribed plastic strain level, the first relaxation sequence was performed at this plastic strain level. During the stress relaxation test, the total strain of the specimen was kept constant. The plastic elongation of the specimen was compensated by a decrease of the elastic part of the total strain. The time interval of relaxation depending on temperature was chosen in order to avoid the sample corrosion, susceptible to affect the macroscopic behavior. At $100°C$, $200°C$ and $300°C$, the interval of relaxation time was chosen equal to 20 hours. However at $400°C$, the interval of relaxation time was chosen equal to 4 hours, because of corrosion.

3. After the first relaxation sequence, the unloading of the specimen was carried out down to 50 MPa. The applied strain rate during unloading was $10^{-4}s^{-1}$.

4. Then, the second relaxation sequence was performed. It lasted 4 hours at $100°C$, $200°C$ and $300°C$. At $400°C$, the relaxation time was 30 minutes, in order to avoid oxygen diffusion inside the material during testing.

This sequence of experiments was repeated at various plastic strain levels in order to measure the response of materials according to different plastic strain levels (which is equivalent to the values of the initial stress). For each test, the value of the plastic strain level associated with the value of stress at which the relaxation test begins, σ_0 is given in appendix II for Zr702 and ZrHf as a function of temperature and the number of relaxation cycle. Note that only small deformations were studied, lower than 3% in order to first neglect the hardening effect and second to consider that the hardening rate is constant.

The accuracy of the measurements during relaxation test with unloading on cylindrical specimen is the following:

- $\Delta\sigma = \pm 2MPa/24\ hours$
- $\Delta L = \pm 0.5\mu m$
- $\Delta\varepsilon = \pm 1.7\ 10^{-5}$
- $\Delta T = \pm 1°C$

Note that this type of experimental set up is able to cover ranges of strain rates between $10^{-3}s^{-1}$ (because of the the dynamic compliance of the machine) and $10^{-9}s^{-1}$ (because of the noise due to the thermal instability of the machine and its environment).

Note that WDS microsonde experiments were carried out in order to quantify the oxygen content which might diffuse during relaxation tests with unloading (4–5 days) between $200°C$ and $400°C$. The results are the following:

- for Zr702, the maximal capture of oxygen is about 1000 wt ppm,
- for ZrHf and the other zirconium alloys doped with oxygen and niobium, no mean capture of oxygen was detected.

For all the materials, the capture of oxygen is more important in a depth of up to $15\mu m$ depth, close to the surface area of the samples. Consequently, the oxygen diffusion during the mechanical tests does not affect the macroscopic response of any material.

VI.4 Conclusion

This chapter allows to introduce the main objectives of the mechanical testing experiments carried out between $20°C$ and $400°C$ for the five zirconium alloys (Zr702, ZrHf, ZrHf–Nb, ZrHf–O, ZrHf–Nb–O), especially elaborated at CEA.
The principal objective of strain rate controlled tensile tests is to obtain the stress versus temperature diagram for Zr702.
The main objective of strain rate changes experiments is to compare the strain rate sensitivity of the five zirconium alloys. For this, the SRS parameter is determined at each temperature as follows:

$$SRS = (\frac{\Delta\sigma}{\Delta \log \dot{\varepsilon}})_{T,\varepsilon_p} \tag{VI.3}$$

The principal aim of relaxation experiments is to obtain information about the deformation mechanisms inh Zr702 and ZrHf by comparing their apparent activation volume at various temperatures, obtained from:

$$V_a = k_B T(\frac{\Delta \log \dot{\varepsilon}_p}{\Delta\sigma})_{T,\varepsilon_p} \tag{VI.4}$$

Chapter -VII-

Experimental results

Contents

Abstract: The aim of this chapter is to show experimental evidence of strain ageing phenomena (strain rate sensitivity, relaxation arrest) in the studied zirconium alloys (Zr702, ZrHf, ZrHf–Nb, ZrHf–O, ZrHf–Nb–O) for different loading conditions (tensile and relaxation tests). In particular, the role of interstitial and substitutional atoms, responsible for strain ageing on the macroscopic response is evidenced.

VII.1 Introduction

Various mechanical tests were carried out, including tensile tests at constant applied strain rates, tensile tests with strain rate changes and relaxation tests with unloading. The strain ageing behavior in the temperatures range $20°C$–$400°C$ was investigated in the five zirconium alloys:

- Zr702, containing 2280 wt *ppm* tin and 1300 wt *ppm* oxygen,
- ZrHf, containing 2.2 wt% hafnium and 100 wt *ppm* oxygen,

- ZrHf–O, containing 2.2 wt% hafnium and 1100 wt *ppm* oxygen,
- ZrHf–Nb, containing niobium and 100 wt *ppm* oxygen,
- ZrHf–Nb–O, containing niobium and 1100 wt *ppm* oxygen.

The following points are discussed:

- the dependence of macroscopic and physical parameters such as SRS and V_a as a function of temperature and plastic strain,
- the role of interstitial and substitutional atoms, responsible for strain ageing on the macroscopic response.

VII.2 Tensile tests

VII.2.1 Results

Tensile tests were carried out at various temperatures and at different applied strain rates. For these experiments, only Zr702 was tested. In the following, we call "transverse Zr702", Zr702 loading in the transverse direction and "longitudinal Zr702", Zr702 loading in the longitudinal direction. The study of the tensile behavior aims at characterizing the influence of various parameters: temperature (between $100°C$ and $300°C$), loading axis (longitudinal and transverse directions), imposed strain rate (between $10^{-5}s^{-1}$ and $10^{-3}s^{-1}$).

Note that, the tensile behavior of Zr702 at $20°C$ was thoroughly studied by Pujol (Pujol, 1994). Prior to the presentation of the results, some main remarks must be done about the experimental set up, used in these tensile tests.
The flat tensile specimens were designed to be mounted on a machine equipped with laser extensometer for detecting local strain heterogeneities (see the plan of sample in chapter VI). This type of sample is not conventional, favoring the localization of deformation. As a standard machine, it can lead to bending of samples during the first stages of mechanical tests. The strain which was cumulated during tension was determined from the cross head displacement. The elastic loading at the beginning of experimental tests also included the adjustment of sample in tensile direction. That is why, we do not discuss about elongation and fracture elongation. Note that most of the samples broke at one end of the specimen and not in the middle of the specimen.

The true stress–true strain responses of transverse Zr702 and longitudinal Zr702 as a function of the various applied strain rates ($10^{-3}s^{-1}$, $10^{-4}s^{-1}$, $10^{-5}s^{-1}$) were compared. Figure VII.1 and figure VII.2 show the comparison between the true stress–true strain responses from specimens of transverse Zr702 and longitudinal Zr702 as a function of the various applied strain rates ($10^{-3}s^{-1}$, $10^{-4}s^{-1}$, $10^{-5}s^{-1}$) at $200°C$ and $300°C$. Note that appendix II gives all the true stress–true strain curves of transverse Zr702 and longitudinal Zr702, as a function of temperature and applied strain rate.

VII.2.2 Concluding remarks

The tensile behavior of Zr702 tested along orthogonal directions exhibits the following characteristics:

- transverse Zr702 exhibits negligible work hardening before necking for each temperature contrary to longitudinal Zr702,
- at $100°C$, the stress level of both Zr702 increases with increasing strain rate as shown figures in appendix II. The strain rate sensitivity is similar for both directions whatever the applied strain rate. Standard viscoplastic behavior is recorded,
- at $200°C$, the strain rate sensitivity between $10^{-4}s^{-1}$ and $10^{-5}s^{-1}$ is larger than between $10^{-3}s^{-1}$ and $10^{-4}s^{-1}$ for both directions as shown in figures VII.1 (a), (b),
- at $300°C$, figures VII.2 (a), (b) show that the plastic flow increases very slightly with increasing strain rate for longitudinal Zr702. Note that, at the beginning of straining (up to a strain of 0.03), the true stress–true strain curve at $10^{-5}s^{-1}$ is significantly above those at $10^{-4}s^{-1}$ and $10^{-3}s^{-1}$. This effect is more pronounced for transverse Zr702 than for longitudinal Zr702.

To conclude, the main points that we observed for tensile tests are the following. For longitudinal Zr702, the strain rate sensitivity is close to zero, indeed negative for deformations smaller than 0.03. Negative strain rate sensitivity is observed for transverse Zr702 at $300°C$, between $10^{-5}s^{-1}$ and $10^{-4}s^{-1}/10^{-3}s^{-1}$. The so–called "athermal plateau" observed in the literature by Derep (Derep et al., 1980), for Zircaloy–4 between $300°C$ and $400°C$ at 3.3 $10^{-5}s^{-1}$ and for strains smaller than 0.03 (see chapter A) can be compared to this observed for transverse Zr702 between $200°C$ and $300°C$ for strains around 0.05 (stress level about 180 MPa).

However, tensile tests, carried out at constant applied strain rate and constant temperature seem to be limited to show experimental evidence of deformation mechanisms, because of the non conventional geometry of the samples and because of the fact that for each experiment the microstructures of samples are different. For the next set of experiments, we decided to carry out strain rate changes on the cylindrical specimens at various temperatures between $20°C$ and $400°C$.

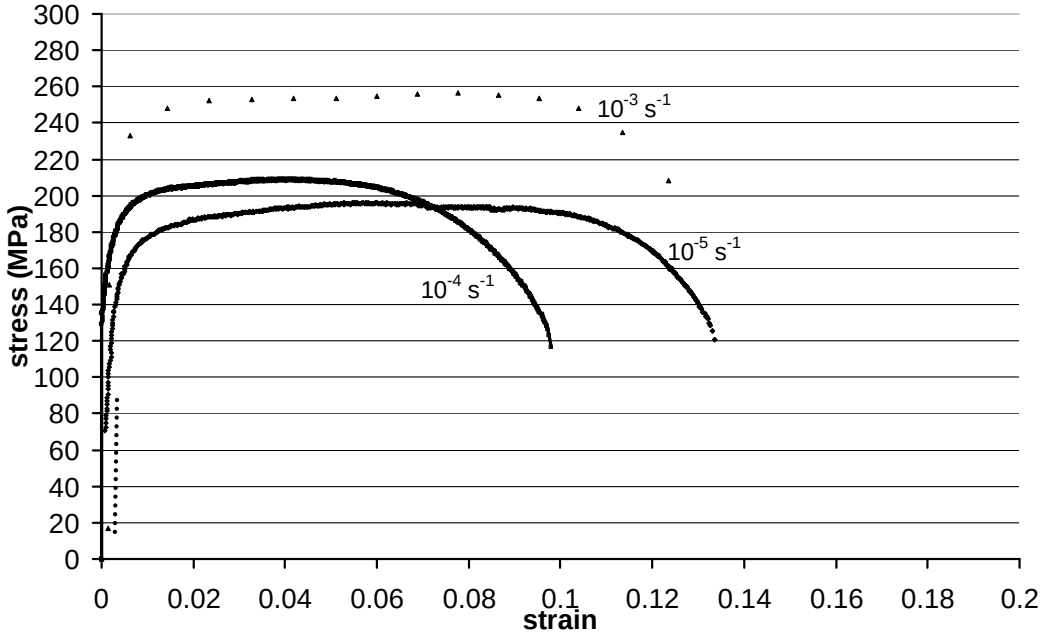

(a)

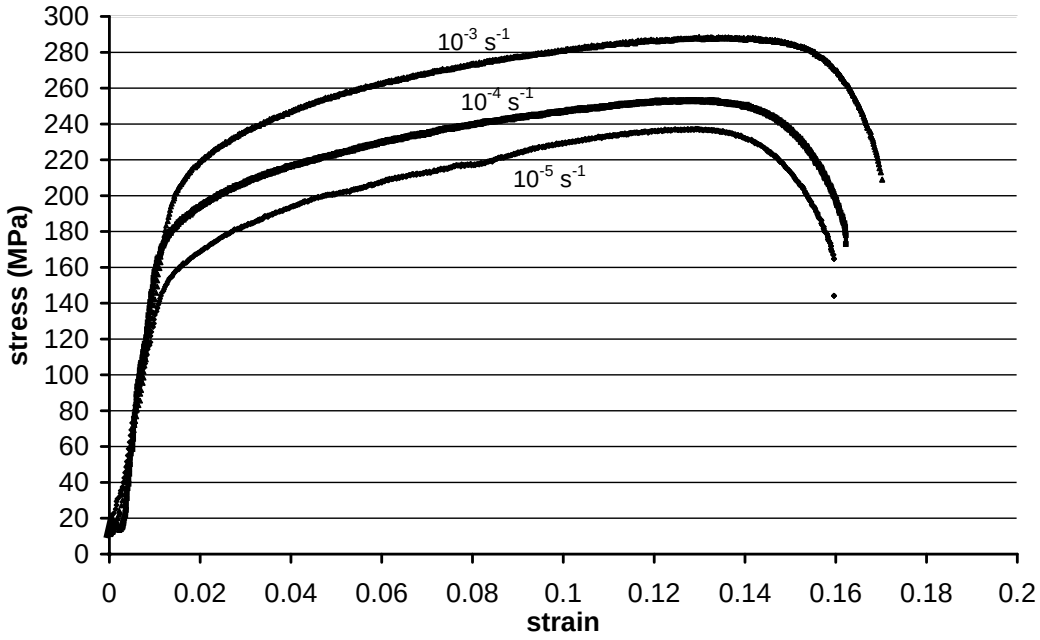

(b)

Figure VII.1 : Influence of applied strain rate on the macroscopic tensile curve at $200°C$ for: (a) transverse Zr702, (b) longitudinal Zr702.

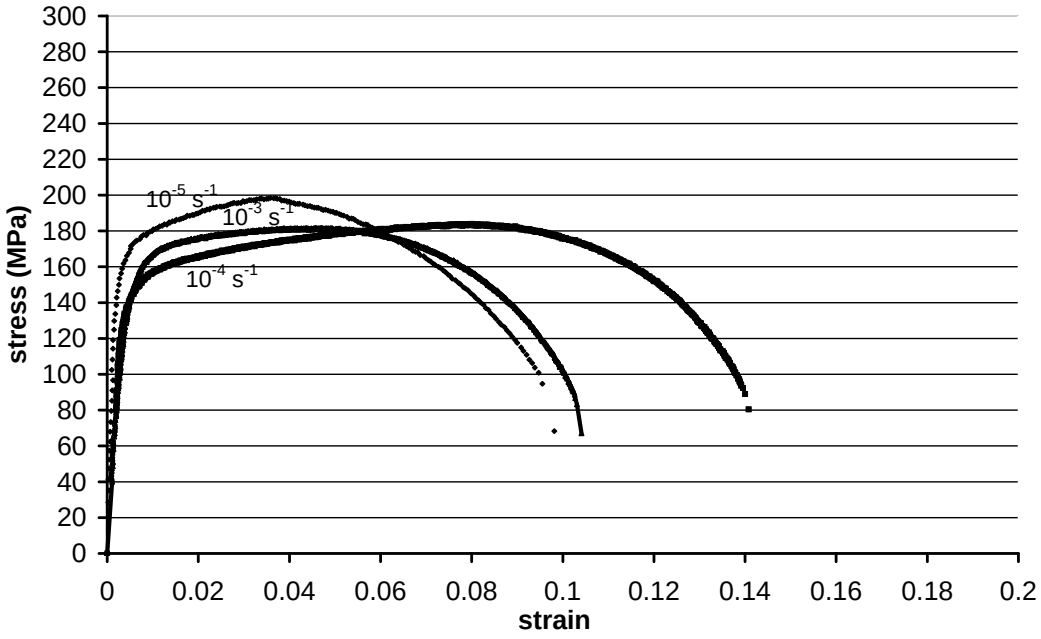

(a)

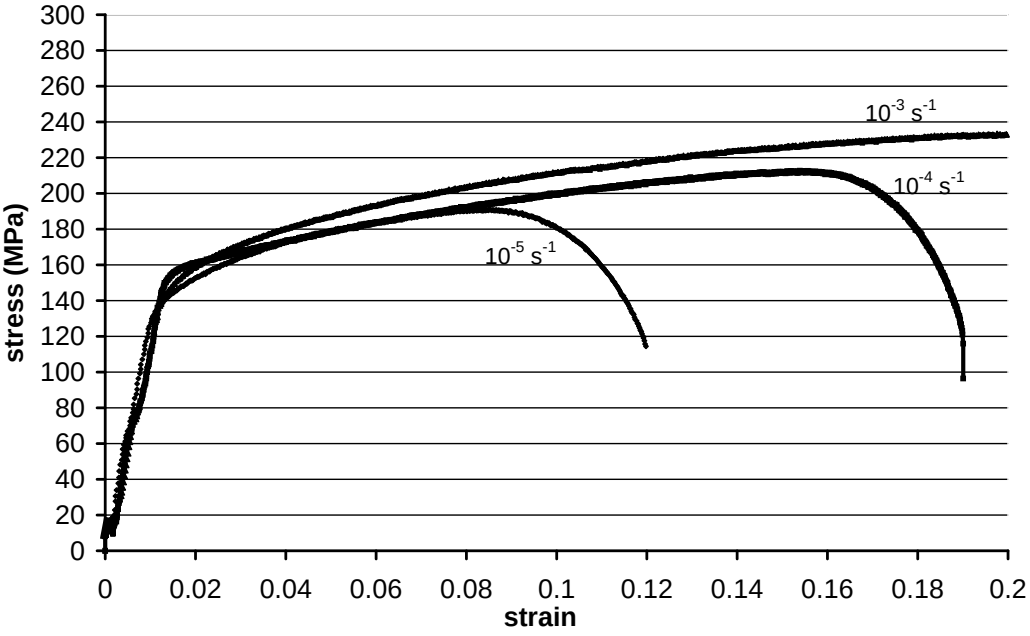

(b)

Figure VII.2 : Influence of applied strain rate on the macroscopic tensile curve at $300°C$ for: (a) transverse Zr702, (b) longitudinal Zr702.

VII.3 Tensile tests with strain rate changes

Tensile tests with strain rate changes were carried out at various temperatures between $20°C$ and $400°C$, using cylindrical specimens (see the plan of the sample in chapter VI). All the specimens were loaded along the transverse direction. Most of the tests with strain rate changes were performed between $10^{-3}\ s^{-1}$ and $10^{-4}\ s^{-1}$. For each test, the plastic strains at which the change occurs are around 0.2%, 0,5%, 1%, 1,5%, 2% and are noted especially in appendix II. The main following points are discussed:

- **influence of temperature,**
  the temperatures tested are $100°C$, $200°C$, $300°C$ and $400°C$,
- **strain rate control,**
  the results of the strain rate changes between $10^{-4}\ s^{-1}$ and $10^{-5}\ s^{-1}$ are compared to those of $10^{-3}\ s^{-1}$ and $10^{-4}\ s^{-1}$ at $300°C$,
- **influence of interstitial and substitutional atoms,**
  the results of tensile tests for ZrHf, ZrHf–Nb, ZrHf–O and ZrHf–Nb–O alloys are compared to those for Zr702 at the various temperatures.

The main objective of these experiments is to determine the SRS parameter, given by equation (VII.1) at each temperature and for each zirconium alloy.

$$SRS = \left(\frac{\Delta\sigma}{\Delta \log \dot{\varepsilon}_p}\right)_{T,\varepsilon_p} = \left(\frac{\sigma_2 - \sigma_1}{\log\left(\frac{\dot{\varepsilon}_2}{\dot{\varepsilon}_1}\right)}\right)_{T,\varepsilon_p} \tag{VII.1}$$

The macroscopic responses of the various zirconium alloys are compared at the various temperatures.

VII.3.1 Results

Young's modulus and 0.2% yield stress

Young's modulus was measured from the unloading branch at $10^{-4}\ s^{-1}$, after 3% of total strain. Figure VII.3 displays the change in Young's modulus with temperature for each zirconium alloy. The influence of solute atoms on the value of Young's modulus as a function of temperature is the following:

- comparing Zr702 and ZrHf, Young's modulus is nearly constant between $20°C$ and $100°C$. Then it decreases when the temperature increases. At $20°C$, $100°C$ and $200°C$, Young's modulus is higher for Zr702 than for ZrHf. However, at $300°C$ and $400°C$, upward values of Young's modulus are almost the same for Zr702 and ZrHf. For the zirconium alloys, ZrHf–O and ZrHf–Nb, the value of Young's modulus is higher at $400°C$ than at $300°C$, contrary to ZrHf–Nb–O,
- the higher niobium content of ZrHf–Nb is associated with a lower value of Young's modulus at $300°C$ and a higher value of Young's modulus at $400°C$, compared to ZrHf,
- the higher oxygen content of ZrHf–O is correlated with a higher value of Young's modulus at each temperature, compared to ZrHf. The comparison between ZrHf–O and Zr702, which have the same oxygen content shows that the nature of substitutional atom plays an important role on the value of Young's modulus. Indeed, up to $200°C$, the values of Young's modulus for Zr702 decrease abruptly with temperature, contrary to ZrHf–O. Moreover from $200°C$, the values of Young's modulus are almost the same

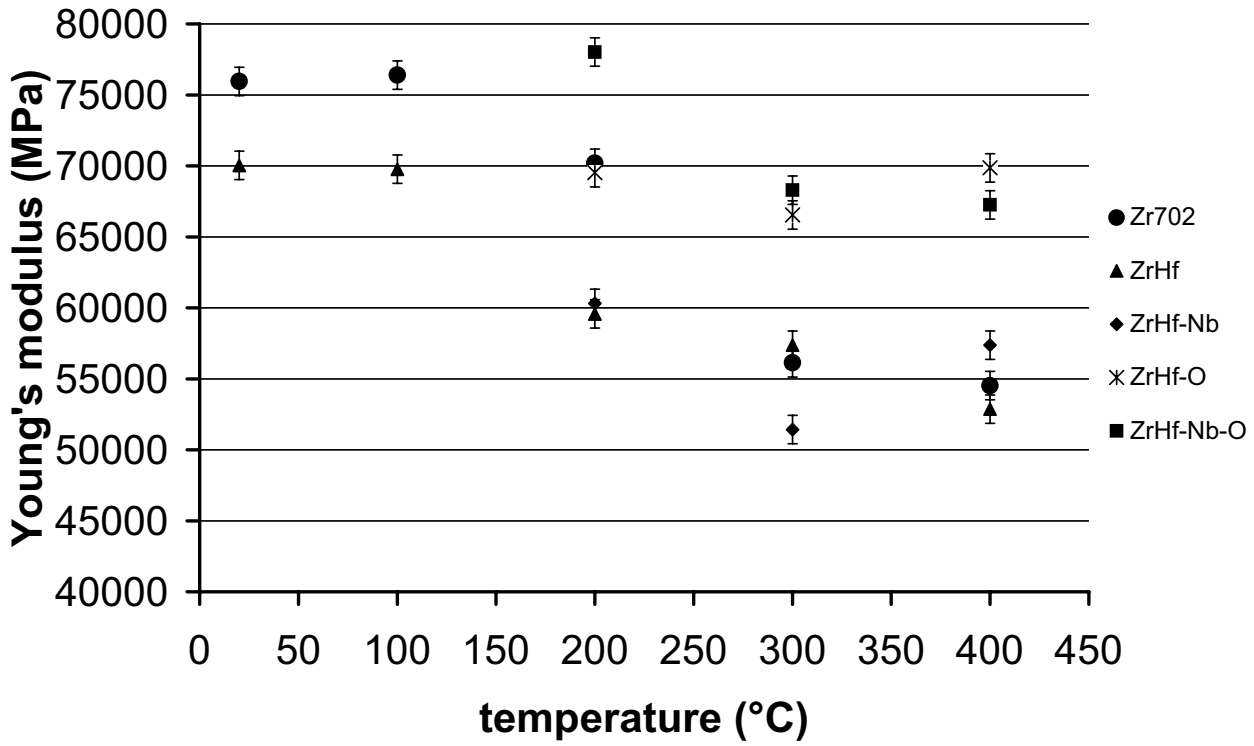

Figure VII.3 : Influence of temperature on Young's modulus measured during unloading at 10^{-4} s^{-1} for Zr702, ZrHf, ZrHf–Nb, ZrHf–O, ZrHf–Nb–O.

for Zr702, ZrHf and ZrHf–Nb, contrary to ZrHf–O and ZrHf–Nb–O which have higher values of Young's modulus.

Figure VII.4 displays the evolution of yield stress at 0.2% plastic strain as a function of temperature for each zirconium alloy. The influence of solute atoms on 0.2% yield stress as a function of temperature is the following:

- on the whole, the values of 0.2% yield stress are twice higher for Zr702 than for ZrHf. The yield stress at 0.2% plastic strain decreases with increasing temperature for both materials,
- the higher niobium content of ZrHf–Nb is correlated with higher yield stress, compared to ZrHf,
- the higher oxygen content of ZrHf–O does not change the value of 0.2% yield stress, compared to ZrHf. For ZrHf–O, ZrHf–Nb and ZrHf–Nb–O, the value of 0.2% yield stress at $400°C$ is higher than this at $300°C$.

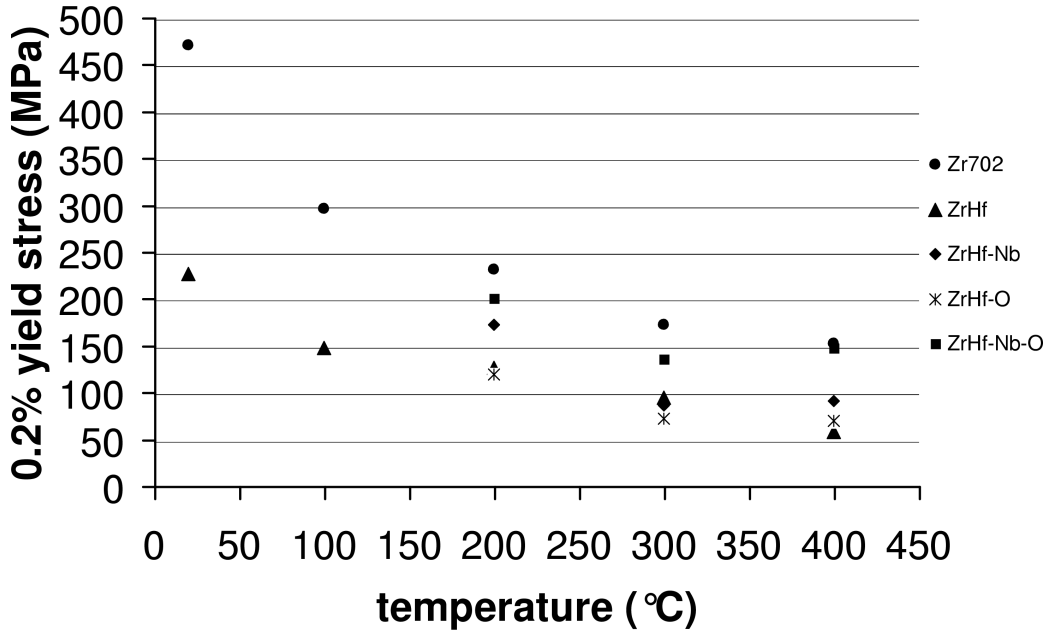

Figure VII.4 : Influence of temperature on yield stress at 0.2% plastic strain after loading at $10^{-4}\ s^{-1}$ for Zr702, ZrHf, ZrHf–Nb, ZrHf–O, ZrHf–Nb–O.

Macroscopic stress–strain curve

Figure VII.5 shows the true stress–plastic strain curves of the tensile tests with strain rate changes between $10^{-4}s^{-1}$ and $10^{-3}s^{-1}$ at $300°C$ for Zr702 and ZrHf. The strain rate control (the plastic strain–time curves) is also displayed on this figure.

Figure VII.6 shows the comparison of macroscopic true stress–plastic strain curves of Zr702 and ZrHf at $200°C$, $300°C$ and $400°C$. Appendix II gives macroscopic true stress–plastic strain curves for the various zirconium alloys at $200°C$ and $300°C$ (Zr702, ZrHf, ZrHf–Nb, ZrHf–O and ZrHf–Nb–O). The influence of oxygen and niobium contents can be summarized as follows:

- for Zr702 and ZrHf, the strain rate sensitivity increases up to $200°C$, then decreases with temperature. Notice that for ZrHf, it becomes nearly equal to zero at $300°C$. It can be negative at some plastic strain levels (1%–1.8%) at $400°C$. For Zr702, the strain rate sensitivity keeps a conventional value, the flow stress increases with increasing strain rate,
- ZrHf and ZrHf–Nb have a comparable strain rate sensitivity. The negative strain rate sensitivity is also observed at $400°C$ for some plastic strain levels (0.08%–1.9%) in both materials,
- a higher oxygen content of ZrHf–O is associated with a higher strain rate sensitivity as shown at $200°C$ and $300°C$, compared to ZrHf. Such an effect is also observed for ZrHf–Nb–O at $300°C$. At $400°C$, the strain rate sensitivity of this alloy is nearly equal to zero for various plastic strain levels (0.1%–1.9%) contrary to ZrHf.

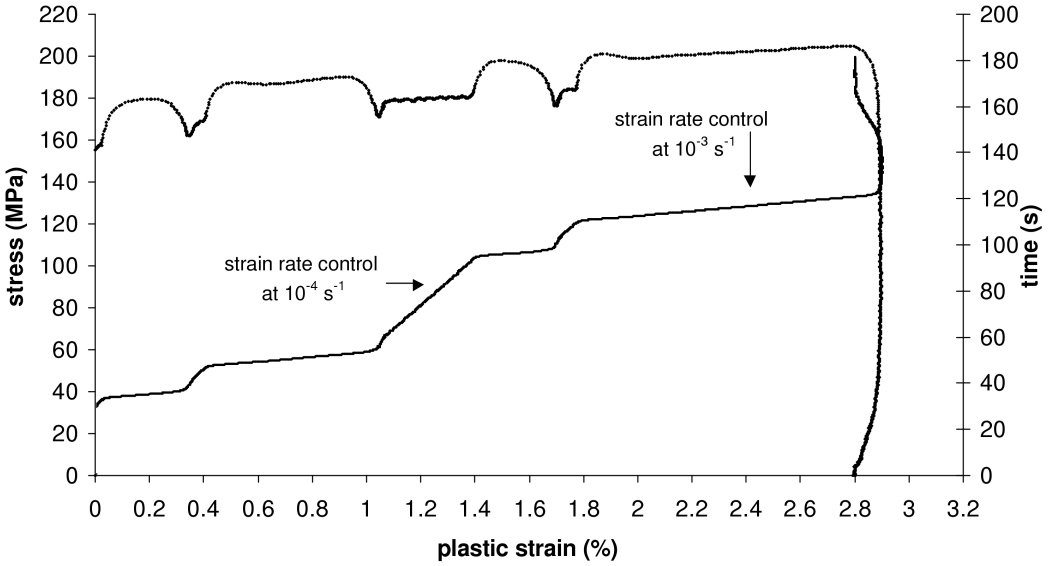

(a)

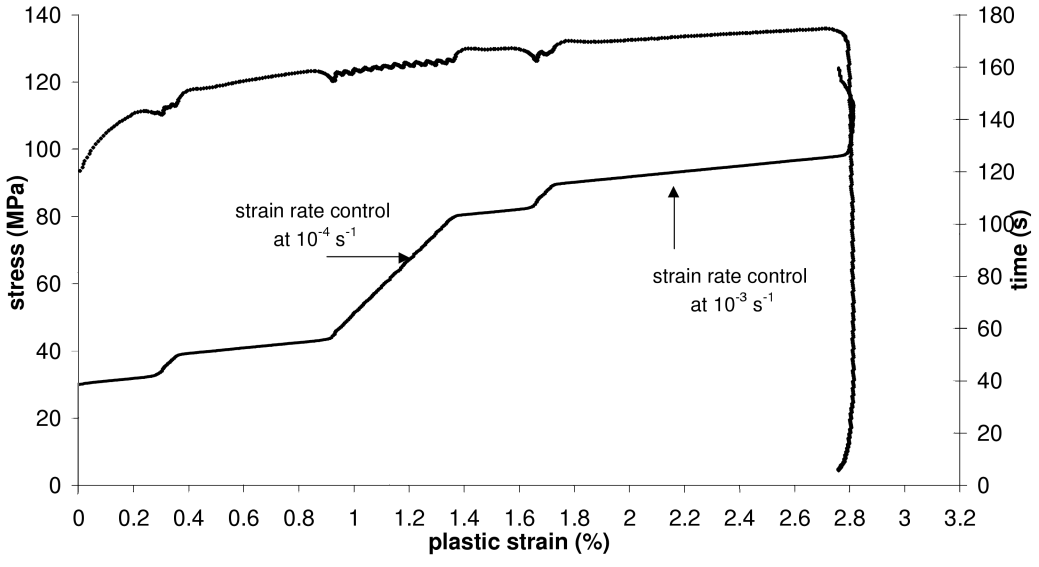

(b)

Figure VII.5 : Macroscopic true stress–true strain curves of tensile tests with strain rate changes at 300°C for: (a) Zr702, (b) ZrHf.

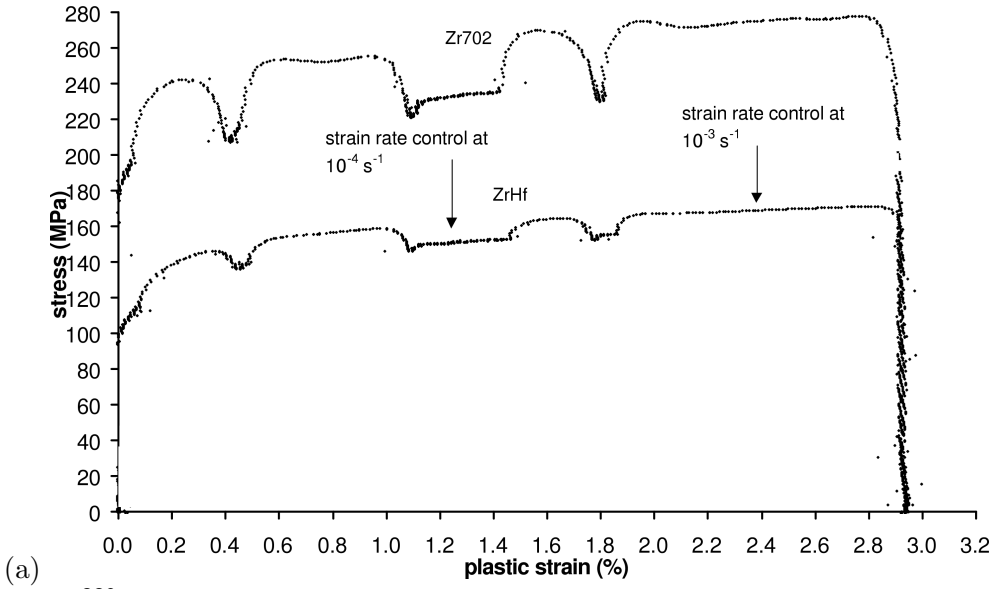

(a)

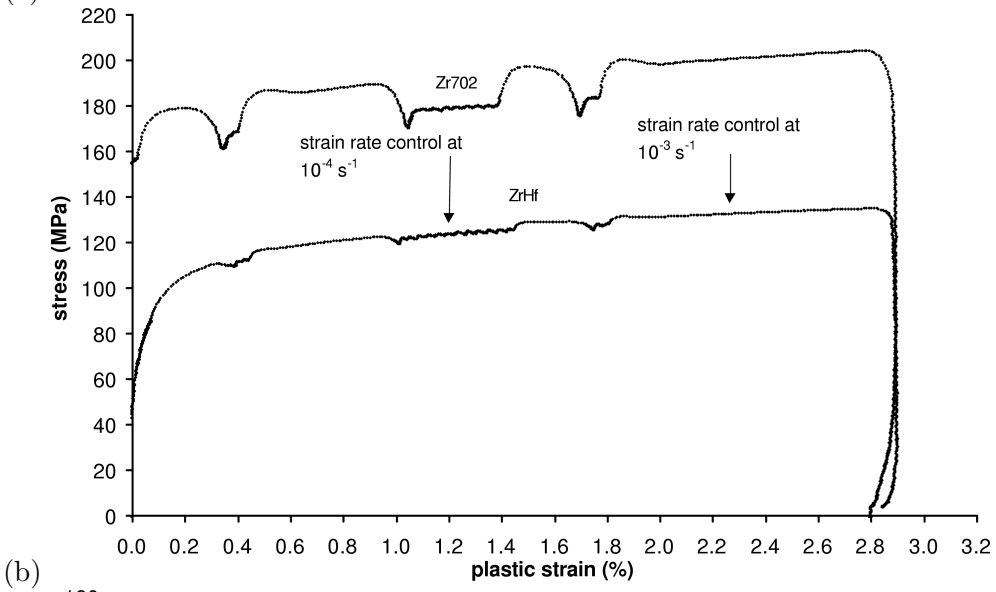

(b)

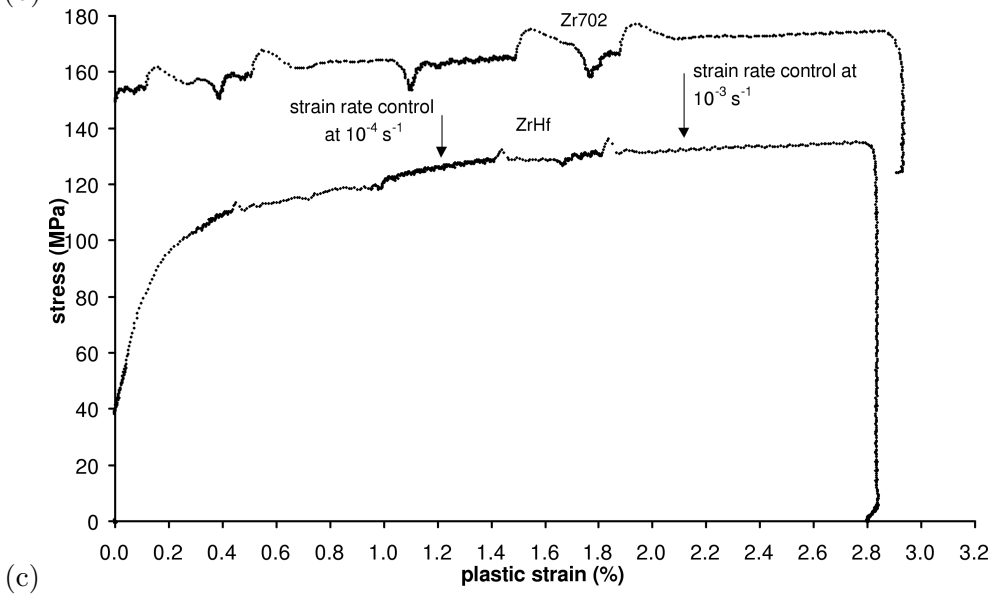

(c)

Figure VII.6 : Comparison of macroscopic true stress–plastic strain curves of tensile tests with strain rate changes for Zr702 and ZrHf : (a) 200°C, (b) 300°C, (c) 400°C.

VII.3.2 Discussion

Strain rate sensitivity

Figures VII.7 and VII.8 show the evolution of the SRS parameter measured between $10^{-3}s^{-1}$ and $10^{-4}s^{-1}$ as a function of temperature for each material at chosen plastic strains of 0.5%, 1.6%, 2%. Notice that the values of SRS for each temperature and each material are given in appendix II.

The main findings deduced from these figures are the following:

- for Zr702, the value of SRS is maximal at $200°C$. Then it decreases with increasing temperature. The minimal value of SRS is nearly equal to 0 MPa at $400°C$ for a plastic strain level of 0.5%. At larger strain levels, it remains always positive at this temperature. On the whole, the values of SRS increase with increasing plastic strain,
- for ZrHf, the value of SRS is maximal at $100°C$. As for Zr702, it decreases with increasing temperature. The value of SRS tends to zero, and can also be negative at $400°C$. On the whole, the values of SRS are almost independent of the plastic strain level, contrary to Zr702,
- the values of SRS are almost the same for ZrHf–Nb and for ZrHf at $200°C$, $300°C$ and $400°C$,
- a higher oxygen content is associated with an increase of the values of SRS at each temperature when ZrHf–O and ZrHf are compared. These values are twice/three times higher than for ZrHf,
- the same observation can be made for ZrHf–Nb and ZrHf–Nb–O. However, the values of SRS at $300°C$ are twice/three times lower than for ZrHf–O. We suggest that oxygen atoms are responsible for the increase in the values of SRS. This effect is suppressed when about 1 wt% niobium is introduced in the lattice.

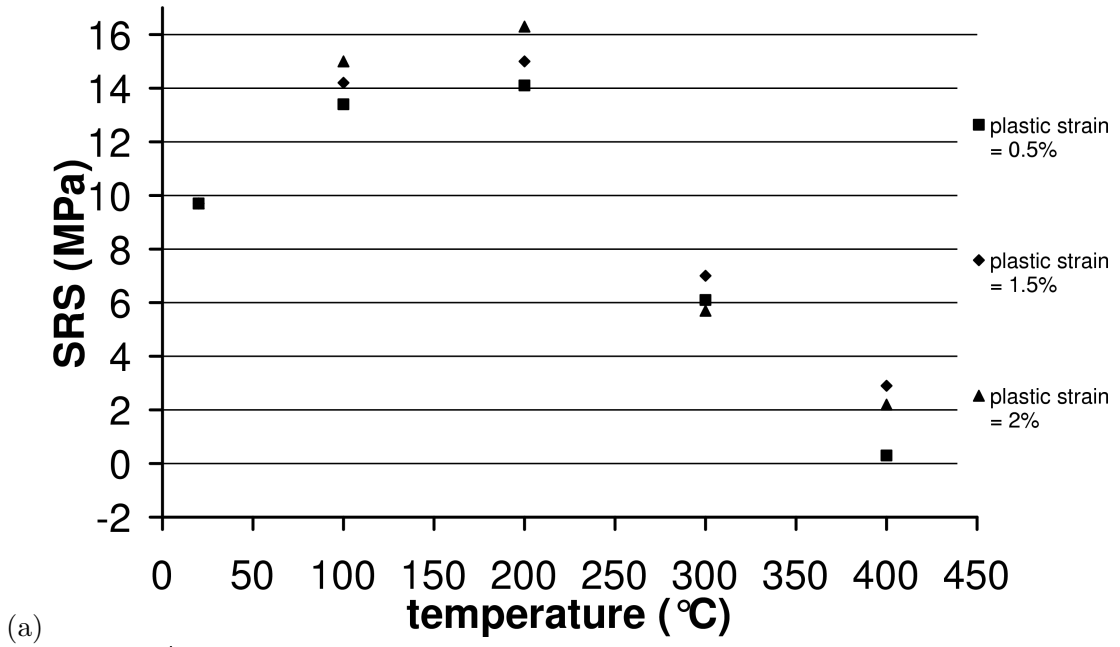

(a)

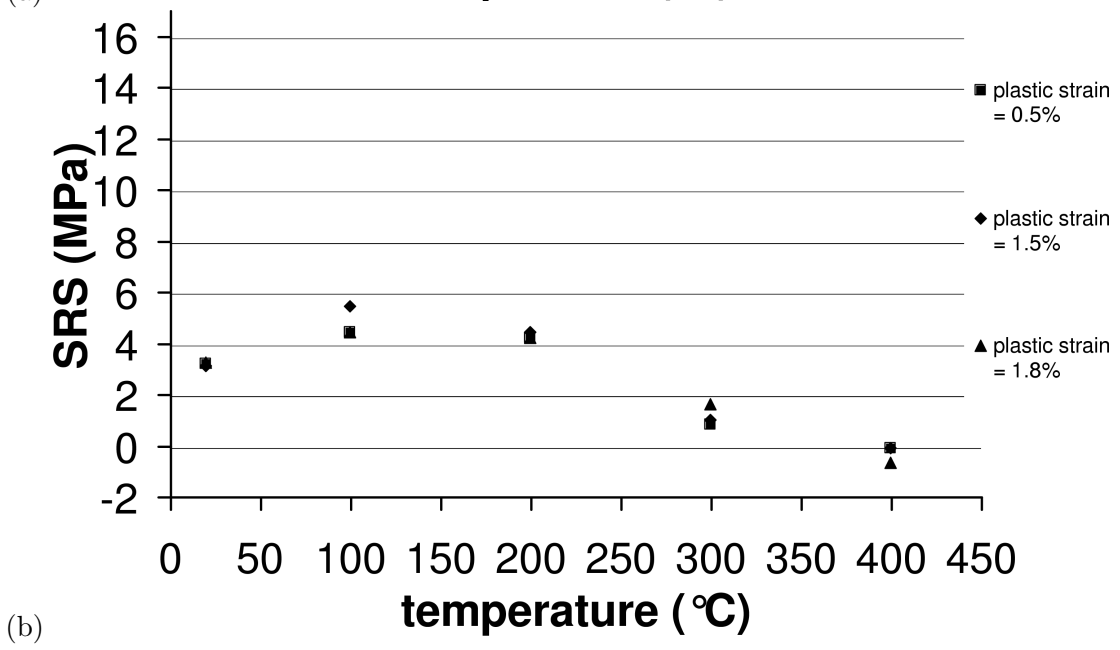

(b)

Figure VII.7 : Influence of temperature and plastic strain level on the SRS parameter, determined between 10^{-4} s^{-1} and 10^{-3} s^{-1} at chosen plastic strain levels close to 0.5%, 1.5%, 1.9% for: (a) Zr702, (b) ZrHf.

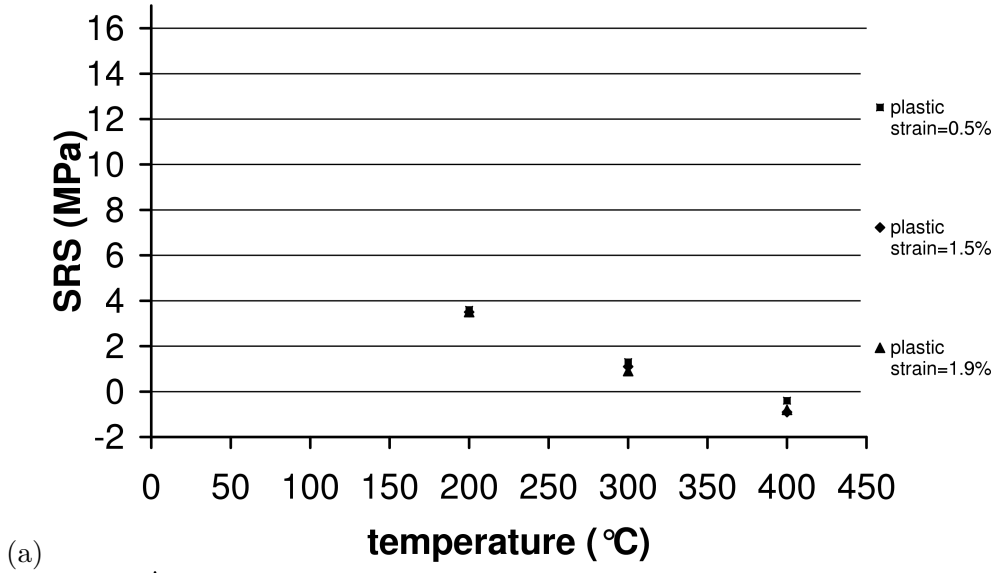

(a)

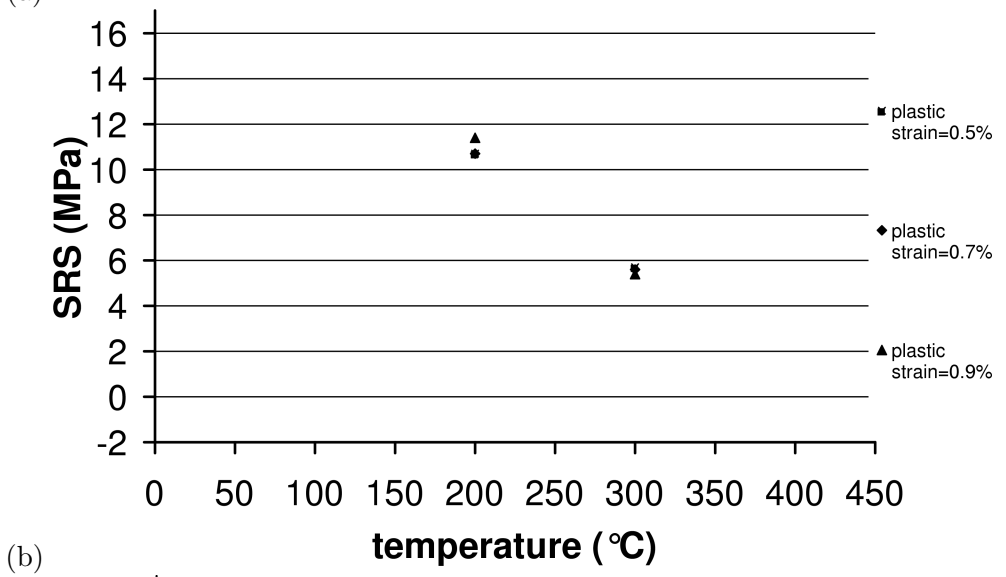

(b)

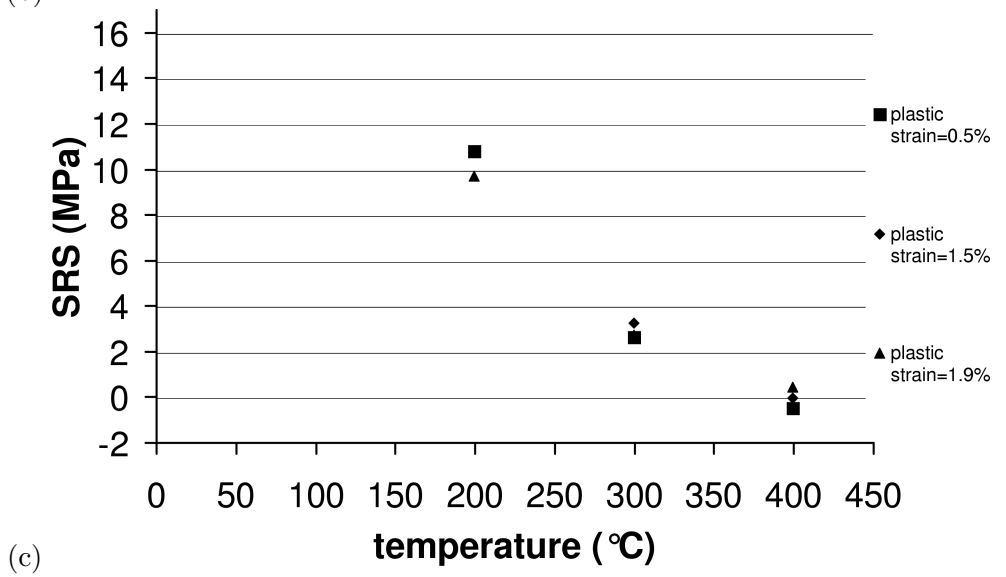

(c)

Figure VII.8 : Influence of temperature and plastic strain level on the SRS parameter, determined between 10^{-4} s^{-1} and 10^{-3} s^{-1} at chosen plastic strain levels close to 0.7%, 1.5% and close to 2% for: (a) ZrHf–Nb, (b) ZrHf–O, (c) ZrHf–Nb–O.

Stress peaks

Stress peaks were observed at 10^{-3} s^{-1} and not at 10^{-4} s^{-1} at various temperatures, when strain rate changes were carried out. They are more pronounced when temperature is higher, as shown figures in appendix II. The shape of stress peaks is characterized by the stress amplitude, labeled $\Delta\sigma_{stress\ peak}$, which is defined in figure VII.9. Table VII.1 gives the features of stress peaks as a function of material and temperature.

Table VII.1 : Characteristics of stress peaks as a function of temperature for Zr702, ZrHf, ZrHf–Nb, ZrHf–O, ZrHf–Nb–O. Features of PLC effect.

Materials	Temperature ($°C$)	Stress peaks $\Delta\sigma_{stress\ peak}$ (MPa)	PLC effect $\Delta\sigma_{PLC}$ (MPa)
Zr702	20	10^{-3} s^{-1}, $\Delta\sigma_{stress\ peak} = 1$	no
	100	10^{-3} s^{-1}, $\Delta\sigma_{stress\ peak} = 2$	no
	200	10^{-3} s^{-1},$\Delta\sigma_{stress\ peak} = 2$	no
	300	10^{-3} s^{-1}, $\Delta\sigma_{stress\ peak} = 3$	10^{-4} s^{-1}; $\Delta\sigma_{PLC} = 1.5$
	400	10^{-3} s^{-1}, $\Delta\sigma_{stress\ peak} = 6$	10^{-4} s^{-1}; $\Delta\sigma_{PLC} = 1.5$
ZrHf	20	10^{-3} s^{-1}, $\Delta\sigma_{stress\ peak} = 0.5$	no
	100	10^{-3} s^{-1}, $\Delta\sigma_{stress\ peak} = 1$	no
	200	10^{-3} s^{-1}, $\Delta\sigma_{stress\ peak} = 1$	no
	300	10^{-3} s^{-1}, $\Delta\sigma_{stress\ peak} = 1$	10^{-4} s^{-1}; $\Delta\sigma_{PLC} = 1.5$
	400	10^{-3} s^{-1}, $\Delta\sigma_{stress\ peak} = 3$	10^{-3} s^{-1}, 10^{-4} s^{-1}; $\Delta\sigma_{PLC} = 1.5$
ZrHf–Nb	20	-	-
	100	-	-
	200	10^{-3} s^{-1}, $\Delta\sigma_{stress\ peak} = 1$	10^{-4} s^{-1}; $\Delta\sigma_{PLC} = 1.5$
	300	10^{-3} s^{-1}, $\Delta\sigma_{stress\ peak} = 1$	10^{-4} s^{-1}; $\Delta\sigma_{PLC} = 1.5$
	400	10^{-3} s^{-1}, $\Delta\sigma_{stress\ peak} = 3$	10^{-3} s^{-1}, 10^{-4} s^{-1}; $\Delta\sigma_{PLC} = 1.5$
ZrHf–O	20	-	-
	100	-	-
	200	$10^{-3}s^{-1}$, $\Delta\sigma_{stress\ peak} = 2$	$10^{-3}s^{-1}$, 10^{-4} s^{-1}; $\Delta\sigma_{PLC} = 2$
	300	$10^{-3}s^{-1}$, $\Delta\sigma_{stress\ peak} = 6$	$10^{-3}s^{-1}$, $10^{-4}s^{-1}$; $\Delta\sigma_{PLC} = 2$
	400	-	-
ZrHf–Nb–O	20	-	-
	100	-	-
	200	10^{-3} s^{-1}, $\Delta\sigma_{stress\ peak} = 1$	10^{-4} s^{-1}; $\Delta\sigma_{PLC} = 1.5$
	300	10^{-3} s^{-1}, $\Delta\sigma_{stress\ peak} = 1$	10^{-4} s^{-1}; $\Delta\sigma_{PLC} = 1.5$
	400	10^{-3} s^{-1}, $\Delta\sigma_{stress\ peak} = 3$	10^{-3} s^{-1}, 10^{-4} s^{-1}; $\Delta\sigma_{PLC} = 1.5$

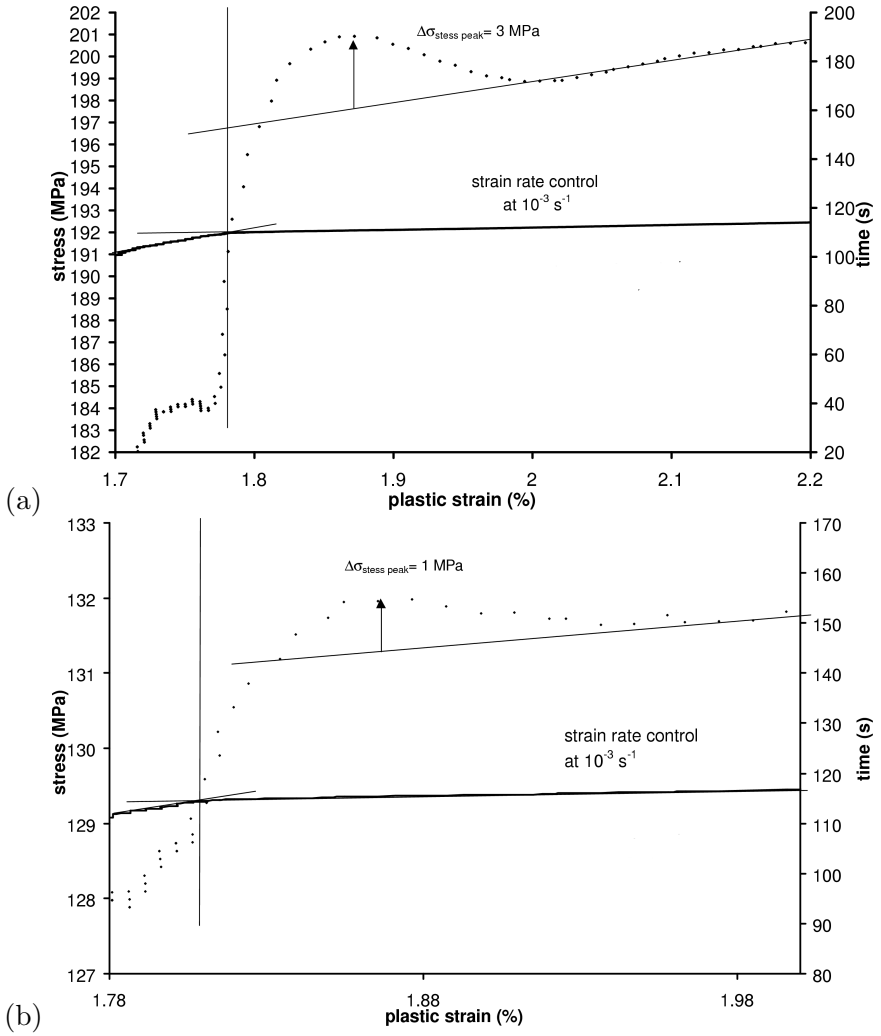

Figure VII.9 : Influence of solute atoms on the shape of stress peaks observed at $300°C$ at 10^{-3} s^{-1} between 2.4% and 3% of total true strain for: (a) Zr702, (b) ZrHf.

Figures VII.9 and VII.10 show the stress peaks observed at $300°C$ for each zirconium alloy. The main findings are the following:

- for all zirconium alloys, the values of $\Delta\sigma_{stress\ peak}$ measured at 10^{-3} s^{-1} increase with increasing temperature in the temperatures range $20°C$–$400°C$. Consequently, this effect is thermally activated in this temperatures range,
- differences can be observed between Zr702 and ZrHf. The values of $\Delta\sigma_{stress\ peak}$ are almost twice as large for Zr702 as for ZrHf. We propose that, such a difference can be explained by the fact that substitutional atoms are not the same for Zr702 (tin) and for ZrHf (hafnium),
- the values of $\Delta\sigma_{stress\ peak}$ are almost the same for ZrHf, ZrHf–Nb and ZrHf–Nb–O. Note that the values of $\Delta\sigma_{stress\ peak}$ for ZrHf–O are higher than for the other zirconium alloys.

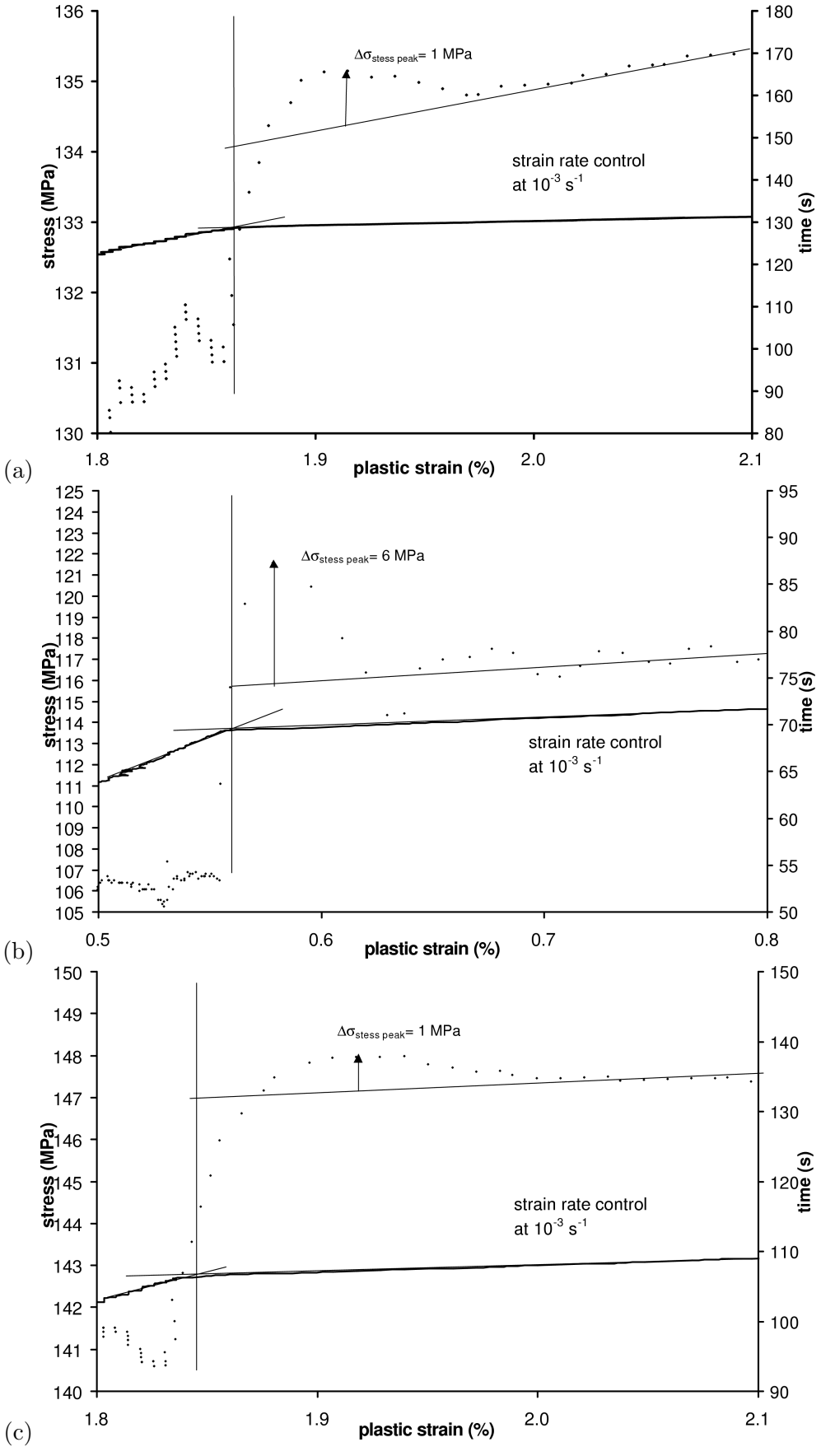

Figure VII.10 : Influence of solute atoms on the shape of the stress peaks observed at $300°C$ at $10^{-3}\ s^{-1}$ between 2.4% and 3% of total true strain for: (a) ZrHf–Nb, (b) ZrHf–O, (c) ZrHf–Nb–O.

Portevin–Le Chatelier effect

PLC effect can be observed for both applied strain rates 10^{-4} s^{-1} and 10^{-3} s^{-1}, at $200°C$, $300°C$ and $400°C$ in the form of slight serrations on the overall stress–strain curves. The observation of PLC serrations on the macroscopic curve depends on material, temperature and applied strain rate. The stress amplitude of PLC serrations, labeled $\Delta\sigma_{PLC}$ are given in table VII.1 as a function of material and temperature. Figure VII.11 shows PLC serrations observed at $300°C$ for Zr702 and ZrHf. Notice that, on these figures, the strain rate control is displayed in order to ensure that such an effect is due to the material and not to a "poor" strain rate control. The main conclusions are the following.

A higher oxygen content is associated with a slight increase of the stress amplitude, $\Delta\sigma_{PLC}$ when ZrHf and ZrHf–O are compared. Moreover, PLC effect is observed for higher applied strain rates for ZrHf–O than for ZrHf at $300°C$.

ZrHf–Nb exhibits PLC effect at $200°C$ at 10^{-4} s^{-1}, but ZrHf does not. ZrHf–Nb–O has nearly the same behavior as ZrHf and ZrHf–Nb, for instance at the same temperatures of $200°C$ and $300°C$.

Some difference can be observed between Zr702 and ZrHf. PLC effect is observed at higher applied strain rate in ZrHf than in Zr702 at $400°C$.

Notice that PLC serrations observed on several material (see table VII.1):

- were always of rather small amplitude, when detectable (1 MPa to 1.5 MPa on figure VII.11). Such effect was observed by Blanc (Blanc, 1987) in 316 stainless steels and in aluminium base alloys where macroscopic PLC bands were detected crossing the gauge length of specimens (the measured stress changes during PLC serrations are 10 to 20 times larger namely 20 MPa to 40 MPa). Notice also that these serrations are rather smooth and tend to appear as periodical stress oscillations in the zirconium alloys studied here as compared to the so–called "jerky flow" reported in the literature for the other materials mentioned,

- were observed for positive values of strain rate sensitivity. This experimental result is apparently in direct contradiction with previous theoretical previsions (Kubin and Estrin, 1991a; Estrin and Kubin, 1995; Estrin and Kubin, 1986) derived from models based on the physics of dislocation dynamics in the presence of interacting impurities atoms, capable of segregating in the stress field of edge dislocations (for instance Cottrell's model (Cottrell, 1953) and the formation of Cottrell's clouds). If this model correctly describes the behavior of an individual dislocation as well as the collective behavior of a few hundred or a few thousand dislocations interacting with one another and with diffusing impurities atoms, it is not clear for the moment how it can be extended to macroscopic specimens containing dislocation substructures (for instance cells, sub–boundaries, phase boundaries), grain boundaries and grains of various sizes and orientations. Yet, when large PLC serrations are recorded on the tensile curves, and macroscopic PLC bands are observed moving across grains and grain boundaries, as in aluminium alloys for example, it is reasonably likely that these microscopic models offer more reliable predictions to experimental observations. On the other hand, when PLC bursts are of limited extension in the material (on the scale of a grain or a few grains), the damping effect of the surrounding material which appears as unaffected by the sudden and localized flow taking place in the neighboring grains will prevent the

application of this microscopic model on the scale of sample. In the case of zirconium alloys, since the plastic flow bursts are restricted to small active domains embedded into inactive bulk surroundings, the measurements do not reflect directly the intense plastic flow taking place in various small size areas scattered in the specimen.

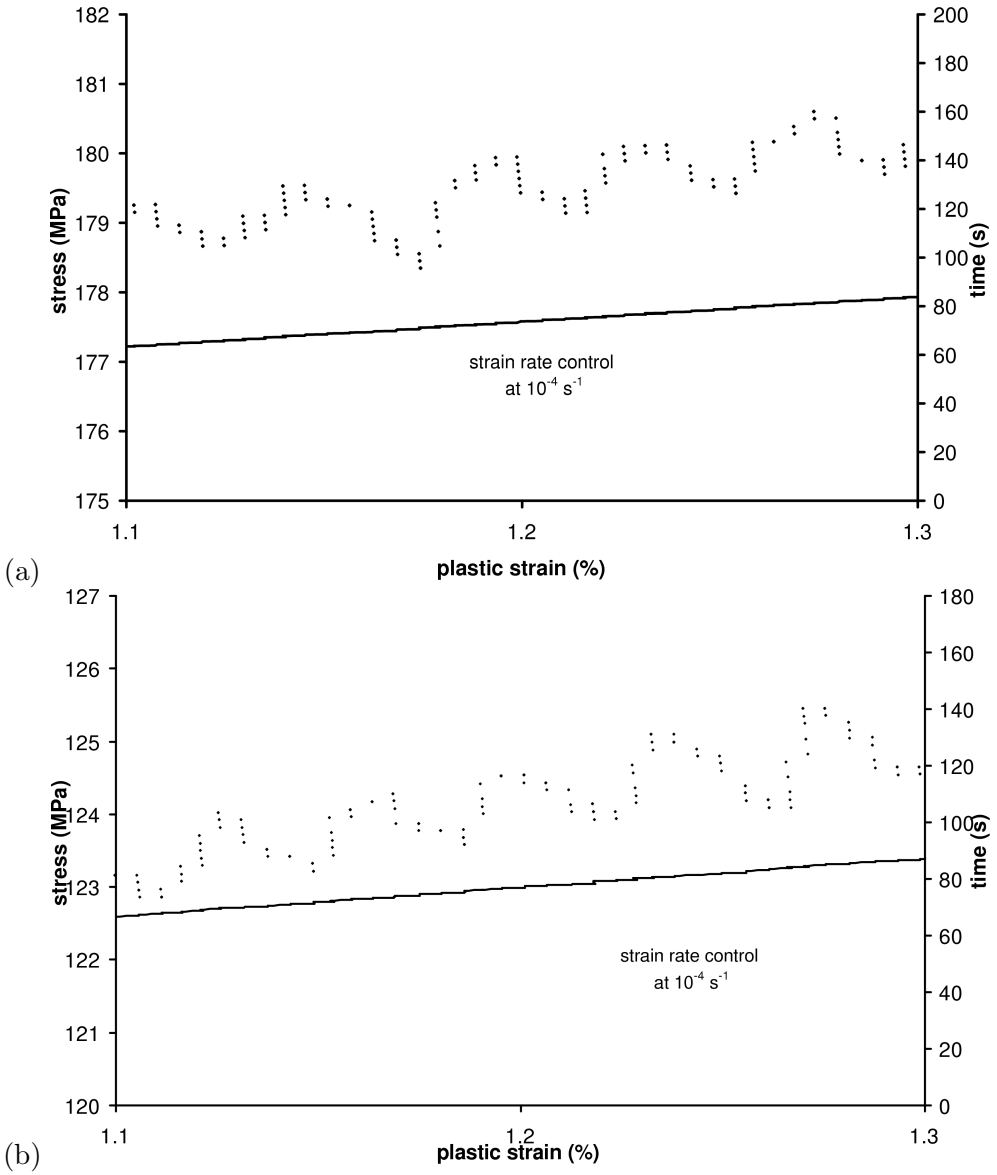

Figure VII.11 : PLC serrations observed at $10^{-4}\ s^{-1}$ and $300°C$ for: (a) Zr702, (b) ZrHf.

Influence of the strain rate control

We showed that negative strain rate sensitivity was observed for transverse Zr702 at $300°C$ between 10^{-5} s^{-1} and 10^{-4} s^{-1} and between 10^{-5} s^{-1} and 10^{-3} s^{-1} during tensile tests on flat specimens and for deformations smaller than 0.03 (see section VII.3). That is why, we chose to carry out tensile tests with strain rate changes between 10^{-5} s^{-1} and 10^{-4} s^{-1} at $300°C$ for the same zirconium alloy. Table VII.2 gives the values of the SRS parameter as a function of plastic strain level in Zr702 at $300°C$ for both experiments with strain rate changes from 10^{-4} s^{-1} to 10^{-3} s^{-1} and from 10^{-4} s^{-1} to 10^{-5} s^{-1}.

Table VII.2 : Evolution of the SRS parameter as a function of plastic strain level for Zr702 at $300°C$ for the strain rate changes from 10^{-4} s^{-1} to 10^{-3} s^{-1} and from 10^{-4} s^{-1} to 10^{-5} s^{-1}.

Strain rate changes experiments	Plastic strain level (%)	SRS (MPa)
from 10^{-4} s^{-1} to 10^{-3} s^{-1}	0.04	8.7
	0.3	6.1
	0.4	5.2
	1.	5.2
	1.4	5.6
	1.7	5.1
	1.8	5.6
from 10^{-4} s^{-1} to 10^{-5} s^{-1}	0.2	0.2
	0.4	3.5
	0.5	3.9
	1.1	3.8
	1.5	3.9
	1.8	3.9
	2.	3.9

At 0.2% plastic strain, the value of SRS is nearly equal to zero for a jump from 10^{-4} s^{-1} to 10^{-5} s^{-1}. On the contrary for a jump from 10^{-4} s^{-1} to 10^{-3} s^{-1}, SRS reaches values around 7 MPa. Consequently, the inverse strain rate sensitivity shown in figure VII.2 (b) is not detected by strain rate change experiments although SRS approaches zero at 0.2% plastic strain for a jump from 10^{-4} s^{-1} to 10^{-5} s^{-1}. We propose that this effect is possibly due to a greater change in microstructure in strain rate changes tests in the case of uniaxial tensile tests or to a sample geometry effect. Indeed the microstructures are likely to be different for a sample tested in tension at constant strain rate and for a sample tested in tension with strain rate changes. Such a microstructure effect was also observed by Thorpe (Thorpe and Smith, 1978b) in Zr–1 wt%Nb alloy.
Whatever the strain rate changes between 10^{-4} s^{-1} to 10^{-5} s^{-1}, the values of SRS are almost independent of plastic strain except at 0.2% plastic strain. The ratio between the SRS values measured between 10^{-4} s^{-1} and 10^{-3} s^{-1} and those measured between 10^{-4} s^{-1} and 10^{-5} s^{-1} is about 2/3 for plastic strain levels superior to 0.3%.

Consequently, it is important to specify at which strain and strain rate level, the strain rate changes are carried out even if the amplitude of the strain rate changes are the same. For Zr702, at a given temperature, the lower the selected strain rates, the lower the measured SRS values.

VII.3.3 Conclusion

It is not necessary to introduce a large quantity of oxygen atoms in order to observe low strain rate sensitivity. The strain rate sensitivity can become negative at $400°C$ for ZrHf, ZrHf–Nb, ZrHf–Nb–O. With only about 80 wt ppm of oxygen atoms, ZrHf and ZrHf–Nb show lower strain rate sensitivities than the other alloys, containing 1100 wt ppm–1300 wt ppm of oxygen atoms. Increasing oxygen content, the strain rate sensitivity increases, as it is the case for ZrHf–O, ZrHf–Nb–O and Zr702. Consequently, we suggest that, according to Veevers (Veevers, 1975) the best conditions to observe lower strain rate sensitivity is to have enough substitutional atoms to distort the lattice, which allows to oxygen atoms to diffuse in the stress field of dislocations. Since strain ageing effects tend to saturate for high concentrations of impurity atoms, one can deduce that there is an optimal concentration of oxygen atoms at which strain ageing is optimal. Probably, this optimal concentration of oxygen atoms lies around 1100 wt ppm–1400 wt ppm if the substitutional content is sufficient.

For lower temperature inferior to $200°C$, oxygen atoms play the role of strain hardening, the SRS–temperature plot moving toward higher values of SRS with introducing oxygen atoms. For higher temperature superior to $400°C$, oxygen atoms play the same role of strain hardening. Between both temperatures, we observe that the minimal value of SRS is not changed, located close to zero around $400°C$, whatever the materials.

Moreover, we show that the shape of the stress peaks and PLC serrations depends on oxygen content. The nature of substitutional atoms seems also to influence the PLC serrations, especially.

In conclusion, tensile tests with strain rate changes from $10^{-4}s^{-1}$ to $10^{-3}s^{-1}$ at constant temperature permit to reach the values of SRS at various temperatures and plastic strain levels. The interpretation of these mechanical tests is given in chapter VIII.
However, the explored range of strain rates is not large enough to show experimental evidence of strain ageing and deformation mechanisms in zirconium alloys. That is why, we preferred stress relaxation experiments, carried out at constant temperature because a wide range of strain rates can be investigated using such tests.

VII.4 Stress relaxation tests with unloading

The main advantage of stress relaxation experiments is to explore the viscoplastic behavior of a material in a large interval of stresses and strain rates, contrary to tensile tests (constant strain rate) and creep tests (constant stress). The aim of this section is to compare the relaxation behavior of two zirconium alloys, Zr702 and ZrHf. For this purpose, stress relaxation tests were carried out on cylindrical specimens between $100°C$ and $400°C$, taken along the transverse direction. Our relaxation test was characterized by the four sequences (the loading, the first relaxation, the unloading down to about 50 MPa and letting the material relax in this latter stress range), described in chapter VI. The macroscopic behavior of Zr702 is compared to that of ZrHf at each temperature.

VII.4.1 Results

Figures VII.12 and VII.13 show the true stress–true strain curves of relaxation tests with unloading for Zr702 and ZrHf at various temperatures ($100°C$, $200°C$, $300°C$ and $400°C$). We can observe that on these macroscopic curves, strain hardening takes place only during the first 1% strain whatever the temperature for both zirconium alloys. Moreover at $200°C$ and $300°C$, stress peaks can be observed for Zr702, as shown in figure VII.13.

The loading and the first relaxation sequence

Figure VII.14 shows the comparison between the true stress–time curves for each relaxation cycle at $100°C$, $200°C$, $300°C$ for Zr702 and ZrHf. We recall that a sequence of relaxation was usually (but not always) composed of about six consecutive 24 hours cycles with the following plastic strain amplitude, ε_p: 0.2–0.2–0.5–0.5–0.2–0.2

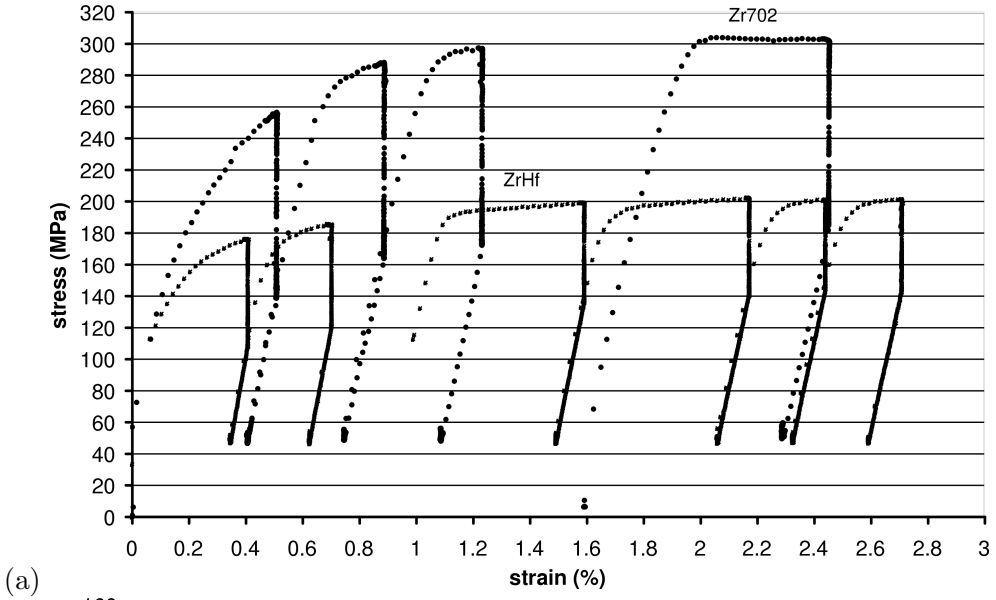

(a)

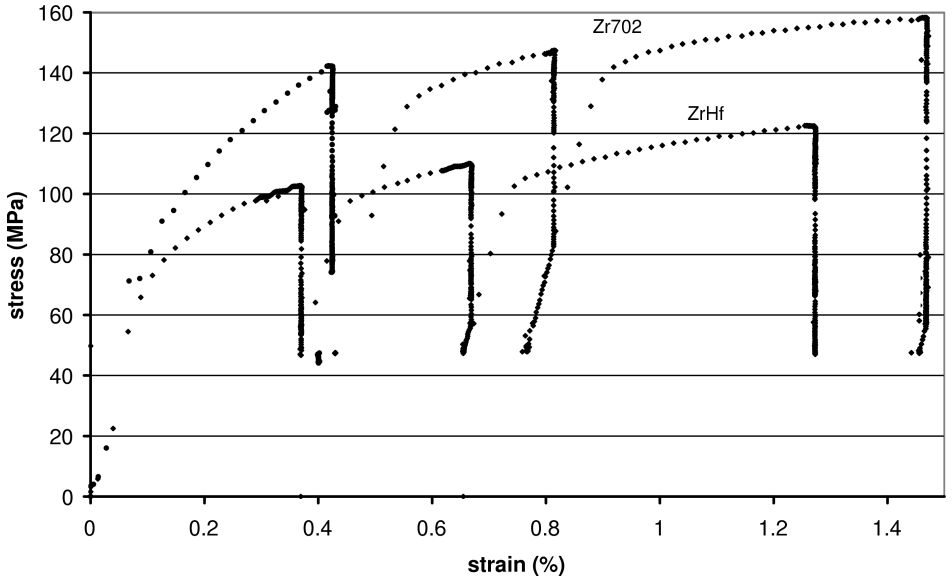

(b)

Figure VII.12 : True stress–true strain curves of relaxation tests with unloading for Zr702 and ZrHf at: (a) $100°C$, (b) $400°C$.

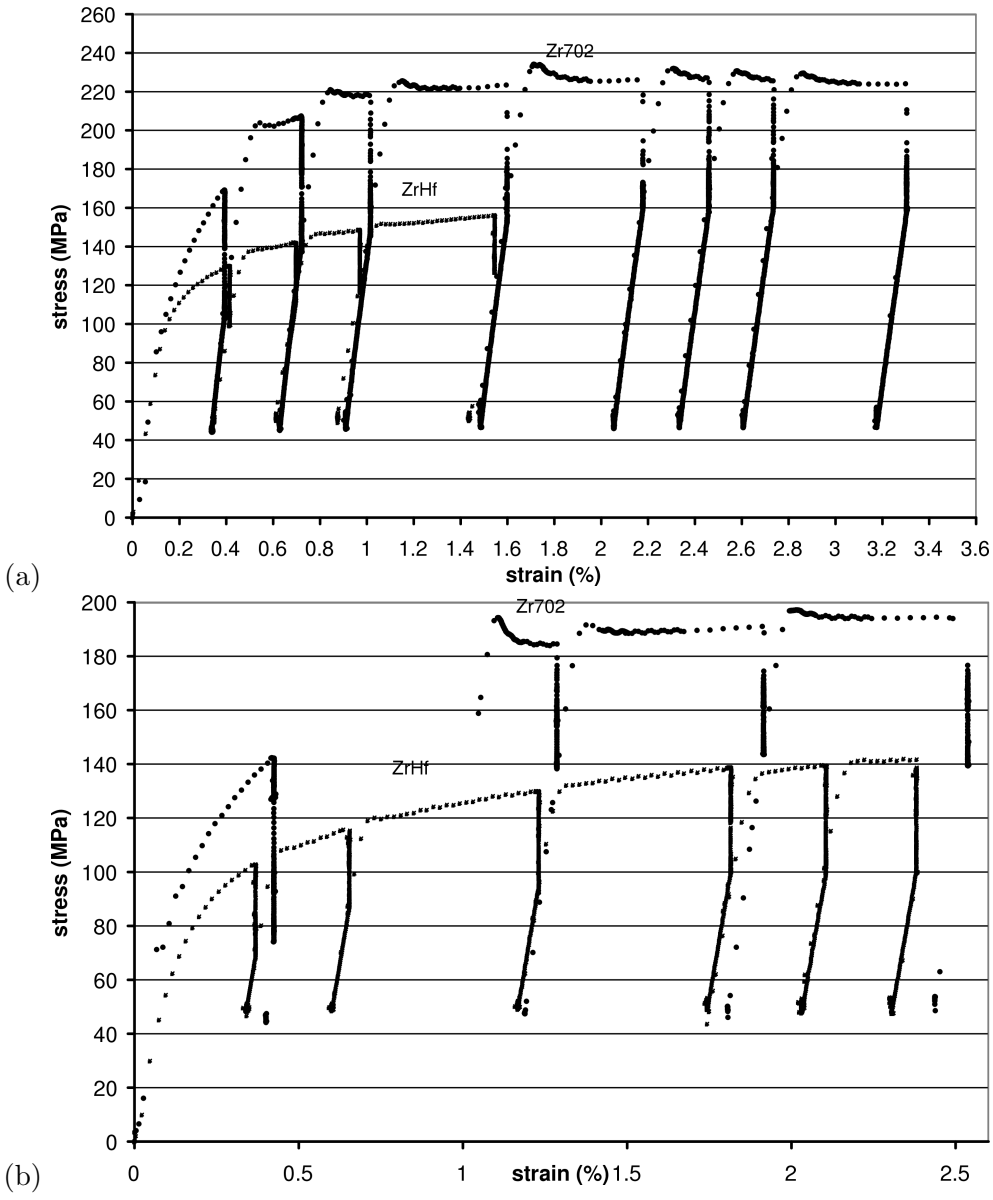

Figure VII.13 : True stress–true strain curves of relaxation tests with unloading for Zr702 and ZrHf at: (a) $200°C$, (b) $300°C$.

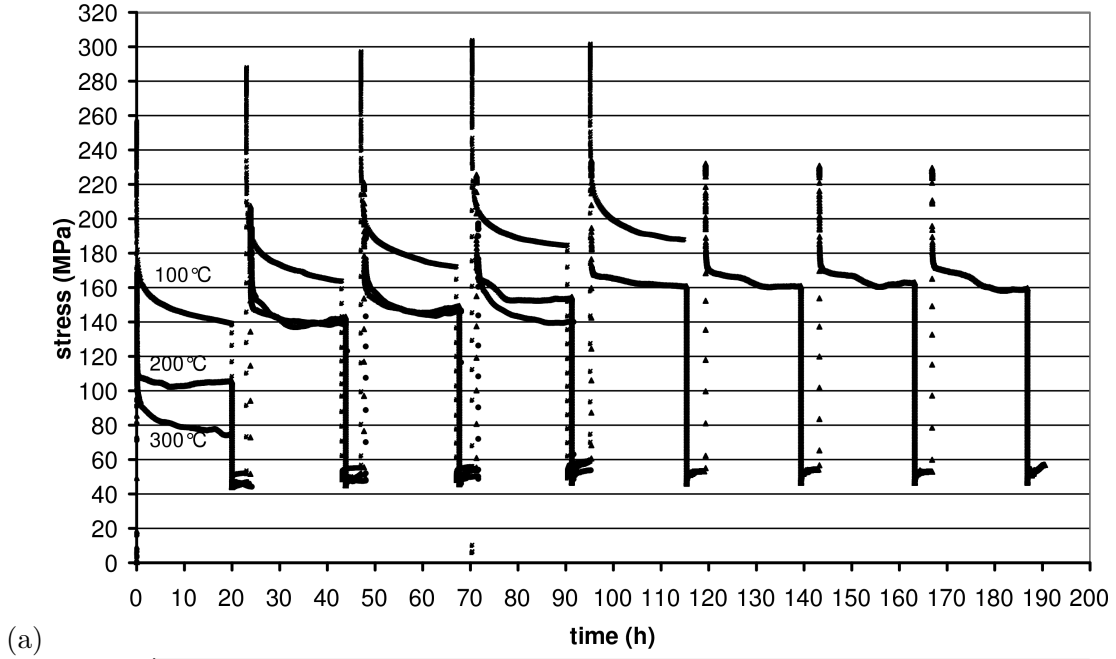

(a)

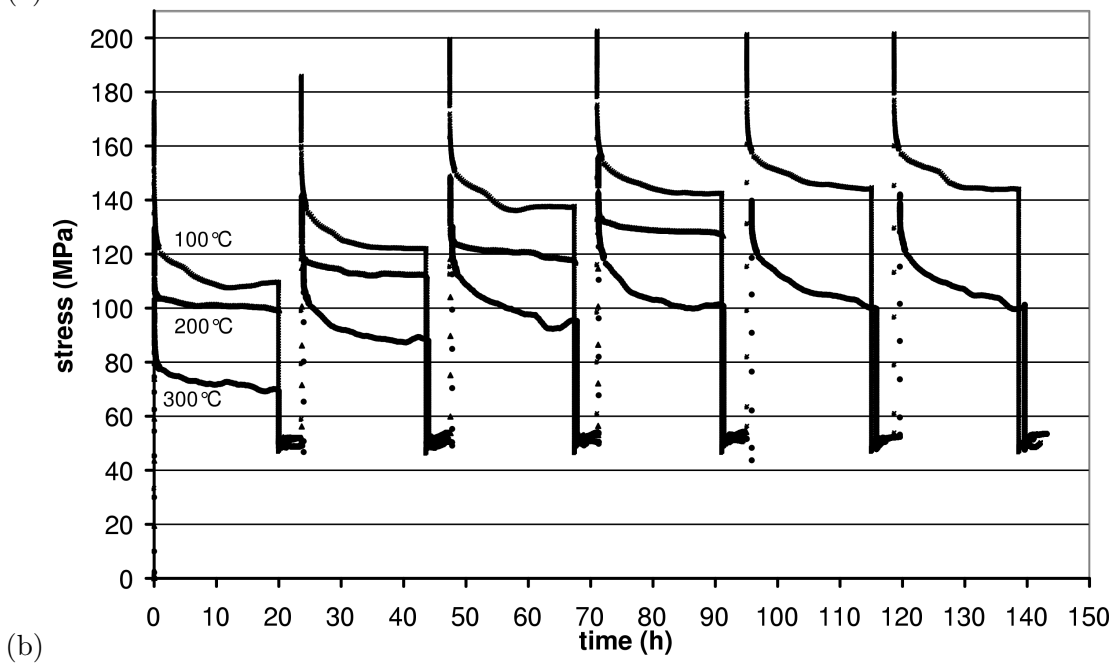

(b)

Figure VII.14 : True stress–time curves for all the relaxation cycles at $100°C$, $200°C$ and $300°C$ for: (a) Zr702, (b) ZrHf.

To have a better view of the relaxation cycles for Zr702, figure VII.15 (a) displays the macroscopic true stress–time curves at $100°C$ and $200°C$ and figure VII.15 (b) at $100°C$ and $300°C$. Figures VII.16 (a), (b) show the comparison between the stress–time curves according to each relaxation cycle at $400°C$ respectively for Zr702 and ZrHf. The values of plastic strain at the end of relaxation test (ε_p^{relax}) and the total decrease of stress during relaxation test ($\Delta\sigma^{relax}$) are given in appendix II as a function of temperature and the number of relaxation cycle for Zr702 and ZrHf. Figure VII.17 shows the evolution of $\Delta\sigma^{relax}$ and ε_p^{relax} as a function of temperature at various plastic strain levels.

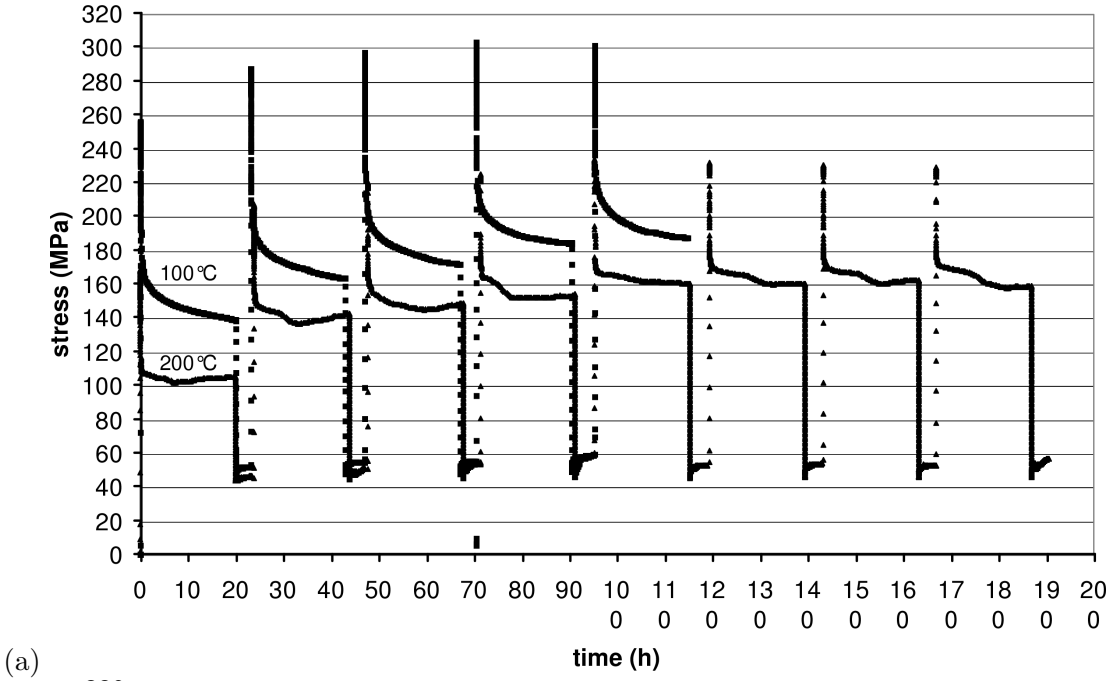

(a)

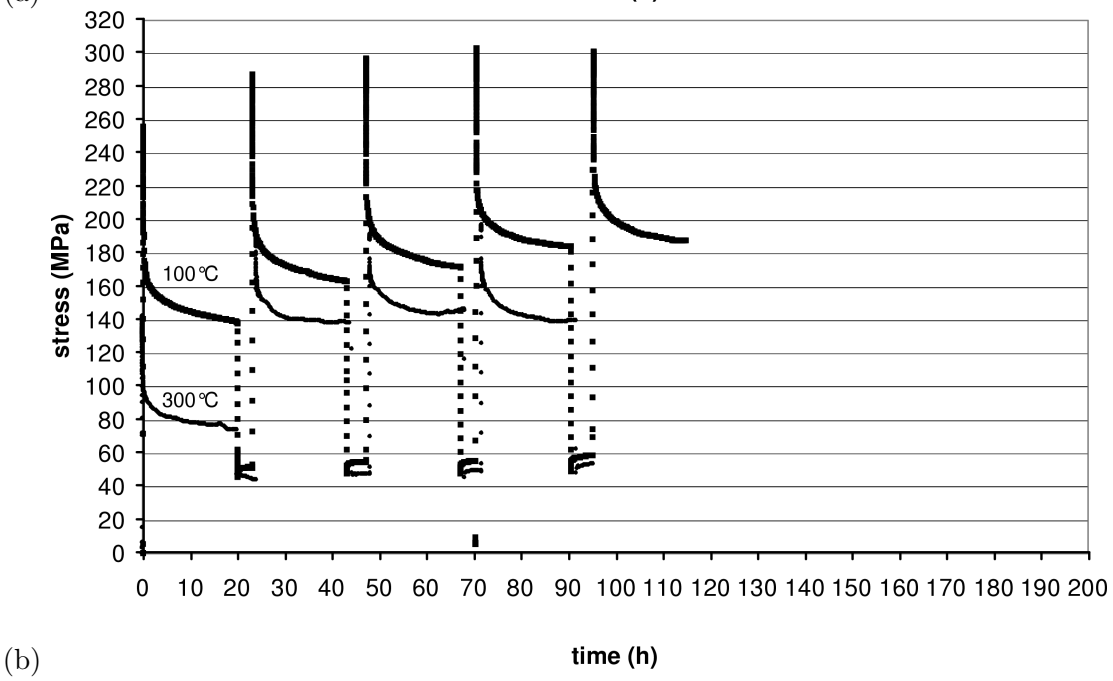

(b)

Figure VII.15 : True stress–time curves for all the relaxation cycles for Zr702 at: (a) $100°C$ and $200°C$, (b) $100°C$ and $300°C$.

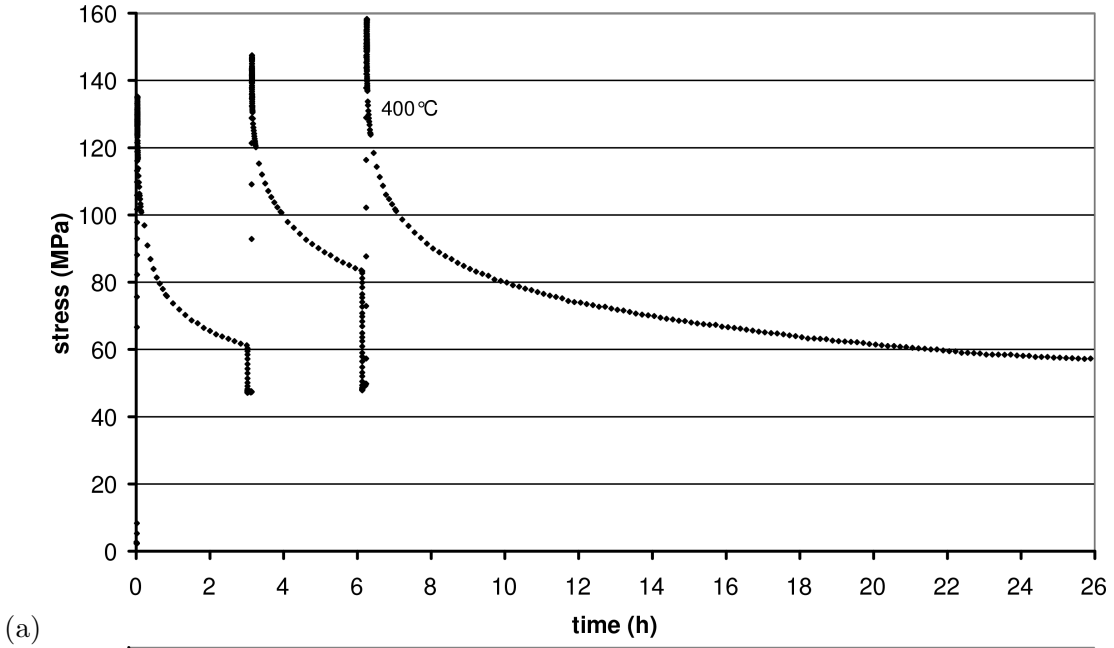

(a)

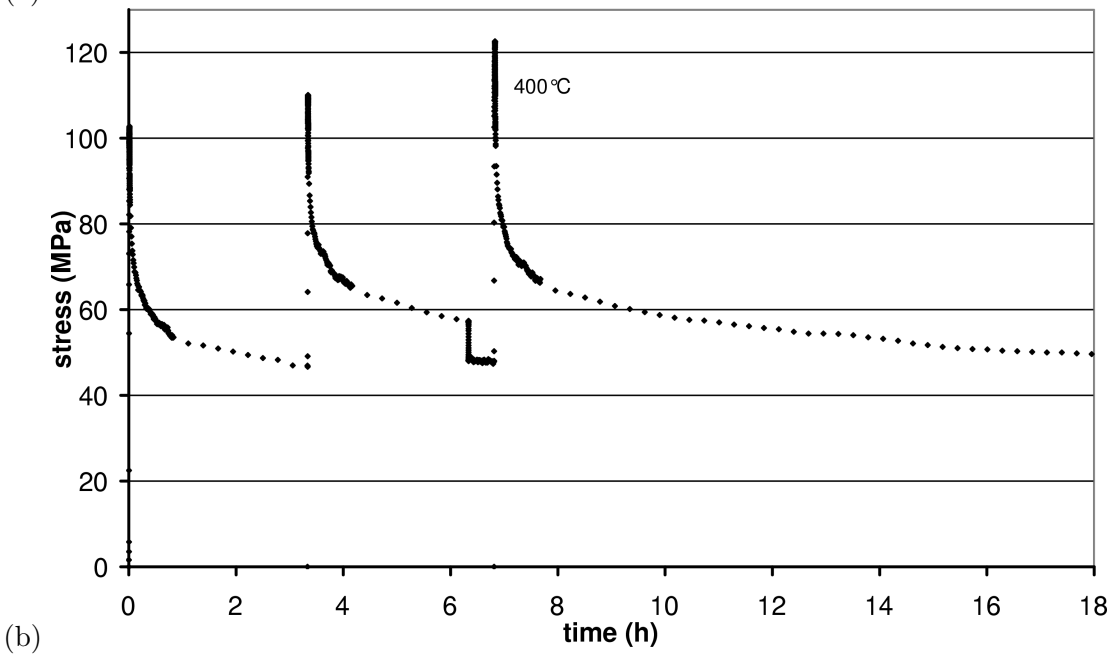

(b)

Figure VII.16 : True stress–time curves for each cycle of relaxation at $400°C$ for: (a) Zr702, (b) ZrHf.

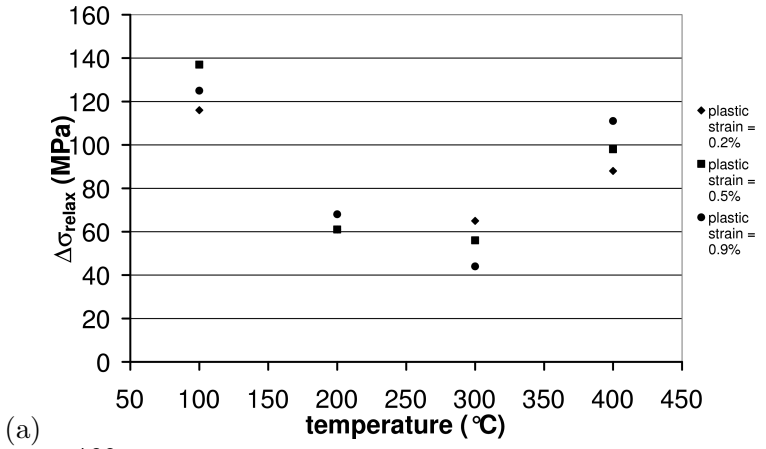

(a)

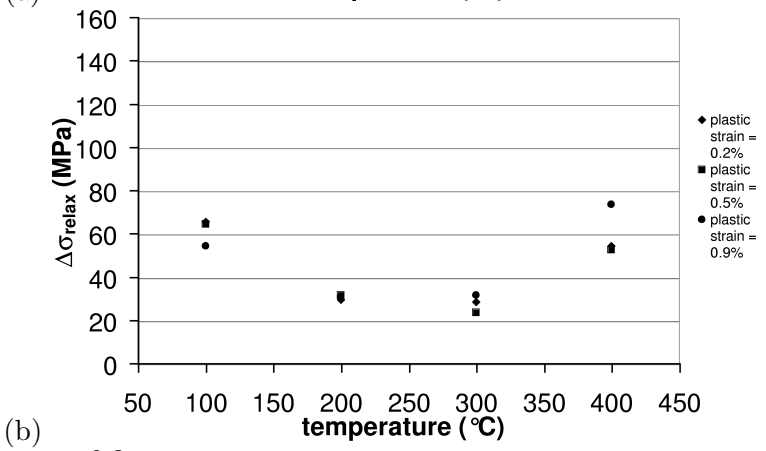

(b)

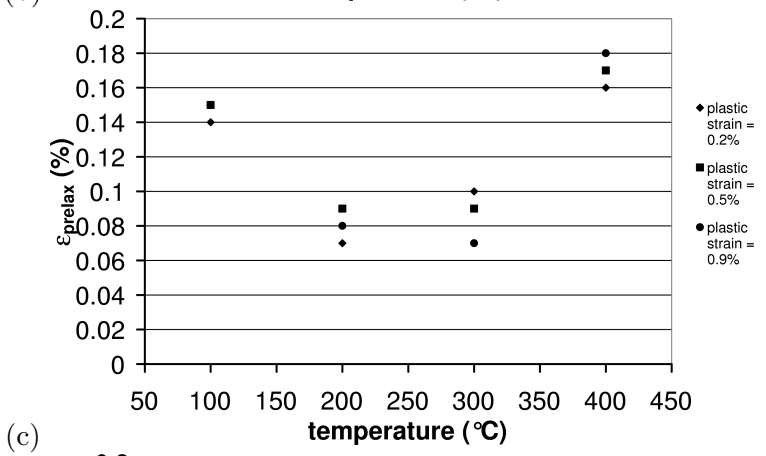

(c)

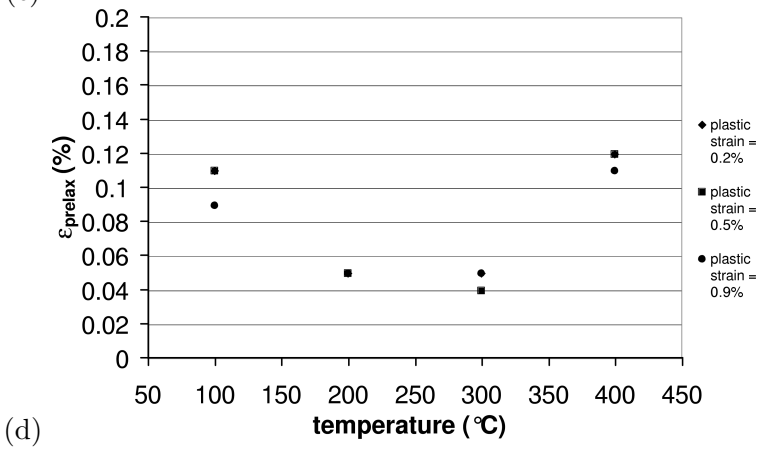

(d)

Figure VII.17 : Variation of $\Delta\sigma^{relax}$ as a function of temperature at 0.2%, 0.5% and 0.9% plastic strain levels for: (a) Zr702, (b) ZrHf and variation of ε_p^{relax} as a function of temperature at the same plastic strain levels for: (c) Zr702, (d) ZrHf.

The relaxation ratio is defined by:

$$\frac{\sigma_0 - \sigma}{\sigma_0} \tag{VII.2}$$

where σ_0 is the stress level at the beginning of relaxation. Figure VII.18 shows the evolution of relaxation ratio as a function of time for Zr702. For standard materials, the relaxation ratio increases with increasing temperature. However for Zr702, the relaxation ratio is lower at $200°C$ and $300°C$ than at $100°C$ and $400°C$. This effect is observed for instance during the third relaxation cycle as shown in figure VII.18. The same observation can be done for ZrHf.

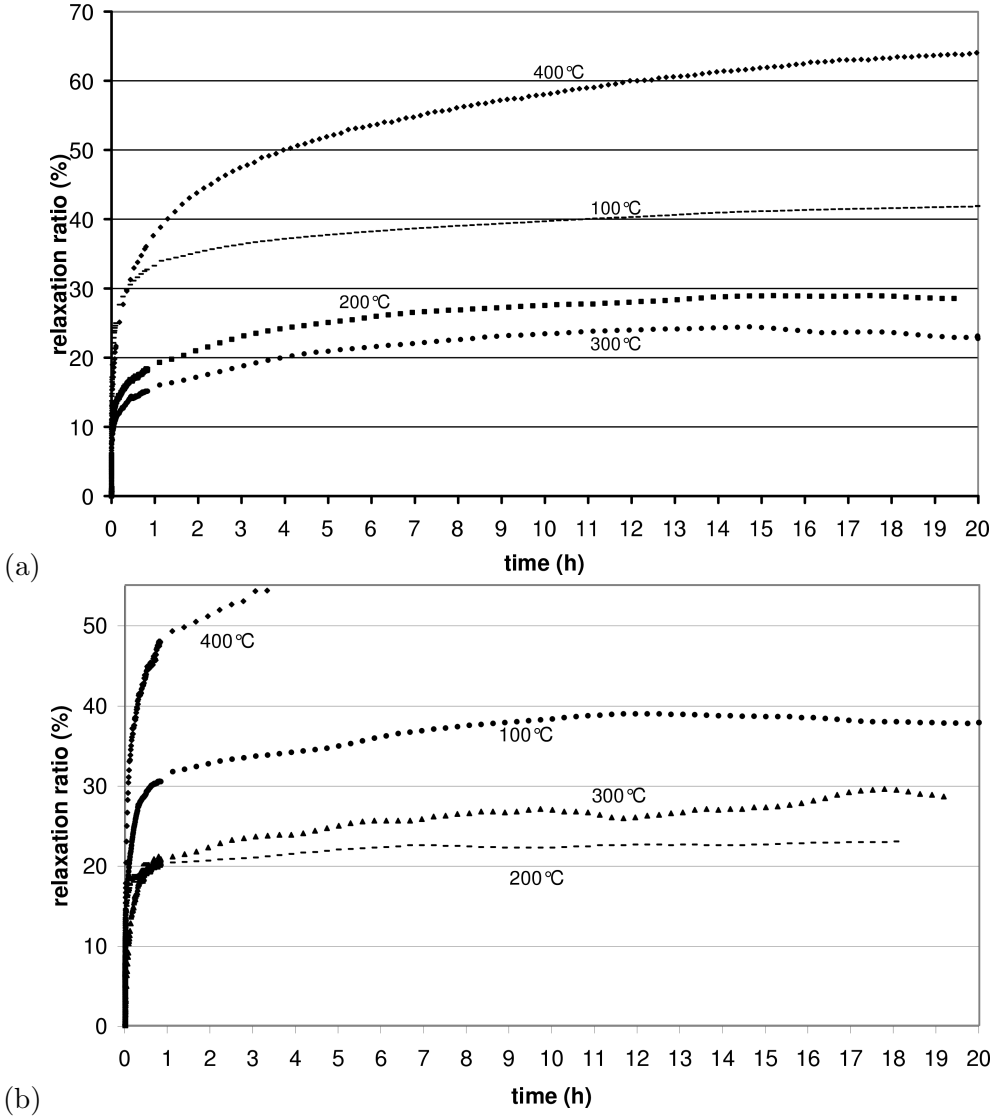

Figure VII.18 : Evolution of the relaxation ratio as a function of time during the third relaxation cycle for: (a) Zr702, (b) ZrHf.

We chose to divide the first relaxation sequence into "two relaxation stages".

At the beginning of the first relaxation sequence, the stress decreases rapidly as a function of time. We call this period, the "stage I of relaxation". Then, the stress can decrease more slowly as a function of time. We call this period, the "stage II of relaxation". This effect is observed for Zr702 at $100°C$ and at $300°C$ during the first and the third relaxation cycles. For ZrHf, the stage II of relaxation is only observed at $100°C$ and $300°C$.
However, this decrease of stress can be arrested. For instance, during the end of the first relaxation sequence, the stress does not decrease as a function of time any more, as shown in figure VII.15 for Zr702 at $200°C$. We call such an effect the "relaxation arrest". The relaxation arrest is then characterized by an abrupt change in the slope of the curve $\dot{\sigma}$–t from a finite to an almost vanishing value of $\dot{\sigma}$. Consequently, figures VII.14, VII.15 show that the relaxation arrest is observed for Zr702 at $200°C$ during all the relaxation cycles and at $300°C$ during the second and the third relaxation cycles. For ZrHf, relaxation arrest is observed at $200°C$ for all the relaxation cycles. Moreover, we call the "threshold stress of relaxation", the stress level associated with the occurrence of the relaxation arrest (the arrest of stress decrease during the relaxation sequence), labeled σ^{thres}.

The main conclusions for the stage I and stage II of relaxation are the following.

1. **Stage I of relaxation**
   For Zr702, during the first 100 seconds (about 0.027 hours), the stress decreases abruptly as shown in figure VII.19 (a). The decrease of stress is higher when temperature is lower. Figure VII.20 (a) shows the decrease of $\Delta\sigma_{stageI}$ during the first 100 seconds as a function of temperature. The effect of plastic strain is also shown on this figure.
   For ZrHf, the decrease of $\Delta\sigma_{stageI}$ during the first 100 seconds is considerably lower than for Zr702 whatever the temperature, as shown in figure VII.20 (b). Moreover, $\Delta\sigma_{stageI}$ is the lowest at $300°C$. At $100°C$, $200°C$ and $400°C$, $\Delta\sigma_{stageI}$ has almost the same value.

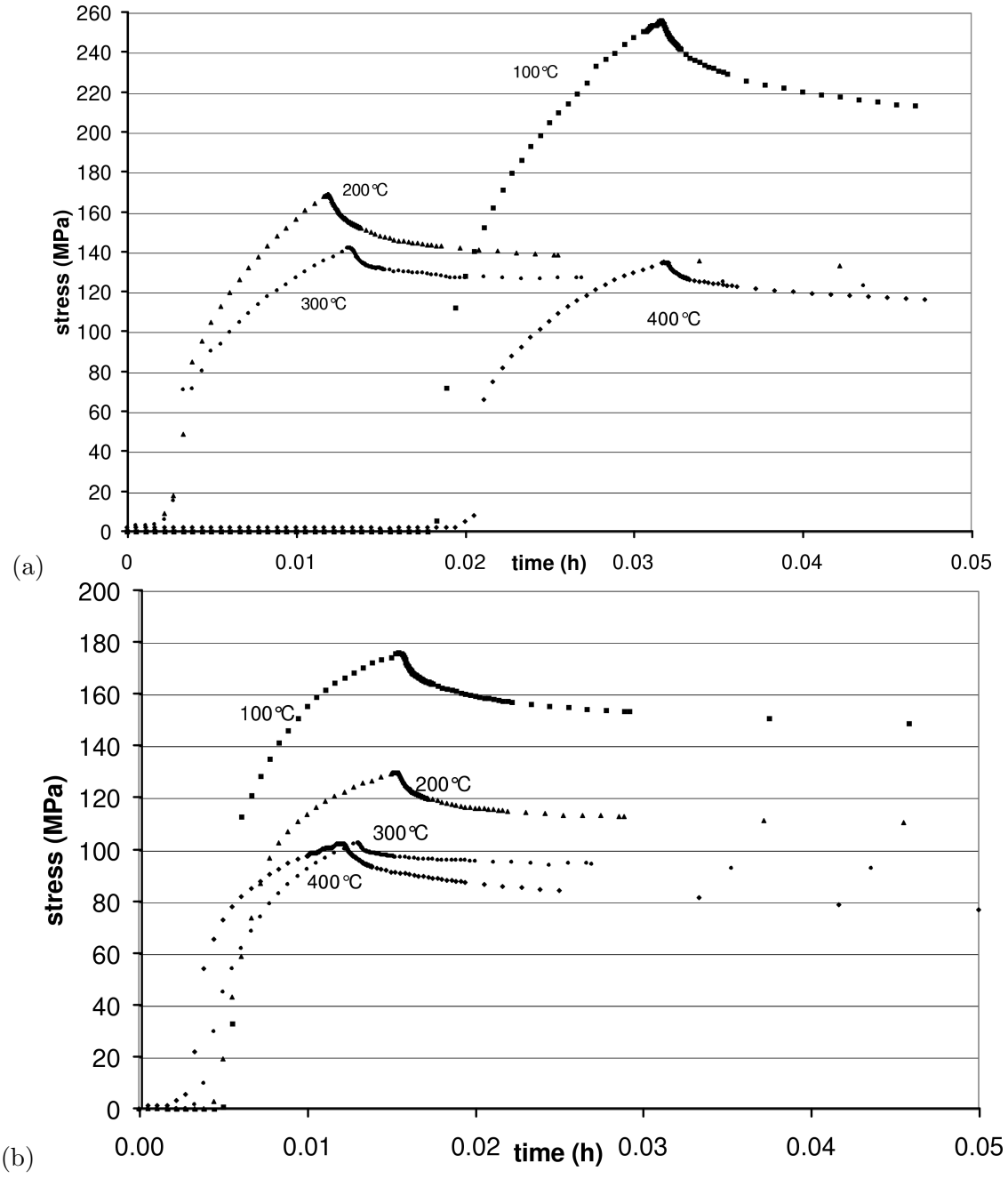

Figure VII.19 : Zoom of the true stress–time curves for the first cycle of relaxation at $100°C$, $200°C$, $300°C$ and $400°C$ for: (a) Zr702, (b) ZrHf.

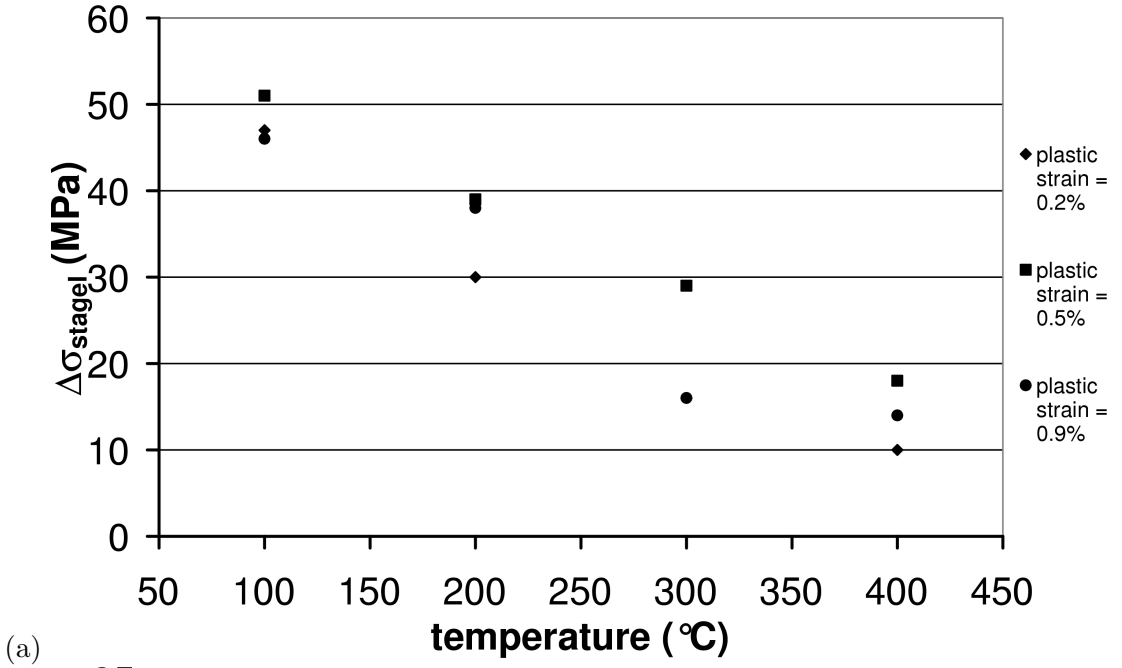

(a)

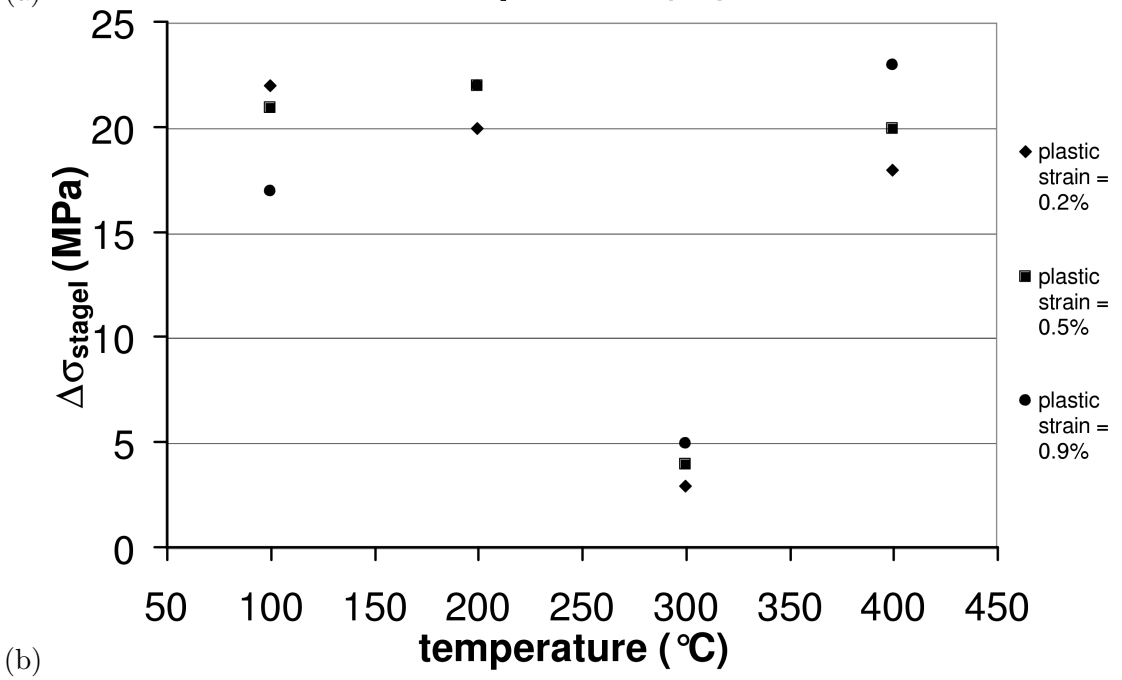

(b)

Figure VII.20 : Evolution of $\Delta\sigma_{stageI}$ during the first 100 seconds of stage I of relaxation for: (a) Zr702, (b) ZrHf.

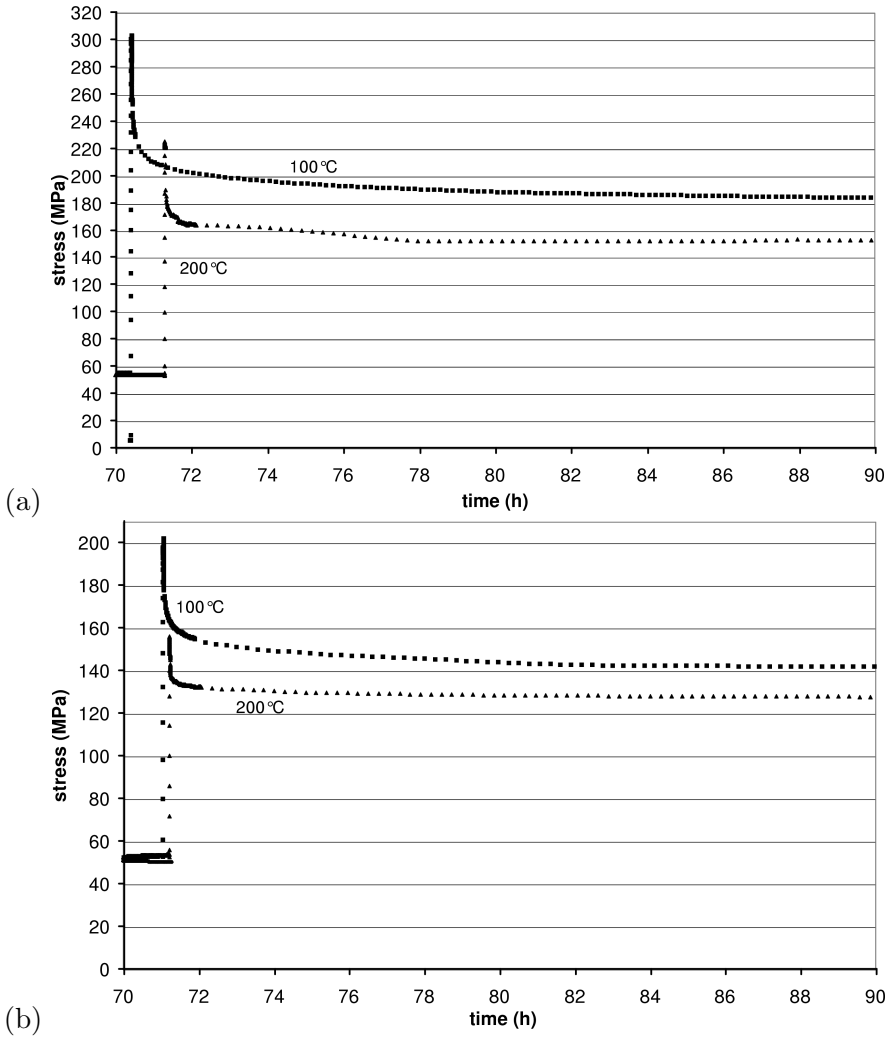

Figure VII.21 : True stress–time curves for the third cycle of relaxation at $100°C$ and $200°C$ for: (a) Zr702, (b) ZrHf.

2. **Stage II of relaxation**
   For Zr702, the stress decreases "classically" at $100°C$ as shown in figure VII.21 (a). However at $200°C$, the stress does not relax anymore. Such an effect is also observed at $300°C$. Note, that relaxation arrest was also observed at $200°C$ for Zr702 by Pujol (Pujol, 1994). Table VII.3 gives the values of σ^{thres} and the difference between σ_0 and σ^{thres}, labeled $\Delta\sigma^{thres}$.

   The main findings are the following:

   - At $200°C$, $\Delta\sigma^{thres}$ is nearly constant between 62 MPa–70 MPa.
   - At $300°C$, $\Delta\sigma^{thres}$ is smaller than at $200°C$, between 47 MPa–54 MPa,

   For ZrHf, relaxation arrest is only observed at $200°C$. The value of $\Delta\sigma^{thres}$ is lower than this for Zr702, nearly constant between 27 MPa–30 MPa.

Table VII.3 : Values of σ_{thres}, $\varepsilon_{p\ thres}$, $\Delta\sigma^{thres} = \sigma_0 - \sigma^{thres}$ as a function of temperature, the number of the relaxation cycle and material.

Material	Temperature ($^\circ C$)	Number of the relaxation cycle	σ^{thres} (MPa)	$\Delta\sigma^{thres}$ (MPa)
Zr702	$200^\circ C$	1	104	62
		2	141	66
		3	149	68
		4	153	70
		5	162	65
		6	163	67
		7	165	66
		8	162	66
	$300^\circ C$	2	140	54
		3	144	47
ZrHf	$200^\circ C$	1	100	29
		2	112	30
		3	120	28
		4	129	27

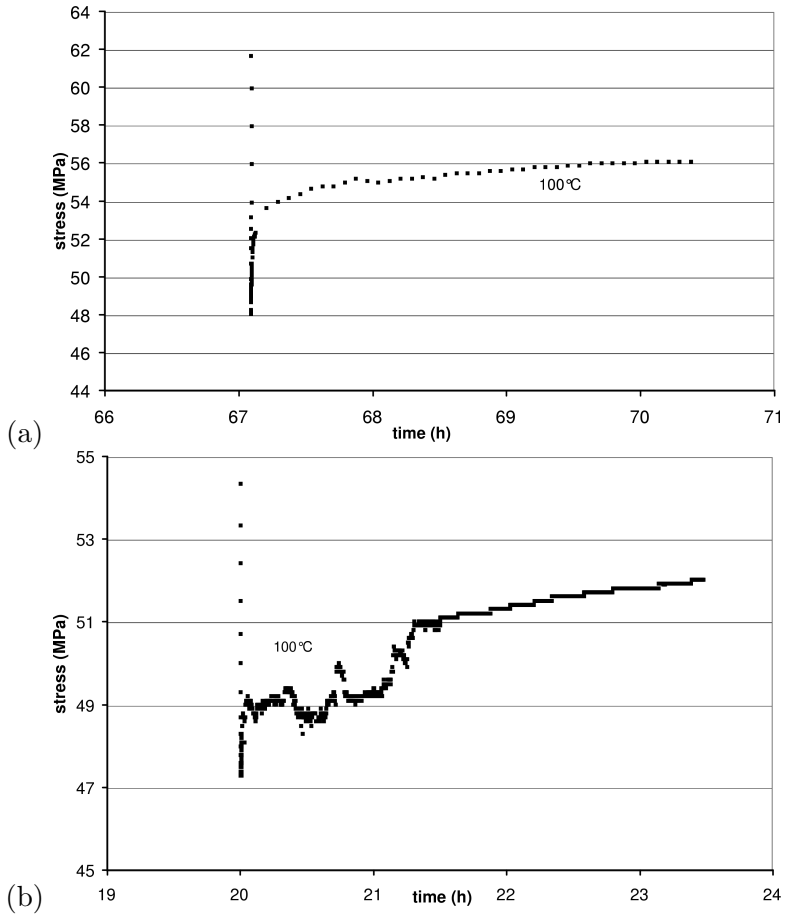

Figure VII.22 : Evidence of the existence of a back–stress (internal stress or kinematic hardening), reloading of the specimen, observed at $100°C$ during the second relaxation sequence after unloading down to 48 MPa: (a) Zr702, (b)ZrHf.

The second relaxation and the unloading sequence

After unloading the specimen down to 50 MPa, a second relaxation sequence was carried out at the total strain level corresponding to this stress level. The effect of time restoration, dependent of the microstructure of material after tensile straining can be observed. Figure VII.22 shows the stress increase instead of stress relaxation which proves the existence of kinematic hardening for Zr702 and ZrHf at $100°C$. If the initial stress level (50 MPa) would be located in the elastic domain, there would be no further stress variation. In contrast, figure VII.22 shows that the stress increases slightly. The specimen tends to shorten its length and the machine must reload the specimen elastically to preserve its length. This is characteristic of the existence of a large internal stress component, labeled X (back stress or kinematic hardening) and a comparatively small elastic domain. The initial stress level lies therefore outside the elastic domain of diameter $2R$ (where R is isotropic hardening) such that $\sigma - X$ is negative. This results in a slight stress increase, instead of the usual stress decrease observed when $\sigma - X$ is positive in relaxation tests. The interpretation of these results is given in chapter VIII.

Note also that during the unloading sequence at $10^{-4}\ s^{-1}$, Young's modulus were obtained at various plastic strain levels. Appendix II gives the values of Young's modulus for Zr702 and ZrHf. The main conclusion is that Young's modulus tends to decrease with increasing plastic strain at $100°C$, $200°C$ and $300°C$, and the opposite is observed at $400°C$ for both materials. Moreover, the values of Young's modulus are maximal at $200°C$ and $300°C$ for Zr702. For ZrHf, Young's modulus tends to decrease with increasing temperature.

VII.4.2 Concluding remarks

The conclusions relative to relaxation tests with unloading are the following:

- for both zirconium alloys, $\Delta\sigma^{relax}$ and ε_p^{relax} have minimal values between $200°C$ and $300°C$ whatever the plastic strain levels,
- the values of $\Delta\sigma^{relax}$ are almost twice as large for Zr702 as for ZrHf. The values of ε_p^{relax} are higher for Zr702 than for ZrHf,
- 90% of the stress relaxation occurs during the first hour and the first minutes at $200°C$ and $300°C$,
- at $100°C$ and $400°C$, no threshold value is observed on the stress which keeps decreasing even after 24 hours,
- for both alloys, a large internal stress component, X and a comparatively small elastic domain, R are detected.

VII.5 Conclusion

To conclude this experimental part, the main findings are summarized as follows.

1. **Tensile tests at constant applied strain rate on flat tensile specimens**
   A negative strain rate sensitivity is observed for transverse Zr702 between 10^{-5} s^{-1} and 10^{-3} s^{-1}/10^{-4} s^{-1} at $300°C$. The constant stress plateau observed between $200°C$ and $300°C$ at $10^{-5}s^{-1}$ and described as an athermal plateau by Derep (Derep et al., 1980) was also observed by Naka (Naka et al., 1988) in titanium (with about 500 wt ppm oxygen) and correctly interpreted as the signature of a thermally activated strain ageing phenomenon.
   Since the long flat samples were meant for a special equipment (Klose et al., 2003b; Traub, 1974), they are neither normalized and nor correctly aligned in the tensile machine that we used. As a consequence, the initial stress peak and the small Lüders plateau reported by Pujol (Pujol, 1994) in the same material namely transverse Zr702, cannot be observed here. Nevertheless, the other curves at all temperatures are entirely similar to those reported earlier.
   At constant temperature and constant strain rate tests, the flow stress levels can be reliably compared between tests carried out at two different strain rates since the internal microstructures pertaining to each strain rate is well established and stabilized in each sample. On the contrary, when using the same sample and performing strain rate changes at a given temperature, the internal microstructure is constantly trying to adjust to a new strain rate value and the flow stress levels cannot be reliably compared. This remark is particularly true in zirconium alloys in which the internal microstructure (dislocation arrangements, work hardening cells, subgrain boundaries and grain boundaries) play a major role in establishing the flow stress.

2. **Tensile tests with strain rate changes on cylindrical specimens**
   The SRS parameter is maximal at $200°C$ for Zr702, and at $300°C$ for ZrHf. A higher niobium content does not change the values of SRS for ZrHf–Nb. A higher oxygen content is associated with an increase of the values of SRS for ZrHf–O.
   After strain rate changes, stress peaks characterized by the parameter $\Delta\sigma_{stress\ peak}$ are observed at 10^{-3} s^{-1} and not at 10^{-4} s^{-1} at the various temperatures for all zirconium alloys. The values of $\Delta\sigma_{stress\ peak}$ increase with increasing temperature. The values of $\Delta\sigma_{stress\ peak}$ are almost twice as large for Zr702 than for ZrHf. A higher niobium content does not almost change the values of $\Delta\sigma_{stress\ peak}$ for ZrHf–Nb. A higher oxygen content is correlated with higher values of $\Delta\sigma_{stress\ peak}$ for ZrHf–O.
   PLC effect is observed at both 10^{-3} s^{-1} and 10^{-4} s^{-1} at $200°C$, $300°C$ and $400°C$. The PLC effect is active at higher applied strain rates for ZrHf than for Zr702 at the same tested temperature. ZrHf–Nb exhibits PLC effect at $200°C$ and 10^{-4} s^{-1}, contrary to ZrHf. A higher oxygen content is associated with a slight increase of the stress amplitude, observed at higher strain rates for ZrHf–O.
   Stress relaxation tests were chosen in order to explore the basic deformation modes present in the specimen. Although relaxation tests are rarely used, their great interest relies on their inherent ability to let the material choose its own plastic deformation modes in a large range of stress levels and strain rates ($10^{-4}s^{-1}$ down to $10^{-9}s^{-1}$ for our equipment) as opposed to tensile tests which try to impose a chosen macroscopic strain rate and to creep tests which impose a constant load for generally rather long periods of time.

3. **Stress relaxation tests with unloading down to 50 MPa**
   The relaxation arrest is observed for Zr702 at $200°C$ during all the relaxation cycles and at $300°C$ during the second and the third relaxation cycles. For ZrHf, relaxation arrest is only observed at $200°C$ for all the relaxation cycles.
   The amplitude of relaxation is minimal between $200°C$ and $300°C$ in Zr702 and ZrHf.
   When relaxation cycles include a relaxation sequence after unloading down to 50 MPa, spontaneous reloading of the specimen is observed, thus providing direct experimental evidence that a strong internal stress develops in the specimen during relaxation tests.

Chapter -VIII-

Interpretation of relaxation tests and other mechanical tests with the catastrophe theory

Contents

Abstract: The purpose of this chapter is to examine and clarify various models suggesting an extension of the microscopic approach based on the physics of interactions between dislocations and solute atoms on the macroscopic scale of mechanical tests where global strain rates are measured and recorded. As suggested earlier by Kubin et al. (Kubin and Estrin, 1989b; Estrin and Kubin, 1989) and by Strudel (Strudel, 1984), the catastrophe theory appears as an appropriate and powerful tool in the interpretation of the results. Two alternative strengthening mechanisms, simultaneously active are possible in a material exhibiting strain ageing effect: hardening by solute drag force exerted on moving dislocations and the usual strain hardening mechanism associated with an increase in dislocation density. The interpretation is mainly based on the determination of apparent activation volumes at constant temperature and constant microstructure, characterizing the various deformation mechanisms in dilute zirconium alloys.

VIII.1 Introduction

Forty years ago, various models were proposed in order to take strain ageing mechanisms into account, trying to explain the anomalous behavior observed on the macroscopic scale, for instance the negative strain rate sensitivity. For that purpose, it is important to correctly define the type of interactions between dislocations and solute atoms and the microscopic associated deformation modes. That is why this chapter deals with the phenomenological interpretation of the experimental results in terms of the main deformation mechanisms in dilute zirconium alloys, detected at constant temperature. Especially, the evolution of these mechanisms is studied as a function of temperature, stress and strain rate. The determination of apparent activation volumes leads to some paradoxes that we will try to solve by introducing the catastrophe theory and the Strudel's studies about interactions between dislocations and impurities (Strudel, 1984).

VIII.2 Competitive deformation modes

VIII.2.1 Analogy between microscopic and macroscopic models

Microscopic models

Two main microscopic models were suggested in the bibliography, based on the same physical phenomenon, the interactions between solute atoms (interstitial and/or substitutional) and dislocations. Various types of solute atoms and dislocations have to be taken into account:

- interaction between mobile dislocations and immobile impurities (shear precipitates, anchoring points of mobile dislocations) (Nabarro, 1947),
- interaction between immobile dislocations and mobile impurities (Cottrell clouds developed by diffusion around immobile dislocations),
- interaction between mobile dislocations and mobile impurities (Cottrell clouds developed by diffusion around mobile dislocations (Cottrell and Bilby, 1949; Yoshinaga and Morozumi, 1971).

The two microscopic models are described as follows.
The Dynamic Strain Ageing (DSA) model is based on the dynamic interaction between mobile dislocations and diffusive solute atoms (Cottrell and Bilby, 1949; Friedel, 1964; Mulford and Kocks, 1979). Note that this model is the oldest, reported by Friedel and used by Cottrell. The dislocations can glide with their diffusive solute cloud (bulk diffusion), called the "Cottrell's cloud" with the hardening vacancies under stress. The main hypothesis is that the dislocation velocity is the same as the velocity of solute atoms. The mean solute atoms velocity v under the force F is given by:

$$v = \frac{DF}{k_B T} = \frac{D\delta}{r^2} \tag{VIII.1}$$

where D is the diffusion coefficient, δ characterizes the diameter of the Cottrell's cloud and r is the minimal distance between the dislocation and impurities. Consequently, the concentration of solute atoms around a dislocation can be larger than that in the lattice, C_0. The advantage of this hypothesis is that the critical velocity v_M for which the Cottrell's cloud is unlocked can be established, associated with the force F_M (see instability 1 on figure VIII.1). Note that v_m is the minimal velocity at which a dislocation can move and still be entirely free of its cloud of solute atoms. Below this minimal velocity, the anchoring of the dislocation becomes

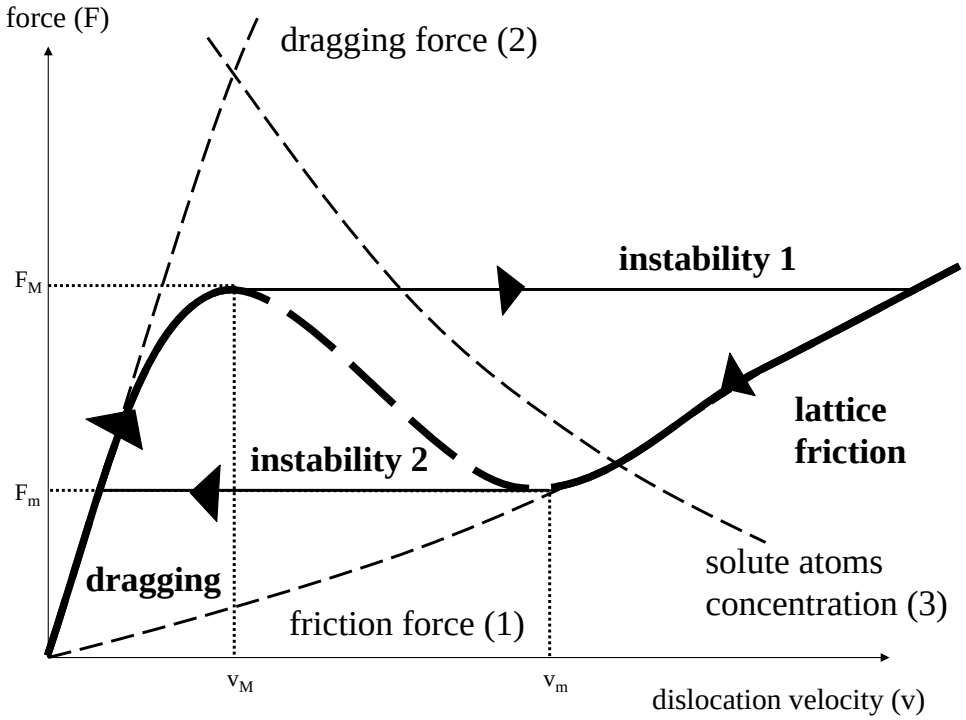

Figure VIII.1 : Force versus dislocation velocity diagram for a mobile dislocation when solute drag effects are operating (Strudel, 1984).

possible with the formation of a new cloud of solute atoms (see instability 2 on figure VIII.1). However, this DSA model does not take the enhanced diffusion rate of solute atoms in the disturbed crystalline structure of the dislocation core into account. In assuming that the speed of a dislocation is uniform, this model is unrealistic. In fact, the glide of a dislocation is non uniform due to the presence of extrinsic obstacles, for instance the forest dislocations. Moreover, its numerical application leads to non realist predictions of the diffusive rate for substitutional atoms. It does not permit to explain properly the PLC effect, in particular the existence of a critical strain at which PLC serrations can be observed on the macroscopic curve.

The Static Strain Ageing (SSA) model is based on the static interaction between slowly moving or immobile dislocations and diffusive solute atoms. This model is related to the Cottrell's model, assuming that δ is high and the dislocation velocity is small or close to zero. The diffusion of the solute atoms is possible when the dislocations are stopped by extrinsic obstacles. Two states in the glide of a dislocation can be considered: the arrest at obstacles and the fast moving of a dislocation among these obstacles. The mean dislocation velocity v is established by the mean time of the dislocation arrest at obstacles t_w, called the "waiting time". These obstacles are in a distance L from each other:

$$v = \frac{L}{t_w + t_p} \tag{VIII.2}$$

where t_p is the time of the dislocation propagation among the obstacles. Consequently, the glide of the dislocation is supposed to be discontinuous with a waiting time behind obstacles and a time of the dislocation course among the obstacles. This model does not distinguish

between dynamic strain ageing and static strain ageing (strengthening takes place during the arrest of deformation, the waiting time is consequently equal to the ageing time). As $t_w >> t_p$, the mean dislocation velocity v can be written as follows:

$$v = \frac{L}{t_w} \tag{VIII.3}$$

Moreover as δ is high, the concentration of solute atoms around dislocation C_s can become superior to their concentration in the lattice C_0. C_s depends on D, the diffusive coefficient and t_w, the waiting time. Note that the diffusion of solute atoms around the dislocation during the waiting time increases, the strengthening of obstacles too. As the waiting time is imposed by the applied strain rate, the unanchoring of the dislocation need an increase of the flow stress, or leads to the creation of new dislocations. Consequently, the hardening increases. A fast and massive unanchoring of dislocations in a localized region of sample can lead to PLC plastic deformation bands.
For this model, different types of diffusion can be taken into account:

1. the vacancies, D_v (McCormick, 1972),
2. the bulk diffusion of solute atoms, D_b (van den Beukel, 1975a),
3. the dislocation cores, D_c (Mulford and Kocks, 1979).

Note that the second and the third mechanisms can be active simultaneously in a cooperative manner. Yoshinaga and Morozumi (Yoshinaga and Morozumi, 1971; Yoshinaga et al., 1976) used the Cottrell's model, simulating the dynamic interaction between moving dislocations and solute atoms in order to calculate the profile of solute atoms concentration around a moving edge dislocation (see figure VIII.2). They improved the equations, allowing to draw more precisely the force versus dislocation velocity diagram for a large range of strain rates, which is not the case for the Cottrell's model. In figure VIII.2 (a), the edge dislocation is assumed to be initially at rest and in thermal equilibrium. When accelerating, the local overconcentration decreases until the velocity of the dislocation reaches v_M and instability 1 is triggered. In figure VIII.2 (b), the edge dislocation is assumed to be initially moving and deprived of any solute atoms concentration but slowing down and attracting more and more solute atoms until v_m is reached and a critical overconcentration is attained which triggers instability 2.

Consequently, the force versus dislocation velocity diagram, as shown in figure VIII.1 can be used to describe both SSA and DSA models. The description of figure VIII.1 is the following.
In pure solids with low Peierls forces such as f.c.c. metals, the velocity of gliding dislocations can be very high when the density of dislocations or other obstacles is low. It is only limited by the rate of energy loss due to interaction with phonons and due to phonon irradiation. When impurities are present in the crystal, lattice friction can be appreciably raised and the retarding force experienced by the dislocation is increasing with its velocity (see curve (1) of figure VIII.1). In the friction mode, the dislocation undergoes the friction force due to solute atoms in the lattice where the diffusive phenomena are inactive. In solid solution of either interstitial or substitutional nature and at high temperature, solute atoms are able to segregate towards an edge dislocation and the localized excess concentration can diffuse along with them when its velocity remains compatible with enhanced diffusion mechanisms (Strudel, 1969). The retarding force or the "drag stress" exerted by moving solute atoms on the mobile dislocation was described in detail by Yoshinaga (Yoshinaga and Morozumi, 1971)

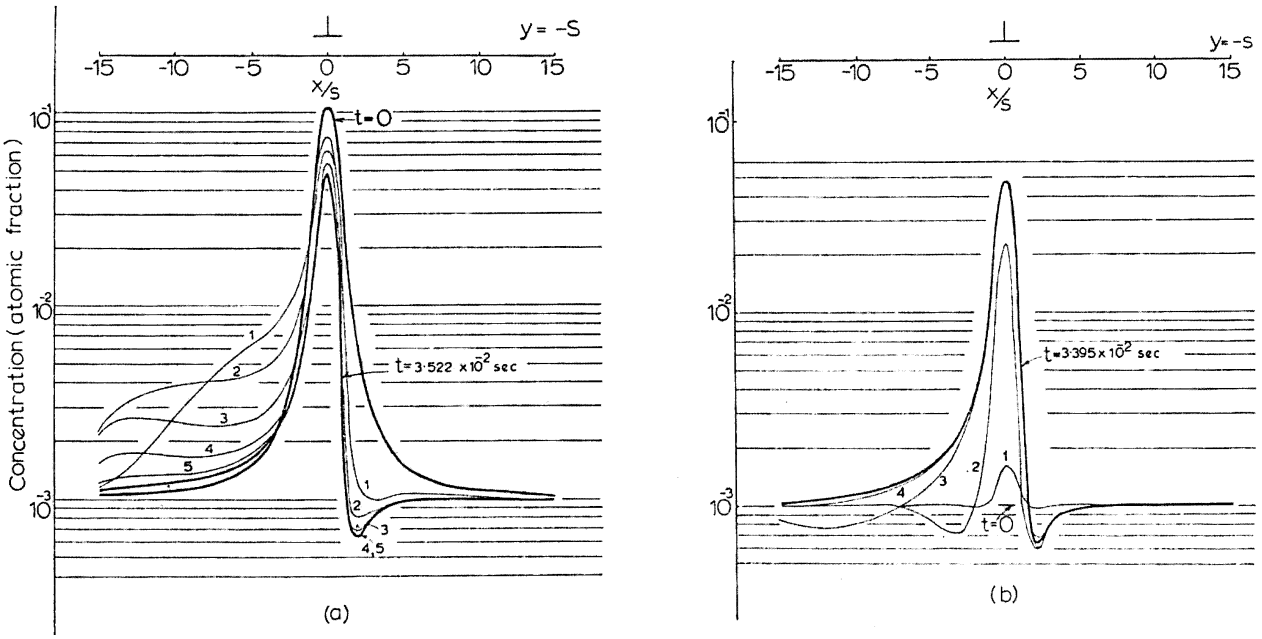

Figure VIII.2 : Changes of the concentration distribution around a dislocation as the dislocation moves. Bold curves show the initial and near to the steady state concentration distributions at $300°C$ and for a dislocation velocity of 2.10^3 Å$.s^{-1}$: (a) the case where the initial atmosphere is the one in thermal equilibrium round a stationary dislocation. The curves numbered 1, 2, 3, 4 and 5 show the concentration distributions after 3.807 10^{-3} s, 7.894 10^{-3} s, 1.434 10^{-2} s, 2.031 10^{-2} s and 2.677 10^{-2} s respectively; (b) the case where the dislocations has no atmosphere initially. The curves numbered 1, 2, 3 and 4 show the concentration distributions after 1.479 10^{-5} s, 1.748 10^{-3} s, 1.163 10^{-2} s and 2.077 10^{-2} s respectively (Yoshinaga and Morozumi, 1971).

in the case of carbon atmospheres in vanadium. This force increases extremely quickly with increasing velocity (see curve (2) of figure VIII.1) until a maximum v_M is reached. Beyond this velocity, the concentration of solute atoms is not sufficient to slow down the dislocation line which tends to accelerate there by reducing further its concentration of solute atoms and rapidly reaches velocities for which the lattice friction alone is operating (see curve (3) of figure VIII.1). In the dragging domain, the force is nearly proportional to the dislocation velocity. The effect of temperature on the force versus dislocation velocity curve underlying the phenomenon was described later by Aubrun (Aubrun, 1975) who introduced a surface describing the local flow behavior of the material as a function of temperature and strain rate. Aubrun (Aubrun, 1975) proposed a synthesis of the behavior of an edge dislocation in interaction with solute atoms. Three domains of strain rate can be distinguished in the force versus dislocation velocity curve as shown in figure VIII.1. Both laws can be observed, separated by an unstable domain with a force decreasing with velocity connecting them.

DSA and SSA models take both modes of the gliding dislocation into account, capable of being active simultaneously under a given stress:

- at low dislocation velocity, the dislocation is in the drag solute mode and undergoes the dragging force, which can be described by Yoshinaga's model or Cottrell's model (part (2) of the curve VIII.1). The friction force can quickly reach high values with increasing stresses because dislocation must move, keeping constant the local concentration of solute atoms,
- at high dislocation velocity, the dislocation is in the friction mode and undergoes a friction force due to impurities present in the lattice. Dislocation is free of its Cottrell's clouds and can move quickly. The dislocation is only limited in its velocity by the friction forces due to the solid solution elements, dispersed or immobilized, creating hard points (part (1) of the curve VIII.1),
- intermediate dislocation velocities are strictly transitory because unstable. The deformation mechanism is composed, on the one hand, of the dragging mode and, on the other hand, of the friction mode.

Macroscopic models

Considering the material on the scale of the sample and ignoring the elementary mechanisms that can cause strain ageing effects on an atomic scale, macroscopic models were developed to take PLC effect into account with macroscopic parameters. PLC effect can be linked to the negative SRS parameter, $SRS = (\frac{\partial \sigma}{\partial log \dot{\varepsilon}})_{T,\varepsilon_p}$.

Two main macroscopic models were suggested, based on the fact that SRS can become negative (Sleeswyk, 1958):

1. the Penning's model (Penning, 1972) describes the behavior of a material at small deformations, showing PLC effect with a hard machine. He was the first to develop a model in which a region of negative strain rate sensitivity is introduced in the macroscopic σ versus $\dot{\varepsilon}$ diagram (see the domain BC on figure VIII.3),
2. the Kubin–Estrin's model (Kubin and Estrin, 1985) is based on this first model and applied it to the case of a soft machine.

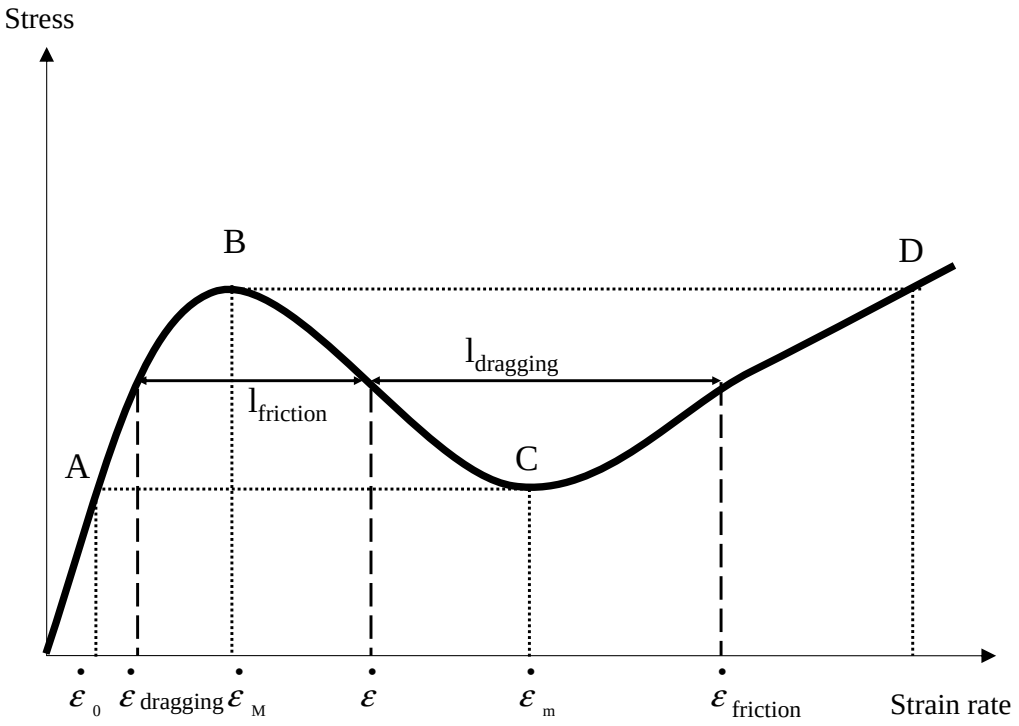

Figure VIII.3 : Stress versus strain rate diagram.

Let us consider a strain rate $\dot{\varepsilon}$ located in this intermediate regime (see the domain BC on figure VIII.3), it can be achieved on the mesoscopic or macroscopic level as the result of the combination of two different strain rates taking place in different areas of the material or in different regions of one tensile sample. We can write:

$$\dot{\varepsilon} = k_1 l_{dragging} \dot{\varepsilon}_{dragging} + k_2 l_{friction} \dot{\varepsilon}_{friction} \tag{VIII.4}$$

by use of the standard "weighting rule" where $k_1 l_{dragging}$ represents the volume fraction of material flowing in the dragging mode (hence proportional to $l_{dragging}$ on figure VIII.3) and $k_2 l_{friction}$ is the volume fraction of material flowing in the friction mode. Notice that this latter quantity, $k_2 l_{friction}$ is much smaller than the former one, $k_1 l_{dragging}$. We can visualize it on a macroscopic scale as the narrow PLC band moving along the gauge length of a tensile specimen (1% of the entire volume of the specimen or less), while the rest of the gauge length (99% of its volume) does not seem to be active in the straining process but yet is slowly straining at a rate $\dot{\varepsilon}_{dragging}$ on its entire volume $k_1 l_{dragging}$. Alternatively, on a mesoscopic scale, considering a large population of dislocations (and no longer an isolated dislocation as on figure VIII.1), the schematic of figure VIII.3 represents how an average strain rate of $\dot{\varepsilon}$ can be achieved in the considered volume where this large population of dislocations is active. This population will spontaneously split into two different colonies, as described also by the mathematical theory of bifurcations (Kubin et al., 1984): one large colony of dislocations proportional to $l_{dragging}$ moving in the dragging mode at a velocity below v_M (see figure VIII.1), hence very slowly, and another very small colony proportional to $l_{friction}$ moving very rapidly in the friction mode at a velocity well above v_m (see figure VIII.1), contributing a strain rate $\dot{\varepsilon}_{friction}$.

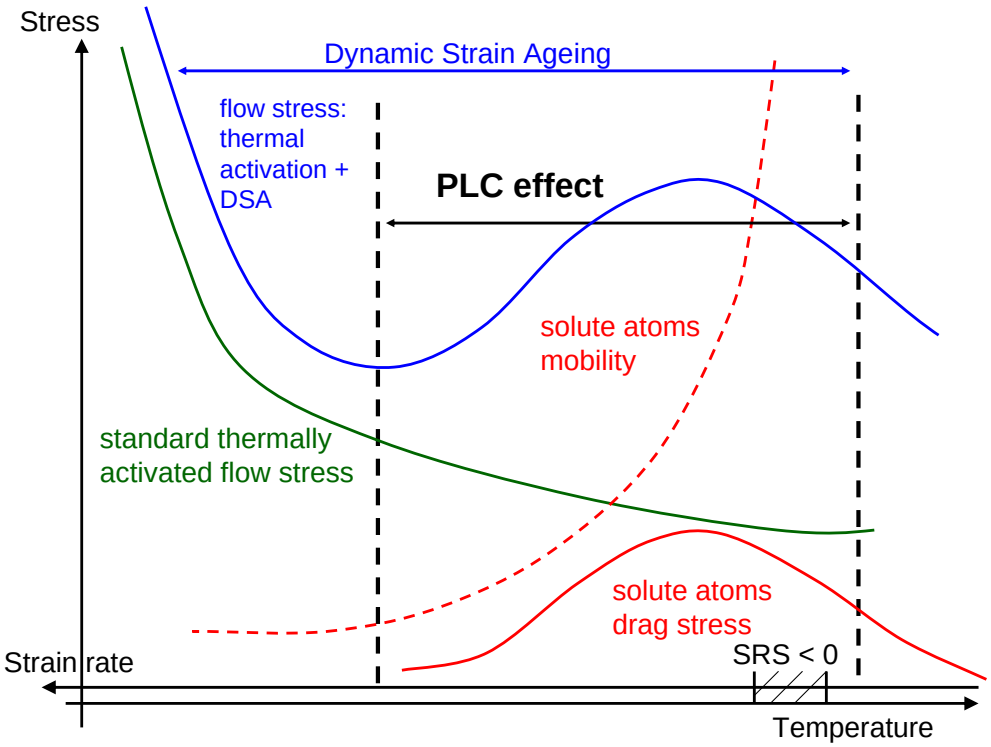

Figure VIII.4 : Flow stress (in blue) resulting from the combined effect of thermal activation and DSA.

Figure VIII.4 shows the contribution of DSA on the flow stress, leading to a negative strain rate sensitivity in a limited range of temperatures and strain rates. Notice that as mentioned in the previous chapter VII, our experimental results do not allow to affirm the hypothesis suggested in literature: "the observation of PLC serrations on the macroscopic curve is equivalent to the detection of a negative strain rate sensitivity". That is why the domain of the existence of PLC effect called PLC domain is plotted in dotted lines in figure VIII.4. $SRS < 0$ is observed only for the upper temperatures end of the PLC domain. The main macroscopic models are based on this principle with some variants.

Concluding remarks

The microscopic diagram F versus v is similar to the macroscopic diagram σ versus $\dot{\varepsilon}$ where $\sigma = F(\dot{\varepsilon})$ is shown in figure VIII.3. The microscopic and the macroscopic properties are the following:

$$F = \sigma b \qquad ; \qquad v = \frac{\dot{\varepsilon}}{\rho_m b} = \frac{L}{t_w} \tag{VIII.5}$$

where ρ_m is the mean density of mobile dislocations with Burgers vector, b. By analogy to the microscopic F versus v diagram, one can define phenomenologically two limiting regimes in the macroscopic σ versus $\dot{\varepsilon}$ diagram: the dragging and the friction modes. However, the intermediate regime is more complex and unstable. This domain is only observable on the macroscopic scale.

Consequently, the splitting of strain rates or the population of dislocations into two different colonies cannot be easily observed. Refined strain field measurement techniques are required to investigate and to quantify them. Indeed in figure VIII.3, the axis is the

plastic strain rate and not the isolated dislocation velocity but the collective group velocity of dislocations. In addition to dislocations motion, considered so far when a crystal is strained, intensive dislocation multiplication is taking place. The following equation takes both phenomena into account:

$$\dot{\varepsilon}_p = \rho_m b v + \dot{\rho}_m b L \tag{VIII.6}$$

where bL is the area swept by the mobile dislocations and v is the mean dislocations velocity. The first term of this equation, often called the Bailey–Orowan's equation describes the glide of mobile dislocations populations. These dislocations are rectilinear, gliding with a mean uniform velocity, labeled v. The second term takes the multiplication of dislocations ($\dot{\rho}_m$) and their glide into account with a mean free distance, L.

That is why, the macroscopic stress necessary to keep a given plastic strain rate can be obtained according to the following mechanisms:

- for extensive mobile dislocations populations, moving slowly, being able to drag their Cottrell's clouds (dragging mode),
- alternatively for a few mobile dislocations populations, moving rapidly, free of any segregation (friction mode),
- and/or for the regular multiplication of dislocations, created by sources with a constant rate, gliding with a fast velocity between long distances obstacles (for instance the dislocations cell walls).

VIII.2.2 Basic features of catastrophe theory

The elementary dislocation mechanisms of solute drag and solid solution hardening can be described, using the catastrophe theory, first developed by mathematicians such as Thom (Thom, 1972) in France and Zeeman (Zeeman, 1977) in USA. The catastrophe theory describes the behavior of unstable systems characterized by a non–linear response to externally imposed conditions. Two radically different deformation modes are possible in the temperatures range where strain ageing is active since two different hardening modes may operate alternatively and/or simultaneously. The catastrophe theory predicts seven elementary catastrophes. Some combinations of catastrophes can be used to describe complex macroscopic behaviors. The simplest catastrophe is the "fold" catastrophe because its representative surface is simply cylindrical.
Catastrophe theory refers to curves such as that of figure VIII.1 in order to generate various surfaces described as cuspsoïds. The surface described in Aubrun's model (Aubrun, 1975) is associated with a 2–dimensional control space or "cusp" catastrophe represented on figure VIII.5 for the dragging mode. It is conical rather than cylindrical. The surfaces shown on the stress versus strain rate (velocity) diagram are generated due to strain hardening effect. Consequently, the point representing the behavior of some elementary volumes of the material will move on this surface during the course of a tensile test. When the effect of solute atoms concentration is considered at a given temperature, another cusp surface can also be drawn with a bifurcation point located at low solute concentrations where the phenomenon obviously vanishes. Strudel (Strudel, 1984) imagined that the solute drag phenomena can be described by a "swallowtail" hypersurface when the effect of the three control variables is included: temperature, stress (or solute atoms concentration) and loading rate (strain or stress rate).

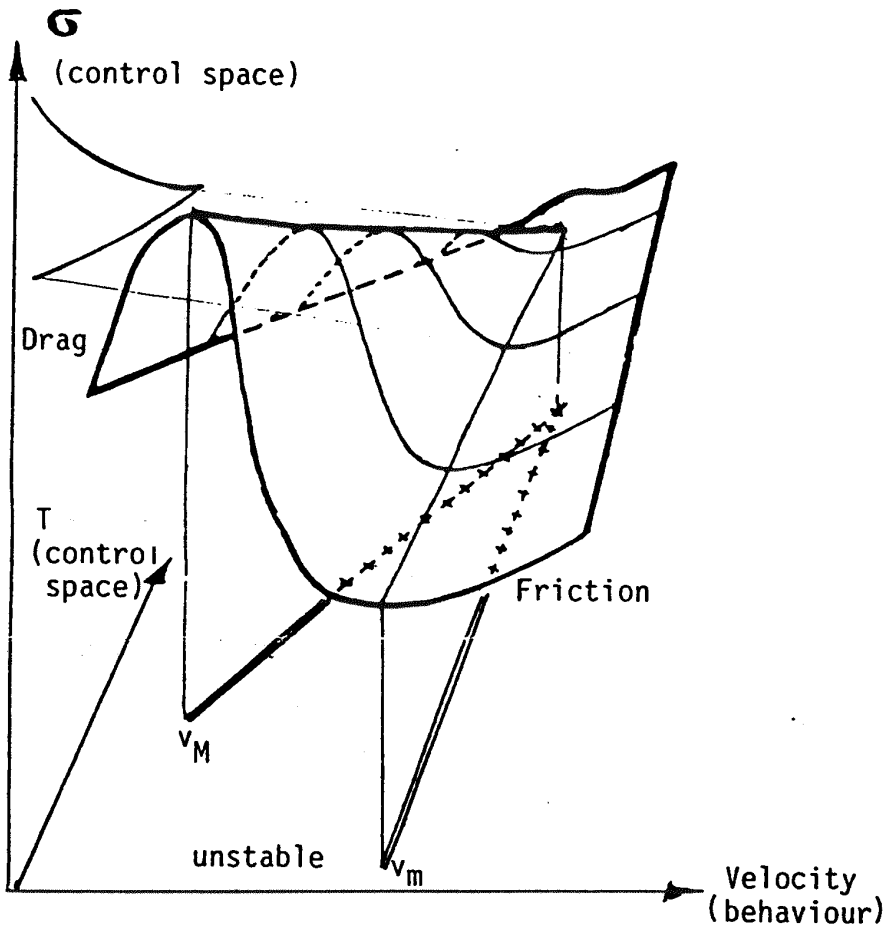

Figure VIII.5 : Representation of the deformation mechanisms in 3–dimensional diagram stress–strain rate(velocity)–temperature using the cusp of the catastrophe theory (Strudel, 1984).

VIII.3 Interpretation of experiments performed on two zirconium alloys

Considering the projection of the 3–dimensional diagram stress–strain rate–temperature on to different sub–spaces (the stress–strain rate plane, the stress–temperature plane and the strain rate–temperature plane), we used this tool in the interpretation of experimental results of relaxation and the other mechanical tests. The materials studied are Zr702 and ZrHf.

VIII.3.1 Limiting curves in the stress versus plastic strain rate plane

Phenomenological approach

In the $\log \dot{\varepsilon}_p$ versus σ diagram, the various plastic or viscoplastic strain rates of a material can be exposed in a large range of strain rates and if necessary for various temperatures or plastic strain levels. This type of diagram shows the various plastic and viscoplastic deformation modes of a material for several plastic strain levels at a given temperature as shown in figure VIII.6. Indeed, in this type of diagram, the slopes of the limiting curves are linked to the viscosity of the material and to the apparent activation volume of the plastic deformation mode, V_a. The material is more viscous when the slope is lower (the apparent activation volume is lower). In contrast, the material is less viscous when the slope is higher (the apparent activation volume is higher).
In most standard materials, the apparent activation volume is the result of several contributions:

- the crossing of the obstacles,
- the multiplication of dislocations,
- the loss of dislocations by recovery processes and the formation of substructures.

However, in materials presenting DSA effects, two different viscoplastic modes may be present simultaneously in different regions of the specimen, which consequently are deforming at drastically different strain rates. When exploring the upper or the lower limits of the temperature–strain rate domain where DSA is observed, one of the two modes becomes dominant and fixes the strain rate of the tested specimen. But in the middle of the domain (see figure VIII.6), no mechanism is prevailing, the behavior of the material is erratic because the straining processes are unstable and the local strain rates can change abruptly in a manner which is not reproducible from one specimen to the next, hence this grey area exists on figure VIII.6 between two well defined regimes.

We recall that at higher plastic strain rate, the macroscopic response observed in the $\log \dot{\varepsilon}_p$ versus σ plot is associated with the friction mode. At lower plastic strain rate, the macroscopic response, observed in the $\log \dot{\varepsilon}_p$ versus σ plot is associated with the dragging mode. Between both modes, the behavior is unstable.

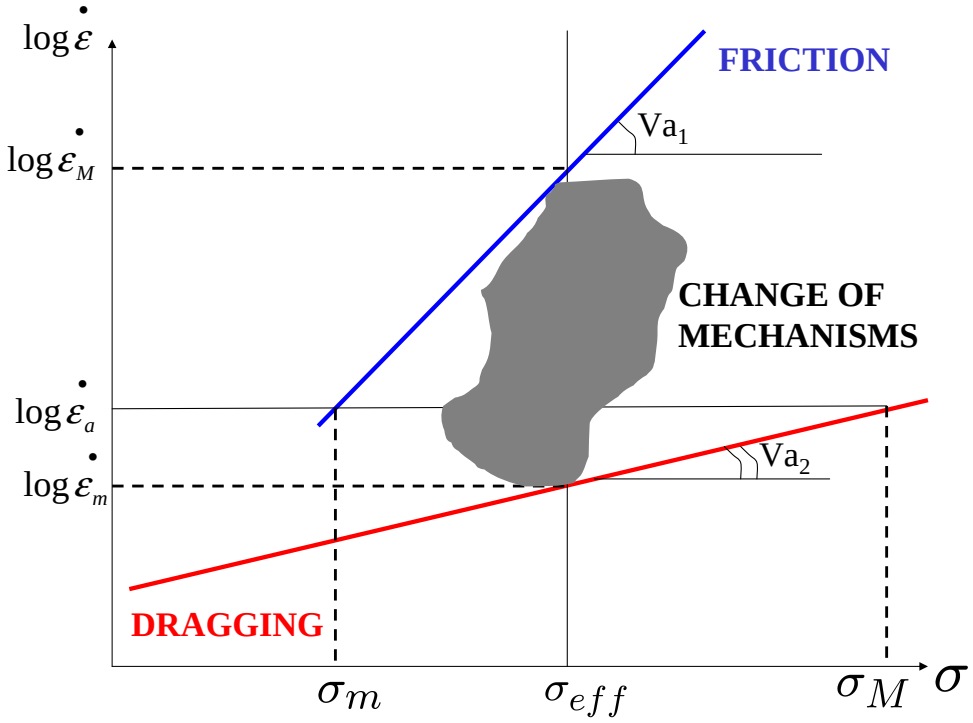

Figure VIII.6 : Schematic diagram of the various deformation mechanisms in the $\log \dot{\varepsilon}_p$ versus σ plot.

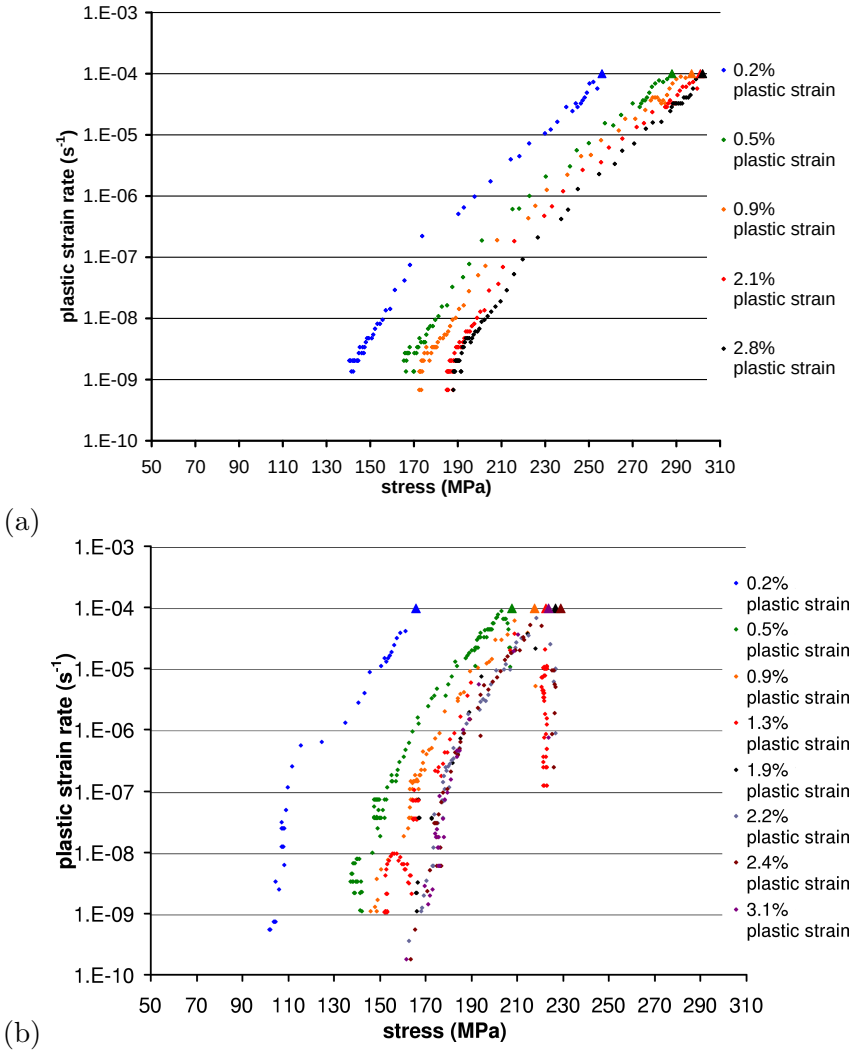

Figure VIII.7 : Effect of the plastic strain level on the $\log \dot{\varepsilon}_p$ versus σ diagrams for Zr702 at: (a) $100°C$, (b) $200°C$.

Relaxation tests performed on Zr702 and ZrHf

Repeated relaxation cycles were performed on Zr702 and ZrHf by loading at a constant strain rate of $10^{-4}s^{-1}$ up to programmed plastic strain values (0.2%, 0.5% for instance) and for several temperatures. Thus, relaxation results for Zr702 and ZrHf are presented and compared as a function of these two parameters: the plastic strain level, ε_p and the temperature, T. Figures VIII.7, VIII.8 show the effect of the plastic strain level, plotting the $\log \dot{\varepsilon}_p$ versus σ diagrams for Zr702 as a function of various temperatures. The exact values of the plastic strain levels at which the relaxation tests were carried out are reported on each figure. The $\log \dot{\varepsilon}_p$ versus σ diagrams for ZrHf as a function of various temperatures are also shown in appendix II. We recall that a deformation mechanism is associated with one single well–defined slope in the $\log \dot{\varepsilon}_p$ versus σ diagram. The intermediate regime is such that no defined slope can be detected.

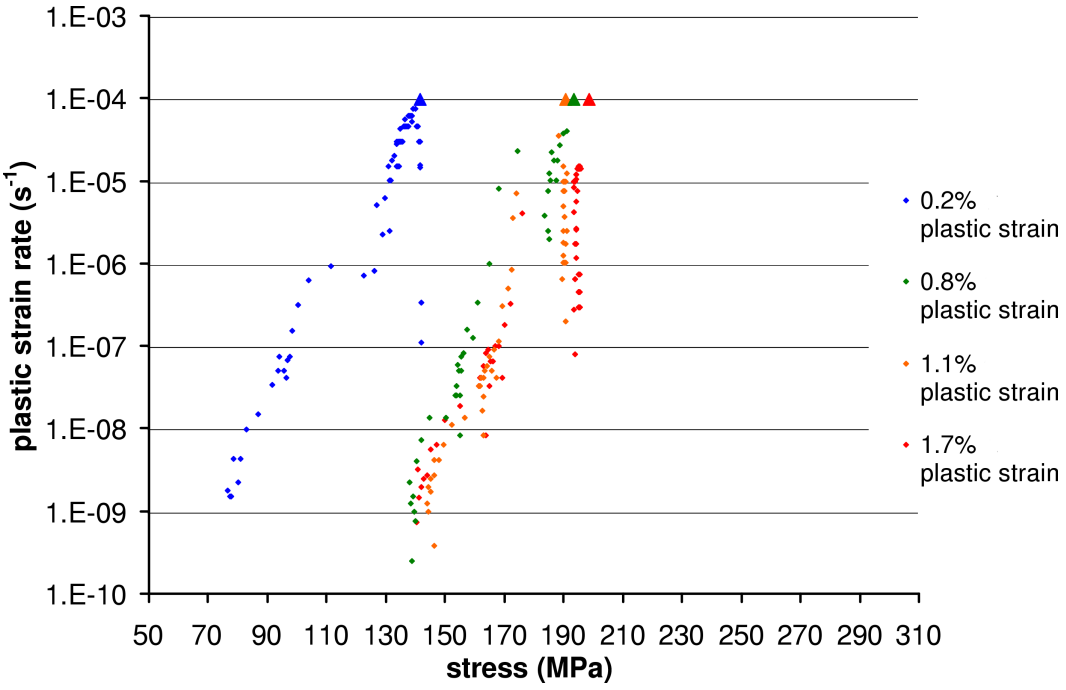

(a)

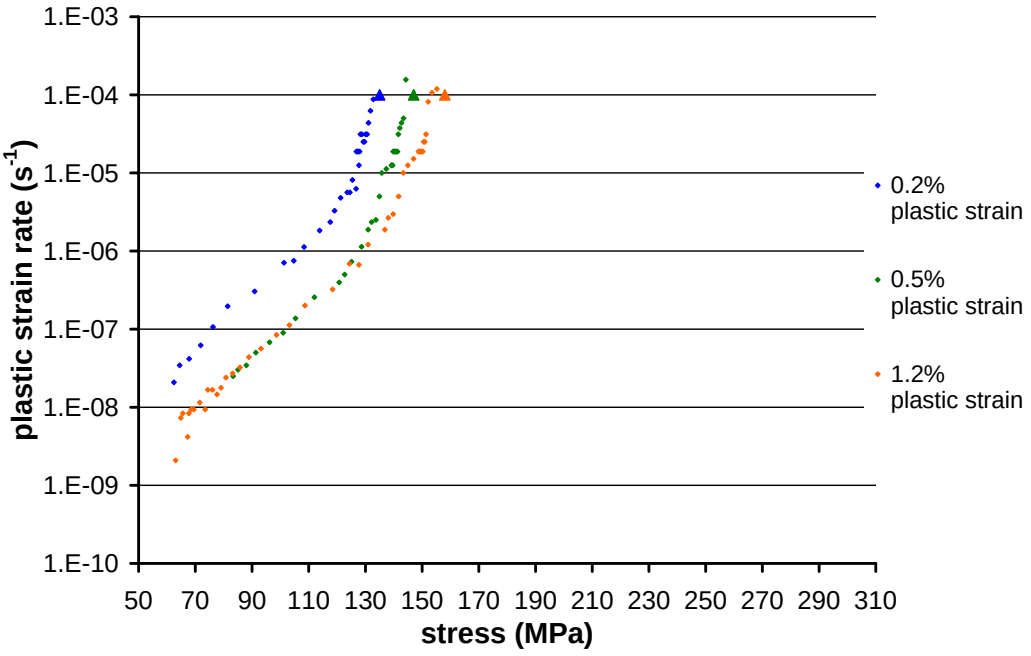

(b)

Figure VIII.8 : Effect of the plastic strain level on the $\log \dot{\varepsilon}_p$ versus σ diagrams for Zr702 at: (a) $300°C$, (b) $400°C$.

For Zr702

- At $100°C$, one slope, characterizing one straining regime is observed. The $\log \dot{\varepsilon}_p$ versus σ curves are shifted toward higher stresses when the plastic strain level is increased. However the hardening rate can be neglected after 0.9% plastic strain level. Indeed the flow stress increases only by 5 MPa from 0.9% to 2.8% plastic strain levels. At the end of the test, when $\dot{\varepsilon}_p$ reaches $10^{-9}s^{-1}$, the beginning of a vertical curve can hardly be detected.

- At $200°C$, the $\log \dot{\varepsilon}_p$ versus σ curves display two slopes. The change in relaxation mode is observed between $\dot{\varepsilon}_p = 10^{-6}\ s^{-1}$ and $\dot{\varepsilon}_p = 10^{-7}\ s^{-1}$. Below these strain rates, the curve is nearly vertical. This second regime with $V_a \longrightarrow \infty$ corresponds to a change in mechanism from friction mode, characterized by V_{a1} and associated with the first regime of this test at $200°C$ (or the entire regime recorded at $100°C$) to the dragging mode, detected alone only at $400°C$ and above, characterized by V_{a2} (see below). The rate controlling mechanism during this so–called friction regime is likely to be a recovery process in which dislocations annihilate by cross–slip and recombine to form cell walls and subgrain boundaries. Mobile dislocations, free of solute atom segregations are the dominant population. Their speed in the friction mode is very fast and does not slow down nor control the macroscopic relaxation rates. Yet, it is playing a major role in setting the flow stress of the material on its lower level for a given strain rate. Notice also that constant strain rate plateau around $10^{-6}s^{-1}$ is recorded on the first relaxation cycle at 0.2% strain level. It will be interpreted in the next paragraph.

- At $300°C$, only a general trend is observed. The slope of the curve is nowhere well defined. A plateau appears again at 0.2% plastic strain for $\dot{\varepsilon}_p = 10^{-6}\ s^{-1}$, as it is already observed at $200°C$. The material is in a transitory state between the two plastic straining modes. They are both present in the material in different locations and different proportions. As the strain rate goes down, the proportion of "the dragging mode" is increasing at the expense of "the friction mode", active at 99% during the loading stage of the test performed at $10^{-4}s^{-1}$. But recovery of the internal microstructure and relaxation of internal stress fields are also taking place simultaneously. As a consequence, local effective stress fields ($\tau_{eff} = \tau_{appl} - \tau_{int}$) may increase and cause, at least, locally and for a limited time a significant straining activity either counterbalancing the general decrease (and the strain rate plateau is formed) or even re–accelerating the plastic strain as observed on figures VIII.7 and VIII.8.

- At $400°C$, two slopes are detected. Contrary to the previous temperatures, the hardening rate is more important. The flow stress increases by about 20 MPa from 0.2% to 1.2% plastic strain levels. At this temperature, the concavity of the curves is opposite to that observed at low temperatures. The last regime is characterized by a single line commun to all relaxation cycles. An apparent activation volume V_{a2} can clearly be identified and measured. Plasticity is no longer unstable and again the change in strain rate is probably controlled by recovery mechanisms involving both cross–slip and climb. This last process is made possible by the higher temperature. Yet, individual dislocations are now moving in the solute atoms dragging mode and experiencing a strong retarding force opposed to the effective forces and reducing it. Similar to the situation previously described for the friction mode, the dislocation velocities in the dragging mode do not control the strain rate nor its changes with time or stress level. But it is providing a significant contribution to the flow stress of the material by setting it to its highest value for a given strain rate.

For ZrHf

- At $100°C$, one slope is detected down to $\dot{\varepsilon}_p = 10^{-8}\ s^{-1}$. Then a change in relaxation mode is observed. Note that a plateau is observed only at 0.2% plastic strain level like in Zr702 at $200°C$ and $300°C$. The hardening rate is very low. The stress increases by about 1 MPa from 1.8% to 2.4% plastic strain level. The beginning of the transition regime with a vertical line seem to appear toward $10^{-9}s^{-1}$ at the end of each cycle.

- At $200°C$, two slopes can be detected. The change in relaxation regime can be observed at about $\dot{\varepsilon}_p = 10^{-7}\ s^{-1}$. Below this strain rate, the curve is nearly vertical. However, the hardening rate is more important than at $100°C$. The flow stress increases by about 15 MPa from 0.5% to 1.3% plastic strain level.

- At $300°C$, the erratic curve evidencing the unstable flow of the transition regime is recorded after the first cycle at 0.2% strain level, but a two–slope is observed after 0.8% strain level with the concave shape of the high temperatures side of the domain. This new observation confirms the fact that ZrHf has a PLC domain shifted by about $50°C$ toward the low temperatures compared to Zr702. However, contrary to $200°C$, the hardening rate is low, the flow stress increasing by about 1 MPa from 1.6% to 2.2% plastic strain levels.

- At $400°C$, two slopes are detected with the concavity specific to the high temperatures domain. A well defined activation volume V_{a2} can be identified as characterizing the dragging mode.

At this stage of the presentation of the results of relaxation tests, we can come to a first and partial set of conclusions:

- the changes in microstructure (recovery processes) control the relaxation behavior of the material in the two explicit modes called the friction mode observed on the low temperatures side of the PLC domain and the dragging mode observed on the high temperatures side. The corresponding activation volumes V_{a1} and V_{a2} are estimated in the next section VIII.3.1,

- in the intermediate temperatures range $200°C$–$300°C$, plasticity (plastic strain rate) is unstable. Relaxation curves exhibit vertical sections with $V_a \longrightarrow \infty$ but also plateau with $V_a \longrightarrow 0$ or even re–acceleration periods at decreasing stress levels with $V_a < 0$. In this transition regime, no interpretation of the quantitative measurements should be attempted,

- in the friction regime, prevailing during loading and also the first part of all relaxation cycles, dislocations are moving rapidly free of any atmosphere for most of them and multiplying at a very high rate. The high value of the flow stress of the material is provided by the strain hardening effect and not by the friction force exerted on the dislocation by its high speed as suggested by the right part of the physical model ($v > v_m$ on figure VIII.1) for an isolated edge dislocation,

- in the dragging regime, only observed in tests carried out at the higher temperatures and/or only at the end of the test, a majority of dislocations is dragging solute atoms atmospheres and experiencing an important retarding force F_m. But, their situation is unstable since the force is only increasing when their speed is below v_M (see figure VIII.1).

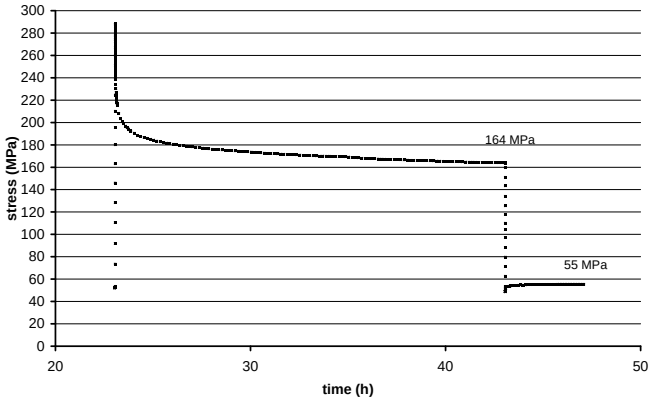

(a)

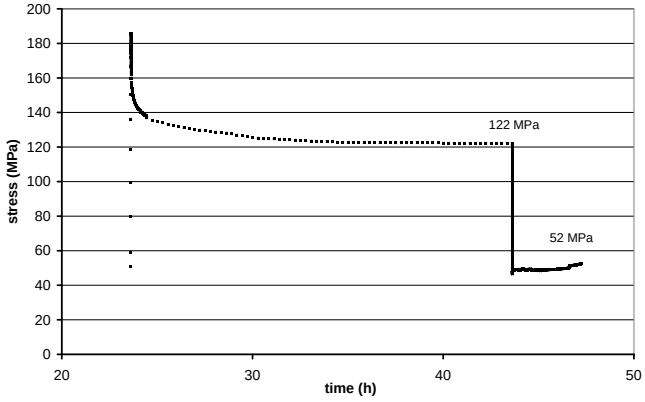

(b)

Figure VIII.9 : True stress–time curves of the first cycle of relaxation at $100°C$ for: (a) Zr702, (b) ZrHf.

Before developing further conclusions further, let us take into consideration some measurements of the internal stress parameters and the apparent activation volumes at several temperatures on these two materials.

Internal stress measurements

When the flow stress was recorded as a function of time after a given loading path was followed, it could be derived once with respect to time and a $\log \varepsilon_p = \dfrac{\sigma}{E}$ was plotted versus σ. This so–called "relaxation curve" is yielding, to a good approximation, taking the value of the flow stress (or yield stress) for a large range of strain rates (here from 10^{-4} seconds down to $10^{-8}s^{-1}$ or $10^{-9}s^{-1}$) into account. For instance the strain rates range of $10^{-8}s^{-1}$–$10^{-9}s^{-1}$ corresponds to the end of the first relaxation sequence on figure VIII.9 (a) for Zr702 and on figure VIII.9 (b) for ZrHf. The flow stress is 164 MPa for Zr702 and 122 MPa for ZrHf.

If furthermore an important stress drop was not applied and the machine did tend to reload the specimen, we can conclude that the entire elastic domain $2R$ was crossed over during this stress drop. Now after only four hours, the plastic strain rate went down to about $10^{-8}s^{-1}$ and the applied stress measured at the end of this second relaxation sequence was 55 MPa for Zr702 and 52 MPa for ZrHf at $100°C$ (see figure VIII.9 (a), (b) respectively).

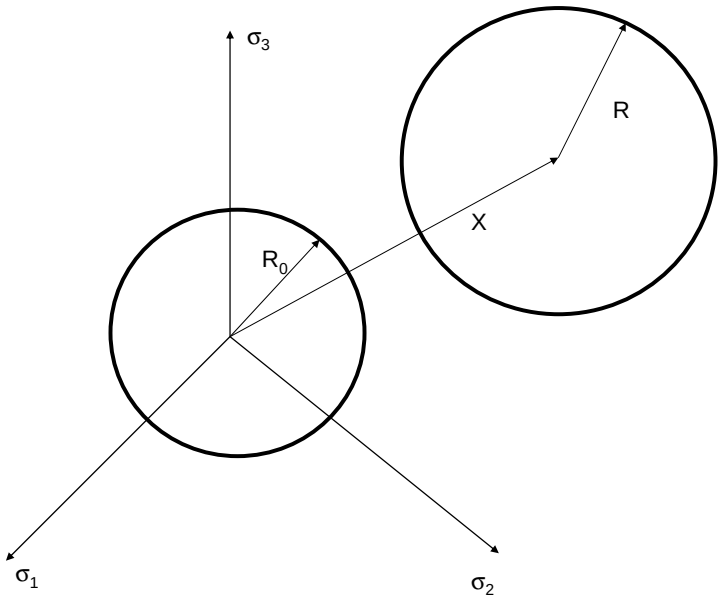

Figure VIII.10 : Stress partition: definition of isotropic stress R and kinematic stress X.

Let us consider Handfield and Dixon's approach to stress partition (Dickson et al., 1984; Handfield et al., 1985) and call the width of the elastic domain $2R$ and X the kinematic hardening which is the stress tensor describing this internal stress as described on figure VIII.10. Making use of this method in connection with figures VIII.11, VIII.12 for Zr702 and ZrHf respectively, these two quantities measured at $10^{-8}s^{-1}$ can be estimated as follows (for instance for the second relaxation of ZrHf at $100°C$):

$$2R = 122 - 52 = 70MPa \quad ; \quad R = 35MPa \tag{VIII.7}$$

$$2X = 122 + 52 = 174MPa \quad ; \quad X = 87MPa \tag{VIII.8}$$

The application of this method to each 24 hours relaxation cycle (including loading and unloading down to 50 MPa) lead to measure the values of R and X at several strain levels (see figures VIII.11 (a) for Zr702, VIII.12 (a) for ZrHf) and at four temperatures $100°C$, $200°C$, $300°C$, $400°C$ (see figures VIII.11 (b) for Zr702, VIII.12 (b) for ZrHf). On these last figures, the flow stress of both materials at $10^{-4}s^{-1}$ measured at the end of the third loading (called $R(2\%)$ for Zr702 and $R(1.5\%)$ for ZrHf) is also plotted for comparison at the four explored temperatures.

In Zr702, kinematic hardening reaches 120 MPa at $100°C$ after 1.8% strain level but drops down to about 50 MPa at $400°C$ when isotropic hardening hardly reaches 60 MPa at $100°C$ after 1.8% strain level and drops down to 40–50 MPa at $300°C$ and to just a few MPa at $400°C$. In ZrHf, kinematic hardening reaches 100 MPa at $100°C$ after 1.8% strain level but drops down to 40 MPa at $400°C$ when isotropic hardening hardly reaches 40 MPa at $100°C$ after 1.8% strain level and drops down to 20 MPa at $300°C$ and to just a few MPa at $400°C$.

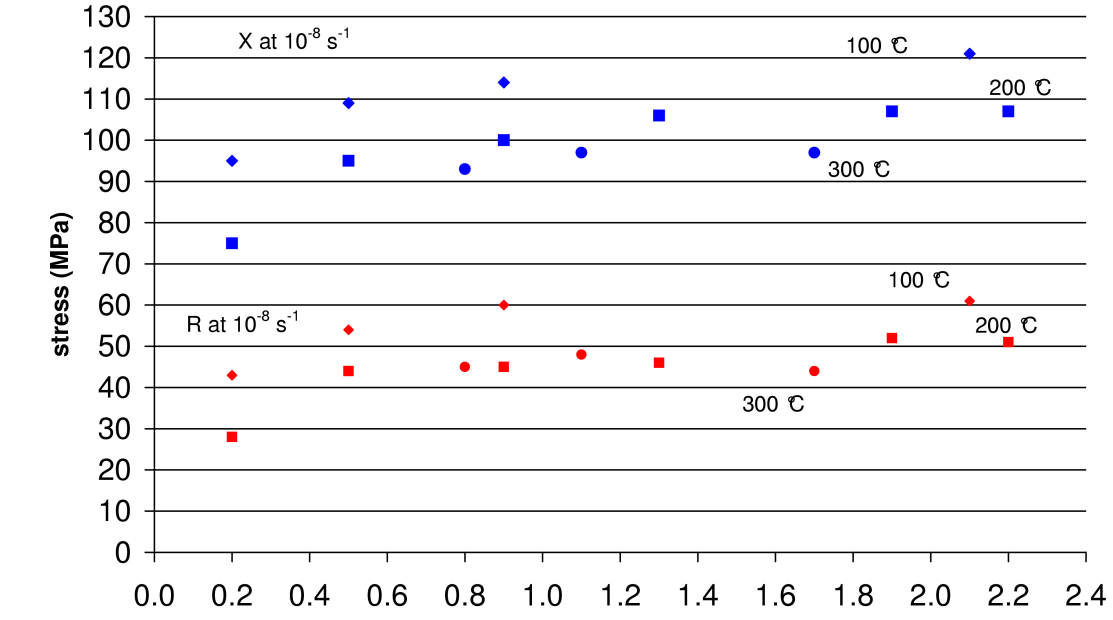

(a)

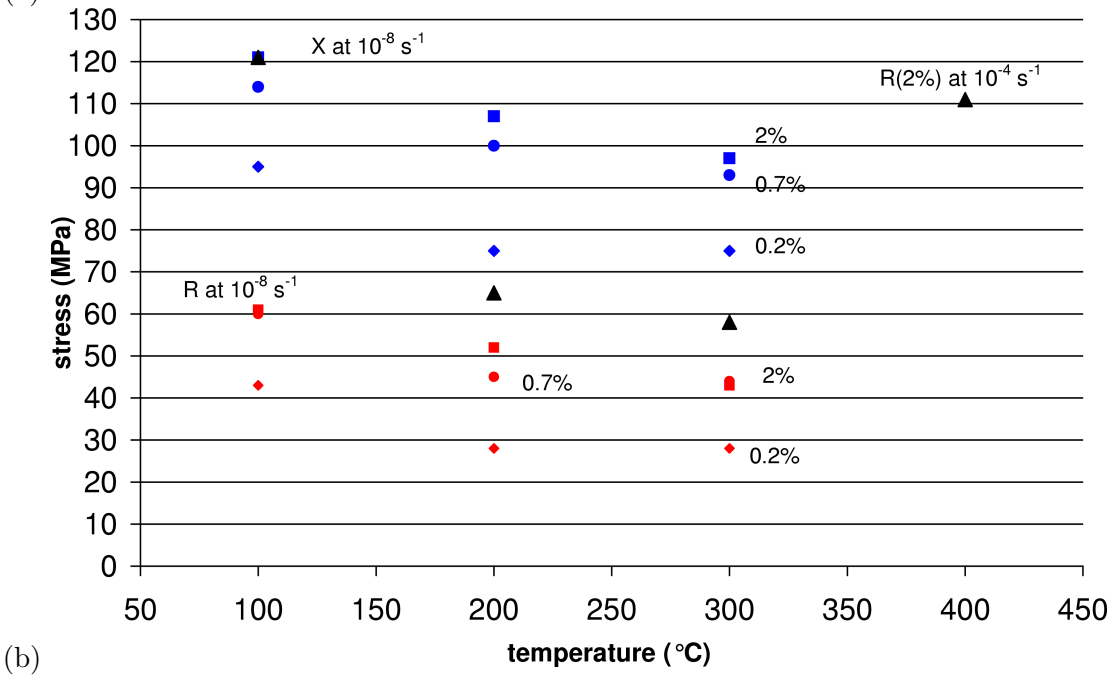

(b)

Figure VIII.11 : Isotropic R and kinematic X hardening for Zr702 as a function of: (a) plastic strain (with R at $10^{-4}s^{-1}$ in the range 75–120 MPa); (b) temperature for various plastic strain levels (X and R measured at $10^{-8}s^{-1}$ with $R(2\%)$ measured at $10^{-4}s^{-1}$).

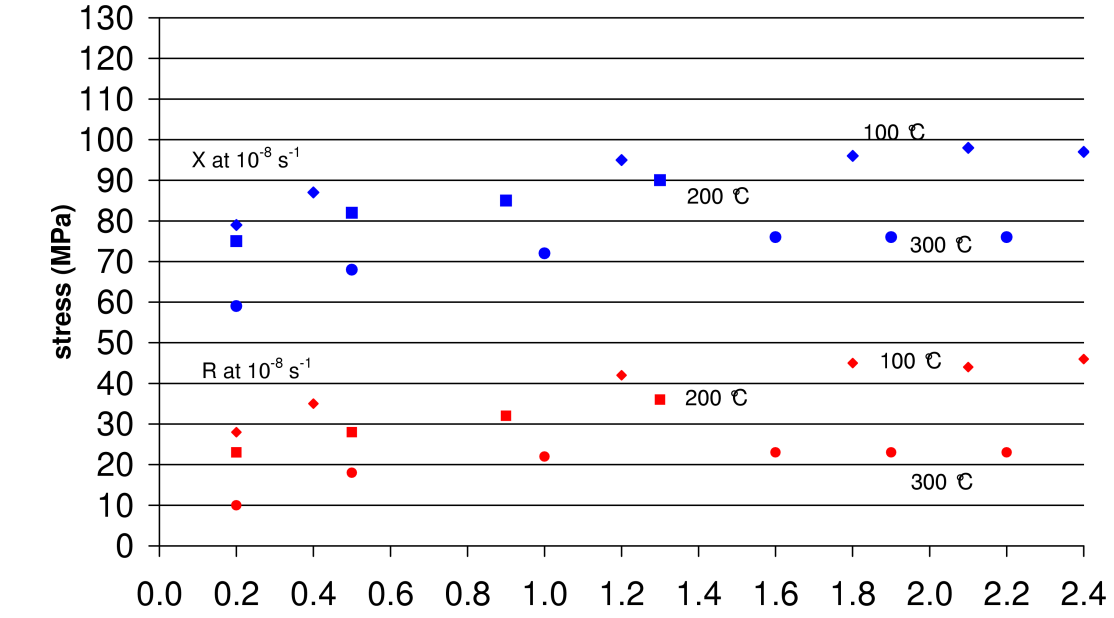

(a)

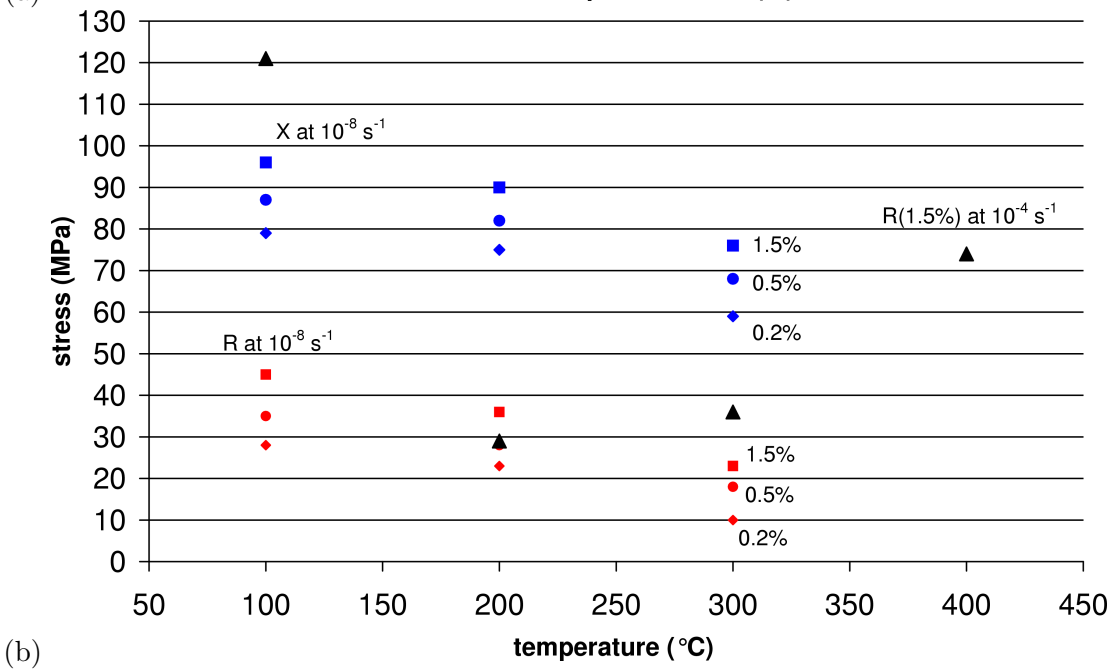

(b)

Figure VIII.12 : Isotropic R and kinematic X hardening for ZrHf as a function of: (a) plastic strain (with R at $10^{-4}s^{-1}$ in the range 60–100 MPa); (b) temperature for various plastic strain levels (X and R measured at $10^{-8}s^{-1}$ with $R(1.4\%)$ measured at $10^{-4}s^{-1}$).

The main conclusions are:

- if isotropic hardening is close to the applied stress, just after loading, at the end of the first 20 hours relaxation cycles, its value is 2 to 2.5 lower than that of the kinematic hardening (internal stress) for Zr702 (35 MPa/85 MPa) and for ZrHf (20 MPa/70 MPa). This proportion is preserved at higher strain values with Zr702 alloy strengthening (50 MPa/105 MPa) than ZrHf alloy (30 MPa/80 MPa),
- both X and R are slightly increasing during the first 1% strain, but R tends to saturate when X still keeps increasing for both materials,
- both quantities are rapidly decreasing with temperature especially above $200°C$ for Zr702. For Zr702, the values of R and X seem to reach a constant depending of the plastic strain level,
- 90% of the amplitude of relaxation is attainned after only a few minutes and a threshold value is reached within a few hours (or less as the temperature increases), about 60 MPa below the applied stress as observed by Pujol (Pujol, 1994) for Zr702,
- the amplitude of relaxation is minimal at $200°C$ and $300°C$ for both zirconium alloys,
- the relaxation arrest is similar to the creep arrest taking place under constant stress. These phenomena are observed in zirconium and titanium alloys as well (Brandes and Mills, 2004) and find their origin in age–hardening as evidence by the fact that the sample can be reloaded carefully after a few hours (slow loading rate) by an amount less than $\Delta\sigma^{thres} = 60MPa$ without exhibiting any detectable strain rate.

Apparent activation volume

The slopes of the $\log \dot{\varepsilon}_p$ versus σ curves are directly linked to the apparent activation volume, which correspond to a macroscopic value. The apparent activation volume characterizes the process controlling the plastic deformation mechanism. The apparent activation volume, V_a is given by:

$$V_a = \frac{1}{k_B T} \left(\frac{\Delta \log \dot{\varepsilon}_p}{\Delta \sigma} \right)_{\varepsilon_p, T} \tag{VIII.9}$$

We recall that V_{a1} is the apparent activation volume associated with the friction mode. It can be measured at the beginning of the low temperatures tests. The apparent activation volume of the dragging mode is called V_{a2}. It can be measured at the end of high temperatures tests. At intermediate temperatures, all possible values of V_a can be defined, indeed for some cases, its value can be negative, nul (constant strain rate plateau) or even infinite.

Figures VIII.13, VIII.14 show the evolution of the apparent activation volume of Zr702 and ZrHf respectively as a function of temperature and plastic strain level. They both increase slightly with temperature and their rather high values (0.4 $nm^3.atom^{-1}$ to 2 $nm^3.atom^{-1}$ characterize recovery processes involving rearrangement of dislocations assemblies such as cell walls and subgrain boundaries. They do not characterize individual dislocation slip or solute drag processes (as would be expected from the physical model of figure VIII.1), which operate with activation volumes 100 times smaller. ZrHf exhibits higher apparent activation volumes (between 0.8 $nm^3.atom^{-1}$ to 2 $nm^3.atom^{-1}$) than Zr702 (between 0.4 $nm^3.atom^{-1}$ and 0.8 $nm^3.atom^{-1}$). This result could be indicate that substructures are finner in Zr702 than in ZrHf.

Note: we use $nm^3.atom^{-1}$ as units for measuring apparent activation volumes rather than b^3 values, often used in the literature because several very different Burgers vectors, b may be active in processes involving plastic and viscoplastic flow. These processes were not studied, hence not identified in the present work. When a process is based on the activated motion of dislocations with Burgers vectors $\overrightarrow{b_2} = \overrightarrow{a} + \overrightarrow{c}$ rather than $\overrightarrow{b_1} = \overrightarrow{a}$ (as in prismatic or basal glide), the ratio of their length is $\frac{b_2}{b_1} = \frac{a+c}{a} = \sqrt{\frac{a^2+c^2}{a^2}} = \sqrt{1+\frac{c^2}{a^2}} = 1.87$. When raised to the third power as in b^3, the meaning of the unit b^3 is completely changed by a factor of 0.65! This situation is not desirable for an unit of measurement.

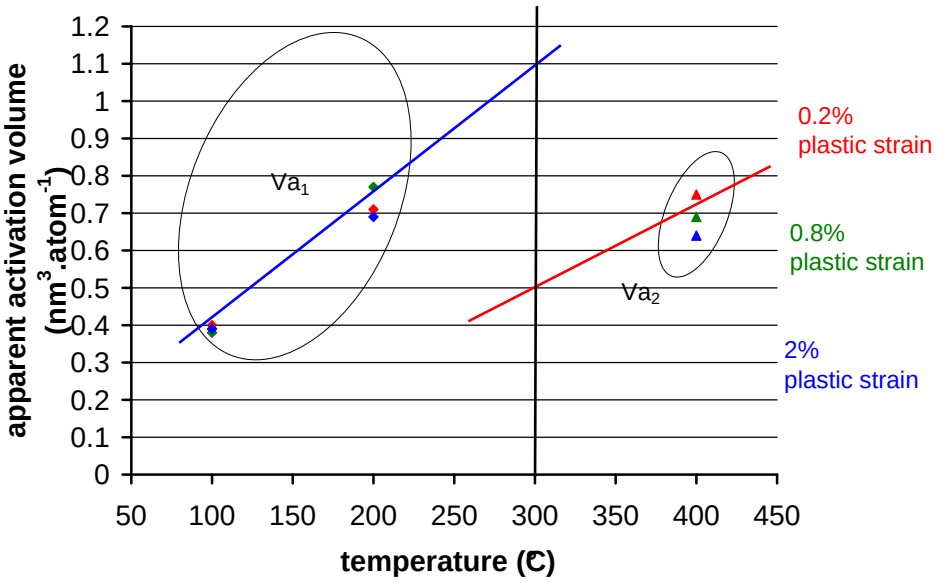

Figure VIII.13 : Evolution of the apparent activation volumes of Zr702 (V_{a1} and V_{a2} for the friction and dragging modes respectively) as a function of temperature and plastic strain level.

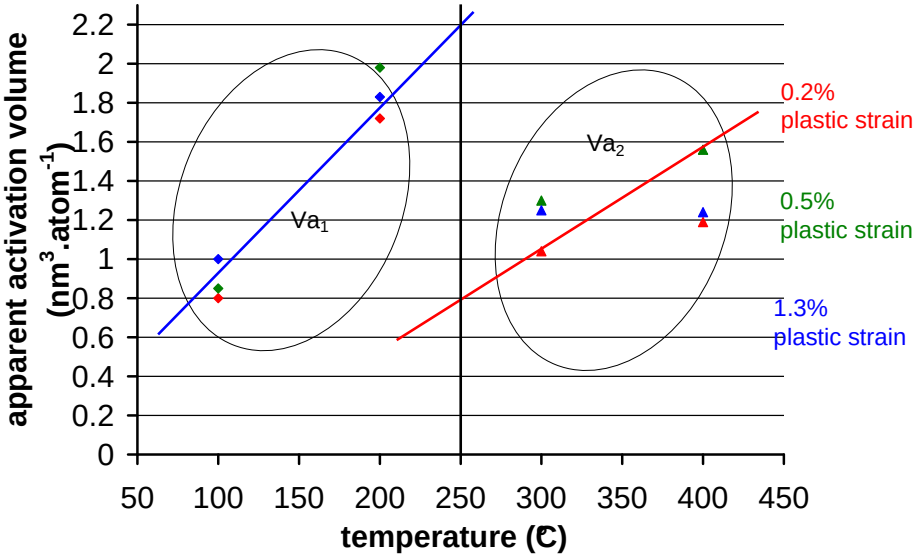

Figure VIII.14 : Evolution of the apparent activation volume of ZrHf (V_{a1} and V_{a2} for the friction and dragging modes respectively) as a function of temperature and plastic strain level.

Reconstruction of the limiting curves

We shall now attempt to reconstruct the limiting curves in the σ versus $\log \dot{\varepsilon}$ space, since it is not possible to observe the entire relaxation curve with its three different domains, directly in a single experiment performed at one temperature:

1. the "friction domain" at high strain rates,
2. the "dragging domain" at low strain rates,
3. the "transition domain", called the "strain ageing domain" when plasticity is essentially split between two active modes without being dominated by one or the other.

We chose to make this reconstruction in the center of the strain ageing domain in temperature, called T_c and in stress level, called σ_c as explicated in table VIII.1.

Table VIII.1 : Reconstruction parameters for Zr702 and ZrHf.

	T_c	σ_c	$\Delta \log \dot{\varepsilon}$	V_{a1}	V_{a2}	$\Delta\sigma$
Zr702	$300°C$	180 MPa	7 decades	1.1 $nm^3.atom^{-1}$	0.5 $nm^3.atom^{-1}$	250 MPa
ZrHf	$250°C$	120 MPa	6 decades	2.2 $nm^3.atom^{-1}$	0.8 $nm^3.atom^{-1}$	130 MPa

The reconstruction appears on figures VIII.15 and VIII.16, which show the effect of temperature, plotting the $\log \dot{\varepsilon}_p$ versus σ diagram for Zr702 at $\varepsilon_p \simeq 0.8\%$ and for ZrHf at $\varepsilon_p \simeq 0.5\%$ respectively. Note that the exact values of the plastic strain levels at which the relaxation tests were carried out are mentionned on each curve. The reconstruction is carried out in the following manner:

- an estimate is made of the total number of strain rate decades when the transition mode is active and the plastic behavior irregular and erratic: 7 decades for Zr702 and 6 decades for ZrHf,
- at a chosen temperature of $300°C$ for Zr702, the extrapolated values of the two well defined viscoplastic processes V_{a1} and V_{a2} are given by figure VIII.13. Similarly, at $250°C$ for ZrHf, they are given by figure VIII.14, reported in table VIII.1,
- notice that the slopes (apparent activation volumes) and the distance (in the stress $\Delta\sigma$ or the number of decades $\Delta \log \dot{\varepsilon}$) between the two limiting curves will vary significantly as the domain is crossed. Hence limiting surfaces must be drawn rather than limiting curves. This will be attempted at the end of this chapter. Here, in the center of the strain ageing domain, if we consider the difference in the flow stress at a given strain rate $10^{-7}s^{-1}$ for Zr702, an increase of 250 MPa is evidenced, which is to be attributed to the dragging of solute atoms. This "drag stress" is simply here a way of measuring the width of the domain in its center. It may never be exerted on a moving dislocation (see figure VIII.1), because it is simply an extension of the first slope of the "dragging force" curve beyond v_M. It is just used here as a tool for comparison between both alloys. For ZrHf, at $250°C$ and for a strain rate of $10^{-6}s^{-1}$, chosen in the center of the strain ageing domain, $\Delta\sigma$ is only equal to 130 MPa, hence about half of the value of the effect measured in Zr702 which contains 1300 wt ppm of oxygen, compared to only 80 wt ppm for ZrHf.

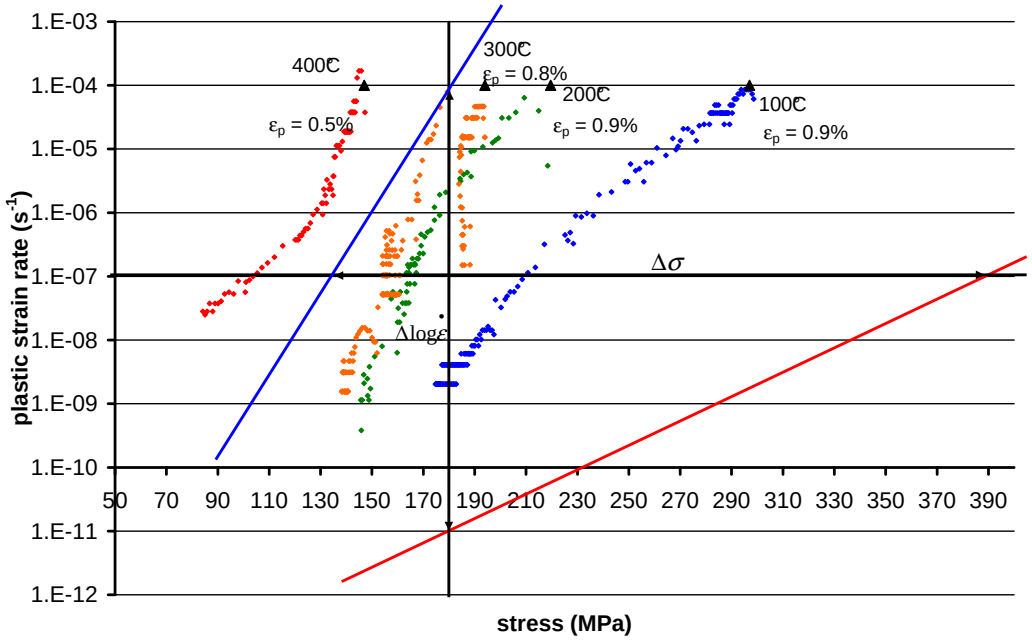

Figure VIII.15 : Effect of temperature plotting the $\log \dot{\varepsilon}_p$ versus σ diagram of Zr702 at $\varepsilon_p \simeq 0.8\%$ and constant temperature at $300°C$

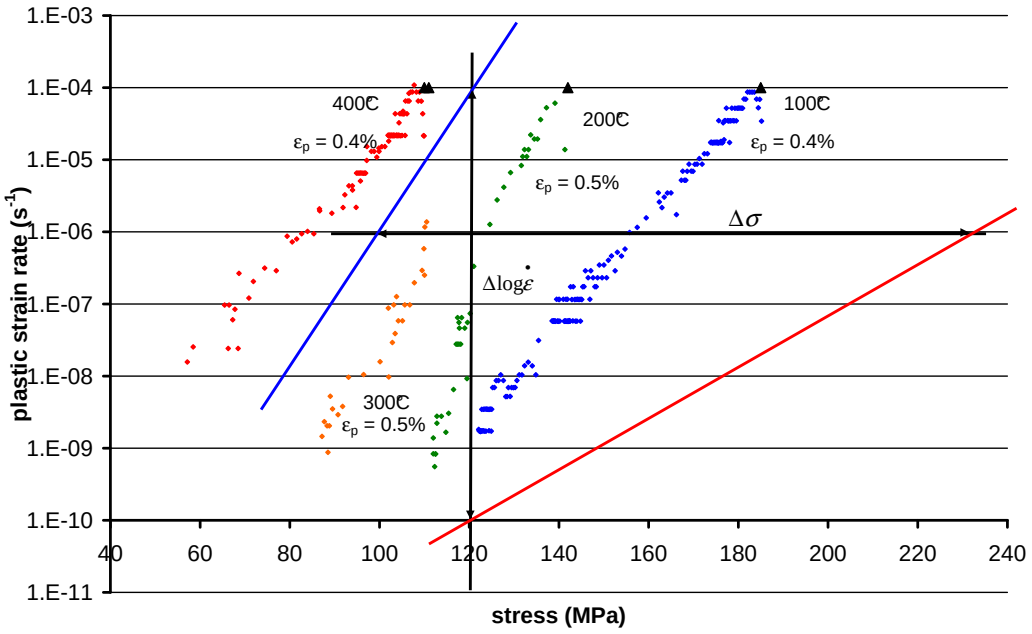

Figure VIII.16 : Effect of temperature on the $\log \dot{\varepsilon}_p$ versus σ diagrams for ZrHf at $\varepsilon_p \simeq 0.5\%$ and constant temperature at $250°C$.

To summarize, figures VIII.17 (a) and (b) show the friction and the dragging modes observed in Zr702 and in ZrHf respectively, associated with their domains of temperatures and strain rates in the $\log \dot{\varepsilon}_p$ versus σ diagram.

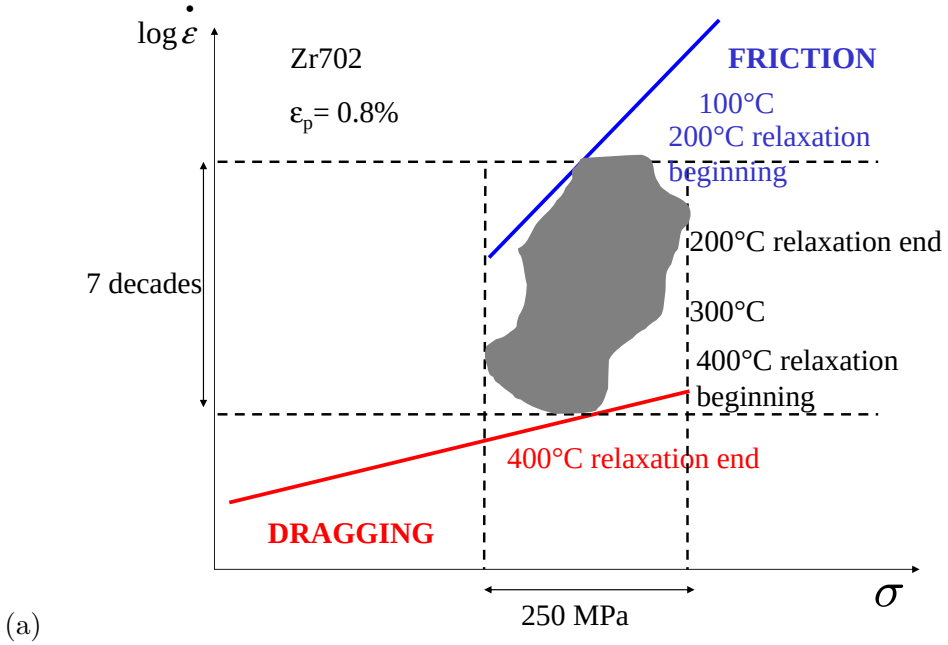

(a)

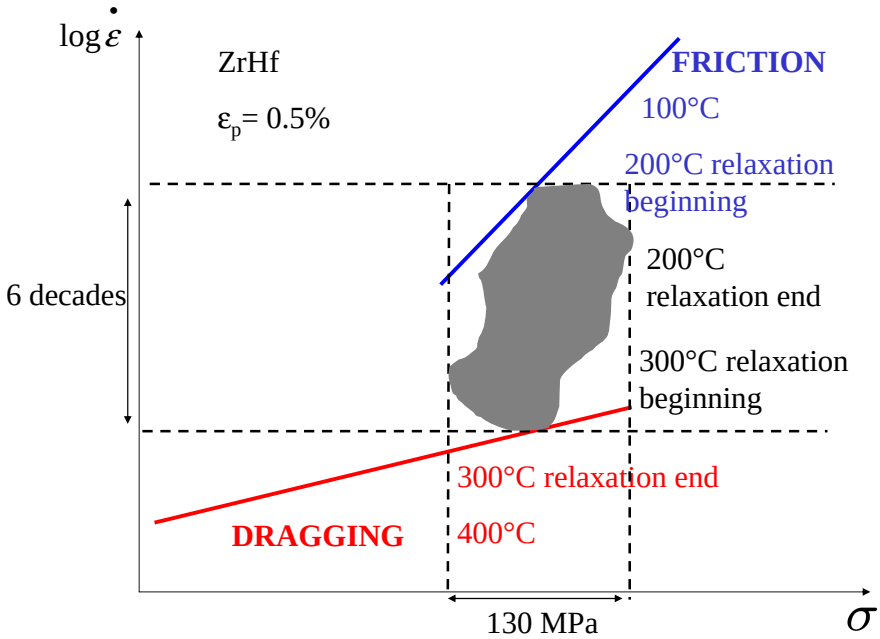

(b)

Figure VIII.17 : The diagram $\log \dot{\varepsilon}_p$ versus σ reveals the friction and dragging modes according to temperature for: (a) Zr702, (b) ZrHf.

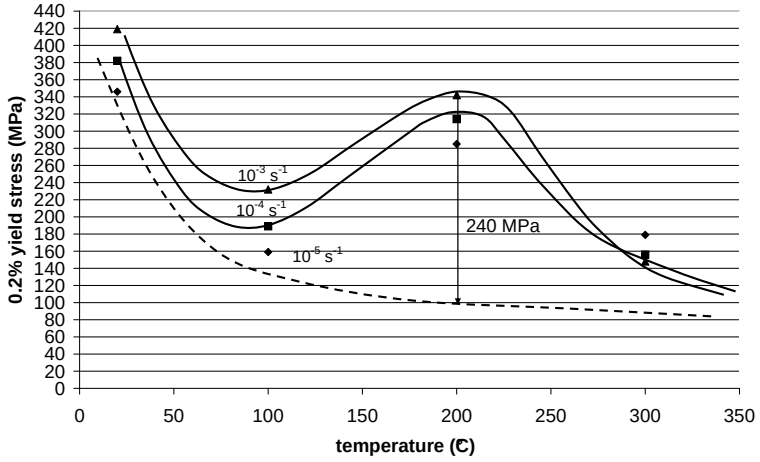

(a)

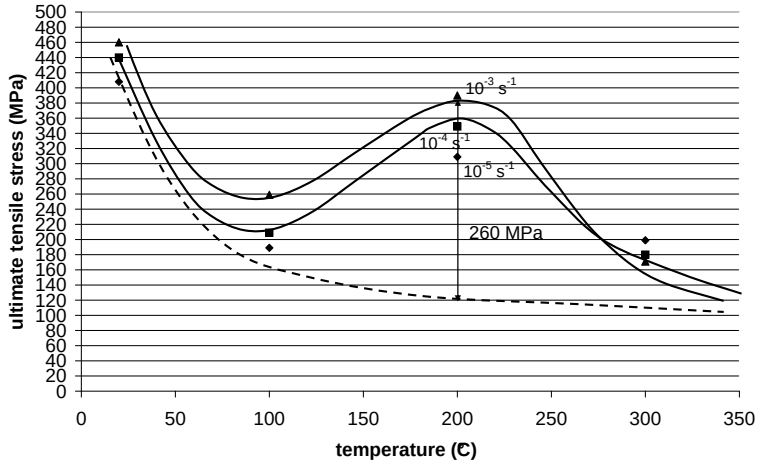

(b)

Figure VIII.18 : For transverse Zr702: (a) 0.2% yield stress versus temperature curves at various strain rates (b) ultimate tensile stress versus temperature curves at various applied strain rates.

VIII.3.2 Limiting curves in the stress versus temperature plane

0.2% yield stress and ultimate tensile stress, obtained from the tensile curves of transverse Zr702 are plotted for a given strain rate as a function of temperature, as shown in figure VIII.18.

The experimental curves merge at high temperature, around $300°C$–$350°C$ for 0.2% yield stress as well as for ultimate tensile stress, into the curve for a standard material, deprived of any DSA or SSA effects (curves in dotted lines on figure VIII.18). Both diagrams give an order of magnitude from strain ageing phenomena as a function of temperature, hardly detectable at $100°C$. Especially at high strain rates, it reaches values of 240 MPa to 260 MPa around $200°C$–$250°C$, in the center of the strain ageing domain and subsides slowly towards $350°C$–$400°C$. Similarly, creep with measurable strain rates is recorded at both ends of the domain: room temperature and $400°C$. In the center of the strain ageing domain, creep arrest and/or relaxation arrest is observed.

VIII.3.3 Limiting curves in the strain rate versus temperature plane

Tensile tests with strain rate changes were carried out in a limited range of loading strain rates in the temperatures range $20°C$–$400°C$ for Zr702 and ZrHf. Standard strain hardening and/or anomalous behavior associated with strain ageing phenomena can be observed for specific temperatures and strain rates.

First, we explored the entire domain where strain ageing phenomena are observable with these tensile tests by varying the strain rate between $10^{-3}s^{-1}$ and $10^{-4}s^{-1}$ back and forth and running tests at five different temperatures ($20°C$, $100°C$, $200°C$, $300°C$, $400°C$). The interpretation of the effect of oxygen atoms on the strain rate sensitivity that we are suggesting is summarized on figure VIII.19.

- On the low temperatures side, the SRS curves are peaked in the temperatures range $100°C$–$200°C$. At constant k_BT, for the explored strain rates, no strain ageing effect is active and the usual positive SRS is measured: increasing the strain rate stimulates dislocations multiplication hence making the population of forest dislocations more dense and increasing the flow stress. In the temperatures range $100°C$–$200°C$, this mechanism by multiplying the length of dislocation segments exposed to strain ageing will increase age–hardening effects and hence the flow stress. An additional age–hardening term will be added to SRS which is more noticeable in materials with higher oxygen content, ZrHf–O here Zr702 and ZrHf–Nb–O (about 1300 wt ppm oxygen) compared to ZrHf and ZrHf–Nb (about 80 wt ppm oxygen). On this low temperature side of the strain ageing domain, the flow stress (and the SRS) is dominated by mobile dislocations, by writing:

  $$\rho_{tot} \simeq \rho_m \tag{VIII.10}$$

  We neglect changes in cell walls and substructures which cannot adjust the frequent strain rate changes. On the other hand, although most dislocations are mobile $\rho_{im} \simeq 0$, a large number can slow down and even become immobile by the combined effect of forest dislocations arrest and increasing impurity atoms concentrations around the arrested segments (Kubin and Estrin, 1989b; Estrin and Kubin, 1989). Thus the derivative $\dfrac{\Delta\rho_{im}}{\Delta log\dot{\varepsilon}}$ is very large and positive.

- On the high temperatures side of the domain $350°C$–$450°C$, the SRS curves are going down to very low or even negative values, just before all strain ageing manifestations will disappear around $500°C$. In that temperatures range, the increased mobility of impurity atoms is such that most dislocations become rapidly saturated and/or are dragging along their impurity clouds except locally in regions of plasticity bursts where they move and multiply very fast. But after such localized events, called the "PLC bands", recovery mechanisms are very active at high temperatures so that schematically we suggest writing:

  $$\rho_{tot} = \rho_m + \rho_{im} \simeq constant \tag{VIII.11}$$

  which implies:

  $$\frac{\Delta\rho_{tot}}{\Delta log\dot{\varepsilon}} \simeq 0 \tag{VIII.12}$$

  and also:

  $$\frac{\Delta\rho_{im}}{\Delta log\dot{\varepsilon}} = -\frac{\Delta\rho_m}{\Delta log\dot{\varepsilon}} \tag{VIII.13}$$

However, in this temperatures range, these last quantities (VIII.13) are negative. When a strain rate jump appears, the material will adjust by mobilizing populations of immobile dislocations rather than by creating some new ones. The velocity of slow dislocations, dragging their impurity clouds will increase at the expense of the solute atoms concentration that will decrease. At the end of this domain, strain hardening and SRS parameter reach their lowest values. In materials where the spatial extension of regions for which $\frac{\Delta\rho_{im}}{\Delta log\dot{\varepsilon}}$ is strongly negative reaches the macroscopic level (PLC bands running across hundred of grains and crossing the entire width of the specimen), the flow stress may even drop down abruptly as the strain rate is raised ($SRS < 0$) or even during a constant strain rate test or period (serrations). Notice though that the occurrence and amplitude of these manifestations do not depend only on the material but also on the compliance of the equipment used. Hence the numerous discrepancies in measurements and in observations which have led to unnecessary controversies.

- In this interpretation, we chose to describe plasticity in terms of dislocation densities named ρ rather than referring to behavior of an individual dislocation (see figure VIII.1). Indeed, the collective behavior of large populations is necessarily involved in phenomena observable on the macroscopic scale. Considering the behavior of a single edge dislocation in the presence of interacting solute atoms is important to understand the physical origin of phenomena. However, when examining the results of macroscopic mechanical tests, the concept of "plasticity modes" is more important. We shall refer to the friction mode when slip activity is very active and quick (here ρ_m) as in localized bands of plasticity that may or may not cross the entire specimen. And also, we shall refer to the dragging mode when plasticity is slow and coupled with age–hardening (here ρ_{im}). Thus special behavior of plasticity, specific to materials where dislocations interact with solute atoms in a restricted domain of temperatures and strain rates is well described by the equations of McCormick which we use in the numerical model presented in part D.

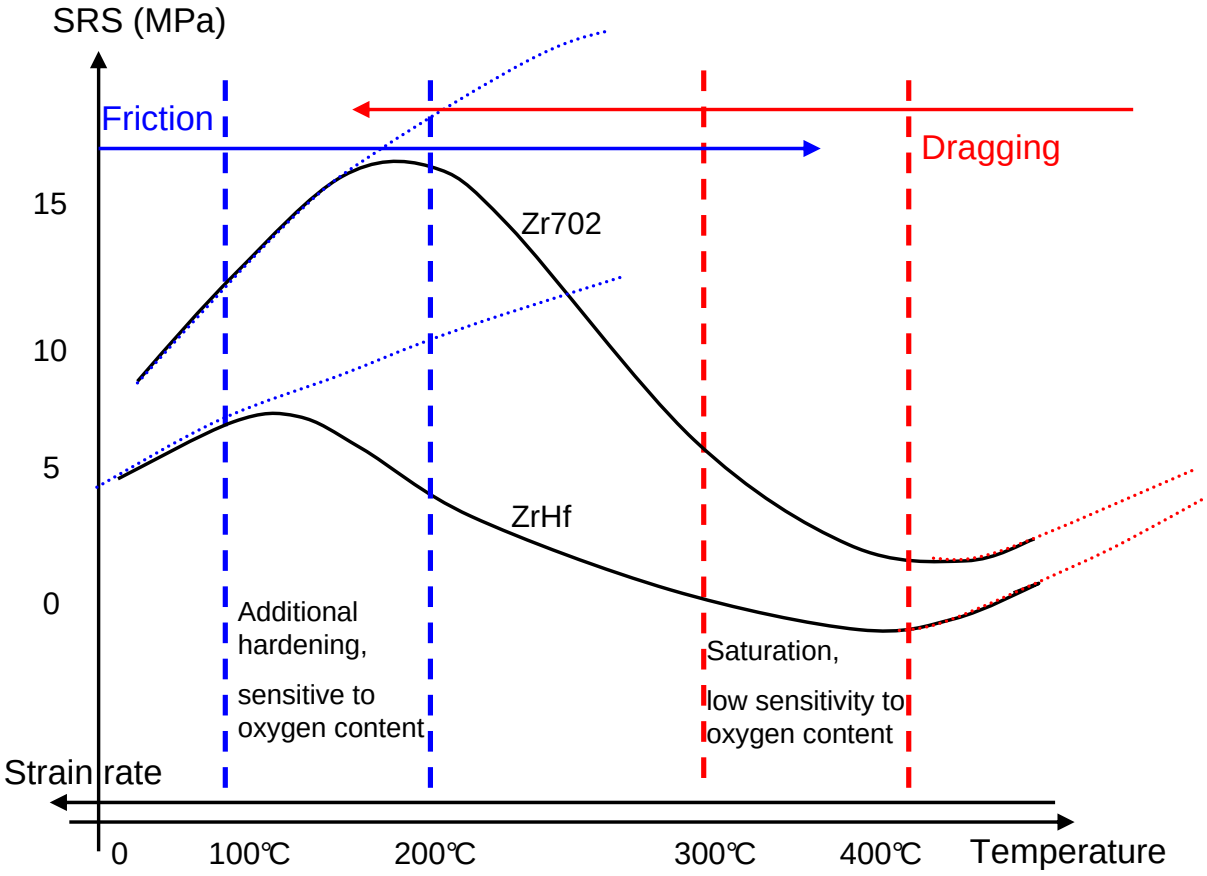

Figure VIII.19 : Schematic diagram describing the various domains where strain ageing phenomena are observed in the presence of oxygen in zirconium alloys. The curve located on the low side can be associated with ZrHf, and the curve located on the high side can be associated with Zr702 or ZrHf–O (strain rate jumps from $10^{-4}s^{-1}$ to $10^{-3}s^{-1}$).

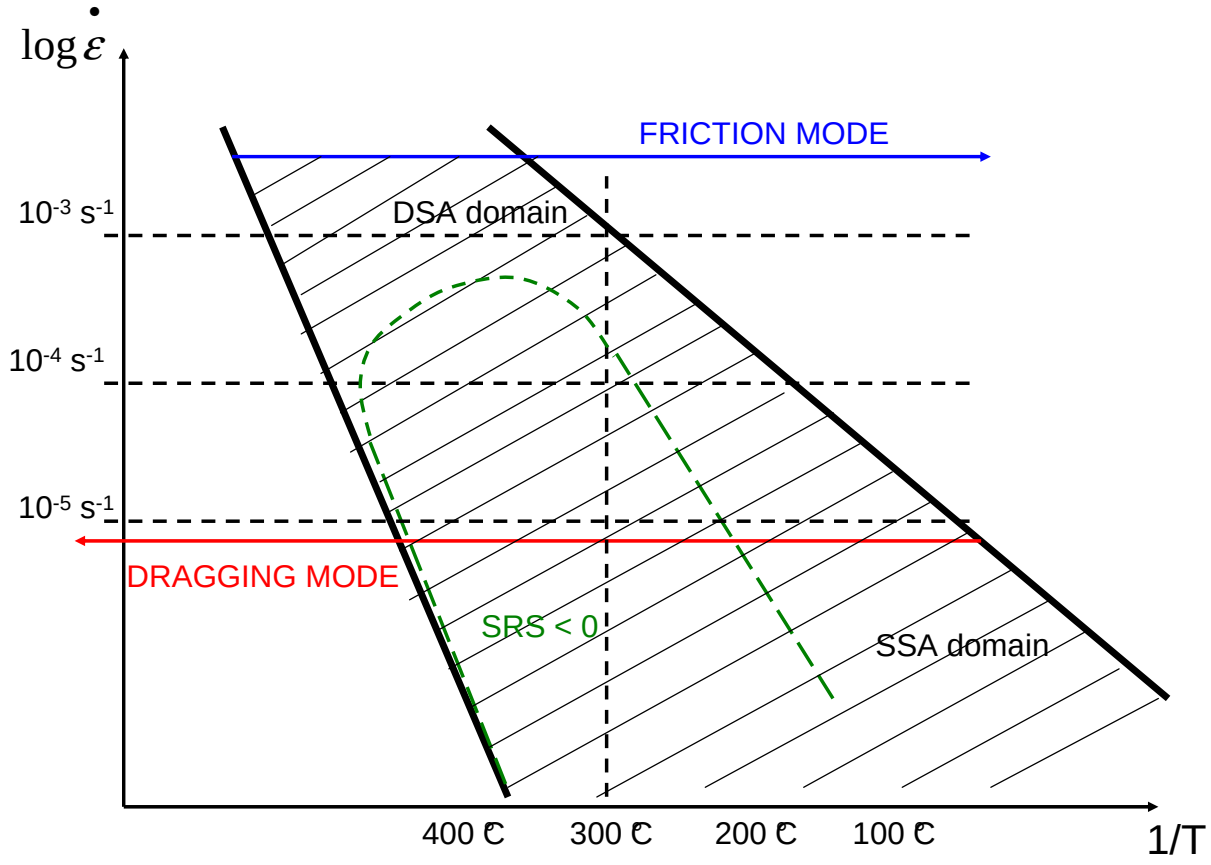

Figure VIII.20 : Strain ageing domain in the $1/T$–$\log \dot{\varepsilon}$ plane for Zr702.

Secondly, the tensile tests (with strain rate changes) allow to plot the schematic $\log \dot{\varepsilon}$ versus $1/T$ diagram where the anomalous behavior is observed, as shown in figure VIII.20 for Zr702 and in figure VIII.21 for ZrHf. The anomalous behavior is defined by the two boundary lines associated with the friction and the dragging modes. We recall that this domain is the strain ageing domain where both modes can be observed leading to especially the occurrence of PLC effect close to limiting curve of the friction mode at higher temperatures. For Zr702, PLC effect is observed at $10^{-4}\ s^{-1}$ for $300°C$ and $400°C$. No PLC effect is observed at $10^{-3}\ s^{-1}$–$10^{-4}\ s^{-1}$ for lower temperatures. For ZrHf, PLC effect is observed at $10^{-4}\ s^{-1}$ for $300°C$ and $400°C$, and also at $10^{-3}\ s^{-1}$ for $400°C$. Note that for higher temperatures at higher and lower strain rates and for lower temperatures at lower strain rates, our experimental investigation was not extensive and systematic enough to determine the exact boundary lines of the domain where PLC effect is active. Note that whenever age–hardening is absent or disappears, it is immediately replaced by strain hardening in order to sustain locally a similar stress level. Yet, this attempt to sustain a constant stress level is not always successful and the flow stress of the material may decrease, even though the local strain rate is increasing. We call this region $SRS < 0$ on figures VIII.20 and VIII.21.

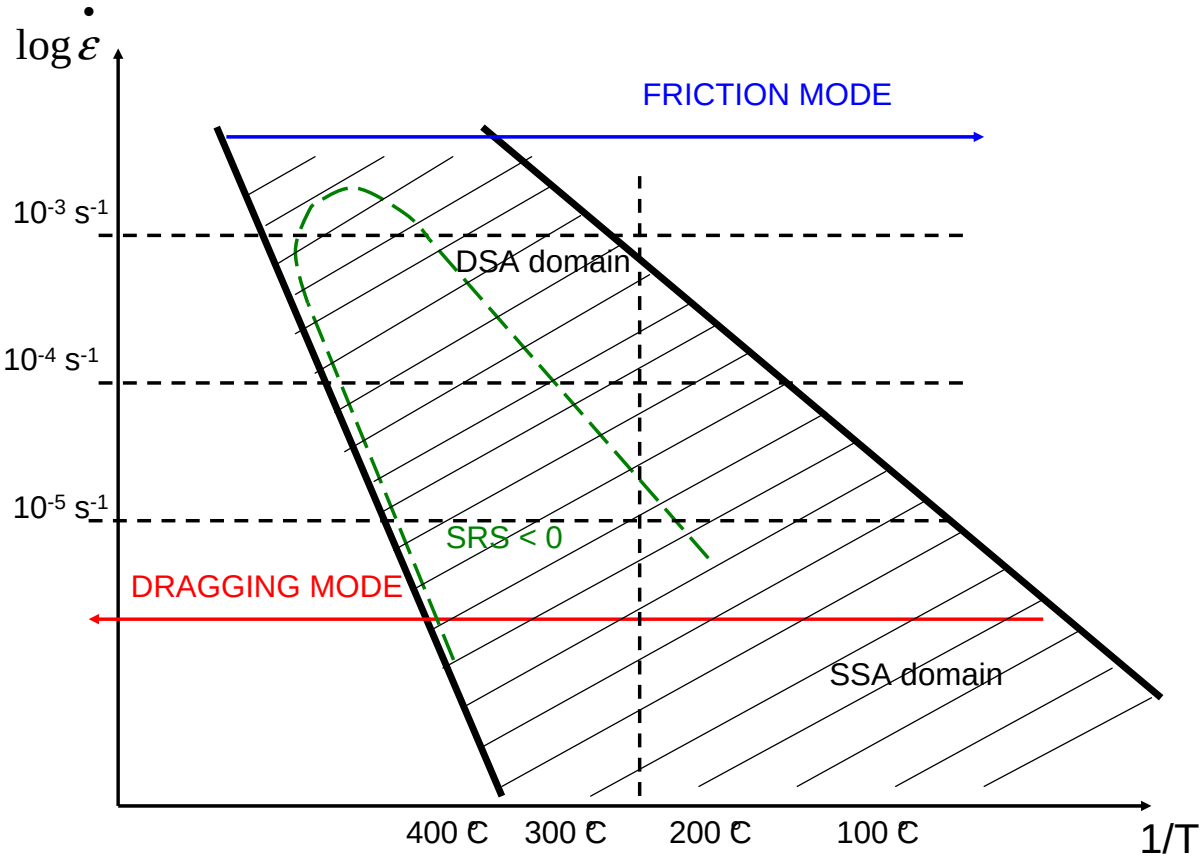

Figure VIII.21 : Strain ageing domain in the $1/T$–$\log \dot{\varepsilon}$ plane for ZrHf.

At low strain rates and/or high temperatures, in the dragging mode, tensile curves are smooth and plastic deformation appears macroscopically uniform. At high strain rates and/or low temperatures, in the friction mode, plastic deformation also appears macroscopically homogeneous and the stress versus strain curves are smooth. In the strain ageing domain, plastic deformation can be heterogeneous on a macroscopic scale.
One can suggest for zirconium alloys, that plastic straining runs along the gauge length of the specimen, but not under the form of propagating PLC bands. Plastically active region remain "sedentary" although they become reactivated periodically as the total strain increases as exposed in part C. In standard materials (steels, Al–Cu, Al–Mg...), at low temperatures, the PLC band may be unique, repeatedly initiated at the same end of the sample and run across the gauge length rather slowly as in the vicinity of the friction mode. At high temperatures, several PLC bands may initiate at various locations along the specimen, move quickly and disappear to initiate again in another section as it is observed near the boundary of the strain ageing domain facing in dragging mode. That is why, in the strain ageing domain (that of the superimposition of mechanisms), dislocations can on the one hand glide in the dragging mode or on the other hand glide in the friction mode.

VIII.4 Concluding remarks

In conclusion, strain ageing is operating in a wide range of temperatures well outside the restricted region where the macroscopically heterogeneous plastic deformation with PLC bands is manifested. Both alternative strengthening mechanisms are possible in a material exhibiting strain ageing phenomenon: hardening by the solute drag force exerted on the moving dislocations, called age–hardening and the usual strain hardening mechanism associated with an increase in the dislocation density. Whenever age–hardening is absent or disappears, it is immediately replaced by strain hardening in order to sustain locally a similar stress level. Yet, this attempt to sustain a constant stress level is not always successful and the flow stress of the material may decrease, even though the local strain rate is increasing (region where $SRS < 0$).
In zirconium alloys, in the presence of about 1300 wt ppm oxygen such as in Zr702, the added flow stress can be estimated at about 250 MPa, peaking around $300°C$, depending on the strain rate. When this retarding force exerted on the moving dislocations by solute atoms is absent or negligible as at $400°C$ but also more surprisingly at room temperature, the material is exhibiting steady state creep. In the center of the strain ageing domain, creep can stop completely. In zirconium alloys, in the presence of about 80 wt ppm oxygen such as in ZrHf, the dragging mechanism is observed for lower temperatures close to $300°C$. The drag stress is estimated at about 130 MPa at the temperature peak of $250°C$. The PLC effect is active at higher applied strain rates for ZrHf than for Zr702 at the same testing temperature.

In order to take all the experimental results into account, the 3–dimensional temperature versus stress versus strain rate diagram is constructed as shown in figure VIII.22. The two surfaces, corresponding to the friction mode and the dragging mode can be distinguished, having one overlapping domain.
On the left side, the surface corresponds to the friction mode at low temperatures. This surface bends drastically to the right at increasing temperatures, passing under the second surface, located at higher stresses and higher temperatures and also bending to the right. At the backside of the diagram, for increasing strain rates, the stresses for both deformation modes increase considerably. Their overlapping is reduced in the range of temperatures and stresses. Note that in the strain ageing domain (on the microscopic scale), Yoshinaga's simulations (Yoshinaga et al., 1976) allow to distinguish the SSA and the DSA phenomenon. Moreover, Strudel suggested to introduce a new surface, corresponding to the stress peak, observed during tensile tests when a re–loading is carried out after a SSA experiment. The SSA surface can be observed on figure VIII.22. This stress peak is observed every time when the strain rate is raised either from zero (start of a tensile test) or from a lower value (experiments with strain rate changes). It is followed by a Lüders plateau (see figure VIII.23 (a)), for instance in steels and aluminium base alloys. It can be loocked upon as a truncation of figure VIII.23 (b) valid for DSA at higher temperatures when the drag stress can be restored dynamically (during straining). The upper limiting curve called dragging can be reached again and again during the course of the experiment.

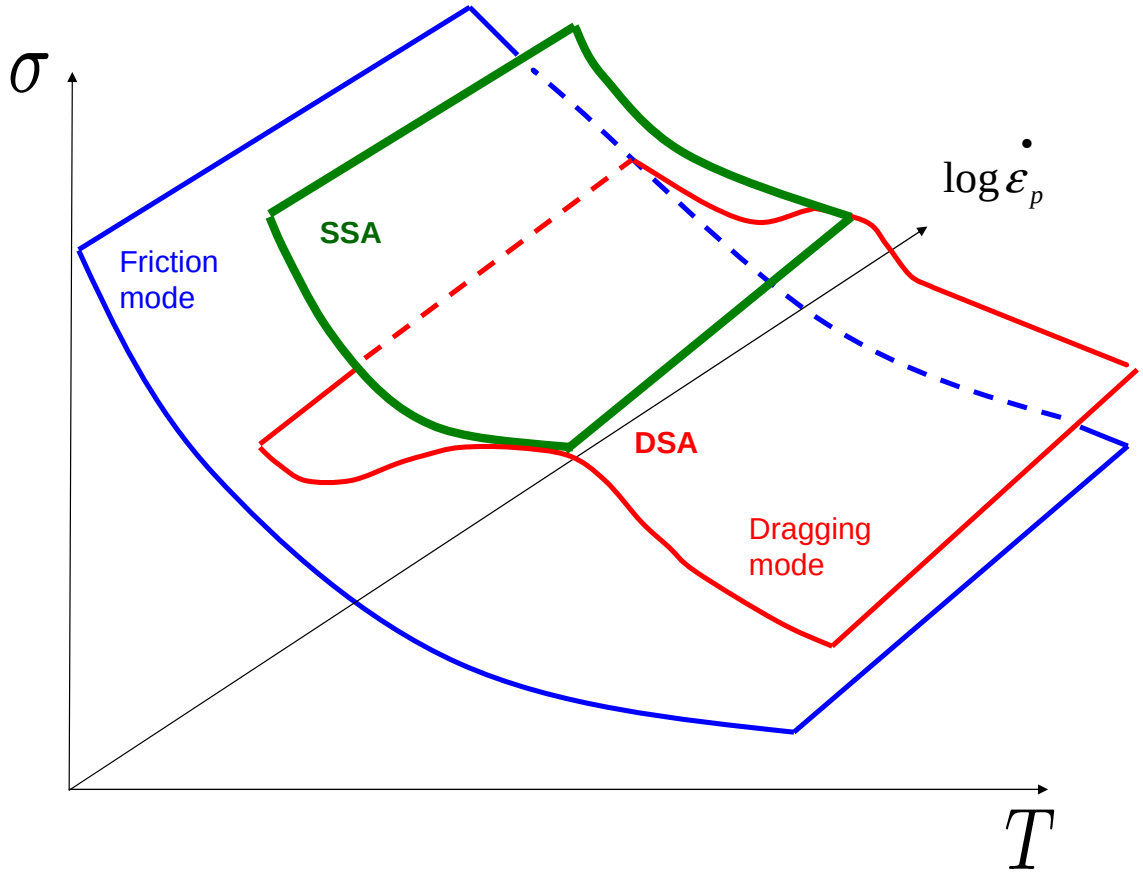

Figure VIII.22 : The 3–dimensional temperature versus stress versus strain rate diagram shows the two surfaces, the friction mode and the dragging mode having one overlapping zone.

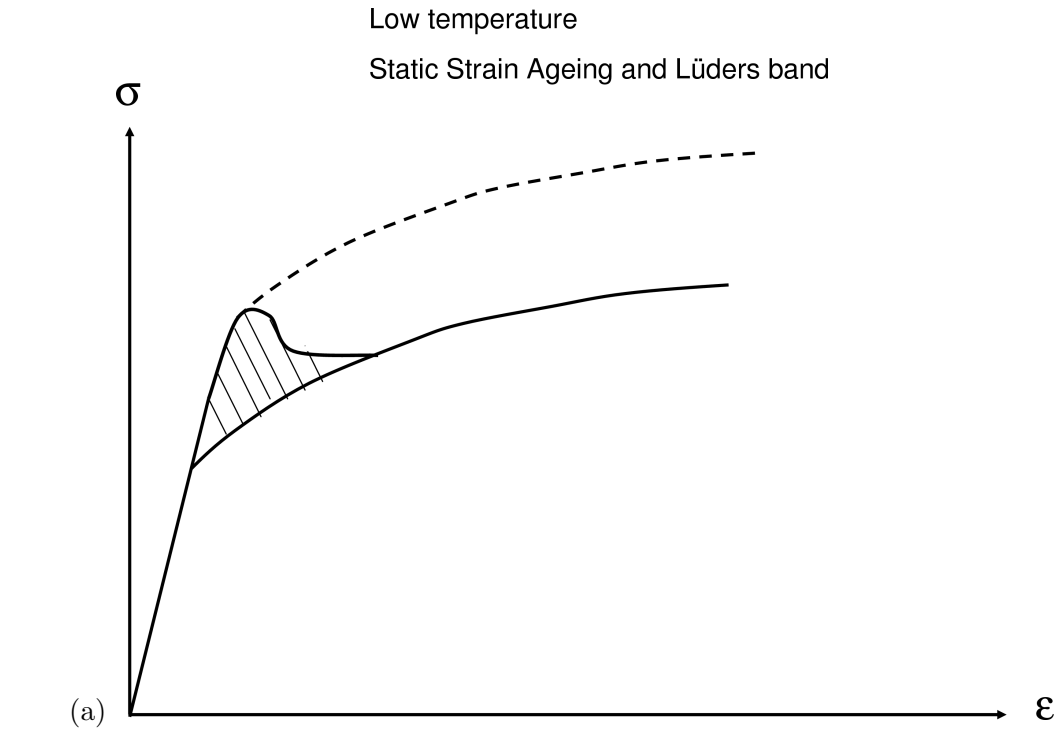

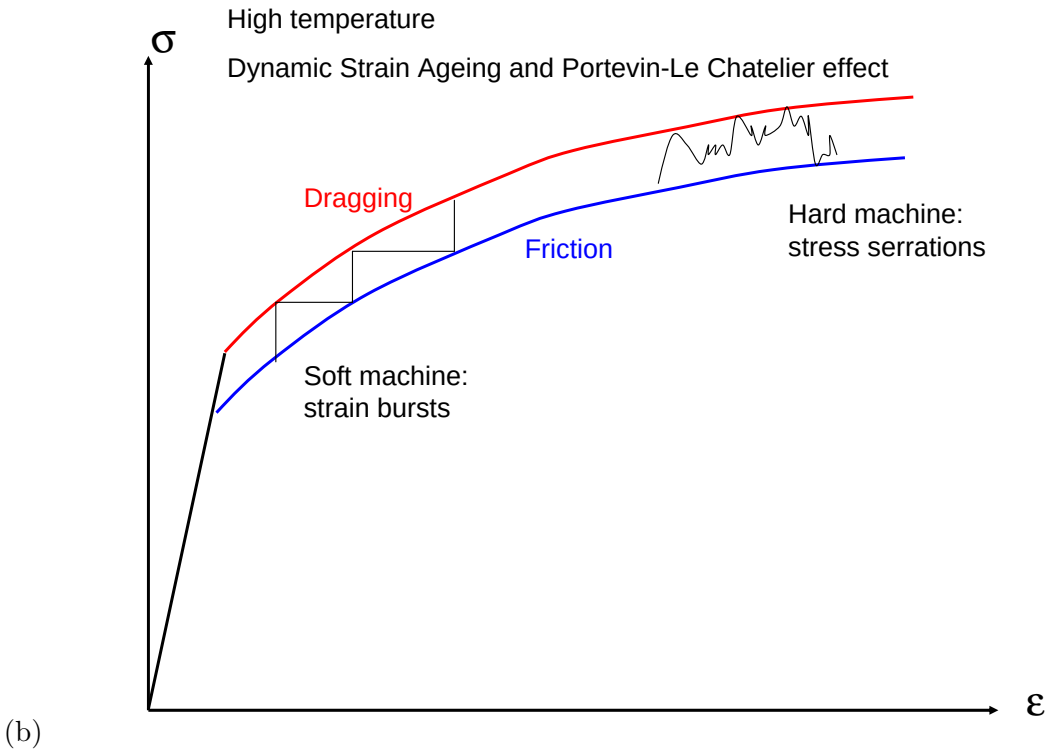

Figure VIII.23 : (a) Schematic of the SSA and the Lüders phenomenon in the stress–strain diagram; (b) Schematic of DSA and the PLC effect with the two stress–strain limiting curves: dragging and friction (Blanc, 1987).

Part C

Field measurements of plastic heterogeneities in strain ageing materials

Chapter -IX-

Investigation of strain heterogeneities by laser scanning extensometry

Contents

Abstract: Laser scanning extensometry was used to detect and characterize propagating plastic instabilities on the millimeter scale such as the Lüders bands and the Portevin–Le Chatelier (PLC) effect. Spatio–temporal plastic heterogeneities are due to either Static or Dynamic Strain Ageing (SSA, DSA) phenomena. Regarding zirconium alloys, different types of heterogeneities are observed, their features strongly depending on mechanical test conditions. In one case, non propagating heterogeneities are observed, associated with SSA effects such as stress peaks after relaxation periods or after unloading steps with waiting times. In other case, they appear as non propagating but are not associated with SSA effects.

IX.1 Introduction

Spatial and temporal homogeneous plastic deformation of crystalline materials can become inhomogeneous in certain ranges of temperatures and plastic strain rates, resulting in the formation and propagation of deformation bands. Only a small part of the specimen volume is activated, in regions which are typically in the range of some μm to some mm wide, depending on material, mechanism and deformation conditions. A variety of such deformation bands have been observed, in particular the Lüders bands in iron and steel at the onset of plastic deformation (Rooyen, 1970) or the PLC effect in aluminum alloys during the deformation process (Klose et al., 2003b). More accurately, such plastic instabilities have been studied by multiple zone laser scanning extensometry in polycrystalline $Al - 15\%Cu$ by Casarotto and Klose (Casarotto et al., 2003).

In numerous zirconium alloys, a non conventional viscoplastic behavior over the temperatures range of approximately $200°C$–$500°C$ has been reported. The phenomena observed included for instance discontinuous plastic flow (Thorpe and Smith, 1978c) and a temperature dependent minimum in strain rate sensitivity (Garde et al., 1975). Many of these phenomena have been related to DSA, and different mechanisms have been proposed such as the interaction between mobile dislocations and interstitial atoms (oxygen, carbon...). Also substitutional atoms (hafnium, tin...) have played an important role in these interactions (Gacougnolle et al., 1970) (see the literature part A).
The aim of the present work is to check whether strain ageing phenomena lead to strain heterogeneities on the millimeter scale in various zirconium alloys. The types of heterogeneities are compared with more standard alloys such as mild steel and aluminum alloys.

IX.2 Presentation of laser scanning extensometry and materials

The materials studied are the following:

- mild steel and Al–Cu4%, denoted as standard alloys (see also (Graff et al., 2004)),
- zirconium 702, labelled Zr702, contained 2280 wt ppm tin and 1300 wt ppm oxygen,
- zirconium with hafnium, labelled ZrHf, contained 2.2 wt% hafnium and 100 wt ppm oxygen.

The main difference between the zirconium alloys is the oxygen level, higher for Zr702 and the substitutional atoms, tin and hafnium respectively for Zr702 and ZrHf.
All specimens were machined a similar way (hot/cold rolling to sheets of about 10 mm thickness) and cut into flat bone-shaped specimens (length 65 mm, width 10 mm, thickness 1.4 mm; active part: length 49 mm, width 4 mm).

The experimental method used in this work is the laser scanning extensometry technique to obtain a high spatial resolution of localized deformation bands. To detect these bands, white stripes (width 1 mm) on a black base layer were applied to the specimens (both capable to sustain high temperatures during the tensile tests). The total gage length scanned and recorded by the extensometer was 24–32 mm and was divided into 25–33 black and white zones (12–16 bright–dark boundaries). Figure IX.1 presents the specimen and the experimental set up. A rotating cubic glass prism scanned a red laser beam along the specimen across the white and black zones painted to its surface at a rotation frequency of 50 Hz. The reflected

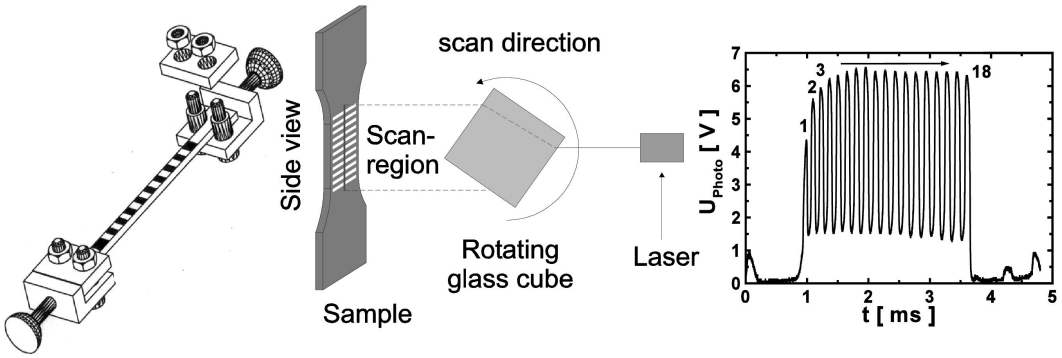

Figure IX.1 : Picture of a prepared sample; Schematic view of the laser scanning extensometer; Voltage of the photodiode which is proportional to the reflected intensity for 18 zones.

signal was focused on a photodiode and its intensity was measured. The second derivative gave the time shift between each intensity alteration referring to the stripe structure. With the reference of the initial state and the known rotation frequency these time intervals can be converted into successive positions in space of all the identified zones. Consequently a practically simultaneous measurement of "local axial strain" can be done with this method along the whole stress–strain curve (strictly speaking, strain was averaged over the 2 mm width of the pair of white and black zones). The resolution of the measured displacement is 1 μm, resulting in a precision of $\delta l/l = 0.05\%$ of a 2 mm wide zone. The time resolution is about 20 ms. What is important is that such plastic heterogeneities or local strains can be detected on the millimeter scale. The investigated volume in any identified painted cell (each pair of white and black zones) is nearly equal to 8 mm^3.
For all the tensile tests, a stiff tensile machine was used. This tensile machine was built by Neuhäuser and Traub (Traub, 1974). The heating of the specimen up to maximum temperature of about $300°C$ was obtained by means of two direct thermocoax heating elements that heat the steel cavities of the specimen holders on both sides of the sample and a removable furnace providing radiation heating to reduce temperature gradients. Taking into account the uncertainties of the measured displacement of the experimental set up, the servo–control of the tensile machine and the temperature, the calculated resolution in strain is ± 0.002.

IX.3 Results and application to zirconium alloys

Detection of the Lüders band in mild steel and application to dynamic strain ageing in aluminum alloys

First, in order to validate the experimental set up of the laser scanning extensometry used for measurements of plastic heterogeneities on the millimeter scale, standard alloys were tested. The first plastic instability is the Lüders band observed in mild steel at room temperature. The strain rate of the tensile test is 8.10^{-4} s^{-1}. The tensile test is carried out with fifteen minutes relaxation periods.

Figure IX.2 shows the macroscopic tensile curve and also the local strain detected by the laser scanning extensometer as a function of the position on the specimen for various strain levels (or the 2 mm width of the pair of white and black zones). The mechanism of the Lüders behavior is the dislocation locking, resulting from an ageing process. A stress

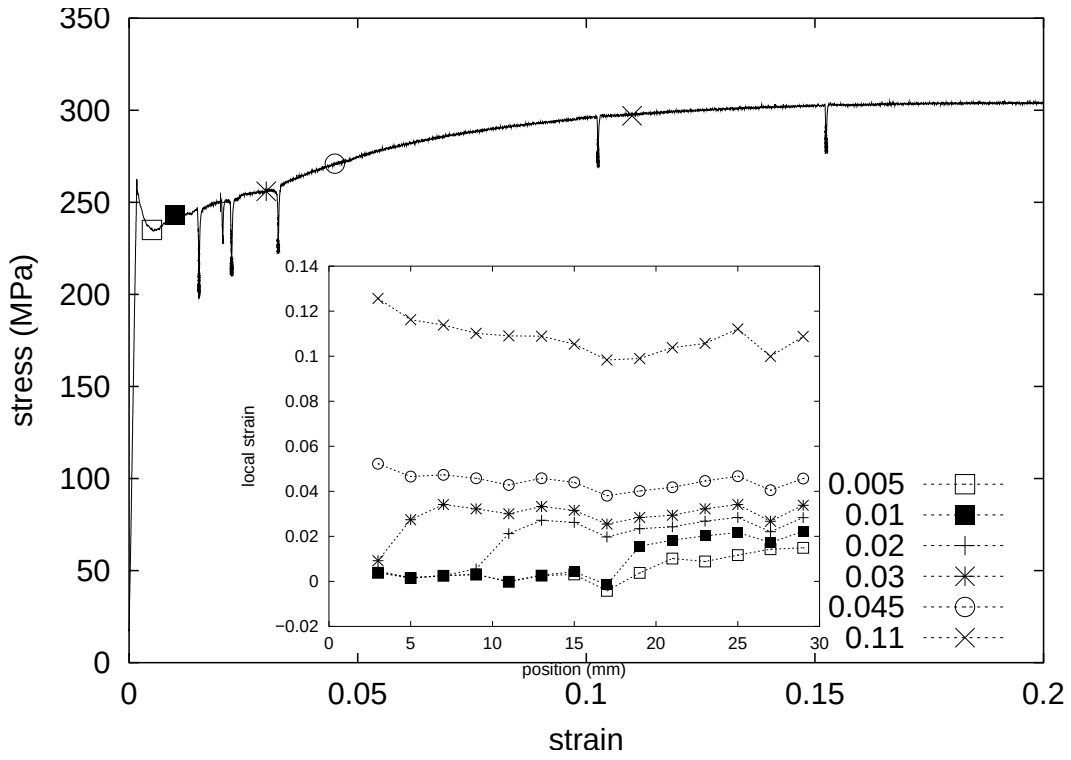

Figure IX.2 : Macroscopic stress–strain curve at room temperature for mild steel obtained during tensile test at a constant strain rate of $8.10^{-4}\ s^{-1}$; Local strain versus position curves for various strain levels selected and identified on the macroscopic curve.

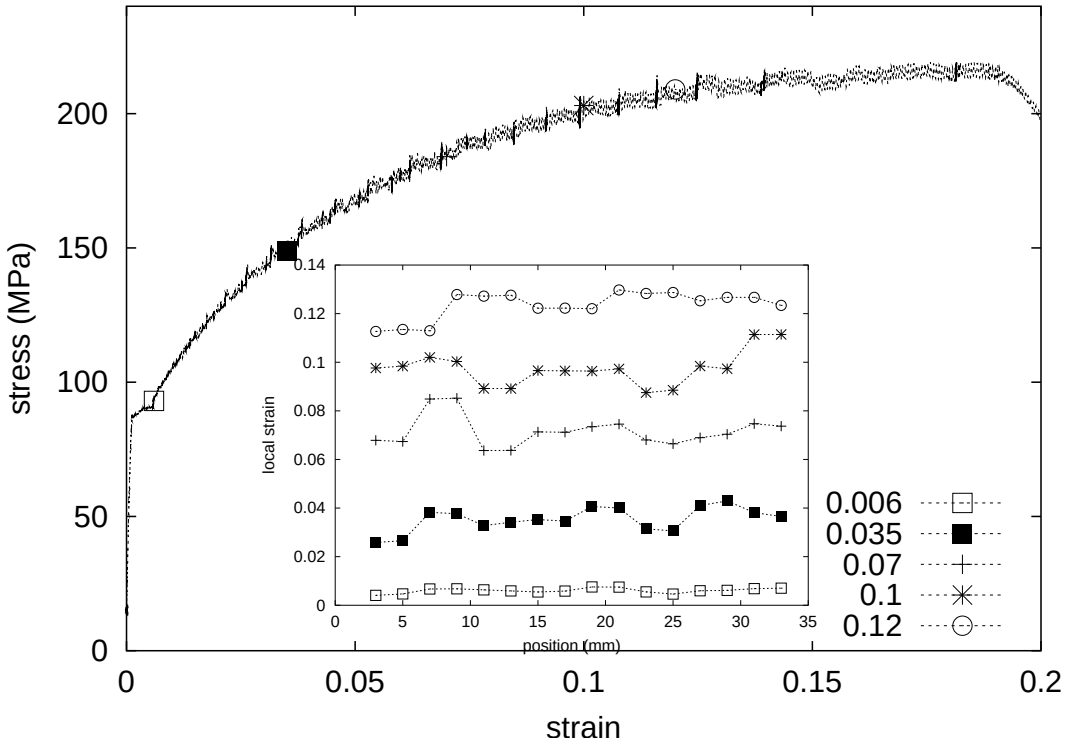

Figure IX.3 : Macroscopic stress versus strain curve at room temperature for $Al-3\%Mg$ obtained during tensile test at a constant strain rate of $10^{-4}\ s^{-1}$; Local strain versus position curves for for various strain levels selected and identified on the macroscopic curve.

is necessary to unlock the dislocations, which is equal to 262 MPa here (the "upper yield stress"). Deformation then localizes into a band usually starting close to the grips. The strain band labeled Lüders band forms with a defined width band, and propagates at a stress level inferior to the upper yield stress (the "lower yield stress"), equal to 247 MPa. A stress peak can be seen on the macroscopic curve of figure IX.2. The Lüders band moves along the entire specimen. Afterwards, the plastic deformation goes on homogeneously following a classic work hardening stress–strain path. Another view of the propagation of the Lüders band front can be observed on the the local strain versus position curve inserted in figure IX.2, which illustrates the propagation mode during straining. We can follow the initiation of the Lüders band near one grip of the specimen and its propagation along the axis of the specimen at various strain levels. The Lüders band is shown to carry 0.003 strain.
Another plastic instability is the PLC effect observed in $Al-3\%Mg$ at room temperature. This jerky flow has been studied in detail by Ziegenbein, Klose et al. (Klose et al., 2003b; Casarotto et al., 2003).

Figure IX.3 shows the macroscopic tensile curve and also the local strain detected by the laser scanning extensometer as a function of the position on the specimen for different strain levels. The serrations observed on the overall tensile curve of figure IX.3, associated with PLC effect are classically labeled as types A, B and C (Hähner et al., 2002) (see part A).

- Type A band appears as a continuous propagation of PLC band, which is usually nucleated with a slight yield point near one specimen grip and propagates with a nearly constant velocity and band width to the other end of the specimen.

- Type B bands propagate discontinuously along the specimen, or more precisely, small

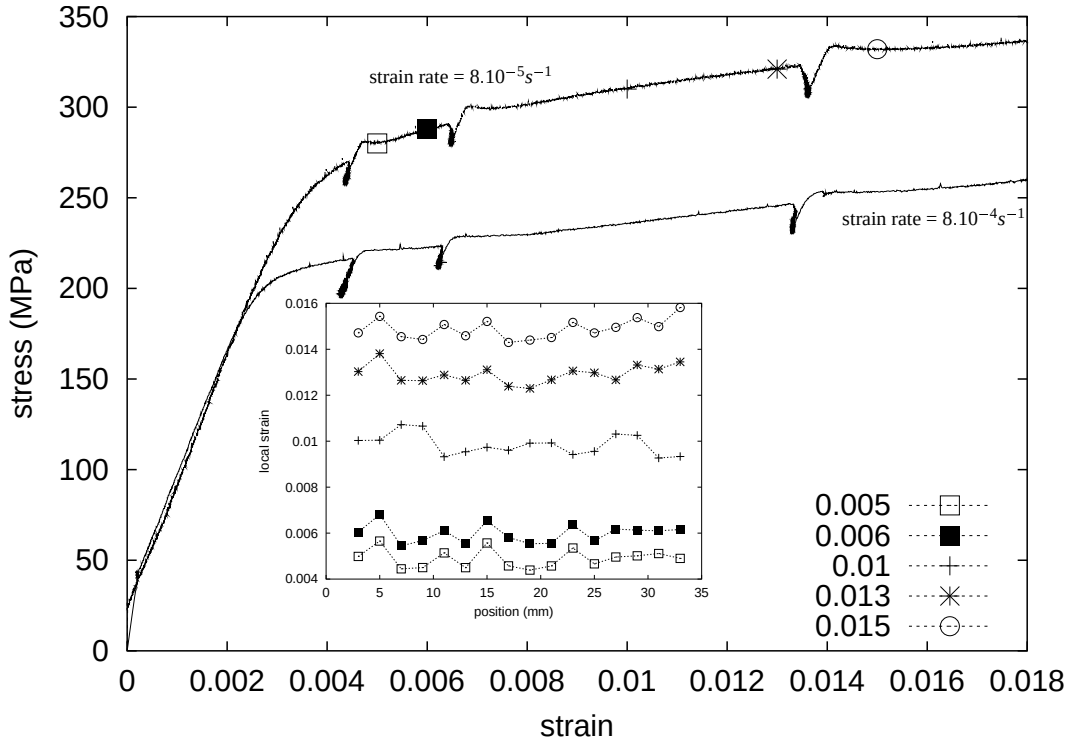

Figure IX.4 : Macroscopic stress versus strain curves at room temperature for $Al-4\%Cu$ obtained during tensile tests at a constant strain rate of $8.10^{-5}\ s^{-1}$ and $8.10^{-4}\ s^{-1}$ interrupted by fifteen minutes relaxation periods; Local strain versus position curves for various strain levels marked on the macroscopic curve.

strain bands nucleate in the surroundings of the former band.

- Type C PLC deformation is characterized by spatially random nucleation of bands without subsequent propagation accompanied by strong, high frequency and irregular load drops.

On the local strain versus position curve inserted in figure IX.3, type B serrations, which are not so easy to recognize on the macroscopic tensile curve, can be clearly identified. For instance, by comparison with 0.035 and 0.07 strain levels, the positions 7 and 10 mm are affected by PLC effect: small strain bands propagate through these two strongly deformed zones. Also at 0.07 and 0.12 strain levels, the positions 11 and 15 mm are affected by localized strain bands which propagate over a short distance.

Figure IX.4 represents the macroscopic curves of two tensile tests performed at a constant strain rate of $8.10^{-4}\ s^{-1}$ and $8.10^{-5}\ s^{-1}$ respectively for $Al-4\%Cu$ alloy at room temperature. During each tensile test, some relaxation periods of fifteen minutes at different strain levels were carried out in order to detect the existence of stress peaks due to SSA during the holding time. The main observation is that this material exhibits an inverse strain rate sensitivity: the macroscopic curve at $8.10^{-5}\ s^{-1}$ is above the one at $8.10^{-4}\ s^{-1}$. The stress peaks observed after each relaxation periods are all the more pronounced as the strain rate is small. Yet the local strain as a function of the position is found to be homogeneous: the value of the local strain heterogeneities detected at various strain levels are smaller than the resolution in strain measurement.

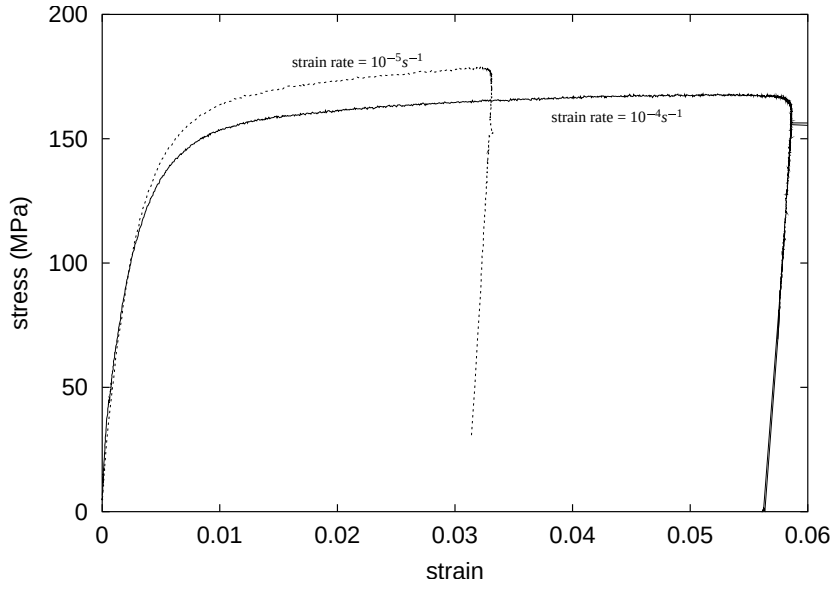

Figure IX.5 : Inverse strain rate sensitivity exhibited by Zr702 at 300°C. The dotted line represents a strain rate of 10^{-5} s^{-1}, the straight line a strain rate of 10^{-4} s^{-1}.

Strain ageing phenomena in zirconium alloys

Various non conventional behaviors have been observed in different zirconium alloys during the last thirty years, for instance:

- the minimum in the strain rate sensitivity versus temperature diagram in Zircaloy–4 (Hong et al., 1983),
- the Lüders band formation in Zr1 wt%Nb (Thorpe and Smith, 1978c),
- the creep arrest in Zr702 (Pujol, 1994).

All these effects, associated with DSA have been observed in the temperatures range 200°C–500°C and for specific imposed strain rates. For such materials exhibiting strain ageing phenomena, the question is to know whether strain heterogeneities exist or not on the millimeter scale. It was previously observed for Al–Mg and mild steel, using the laser scanning extensometry. The aim of this work is also to characterize the type of strain heterogeneities by comparison with standard materials presented in the previous section.

The first tested zirconium alloy is transverse Zr702. This material exhibits an inverse strain rate sensitivity at 300°C as shown in figure IX.5, where the macroscopic curves of two tensile tests realized at the constant strain rates of 10^{-4} s^{-1} and 10^{-5} s^{-1} respectively are presented (zoom at the beginning of the straining). This effect is usually attributed to DSA phenomena up to 0.03 strain, due to the interaction between oxygen atoms and mobile dislocations (Hong et al., 1983).

Tensile tests at a constant strain rate of 8.10^{-5} s^{-1} with relaxation periods of fifteen minutes were realized for the temperatures 20°C, 100°C and 250°C.

The macroscopic curves of figure IX.6 show that Zr702 exhibits SSA only at 250°C. The stress peaks after relaxation periods are rather bulgy. For the same various strain levels at 20°C and 250°C, the local strains were measured and plotted as a function of the position in figure IX.7(a) at 20°C and in figure IX.7(b) at 250°C. A conventional behavior associated with an homogeneous response is observed for the different strain levels at 20°C.

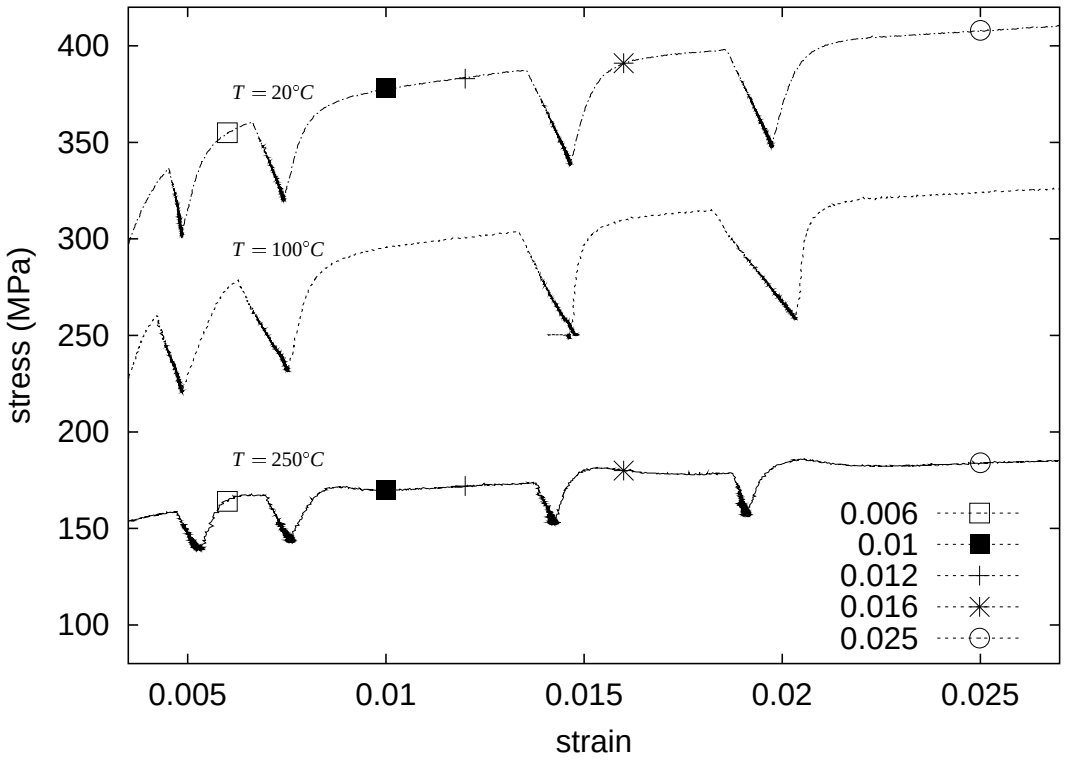

Figure IX.6 : Macroscopic stress versus strain curves at $20°C$, $100°C$ and $250°C$ for Zr702 obtained during tensile tests at a constant strain rate of 8.10^{-5} s^{-1} interrupted by fifteen minutes relaxation periods.

However, at $250°C$ strain heterogeneities are observed on the millimeter scale. Initially for small deformations, for instance at 0.006 strain level, strain inhomogeneities are detected in all the zones. Comparing with the mild steel and the $Al - 3\%Mg$ alloy, this type of strain heterogeneity during straining is not a propagating one like the Lüders band and is not a PLC instability.

Ferrer et al. showed in a zirconium alloy labeled M5 that for small deformations (about 0.02 strain level), after a tensile test carried out at a constant strain rate of $5.10^{-5}\ s^{-1}$ at $200°C$, glide lines were not observed in all the grains: the strain was localized in some specific grains (Ferrer, 2000). This strain localization effect is however at a different scale.

Other mechanical tests are now considered namely tensile tests with partial unloading steps and waiting times. Figure IX.8 shows the macroscopic curves obtained at an imposed strain rate of $8.10^{-5}\ s^{-1}$ at $20°C$ and $250°C$. SSA is observed only at $250°C$ and the stress bulges are similar to those observed in figure IX.6. The stress peak is more pronounced at the first partial unloading because the waiting time is 24 hours contrary to the other partial unloadings with holding times of just a few minutes. The curves which represent the local strain as a function of the position for different strain levels on figure IX.8 are those obtained at $20°C$. Even though there is no clear SSA effect on the macroscopic curve at $20°C$, strain heterogeneities are observed on the millimeter scale. This effect can be explained by the fact that the strain inhomogeneities are detected after the first partial unloading with the waiting time of 24 hours. Consequently, during this holding time, the diffusion of solute atoms could lead to the initiation of plastic strain inhomogeneities. Moreover, the strain heterogeneities are of the same type as those found during the tensile test with relaxations at $250°C$. Such heterogeneities are also observed at $250°C$ where SSA occurs. For this example, the amplitude of strain heterogeneities can reach 0.015.

For comparison, we tested another zirconium alloy, especially ZrHf. The same mechanical tests as the previous ones were performed. Regarding the tensile tests with partial unloading steps and waiting times at a constant strain rate of $8.10^{-5}\ s^{-1}$ at $20°C$ and $250°C$, figure IX.9 shows that ZrHf exhibits SSA effect, characterized by an increase of stress after each unloading step at $250°C$. Such an effect is seen in Zr702 at the same temperature.

At $20°C$, no strain heterogeneity is measured up to 0.02 strain level, contrary to Zr702 in which initial heterogeneities are observed at the beginning of straining (see figure IX.8). This effect can be explained by the fact that Zr702 contains ten times more oxygen atoms than ZrHf. Thus in zirconium alloys, the presence of both oxygen and substitutional element (tin in Zr702 and hafnium in ZrHf) seems to be a necessary condition for the observation of strain ageing phenomena. Consequently, we can suggest that although $20°C$ is not a temperature for which the diffusion of solute atom is efficient in zirconium alloys, if the content of oxygen atoms is high enough, plastic strain heterogeneities can be detected. Moreover as in Zr702, the strain heterogeneities are non propagating.

Figure IX.10 shows the macroscopic curves obtained during the tensile tests with relaxation periods realized at a constant strain rate of $8.10^{-5}\ s^{-1}$ at $20°C$ and $100°C$. For the two temperatures, there is no strain ageing after relaxation periods as observed in Zr702 at $20°C$ and $100°C$ (see figure IX.6). The strain level for which strain heterogeneities are detected is equal to 0.016 at $100°C$ contrary to Zr702 (the initial heterogeneities are observed at 0.0075 strain level). This is the main difference between the two zirconium alloys studied. As the results of the tensile tests with partial unloading steps and waiting times, one can argue that the oxygen atoms can favor the initial heterogeneities for Zr702. The values of the stress peak after relaxation period and unloading are equal to 9 MPa and 5 MPa for Zr702 and ZrHf respectively (see tables IX.2, IX.3).

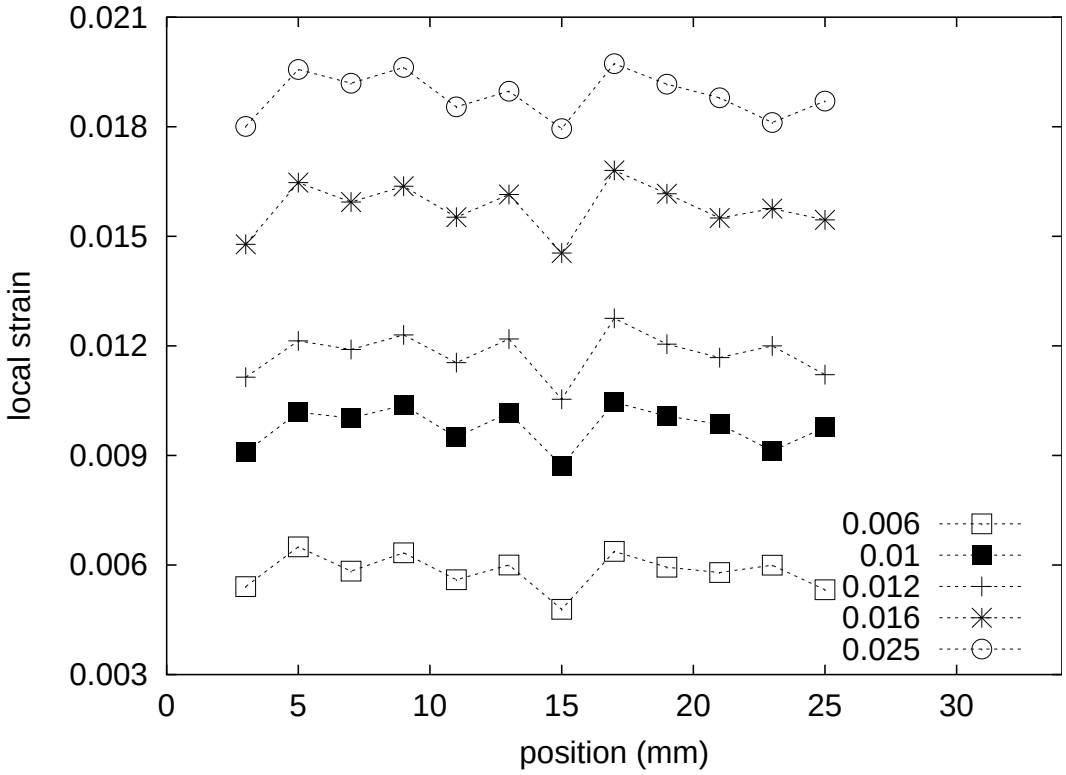

(a)

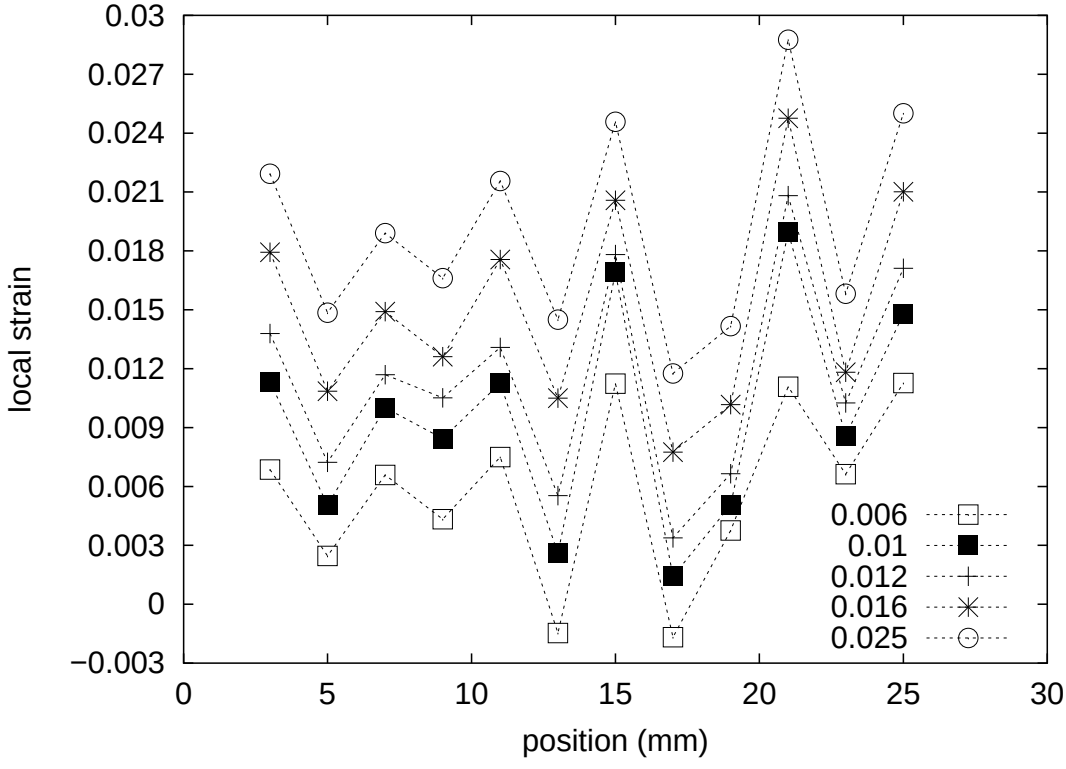

(b)

Figure IX.7 : Local strain versus position curves for Zr702 corresponding to the tensile test at a constant strain rate of $8.10^{-5}\ s^{-1}$ for various strain levels marked on the macroscopic curve (see figure IX.5) at $20°C$ (a) and at $250°C$ (b).

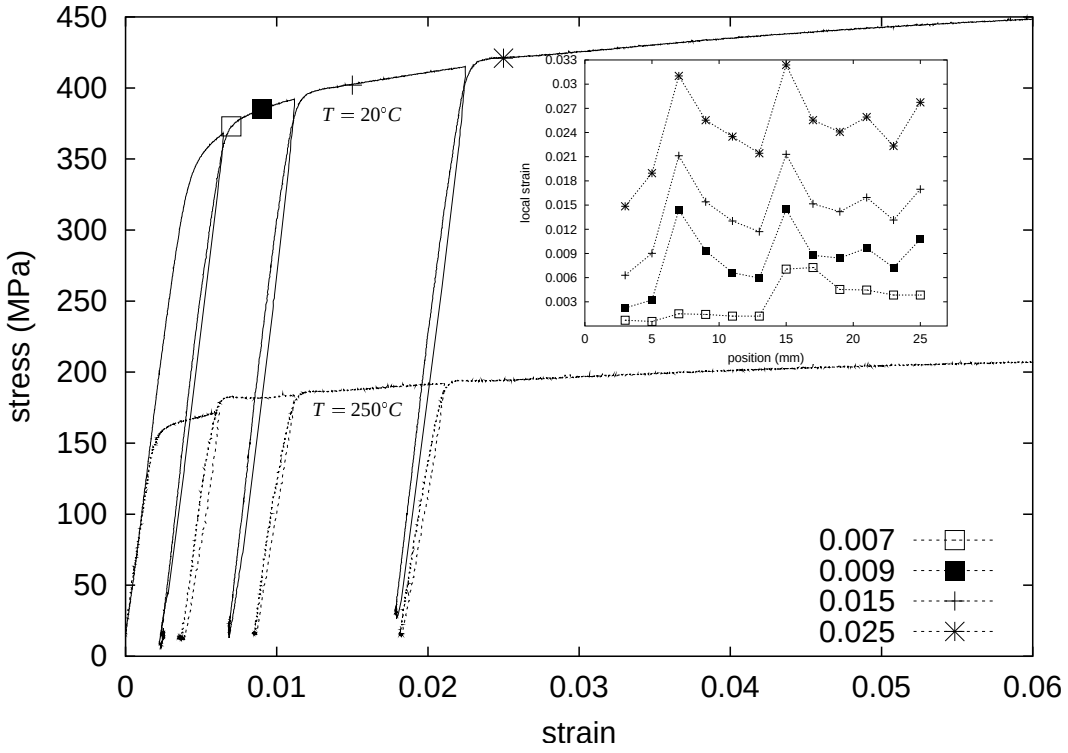

Figure IX.8 : Macroscopic stress versus strain curves at $20°C$ and $250°C$ for Zr702 obtained during tensile tests at a constant strain rate of $8.10^{-5}\ s^{-1}$ interrupted with unloading steps and waiting times (the waiting time after the first partial unloading is 24 hours contrary to the other partial unloadings with holding times of just a few minutes); Local strain versus position curves for various strain levels shown on the macroscopic curve at $20°C$.

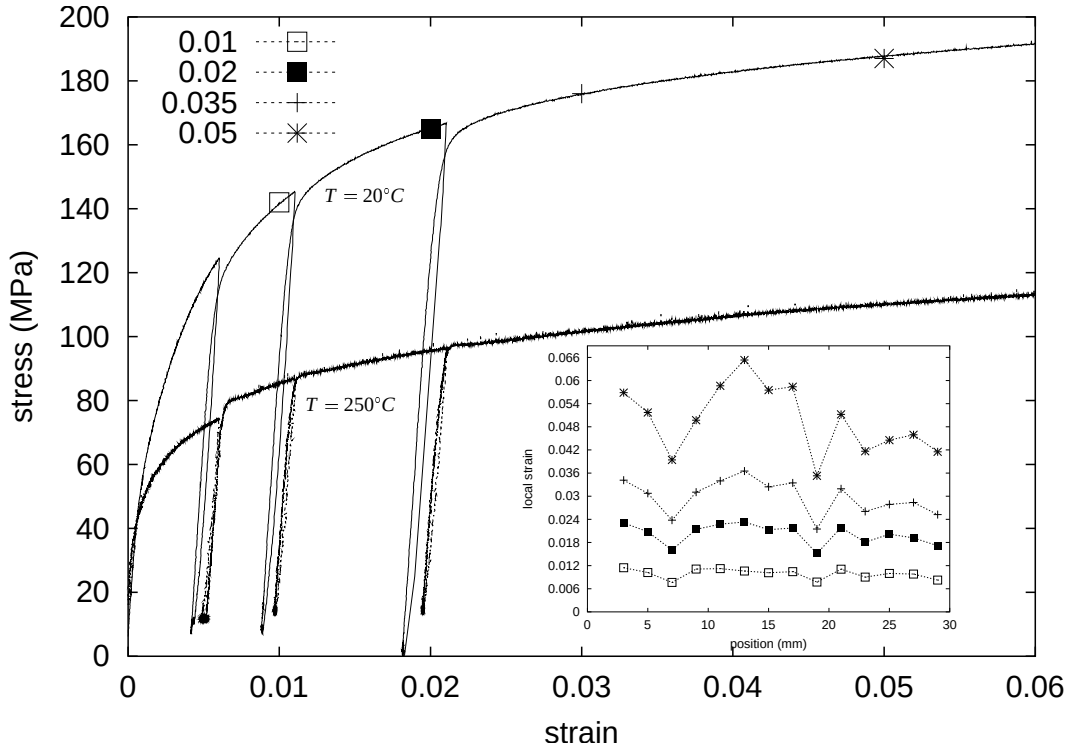

Figure IX.9 : Macroscopic stress versus strain curves at $20°C$ and $250°C$ for ZrHf obtained during tensile tests with unloading steps and waiting times (the waiting time after the first partial unloading is 24 hours contrary to the other partial unloadings with holding times of just a few minutes); Local strain versus position curves for various strain levels marked on the macroscopic curve at $20°C$.

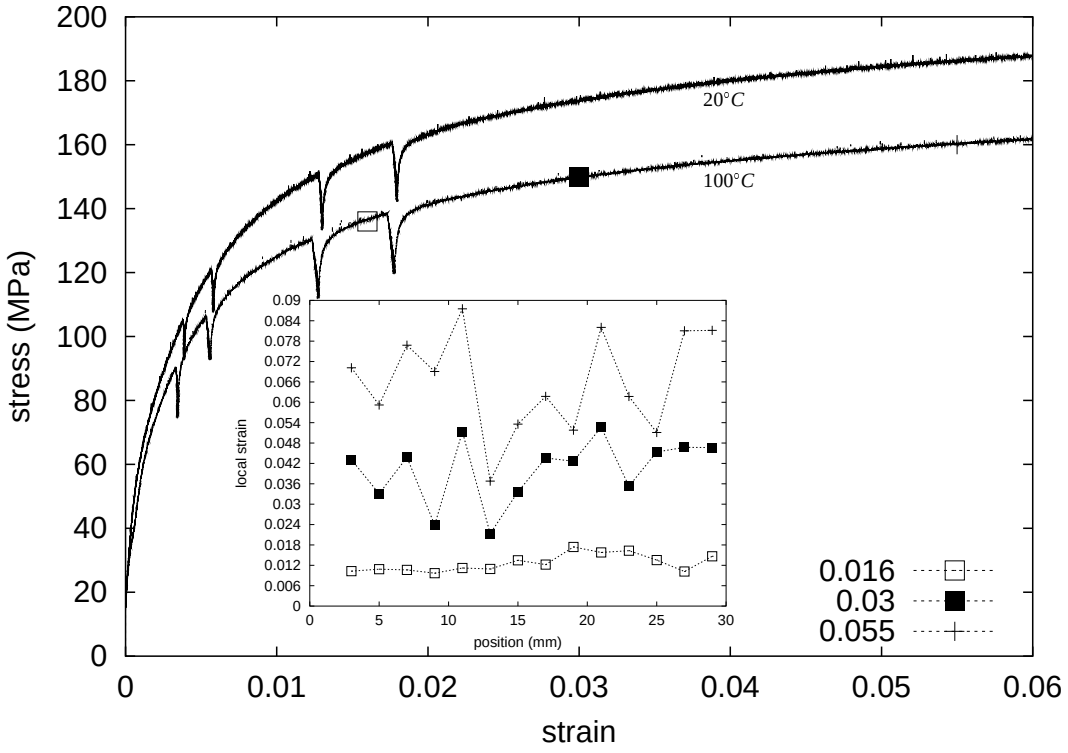

Figure IX.10 : Macroscopic stress versus strain curves at $20°C$ and $100°C$ for ZrHf obtained during tensile tests at a constant strain rate of $8.10^{-5}\ s^{-1}$ interrupted with relaxation periods; Local strain versus position curves for various strain levels marked on the macroscopic curve at $100°C$.

IX.4 Conclusion

Laser scanning extensometry is an appropriate method to identify and characterize plastic strain heterogeneities on the millimeter scale.
Table IX.1 gives the classification of SSA and DSA phenomena during tensile tests carried out at constant strain rates for standard materials such as the mild steel, $Al-3\%Mg$ and $Al-4\%Cu$ alloys.

Table IX.1 : Classification of SSA and DSA phenomena during tensile tests carried out constant strain rates for the standard materials.

Materials	Temperature ($^{\circ}C$)	Strain rate (s^{-1})	SSA	DSA	Strain heterogeneities
Mild steel	20	8.10^{-4}	upper yield stress, lower yield stress, Lüders band	no	yes
$Al-3\%Mg$	20	10^{-4}	Lüders band	PLC serrations	yes
$Al-4\%Cu$	20	8.10^{-5}	stress peaks after relaxation periods	inverse strain rate sensitivity	no
$Al-4\%Cu$	20	8.10^{-4}	stress peaks after relaxation periods	inverse strain rate sensitivity	no

Table IX.2 and table IX.3 display the classification of SSA and inverse strain rate sensitivity phenomena during tensile tests carried out at constant strain rates respectively including relaxation periods and unloading steps with waiting times for the tested zirconium alloys.

Table IX.2 : Classification of SSA and inverse strain rate sensitivity phenomena during tensile tests carried out at constant strain rates with relaxation periods for both zirconium alloys.

Materials	Temperature ($°C$)	Strain rate (s^{-1})	SSA	Inverse strain rate sensitivity	Strain heterogeneities
Zr702	20	8.10^{-5}	no	no	no
Zr702	100	8.10^{-5}	no	no	yes
Zr702	250	8.10^{-5}	stress peaks after relaxation periods $\Delta\sigma = 9MPa$	no	yes
ZrHf	20	8.10^{-5}	no	no	no
ZrHf	100	8.10^{-5}	no	no	yes
ZrHf	250	8.10^{-5}	stress peaks after relaxation periods $\Delta\sigma = 5MPa$	no	yes

Table IX.3 : Classification of SSA and inverse strain rate sensitivity phenomena during tensile tests carried out at constant strain rates with unloading steps and waiting times for both zirconium alloys.

Materials	Temperature ($°C$)	Strain rate (s^{-1})	SSA	Inverse strain rate sensitivity	Strain heterogeneities
Zr702	20	8.10^{-5}	no	no	yes
Zr702	100	8.10^{-5}	no	no	yes
Zr702	250	8.10^{-5}	stress peaks after unloading steps and waiting times $\Delta\sigma = 9MPa$	no	yes
ZrHf	20	8.10^{-5}	no	no	yes
ZrHf	100	8.10^{-5}	no	no	yes
ZrHf	250	8.10^{-5}	stress peaks after unloading steps and waiting times $\Delta\sigma = 5MPa$	no	yes

Taking these observations and the experimental results of local strain versus position curves into account, we can propose the following classification of the different plastic strain heterogeneities, detected by laser scanning extensometry.

1. The Lüders phenomenon is a continuous propagation of strain band front moving along the entire specimen at a nearly constant velocity and at a nearly constant stress: for example in mild steel.

2. Regarding PLC effect:

   - PLC type A bands are strain bands usually propagating continuously with a nearly constant velocity and band width. They reach the other end of the specimen and can be reflected. PLC bands sweep across the gauge length periodically.
   - PLC type B bands are small strain bands which nucleate, propagate and vanish at random in various regions of the specimen: for example in $Al - 3\%Mg$ alloy.
   - PLC type C bands are characterized by a spatially random nucleation of strain bursts with short life time and without significant propagation.

3. No plastic strain heterogeneities are detected but SSA effects such as stress peaks after relaxation periods can be observed: for example in $Al - 4\%Cu$ alloy.

4. Non propagating strain heterogeneities associated with SSA effects such as stress peaks after relaxation periods or unloading steps with waiting times can be detected: for example in Zr702 and ZrHf at $250°C$.

5. Non propagating strain heterogeneities associated with no SSA effects can be observed: for example in Zr702 and ZrHf at $100°C$.

As complex strain localization phenomena take place in zirconium alloys, it should be interesting to make some investigations on the sub–millimeter scale, to have a better view of the diffusion processes of solute atoms on plastic strain heterogeneities. Some questions can be asked:

- How do plastic heterogeneities initiate?
- What is the role of the interstitial atoms like oxygen atoms?
- How are plastic instabilities preserved when strain increases?

Acknowledgements:

I wish to thank H. Dierke for his help with the laser extensometer experiments applied to zirconium alloys studied at $20°C$, $100°C$ and $250°C$ and Professor H. Neuhäuser for our interesting discussions as well as the DFG and the EU (DEFINO RTN network) for their financial support of this research.

Chapter -X-

Additional comments about investigation of strain heterogeneities by laser scanning extensometry

Contents

Abstract: A collection of the essential features and general characteristics of PLC effect from a phenomenological point of view is based on the experimental results obtained for aluminum alloys. Regarding zirconium alloys, additional analysis of the observed plastic strain heterogeneities is given in the relevant description of local strain versus time curve at various temperatures. The main finding is that the plastic strain heterogeneities detected on the millimeter scale are non propagating, and also the cumulated plastic strain can increase locally along the stress versus strain curve in some cases.

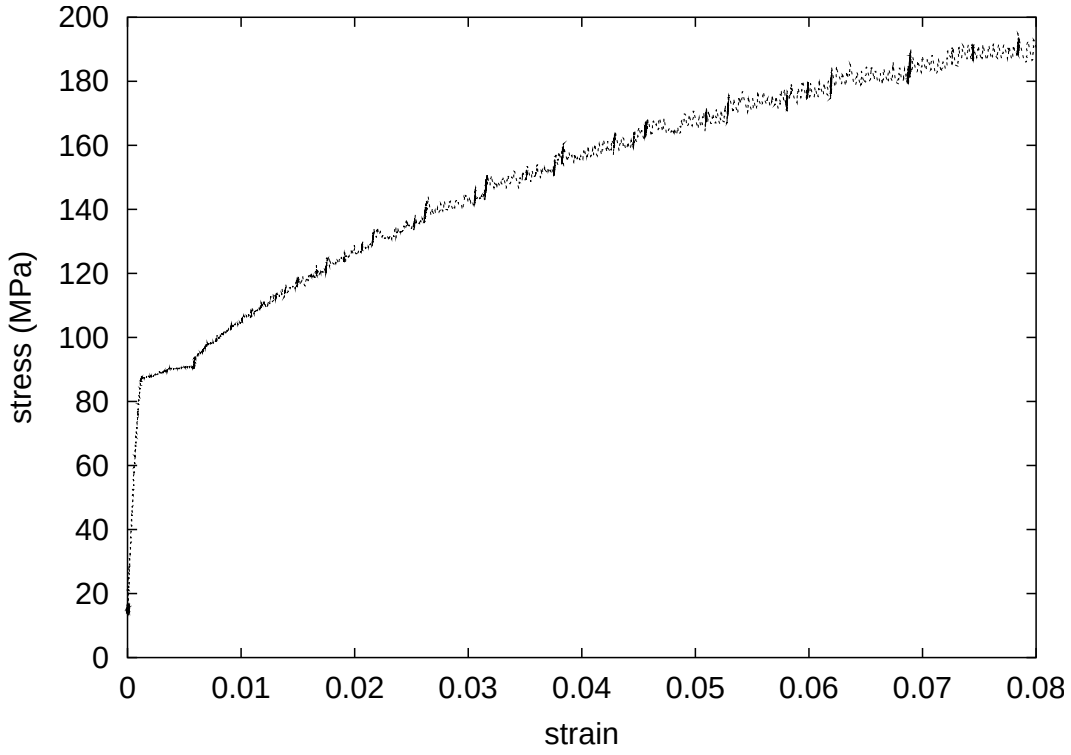

Figure X.1 : Macroscopic stress versus strain curves for the deformation of $Al-3\%Mg$ alloy at $20°C$ in a strain rate controlled mode with $\dot{\varepsilon} = 10^{-4}\ s^{-1}$ (Dierke, 2005).

X.1 Experimental spatio–temporal analysis of strain ageing in aluminum alloys

This section presents a more detailed examination of PLC unstable behavior in $Al-3\%Mg$ alloy and strain ageing phenomena in zirconium alloys by means of the laser scanning extensometry.

Regarding $Al-3\%Mg$ alloy, strain rate controlled tests were carried out at $20°C$ at a strain rate of $10^{-4}\ s^{-1}$. The macroscopic stress–strain behavior is shown in figure X.1.

The unstable deformation starts with a Lüders band. Starting from a nucleation region, where some stress concentration is acting (near the grips or at a geometric non uniformity of the specimen) and/or where the microstructure is softer than elsewhere, a local region of high strain is spreading in the virgin part of the specimen with the help of local stresses generated at the border between the sheared and not yet sheared material. Together with the local work hardening, which terminates shear in the rear of the band, this results in a soliton–like propagation behavior. Figure X.2 shows the Lüders band in the stress versus time diagram between 50 s and 60 s. Then the stress versus time curves of the figure X.2 between 160 s and 200 s and between 280 s and 305 s show type B serrations. In addition to the global stress versus time/stress versus strain curves, the classification of the PLC events can be done unambiguously on the basis of the local strain data for the 2 mm wide regions of the specimen data which are achieved by means of the laser scanning extensometry. Figure X.3 shows the so–called "correlation diagrams" in which the position of local strain bursts is plotted versus its time of occurrence for all local strain measurements. In figure X.3, correlation diagrams and local strain as a function of time are shown for different intervals of time. These two types of description immediately permit to have a better view of the possibility of the propagating

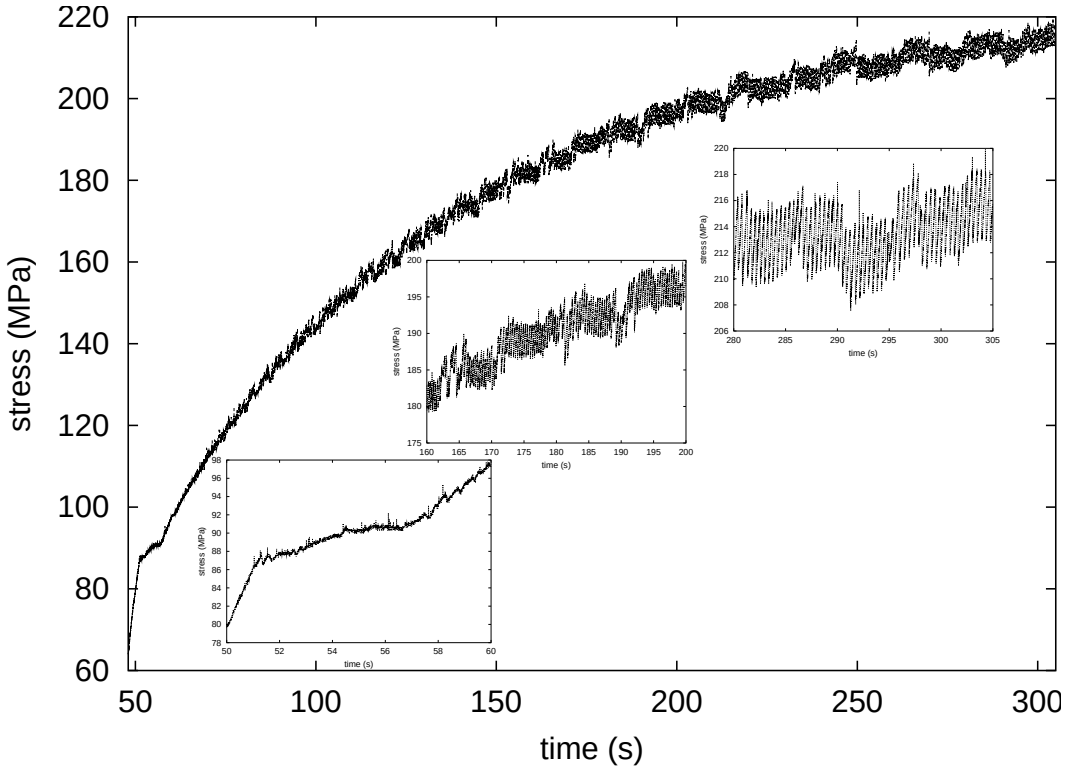

Figure X.2 : Stress versus time curves for $Al-3\%Mg$ alloy at $20°C$, at a constant applied strain rate of $10^{-4}\ s^{-1}$. Note the evolution of the work hardening and the transition from type A to type B behavior at about 0.0045 strain level.

and/or increasing strain behavior during the mechanical test: propagation mode, speed and strain increment.

The velocity of the Lüders band is deduced from the correlation diagram of figure X.3 (a): $v_b = 6.67\ mm.s^{-1}$. The discontinuous jerky propagation of type B band is recognized in the global strain versus time curve with small strain increments. The intermittent propagation of the band within one zone, for instance the position 15 mm with three jumps is seen in figure X.3 (f) between 291 s and 302 s. These three events are indicated in the correlation diagram (see the three crosses of figure X.3 (e)) in the respective position 21 mm . The "reflection" of type B bands is more frequent at larger strains as shown in figure X.3 (e). This effect means that the nucleation of the next band occurs preferably at those sites where the last band has just come to a stop (where the less aged dislocations represent the smallest threshold for a re–nucleation assuming an homogeneous work hardening level along the specimen axis) (Schwarz, 1985b).

This last paragraph deals with the comparison between the local strain versus time curves of both aluminum alloys at $20°C$: the $Al-3\%Mg$ and the $Al-4\%Cu$. In the first chapter, we observed that at $20°C$ the local strain is found to be homogeneous, although $Al-4\%Cu$ alloy exhibits both an inverse strain rate sensibility and stress peaks after each relaxation period. $Al-3\%Mg$ exhibits also an inverse strain rate sensibility (Graff et al., 2005), but the local strain is heterogeneous. Macroscopic PLC serrations can be observed on the stress versus strain curve of figure X.2 for $Al-3\%Mg$ alloy. Figure X.4 shows the local strain as a function of time for three zones: (a) for $Al-3\%Mg$ and (b) for $Al-4\%Cu$ alloy.

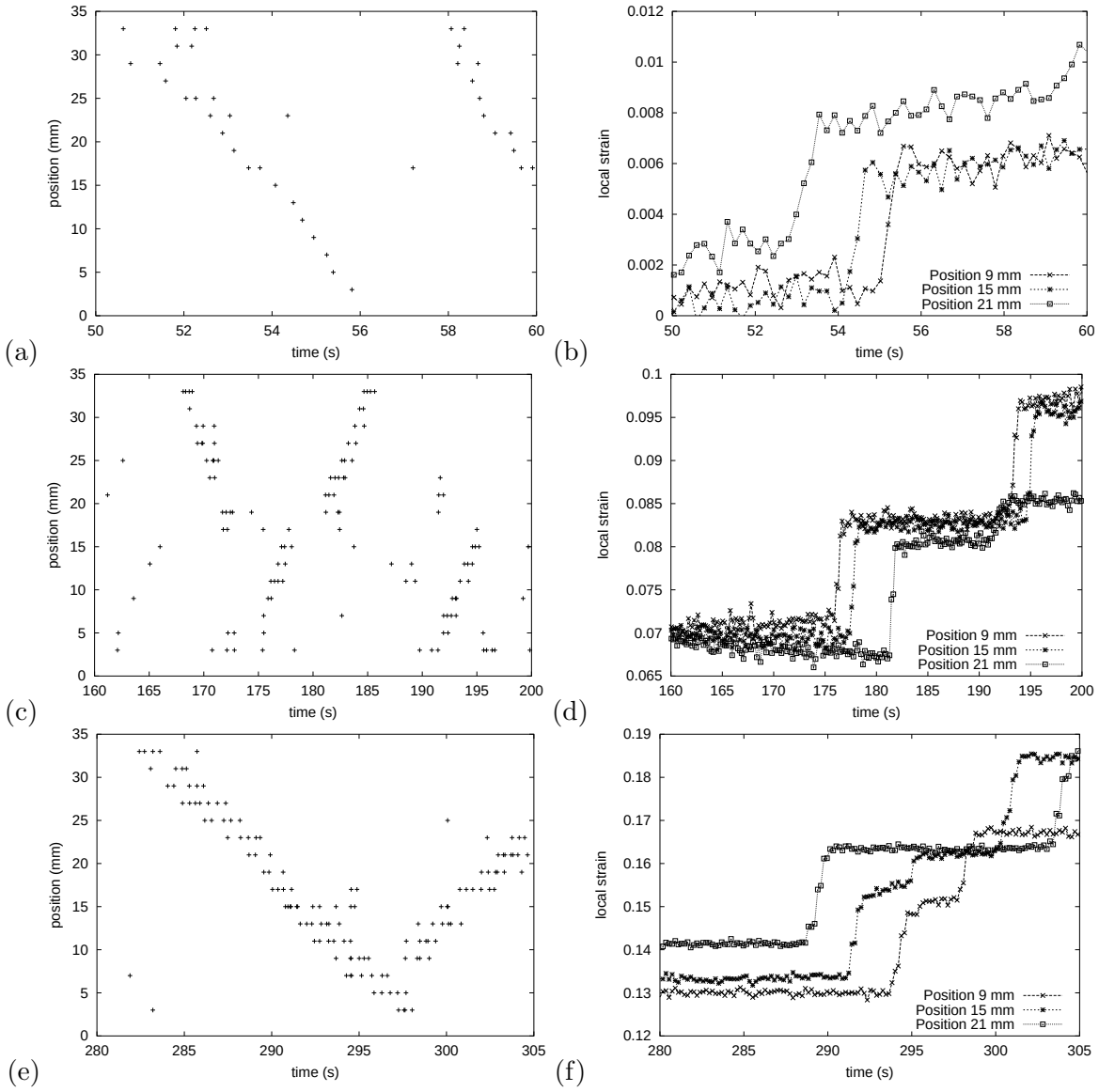

Figure X.3 : "Correlation diagrams" (a), (c), (e) and local strain as a function of time (b), (d), (f) for different intervals of time for $Al - 3\%Mg$ alloy at $20°C$, at a constant applied strain rate of $10^{-4}\ s^{-1}$. (a), (b) show the extended view of the Lüders band regime. (f) shows a PLC type B event which is reflected at positions 5–7 mm (almost at one end of the gage length).

The local strain difference between the various zones increases during straining. For instance for the positions 7, 9, 11 mm:

- between 0 s and 70 s, the maximal local strain difference is about 0.004,
- between 160 s and 200 s, the maximal local strain difference is about 0.015,
- between 280 s and 305 s, the maximal local strain difference is about 0.033.

This shows that the PLC bands are propagating. Up to about 150 s, the local strain level of the position 7 mm is similar to this of the position 9 mm. Then up to 270 s, the local strain level of the position 9 mm becomes superior to this of the position 7 mm. Consequently the strain heterogeneities increase during straining. Contrary to $Al-3\%Mg$ alloy, the increments of the local strain for $Al-4\%Cu$ alloy are not due to some PLC events. They correspond to each relaxation period. The maximal local strain difference between the positions 23 and 27 mm is about 0.0009 which is inferior to 0.002, the estimated strain of the resolution. After each relaxation period, the quantity of strain for both positions increases with the same value. Consequently the behavior of this material tends to become homogeneous and no plastic strain localization phenomena are observed for $Al-4\%Cu$ alloy tested at the applied strain rate of $8.10^{-5}\ s^{-1}$ at $20°C$.

X.2 Application to zirconium alloys

The aim of this section is to give some additional comments about plastic strain localization phenomena observed in both zirconium alloys tested at different temperatures in the description of local strain versus time curve for some relevant positions.

In the previous chapter, tensile tests at constant strain rate of $8.10^{-5}\ s^{-1}$ with relaxation periods are presented for Zr702. Figures X.5 (a), (b) are other representations of the tests showing the local strain versus time for various positions. At $20°C$, an homogeneous response is observed in figure X.5 (a): the positions 7 and 17 mm have the same value of local strain during the straining of the specimen. After each relaxation period, the quantity of strain for both positions increases with the same value. This material exhibits also a conventional macroscopic behavior. The four strain steps observed correspond to the four relaxation periods of about fifteen minutes and consequently they are not associated with increments of local strain due to PLC effect as shown in figure X.3 for $Al-3\%Mg$ alloy. At $250°C$, figure X.5 (b) shows that at the beginning of straining, plastic strain heterogeneities are observed in the various zones. In particular between the positions 13 and 15 mm, the maximal local strain difference is about 0.011. During the deformation, after each relaxation period and according to the position, the local strain does not increase with the same value. This effect can be observed for instance at the positions 7 and 13 mm after the third relaxation period. The local strain of the position 13 mm is twice bigger than this of the position 7 mm. Contrary to measurements at $250°C$, where stress peaks are observed after each relaxation period, on the macroscopic curve, this effect is also observed at $100°C$, although no SSA phenomenon is observed on the macroscopic curve.

Then tensile tests with partial unloading steps and waiting times were carried out at the applied strain rate of $8.10^{-5}\ s^{-1}$ for various temperatures. At $20°C$, figure X.6 (a) shows the local strain versus time curves for the positions 9, 11 and 13 mm between 0 s and 600 s. The main observation is that locally the partial unloading step has not the same impact according to the different zones. For instance, the strain drop is larger for the position 11 mm than for the position 13 mm. Just after the first partial unloading step, the local strain of the position

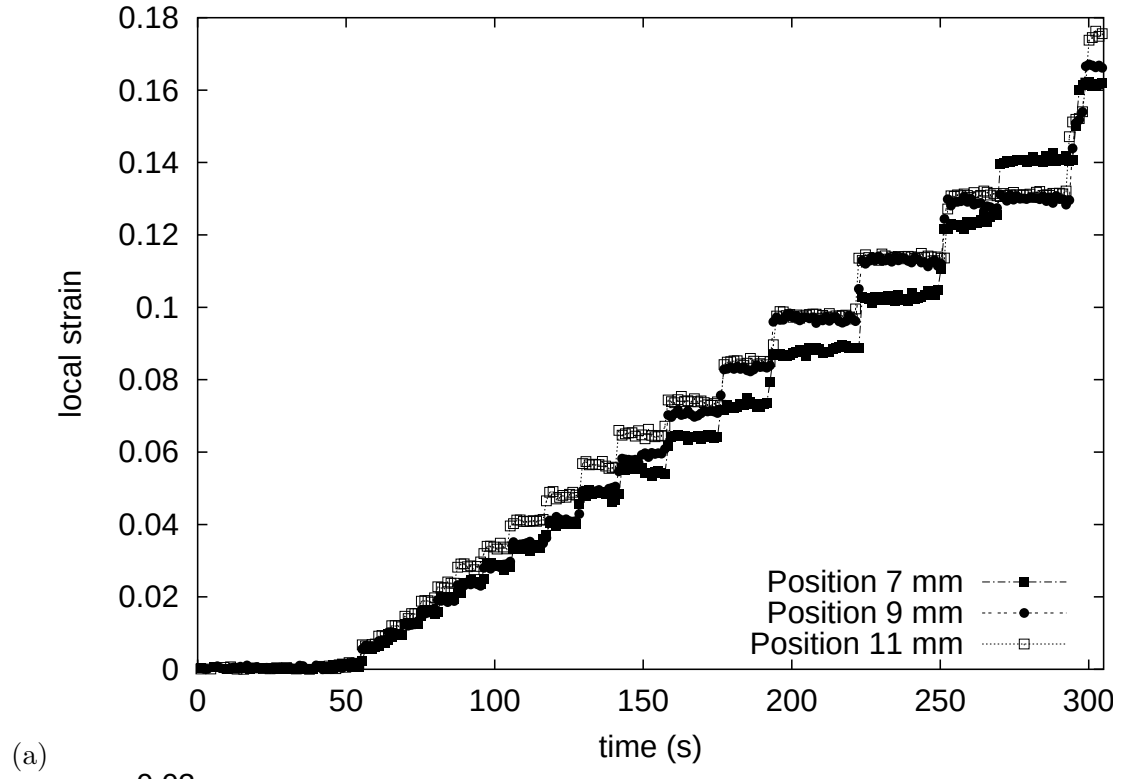

(a)

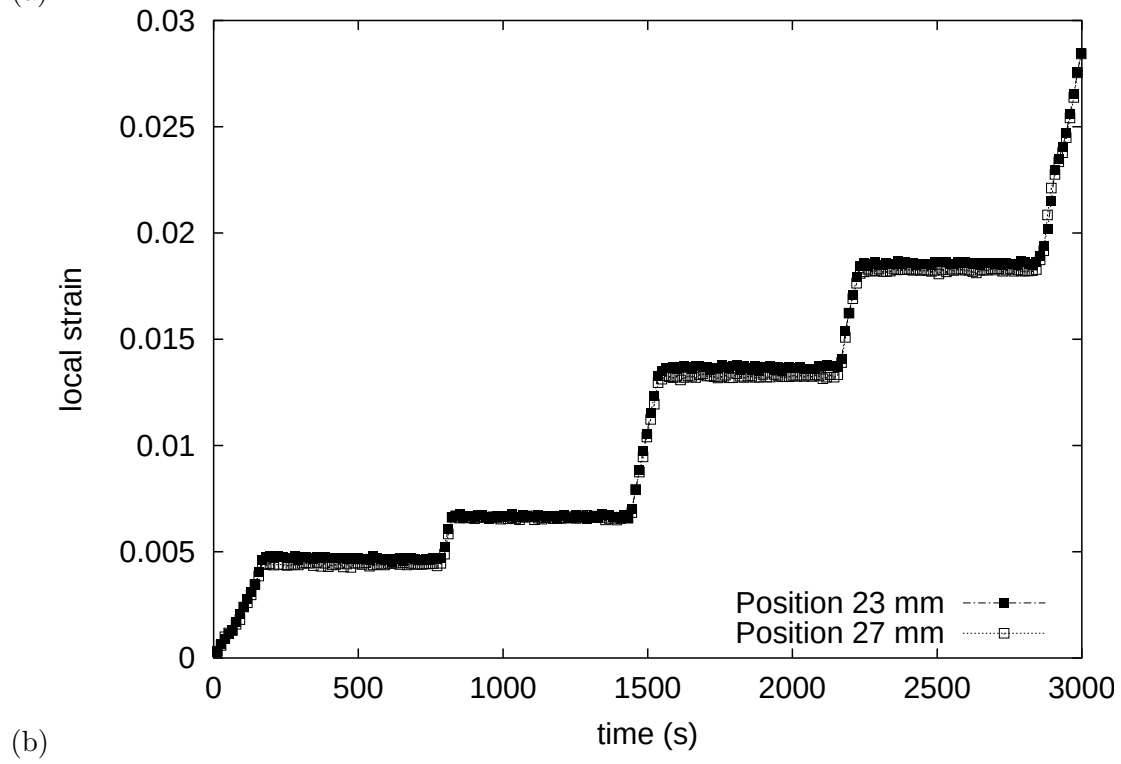

(b)

Figure X.4 : Local strain for various positions as a function of time for: (a) the tensile test at constant applied strain rate of $10^{-4}\ s^{-1}$ at $20°C$ for $Al-3\%Mg$ alloy, (b) the tensile test at constant applied strain rate of $8.10^{-5}\ s^{-1}$ with relaxation periods at $20°C$ for $Al-4\%Cu$ alloy.

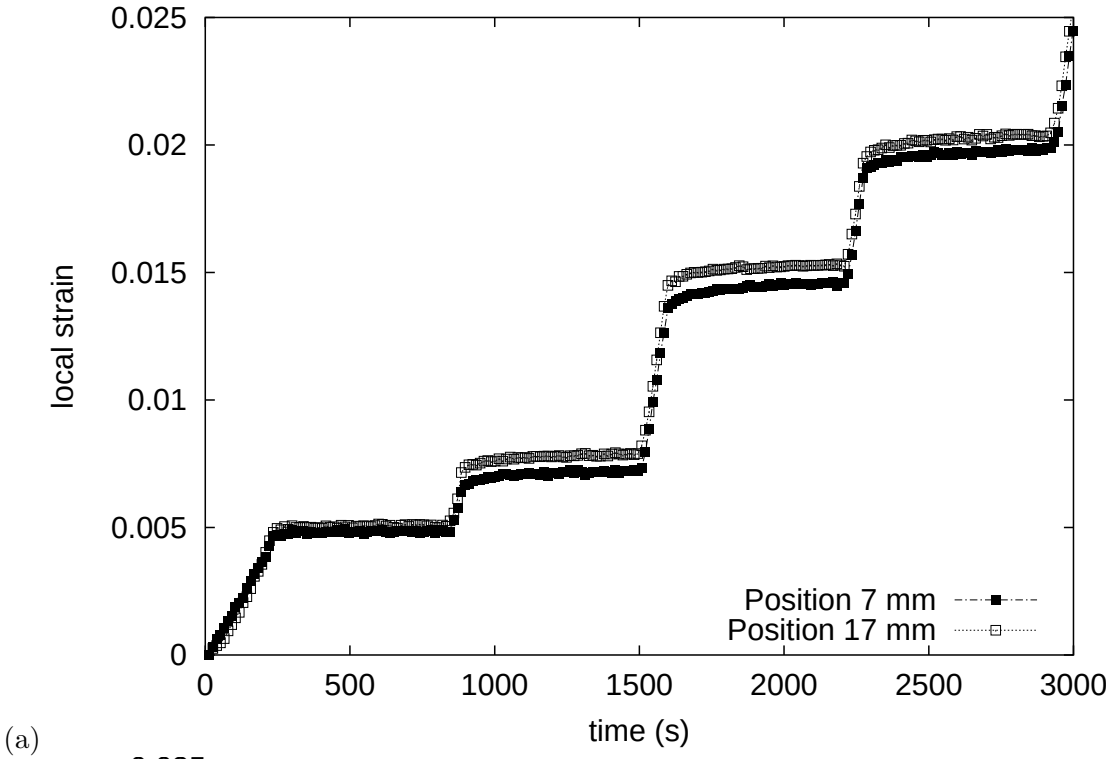

(a)

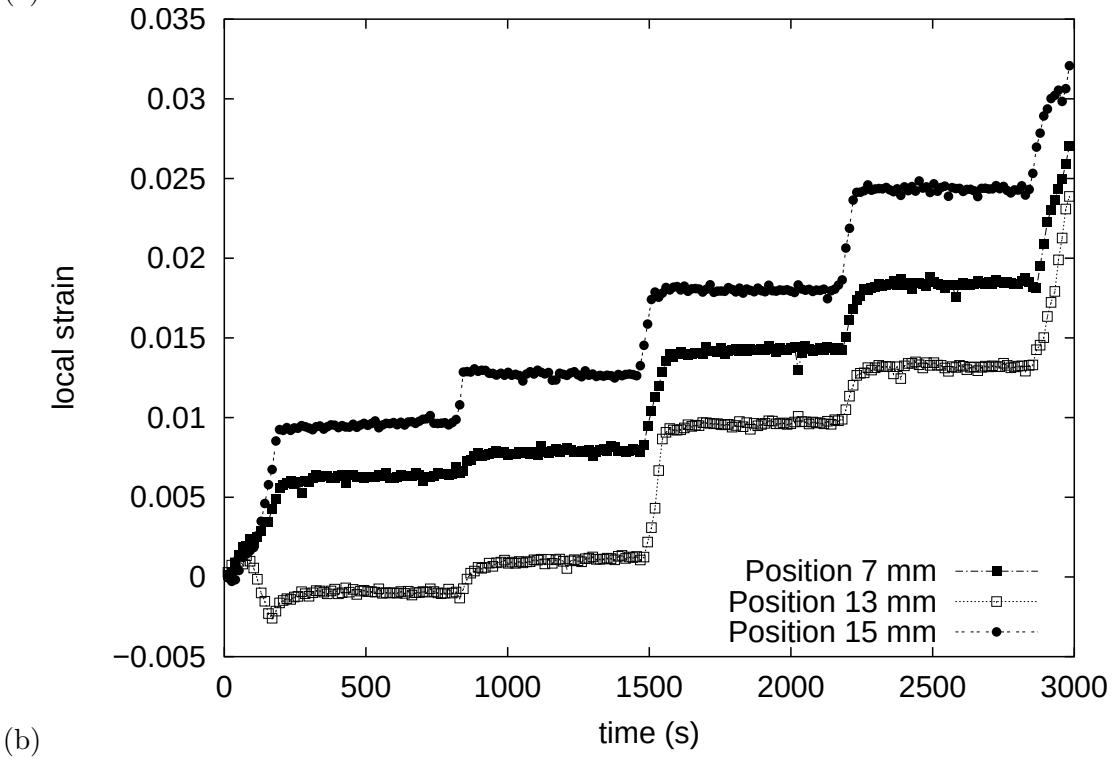

(b)

Figure X.5 : Local strain for various positions as a function of time for: (a) the tensile test at a constant applied strain rate of 8.10^{-5} s^{-1} with relaxation periods at $20°C$ for Zr702, (b) the tensile test at a constant applied strain rate of 8.10^{-5} s^{-1} with relaxation periods at $250°C$ for Zr702.

13 mm increases contrary to the position 11 mm for which the local strain decreases before reaching the stationary regime of the waiting time. Figure X.6 (b) compares the evolution of these three positions after the second and the third partial unloadings with waiting times. The main observation is that the local strain of the position 11 mm becomes larger than for the position 13 mm during the straining. Consequently the strain of the position 11 mm grows contrary to the position 13 mm. Such effects are also observed at $100°C$ and $250°C$.

Consequently the partial unloading steps of the tensile tests at constant applied strain rate lead to increase locally the cumulated plastic strain, which is not the case for the relaxation periods of the tensile tests. This effect can be explained by the fact the static strain ageing during the waiting time of mechanical test with the partial unloading steps is more efficient than the waiting time of the relaxation test. Indeed, the waiting time after the first partial unloading step is 24 hours contrary to the relaxation period of fifteen minutes.

The same mechanical tests as the previous ones, in the same experimental conditions were performed with the zirconium alloy with hafnium (ZrHf). Regarding the tensile tests with relaxation periods, at $100°C$, figure X.7 (a) shows that up to the first relaxation period, the local strain is homogeneous in all the positions 3, 5 and 11 mm. Then the behavior exhibits strain heterogeneities between the various zones although no stress peak after the relaxation periods are observed on the macroscopic curve (see the previous chapter). For example, after the third relaxation periods, the quantity of strain does not increase with the same value according to the various positions: for the position 3 and 11 mm, the quantity of strain is about 0.007 and for the position 5 mm, the quantity of strain is about 0.005. However at $20°C$, no plastic inhomogeneities associated with no static strain ageing effect on the macroscopic curve are detected. At $250°C$, ZrHf displays the same type of local strain heterogeneities than Zr702, which are associated with stress peaks after each relaxation period on the macroscopic curve. These stress peaks are similar to those observed for Zr702 at the same temperature. Figure X.7 (b) is a zoom of the macroscopic stress versus strain curve up to 0.01 strain level.

Regarding the tensile tests with partial unloading steps and waiting times at $20°C$, figure X.8 (a), which is a zoom between 44500 and 45500 s, shows that the local strain for the various positions 9 and 17 mm is homogeneous. Then increasing the deformation, plastic strain heterogeneities are detected from 0.02 strain level contrary to Zr702 in which initial heterogeneities are observed after the first unloading step and waiting time. The same scenario is observed at $100°C$. At $250°C$, the local strain for the various positions 7 and 29 mm is homogeneous up to 0.002 strain level i.e. before the first partial unloading step. Then plastic strain heterogeneities appear after the first partial unloading step and waiting time as shown in figure X.8 (b).

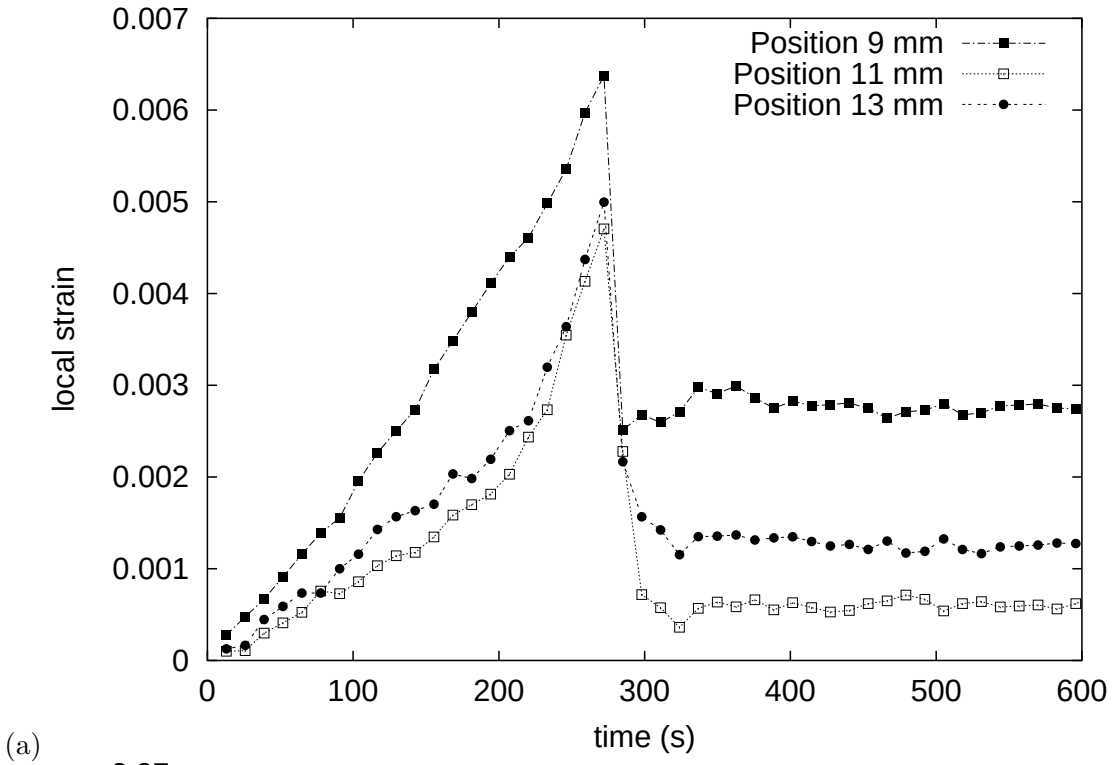

(a)

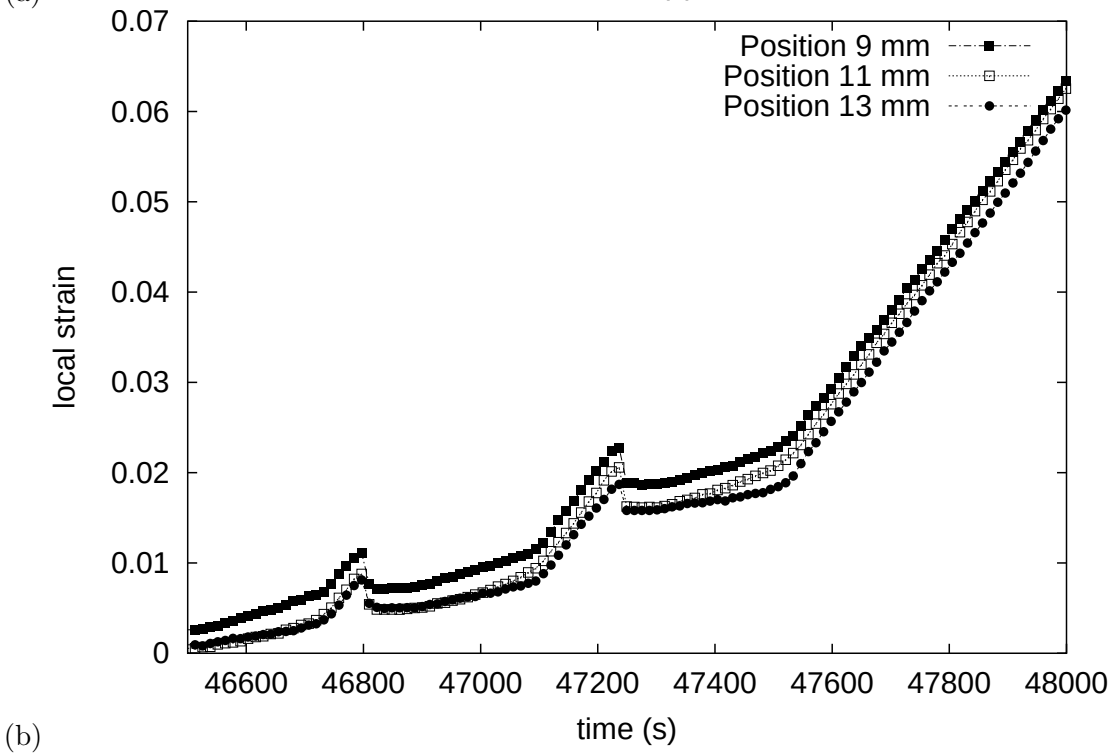

(b)

Figure X.6 : Local strain for various positions as a function of time for the tensile test at the applied strain rate of $8.10^{-5}\ s^{-1}$ with partial unloading steps and waiting times at $20°C$ for Zr702: (a) between 0 and 600 s (the first partial unloading step and waiting time), (b) between 46500 and 48000 s (the second and the third partial unloading steps and waiting times).

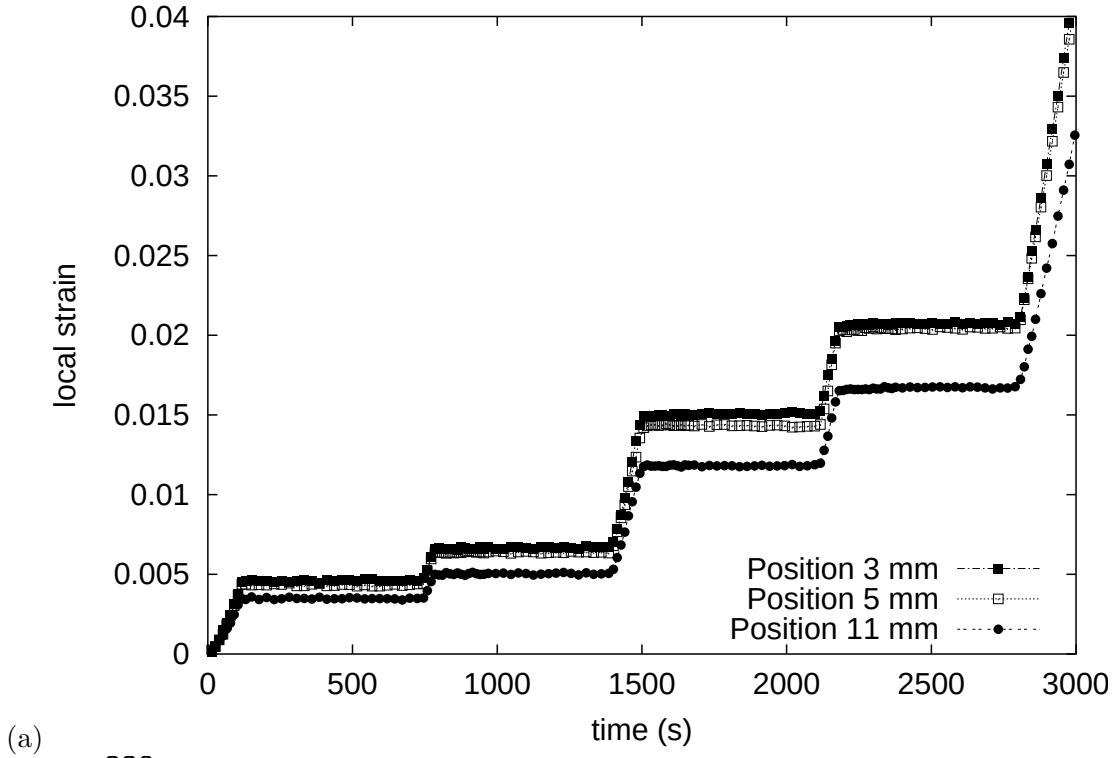

(a)

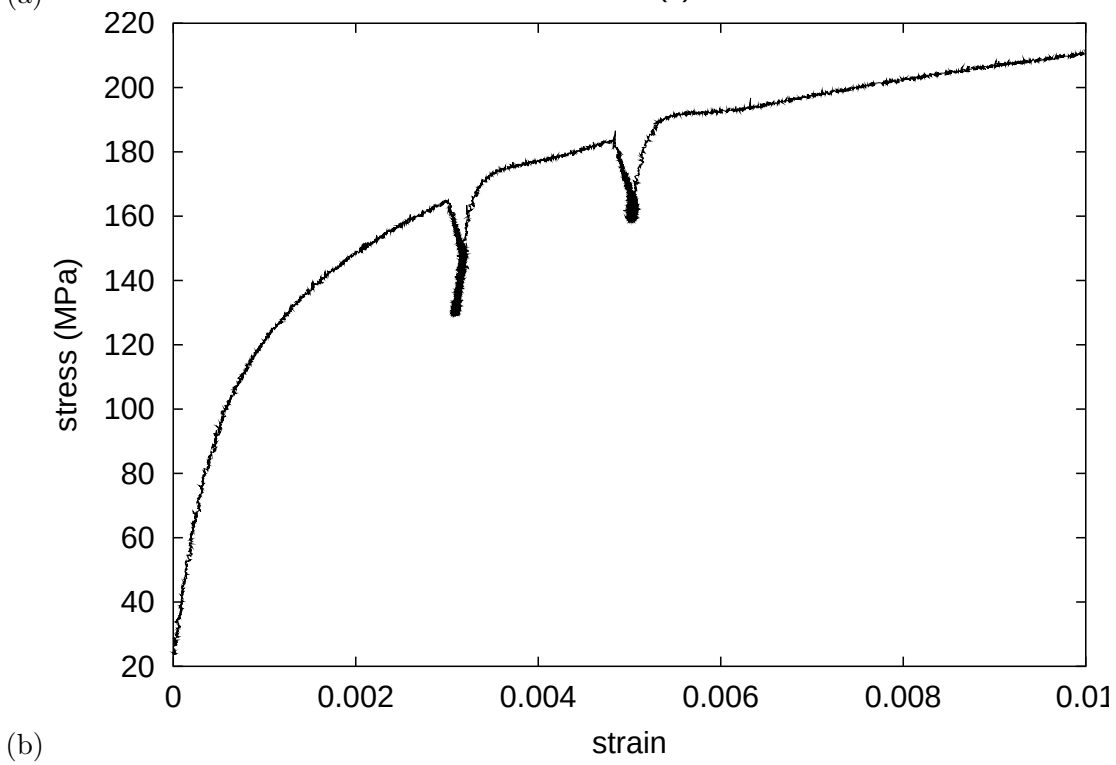

(b)

Figure X.7 : Local strain for various positions as a function of time for tensile tests at constant applied strain rate of $8.10^{-5}\ s^{-1}$ with relaxation periods for ZrHf: (a) at $100°C$; (b) Zoom of the macroscopic stress versus strain curve for the tensile test at constant applied strain rate of $8.10^{-5}\ s^{-1}$ with relaxation periods at $250°C$ for ZrHf.

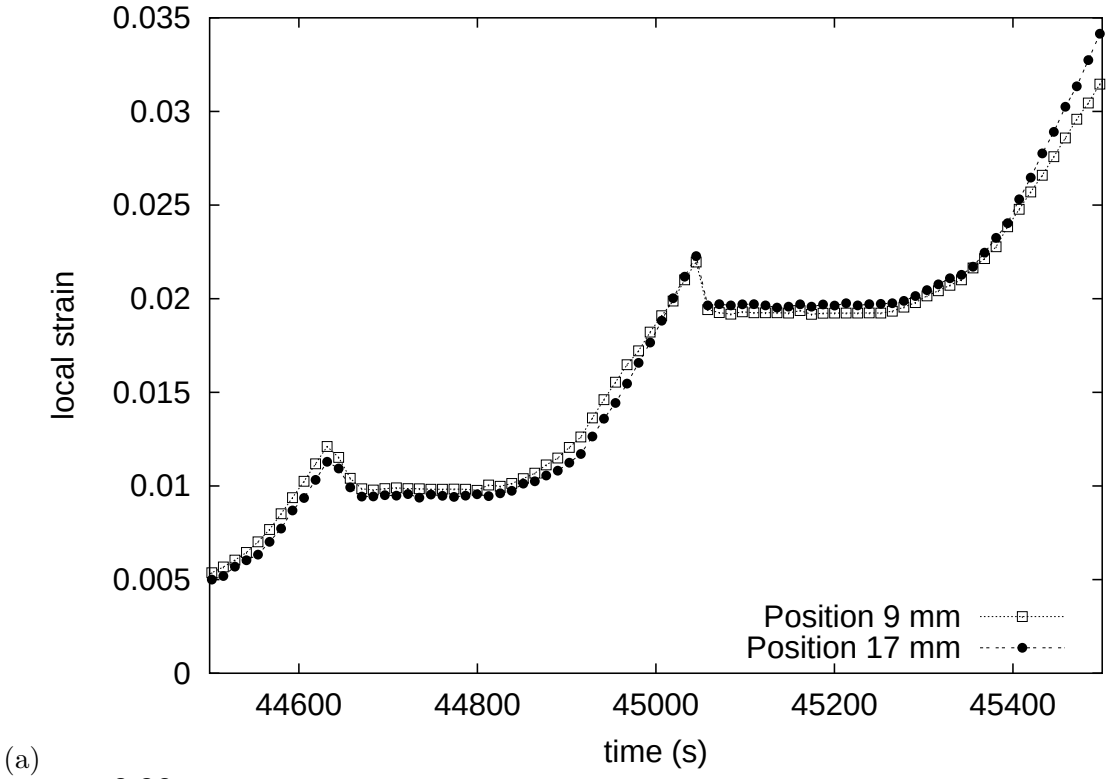

(a)

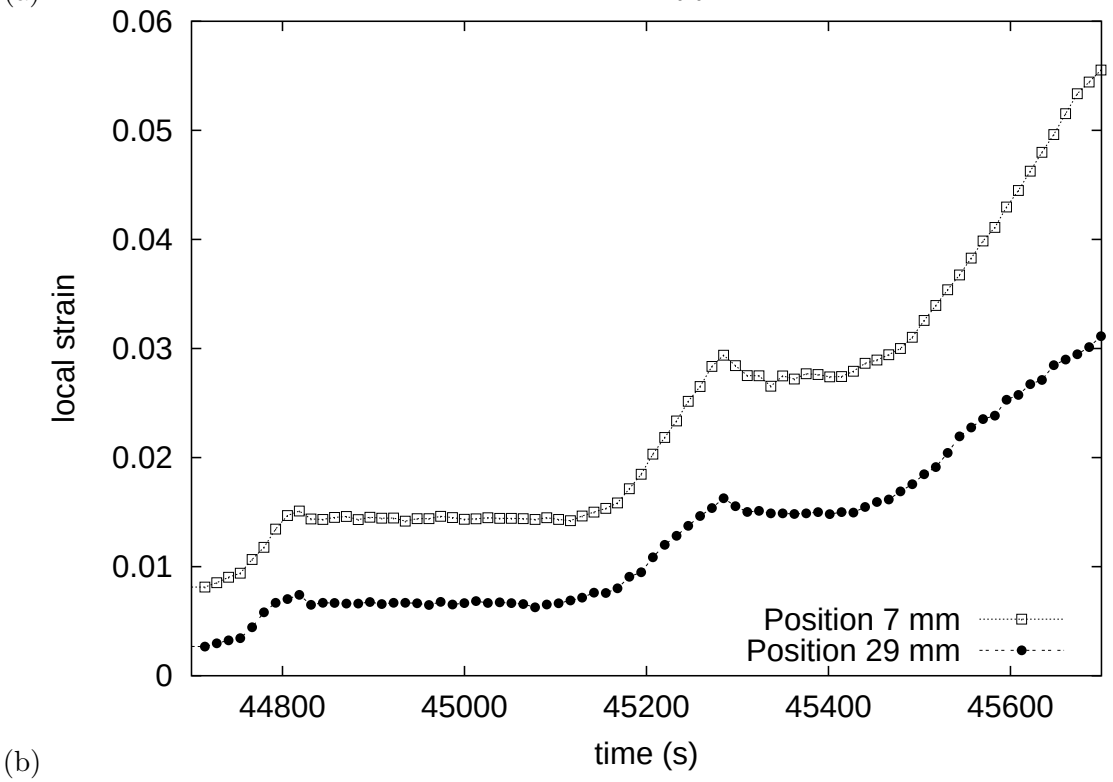

(b)

Figure X.8 : Local strain for various positions as a function of time for the tensile test at the applied strain rate of $8.10^{-5}\ s^{-1}$ with partial unloading steps and waiting times for ZrHf: (a) at $20°C$ between 44500 and 45500 s i.e. the second and the third partial unloading steps and waiting times, (b) at $250°C$ between 44700 and 45700 s (the second and the third partial unloading steps and waiting times).

Conclusion

Spatio–temporal plastic instabilities, during straining of strain ageing materials were investigated by means of laser scanning extensometry and tensile tests at constant applied strain rate according to different experimental conditions (with relaxation periods or unloading steps with waiting times). This experimental method is relevant because it allows to identify and to characterize local plastic strain heterogeneities on the millimeter scale. Another advantage of this technique is to have a better view of the development of plastic strain during deformation. After validating the experimental set up by testing standard alloys such as mild steel and aluminum alloys, measurements of local strain by laser scanning extensometer were obtained for several zirconium alloys. Two zirconium alloys were chosen in order to show the influence of interstitial and substitutional atoms like oxygen and hafnium on the strain ageing phenomena and the plastic instabilities: Zr702 (2280 wt ppm tin and 1300 wt ppm oxygen) and ZrHf (2.2 wt% hafnium and 100 wt ppm oxygen).

Taking the main findings shown in both chapters for the standard alloys and the zirconium alloys into account, a classification of plastic strain heterogeneities associated with strain ageing phenomena (SSA, DSA) is proposed. Complex strain localization phenomena take place in both zirconium alloys, investigated by laser scanning extensometry. We showed that in zirconium alloys, plastic strain heterogeneities are observed experimentally on the millimeter scale. At $20°C$ and $100°C$, Zr702 and ZrHf don't display SSA and DSA effects, which can be observed on the macroscopic curve contrary to $250°C$ for which stress peaks after relaxation periods and unloading steps with waiting times are observed on the macroscopic stress versus strain curve. According to the type of mechanical tests (the strain rate controlled tensile tests with relaxation periods and unloading steps with waiting times), both zirconium alloys do not exhibit the same response.

- At $20°C$, plastic strain heterogeneities are detected for the tensile test with unloading steps and waiting times, contrary to the tensile test with relaxation periods. Such a difference can be explained by the fact that static strain ageing phenomena can occur during the waiting time of 24 hours after the first unloading step, contrary to the relaxation periods for which the total strain is kept constant during only fifteen minutes. Consequently this effect suggests that if the waiting time is high enough and if the applied strain rate is appropriate, even if the temperature is not a "relevant temperature" (for which strain ageing is active), plastic stain heterogeneities due to the diffusion of solute atoms can be detected.

- Using the relationship between time–temperature and increasing the temperature, for instance at $100°C$, this hypothesis is supported by the fact that because no SSA and DSA effects are shown macroscopically. However, on the millimeter scale plastic strain heterogeneities are detected for both types of tensile tests: diffusion of solute atoms is emphasized.

- Then at $250°C$, plastic strain heterogeneities are observed on the millimeter scale but also on the macroscopic scale. The plastic strain inhomogeneities detected by laser scanning extensometry are non propagating and also the cumulated plastic strain can increase locally along the stress versus strain curve for both zirconium alloys.

Part D

Constitutive laws and finite element modeling of strain ageing phenomena

Chapter -XI-

Review of the constitutive models of negative strain rate sensitivity

Contents

Abstract: The aim of this chapter is to compare the various constitutive models of the negative strain rate sensitivity described in the literature and the strain, strain rate localization criteria associated with these models. Two main models are proposed.

- The phenomenological elastic–viscoplastic constitutive model accounting for negative strain rate sensitivity is based on the empirical material law proposed by Penning (Penning, 1972) and improved by Kubin–Estrin (Kubin and Estrin, 1985), introducing the evolutionary behavior of the coupled densities of mobile and forest dislocations. In particular, this model was used by Benallal (Benallal et al., 2006) in a finite element code, based on available experimental data for an aluminium alloy, and also by Kok (Kok et al., 2003) and Schmauder (Lasko et al., 2005).
- The constitutive model of strain ageing accounting for Portevin–Le Chatelier (PLC) effect by introducing the local solute composition at temporarily arrested dislocations, depending on an internal variable t_a called the ageing time was suggested by McCormick (McCormick, 1988). This model was used by Zhang (Zhang et al., 2000) and then by Graff (Graff et al., 2004; Graff et al., 2005) in finite element codes. The stability of the system and its post–instability behavior were analyzed by Mesarovic (Mesarovic, 1995).

XI.1 Introduction

The McCormick's constitutive model studied by Mesarovic (Mesarovic, 1995) and used by Zhang (Zhang et al., 2000) in finite element simulations is based on dislocation–solute interaction, describing strain ageing behavior (McCormick, 1988). It is compared with the Kubin–Estrin's phenomenological constitutive model, first suggested by Penning (Penning, 1972; Kubin and Estrin, 1985) and used by Benallal (Benallal et al., 2006) in a finite element code.
The McCormick's model is rate dependent and includes a time–varying state variable, representing the mean local concentration of impurity atoms at dislocations, C_s, which depends on an internal variable t_a, called the ageing time. The hypotheses is that strain ageing in alloys is associated with the time dependent segregation of mobile solute atoms to temporarily arrested dislocations, which partially impedes dislocation motion. A stage of deformation with abundant mobile and forest dislocations is considered. Dislocation glide is assumed to be discontinuous with a long waiting time at obstacles, t_w and a very short flight time between them. The yield stress is determined by the strength of obstacles. This strength, in turn, depends on the local concentration of diffused impurity atoms in the cores of temporarily arrested dislocations and in their neighborhoods. During the average waiting time of dislocations at obstacles, the diffusion of solute atoms is available, characterized by the ageing time, t_a. It is inversely proportional to strain rate. Qualitatively, low strain rates or low temperatures result in long characteristic diffusion times and long waiting times, so that in the limit, dislocations glide by breaking off from their equilibrium segregated (hence, often practically saturated) cores and atmospheres. This scenario excludes the dragging of solute atoms by moving dislocations. Intermediate strain rates and temperatures lead to the competition between two processes:

- the nature of thermal activation is such that the flow strength increases with increasing strain rate,
- an increase in strain rate shortens the time available for diffusion and thus weakens the obstacle, leading to a decrease in flow strength.

When the second effect dominates, the steady state strain rate sensitivity, $SRS_{ss} = \dfrac{\Delta\sigma_{ss}}{\Delta \log \dot{\varepsilon}}$, which includes the effect of the steady state strain rate dependence of C_s becomes negative as shown in figure XI.1. Transient behavior in the positive strain rate jump experiment is always characterized by positive stress jump (positive instantaneous strain rate sensitivity, $SRS_i > 0$). The negative steady state strain rate sensitivity is substantiated experimentally by Estrin and Kubin (Kubin and Estrin, 1989b) for Al–5%Mg alloy or by Nadai for iron (Nadai, 1950). Estrin and Kubin (Estrin and Kubin, 1989), then Ling and McCormick (Ling and McCormick, 1990) obtained large negative strain rate sensitivity for Al–5%Mg alloy in the order of -1.5 MPa. The stability of the system and its post–instability behavior is considered, suggested by Mesarovic (Mesarovic, 1995). The used methods include analytical and numerical stability and bifurcation analysis with a numerical continuation technique. The distinction between the temporal and the spatial (loss of homogeneity of strain) instabilities is emphasized. While the present model is based on physical processes which occur at a dislocation scale, the formulation is macroscopic and phenomenological, so that the number of independent parameters is minimized. The state variable formulation can include a variety of materials and microscopic strain ageing mechanisms.

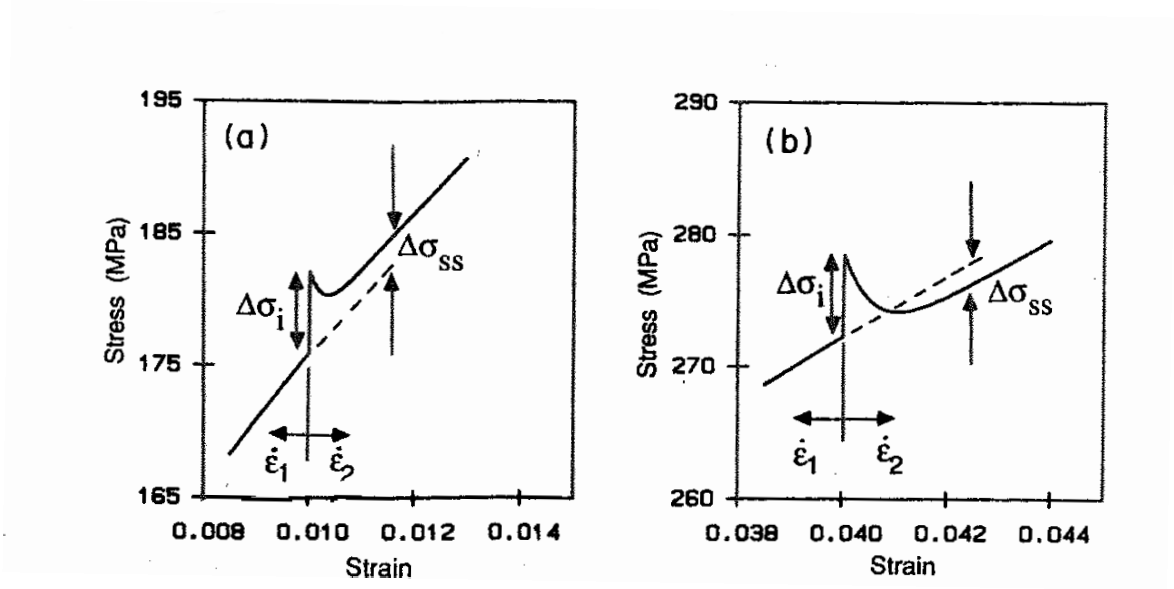

Figure XI.1 : Calculated stress transient associated with a discontinuous increase in strain rate: (a) $\dot{\varepsilon}_1 = 4.10^{-5}s^{-1}$, $\dot{\varepsilon}_2/\dot{\varepsilon}_1 = 10$, $\varepsilon = 0.01$ for low carbon steel; (b) $\dot{\varepsilon}_1 = 4.10^{-5}s^{-1}$, $\dot{\varepsilon}_2/\dot{\varepsilon}_1 = 10$, $\varepsilon = 0.04$ for low carbon steel (McCormick, 1988).

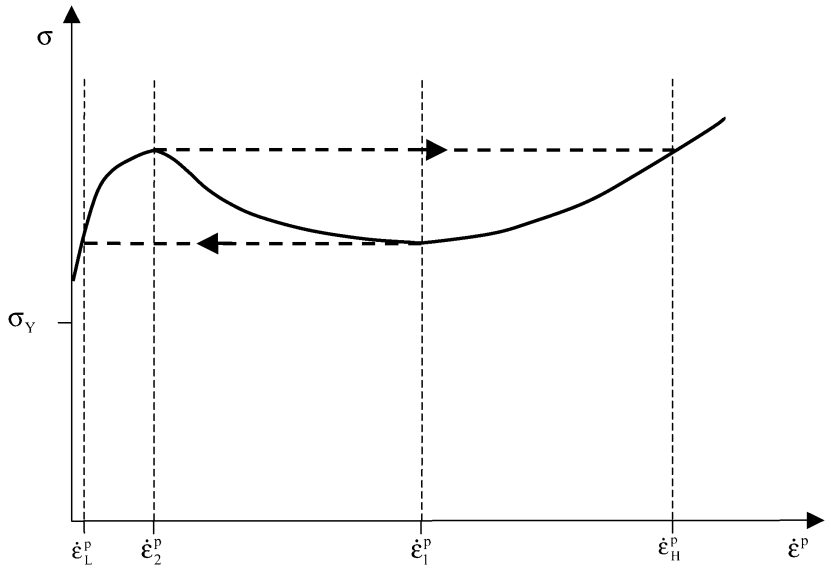

Figure XI.2 : Jumps in plastic strain rates from $\dot{\varepsilon}_2^p$ to $\dot{\varepsilon}_H^p$ for increasing strain rate and from $\dot{\varepsilon}_1^p$ to $\dot{\varepsilon}_L^p$ for decreasing strain rate (Benallal et al., 2006).

The Kubin–Estrin's model accounts for the negative strain rate sensitivity, based on the assumption suggested by Penning (Penning, 1972) that whenever the plastic strain rate reaches a critical value $\dot{\varepsilon}_2^p$, it must jump to the value $\dot{\varepsilon}_H^p$, as shown in figure XI.2. Similarly, there is a jump for decreasing strain rates from $\dot{\varepsilon}_1^p$ to $\dot{\varepsilon}_L^p$. We recall that the result is that plastic strain rates in the region between $\dot{\varepsilon}_2^p$ and $\dot{\varepsilon}_1^p$ will never occur at material level.

The aim of this chapter is to compare the criteria for the onset of flow localization used on the one hand in the strain ageing model suggested by McCormick (McCormick, 1988) and on the other hand in the phenomenological model proposed by Penning and improved by Kubin–Estrin (Penning, 1972; Kubin and Estrin, 1985). This comparison is based on the studies of Mesarovic (Mesarovic, 1995) for the McCormick's model and Benallal (Benallal et al., 2006) for the Kubin–Estrin's model.

XI.2 The McCormick's model

XI.2.1 Basic hypotheses

The development of the constitutive model of McCormick (McCormick, 1988), exhibiting negative steady state strain rate sensitivity SRS_{ss} and positive instantaneous strain rate sensitivity SRS_i is based on the following hypotheses.

Cottrell and Bilby (Cottrell and Bilby, 1949) first developed the theory of strain ageing in iron based on the segregation of carbons atoms to temporarily arrested dislocations, in the limit of dilute concentrations. While their theory predicts negative strain rate sensitivity, it does not include the saturation of solute atoms at dislocations and will, if included in the present model, predict large negative strain rate sensitivity at low strain rates, contrary to experiments. Assuming Cottrell–Billby strain ageing kinetics (Cottrell and Bilby, 1949), the

solute composition, labeled C_s may be expressed as:

$$C_s = C_0(KDt_a)^{2/3} \tag{XI.1}$$

where C_0 is the alloy solute composition ($C_s \ll C_0$), D is the solute diffusion coefficient and K is a constant which includes the solute dislocation binding energy. These authors were the first to introduce t_a, the effective time that arrested mobile dislocations have spent at obstacles. Note that equation (XI.1) is valid only for the initial stage of ageing.

Van den Beukel (van den Beukel, 1975a) demonstrated that the strain ageing model which includes saturation behavior results in a negative strain rate sensitivity region. This author first showed that a negative strain rate dependence of the flow stress can result from the diffusion of solute atoms to dislocations temporarily arrested at obstacles in the slip path. At temperatures and strain rates where solute diffusion to dislocations is active (Sleeswyk, 1958; Bodner and Baruch, 1967a), the local solute composition at arrested dislocations, C_s given by equation (XI.1) is a function of the average waiting time at extrinsic obstacles, t_w. So, the effective time that arrested mobile dislocations have spent at obstacles t_a suggested by Cottrell–Bilby is assumed to be equal to the average waiting time, t_w. This waiting time, t_w is linked to the average dislocation velocity, v and the distance between extrinsic obstacles, L:

$$v = \frac{L}{t_w} \tag{XI.2}$$

The Cottrell–Bilby ageing kinetics were modified by Louat (Louat, 1981) to include saturation of solute atoms. This author simply included the fact that the probability of the solute atom coming to a core site is proportional to the fraction of available core sites. Also, Louat's generalization of the Cottrell–Bilby analysis to include saturation at longer ageing times gives (Louat, 1981):

$$C_s = C_m[1 - exp(-\frac{C_0}{C_m}\left(\frac{t_a}{t_d}\right)^{2/3})] \tag{XI.3}$$

where C_m is the saturation value of C_s (the maximal saturated concentration of solute atoms around dislocations) and t_d is the characteristic solute diffusion time $t_d = \frac{1}{KD}$. It is emphasized that C_s is not equal to the local solute concentration at an isolated dislocation, but rather a quantity determined from an average over all mobile dislocations. It is also important to note that t_a is equal to the current value of the average waiting time of dislocations at obstacles, t_w only for steady state conditions (the time for dislocations to undergo the anchoring due to diffusive solute atoms while they are stopped by extrinsic obstacles).

Springer and Schwink (Springer and Schwink, 1991) supported an exponent of 1/3 instead of 2/3 in the above formula (XI.3). The physical basis for such a difference is thought to be pipe diffusion along dislocation lines. Ling (Ling and McCormick, 1993) performed numerical time integration, with the 1/3 exponent, to demonstrate the similarity of predicted oscillations to the experimental results. This exponent, linked to the size effect between the lattice and the solute atoms will be labeled n in the following.

McCormick (McCormick, 1988) was the first to show that C_s does not respond instantaneously to the strain rate change of tensile tests with strain rate changes. As a consequence, a transient period may be expected to follow the change in strain rate as C_s adjusts to its new quasi–steady state value (see figure XI.1). In the transient region

time dependent variation of the flow stress is determined by the rate of change of the flow stress associated with the time dependent change in C_s and the rate of strain hardening. Although the actual process by which the new steady state value of C_s is reached may differ for increasing and decreasing, respectively in strain rate, van den Brink and McCormick (van den Brink et al., 1975) suggested that the time constant of the transient period is of the order of t_w of the new strain rate. For example, if the strain rate is abruptly decreased, the mobile dislocations must on the average wait for a period of time about t_w before acquiring the higher steady state composition characteristic of the new strain rate by solute diffusion. For an increase in strain rate, it appears that the dislocations on the average must move at least once before steady state conditions are restored. That is why McCormick suggested that the strain rate sensitivity parameter follows a relaxation kinetics:

$$SRS = SRS_i + (SRS_{ss} - SRS_i)[1 - exp(\frac{t}{\tau})] \tag{XI.4}$$

where SRS_i is the instantaneous strain rate sensitivity and SRS_{ss} is the steady state strain rate sensitivity defined by:

$$SRS_i = \frac{\Delta\sigma_i}{\Delta \log \dot{\varepsilon}} \quad ; \quad SRS_{ss} = \frac{\Delta\sigma_{ss}}{\Delta \log \dot{\varepsilon}} \tag{XI.5}$$

Figure XI.1 illustrates both strain rate sensitivities. Note that measured values of SRS_i are positive at all strains, while SRS_{ss} decreases with increasing strain, becoming negative prior to the onset of the PLC effect. This parameter becomes negative at some specific value of the deformation, called the critical strain, ε_c.

Then, McCormick was the first to introduce the relaxation kinetics (Avrami's equation) followed by t_a:

$$\frac{dt_a}{dt} = -\frac{t_a - t_w}{\tau} \tag{XI.6}$$

Equation (XI.6) gives t_a as an implicit function of strain and strain rate history of the material, which can be determined from a hereditary integral, if $t_w(t)$ is known. If $t_w \gg t_a$, then from equation (XI.6), $\frac{dt_a}{dt} \propto 1$ using the following hypotheses $\tau \longrightarrow t_w$. This is in agreement with the fact that the solute concentration at arrested dislocations cannot increase faster than that allowed by the passage of time. In the limit of the vanishing strain rate, the average waiting time should approach the real time $\dot{t}_a \longrightarrow 1$. Hence, the characteristic relaxation time must be equal to the new steady state average time. If the strain rate is continuously varying, the steady state waiting time is as a "moving target" for the average waiting time. The time dependent character of C_s is of fundamental importance in the modeling of strain ageing behavior.

Kubin and Estrin (Kubin and Estrin, 1989b; Estrin and Kubin, 1989) were the first to develop the idea that mobile dislocations can age when interacting with forest dislocations which are extrinsic obstacles. The elementary strain, ω incorporates the microstructural features on the dislocation level. More precisely, considering the evolution of two coupled dislocation densities, it was shown that the whole variety of experimentally observed situations with regard to the strains ranges of existence of the PLC effect can be accounted for. This consideration outlined is neutral to the particular choice of the model, describing strain ageing effects. The main characteristics of the model proposed by Kubin–Estrin are recalled in section XI.3.

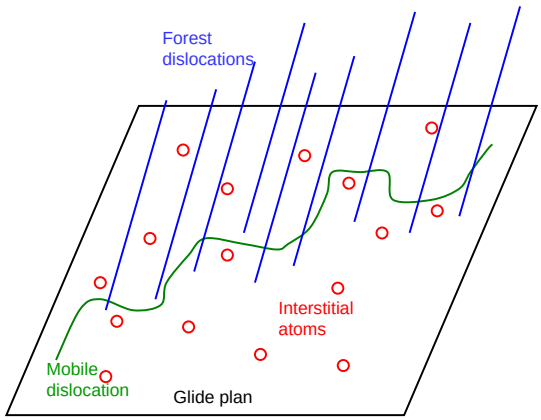

Figure XI.3 : Interaction between mobile and forest dislocations in the strain ageing model (Estrin and Kubin, 1989; Kubin and Estrin, 1989b).

Figure XI.3 illustrates the interaction between mobile and forest dislocations.

Solute atoms can diffuse towards the mobile dislocations stopped by forest dislocations in the presence of solute atoms. The densities of mobile and forest dislocations evolve inversely during straining. A high concentration of forest dislocations favors the anchoring of mobile dislocations. Hardening due to solute atoms around obstacles depends on this interaction between mobile and forest dislocations. The elementary strain amplitude for an obstacle jump depends on deformation. At low strain, the mobile dislocations density increases rapidly. The forest dislocations density is practically constant. So, the elementary deformation, ω carried by dislocations increases rapidly. At high strain, the mobile dislocations density saturates and the forest dislocations density increases and then saturates. The elementary deformation, ω follows qualitatively the curve of figure XI.4.

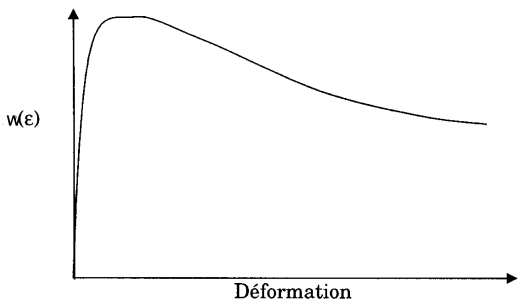

Figure XI.4 : Evolution of the elementary deformation ω as a function of strain (Estrin and Kubin, 1989).

XI.2.2 Criterion for the onset of flow localization

Mesarovic (Mesarovic, 1995) slightly modified the constitutive equations of McCormick in order to study the stability of the system and its post-instability.
Assuming that obstacle controlled glide is the dominant mechanism for plastic deformation for the investigated temperatures and strain rates ranges, one can regard plastic straining as a thermally activated process (Kocks et al., 1975):

$$\dot{\varepsilon} = \dot{\varepsilon}_0 exp(-\frac{\Delta G}{k_B T}) \tag{XI.7}$$

where $\dot{\varepsilon}_0$ is a reference strain rate, which clearly depends on the current strain i.e. current dislocation densities and stress. However, for strong obstacles, the exponential varies strongly with stress so that pre–exponential can be regarded as constant. Frost and Ashby (Frost and Ashby, 1982) found that the value $\dot{\varepsilon}_0 = 10^6\ s^{-1}$ fits experimental data for both f.c.c. and b.c.c. metals. In equation (XI.7), T is the temperature , k_B is the Boltzmann constant and ΔG is the free enthalpy of activation, referred to as activation energy in the sequel.
ΔG depends on the excess stress, $\sigma - \hat{\sigma}$ and on the solute atoms concentration C_s, where $\hat{\sigma}$ is the average stress at 0 K for a given nominal solute concentration and dislocation density, depending also on strain ε. It is the average energy barrier encountered by dislocations at obstacles to be overcome by thermal fluctuations. In the case of discrete obstacles, the free flight time between obstacles is negligible compared to the average waiting time, so that the Orowan equation, relating plastic strain rate to dislocation densities and velocity may be written as follows:

$$\dot{\varepsilon} = \rho_m b \frac{L}{t_w} = \frac{\rho_m b \rho_f^{-1/2}}{t_w} = \frac{\omega}{t_w} \tag{XI.8}$$

where ρ_m and ρ_f are the densities of mobile and forest dislocations respectively, L is the mean free path between obstacles, b is the length of the Burgers vector. ω is the elementary strain increment accumulated when all mobile dislocations are displaced by a distance equal to L. Clearly, ω varies with dislocation densities and thus, with the accumulated plastic strain. Both ρ_m and ρ_f evolve with strain and are generally strain rate dependent. As a first approximation, it may be assumed that $\tau = t_w$ (McCormick, 1988). Models for such variation can be found in Kubin and Estrin (Kubin et al., 1992) and Balik and Lukac (Balik and Lukac, 1993). The main result is that the PLC effect can occur only for some intervals of accumulated plastic strain. Here this variation is not considered. Linearizing the activation energy dependence on the excess stress and on the solute atoms concentration, one defines:

$$\frac{1}{SRS_i} = -\frac{\partial}{\partial(\sigma - \hat{\sigma})}(\frac{\Delta G}{k_B T}) = (\frac{\partial \log \dot{\varepsilon}}{\partial \sigma})_{C_s = cte} \quad ; \quad H = \frac{\partial}{\partial C_s}(\frac{\Delta G}{k_B T}) = -(\frac{\partial \log \dot{\varepsilon}}{\partial C_s})_{\sigma = cte} \tag{XI.9}$$

The stress variation during PLC and yield point phenomena is small compared to the total stress. Linearizing activation energy with respect to stress is thus plausible. The linearizing of activation energy with respect to C_s is phenomenological. Note that Mesarovic used the following equation for C_s, as suggested by McCormick:

$$C_s = 1 - \exp[-(\frac{t_a}{t_d})^{\alpha}] \tag{XI.10}$$

The plastic strain (rate)–stress relation can be cast into the following equivalent forms:

$$d\sigma = h d\varepsilon + SRS_i(d \log \frac{\dot{\varepsilon}}{\dot{\varepsilon}_0} + H dC_s) \quad ; \quad \dot{\varepsilon} = \dot{\varepsilon}_0 \exp(\frac{\sigma - \hat{\sigma}}{SRS_i} - HC_s) \tag{XI.11}$$

where $h = \dfrac{d\sigma}{d\varepsilon}$ is strain hardening. Under the condition of constant plastic strain rate, the constitutive equations can be integrated to give:

$$\sigma_{ss} = \hat{\sigma} + SRS_i[\log \frac{\dot{\varepsilon}}{\dot{\varepsilon}_0} + H(1 - exp(-(\frac{\omega}{\dot{\varepsilon} t_d})^n))] \tag{XI.12}$$

The steady state strain rate sensitivity SRS_{ss} is given by:

$$SRS_{ss} = \frac{d\sigma_{ss}}{d\log\dot{\varepsilon}} = SRS_i[1 - Hn(\frac{\omega}{\dot{\varepsilon} t_d})^n exp(-(\frac{\omega}{\dot{\varepsilon} t_d})^n)] \tag{XI.13}$$

Clearly SRS_{ss} can take negative values for intermediate strain rates. Other state variables may be introduced such as mobile and forest dislocation densities. Indeed the appearance of PLC is conditioned by accumulated dislocation densities. Their evolution law is discussed in (Kubin et al., 1992) and (Balik and Lukac, 1993). The variation of these densities with strain is slow. Here, we are interested in fast instabilities, dominated by rate sensitivity variations. Dislocation densities can then be treated as constant. Nevertheless, the required dislocation densities are included in the resulting stability condition though the current values of ω and h.

The stability and bifurcations of the 3–dimensional system ($\varepsilon(x,t)$, $t_a(x,t)$, $\sigma(x,t)$) are first analyzed using the linear perturbation theory. The main results are the following. The criterion for the onset of flow localization is given by two possibilities:

1. $$h - \sigma \leq -\frac{SRS_i}{\omega}(1 - \Gamma) \tag{XI.14}$$

   with $\Gamma(t_a) = H\alpha(\dfrac{t_a}{t_d})^\alpha \exp[-(\dfrac{t_a}{t_d})^\alpha]$

2. If the pre–bifurcation state is close to the steady state:

   $$h - \sigma \leq -\frac{SRS_{ss}}{\omega} \tag{XI.15}$$

   because $\Gamma(t_{a,ss}) = \dfrac{1 - SRS_{ss}}{SRS_i}$.

The equation (XI.15) is the criterion for the onset of flow localization used by McCormick (McCormick, 1988) using the definition of SRS_{ss} given by the following equation:

$$SRS_{ss} = SRS_i(1 - \frac{2HC_s}{3}) \tag{XI.16}$$

A comparison can be done with the experimental form of SRS_{ss} given by van den Beukel (van den Beukel, 1975a) as follows:

$$SRS_{ss} = SRS_i(1 - K_1\frac{\varepsilon^{m+\beta}}{\dot{\varepsilon}}) \tag{XI.17}$$

with K_1, m and β are constant.

Mesarovic (Mesarovic, 1995) showed that the only difference between the characteristic exponents of the spatial and temporal instabilities is due to equivalent elastic stiffness of the specimen and the machine. The instability occurs when the real part of the characteristic exponent becomes positive. The bifurcation is a Hopf bifurcation, and the emerging solution is a limit cycle. Therefore for a given material composition, temperature and accumulated dislocation densities (hardening stage), there is a critical equivalent stiffness above which no temporal bifurcation is possible. It is shown that in the neighborhood of instability, the fundamental solution varies rapidly. Due to the negative strain rate sensitivity, the system moves through the bifurcation point quickly towards the target strain rate imposed by the cross–head velocity. The behavior of the system "in the large" is then determined by the state corresponding to the target strain rate, and not by the state near the bifurcation point. It is therefore instructive to examine the variation of characteristic exponents as the fundamental solution moves through the range of strain rates.

The yield point behavior is a property of the fundamental solution. It occurs even if spatial homogeneity is enforced. Without this enforcement, an instability, such as Lüders band or serrated yielding is expected. Serrated yielding emerges as an interplay between rate dependence, state variable evolution and elastic properties of the system. The oscillatory behavior requires a mechanism for stress drops. Without localization, this kind of behavior is limited by the machine stiffness: high equivalent elastic stiffness prevents serrated yielding and sharpens the upper yield point. Further, when serrated yielding occurs, increasing equivalent stiffness lowers the amplitude of serrations. Saitou (Saitou et al., 1988) demonstrated very systematically and clearly the effects of the machine stiffness on the amplitude of serration, in agreement with the present model on 7075–Al alloy. In the van den Brink (van den Brink et al., 1977) experiments on Al–Cu alloy, the machine stiffness influenced the type of serration and their onset. In all experiments, localization begins at the grips, where the stress and strain rate states are different than in the middle of the specimen. Experimental evidence of the dependence of bandwidth on specimen dimensions (van den Brink et al., 1977) suggests that the length scale is determined on the macroscopic continuum level.

XI.2.3 The McCormick's model in finite element codes

In order to solve mechanical problems, with the generalization of numerical methods, such as the finite elements method, numerical simulations of DSA can be found in literature. The main difficulty of such models is to be able, on the one hand to take the structure effect of the mechanical problem (especially, the simulation of the localized plastic strain deformation) into account and on the other hand to take the physical aspects of DSA into account. The fact that physical mechanisms are introduced in numerical constitutive laws allows to simulate the PLC effect (DSA) but also the Lüders phenomenon (Static Strain Ageing, SSA). Both phenomena depend on temperature and strain rate, which leads to some difficulties. The DSA constitutive laws suggested by McCormick (McCormick, 1988) are introduced in finite element codes. The main results are the following:

- In 1993, McCormick and Ling (McCormick and Ling, 1995) meshed a 1-dimensional round bar in 250 parts, and a geometric heterogeneity was introduced to allow the initiation of a plastic strain rate localized band. They simulated a strain discontinuity along the sample. The results were in good accordance with experiments: both type A and type B PLC serrations were simulated. However, in the section of the sample only one element was taken into account. Consequently, the velocity of the band cannot be determined, but the behavior of the band regarding geometry effects (for instance

the angle of the band with the tensile axis, the initiation of the band localized in the grips...) was not studied.

- In 2000, Zhang and McCormick (Zhang et al., 2000) used a 2-dimensional finite element mesh of the geometry of the sample. They studied the morphology of the bands. They found that the angle of the band with respect to the tensile axis is equal to $35° - 37.5°$.

XI.3 The Kubin–Estrin's model

XI.3.1 Basic hypotheses

From the phenomenological point of view, Penning (Penning, 1972) was the first to assume an intermediate range of strain rates where the strain rate sensitivity is negative to explain the PLC effect. Then, Kubin and Estrin (Kubin and Estrin, 1985; Kubin and Estrin, 1991a) examined the dynamics of repeated discontinuous yielding for materials exhibiting a bounded region of negative strain rate sensitivity. They proposed a constitutive model of plastic deformation based on two structure parameters related to the dislocation density. Their model predicts the existence of a negative branch of the strain hardening rate at small plastic strains (Estrin and Kubin, 1986).

- The simplest coupling mechanisms lead to a Laplacian term that is included in time–dependent constitutive equations. When coupling can be described by a stress term, the constitutive equation takes the following form:

$$\sigma = h\varepsilon + F(\dot{\varepsilon}) + C\nabla^2\varepsilon \tag{XI.18}$$

  where ε is plastic strain, h is strain hardening $h = (\frac{\partial\sigma}{\partial\varepsilon})_{\partial\dot{\varepsilon}}$ and $F(\dot{\varepsilon})$ is the N–shaped strain rate function adopted from purely temporal models, as shown in figure XI.2. C is a coupling parameter which incorporates a length scale representing the interaction distance for the underlying mechanism.

- Benallal (Benallal et al., 2006) proposed the following equation to investigate the effects of the negative strain rate sensitivity on the material's behavior:

$$\sigma = \sigma_Y + R(\varepsilon) + \sigma_v(\dot{\varepsilon}) \tag{XI.19}$$

  where σ_Y is yield stress, R is strain hardening and σ_v is viscous stress, governing the strain rate sensitivity of the flow stress as shown in figure XI.2. It is assumed that the viscous stress is non–negative, but in order to include negative strain rate sensitivity, σ_v is taken as a decreasing function of $\dot{\varepsilon}$ in a bounded region of the plastic strain rate. Typical stress versus plastic strain rate curves including negative strain rate sensitivity are shown in figure XI.5.

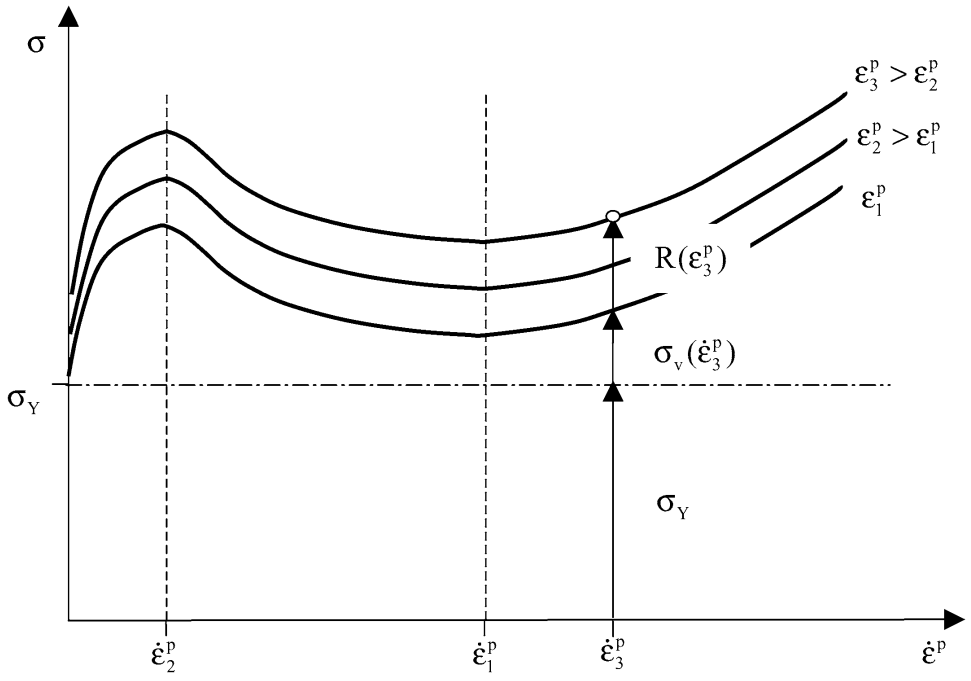

Figure XI.5 : Uniaxial stress–strain rate curves including negative strain rate sensitivity (Benallal et al., 2006).

XI.3.2 Criterion for the onset of flow localization

Kubin and Estrin (Kubin and Estrin, 1985; Estrin and Kubin, 1989) suggested a classification of viscoplastic instabilities, based on the following equation:

$$d\sigma = hd\varepsilon + SRSd(\log \dot{\varepsilon}) \tag{XI.20}$$

where $h = (\frac{\partial \sigma}{\partial \varepsilon})_{\dot{\varepsilon}}$ is the strain hardening of the material and $SRS = (\frac{\partial \sigma}{\partial \log \dot{\varepsilon}})_{\varepsilon}$ is the strain rate sensitivity of the material. The criterion for the flow localization is given by:

$$\frac{\sigma - h}{SRS} > 0 \tag{XI.21}$$

Two conditions for the flow localization are determined:

1. $h < \sigma$ and $SRS > 0$

2. $h > \sigma$ and $SRS < 0$

The first condition is called type h instability and corresponds to the Lüders behavior. The second condition is called type S instability and corresponds to the PLC effect. Consequently, for $h > \sigma$ homogeneous plastic deformation is unstable when SRS is negative. Whenever this region is reached, whether by increasing strain or stress, discontinuous jumps in strain rate across the unstable region should occur. Moreover, the criterion obtained by Kubin and Estrin (Estrin and Kubin, 1986), using the constitutive model of plastic deformation based on two structure parameters related to dislocation density shows that plastic flow necessarily begins in a nonuniform manner, the local strain hardening rate being negative in the initial stage of plastic deformation. Slip pattern formation is related to this behavior of the hardening.

XI.3.3 The Kubin–Estrin's model in finite element codes

The phenomenological elastic–viscoplastic constitutive model that accounts for negative strain rate sensitivity, suggested by Penning (Penning, 1972) and improved by Kubin–Estrin (Kubin and Estrin, 1991a) is implemented in finite element codes by several authors. The main results are the following:

- In 2003, Kok (Kok et al., 2003) used a polycrystalline model. He was able to simulate the PLC effect with localized bands, as shown in figure XI.6. The polycrystal was meshed by finite element (1440 elements) and no initial defect was introduced, contrary to the simulation of McCormick (McCormick and Ling, 1995). The band is initiated by the heterogeneities due to the crystallographic orientations introduced in the mesh. This type of model allows to reproduce the type A, B, C serrations by changing the applied strain rate (Lebyodkin et al., 2000). However, the temperature dependence was not tested.

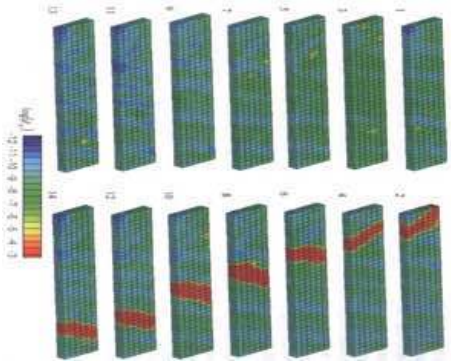

Figure XI.6 : Simulations of the Portevin–Le Chatelier bands in a polycrystal (Kok et al., 2003).

- Benallal (Benallal et al., 2006) studied the PLC effect in smooth and pre–notched, axisymmetric tensile specimens. By comparison with experimental data for an aluminium alloy, the PLC effect in pre–notched specimens was investigated. Figure XI.7 shows fringe plots of the band propagation in pre–notched specimens with initial notch root of 0.4 mm. In this type of specimen, Benallal showed that the band can suddenly leave the notch area and can propagate through one shoulder of the specimen. Then it can be re–initiated at the other side of the notch and can travel through the other shoulder of the specimen. The reason for this is that the strength in the minimum cross–section increases due to strain hardening and is at this point higher than in the surrounding material in the straight part of the specimen.

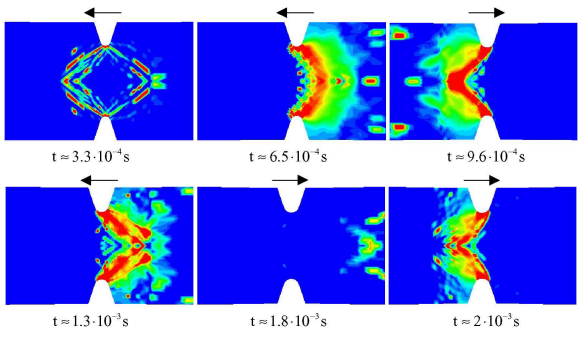

Figure XI.7 : Strain rate fringe plots of band propagation in simulation of a notched specimen with initial notch root radius of 0.4 mm (Benallal et al., 2006).

XI.4 Conclusion

It is well established that in the absence of strain ageing, plastic deformation at constant temperature may be characterized by constitutive relations of the form: $\dot{\varepsilon} = f(\sigma, \rho_i, \rho_j ...)$ where ε and σ are extrinsic state variables and ρ_i, ρ_j...are intrinsic state structure variables. To include the effect of DSA, McCormick (McCormick, 1988) suggested to take an additional state parameter, C_s into account in the constitutive relation, which is associated with an internal variable, t_a representing the ageing time. Therefore $\dot{\varepsilon} = f(\sigma, \rho_i, \rho_j, t_a ...)$. The effective solute composition is essentially a "fast" evolving variable due to t_a which obeys to relaxation kinetics $\dot{t}_a = 1 - \dfrac{t_a}{t_w}$. The time dependent character of C_s is fundamental to DSA phenomena. If C_s was an instantaneous function of strain and strain rate, transient effects would not be observed and the strain rate sensitivity would be described by the single parameter labeled SRS. In this case $SRS < 0$ would be a valid criterion for localized yielding (Penning, 1972; Estrin and Kubin, 1995). However, the flow localization is determined by both the local strain hardening rate and the rate of change of C_s. Consequently, McCormick's constitutive model can take both the yield point behavior and serrated yielding into account. The temperature and strain rate bounds for these phenomena are derived. This model was studied by Mesarovik (Mesarovic, 1995) in terms of analytical and numerical stability of the system and bifurcation analysis. The oscillatory behavior is relaxation oscillation type, with abrupt changes followed by periods of relative stability. On the other hand, this model is compared with Kubin's model which is a phenomenological model of plastic deformation, based on Penning's formulation which introduced the concept of negative strain rate sensitivity of the flow stress whose relation to the PLC effect was emphasized by Sleeswyk (Sleeswyk, 1958) and Bodner and Rosen (Bodner and Baruch, 1967a; Bodner and Baruch, 1967b). A linear perturbation approach was used Benallal (Benallal et al., 2006) in the general case of multiaxial loadings.

The various criteria for flow localization are summarized in table XI.1.

Table XI.1 : Comparison of the various criteria for flow localization recalled in the bibliography.

Authors	Criterion for flow localization
McCormick (McCormick, 1988)	$h - \sigma \leq -\dfrac{SRS_{ss}}{\omega}$
Mesarovic (Mesarovic, 1995) (Mesarovic, 1995)	$h - \sigma \leq -\dfrac{SRS_i}{\omega}(1 - \Gamma)$
Kubin–Estrin / Benallal (Kubin and Estrin, 1985) / (Benallal et al., 2006)	$\dfrac{h - \sigma}{SRS} < 0$

We chose to use McCormick's model in order to simulate DSA phenomena, especially in aluminium, steel and zirconium alloys because this model uses an internal variable t_a so that it is numerically easier to implement and to time integrate than Kubin–Estrin's model. Consequently, the next chapters present various applications of the McCormick's strain ageing model (McCormick, 1988; Zhang et al., 2000). Simulations and experiments are in most cases compared when possible. The main subjects that we treated are the following:

- strain localization phenomena associated with SSA and DSA in notched specimens,
- finite element simulations of DSA effects at V–notches and crack tips,
- finite element simulations of the PLC effect in metal–matrix composite (appendix IV).

Chapter -XII-

Additional comments about the strain ageing model

Contents

Abstract: The constitutive equations of the macroscopic strain ageing model, suggested by McCormick (McCormick, 1988) and used in finite element by Zhang and McCormick (Zhang et al., 2000) were re–written in order to simplify and to better understand this model. The influence of the parameters on a material volume element is studied. The aim of this simplification is to know how to control the shape of the σ–$\dot{p}$ curves in tensile conditions (to locate precisely the domain of inverse strain rate sensitivity, associated with plastic strain heterogeneities). This chapter is important because it is used to identify the parameters of the strain ageing model applied to the studied materials (steels, aluminium and zirconium alloys).

XII.1 Introduction

The aim of this chapter is to discuss the possibilities and limitations of the macroscopic strain ageing model, developed by McCormick (McCormick, 1988; Zhang et al., 2000). The influence of the parameters is studied on the constitutive law σ–$\dot{p}$ under tensile loading conditions using a material volume element. In this chapter, the final retained expression of the strain ageing model is introduced, to be applied to zirconium alloys (see chapter XIII). The constitutive equations of the macroscopic strain ageing model were simplified, in order to identify the role of each parameter, controlling the shape of the σ–$\dot{p}$ curve. This chapter gives answers to the following questions:

- Does the exponential and hyperbolic sine function of the vicoplastic flow rule have an influence on the shape of the σ–$\dot{p}$ curve?
- What are the parameters which control the domain of negative strain rate sensitivity?

This important chapter is used to identify the parameters of the strain ageing model applied to the studied materials (steels, aluminium and zirconium alloys).

XII.2 Presentation of the constitutive equations

The model of the macroscopic strain ageing, suggested by McCormick (McCormick, 1988; Zhang et al., 2000) is based on constitutive elasto–viscoplastic equations, taking thermal activation of plastic strain and static or dynamic strain ageing effects into account. This model used in finite element method is able to account for plastic strain localization phenomena such as Lüders bands and PLC effect. First, we cast the evolution equations in a form complying with thermodynamics of thermally activated processes (see chapters IV and V) and then we re–wrote the constitutive equations of the macroscopic strain ageing model, in order to simplify and better understand this model. The main differences, compared with the McCormick's model (McCormick, 1988; Zhang et al., 2000) are the following.
The expression of the viscoplastic multiplier for cumulated viscoplastic strain rate, $\dot{p}$ evolved according to our various studies. The plastic flow is thermally activated, that is why our simplified strain ageing model takes temperature and thermally activated processes into account.

1. Influence of notches in chapter IV:

$$\dot{p} = \dot{\varepsilon}_0 \exp(-\frac{E_\mathrm{a}}{k_\mathrm{B}T}) \exp(\frac{< f(\underset{\sim}{\sigma}) > V_\mathrm{a}}{k_\mathrm{B}T}) \tag{XII.1}$$

2. Comparison with a standard elasto–plastic model neglecting PLC effects in chapter V:

$$\dot{p} = \dot{\varepsilon}_0 \exp(-\frac{E_\mathrm{a}}{k_\mathrm{B}T}) \sinh(\frac{< f(\underset{\sim}{\sigma}) > V_\mathrm{a}}{k_\mathrm{B}T}) \tag{XII.2}$$

3. Influence of metal–matrix composites in appendix IV:

$$\dot{p} = \dot{p}_0 \exp\left(\frac{< f(\underset{\sim}{\sigma}) > V_\mathrm{a}}{k_\mathrm{B}T}\right) \tag{XII.3}$$

   In the last form, $\dot{p}_0$ is equal to $\dot{\varepsilon}_0 \exp(-\frac{E_\mathrm{a}}{k_\mathrm{B}T})$ at given temperature.

The expression of the viscoplastic multiplier can be written with the hyperbolic sine or exponential function. Note that Nabarro (Nabarro, 2003) analyzed the thermal activation under shear stress in different models. In its model, many dislocations are held in equilibrium for backward jumps as for forward jumps. He showed that the experimental activation under applied stress is different from the true activation volume. The conventional model of dislocations jumping forwards and backwards over isolated is also not physically realistic. There is no steady state. A dislocation which has jumped forward over its obstacle runs away to infinity, and there are no dislocation held in equilibrium to jump backwards. In conclusion, due to inconsistencies the relevance of the hyperbolic sine function for moderately low stresses is shown to be very limited and the indiscriminate use of the hyperbolic function to take the back fluctuations into account is not justified.

Physical parameters such as the activation energy of the plastic deformation mechanisms E_a and the activation volume V_a which depends on temperature (and also on plastic strain) were introduced in order to comply with the thermodynamics of thermally activated processes. Note that the activation volume V_a is related to the instantaneous strain rate sensitivity SRS_i, which is always positive, but also with plastic strain. The negative strain rate sensitivity SRS_{ss} is taken into account in the strain ageing expression P_1C_s. We showed in the experimental part B that both mechanisms associated with friction and dragging modes can be observed in zirconium alloys, according to the relaxation experiments. Apparent activation volumes, associated with both deformation mechanisms were established, by plotting $\log \dot{\varepsilon}_p$–σ curves for various temperatures and plastic strain levels.

The plastic strain increment, ω is constant in our simplified strain ageing model, neglecting the strain dependence.

McCormick's model contains 14 parameters and our simplified strain ageing model contains 9 parameters.

We remind the general characteristics of both macroscopic strain ageing models (McCormick, 1988; Zhang et al., 2000) and (Graff et al., 2004; Graff et al., 2005), as follows.

- The yield criterion used is a von Mises type criterion.

- The hardening R is isotropic, where R_0 is the initial yield stress, depending on the cumulated plastic strain p, Q is the saturated value of hardening and b is the rate at which the saturation is reached.

- The age–hardening P_1C_s is also isotropic, due to the contribution of strain ageing (static or dynamic). This term depends on the cumulated plastic strain p and the ageing time t_a, which are internal variables. With this expression, the stress due to the "dislocation anchoring" can be simulated. C_s is also the saturated fraction of solute atoms, diffusing around the dislocation, temporarily stopped by extrinsic obstacles such as forest dislocations. The value of C_s lies between 0 and 1, increasing with time. P_1 is a constant, depending on temperature.

- P_2 and α depend on temperature. Both terms define the dependence of dislocation anchoring with the cumulated plastic strain p.

- The exponent n depends on the type of diffusion. For instance for "pipe diffusion" in aluminium alloys, n is equal to 2/3 and for zirconium alloys, n is equal to 1/3 for bulk diffusion (see the bibliography chapter A).

- The evolution of solute atoms concentration around dislocations temporarily stopped by extrinsic obstacles is described by a relaxation–saturation kinetics of t_a, also labeled Avrami's kinetics. Note that ageing time t_a differs from waiting time t_w. Indeed, this effective ageing time of dislocations t_a evolves with a delay in order to reach the saturation value t_w, which is the mean waiting time of dislocation behind obstacle.

- ω is the plastic strain increment produced when all the dislocations, temporarily stopped by their extrinsic obstacle overcome them. Its value depends on forest dislocations density. However, a constant value is adopted in our simplified strain ageing model.

XII.3 Influence of strain ageing parameters on the constitutive law σ–$\dot{p}$

XII.3.1 Constitutive law σ–$\dot{p}$ under tensile loading conditions

In order to study the σ–$\dot{p}$ curve analytically, various hypotheses are introduced.

The test is uniaxial tension.

The cumulated plastic strain $\dot{p}$ is imposed and constant: $p = \dot{p}t$.

Using the initial condition that at $t = 0 \quad ; \quad t_{a0} = 0$, the solution of the differential equation $\dot{t_a} = 1 - \frac{t_a}{\omega}\dot{p}$ is given by:

$$t_a = \frac{\omega}{\dot{p}}[1 - \exp(-\frac{p}{\omega})] \tag{XII.4}$$

Using the equation $f(\sigma) = |\sigma| - R - P_1 C_s$, the stress is deduced as a function of the cumulated plastic strain rate according to both exponential or hyperbolic sine functions of the yield criterion:

- Exponential approximation of the viscoplastic flow:

$$\sigma = K \log(\frac{\dot{p}}{\dot{p}_0}) + R + P_1 C_m[1 - exp(-P_2 p^{\alpha} t_a^n)] \tag{XII.5}$$

- Hyperbolic sine approximation of the viscoplastic flow:

$$\sigma = K sinh^{-1}(\frac{\dot{p}}{\dot{p}_0}) + R + P_1 C_m[1 - exp(-P_2 p^{\alpha} t_a^n)] \tag{XII.6}$$

Plotting the stress σ as a function of cumulated plastic strain rate $\dot{p}$ (or total strain rate $\dot{\varepsilon}$), the curve has a "S" shape. According to equations XII.4 and XII.5, the influence of the 9 parameters is tested on the σ–$\dot{p}$ curve at constant plastic strain, taken at 0.02 plastic strain in a preliminary study of this thesis (Graff, 2002). For this, the values of the parameters vary one by one, keeping the others constant. We studied the effect of both exponential or hyperbolic sine functions of the yield criterion.

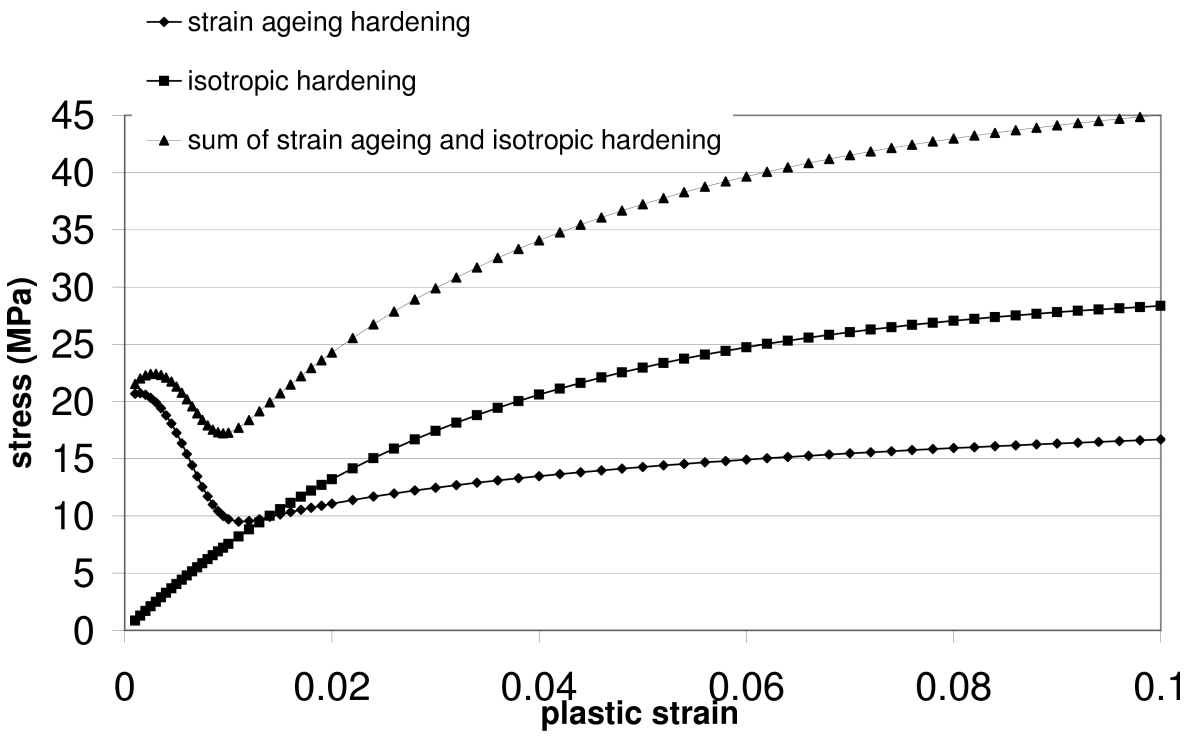

Figure XII.1 : Contribution of classical isotropic hardening $R-R_0$ and age–hardening P_1C_s on the evolution of the stress component as a function of the cumulated plastic strain in the case of the Lüders phenomenon with the the following hypotheses: $\dot{p} = 10^{-3}\ s^{-1}$, $t_{a0} = 0s$.

XII.3.2 Competition between the various mechanisms

The strain ageing contribution can be divided into two terms: t_a^n and $P_2\ p^\alpha$.

Regarding the Lüders phenomenon, the dominating term is t_a^n. The initial state is obtained for a high value of $t_{a0} = t_a(t = 0)$. When plasticity appears, t_a decreases to reach its asymptotic value t_w, close to zero in the Lüders case. The variable C_s is initially equal to 1, decreasing to zero. The decrease of P_1C_s is responsible for the shape of the intrinsic softening law, as shown in figure XII.1.

Regarding the PLC effect, the dominating term is P_2p^α. This term is associated with dislocation anchoring during straining and with the effect of forest dislocations. The component P_2p^α increases with increasing cumulated plastic strain. The p^α dependence controls the critical plastic strain ε_c at which the PLC serrations can be observed on the macroscopic curve. Figure XII.2 shows the evolution of the stress σ as a function of cumulated plastic strain rate $\dot{p}$ in the case of the PLC effect. Contrary to the Lüders phenomenon, the term P_1C_s is generally initially equal to zero and increases during straining. At constant plastic strain rate, t_a increases up to reach the asymptotic value $\dfrac{\omega}{\dot{p}}$ as shown in figure XII.3. Then t_a is constant unless a change of the strain rate.

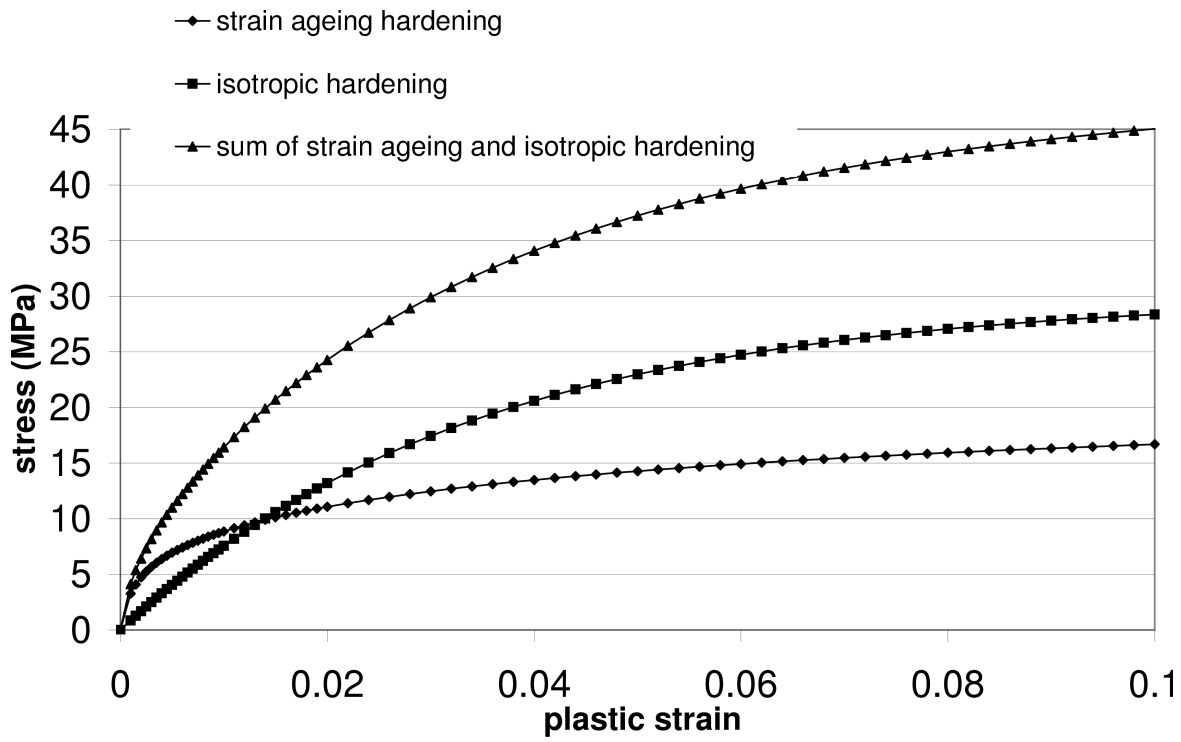

Figure XII.2 : Contribution of classical isotropic hardening $R - R_0$ and age–hardening $P_1 C_s$ on the evolution of the stress component as a function of the cumulated plastic strain in the case of the PLC effect with the following hypotheses: $\dot{p} = 10^{-3}\ s^{-1}$, $t_{a0} = 10^5 s$.

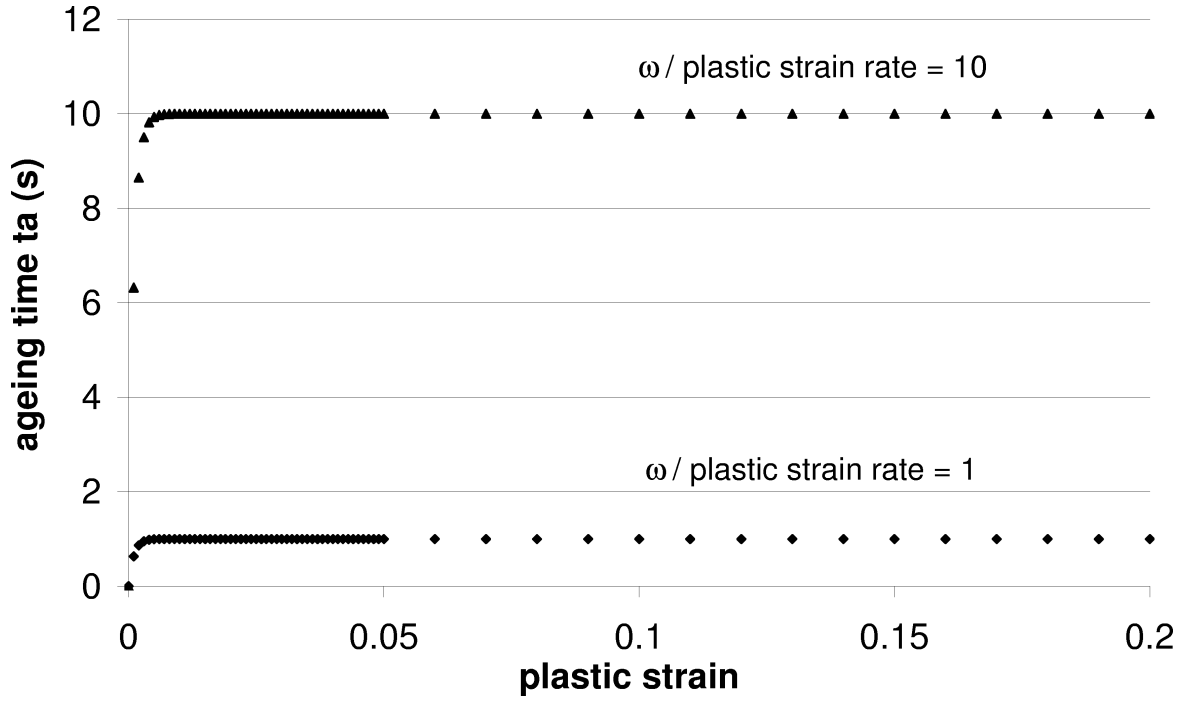

Figure XII.3 : Evolution of t_a as a function of the cumulated plastic strain at two given plastic strain rates in the case of the PLC effect.

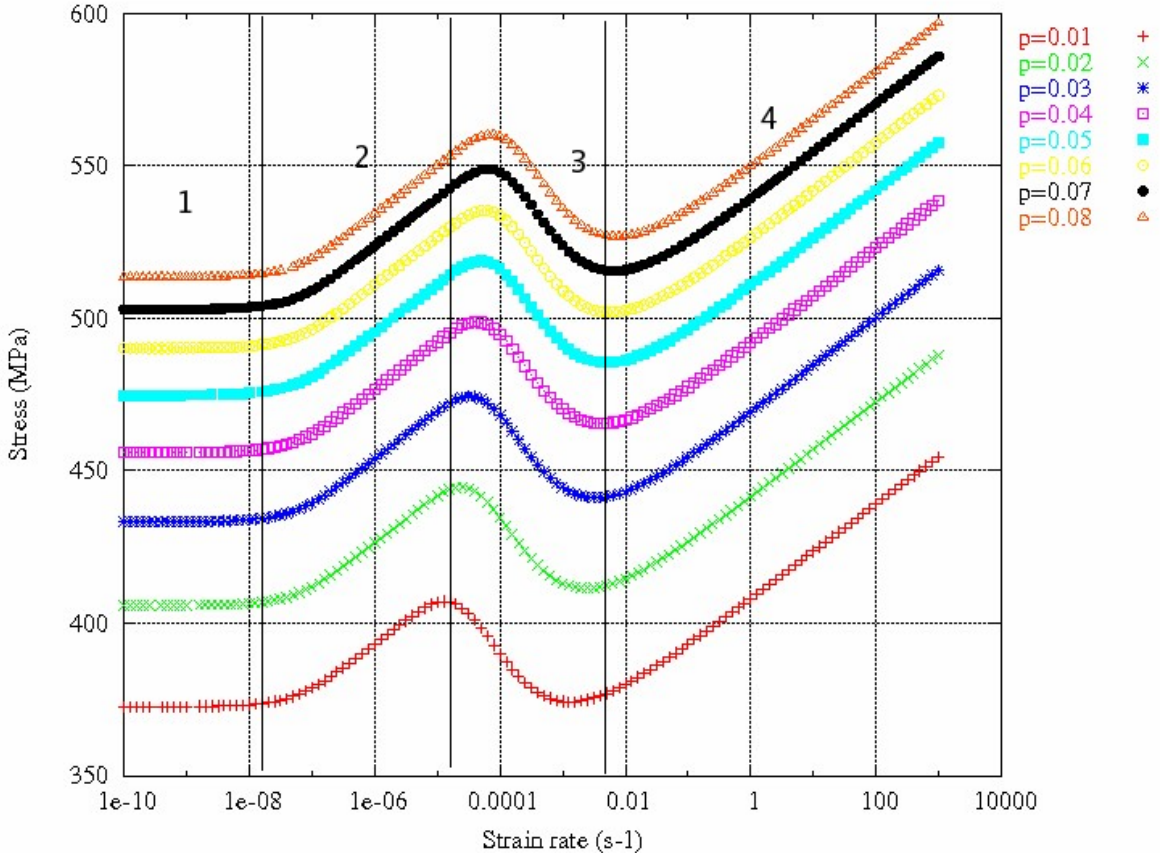

Figure XII.4 : Evolution of the stress as a function of strain rate at various strain levels (simulations of tensile tests on a volume element for 8 different plastic strain levels using exponential function of the yield criterion).

XII.3.3 Parametric study of the strain rate sensitivity

The aim of this study is to relate the values of material parameters and of negative strain rate sensitivity domain. It is necessary to identify the parameters for the materials studied in this work (steels, aluminium alloys, zirconium alloys). The main results of the parameter influence on the constitutive law σ–$\dot{p}$ in uniaxial tensile conditions are taken from a previous study related in appendix IV (Graff, 2002). For this purpose, the idea is to perform calculations on a volume element with a program, which simulates a tensile test at constant strain rate up to a given strain level. This test is repeated for various strain rates, between 10^{-10} s^{-1} and 100 s^{-1}. Then the results are plotted on the stress σ versus plastic strain rate $\dot{p}$ diagram at constant plastic strain p.

Figure XII.4 shows the evolution of the stress as a function of the strain rate occurs for various strain levels at a given temperature, whatever the exponential or hyperbolic sine approximations of the yield criterion. Note that each point observed on the curves correspond to one simulation of a tensile test on a volume element, carried out at given strain rate and up to a given strain level. We can observe that the curves are translated toward higher strain rates and stresses when plastic strain level increases.

Each curve can be divided into four domains, introduced as follows.

1. In domain 1, the stress is independent of the strain rate because the applied strain rate is lower than the threshold strain rate whatever the exponential or hyperbolic sine function used.

2. In domain 2, the stress increases with increasing strain rate. It is due to viscosity K, defined in the thermal activation term $Ksinh^{-1}(\frac{\dot{p}}{\dot{p}_0})$ or $K\log(\frac{\dot{p}}{\dot{p}_0})$ of the strain ageing model.

3. In domains 1 and 2, C_s is equal to 1.

4. In domain 3, the stress decreases with increasing strain rate. A negative strain rate sensitivity can be observed. The term P_1C_s has not its saturated value and decreases. Consequently, the stress decreases too. However the thermal activation term goes on increasing.

5. In domain 4, the strain ageing term P_1C_s is equal to zero and the increase of the stress with strain rate is due to the classical viscosity term K.

6. The parameter, controlling the viscosity (the slope of the curves in the exponential function) is K for both friction mode defined by domain 4 and dragging mode defined by domain 1.

The parameter P_1 controls the amplitude of dislocation anchoring. We recall that the strain ageing term is P_1C_s, where C_s is between 0 and 1. Note that for the high strain rates i.e. the short times, the strain ageing term does not interfere. The stress amplitude is higher when the value of P_1 is higher for low strain rates.

The parameters ω, P_2, α and n have a strong influence on the σ–$\dot{p}$ curve. The main conclusions are the following.
When ω decreases, domain 3 is translated toward lower stress and lower strain rate levels. This effect is expected because ω is the increment of strain produced when all the dislocations overcome their obstacles. The cumulated plastic strain rate is higher when ω is higher. Note that for high values of ω ($> 10^{-2}$), the curves exhibit partial dislocation anchoring for the high strain rates.
When α decreases, domain 3 is translated toward lower strain rate levels. This term is the exponent of cumulated plastic strain, defining the dependence of the dislocation anchoring with plastic strain.
When P_2 decreases, domain 3 is translated toward lower stress and lower strain rate levels. This term also controls the dependence of dislocation anchoring with cumulated plastic strain $\dot{p}$ and the dependence of dislocation anchoring with ageing time t_a.
The stress amplitude of the S shape of the curves is constant whatever the values of ω, P_2, α which is controlled by the parameter n.

XII.4 Conclusion

The strain ageing model is able to simulate the negative strain rate sensitivity domain in the σ–$\dot{p}$ diagram on a material volume element. The simplification of the constitutive equations allows to identify the role of each parameter, controlling the shape of the σ–$\dot{p}$ curve under tensile loading conditions. This study shows that the parameters which sets the negative strain rate sensitivity domain are ω, P_2 and α. The stress amplitude of the S shape of the curves is controlled by the parameter n. The exponential or the hyperbolic sine function of the viscoplastic flow rule have no influence on the shape of the σ–$\dot{p}$ curve.
The main inconvenience of the strain ageing model is that the slope of both deformation mechanisms (friction and dragging modes) is the same, equal to K using the exponential function of the yield criterion.
This important chapter is used to identify the parameters of the strain ageing model applied to the studied materials (steels, aluminium and zirconium alloys).

Chapter -XIII-

Application to the viscoplastic behavior of zirconium alloys

Contents

Abstract: The aim of this chapter is to propose a predictive approach of the strain ageing effects observed in zirconium alloys especially Zr702, based on low or negative strain rate sensitivity, creep arrest and relaxation arrest at the appropriate temperatures. For this the parameters of the strain ageing model suggested by McCormick were identified using the experimental characterization of the range of temperatures and strain rates where strain ageing is effective. Then a comparison between simulations of a plate tensile specimen and experiments is presented, based the development of strain and strain rate heterogeneous fields.

XIII.1 Introduction

We chose to model the anomalous strain rate sensitivity over the temperature ranges $100°C$–$300°C$ in transverse Zr702, related to the existence of a strain ageing phenomenon which results from the combined action of the thermally activated diffusion of foreign atoms to and along the dislocation cores and the long range dislocations interaction. After characterizing the range of temperatures and strain rates where strain ageing is active on the macroscopic and mesoscopic scales, a predictive approach of the strain ageing effects is proposed, using the simplified macroscopic strain ageing model, studied in chapter XII. Some consequences on the development of strain and strain rate heterogeneous fields are also presented, based on the comparison between experiments and simulations of the tension of a plate specimen.

The main experimental results associated with static and dynamic strain ageing effects for the zirconium alloy studied are recalled:

- regarding tensile tests at constant applied strain rates and temperatures, low or even negative strain rate sensitivity is observed at $300°C$ between 10^{-3} s^{-1}, 10^{-4} s^{-1} and 10^{-5} s^{-1},
- creep arrest is observed at $200°C$,
- relaxation arrest is observed at $200°C$.

In this chapter, the material parameters of the strain ageing model are first identified only in tension along the transverse direction for Zr702, using a numerical procedure, based on the minimization of the difference between simulations and experiments. The tensile tests that we chose were carried out at the various applied strain rates ($10^{-3}s^{-1}$, $10^{-4}s^{-1}$, $10^{-5}s^{-1}$) and temperatures ($100°C$, $200°C$, $300°C$) on flat specimens. This choice is justified by the fact that there is no enough information in relaxation.

XIII.2 Parameters identification for Zr702

The first objective is to identify the material parameters of the simplified macroscopic strain ageing model for Zr702, taking the dependence of temperature and strain rate into account. In chapter XII, we studied the influence of the various parameters on the shape of the σ–$\dot{p}$ curve. We recall that three different mechanisms can be taken into account, associated with a set of parameters established for each temperature ($100°C$, $200°C$ and $300°C$):

- thermal activation (also labeled viscosity): E_a, V_a or equivalently K, $\dot{p}_0$,
- classical isotropic hardening: R_0, Q, b,
- static or dynamic strain ageing: t_{a0}, ω, P_1, P_2, α, n.

The classical parameters are determined using the identification for "unaged material" application package of Zset code on a volume element. First we investigated the isotropic hardening parameters (R_0, Q, b), taking P_1 equal to zero (the strain ageing is not taken into account) at each temperature. We recall that R_0 is the yield stress. Then, we identified the parameters of the thermal activation (K and $\dot{p}_0$). Secondly, we determined the strain ageing parameters for Zr702 at the three temperatures, tested experimentally. The value of n, associated with the kinetics of dislocation anchoring can be found in the literature, equal to 1/3 for zirconium alloys (see the chapter A). The initial value t_{a0} controls the occurrence of the Lüders peak. For Zr702, t_{a0} is equal to zero, because no Lüders peak was observed experimentally although after strain rate changes, stress peaks were observed especially at $10^{-3}s^{-1}$. The other strain ageing parameters P_1 and P_2, α, ω, which control the domain of negative strain rate sensitivity are identified using the identification package of Zset code. These four parameters are determined at each temperature by using approximations of the σ versus $\dot{\varepsilon}$ simulated plots on a volume element at the various strain rates ($10^{-3}s^{-1}$, $10^{-4}s^{-1}$ and $10^{-5}s^{-1}$). Plotting, the stress as a function of the strain rate, the objective is to find the domain where the strain rate sensitivity is low or negative in the correct range of strain rates:

- at $100°C$, the strain rate sensitivity is nearly constant whatever applied strain rate,
- at $200°C$, the strain rate sensitivity increases with increasing applied strain rate,

- at $300°C$, the strain rate sensitivity is close to zero or slightly negative (the macroscopic curve at $10^{-5}s^{-1}$ is above these at $10^{-3}s^{-1}$ and $10^{-4}s^{-1}$ for plastic strain between 0.005 and 0.03).

The identification of the material parameters led to the set of parameters according to the various temperatures, assessed in table XIII.1. Young's modulus for each temperature is this deduced from the classical tensile test (see chapter VII) and the Poisson ratio is equal to 0.3. Using the parameters of table XIII.1, the intrinsic σ–$\dot{\varepsilon}$ curves are plotted at each temperature. Figures XIII.1 show the simulated σ–$\dot{\varepsilon}$ curves at $100°C$, $200°C$, $300°C$ for Zr702, compared with experimental data at 2% strain level. Note that at these temperatures, the identification of the material parameters allows to obtain a correct agreement between simulations and experiments, what can be improved at $300°C$ for strain levels up to 1% and after 3.5%.

Table XIII.1 : Parameters of the strain ageing model applied to Zr702 according to the different temperatures.

Parameters	Unit	$100°C$	$200°C$	$300°C$
R_0	MPa	213	70	130
Q	MPa	60	119	2.7
b	-	124	274	201
K	MPa^{-1}	1.67	15.4	7.74
P_1	$MPa\%atom.^{-1}$	0	35.6	73
P_2	s^{-n}	-	2.96	4.22
ω	-	-	$3.4\ 10^{-4}$	$2.15\ 10^{-4}$
α	-	-	3.25	5.4
n	-	0.33	0.33	0.33
$\dot{p}_0$	s^{-1}	$1.96\ 10^{-6}$	$5.36\ 10^{-5}$	$9.13\ 10^{-5}$
C_m	$\%atom$	-	1	1

The comparison between simulated and experimental σ–ε curves is given in figure XIII.2 for Zr702 at $100°C$, $200°C$, $300°C$. The experimental curves are in dot lines and the numerical curves are in continuous lines.

XIII.3 Prediction of the unconventional behavior

The identified strain ageing model for Zr702 (identification only on the classical tensile tests) is also used to predict the strain ageing effects, observed in this zirconium alloy:

- creep arrest, observed by Pujol (Pujol, 1994) at $200°C$,
- relaxation arrest, that we observed at $200°C$ (see relaxation experiments with unloading in chapter VI),
- strain heterogeneities, that we observed for instance at $150°C$ (see local strain measurements by laser scanning extensometry in chapter IX).

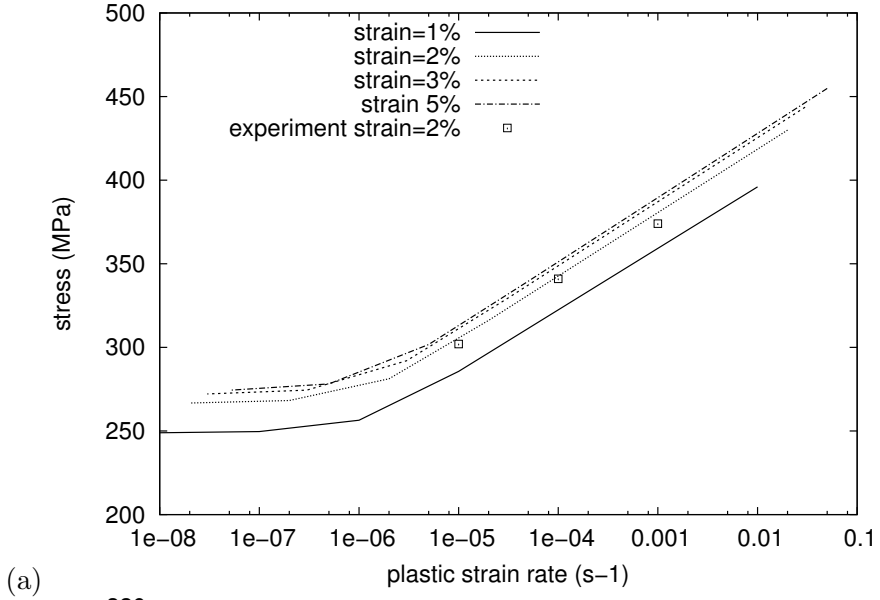

(a)

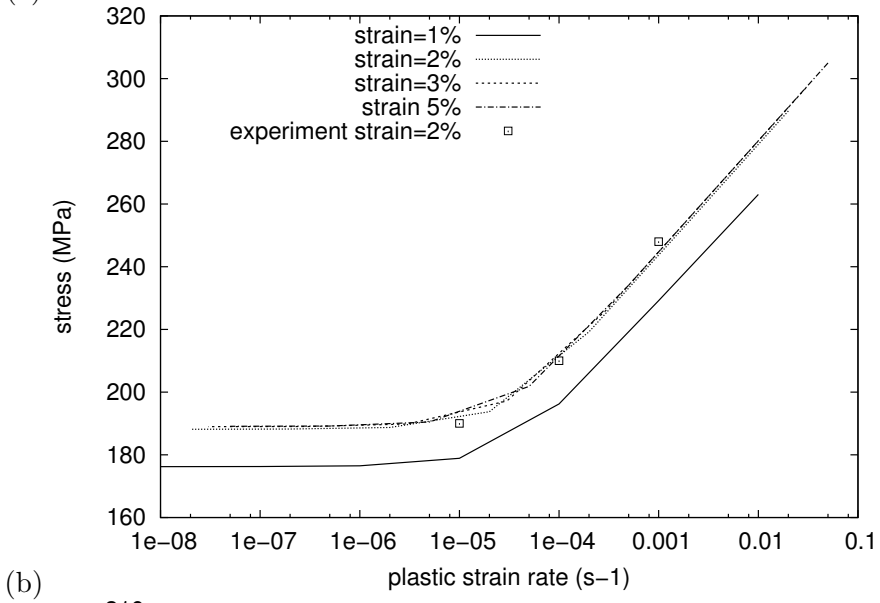

(b)

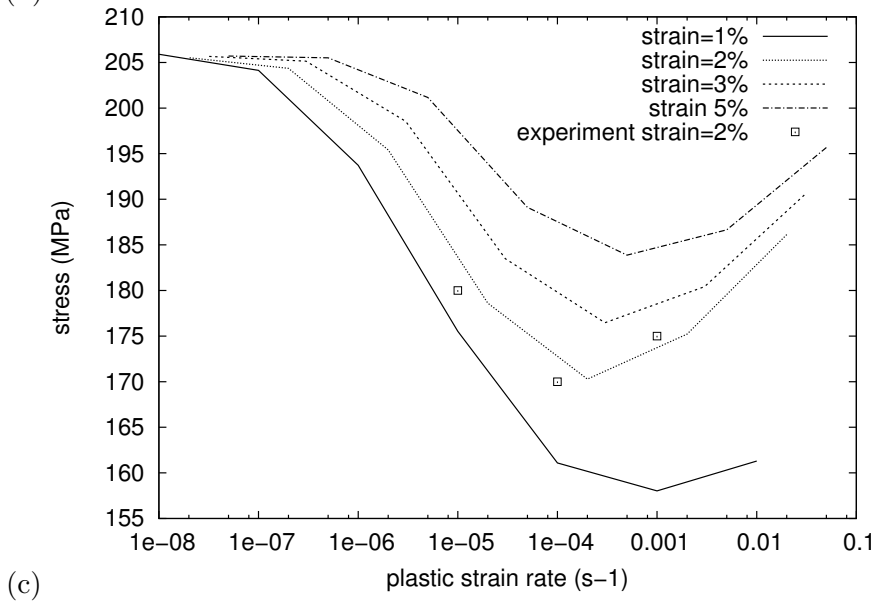

(c)

Figure XIII.1 : Simulated intrinsic σ–$\dot{\varepsilon}$ curve for Zr702 at: (a) $100°C$, (b) $200°C$, (c) $300°C$.

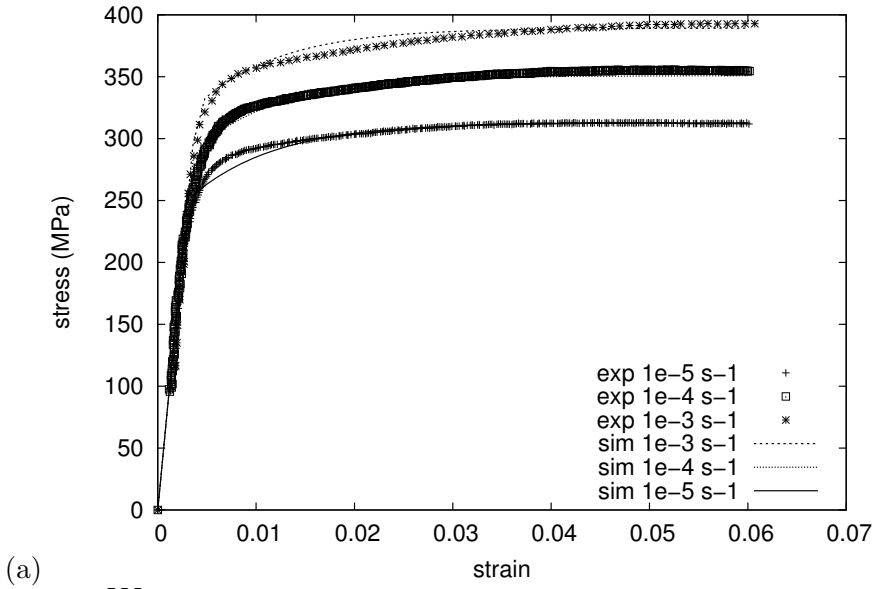

(a)

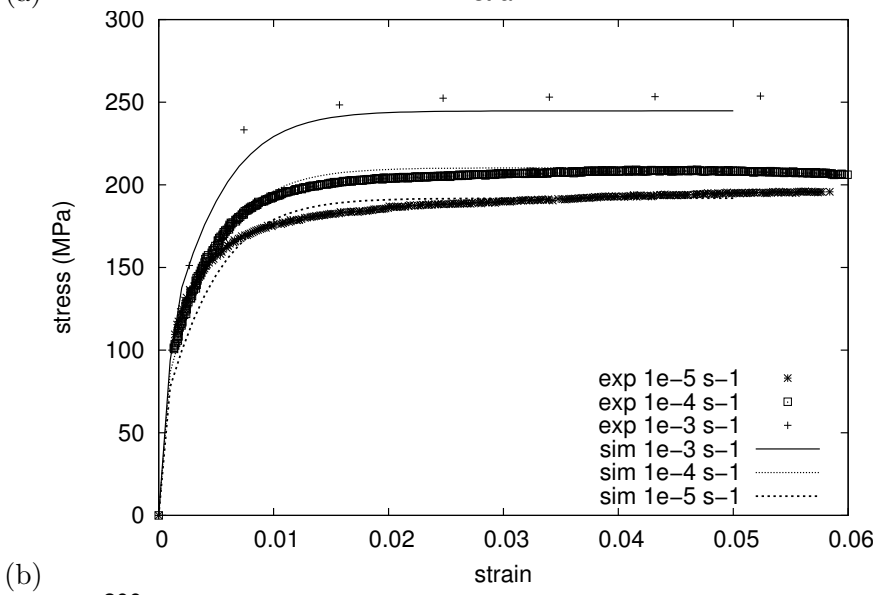

(b)

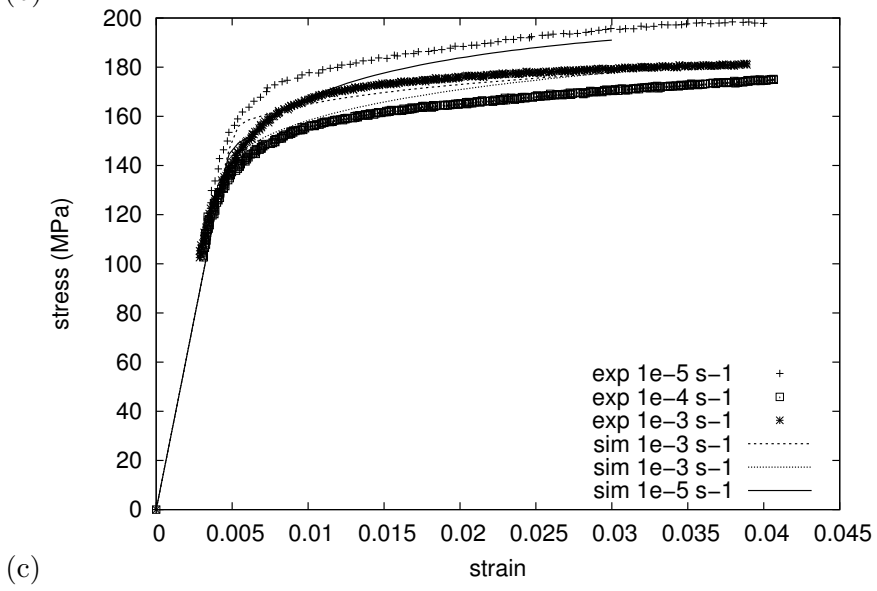

(c)

Figure XIII.2 : Comparison between simulated and experimental tensile curves for Zr702 at: (a) $100°C$, (b) $200°C$, (c) $300°C$.

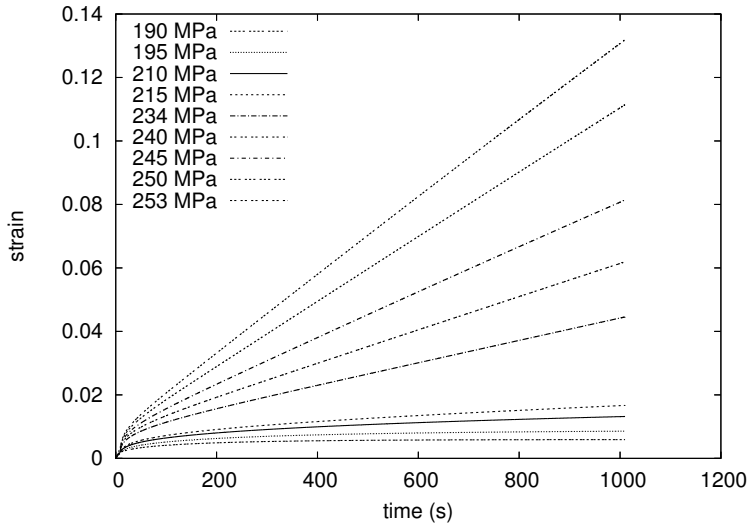

Figure XIII.3 : Creep simulation at 200°C for Zr702: ε–t curve at the various applied stresses: 195 MPA, 215 MPa, 240 MPa, 245 MPa, 250 MPa, 253 MPa.

First we simulated the response of a material volume element of creep and relaxation tests. Then, we simulated tensile tests using a flat tensile specimen (2D in plane stress). Experiments and simulations were compared in order to validate the identified strain ageing model for Zr702.

XIII.3.1 Prediction of creep arrest

The conditions for creep simulation are the following:

- the parameters of the strain ageing model are those at 200°C for Zr702,
- the volume element is loaded up to a prescribed stress level. Then the stress level is kept constant during 10000 seconds,
- during the simulation of creep test, the strain is stored as a function of time.

Figure XIII.3 shows the ε–t curve at 200°C at the various applied stresses: 195 MPA, 215 MPa, 240 MPa, 245 MPa, 250 MPa, 253 MPa. This type of diagram allows to show a strong stress sensitivity at this temperature. The simulations show that creep arrest can be predicted at 200°C for the stress level equal to 195 MPa. An increase of 5 MPa on the applied stress leads to increase the creep strain rate. We recall that Pujol (Pujol, 1994) defined two domains of stress D1 and D2 for which the shape of the the ε–t curve is different (see the bibliography part A). In the domain D1, the saturation of deformation can be reached: $\sigma < 195MPa$. This phenomenon implies a creep rate nearly equal to zero. In the domain D2, the creep behavior is more classical: $\sigma > 195MPa$. The limit between the domains D1 et D2 is defined by the critical stress σ_c predicted at 195 MPa. Figure XIII.4 shows the comparison between experiments related in Pujol's thesis (Pujol, 1994) and simulations at 200°C for Zr702. Pujol showed that the critical stress between domains D1 and D2 at 200°C for Zr702 loaded in transversal direction is found equal to 190–195 MPa. In conclusion, simulations and experiments are in good agreement. The critical stress, equal to 195 MPa associated with creep arrest is well predicted at 200°C for Zr702.

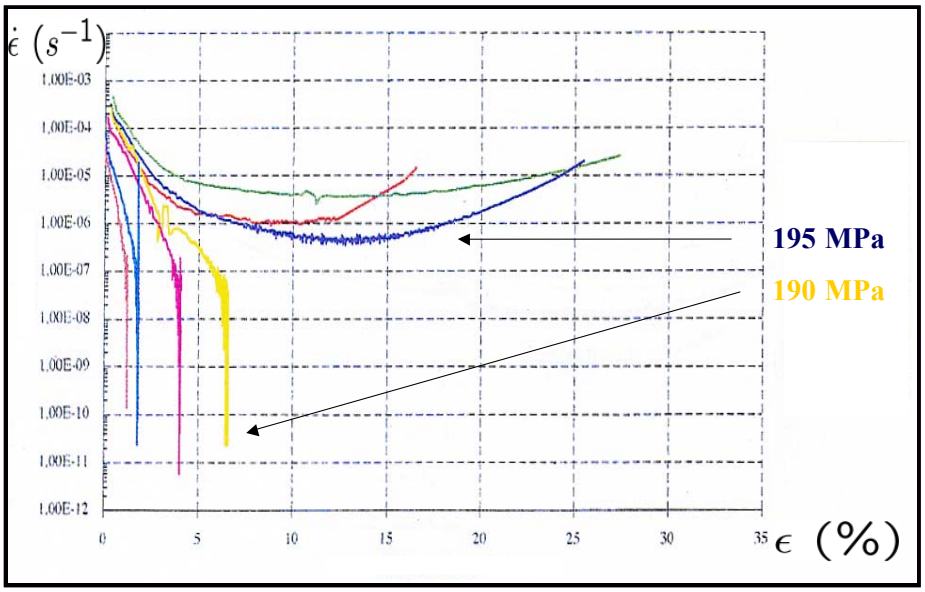

(a)

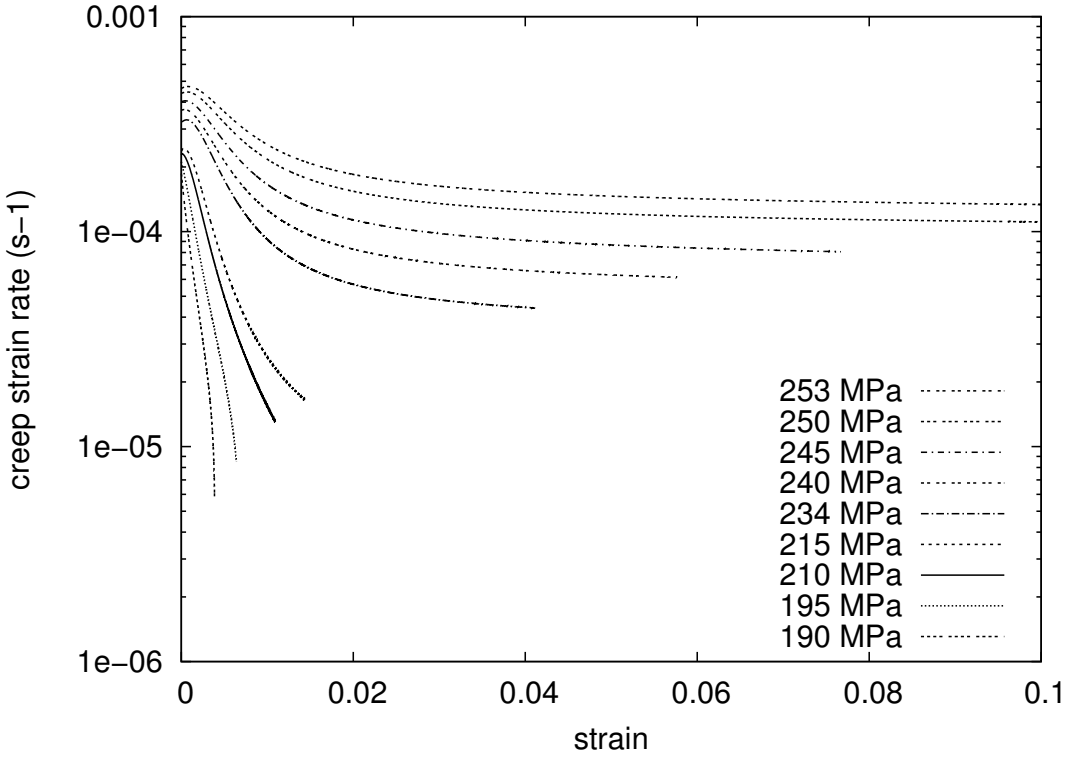

(b)

Figure XIII.4 : Creep simulation at 200°C for Zr702: comparison between: (a) experiments (Pujol, 1994) and (b) simulations.

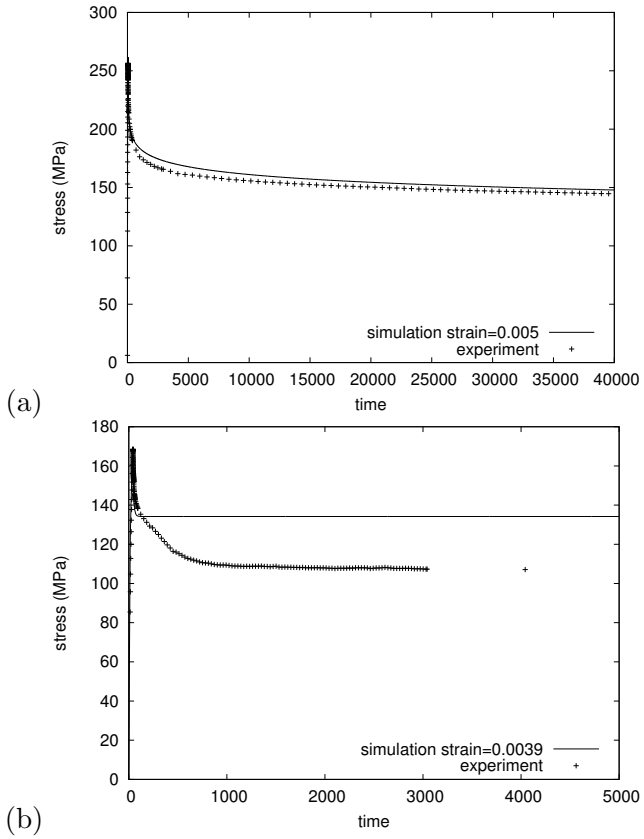

Figure XIII.5 : Comparison between the experimental curve in dot line and the simulated curve in continuous line for relaxation tests at: (a) $100°C$ for a relaxation strain of 0.005, (b) $200°C$ for a relaxation strain of 0.0039.

XIII.3.2 Prediction of relaxation arrest

The conditions for relaxation simulation are the following:

- the parameters of the strain ageing model are those at $100°C$ and $200°C$ for Zr702,
- the volume element is loaded up to a prescribed strain level. Then this strain level is kept constant during 40000 seconds,
- during the simulation of the relaxation test, the stress is stored as a function of time.

Figure XIII.5 shows the σ–t curve for a relaxation strain of 0.005 at $100°C$ and for a relaxation strain of 0.0039 at $200°C$. The simulated curve in continuous line is compared to the experimental curve in dot line (see chapter VII). We recall that Pujol (Pujol, 1994) studied the relaxation behavior of Zr702 at $20°C$ and $200°C$. The author observed that there are differences between the macroscopic behavior at $20°C$ and $200°C$. Up to about 100 hours, the relaxation is always effective at $20°C$ contrary to $200°C$ at which the relaxation is significantly smaller. Moreover, we showed that relaxation arrest is observed at $200°C$ and $300°C$ for Zr702 (see chapter VII). In conclusion, relaxation arrest is well predicted at $100°C$. At this temperature the stress decreases classically. However the threshold stress σ^{thres} of relaxation has to be improved at $200°C$. We recall that experimentally we found that $\sigma^{thres} = 104MPa$ at $200°C$ for the first relaxation cycle.

XIII.3.3 Prediction of strain heterogeneities

It is essential to distinguish the response of a material volume element from the response of a tensile specimen which must be regarded as a structure. That is why we present here finite element simulations of the tension of a plate using the identified strain ageing model for Zr702. We focus our attention on the possible occurrence of strain heterogeneities across the width of the sample during deformation. For this, we simulated a tensile test at $300°C$ with applied strain rates of $10^{-4}s^{-1}$ and $10^{-5}s^{-1}$ using the finite element method. The flat tensile specimen simulated and the bounding conditions are presented in the experimental chapter C. Plane stress conditions are enforced.

Figures XIII.6 shows the simulated plastic strain rate and plastic strain maps at various strain levels for the simulation of the tensile test at $300°C$ with both applied strain rates. The σ–ε curves of the simulated tensile tests at $10^{-5}s^{-1}$ and $10^{-4}s^{-1}$ using flat tensile specimen are shown in figure XIII.7. The simulation result for tensile test at $10^{-5}s^{-1}$, using a volume element is compared also to this for the tensile test at $10^{-5}s^{-1}$ using the flat tensile specimen. After a certain amount of plastic strain, peculiar serrations appear on the macroscopic σ–ε curve at $10^{-5}s^{-1}$, which is not the case at $10^{-4}s^{-1}$, the macroscopic curve showing a "classical" hardening. We are not able to classify such serrations, which do not seem to be A or B or C type as it is the case for PLC effect (see chapters IV and V). Regarding plastic strain rate and plastic strain maps for the various strain levels at $10^{-5}s^{-1}$, localization bands start to develop on each side of the initial defect (here a slightly lower yield stress in one element). They seem to propagate through short millimeter distances (the mesh size is 0.25×0.25) on the width of the flat specimen and then vanish. The higher serration observed on the macroscopic curve at about 0.009 can be associated with the reflection at the bottom boundary of the deformation band. This reflection is not complete because new deformation band appear again near the initial defect. Moreover, the calculations show that at the beginning of straining, the plastic strain bands can be associated with the plastic strain rate bands. Then after a strain level of about 0.012 start, plastic strain is cumulated here where the plastic strain rate bands have been propagated themselves.

Figure XIII.8 shows the strain as a function of a line taken on the left horizontal edge of the sample at $300°C$ for various strain levels of 0.01, 0.013 and 0.02. The simulated local strain at $300°C$ for the applied strain rate of $10^{-5}s^{-1}$ can be compared to the local strain detected by laser scanning extensometry at $250°C$ for the applied strain rate of $10^{-4}s^{-1}$ for the same strain levels. We recall that at $250°C$, strain heterogeneities were observed on the millimeter scale. Strain inhomogeneities were detected at the beginning of straining. We deduced that the type of these strain heterogeneities is not a propagating one like the Lüders band and is not a PLC instability. Regarding figure XIII.8, simulation and experiment are in good agreement. The simulated and experimental local strain amplitudes can be compared at the same level. In conclusion, complex plastic strain localizations associated with negative strain rate sensitivity can take place in Zr702 around $300°C$.

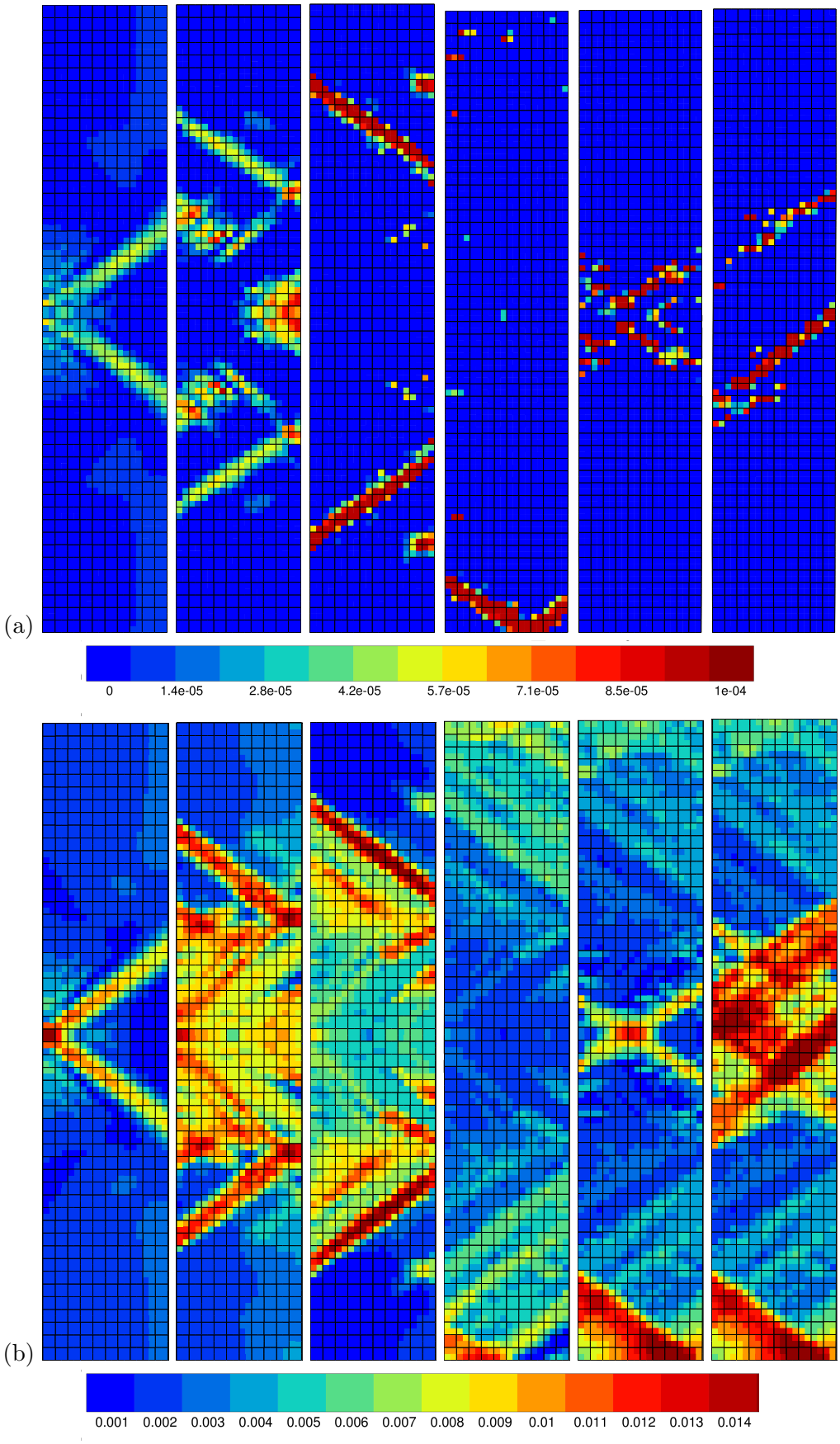

Figure XIII.6 : Simulation of a tensile test at $300°C$ and $10^{-5}s^{-1}$ for Zr702 at various macroscopic strain levels of 0.006, 0.007, 0.008, 0.009, 0.01, 0.012: (a) plastic strain rate maps, (b) plastic strain maps.

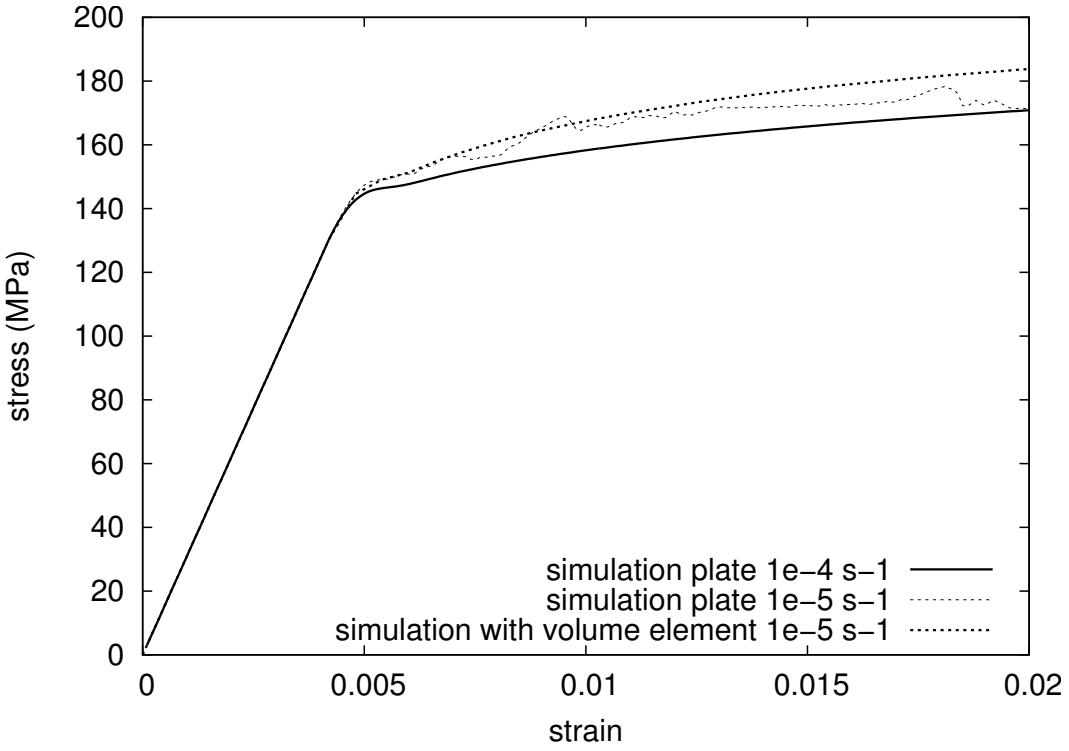

Figure XIII.7 : The σ–ε curves of the simulated tensile tests at $10^{-5}s^{-1}$ and $10^{-4}s^{-1}$ using flat tensile specimen. These curves are compared with the simulation of the tensile tests at $10^{-5}s^{-1}$, using a volume element.

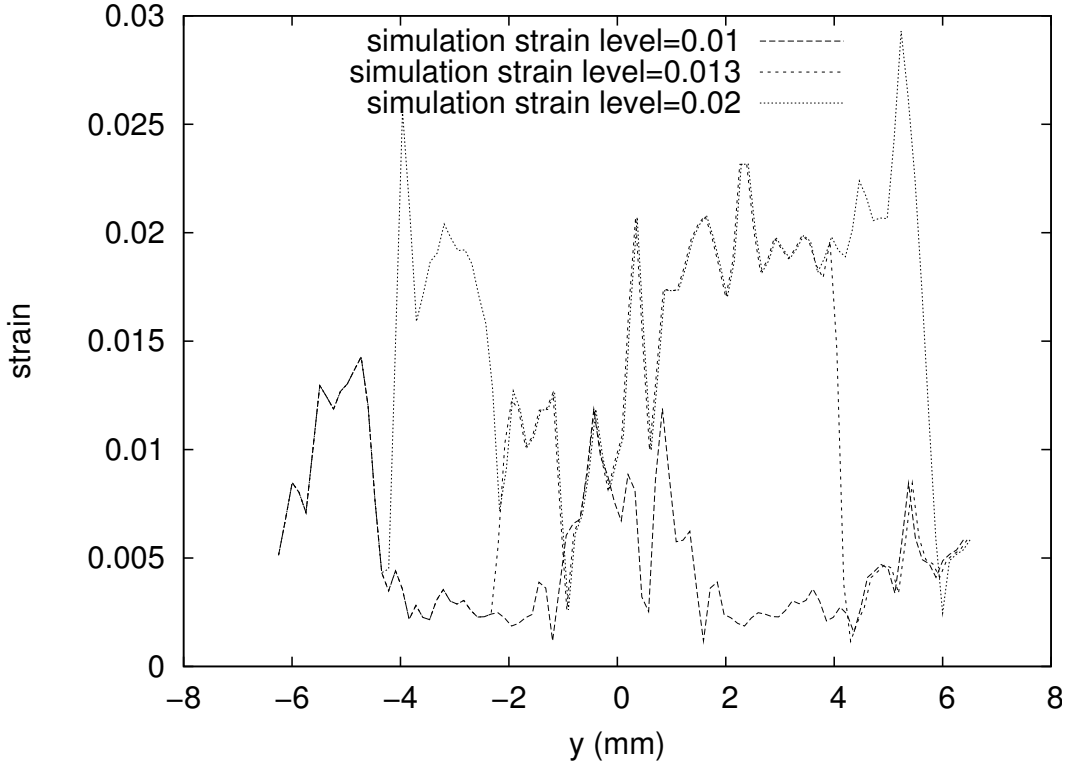

(a)

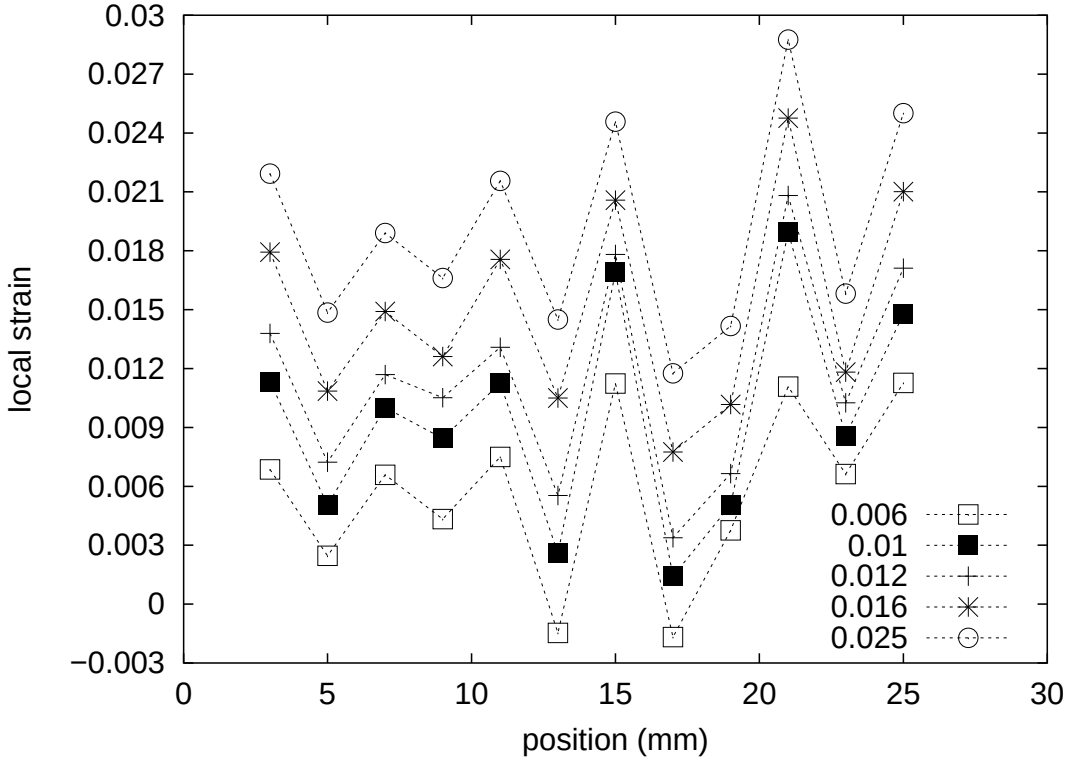

(b)

Figure XIII.8 : Comparison between: (a) simulated local strain at $300°C$ for the applied strain rate of $10^{-5}s^{-1}$, (b) local detected by laser scanning extensometry at $250°C$ for the applied strain rate of $10^{-4}s^{-1}$ at various strain levels of 0.01, 0.013, 0.02.

XIII.4 Introduction of kinematic hardening

The existence of an internal stress component X was evidenced at several places in this work (see for instance section VIII.3.1). Internal stresses are induced by the formation of dislocation structures. It is not known how strain ageing influences the partition of hardening into isotropic and kinematic parts. In this work, strain ageing effects are incorporated into the isotropic hardening part only. We show here that a kinematic hardening variable $\underset{\sim}{\mathbf{X}}$ can be introduced in the strain ageing model to improve the description of relaxation tests. The assumption is made that the kinematic hardening law is unaffected by the strain ageing variable t_a. Therefore, kinematic hardening is introduced in a standard way in the J_2 of viscoplasticity theory (Besson et al., 2001). The von Mises plasticity criterion is modified as follows:

$$f(\underset{\sim}{\sigma}, \underset{\sim}{\mathbf{X}}, R) = J_2(\underset{\sim}{\sigma} - \underset{\sim}{\mathbf{X}}) - R \tag{XIII.1}$$

The isotropic hardening variable is still given by:

$$R = R_0 + Q(1 - \exp(-bp)) + P_1 C_s \quad \text{with} \quad C_s = C_m(1 - \exp(-P_2 p^\alpha t_a^n)) \tag{XIII.2}$$

The flow rule and evolution equation for t_a are unchanged:

$$\dot{p} = \dot{\gamma}_0 \sinh(< f > /K) \quad ; \quad \dot{t}_a = \frac{t_w - t_a}{t_w} \quad ; \quad t_w = \frac{\omega}{\dot{p}} \tag{XIII.3}$$

A nonlinear kinematic hardening law is adopted:

$$\underset{\sim}{\mathbf{X}} = \frac{2}{3} C \underset{\sim}{\alpha} \quad ; \quad \dot{\underset{\sim}{\alpha}} = \dot{\underset{\sim}{\varepsilon}}^p - D\dot{p}\underset{\sim}{\alpha} \tag{XIII.4}$$

where C and D are material parameters depending on temperature. The previous equations are specialized in the case of simple tension:

$$f(\sigma, X, Cs) = |\sigma - X| - R_0 - P_1 C_s \tag{XIII.5}$$

$$\dot{p} = \dot{\gamma}_0 \sinh(< f > /K) \tag{XIII.6}$$

$$C_s = C_m(1 - \exp(-P_2 p^\alpha t_a^n)) \tag{XIII.7}$$

$$\dot{t}_a = \frac{t_w - t_a}{t_w} \quad ; \quad t_w = \frac{\omega}{\dot{p}} \tag{XIII.8}$$

$$\dot{X} = C\dot{\varepsilon}_p - D\dot{p}X - \left(\frac{|X|}{M}\right)^m sign(X) \tag{XIII.9}$$

where X is the axial internal stress or back–stress component. The material parameters were identified from a relaxation test at two strain levels at 200°C. The results of this identification is shown in figure XIII.9. The existence of reverse plastic flow after the change in relaxation strain from $\varepsilon^1 = 0.0039$ to $\varepsilon^2 = 0.0034$ is correctly accounted for, which is not possible based on pure isotropic hardening. The values found are:

$$R_0 = 10\text{MPa} \quad ; \quad P_1 = 20\text{MPa} \quad ; \quad C = 42000\text{MPa} \quad , \quad D = 300$$

$$P_2 = 900 \quad ; \quad \alpha = 1.2 \quad ; \quad \omega = 3.4.10^{-6}$$

The magnitude of internal stress, X is compatible with the analysis of internal stresses performed in section VIII.3.1. Note that the initial yield stress, R_0 is considerably reduced

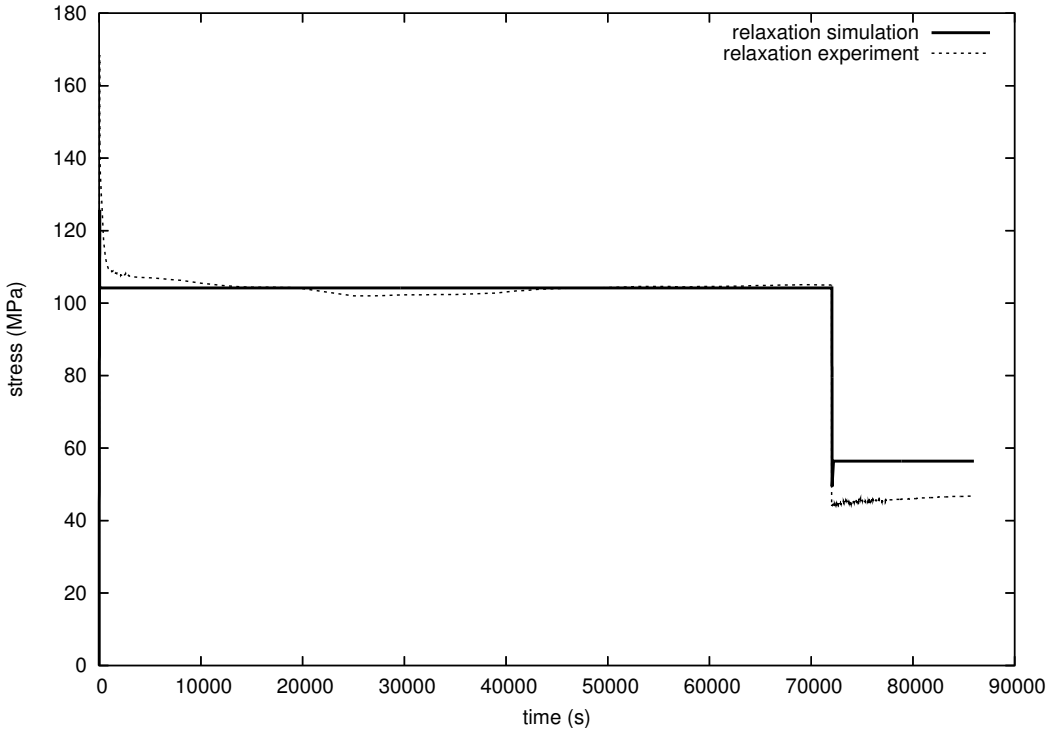

Figure XIII.9 : Relaxation test at $200°C$ at two successive strain levels in Zr702: $\varepsilon^1_{relax} = 0.0039$, $\varepsilon^2_{relax} = 0.0034$. Simulation versus experiment. The model includes a kinematic hardening variable, X.

in comparison to the value in table XIII.1, the values of Q and b being unchanged. These parameters are compatible with a still correct description of the tensile test at different strain rates, as shown in figure XIII.10. However, it is apparent on these curves that the initial yield stress is too small. This underlines a standard difficulty in constitutive modeling of both tensile and relaxation tests.

This could be improved in two ways at least:

- several kinematic hardening variables associated with various plastic strains ranges (Besson et al., 2001),
- introduction of a static recovery term:

$$\dot{X} = C\dot{\varepsilon}_p - D\dot{p}X - \left(\frac{|X|}{M}\right)^m sign(X)$$

with parameters M, m, describing time–dependent dislocation structure rearrangement. However, strain ageing may have some influence at this stage in recovery processes, which remains to be studied.

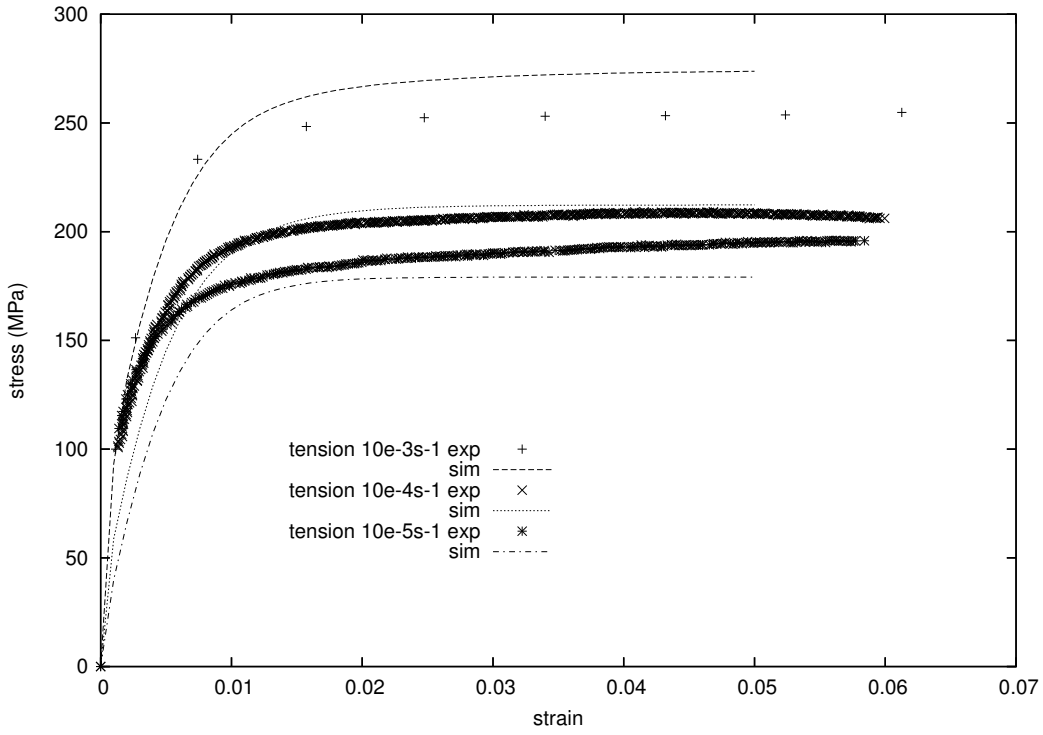

Figure XIII.10 : Impact of the kinematic hardening variable on the description of tensile tests at various strain rates in Zr702 at $T = 200°C$. Simulation versus experiment.

XIII.5 Conclusion

In this chapter, we propose a predictive approach of the strain ageing effects observed in zirconium alloys especially Zr702. This work is based on low or negative strain rate sensitivity observed at $200°C$ and $300°C$ for Zr702. The parameters of the strain ageing model identified for Zr702 are taken from the results of chapter XII. The main conclusions are the following:

- low or negative strain rate sensitivity is simulated at $200°C$ and $300°C$,
- creep arrest is well predicted by the model at $200°C$,
- relaxation behavior is well predicted at $100°C$, but relaxation arrest can be improved at $200°C$, the threshold stress being over–predicted and the threshold strain being below–predicted,
- the development of strain and strain rate heterogeneous fields is predicted,
- a kinematic hardening model is proposed to better describe relaxation tests. The assumption that internal stresses are not affected by strain ageing is compatible with the experimental results as a first approximation.

In prospect, the strain ageing model applied to zirconium alloys can be improved and the material identification is incomplete.
The specific effect of strain ageing on isotropic and kinematic hardening components must be investigated further, especially taking static recovery phenomena into account.
The 2–dimensional field measurements on the millimeter scale associated relaxation tests with unloading and creep tests have to be taken into account in the material parameters identification.
The viscosity parameter, K which is associated with the activation volume has to be different according to the dragging mode or the friction mode. The dependence of K with the ageing time t_a and temperature T has to be taken into account.

General conclusion and prospects

The relaxation modes theory of paired point defects in h.c.p. crystals and internal friction measurements reveal that anelastic effects, attributed to the stress induced ordering of substitutional–interstitial atom pairs in zirconium alloys are responsible for jumps of oxygen interstitial atoms, parallel to the basal plane. The three phenomena, Static Strain Ageing (SSA), Dynamic Strain Ageing (DSA) and Portevin–Le Chatelier (PLC) effect have the same physical origin: the interaction between oxygen atoms (interstitial elements) interacting at short range distance with substitutional elements and dislocation stress. The oxygen content and the nature of the substitutional atoms play an important role on strain ageing phenomena. The temperature dependence of the stress peak, associated with SSA is strongly affected by the substitutional alloying element and the height of this peak increases with the oxygen content. Strain ageing also has a strong effect on the creep behavior. In particular, creep arrest which is characterized by a saturation of deformation in the creep strain–time diagram was observed by Pujol (Pujol, 1994) in type 702 zirconium called Zr702 at $200°C$.

The experimental aim of this work was to characterize the range of temperatures and strain rates where strain ageing phenomena are effective on the one hand on the macroscopic scale and on the other hand on the mesoscopic scale. For this purpose, specific zirconium alloys were elaborated starting from a crystal bar of zirconium with 2.2 wt% hafnium and with a very low oxygen content (80 wt ppm) called ZrHf. Another substitutional atom was added to the solid solution under the form of 1 wt% niobium. Some zirconium alloys were doped with oxygen (ZrHf–O, ZrHf–Nb–O), others were not (ZrHf–Nb). All of them were characterized by various mechanical tests (standard tensile tests, tensile tests with strain rate changes, relaxation tests with unloading). The experimental results were compared with the standard oxygen doped zirconium alloy studied by Pujol and called Zr702 (Pujol, 1994). The following experimental evidences of the age–hardening phenomena were collected and analysed.

- Regarding the standard tensile tests, negative strain rate sensitivity was observed for transverse Zr702 between $10^{-5}\ s^{-1}$ and $10^{-3}\ s^{-1}$ / $10^{-4}\ s^{-1}$ at $300°C$. The yield stress plateau observed between $200°C$ and $300°C$ at $10^{-5}s^{-1}$ and improperly regarded as an athermal plateau by Derep (Derep et al., 1980) was also observed by Naka (Naka et al., 1988) in titanium (with about 500 ppm oxygen) and correctly interpreted as the signature of a thermally activated DSA phenomenon.

- The tensile tests with strain rate changes were carried out for the five zirconium alloys at various temperatures for two applied strain rates $10^{-3}s^{-1}$ and $10^{-4}s^{-1}$. The strain rate sensitivity parameter, SRS is maximal at $200°C$ for Zr702, and at $300°C$ for ZrHf. A higher niobium content does not change the values of SRS for ZrHf–Nb. A higher oxygen content is associated with an increase in the values of SRS for ZrHf–O. PLC effect is observed at both $10^{-3}\ s^{-1}$ and $10^{-4}\ s^{-1}$ at $200°C$, $300°C$ and $400°C$. The PLC effect is effective at higher applied strain rates for ZrHf than for Zr702 at the same testing temperature. ZrHf–Nb exhibits PLC at $200°C$ and at $10^{-4}\ s^{-1}$, contrary to ZrHf. A higher oxygen content is associated with a slight increase of the stress amplitude, observed at higher strain rates for ZrHf–O.

- Stress relaxation tests were chosen in order to explore the basic deformation modes present simultaneously in the specimen: the friction and dragging modes. Although relaxation tests are seldom used, their great interest relies on their inherent ability to let the material choose its own plastic deformation modes in a large range of stress levels and strain rates ($10^{-4}s^{-1}$ down to $10^{-10}s^{-1}$ for our equipment) as opposed to tensile tests which try to impose a chosen macroscopic strain rate and to creep tests which impose a constant load for generally rather long periods of time. We studied the effect of strain ageing phenomena on relaxation behavior, especially for transverse Zr702 and ZrHf at various temperatures in the range of $20°C$–$400°C$.We evidenced the existence of relaxation arrest which is characterized by an abrupt change of the slope of the curve $\dot{\sigma}$–t from a finite to an almost infinite value of $\dot{\sigma}$. This effect was observed at $200°C$ and $300°C$ for Zr702 and at $200°C$ for ZrHf. When relaxation cycles include a relaxation sequence after unloading down to 50 MPa, spontaneous reloading of the specimen is observed, thus providing direct experimental evidence that a strong internal stress develops in the specimen during relaxation tests. In Zr702, kinematic hardening reaches 100 MPa at $100°C$ after 1.8% strain level but drops down to 40 MPa at $400°C$ when isotropic hardening hardly reaches 40 MPa at $100°C$ after 1.8% strain level and drops down to 20 MPa at $300°C$ and to just a few MPa at $400°C$. Relaxation experiments give information about deformation mechanisms, which are associated with one single well-defined slope in the $\log \dot{\varepsilon}$ versus σ diagram. The intermediate regime is such that no definite slope can be detected. At lower plastic strain rates, the macroscopic response is associated with the dragging mode (higher temperatures) and at higher plastic strain rates, the macroscopic response is associated with the friction mode (lower temperatures). Between these two limiting modes, the behavior is unstable. For Zr702, the behavior observed at $100°C$ is associated with the friction mode. A change in the deformation mechanism was observed between $200°C$ and $400°C$. For temperatures larger than $400°C$, the dragging mode is active. The apparent activation volumes associated with friction and dragging modes are almost the same for Zr702, close to 0.7 $nm^3.atom^{-1}$. By reconstruction of the entire relaxation curve at the temperature peak of $300°C$ for strain ageing in Zr702, an estimated "drag stress" of about 250 MPa was determined. A similar value was deduced from the flow stress versus temperature curve (0.2% yield stress or ultimate tensile stress) for this reference alloy doped with 1300 wt ppm of oxygen. For ZrHf, the dragging mechanism was observed for lower temperatures close to $300°C$. For this zirconium alloy, the change in the deformation mechanism was observed between $200°C$ and $300°C$. The apparent activation volumes are close to 2 $nm^3.atom^{-1}$ for the friction mode and 1 $nm^3.atom^{-1}$ for the dragging mode. For this alloy which contains only about 80 wt ppm of oxygen, the "drag stress" was estimated at about 130 MPa.

Field measurements of plastic strain heterogeneities during straining of materials exhibiting strain ageing effects were carried out by means of laser scanning extensometry and tensile tests at constant applied strain rate according to various experimental conditions: with relaxation periods and unloading steps with waiting times. This experimental method is very potent in identifying and characterizing local plastic strain heterogeneities on the mesoscopic scale. We chose two zirconium alloys, Zr702 and ZrHf that we compared to standard materials such as mild steel and $Al - Mg$ alloy. We showed that complex strain localization phenomena take place in both zirconium alloys. We observed that at $20°C$ and $100°C$, plastic strain heterogeneities can be detected for both zirconium alloys although no effect due to strain ageing phenomenon is observed on the macroscopic curve. At $250°C$,

plastic strain heterogeneities were observed both on the millimeter and macroscopic scales. Then, we concluded that the plastic strain heterogeneities detected for Zr702 and ZrHf are neither Lüders bands (mild steel) nor PLC serrations (aluminium alloy). They are complex and non–propagating plastic strain heterogeneities, associated with low or even locally negative strain rate sensitivity.

The other important contribution of the thesis is the modeling of strain ageing effects observed experimentally in dilute zirconium alloys. In the bibliography we reported two main constitutive models. First, the Kubin–Estrin's model (Kubin and Estrin, 1985) is a phenomenological model of plastic deformation based on Penning's formulation which introduces the concept of negative strain rate sensitivity of the flow stress. The second model is the McCormick's model (McCormick, 1988) which includes in the constitutive relation an additional state parameter C_s, the concentration of solute atoms which can segregate around mobile dislocations stopped by extrinsic obstacles. This parameter is associated with an internal variable t_a, the ageing time. The effective solute composition is essentially a "fast" evolving variable due to t_a which obeys relaxation kinetics.
We chose to use the constitutive model of McCormick (McCormick, 1988) because this model uses the internal variable t_a so that it is numerically easier to implement and time integrate than Kubin–Estrin's model. The main conclusions are the following.

- First, we tested this model, simulating the deformation of notched and CT specimens in tension for standard materials such as mild steel and aluminium alloys. We showed that simulations and experiments are in good accordance for Al–Cu alloy and mild steel. Serrations on the overall load/displacement curves showed to disappear progressively when the notch radius decreases. Strain rate localization bands initiation and propagation are still predicted by the computation but the spatial propagation range strongly decreases. However, strain localization bands can escape from the notched zone. For instance, intense strain rate localization bands were produced at the crack tip in pre–cracked CT specimen. They are curved by the complex multiaxial stress state. The propagation of these intense strain rate bands neither affects the shape nor the extension of the plastic zone when compared to simulations with a standard elastoplastic model. These results showed the important role that DSA effects can play on the subsequent fracture materials.

- After validating this model with various standard alloys, we identified the material parameters for transverse Zr702 using the classical tensile tests at constant applied strain rates ($10^{-3}s^{-1}$, $10^{-4}s^{-1}$, $10^{-5}s^{-1}$) and temperatures ($100°C$, $200°C$, $300°C$). The main conclusions of the predictive approach of the strain ageing effects observed in Zr702 are the following. Low and/or negative strain rate sensitivity can be simulated at $200°C$ and $300°C$. Creep arrest, observed experimentally by Pujol (Pujol, 1994) is correctly predicted at $200°C$. Relaxation behavior can be also predicted at $100°C$ and $200°C$, including relaxation arrest phenomenon. A kinematic hardening model was elaborated in order to better describe the relaxation tests. The assumption that internal stresses are not affected by strain ageing is compatible with the experimental results as a first approximation. The development of strain and strain rate heterogeneous fields observed by laser scanning extensometry at $250°C$–$300°C$ are also predicted by the model. The simulated and experimental local strain amplitudes can be compared at the same level.

This work leads to the following prospects:

- From the experimental side, we propose to investigate the following points. First, tensile tests with strain rate changes should be carried out for zirconium alloys with lower oxygen content (inferior to 20 wt ppm) in order better characterize the influence of oxygen content on the macroscopic response such as in the SRS versus temperature diagram and the relaxation behavior. Besides, relaxation tests with unloading should be carried out at temperatures, higher than $400°C$, for instance $500°C$, $600°C$ in order to give more accurately not only the deformation mechanisms, especially for the dragging mode of Zr702, but also the various recovery mechanisms and their kinetics.

- Regarding numerical aspects, we suggest to identify the material parameters for Zr702 with all the experimental data, including tensile tests with strain rate changes and relaxation tests at various temperatures ($100°C$, $200°C$, $300°C$, $400°C$). The viscosity parameter K which is closely associated with the apparent activation volume, and its variations with the ageing time, t_a and with the temperature should be introduced in the constitutive equations. The two dimensional field measurements observed on the millimeter scale and the identification of the strain ageing model using calculations with a structure should be associated.

- Multiscale modeling of strain ageing modeling should be investigated at the grain level and at the dislocation level. The various scale transitions necessary to go from the single–crystal to the polycrystalline behavior must be explored.

- The localization phenomena observed for both zirconium alloys Zr702 and ZrHf on the millimeter scale in laser scanning extensometry and predicted by the strain ageing model, though not visible on the macroscopic curves, may play a significant role in fracture processes. This major point should be investigated in the future in the temperatures range $20°C$–$600°C$ for zirconium alloys.

- Other materials such as C–Mn steels are subjected to SSA and DSA, that induce Lüders or PLC strain localizations and a reduction in fracture toughness. Especially, C–Mn steels used for the secondary cooling systems of PWR are sensitive to strain ageing at in–service temperature. The study of Belotteau (Belotteau, 2004) is devoted to the prediction of the mechanical behavior and especially the fracture resistance of C–Mn steels in presence of DSA.

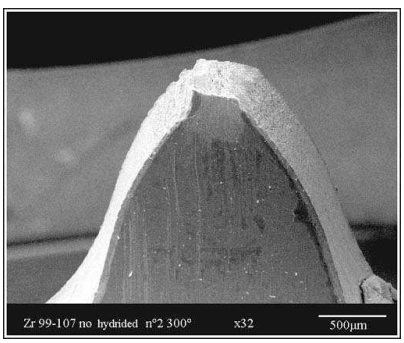

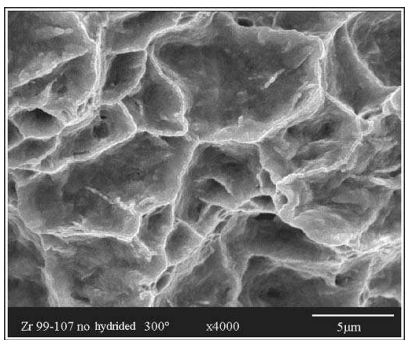

Appendices

Chapter -I-

Zirconium and its alloys

This appendix gives some generalities about zirconium and its alloys, mainly taken in (Bailly et al., 1996; Lemaignan, 2004).

I.1 Physical properties and crystalline structure of the h.c.p. zirconium

Zirconium is a metal of the second class of transition. Zirconium exhibits two allotropic phases, the h.c.p. α phase (stable at low temperatures) and the c.c. β phase (at high temperatures). In the periodic table of elements, zirconium is in the IV B column between titanium and hafnium. The α–β transition is observed at $864°C$. The melting temperature is $1855°C$, which is the bound of the heat–resistant metals. The main physical properties are copied out in table I.1.

Table I.1 : The main physical properties of zirconium.

Property at room temperature	Unity	Mean (or for a tube)	<a> direction	<c> direction
Young modulus	GPa	axial = 102 radial = 92	99	125
Dilatation coefficient	K^{-1}	axial = $5.6.10^{-6}$ radial = $6.8.10^{-6}$	$5.2.10^{-6}$	$7.8.10^{-6}$
Crystalline parameter	nm	-	0.3233	0.5147
Specific heat	$J.kg^{-1}.K-1$	276	-	-
Thermic conductibility	$W.m^{-1}.K^{-1}$	22	-	-
Capture section of thermal neutrons	barn	0.185	-	-

Table I.1 shows that zirconium exhibits a high anisotropy for many physical properties.

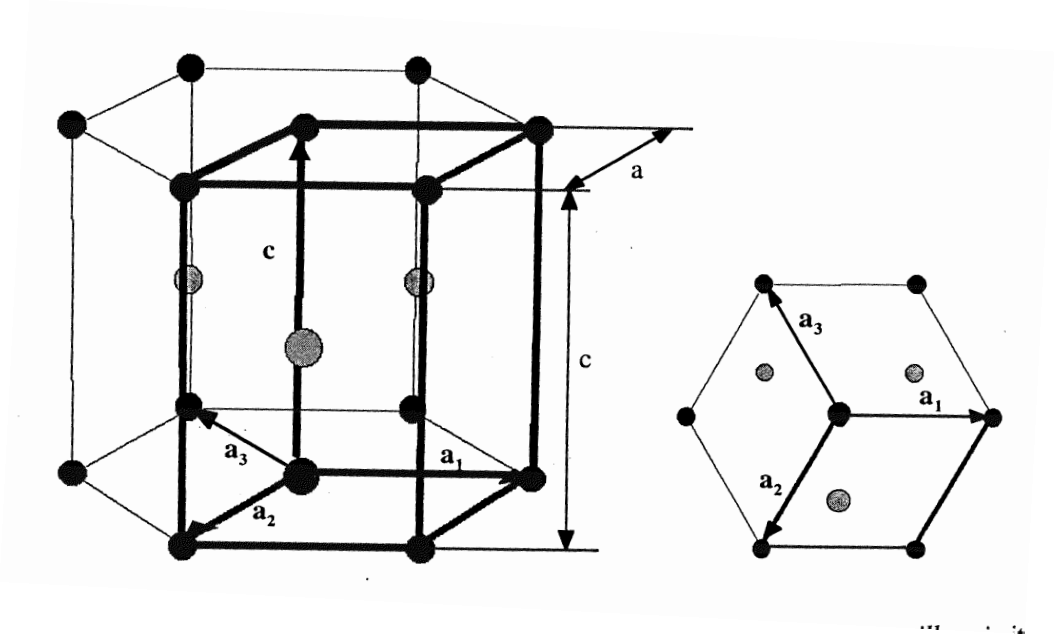

Figure I.1 : Crystalline h.c.p. mesh.

This characteristic of the hexagonal structure is also important for the deformation mechanisms or the diffusion processes. Indeed, the elementary mesh of α zirconium, hexagonal compact showed in figure I.1 has a ratio $c/a = 1.583$, corresponding to a slight expansion in the <a> direction contrary to the ideal pile ($2\sqrt{2/3}$). However, this anisotropy leads to be reduced with increasing temperatures due to higher thermal dilatation in the <c> direction. The h.c.p. structure corresponds to a compact pile of dense plans, parallel to the basal plane. The pile sequence is ABAB. This structure can be represented by an elementary mesh with two atoms A and B with coordinates (0, 0, 0) and (2/3, 1/3, 1/2) respectively (see figure I.1).

The two parameters which define this structure are the edge a of the basal hexagon and the height c of the prism. The perfect compactness ratio, corresponding to the hard sphere model is $c/a = \sqrt{(8/3)}$, but none metal have the perfect compactness. Generally, the hexagonal metals are classified conventionally in two classes according to the value of c/a inferior or superior to the ideal value. In α zirconium, the ratio is inferior to this value. It changes slightly as a function of temperature and is equal to 1.593 at room temperature (Lustmann and Kerze, 1955). In order to define the crystallographic plans, four axis with the following coordinates are considered:

- three axis a_1, a_2 and a_3 at 120° in the basal plan with $a_3 = -(a_1 + a_2)$,
- the c prismatic axis.

The directions and the atomic plans are indicated according to the Miller–Bravis method. In this case, the normal of the plan with index (h k i) has for indexes [h k i$\frac{3}{2}(\frac{a}{c})^2$l].

In the crystalline lattice, two types of interstitial sites are present, the tetrahedral sites and the octahedral sites. The radius of these sites for the h.c.p. zirconium structure are given in table I.2. The atomic radius of the interstitial and substitutional elements are given in table I.3. Comparing these values, it is clear that only the octahedral sites can contain interstitial elements another than hydrogen.

Table I.2 : Radius of interstitial sites in zirconium

Nature of the interstitial site	Radius of the site when $c/a > \sqrt{(8/3)}$	α zirconium
Octahedral	$\frac{1}{2\sqrt{3}}[\sqrt{4+3/4(c/a)^2}-\sqrt{1+3/4(c/a)^2}]a$	0.68
Tetrahedral	$\frac{1}{2\sqrt{3}}[\sqrt{2+4/3(a/c)^2+3/4(c/a)^2}-\sqrt{1+3/4(c/a)^2}]a$	0.37

Table I.3 : Atomic radius of interstitial elements

Interstitial elements	Atomic radius (Å)
H	0.46
O	0.60
N	0.71
C	0.77
Substitutional elements	Atomic radius (Å)
Sn	1.40
Nb	1.43
Hf	1.56

I.2 Deformation mode observed in the h.c.p. zirconium

Perfect and non perfect dislocations in hexagonal metals

The potential Burgers vectors for the glide directions are represented in a double tetrahedron of Thompson (see figure I.2). Three types of perfect dislocations and three types of non perfect dislocations, resulting from the dissociation of perfect dislocations are present in the hexagonal metals (see table I.4). The energy of these dislocations are proportional to the square of burgers vector.

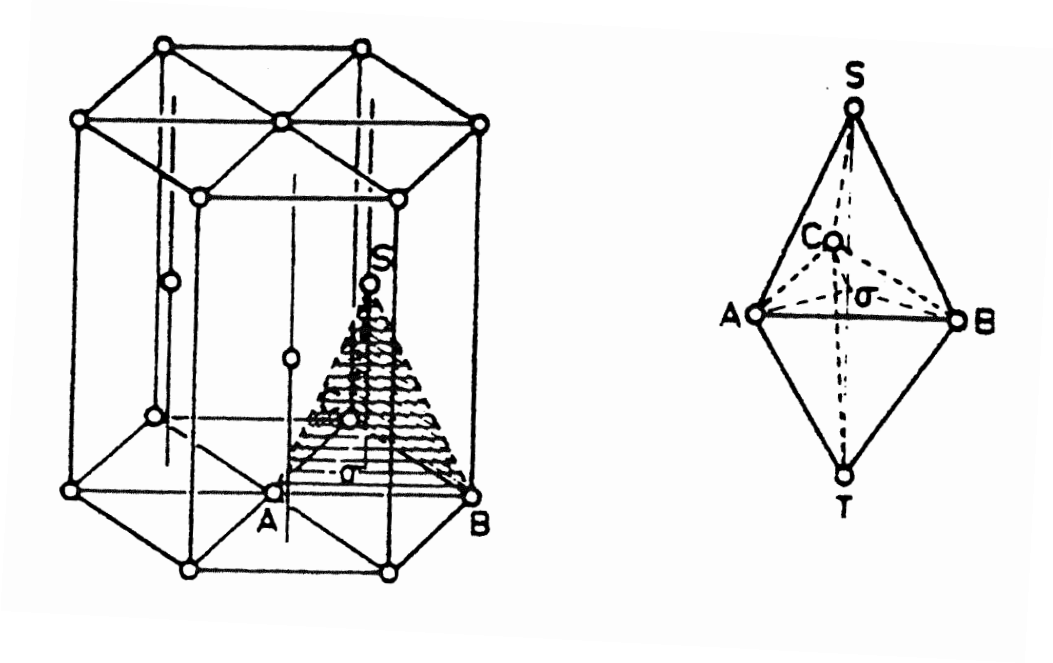

Figure I.2 : Double tetrahedron of Thompson.

Table I.4 : Perfect and non perfect dislocations in hexagonal metals

Crystallographic notation	Vector notations	Representation above the tetrahedron	Nature of the dislocation
1/3<11-20>	$\overrightarrow{a}$	AB	perfect
[0001]	$\overrightarrow{c}$	ST,TS	perfect
1/3<11-23>	$\overrightarrow{c} + \overrightarrow{a}$	ST+AB	perfect
1/3<10-10>	$\overrightarrow{p}$	Aσ, Bσ	non perfect
1/6<20-23>	$1/2\overrightarrow{c} + \overrightarrow{p}$	AS, BS	non perfect
1/2[0001]	$1/2\overrightarrow{c}$	σS, σT	non perfect

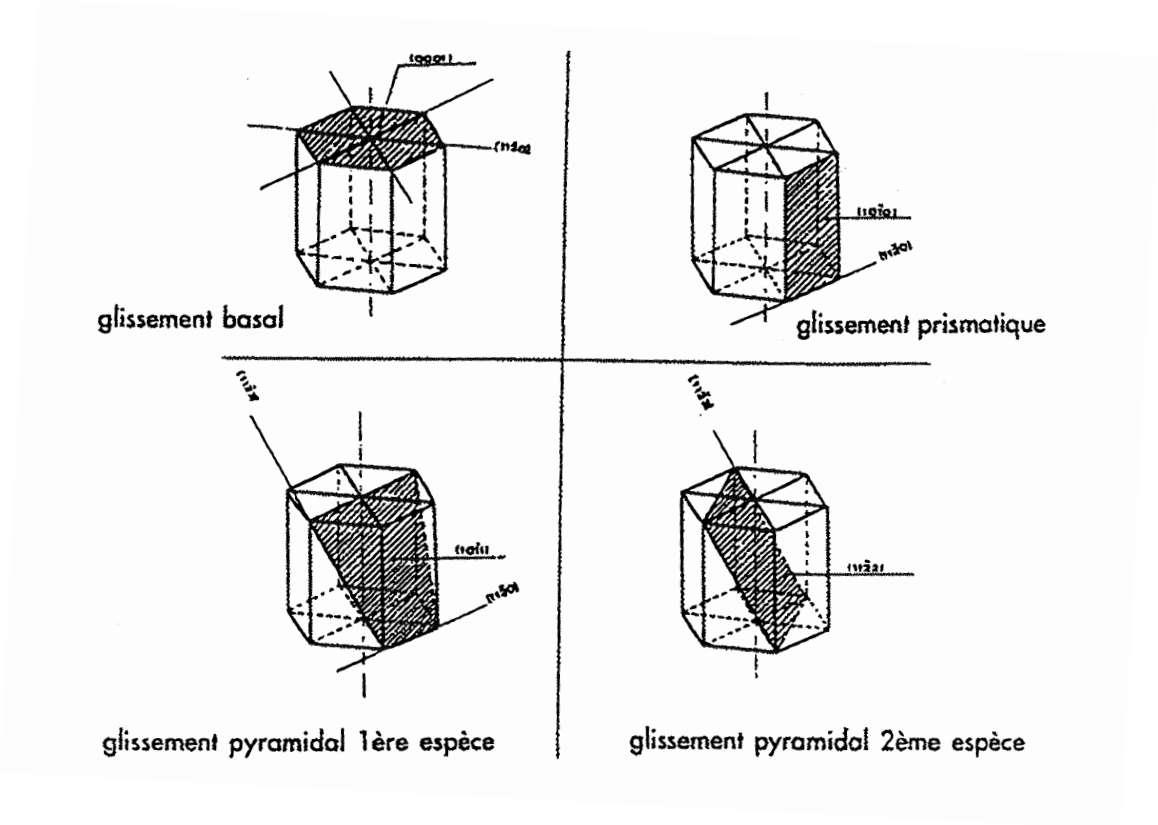

Figure I.3 : Various glide modes observed in hexagonal metals.

Various glide modes observed in hexagonal metals

Tenckhoff (Tenckhoff, 1988) studied the deformation modes in zirconium. Four glide modes are generally observed in hexagonal metals:

- the basal glide (0001)1/3<11-20>,
- the prismatic glide (10-10)1/3<11-20>,
- the first specie pyramidal glide (10-11)1/3<11-20> ou 10-111/3<11-23>,
- the second specie pyramidal glide (11-22)1/3<11-23>.

Figure I.3 summarizes the various glide modes observed in hexagonal metals. Generally, one glide mode is easier to activate than the others, labeled the main glide. For zirconium, the main glide is the prismatic glide. The basal glide and the two pyramidal glides are the secondary glides.

I.3 Development of zirconium alloys

As we know, there are two interstitial sites in the zirconium lattice. Only octahedral sites are able to receive most of the solute elements because the volume of tetrahedral site is lower than this of octahedral site. The main alloying elements are the following: tin, chromium, iron, niobium and oxygen. These elements were chosen in order to improve the mechanical properties and the corrosion strengthening of zirconium, used in the nuclear industry.

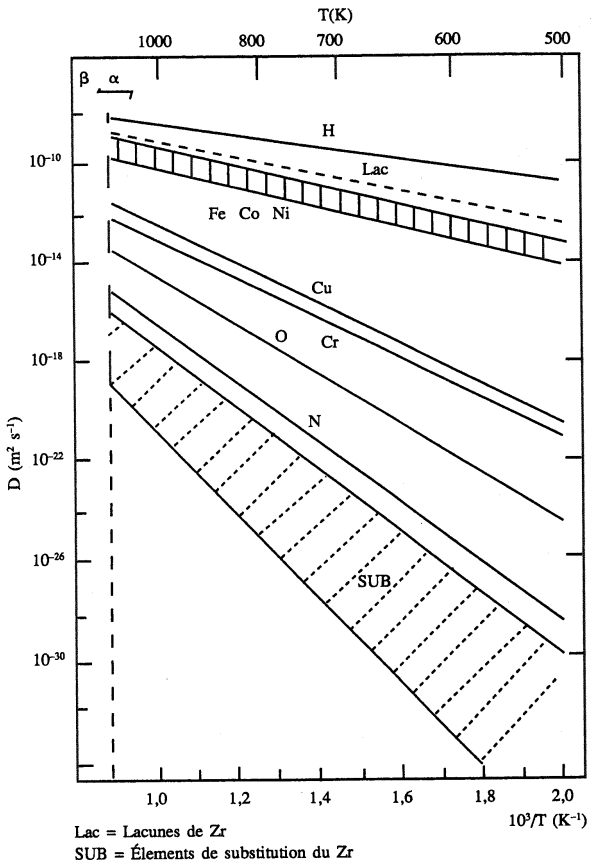

Figure I.4 : Diffusion coefficient of the main solute elements in zirconium (Hood, 1988).

For instance:

- oxygen (interstitial–octahedral site) is an hardening element at low temperatures. This atom stabilizes the α phase,
- tin (substitutional site) which is the starting point of the elaboration of Zircaloy. This element leads to the reduction of the β domain. It involves the corrosion strengthening and is an hardening element at higher temperatures, in particular in creep behavior,
- niobium (substitutional site) which is the main element of the second class of industrial alloys. This element is solvable at any content in the β phase and improves the creep strengthening at low stresses, contrary to high stresses. Niobium improves also the corrosion strengthening.

Figure I.4 shows the diffusion coefficients of the solute elements in zirconium. The substitutional elements are also mobile and their diffusivity is highly dependent on the crystalline direction.
Note that tin (substitutional atom), but also nickel and copper diffuse faster than oxygen (interstitial atom). Hood (Hood, 1988) suggested that these elements diffuse with a dissociative mechanism.

Chapter -II-

Additional experimental results

This appendix is divided into three sections, presenting: the macroscopic curves of tensile tests at constant applied strain, the strain rate changes experiments and the relaxation with unloadings tests. All these mechanical tests were carried out at various temperatures between $20°C$ and $400°C$.

II.1 Tensile tests at constant applied strain rate

In chapter B, the macroscopic responses are compared taking the effect of applied strain rate at each temperature into account. An other view is to plot the true stress–true strain responses of transverse Zr702 and longitudinal Zr702 as a function of temperature ($100°C$, $200°C$, $300°C$), keeping constant the applied strain rate ($10^{-3}s^{-1}$, $10^{-4}s^{-1}$, $10^{-5}s^{-1}$) as shown in figures II.1, II.2, II.3.

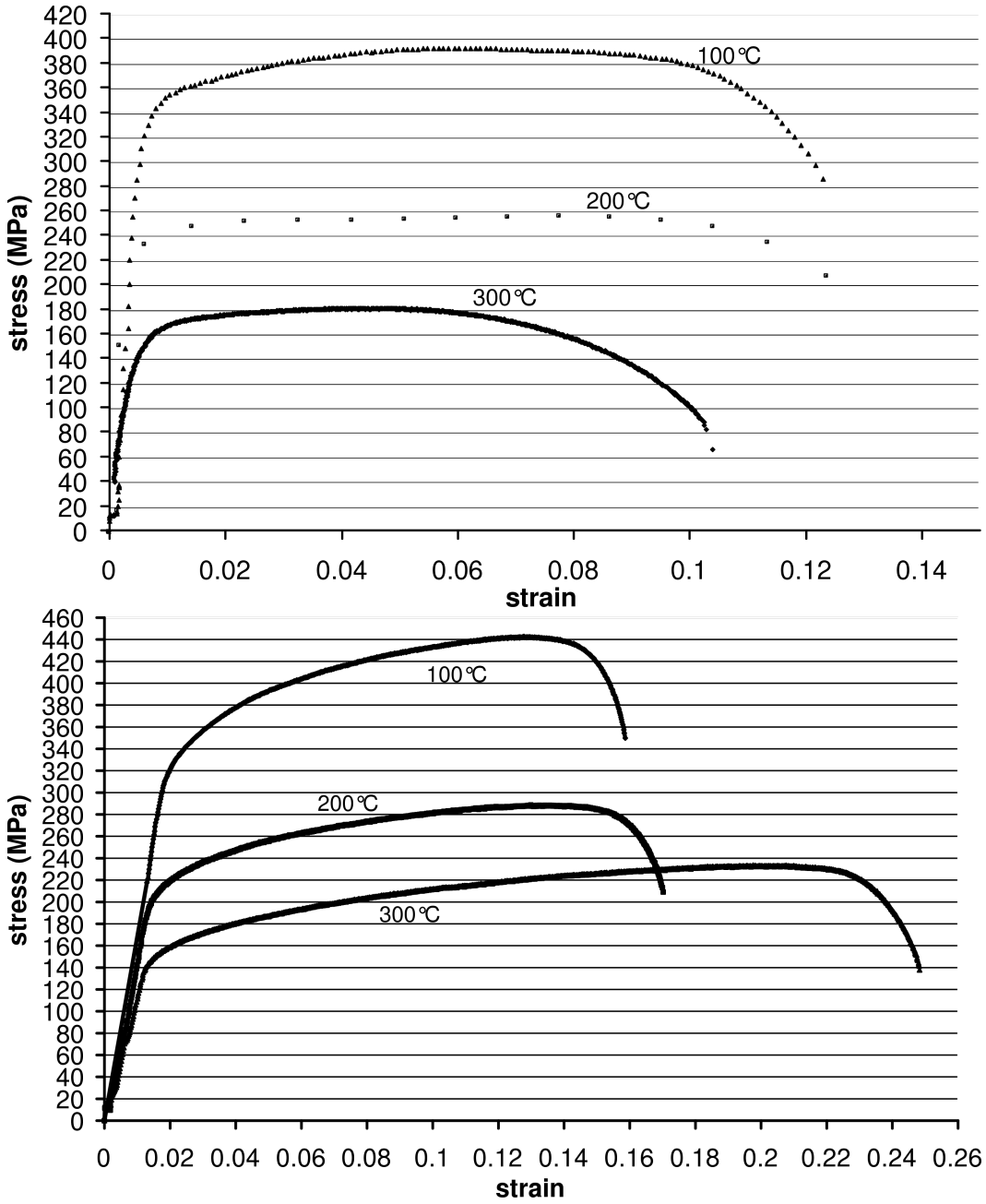

Figure II.1 : Influence of temperature on the macroscopic tensile curve at $10^{-3}s^{-1}$: (a) transverse Zr702, (b) longitudinal Zr702.

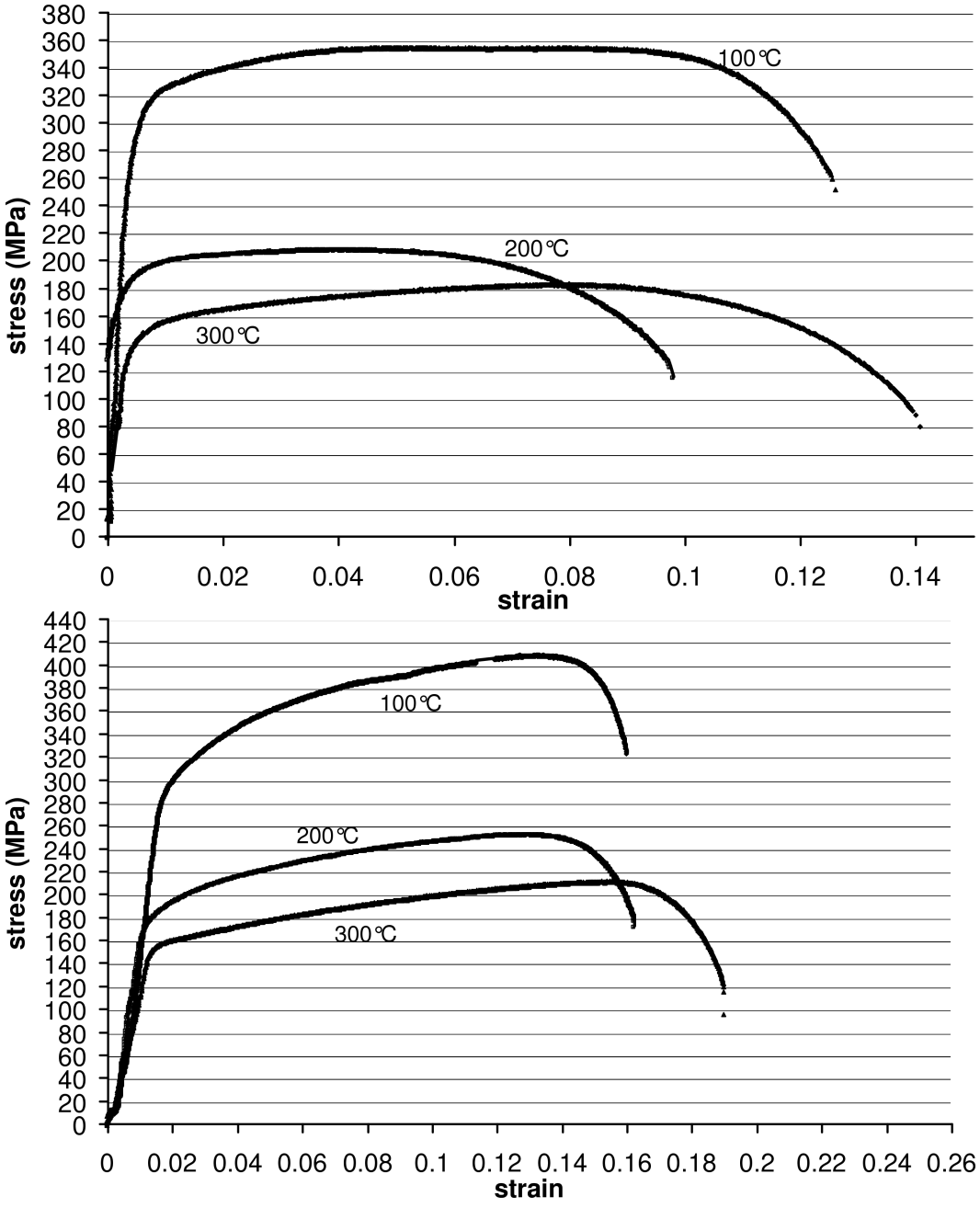

Figure II.2 : Influence of temperature on the macroscopic tensile curve at $10^{-4}s^{-1}$: (a) transverse Zr702, (b) longitudinal Zr702.

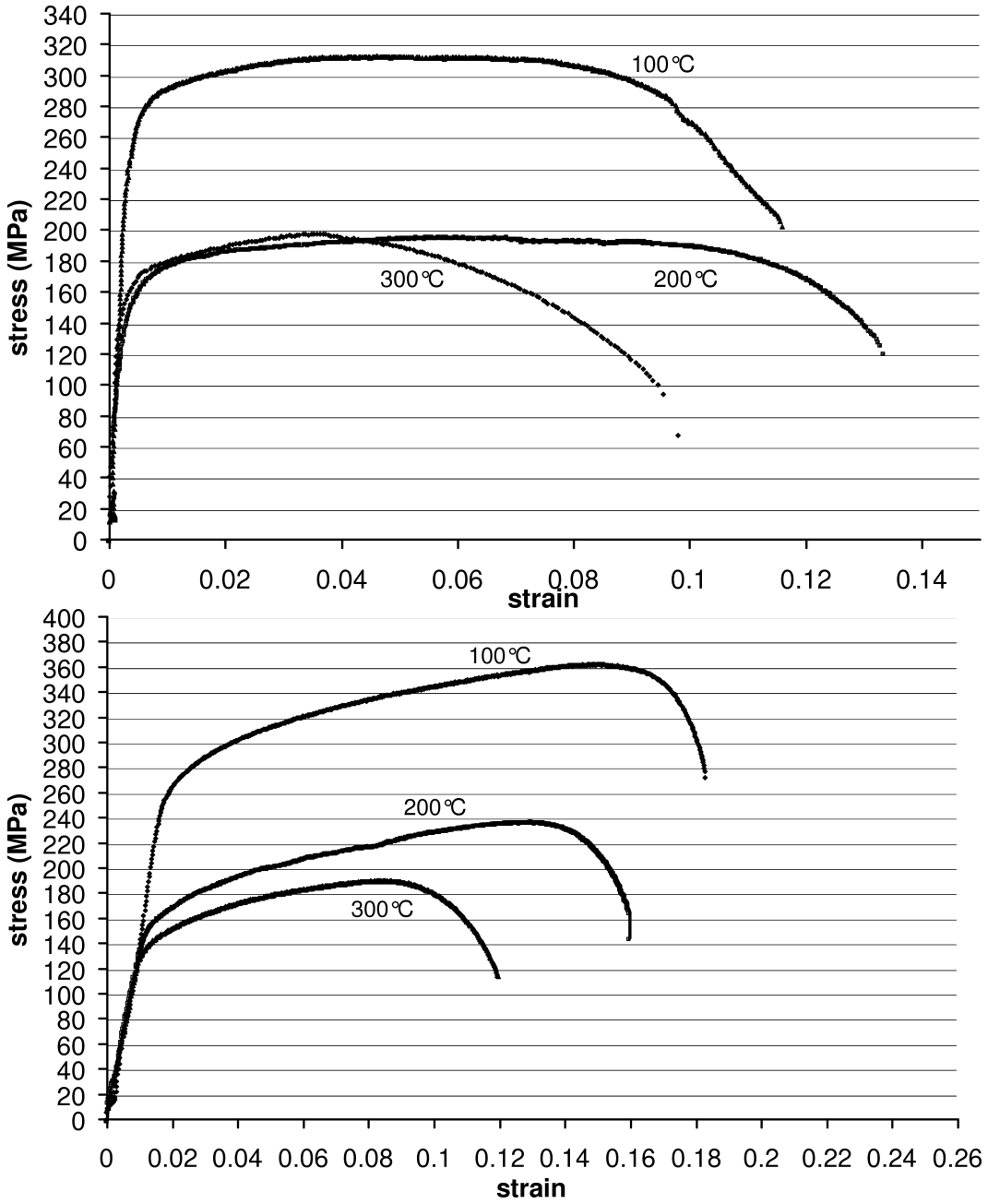

Figure II.3 : Influence of temperature on the macroscopic tensile curve at $10^{-5}s^{-1}$: (a) transverse Zr702, (b) longitudinal Zr702.

II.2 Tensile tests with strain rate changes

Table II.1 gives the values of the 0.2% yield stress at $10^{-4}s^{-1}$ and Young's modulus measured from the unloading branch at $10^{-4}s^{-1}$ as a function of temperature for all the materials tested.

Table II.1 : Evolution of the 0.2% yield stress at $10^{-4}s^{-1}$ and Young's modulus determinated at unloading of $-10^{-4}s^{-1}$ as a function of temperature for Zr702, ZrHf, ZrHf–Nb, ZrHf–O, ZrHf–Nb–O.

Materials	Temperature ($°C$)	0.2% yield stress (MPa)	Young's modulus (GPa)
Zr702	20	473	77
	100	298	76
	200	234	70
	300	174	56
	400	154	54
ZrHf	20	229	70
	100	150	69
	200	129	65
	300	97	52
	400	60	64
ZrHf–O	20	-	-
	100	-	-
	200	122	69
	300	74	66
	400	72	69
ZrHf–Nb	20	-	-
	100	-	-
	200	175	60
	300	88	51
	400	93	57
ZrHf–Nb–O	20	-	-
	100	-	-
	200	203	78
	300	138	68
	400	150	67

To have a better view of the influence of oxygen and niobium contents, figures II.5, II.4, II.6 show the comparison of the macroscopic true stress–plastic strain curves between Zr702 and ZrHf–O, ZrHf–Nb and ZrHf–Nb–O respectively at various temperatures.

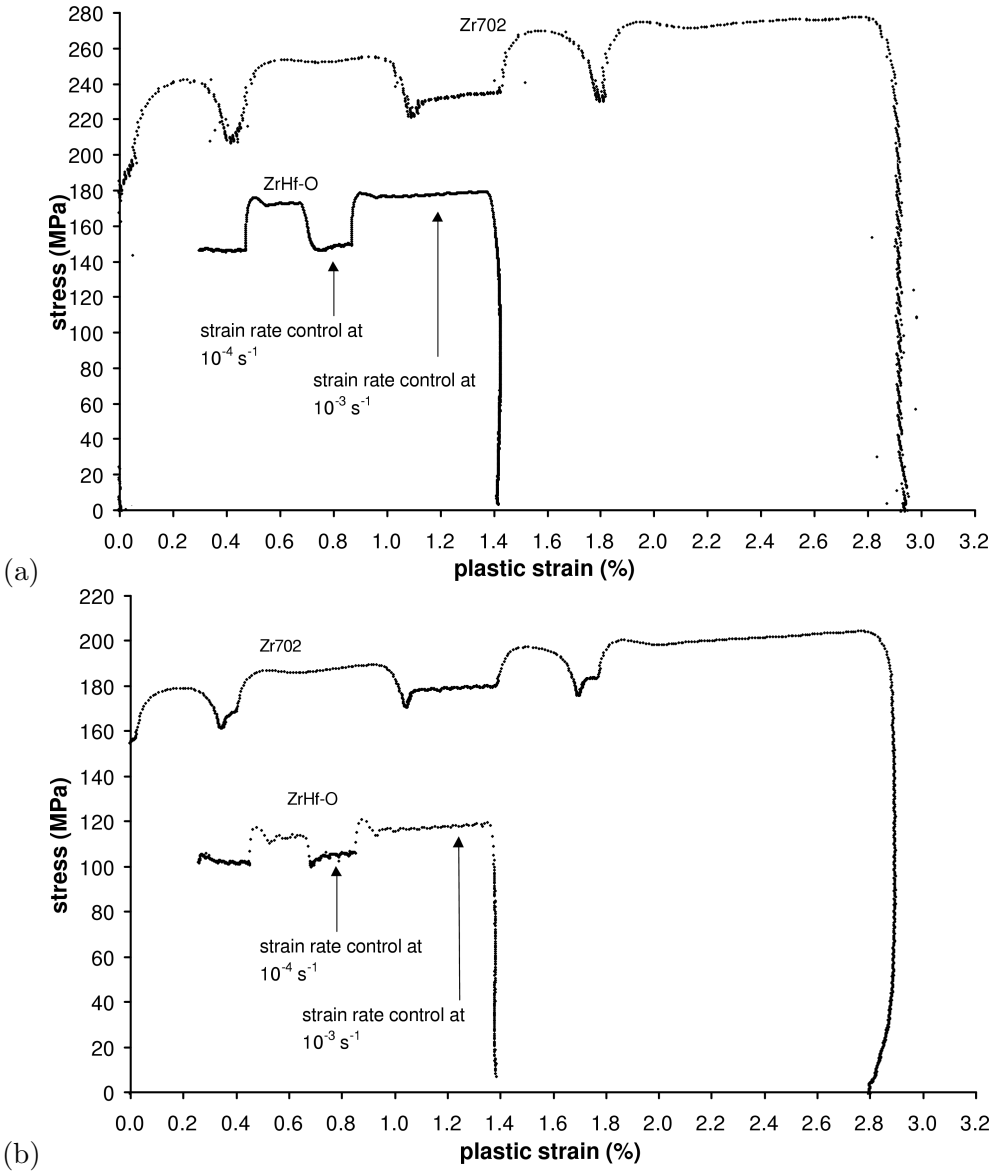

Figure II.4 : Influence of interstitial and substitutional atoms on the macroscopic true stress–plastic strain curves of the tensile tests with strain rate changes of Zr702 and ZrHf–O at : (a) $200°C$, (b) $300°C$.

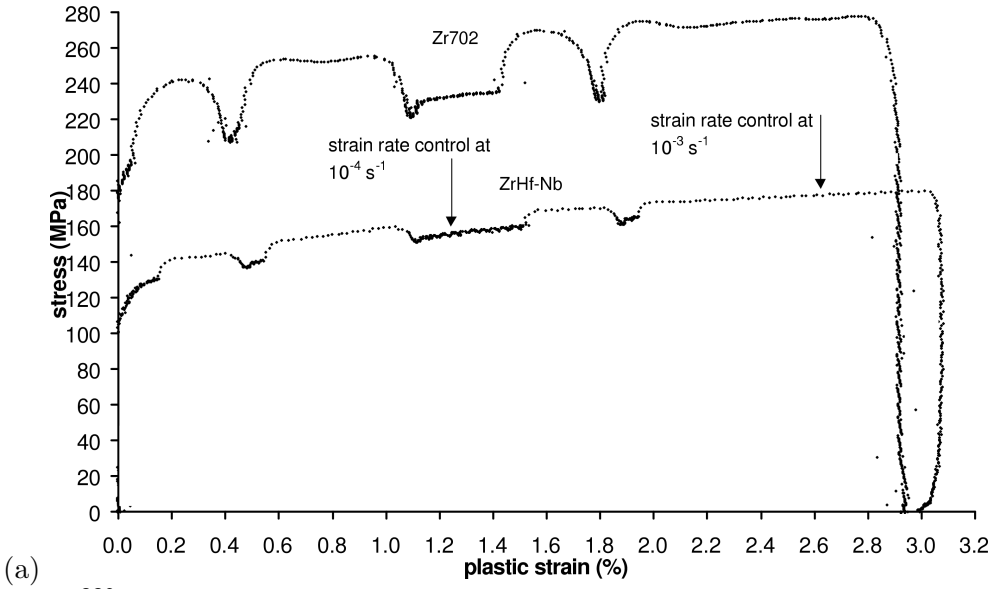

(a)

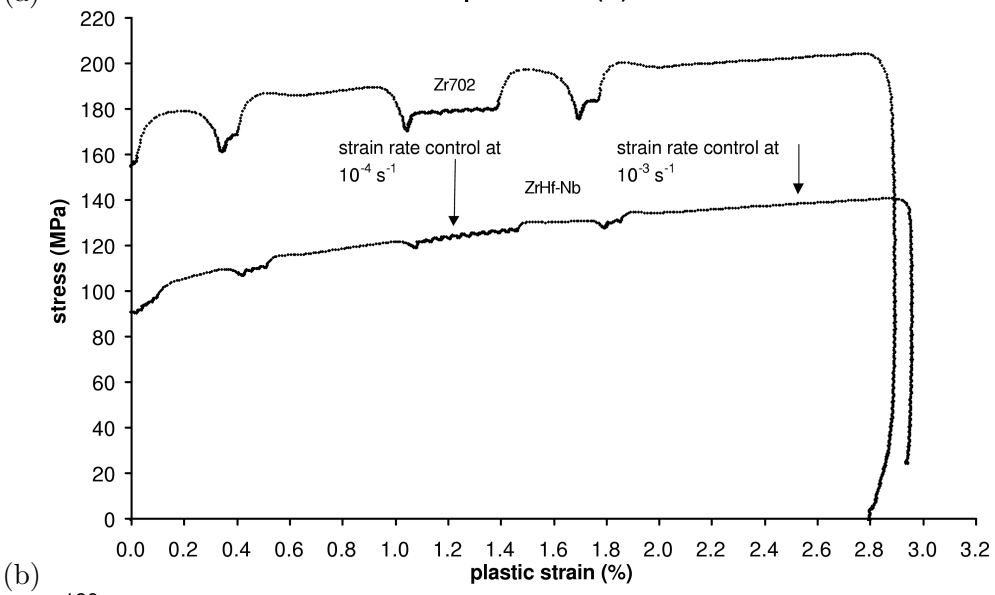

(b)

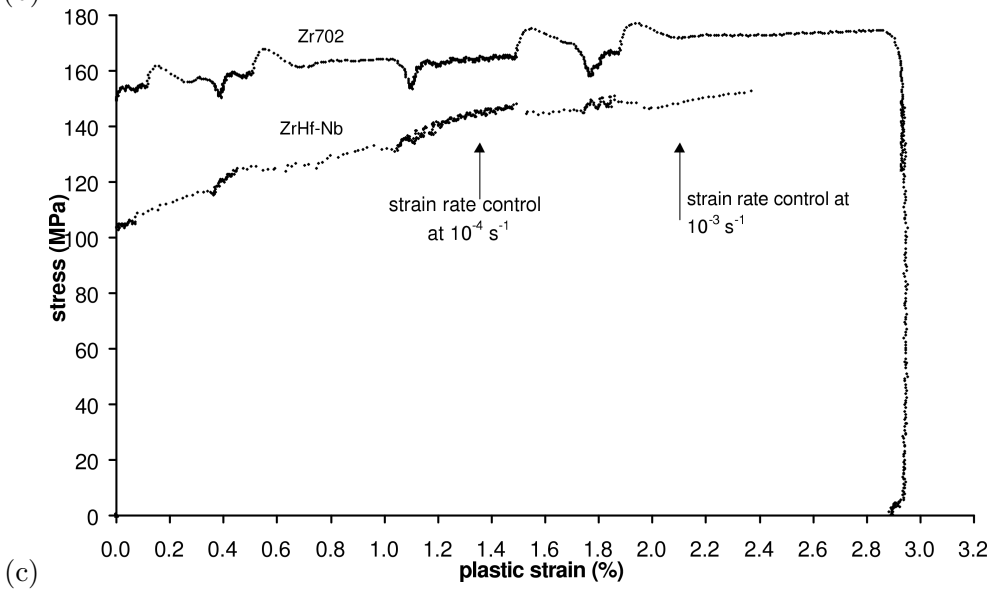

(c)

Figure II.5 : Influence of interstitial and substitutional atoms on the macroscopic true stress–plastic strain curves of the tensile tests with strain rate changes of Zr702 and ZrHf–Nb at : (a) 200°C, (b) 300°C, (c) 400°C.

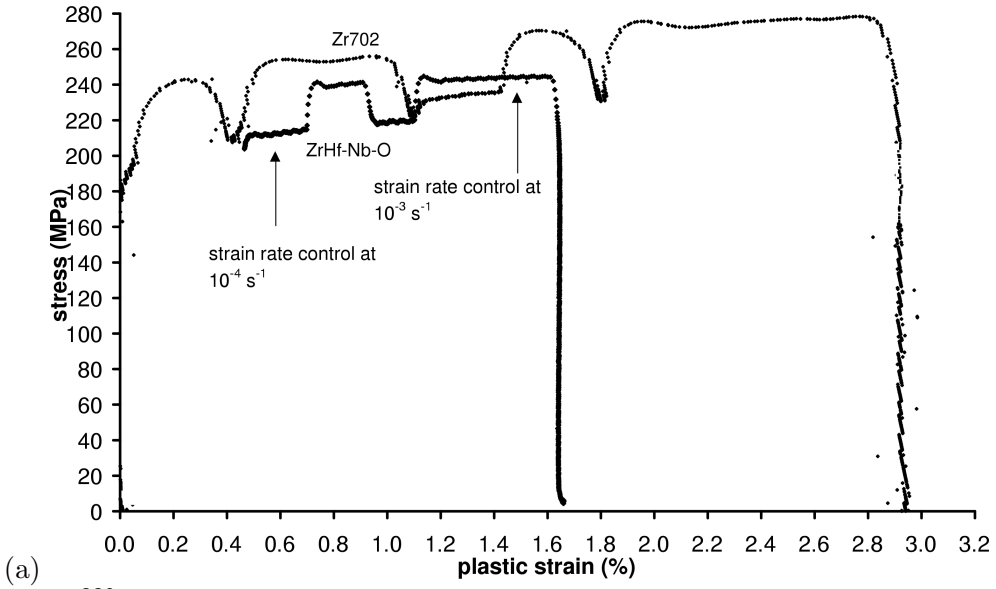

(a)

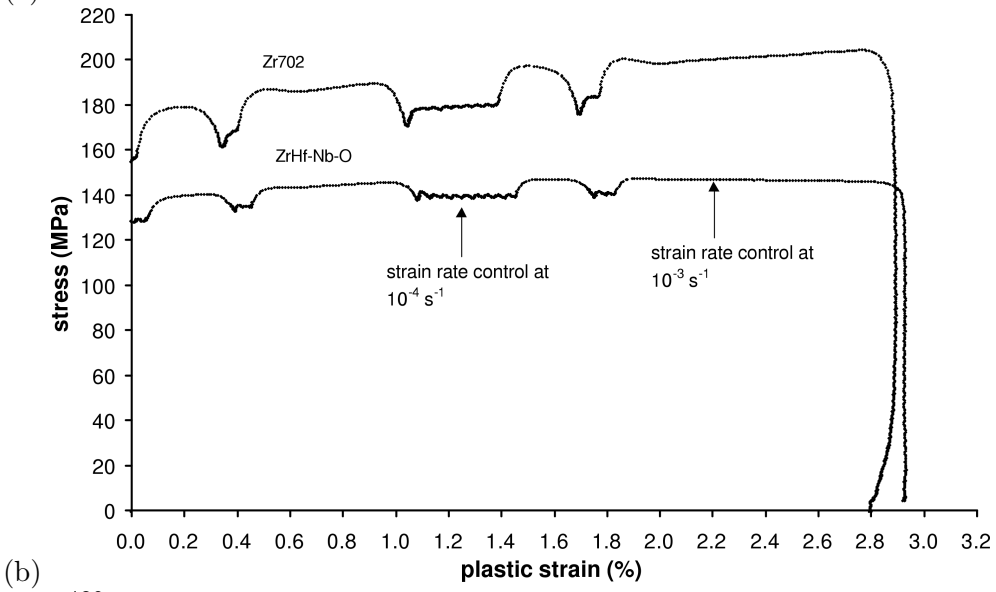

(b)

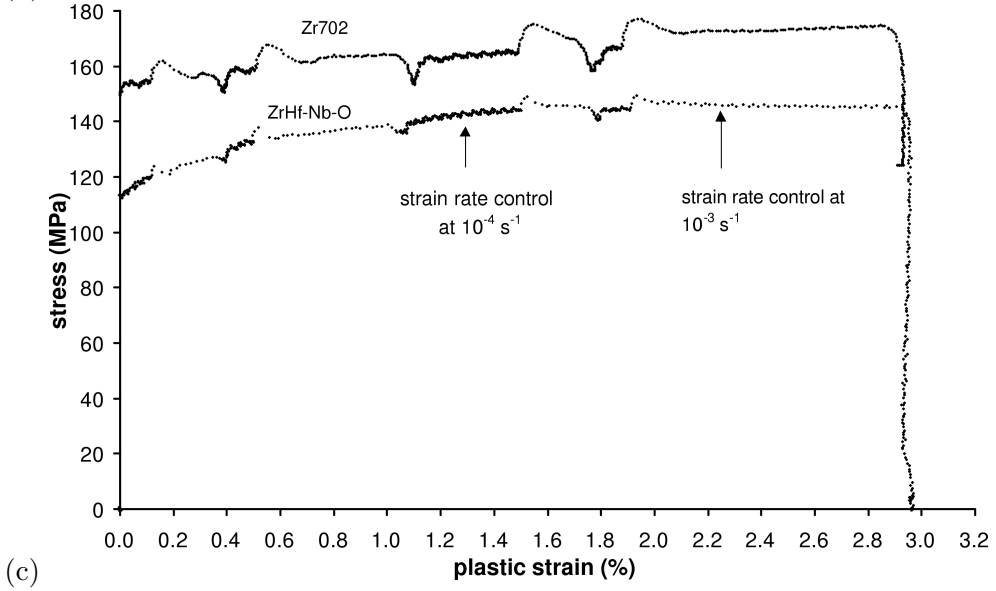

(c)

Figure II.6 : Influence of interstitial and substitutional atoms on the macroscopic true stress–plastic strain curves of the tensile tests with strain rate changes of Zr702 and ZrHf–Nb–O at : (a) 200°C, (b) 300°C, (c) 400°C.

Tables II.2, II.3, II.4, II.5, II.6 give the values of Strain Rate Sensitivity (SRS) for ZrHf–O, Zr702, ZrHf, ZrHf–Nb, ZrHf–Nb–O respectively.

Table II.2 : Evolution of SRS as a function of temperature and plastic strain for ZrHf–O.

Materials	Temperature ($°C$)	SRS (MPa)	Plastic strain (%)
ZrHf–O	200	10.7	0.5
		10.7	0.7
		11.4	0.9
	300	5.7	0.5
		5.6	0.7
		5.6	0.9

Table II.3 : Evolution of SRS as a function of temperature and plastic strain for Zr702.

Materials	Temperature ($°C$)	SRS (MPa)	Plastic strain (%)
Zr702	20	9.7	0.2
		9.8	0.4
		9.8	0.5
		8.7	1.1
		10.9	1.5
		10.8	1.8
		7.9	2.
	100	6.3	0.1
		11.6	0.4
		11.7	0.5
		15.4	1.1
		13.9	1.5
		15.2	1.7
		15.3	1.8
	200	18.5	0.07
		14.1	0.4
		12.6	0.5
		11.9	1.1
		14.1	1.4
		14.2	1.7
		14.1	1.8
	300	8.7	0.04
		6.1	0.3
		5.2	0.4
		5.2	1.
		5.6	1.4
		5.1	1.7
		5.6	1.8
	400	1.4	0.1
		0	0.4
		1.4	0.5
		1.5	1.1
		2.9	1.5
		2.2	1.8
		2.1	1.9

Table II.4 : Evolution of SRS as a function of temperature and plastic strain for ZrHf.

Materials	Temperature ($°C$)	SRS (MPa)	Plastic strain (%)
ZrHf	20	2.2	0.08
		3.3	0.3
		2.2	0.5
		4.3	1.
		3.3	1.5
		3.8	1.7
		3.3	1.9
	100	3.	0.07
		4.5	0.4
		4.5	0.5
		5.4	1.
		5.4	1.4
		5.4	1.7
		4.5	1.8
	200	2.9	0.1
		4.3	0.4
		4.3	0.5
		5.1	1.1
		4.3	1.5
		4.3	1.7
		4.3	1.8
	300	0.	0.1
		0.9.	0.3
		1.2	0.5
		1.2	1.
		1.2	1.5
		1.2	1.7
		1.7	1.8
	400	0	-
		0	0.3
		0	0.4
		-1.7	1.
		-1.3	1.4
		-1.2	1.7
		-0.6	1.8

Table II.5 : Evolution of SRS as a function of temperature and plastic strain for ZrHf–Nb.

Materials	Temperature ($°C$)	SRS (MPa)	Plastic strain (%)
ZrHf–Nb	200	3.6	0.2
		3.6	0.4
		3.6	0.5
		4.3	1.1
		3.5	1.5
		3.5	1.8
		3.5	1.9
	300	1.7	0.1
		1.3	0.4
		1.3	0.5
		1.2	1.
		1.1	1.5
		0.8	1.8
		0.9	1.9
	400	-0.4	0.08
		-0.4	0.3
		-0.4	0.4
		-0.5	1.
		-0.9	1.5
		-0.8	1.7
		-0.8	1.9

Table II.6 : Evolution of SRS as a function of temperature and plastic strain for ZrHf–Nb–O.

Materials	Temperature ($°C$)	SRS (MPa)	Plastic strain (%)
ZrHf–Nb–O	200	10.9	0.7
		9.8	1
		9.8	1.2
	300	3.3	0.08
		2.7	0.4
		3.2	0.5
		2.7	1.1
		3.3	1.5
		2.8	1.7
		2.8	1.8
	400	0.	0.1
		-0.4	0.4
		0.	0.5
		0.	1.1
		0.	1.5
		0.4	1.8
		0.5	1.9

II.3 Relaxation tests with unloading

Tables II.7, II.8 give the values of the stress at which relaxation test begins σ_0 and Young's modulus as a function of the number of relaxation cycle associated with the cumulated plastic strain level (which is the sum of plastic strain due to loading and induced from the relaxation), for Zr702 and ZrHf respectively.

Table II.7 : General characteristics of the various relaxation cycles for Zr702.

Temperature ($°C$)	Number of the relaxation cycle	Cumulated plastic strain level (%)	σ_0 (MPa)	Young's modulus (MPa)
$100°C$	1	0.2	255	89200
	2	0.5	288	81184
	3	0.9	297	78115
	4	2.1	302	71129
	5	2.8	302	69864
$200°C$	1	0.2	166	105540
	2	0.5	207	100390
	3	0.9	218	95432
	4	1.3	223	94131
	5	1.9	227	92355
	6	2.2	224	89573
	7	2.4	225	88384
	8	3.1	224	87172
$300°C$	1	0.2	142	123800
	2	0.8	194	93905
	3	1.1	191	93589
	4	1.7	199	92063
$400°C$	1	0.2	135	71069
	2	0.5	147	71879
	3	1.2	158	73883

Table II.8 : General characteristics of the various relaxation cycles for ZrHf.

Temperature ($^\circ C$)	Number of the relaxation cycle	Cumulated plastic strain level (%)	σ_0 (MPa)	Young's modulus (MPa)
$100^\circ C$	1	0.2	175	100200
	2	0.4	185	93405
	3	1.2	192	89829
	4	1.8	204	83767
	5	2.1	204	82532
	6	2.4	205	81673
$200^\circ C$	1	0.2	129	75762
	2	0.5	142	79298
	3	0.9	148	71660
	4	1.3	156	70959
$300^\circ C$	1	0.2	98	73194
	2	0.5	111	73790
	3	1.	127	71790
	4	1.6	138	72436
	5	1.9	138	69906
	6	2.2	139	71306
$400^\circ C$	1	0.2	102	-
	2	0.4	110	65214
	3	1.1	122	-

Tables II.9, II.10 give the values of plastic strain created during the relaxation test ($\varepsilon_{p\ relax}$), the total decrease of stress during relaxation test ($\Delta\sigma_{relax}$) as a function of temperature and the number of relaxation cycle for Zr702 and ZrHf respectively.

Table II.9 : Relaxation characteristics of the various relaxation cycles for Zr702.

Temperature ($^\circ C$)	Number of the relaxation cycle	$\varepsilon_{p\ relax}$ (%)	$\Delta\sigma_{relax}$ (MPa)	Apparent activation volume V_a ($nm^3.atom^{-1}$)
$100^\circ C$	1	0.14	116	$V_{a1} = 0.40$
	2	0.15	137	$V_{a1} = 0.35$
	3	0.15	125	$V_{a1} = 0.38$
	4	0.14	121	$V_{a1} = 0.39$
	5	0.13	114	$V_{a1} = 0.41$
$200^\circ C$	1	0.07	61	$V_{a1} = 0.71$
	2	0.07	65	$V_{a1} = 0.67$
	3	0.08	68	$V_{a1} = 0.77$
	4	0.09	82	$V_{a1} = 0.90$
	5	0.06	65	$V_{a1} = 0.69$
	6	0.07	67	$V_{a1} = 0.74$
	7	0.07	65	$V_{a1} = 0.67$
	8	0.07	66	$V_{a1} = 0.82$
$300^\circ C$	1	0.1	65	Non defined slope
	2	0.09	56	Non defined slope
	3	0.07	44	Non defined slope
	4	0.09	58	Non defined slope
$400^\circ C$	1	0.16	88	$V_{a2} = 0.75$
	2	0.17	98	$V_{a2} = 0.69$
	3	0.18	111	$V_{a2} = 0.64$

Table II.10 : Relaxation characteristics of the various relaxation cycles for ZrHf.

Temperature ($^\circ C$)	Number of the relaxation cycle	$\varepsilon_{p\ relax}$ (%)	$\Delta\sigma_{relax}$ (MPa)	Apparent activation volume V_a ($nm^3.atom^{-1}$)
$100^\circ C$	1	0.11	66	$V_{a1} = 0.80$
	2	0.15	137	$V_{a1} = 0.85$
	3	0.15	125	$V_{a1} = 1.0$
	4	0.14	121	$V_{a1} = 0.86$
	5	0.13	114	$V_{a1} = 0.99$
	6	0.13	114	$V_{a1} = 0.99$
$200^\circ C$	1	0.05	30	$V_{a1} = 1.72$
	2	0.05	32	$V_{a1} = 1.83$
	3	0.05	31	$V_{a1} = 1.98$
	4	0.05	29	$V_{a1} = 1.99$
$300^\circ C$	1	0.05	29	$V_{a2} = 1.35$
	2	0.04	24	$V_{a2} = 1.3$
	3	0.05	32	$V_{a2} = 1.25$
	4	0.06	36	$V_{a2} = 1.22$
	5	0.06	36	$V_{a2} = 1.19$
	6	0.06	36	$V_{a2} = 1.04$
$400^\circ C$	1	0.12	55	$V_{a2} = 1.49$
	2	0.12	53	$V_{a2} = 1.56$
	3	0.11	74	$V_{a2} = 1.24$

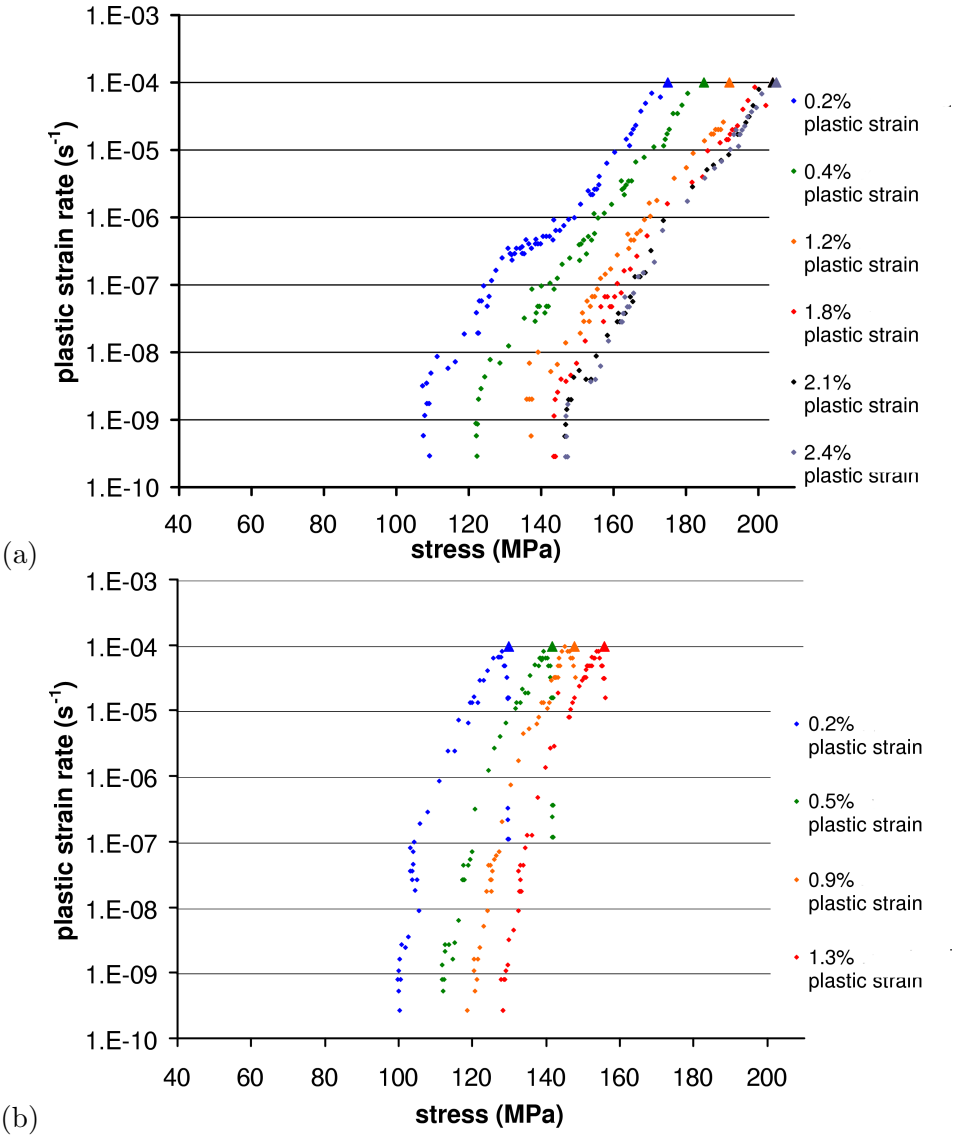

Figure II.7 : Effect of the plastic strain level, plotting the $\log \dot{\varepsilon}_p$ versus σ diagrams for ZrHf at: (a) $100°C$, (b) $200°C$.

The effect of the plastic strain level, plotting the $\log \dot{\varepsilon}_p$ versus σ diagrams for ZrHf at $100°C$, $200°C$, $300°C$ and $400°C$ are shown in figures II.7 and II.8.

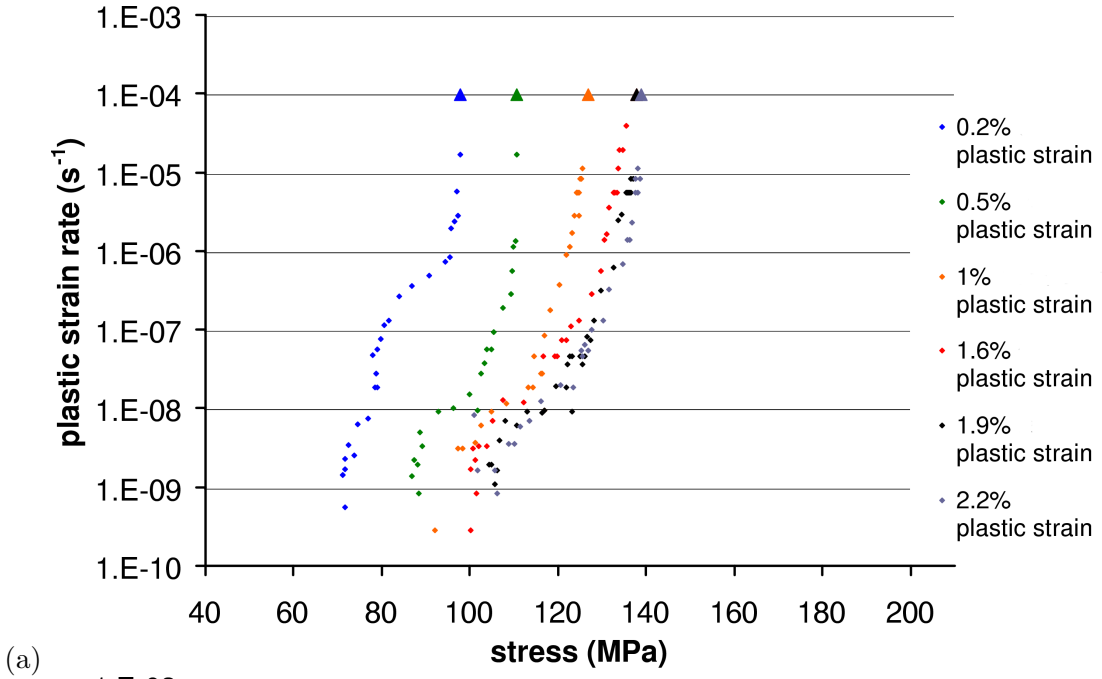

(a)

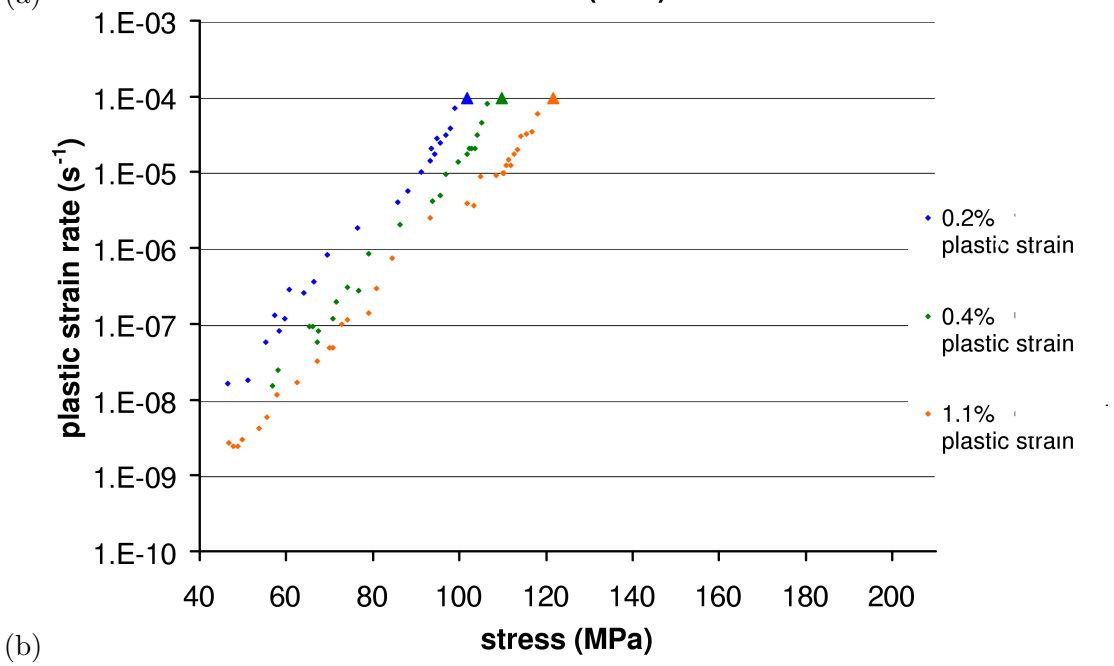

(b)

Figure II.8 : Effect of the plastic strain level, plotting the $\log \dot{\varepsilon}_p$ versus σ diagrams for ZrHf at: (a) $300°C$, (b) $400°C$.

Chapter -III-

The method of the laser scanning extensometry

This appendix is divided into five sections: the selection of materials, the laser extensometer for local strain measurements, the tensile machine and the data analysis. The information given as follows is taken from the thesis of Klose (Klose, 2004).

III.1 Materials, preparation and specimens

To validate the experimental set up before applying it to the zirconium alloys, we chose different materials that we know their mechanical behavior and for which some tests using the laser scanning extensometry were carried out. The materials that we chose are the following:

- the mild steel is a c.c structured interstitial solid solution within the α–phase. It contained 0.15% to 0.25% C,
- the $Al - 3\%Mg$ alloy is a f.c.c structured substitutional solid solution within the α–phase, showing Mg based precipitates, The chemical composition of this technical alloy AA5754 was in all wt.%: 96.15% Al, 3.14% Mg, 0.25% Si, 0.23% Fe, 0.21% Mn,
- the $Al - 4\%Cu$ alloy is a f.c.c disorganized solid solution within the α–phase. It contained in wt.%: 2.6 % Cu, 0.35% Mg.

The preparation for laser extensometric measurements was restricted to apply some white color first and upon this layer black stripes (distance and width 1 mm) were applied. At this state the sample geometry was measured: complete active length, width and thickness. A schematic of a prepared specimen within the specimen holder for tensile tests is shown in figure III.1.

III.2 Laser scanning extensometer

In the following, the operating mode of the commercial laser scanning extensometer [1] is explained, referring to its advantages and limitations especially with respect to the detection

[1] Fiedler Optoelektronik GmbH, Lützen, Germany, http://www.fiedler-oe.de

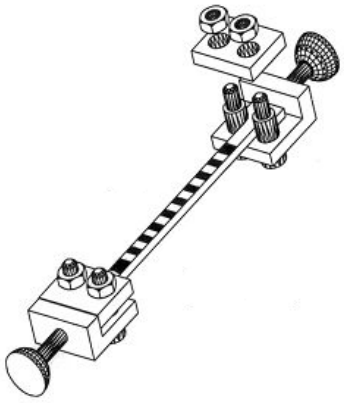

Figure III.1 : Schematic of a prepared specimen within the specimen holder for tensile tests.

of plastic strain inhomogeneities. Figure III.2 shows a schematic of the operating mode of laser extensometer.

A rotating cubic glass prism with a permanently measured rotation frequency of approximately 54 Hz scanned a red laser beam across the sprayed stripy markings. The reflected signal was focused on a photodiode and its intensity was measured. The second derivative gave the time shift between each intensity alteration referring to the stripe structure. With the reference of the initial state and the known rotation frequency those time intervals could be converted to the position or distance in space for all numbered stripes. Changes of the intervals in time, for example due to localized plastic strain as in PLC bands, cracks...showed an increase in strain for the affected markings.

The gage length of the extensometrically recorded sample parts amounts to 30 mm with a grid of up to 12 black and white zones (24 bright–dark boundaries) along the specimen axis. The resolution of displacement is 1 μm ($\delta\Delta\varepsilon = \delta l/l = 0.05\%$ of a 2 mm wide zone). The maximum sampling frequency for stress amount to about 216 Hz for strain, to about 50 Hz due to non ideal polynomials for the description of the four prism faces. On the short specimen length, two thermocouples were fixed additionally.

The main advantages of laser extensometric strain measurements are the variable extensometer gage length up to 50 mm, the contactless and independent measurement of quantity, the location, the extent and kinetics of strain localizations (propagating band width, velocity, strain concentration, strain rate) with high resolution in time and space with the synchronously recorded stress and strain data.

III.3 Tensile machine

For an experimental exploration of PLC effect during strain and stress rate controlled plastic deformation, respectively, a stiff machine was used which could optionally be "softened" by an additional spring within the horizontal tensile axis. In order not to falsify the load cell signal during rapid plastic events the spring was inserted between the pull rod and the specimen. The tensile machine was built by Neuhäuser and Traub (Traub, 1974). The maximum cross head velocity amounts to about 2 mm/s. The load is transmitted to the tensile rod via a ball bearing spindle to reduce friction. The heating up to maximum temperatures of about $300°C$ was obtained by means of two direct thermocoax heating elements that heated the steel cavities of the specimen holders on both sides of the sample. To minimize temperature gradients especially at elevated temperatures a removable furnace providing radiation heating

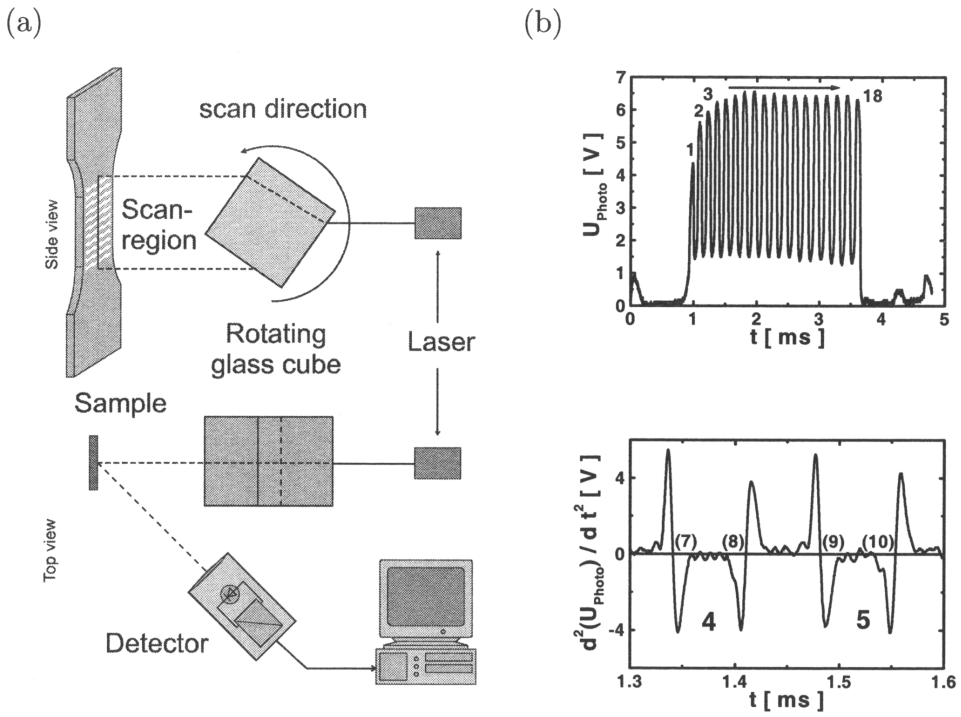

Figure III.2 : (a) Schematic of the laser scanning extensometer showing side and top view; (b) Voltage of the photo diode which is proportional to the reflected intensity for 17 stripes and 2nd derivative of the intensity signal.

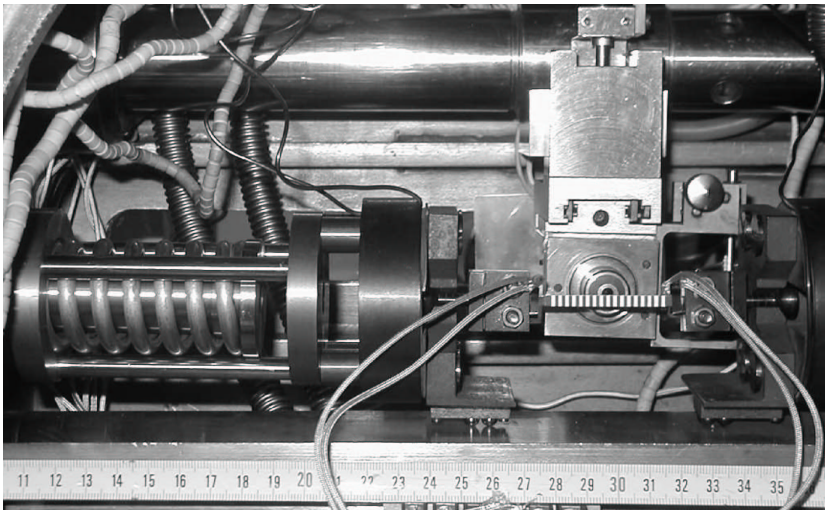

Figure III.3 : View into the vessel. Starting from the left hand side: spring construction, spacers, left heating coil, tensile jaw, clamped specimen with two thermocouples and markings for laser extensometry.

was used. The temperature was recorded by means of Ni/NiCr thermocouples at the radiation heating element and at both ends of the sample. Temperature fluctuations amount to ± 1 K during stationarity and up to 6 K during the measurements probably due to slight slipping of the thermocouples on the specimen surface at high deformation rates tests. In order to avoid uncontrolled thermal expansion, on both sides beyond the heating elements (the tensile rod and the load cell), a thermal decoupling was achieved by spacers and water cooling of universal–joint shafts of stainless steel. An amplifier (HBM, model KWS 3/5 carrier frequency 50 Hz) and an AD/DA converter (20 Hz) were connected to the load cell. The digitized voltages were recorded as mechanical load by means of two computers. One of them recorded the laser extensometric data including the load, the second computer controlled the measurement. The load cell was calibrated prior to the measurements presented here.

III.4 Data analysis

From raw data to physical data

The data were recorded in a binary format with both computers for a reduced amount of raw data, such that a conversion to an ASCII format for further analysis was necessary. This was realized by a program for data of the load control computer, that calculated the stress time data and by a commercial program for the laser extensometric data. This program provided the time dependence of local and global strain depending on the demanded zone intervals, global force and stress and the stress–strain data. For all data presented here, the local strain was averaged over 2 mm (three bright dark boundaries). The following algorithm and parameters were used for the automatic detection of local and global strain bursts, their time and place of appearance and their amount of strain. Due to the scattering of the strain data and the small number of data points within rapid strain increase an average process over the number M of data points was necessary, especially for the smallest strain increase (at small strains) and especially for type B and C bands. Afterwards an adjacent forward differentiation over D data points detected the average slope of those D data points. The exceeding of such slopes over a minimum slope ST and the exceeding of the corresponding

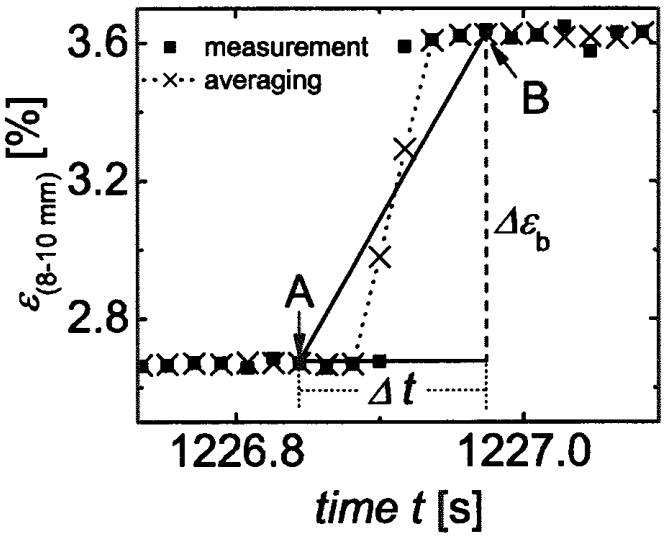

Figure III.4 : Typical example of a local strain increase during PLC band propagation. The parameters $\Delta\varepsilon_b, \delta t, \varepsilon_{loc,t}$ are extracted for all laser extensometric zones.

strain increase within those D data points over an initial minimum amount of strain increase ISH, respectively was the first condition for the detection of a strain burst. The first data point (A) that fulfilled this condition defined the time of the strain increase within the actual location (laser extensometric zone interval) if a second condition was fulfilled: if the actual slope fell below 1/20 of ST (this data point (B) defined the end of the increased local strain) and if the whole strain increase within the interval of averaged strain data [A, B] exceeded a minimum amount of the actual entire strain bursts SH these times of (A) and (B), the time difference δt between them the amount of strain within the actual jump $\Delta\varepsilon_b$ were recorded. This process was continued at data point (B) for the detection of further strain bursts up to the end of the file and repeated for the local strain data of all zones as well as for the global strain data between the first and the last zone. An example of a typical strain increase and the relevant parameters deduced are shown in figure III.4.

At the end of this procedure the following data for further physical analysis are available: the global stress/force and the global strain burst (averaged over all laser extensometric zones) which contained the initial times of occurrence of PLC events, the accumulated strain within the actual strain avalanche, the duration of the avalanche and the strain at the end of the actual avalanche. Furthermore there are the data extracted from the local strain bursts: the initial time t, the position (labeled also zone) x, the concentrated strain $\Delta\varepsilon_b$, the event duration Δt and the strain at the end of the strain increase $\varepsilon(t + \Delta)$. Further characteristics and PLC parameters like mode of propagation, band velocity, width and local strain rate in the band had to be analyzed separately.

From data to characteristic physical parameters

- Strain and strain rate: local and global strain concentrations within the PLC bands $\Delta\varepsilon^{loc/glob}$ were directly deduced from the data as described above. Difficulties with the accurate detection of strain bursts with respect to their time of occurrence did not affect the strain values because during PLC bands the strain is concentrated within the

small PLC bands and almost no plastic strain takes place elsewhere. Therefore a slight time shift for the start and stop of the strain increase within the almost stationary part of the strain time curve did not affect the amount of cumulated strain.

- Propagation mode and propagation velocity: the plot of the position where a strain burst was detected over the time of its occurrence is denominated as a "correlation diagram". Phenomenologically, the mode of propagation (PLC type A solitary wave, B intermittent, C random nucleation) could be characterized unambiguously. Furthermore the velocities of the PLC bands could easily be deduced from the "correlation diagram" for strain rate controlled tests via linear fits for the individual bands due to their homogeneous propagation with a constant average velocity for both types A and B.

- Bandwidth: the last characteristic PLC parameter is the width of the band w_b (the extension of the plastically active region starting with the band front up to the wake of the band where the dislocations are arrested). An analysis of the band width has been quite simple for propagating solitary waves (type A) during strain rate controlled deformation. In that case that can be determined by:

$$w_b = v_b \Delta t - \Delta p \tag{III.1}$$

with the zone width Δp. The assumption of PLC bands as solitary plastic waves provides a constant front velocity with a constant shape of the deformation band. The path $v_b \Delta t$ is covered by the band front within the duration of the strain increase $\Delta\varepsilon$, equal to the band width plus the width of the actual zone that has to be subtracted.

Chapter -IV-

Strain localization phenomena associated with static and dynamic strain ageing in notched specimens : experiments and finite element simulations

Contents

This chapter was published in Materials Science and Engineering A in 2004 (Graff et al., 2004).

Abstract : The aim of the present work is to use an available constitutive model for the description of the PLC effect to simulate the deformation of notched specimens in tension (smooth and sharp U–notched specimens). This model can be used to account for dynamic strain ageing as suggested by Zhang, McCormick and Estrin [S. Zhang, P.G. McCormick, Y. Estrin, Acta Mater. 49, (2000), 1087–1094] but also static strain ageing as suggested by Estrin, Kubin and Perrier [L.P. Kubin, Y. Estrin, C. Perrier, Acta Metall. Mater. 40, (1992), 1037–1044]. The experimental material studied is an Al–Cu alloy, displaying dynamic strain ageing at room temperature. Regarding Lüders band propagation, the experimental material studied is a mild steel. This work shows that the PLC serrations disappear progressively on the macroscopic curve when the notch radius decreases. However, strain localization still takes place in the deformed notched zone, and can escape from the notched zone. Regarding the Lüders behavior, the computed spreading of deformation bands is in agreement with experimental observations.

IV.1 Introduction

Many engineering materials exhibit strain ageing effects during plastic deformation of flat tensile specimens. Serrations can be observed on the macroscopic load/displacement curve, usually attributed to DSA and associated with the multisite initiation and propagation of strain rate localization bands (van den Beukel, 1975b; Kubin and Estrin, 1991a). Moreover, SSA can lead to the propagation of strain localization bands called Lüders bands. One frequent claim for doing this is that, contrary to flat tensile specimens, in real components, the complex geometry including the presence of stress concentrations such as holes and notches generates non–uniform strain fields which tend to absorb and/or disperse strain localization events. The objective of this work is to check that argument both numerically and experimentally.

IV.2 Constitutive equations of the macroscopic strain ageing model

The instabilities simulated in this work occur in some material, containing interstitial or substitutional elements, which may segregate at dislocations and lock them. The constitutive model used in (Zhang et al., 2000) incorporates in a set of phenomenological constitutive equations several features of the intrinsic behavior of strain ageing materials. It tries to mimic, in a phenomenological way, the mechanisms at work in a material volume element : repeated breakaway of dislocations from their solute clouds and recapture, for instance, by mobile solutes. We cast the evolution equations into the following form in order to comply with the thermodynamics of thermally activated processes. The total deformation is the sum of elastic and plastic strains tensors :

$$\underset{\sim}{\varepsilon} = \underset{\sim}{\varepsilon}^{\mathrm{e}} + \underset{\sim}{\varepsilon}^{\mathrm{p}} \qquad ; \qquad \underset{\sim}{\sigma} = \underset{\sim}{\underset{\sim}{\mathbf{C}}} : \underset{\sim}{\varepsilon}^{\mathrm{e}} \tag{IV.1}$$

where $\underset{\sim}{\underset{\sim}{\mathbf{C}}}$ is the fourth–rank tensor of elastic moduli. The yield criterion is defined by the equation :

$$f(\underset{\sim}{\sigma}) = J_2(\underset{\sim}{\sigma}) - R \tag{IV.2}$$

The second invariant of the stress tensor is denoted by J_2. The plastic flow rule is deduced from the normality rule :

$$\dot{\underset{\sim}{\varepsilon}}^{\mathrm{p}} = \dot{p}\,\frac{\partial f}{\partial \underset{\sim}{\sigma}} \qquad ; \qquad \dot{p} = \dot{\varepsilon}_0 \exp(-\frac{E_{\mathrm{a}}}{k_{\mathrm{B}}T}) \exp[\left(< f(\underset{\sim}{\sigma}) > V_{\mathrm{a}}\right) / (k_{\mathrm{B}}T)] \tag{IV.3}$$

where $\dot{p}$ is the viscoplastic multiplier and $< f(\underset{\sim}{\sigma}) >$ means the maximal of ($f(\underset{\sim}{\sigma})$, 0). In a viscoplasticity theory, the multiplier is given by an independent equation (IV.3), where T is the absolute temperature, V_a is the activation volume, and E_a is the activation energy. Strain hardening is assumed to be isotropic and includes also the strain ageing term ($P_1 C_s$) :

$$R = R_0 + Q[1 - \exp(-bp)] + P_1 C_{\mathrm{s}} \qquad ; \qquad C_{\mathrm{s}} = C_{\mathrm{m}}\,[1 - \exp(-\mathrm{P_2 p}^{\alpha} \mathrm{t}_{\mathrm{a}}^{\mathrm{n}})] \tag{IV.4}$$

where R_0, Q, b and P_1 are constant. C_{s} is the concentration of solute atoms segregating around the dislocations which are temporarily immobilized by extrinsic obstacles ("forest dislocations"). C_{m} is the saturated concentration around the dislocations. The time dependence of this segregation process can be described as the "relaxation–saturation" kinetics of Avrami and can be expressed by equation (IV.5), as suggested in (Zhang et al., 2000) :

$$\dot{t}_{\mathrm{a}} = \frac{t_{\mathrm{w}} - t_{\mathrm{a}}}{t_{\mathrm{w}}} \qquad ; \qquad t_{\mathrm{w}} = \frac{\omega}{\dot{p}} \tag{IV.5}$$

The ageing time t_a is the time of the diffusion of the solute atoms towards or along the dislocations. The waiting time t_w is the mean waiting time of dislocations, which are temporarily stopped by extrinsic obstacles. It depends on the plastic strain rate and can be expressed by equation (IV.5). ω is the increment of the plastic strain, which is produced when all the stopped dislocations overcome their obstacles.
The previous model was implemented in the finite element program $Z-set$ (Z-set package, 1996). The differential equations were integrated at each Gauss point of each element using a Runge–Kutta method of fourth order with automatic time–stepping. The resolution method for equilibrium was based on an implicit Newton algorithm. The elements used in all presented simulations were 8–node quadratic elements with reduced integration (four Gauss points per element) under plane stress conditions.

IV.3 Finite element simulations

The parameters used are given in table IV.1, for Al–Cu alloy (hardened duralumin with $4wt\%$ Cu) and the mild steel alloy (0.15%) at room temperature.

Table IV.1 : Parameters used to simulate the PLC effect in an Al–Cu alloy (after (Zhang et al., 2000)) and the Lüders behavior in a mild steel (after (Forest, 1997))

Parameters	Units	Al–Cu	Mild steel
Young's modulus	MPa	70200	210000
Poisson's ratio	-	0.3	0.3
R_0	MPa	140	220
Q	MPa	140	42
b	-	29	20
P_1	MPa (atom %)$^{-1}$	11	30
P_2	s^{-n}	3.91	0.01
w	-	10^{-4}	2.10^{-4}
α	-	0.44	0
n	-	0.33	1
E_a	eV	0.15	1
V_a	nm^3 (atom %)$^{-1}$	11	4000
C_m	atom %	2	1
$\dot{\varepsilon}_0$	s^{-1}	10^{-5}	10^2
Initial t_a	s	0	1000

The main difference in both sets of parameters is the initial value of t_a, which is chosen such that initially the concentration of solute atoms C_s is either minimal or maximal.
Three types of flat tensile specimens are considered : straight specimens, as well as smooth and sharp U–notched specimens. The ligaments of the notched specimens are identical, equal to 20 mm. Three finite element meshes are shown in figure IV.1.

The vertical displacement at the bottom is fixed to 0. The vertical displacement of the top is prescribed at a constant displacement rate equal to 3.33×10^{-2} mm.s^{-1} for the straight specimen and equal to 7.5×10^{-2} mm.s^{-1} for the U–notched specimens. One node is fixed

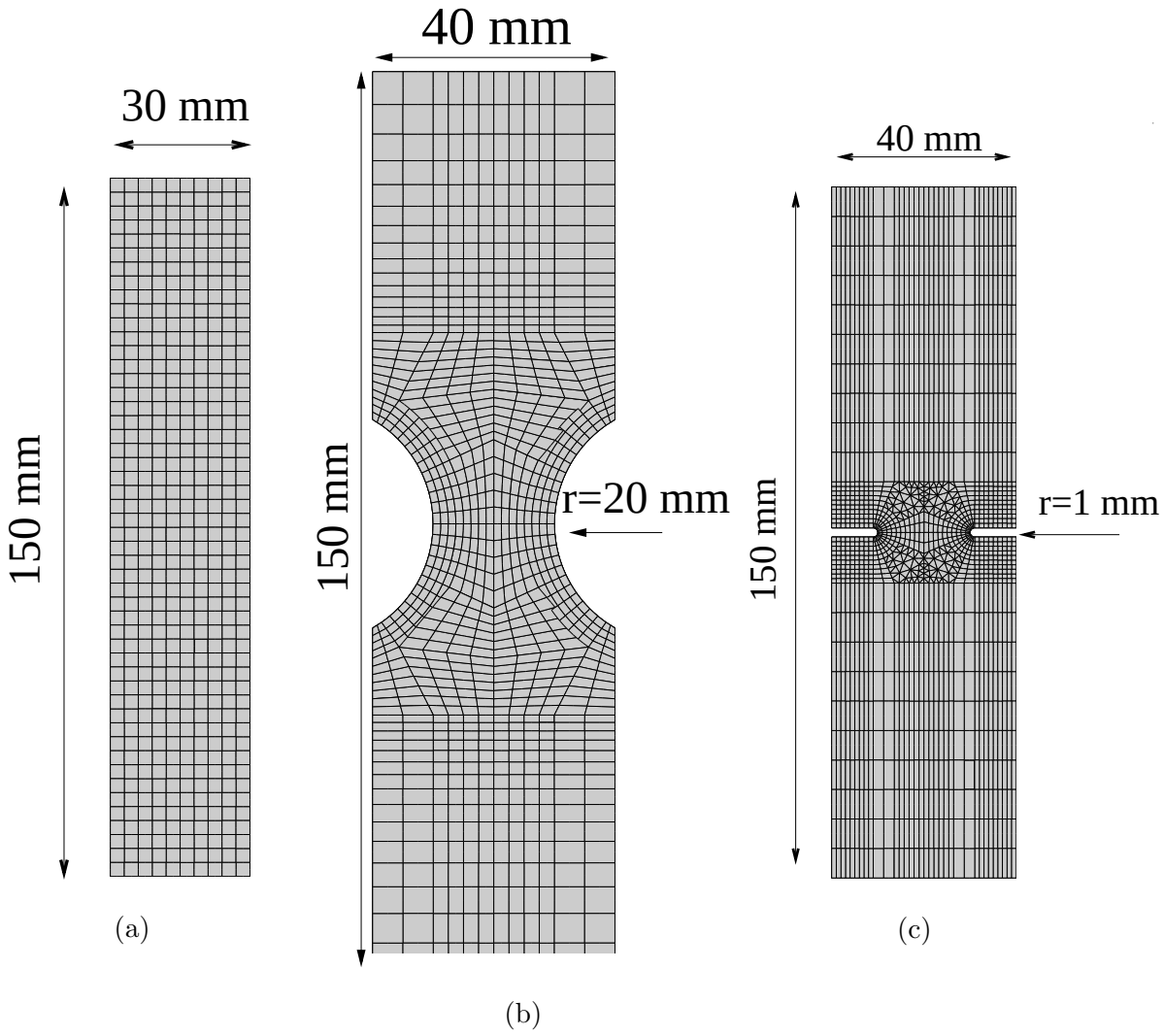

Figure IV.1 : Finite element meshes of computed specimens : (a) Straight, (b) Smooth U–notched, (c) Sharp U–notched specimens

also with respect to the horizontal direction. In our simulations, plastic strain do not exceed 5% in the deformed part of the specimens.

IV.4 Simulations of the PLC effect in notched Al–Cu alloy specimens

Simulations of the PLC effect on straight specimens in 2D and 3D are reported in (Zhang et al., 2000). We carried out similar computations to validate our finite element implementation. After a certain amount of plastic strain, slight serrations appear on the macroscopic stress/strain curve. Simultaneously, two strain rate localization bands start to develop on each side of an initial defect (here a slightly lower yield stress in one element). They propagate through the whole specimen and are reflected at the top and bottom boundaries. If fillets are introduced, they generate stress concentrations that are sufficient to trigger similar strain rate localization bands. Each serration on the overall curve is associated with a reflection of the band at one end of the specimen.
Tensile tests were simulated on different U–notched specimens. The results can be divided into two groups. The overall load divided by the area/displacement curves are obtained from a smooth U–notched specimen, displaying serrations as in the case of straight tensile specimen (see figure IV.2). Plastic strain rate bands start from the location of stress concentrations at the notches and propagate in the plastically deformed zone.

These different steps are shown in figure IV.3.

The contour maps show the variable $\dot{p}$. Note that some bands are able to escape from the main deformation zone. The scenario is almost similar in the case of sharp U–notched specimens. However, serrations are not observed on the overall load/displacement curve contrary to the smooth U–notched specimen considered above. The calculations show that strain rate localization, band initiation and propagation over short distances do exist even though serrations are not seen on the overall curve.

IV.5 Simulations of the Lüders behavior in notched mild steel specimens

The equations of the model recalled in section IV.2 can be used to describe tensile behavior with an initial yield drop, as seen in many mild steels. When applied to the straight flat tensile specimen of figure IV.1(a), such a constitutive response, leads to the formation of a plastic strain localization band starting from an initial defect. The band then propagates over the entire specimen but does not reflect at the specimen ends, contrary to the previous PLC strain rate bands. The specimen then deforms homogeneously, due to the hardening part, as explained in (Forest, 1997; Tsukahara and Iung, 1998).
Tensile tests were simulated on different U–notched specimens. The overall load divided by the area/displacement curves display an initial yield drop, which is less pronounced than in straight specimens. The strain bands start from the location of stress concentration at the notches and they migrate toward the center of the main deformation zone. The overall tensile curves of the U–notched flat specimens can be seen on figure IV.4. The initial yield drop decreases with the decrease of the notch radius.

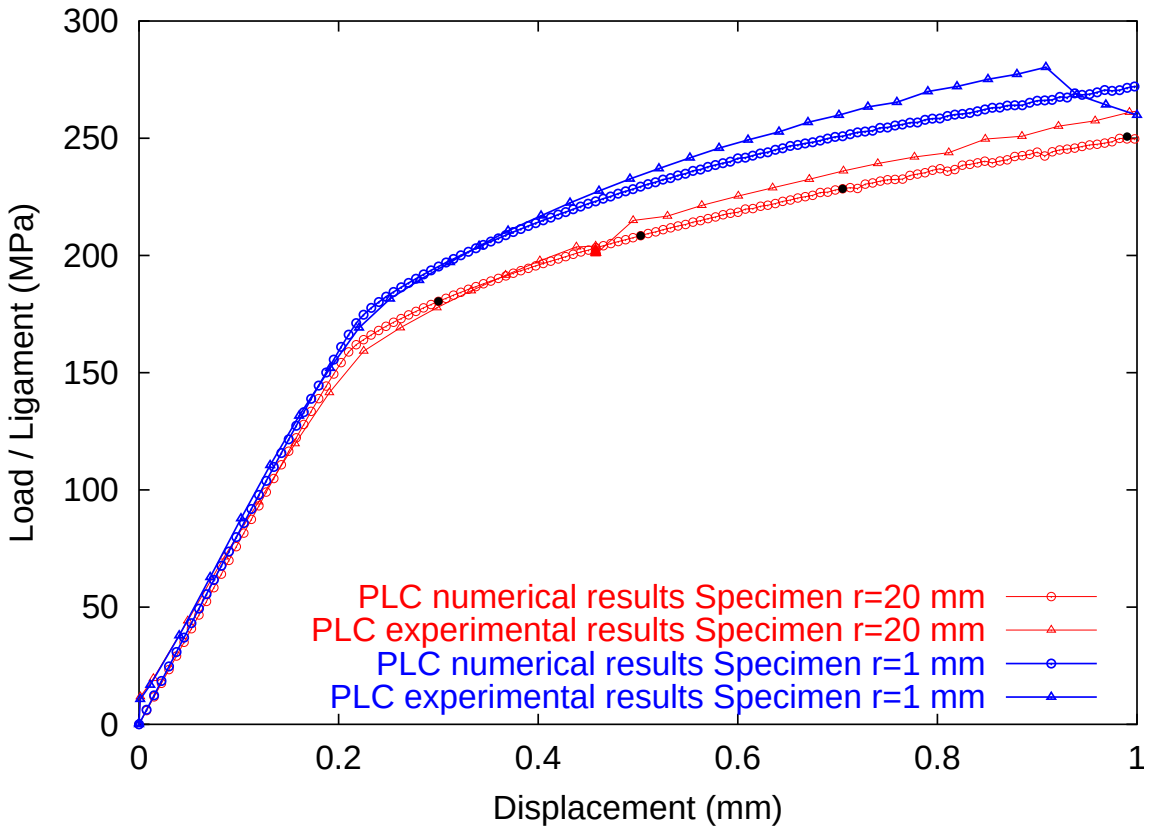

Figure IV.2 : Normalized overall PLC load divided by the area/displacement curves for the simulated U–notched specimens and the experimental U–notched specimens (r=20 mm and r=1 mm). The points correspond to different overall displacement levels (0.3 mm, 0.5 mm, 0.7 mm, 1 mm), as presented on figure IV.3.

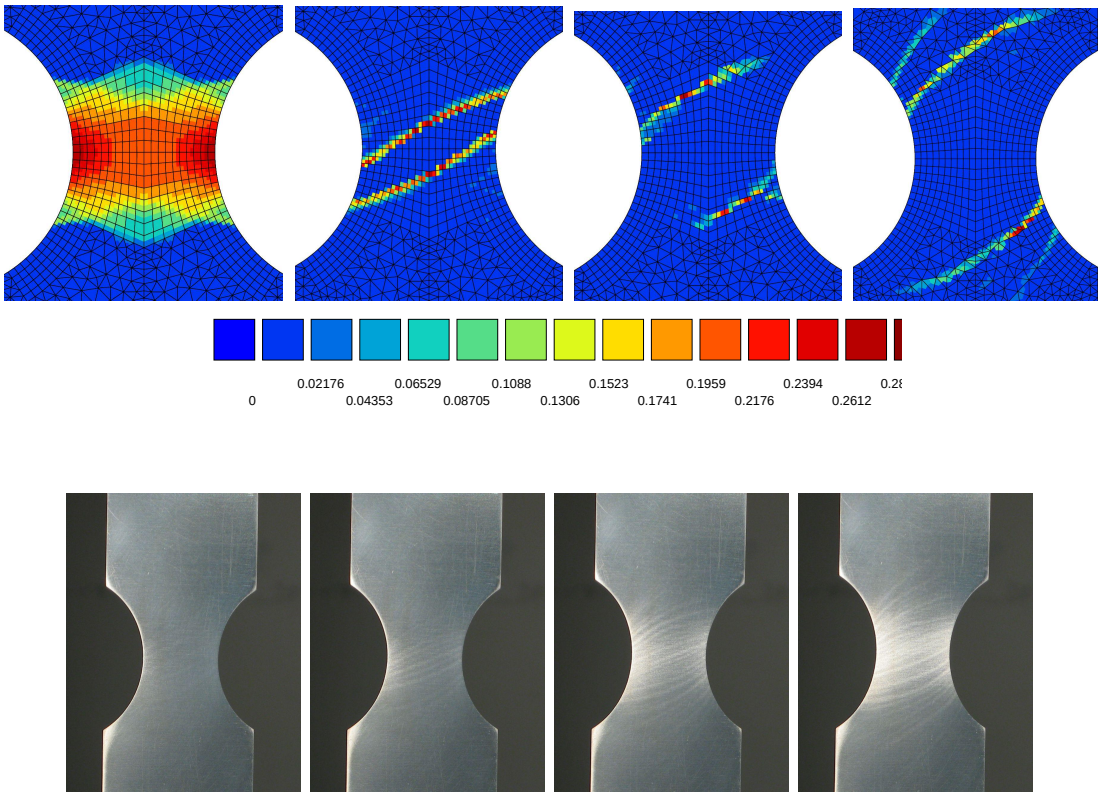

Figure IV.3 : The PLC effect in a simulated smooth U–notched specimen and an experimental smooth U–notched specimen : plastic strain rate maps at different overall displacement levels (0.3 mm, 0.5 mm, 0.7 mm, 1 mm), which are defined by the points on figure IV.2.

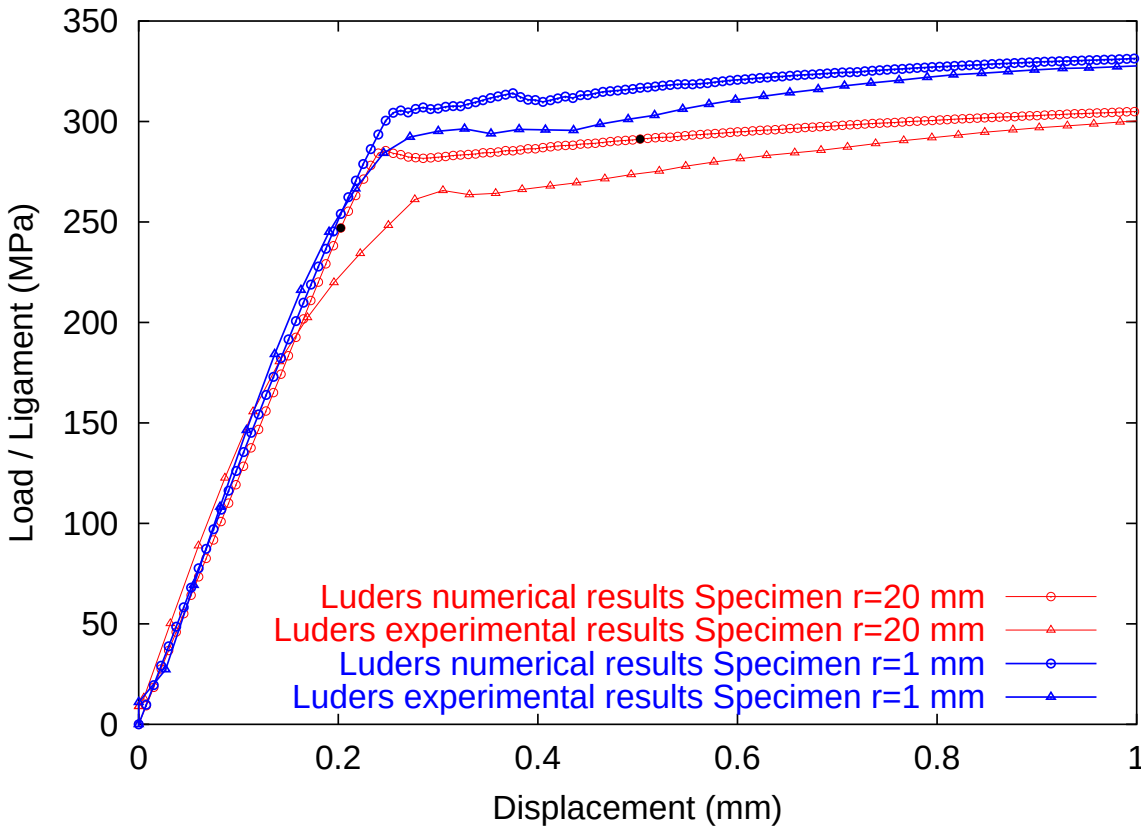

Figure IV.4 : Normalized overall Lüders load divided by the area/displacement curves for the simulated U–notched specimens and the experimental U–notched specimens (r=20 mm and r=1 mm). The points correspond to different overall displacement levels (0.2 mm, 0.5 mm, 1.2 mm, 1.8 mm), as presented on figure IV.5.

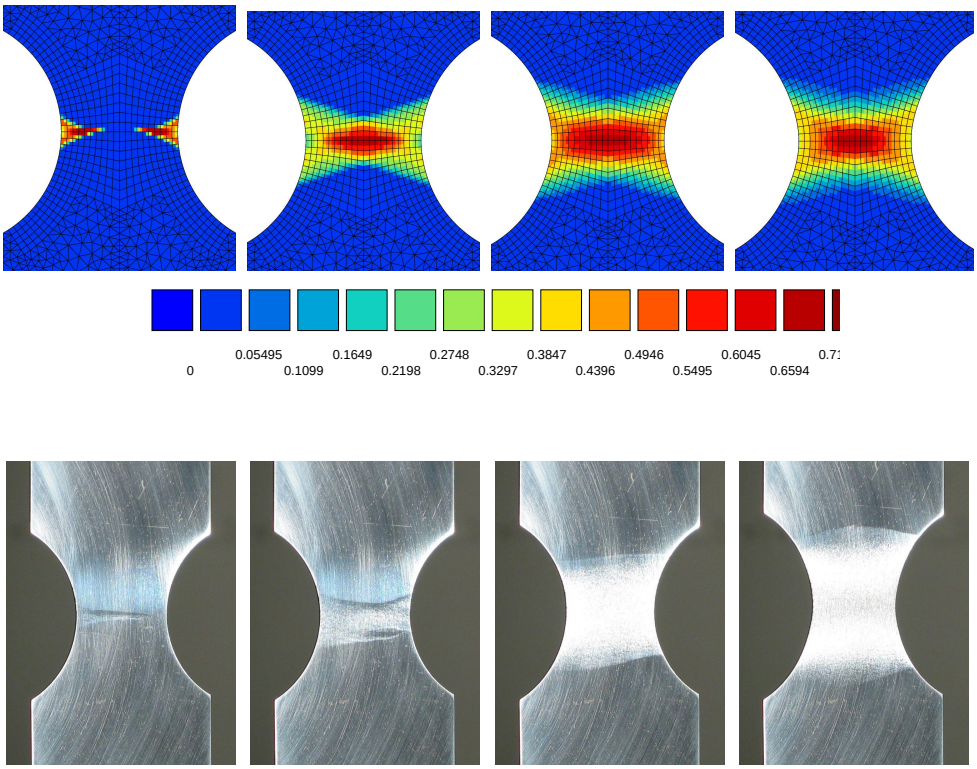

Figure IV.5 : The Lüders behavior in a simulated smooth U–notched specimen and an experimental smooth U–notched specimen : plastic strain maps at different overall displacement levels (0.2 mm, 0.5 mm, 1.2 mm, 1.8 mm), which are defined by the points on figure IV.4.

IV.6 Experiment vis–à–vis simulation results

Tensile tests were carried out for the different geometries of flat specimens, shown in figure IV.1 and for both materials Al–Cu alloy and mild steel at room temperature. The thickness of the specimen is equal to 1 mm. The tests were carried out at the same mean strain rate for the straight specimens and also for the notched specimens. An experimental set–up was developed in order to observe the evolution of polished specimens during the tests. It is composed by a digital camera, a halogen lamp, a tensile machine and a computer.
Considering the PLC effect, the main consequence is that the serrations on the macroscopic experimental and simulated curves disappear when the notch radius decreases. Even though serrations are not observed on the macroscopic experimental curve for the sharp U–notched specimen, the simulations predict strain rate localization bands, which are able to escape from the notched zone. Comparisons between experiments and numerical results are made based on figures IV.2, IV.3. Considering the Lüders behavior, experiments and simulations are in good accordance. However, the identification of model parameters for mild steel needs to be improved. Comparisons between experiments and numerical results are made on the basis of figures IV.4, IV.5.

In addition to that, the simulations, which show the localized stress concentrations, are in good accordance with the fracture processes. Indeed, experimentally, the smooth U–notched specimens tend to fracture in the middle of the deformed zone for both materials, and the sharp U–notched specimens tend to fracture at the notches for both materials.

IV.7 Conclusion

This work shows that the available constitutive model considered simulates the PLC and the Lüders effects for different notched specimens in tension : on the whole, the simulations and the experiments for Al–Cu alloy and the mild steel are in good accordance. Serrations on the overall load/displacement curves are shown to disappear progressively when the notch radius decreases. Strain rate localization bands initiation and propagation are still predicted by the computation but the spatial propagation range strongly decreases. For instance, strain localization bands can escape from the notched zone. The same methodology is used in the case of Lüders band propagation.
These localization phenomena, though not visible on the macroscopic curves, can play a significant role in early fracture processes.

Chapter -V-

Finite element simulations of dynamic strain ageing effects at V–notches and crack tips

Contents

This chapter was published in Scripta Materialia in 2005.

Abstract : Finite element simulations of the PLC effect in notched and CT (Compact Tensile) specimens of aluminium alloys are presented, based on a macroscopic strain ageing constitutive model. They predict the formation and propagation of intense strain rate localization bands. In particular, the predicted size of the plastic zone around the crack tip in a pre–cracked CT specimen is compared to the value found when using a standard elastoplastic model neglecting the PLC effect.

V.1 Introduction

The PLC effect is the manifestation of dynamic strain ageing. This effect can be associated with negative strain rate sensitivity (Kubin and Estrin, 1991a). It is characterized by the presence of stress serrations on the macroscopic load/displacement curve in constant strain rate tests or strain bursts in constant stress rate tests (Hähner et al., 2002). These serrations are associated with the multisite initiation and propagation of strain rate localization bands. Such phenomena were shown experimentally in the polycrystalline Al–Cu alloy in (Casarotto et al., 2003). A multiscale modeling approach for polycrystal plasticity was used to model the jerky flow in Al–Mg polycrystals in (Kok et al., 2003). For the sake of simplicity, however, these engineering materials are usually modeled by constitutive elastoplastic equations, that

do not take these strain or strain rate localization phenomena into account. A frequent claim for doing that is that, contrary to flat tensile specimens, the complex geometry of real components induces stress concentrations and generates non–uniform strain fields which tend to absorb and/or disperse strain localization events. The main objective of this work is to examine this argument by means of finite element simulations in the case of V–notched and CT specimens.

In a previous work (Graff et al., 2004), PLC effect and Lüders band propagation were simulated in flat and U–notched specimens of different curvature radii using the phenomenological model proposed in (Zhang et al., 2000). The numerical results are in good agreements with experimental results obtained for an Al–Cu alloy and a mild steel. In the present work, finite element simulations were performed to predict the response at V–notches and at a crack tip in a pre–cracked CT specimen. For the same material, two models are compared: a standard von Mises elastoplastic model that neglects DSA effects, on the one hand, and the strain ageing model taken from (Zhang et al., 2000), on the other hand. Attention is drawn on the comparison of plastic zone sizes in both cases.

V.2 The macroscopic strain ageing model

The constitutive model presented in (Zhang et al., 2000) is available to simulate instabilities in materials, containing interstitial or substitutional elements that can segregate at dislocations and lock them. It can be used to simulate both the PLC effect and the Lüders behavior, as shown in (Graff et al., 2004). The evolution equations try to mimic the mechanisms of repeated breakaway of dislocations from their solute clouds and recapture, for instance, by mobile solutes. The total deformation is the sum of elastic and plastic strains:

$$\underset{\sim}{\varepsilon} = \underset{\sim}{\varepsilon}^{\mathrm{e}} + \underset{\sim}{\varepsilon}^{\mathrm{p}} \quad ; \quad \underset{\sim}{\sigma} = \underset{\sim}{\mathbf{C}} : \underset{\sim}{\varepsilon}^{\mathrm{e}} \tag{V.1}$$

The tensor $\underset{\sim}{\mathbf{C}}$ is the fourth–rank tensor of elastic moduli. The yield criterion is:

$$f(\underset{\sim}{\sigma}) = J_2(\underset{\sim}{\sigma}) - R \tag{V.2}$$

where J_2 is the second invariant of the stress tensor. The plastic flow rule is deduced from the normality law :

$$\dot{\underset{\sim}{\varepsilon}}^{\mathrm{p}} = \dot{p}\,\frac{\partial f}{\partial \underset{\sim}{\sigma}} \quad ; \quad \dot{p} = \dot{\varepsilon}_0 \exp(-\frac{E_{\mathrm{a}}}{k_{\mathrm{B}}T}) \sinh\left(\frac{< f(\underset{\sim}{\sigma}) > V_{\mathrm{a}}}{k_{\mathrm{B}}T}\right) \tag{V.3}$$

where $\dot{p}$ is the viscoplastic multiplier; $\dot{\varepsilon}_0$ is a constant; $< f(\underset{\sim}{\sigma}) >$ means the maximum of ($f(\underset{\sim}{\sigma})$, 0); T is the absolute temperature; V_a is the activation volume; and E_a is the activation energy. In this study, strain hardening is assumed to be isotropic and includes also the strain ageing term $P_1 C_s$:

$$R = R_0 + Q[1 - \exp(-bp)] + P_1 C_{\mathrm{s}} \quad ; \quad C_{\mathrm{s}} = C_{\mathrm{m}}\,[1 - \exp(-\mathrm{P}_2 \mathrm{p}^{\alpha} \mathrm{t}_{\mathrm{a}}^{\mathrm{n}})] \tag{V.4}$$

where R_0, Q, b, P_1, P_2, α and n are material parameters. C_{s} is the concentration of solute atoms segregating around the dislocations which are temporarily immobilized by extrinsic obstacles. C_{m} is the saturated concentration around the dislocations. The time dependence of this segregation process can be described by the "relaxation–saturation" kinetics of Avrami:

$$\dot{t}_{\mathrm{a}} = \frac{t_{\mathrm{w}} - t_{\mathrm{a}}}{t_{\mathrm{w}}} \quad ; \quad t_{\mathrm{w}} = \frac{\omega}{\dot{p}} \tag{V.5}$$

The ageing time, t_a is the time of the diffusion of the solute atoms towards or along the dislocations. The time t_w is the mean waiting time of dislocations, which are temporarily stopped by extrinsic obstacles. It depends on the plastic strain rate. The parameter, ω is the increment of the plastic strain produced when all stopped dislocations overcome their obstacles.

The strain ageing model was implemented in a finite element program (Graff et al., 2004). The differential equations were integrated at each Gauss point of each element using a Runge–Kutta method of fourth order with automatic time–stepping. The resolution method for global balance was based on a Newton algorithm. The elements used in all presented simulations were 8–node quadratic elements with reduced integration under plane stress conditions.

Two aluminium alloys are considered in the following finite element simulations : Al–Cu alloy studied in (Graff et al., 2004), and 2091 Al–Li alloy investigated in (Delafosse et al., 1993). The material parameters of the strain ageing model identified from tensile tests on straight samples are to be found in (Graff et al., 2004) for the first alloy, and in table V.1 for the second one.

Table V.1 : Parameters of the strain ageing model in 2091 Al–Li alloy at $-20°C$ (after (Delafosse et al., 1993)).

Parameters	Units	2091 Al–Li
R_0	MPa	320
Q	MPa	140
b	-	29
P_1	MPa (atom %)$^{-1}$	11
P_2	s^{-n}	3.91
ω	-	10^{-4}
α	-	0.44
n	-	0.33
E_a	eV	0.15
V_a	nm^3 (atom %)$^{-1}$	11
C_m	atom %	2
$\dot{\varepsilon}_0$	s^{-1}	10^{-5}

In order to simulate the PLC effect, the initial value of t_a is set to zero (see equation (V.5)).

A standard von Mises elastoplastic model is also used in the following for comparison. It is obtained simply by suppressing the ageing term $P_1 = 0$ in equation (V.4), the remaining parameters being left unchanged.

V.3 PLC effect in V–notched specimens

The tensile deformation of flat specimens with two symmetric V–notches were computed for two different angles: 60°–V–notches and 90°–V–notches. All the V–notched specimens are the same ligament size of 20 mm, and the same total length of 50 mm. All the tests were simulated under a constant displacement rate such that the mean strain rate reached in

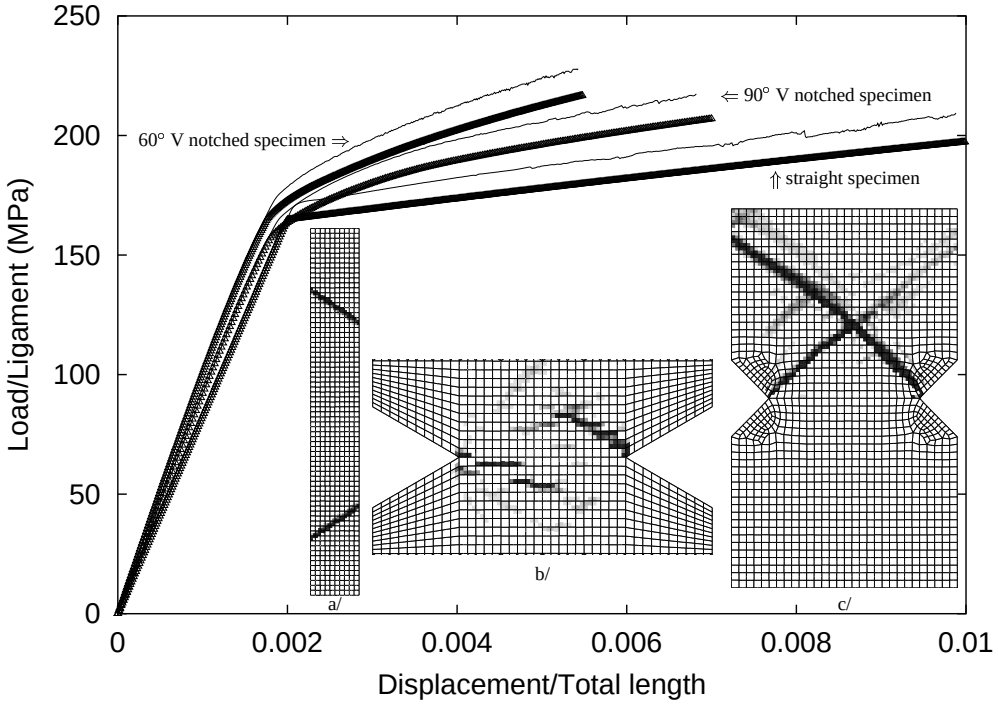

Figure V.1 : Overall load/displacement curves for the tensile deformation of straight, 60° and 90°–V–notched specimens. The thick (resp. thin) curve is the result of the simulation with a standard (resp. strain ageing) model. The total length is 50 mm. Plastic strain rate maps at overall strain 0.0025 for: a/ straight specimens; b/ 60° V–notched specimen; c/ 90° V–notched specimen. The black color corresponds to $\dot{p} > 0.2$ % s^{-1}.

the notched deformed zone is equal to 4.10^{-4} s^{-1}. Figure V.1 shows the overall normalized load/displacement curves. For comparison, the response of a straight specimen with a width of 20 mm is also given.

For each specimen, two curves are provided: the one obtained with the PLC model, and the one obtained with the standard model. Two main differences arise. The stress level reached with the PLC model is higher than for the standard model. This is due to the suppression of the hardening component $P_1 C_s$ in equation (V.4) for the standard model. The more significant difference is the presence of serrations after a certain amount of plastic strain on the curves simulated with the PLC model. The amplitude of the serrations is smaller in the 60°–V–notched specimen than in the 90°–V–notched specimen. The apparent yield stress for the 60°–V–notched specimen is larger than for the sharp 90°–V–notched specimen. This can be explained by a triaxiality effect (Thomason, 1990).

Figure V.1 also shows maps of plastic strain rate $\dot{p}$ in the straight and notched samples. In the straight specimen, two strain rate localization bands start to develop simultaneously from an initial defect which is numerically introduced. Then, they propagate through the whole specimen and are reflected at the top and bottom boundaries. One of them vanishes progressively, whereas the other one goes up and down at a constant speed. Each serration on the corresponding macroscopic curve is associated with the reflection of the band at one end of the specimen. In the case of V–notched specimens, the plastic strain rate bands start from

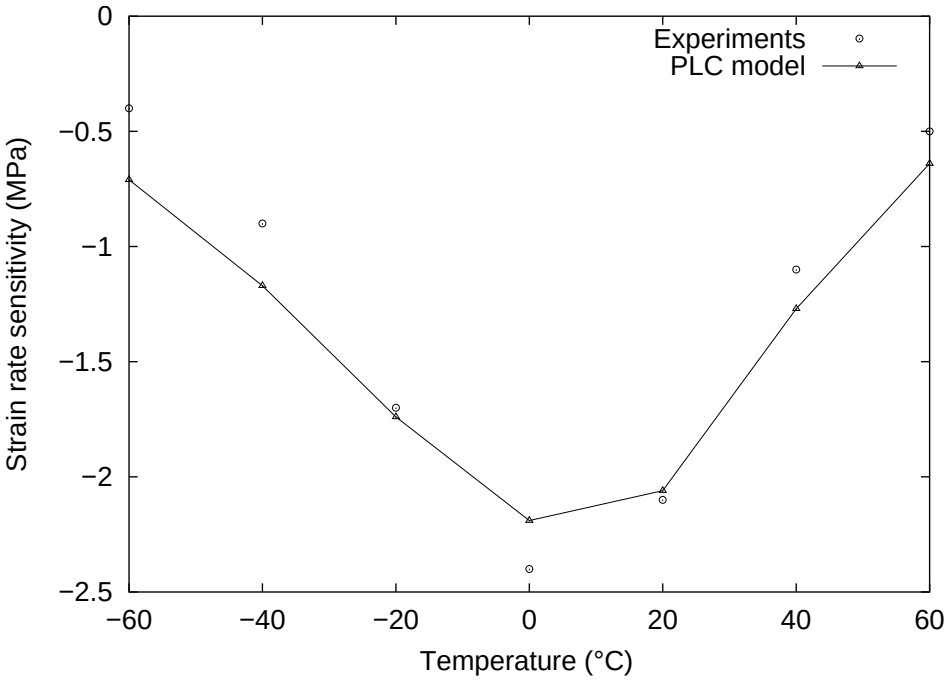

Figure V.2 : Strain rate sensitivity as a function of temperature at 2 % plastic strain : experimental results (after (Delafosse et al., 1993)) versus numerical identification of the strain ageing model.

the location of stress concentrations at the notches and propagate in the plastically deformed zone. They propagate on a short distance, disappear and new ones form starting from the notches. The plastic strain rate bands of the 60°–V–notched specimens remain confined in the region close to the ligament. In contrast, in sharp 90°–V–notched specimens, the intense strain rate bands extend far beyond the notched region. This feature can be related to the fact that the serrations on the overall curve of the 60°–V–notched specimen are less pronounced. Each band is found to bring about 3 % of plastic strain. The propagation of strain rate bands starts earlier (for a smaller overall plastic strain) in the 60°–V–notched specimen than in the 90°–V–notched specimen. This can be explained by a triaxiality effect (Thomason, 1990).

It is possible to draw a qualitative comparison of the numerical results with the experimental ones presented in (Delafosse et al., 1993). These authors investigated the influence of DSA on ductile tearing in 2091 Al–Li alloy. This alloy exhibits the PLC effect at $-20°C$ during unixial deformation tests, which is associated with a depletion of the Strain Rate Sensitivity (SRS). This effect is shown on Figure V.2 which gives the SRS as a function of the temperature at 2% of plastic strain. These results are used to identify the material parameters of the strain ageing model for this alloys (see table V.1). For the identification over the considered temperature range, a temperature dependence of the activation volume V_a is introduced. It varies between 3 and 11 $nm^3(atom\%)^{-1}$. The authors in (Delafosse et al., 1993) used CT specimens without pre–cracking, with a 60° V–notch and a ligament of 17.3 mm. Figure V.3 compares the experimental and simulated deformed zones at the notch.

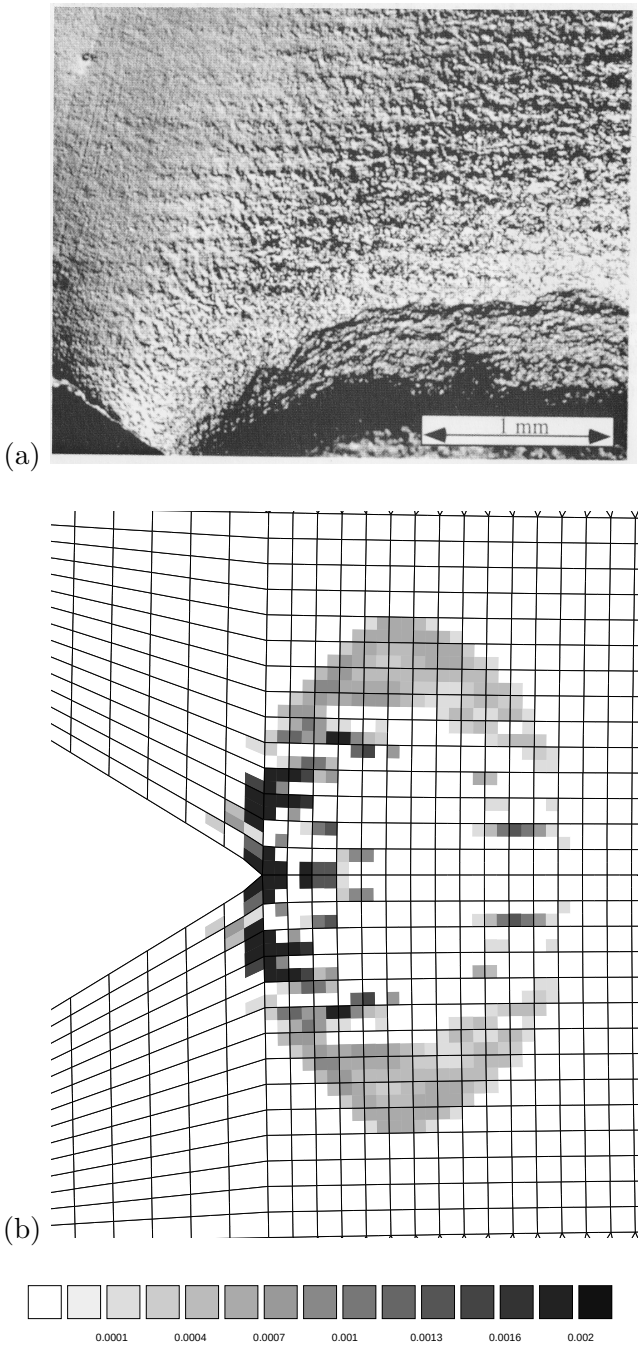

Figure V.3 : (a) Micrograph obtained in Nomarski contrast near the notch tip of 2091 Al–Li alloy specimen at $-20°C$ (after (Delafosse et al., 1993)); (b) Plastic strain rate (s^{-1}) map at relative displacement of the pins of 0.8 mm. The element size in the deformed zone is 150 μm. The unit of the color scale is s^{-1}.

The specimen was torn at $-20°C$ with a cross head velocity of 0.2 mm.mn^{-1} to a crack extension of 3 mm. The existence of horizontal bands is evidenced. The simulated map represents the plastic strain rate $\dot{p}$ at a displacement equal to 0.4 mm. Horizontal strain rate bands in front of the crack tip are correctly predicted by the simulations. However, the band spacing depends on the mesh size which is set to 150 μm in the notched region.

V.4 PLC effect at a crack tip

Finite element simulations of the deformation behavior of a pre–cracked Al–Cu CT specimen were performed for a ligament of 22 mm and 16 mm crack length. The main purpose of this part is to compare the plastic zone sizes obtained around the crack tip for the strain ageing and standard models. The mesh size at the crack tip is equal to 10 μm. Figure V.4 shows six maps comparing the strain ageing model and the standard model at two different overall loadings : relative displacement of the pins of 0.07 mm and 0.13 mm. The maps (a) and (b) represent the PLC plastic strain rate fields $\dot{p}$.

Multiple intense strain rate bands form at the crack tip and propagate in the plastic zone. The curvature of the observed bands is due to the strongly multiaxial stress field around the crack tip. On the map (b) each PLC plastic strain rate band brings about 2 % plastic strain. The band spacing and band width are respectively equal to about 30 μm and 15 μm. The maps (c) and (d) represent the corresponding PLC plastic strain field at the same loading steps. They must be compared to the maps (e) and (f) obtained with the standard elastoplasticity model. Regions where the cumulated plastic strain p is less than 0.2 % are in white. It turns out that both models lead to about the same plastic zone shape and size. This indicates that the very complicated and heterogeneous propagation of strain rate bands takes place inside the same plastically deformed zone than for a standard model. The elliptical shape of the plastic zone in figures V.4 (c), (d), (e), (f) are in agreement with the observations reported in (Delafosse et al., 1993).

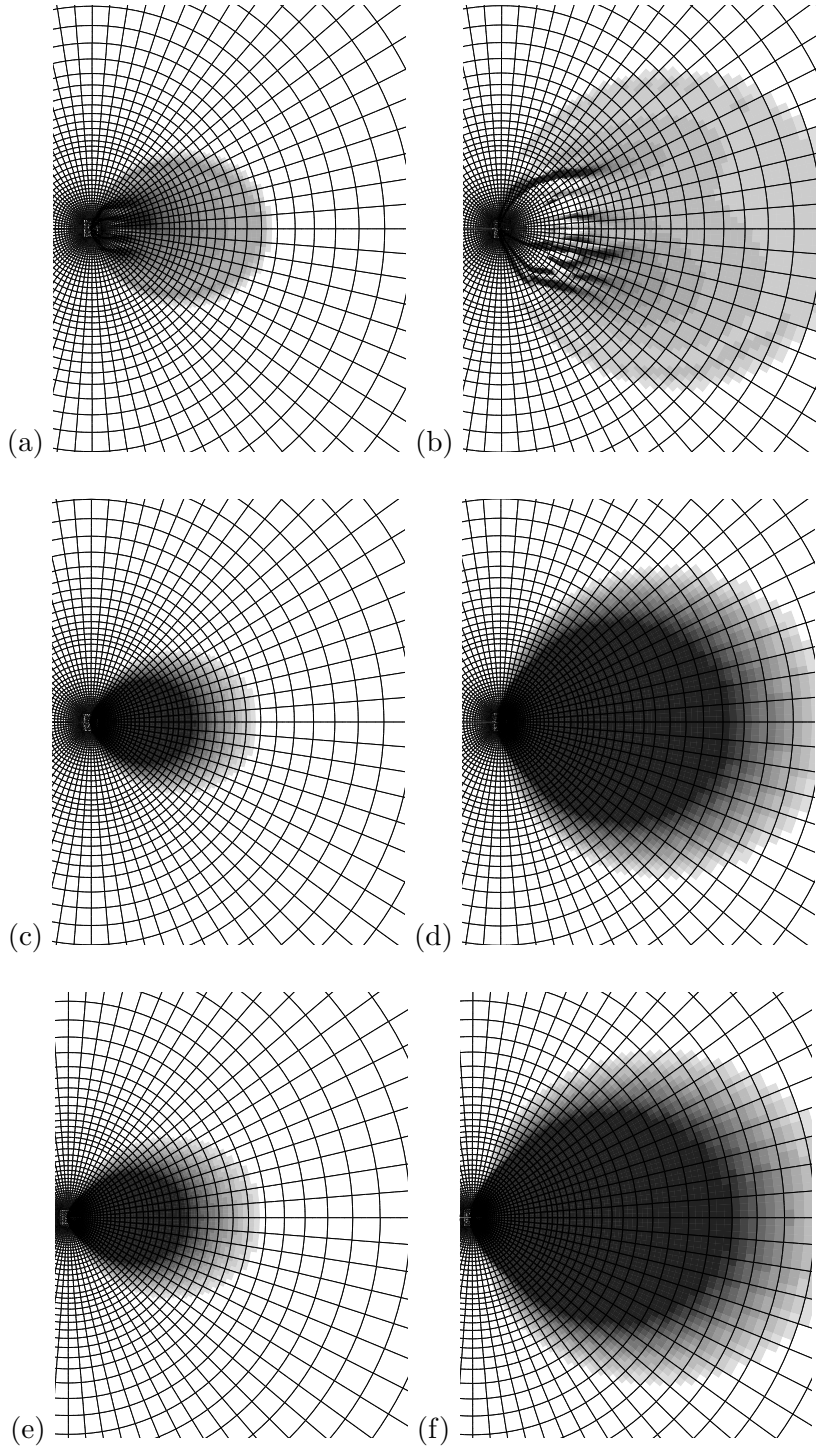

Figure V.4 : Strain rate maps at the crack tip at relative pins displacements 0.07 mm (a) and 0.13 mm (b) for the simulation of a pre–cracked specimen with the strain ageing model. Plastic strain maps at the same displacements : simulations with the strain ageing model ((c), (d)), and with a standard model ((e), (f)). The color scale is the same as figure V.3. The unit for (a) and (b) is s^{-1} and the maps (c), (d), (e) and (f) are dimensionless.

V.5 Discussion and prospects

The following PLC effect arising in notched and cracked specimens is evidenced in the previous simulations:

1. Serrations on the overall load/displacement curves are found for both 60° and 90°–V–notches. They are associated with the formation and propagation of multiple strain rate localization bands starting from the notches. These bands remain confined in the ligament zone in 60°–V–notched specimens and extend far beyond the ligament region in the case of 90°–V–notches. These results are similar to that found for U-notched specimens simulated and experimentally tested in (Graff et al., 2004). The predicted horizontal bands in the deformed zone are in qualitative agreement with the experimental observations in (Delafosse et al., 1993).

2. Intense strain rate localization bands are produced at the crack tip in pre–cracked CT specimens. They are curved by the complex multiaxial stress state. The propagation of these intense strain rate bands does not affect the shape and the extension of the plastic zone, when compared to simulations with a standard elastoplastic model.

Complex strain localization phenomena take place at notches and crack tips in strain ageing materials. Accordingly, neglecting them in the design of engineering components is not without consequence regarding failure assessment. Even though the plastic zone sizes predicted by the strain ageing and standard models are very close, the locally higher and strongly heterogeneous stresses associated with the strain ageing model may well play a significant role in the subsequent ductile fracture of the materials which was not investigated here. This will be the subject of future analysis.

Acknowledgements.

S. Graff and S. Forest thank L.P. Kubin (LEM/CNRS/ONERA, France) and D. Delafosse (Ecole des Mines de Saint–Etienne, France) for providing additional information about the results in (Delafosse et al., 1993) and for stimulating discussions.

Chapter -VI-

Finite element simulations of the Portevin–Le Chatelier effect in metal–matrix composites

Contents

Abstract: The Portevin–Le Chatelier (PLC) effect in $Al-3\%Mg$ alloys reinforced with Al_2O_3 second phase particles is studied both experimentally and by computer simulation. Plastic instabilities and inhomogeneities in such materials are caused by correlated movement of dislocations during deformation. By addition of unshearable obstacles, the propagation of correlated dislocation groups is restricted to shorter distances thus reducing the amplitude of the PLC serrations. This work aims at comparing the observed and simulated macroscopic behaviors of the AA5754 metal–matrix composite (MMC) for various volume fractions of particles. The macroscopic strain ageing model presented in [Material Science and Enginering A 5 (2004) 387] is used to account for PLC effect in the MMC. The 2–dimensional finite element simulations are based on computational homogenization methods. They show that the addition of particles in the MMC leads to a reduction of the critical strain for serrations ε_c and to a weakening of the PLC serrations on the macroscopic curve. These findings are in good agreement with the presented experiments.

VI.1 Introduction

The PLC effect is often observed in $Al-Mg$ alloys (Chihab et al., 1987). Microscopically, they result from the dynamic interaction of mobile dislocations and solute atoms. Mobile dislocations move by successive jerks between forest dislocations (other dislocations piercing their slip plane). Solute atoms diffuse to and saturate dislocations while they are temporarily arrested at these obstacles (van den Beukel, 1975b). Referred to as Dynamic Strain Ageing (DSA), this mechanism can lead to negative Strain Rate Sensitivity (SRS) in a range of applied strain rates, $\dot{\varepsilon}$ where dislocations and solute atoms have comparable mobility (Estrin and Kubin, 1995; Kubin and Estrin, 1991a). If the applied strain rate falls into such an appropriate range and if sufficient interaction between dislocations (via their long–range stress fields) occurs (Hähner, 1997), plastic flow becomes heterogeneous. Plastic strain and plastic strain rate are highly localized in narrow bands in the deformed specimen. Such bands remain either stationary or propagative in a continuous or discontinuous manner. In this work, these bands are called "plastic strain rate bands". The nature of PLC effect depends on the influence of testing conditions (Pink and Grinberg, 1982; Ziegenbein, 2000; Ranc and Wagner, 2005): (i) applied strain rate (Klose et al., 2003b), (ii) temperatures range (Ling and McCormick, 1993), (iii) stress state (Hähner et al., 2002). Mg content superior to 2–3% in $Al-Mg$ alloys lead to pronounce PLC effect according to (Chihab et al., 2002).

The $Al-Mg$ alloys are used in a large variety of industrial applications owing to their high mechanical strength and low density. Their practical benefit is limited by PLC instabilities and strain inhomogeneities. The study of Estrin and Lebyodkin (Estrin and Lebyodkin, 2004) and the experimental study of Dierke (Dierke, 2005; Dierke et al., 2006) explored the assumption that the addition of second phase dispersion Al_2O_3 particles to the parent $Al-3\%Mg$ alloy has a strong influence on the unstable deformation and the critical conditions for the occurrence of PLC instabilities.

The present work is motivated by recent progress in the simulation of PLC effect. It is possible to reproduce the types of PLC bands observed in the experiments as well as their dynamic behavior using finite element (FE) simulations. The basic assumption is the DSA mechanism which is introduced in the Kubin–Estrin's model in a phenomenological way (Kubin et al., 1992). Zhang and McCormick (McCormick, 1988; Zhang et al., 2000) proposed a 3–dimensional macroscopic constitutive model including the time dependence of the solute concentration at temporarily arrested dislocations, called the McCormick's model. Their FE simulations showed the occurrence of propagative zones of localized strain for an $Al-Mg-Si$ alloy in flat and round specimens associated with serrations on the macroscopic stress–strain curve during tensile tests at constant strain rate.

Beaudoin et al. (Kok et al., 2003) proposed a polycrystalline plasticity constitutive model embedded in a FE framework. Their simulations reproduce both the propagative and statistical nature of PLC bands.

The model of Schmauder and Hähner (Lasko et al., 2005; Saraev and Schmauder, 2003) introduced an activation enthalpy for dislocation motion which is considered as an intrinsic variable governing the extent to which dislocations are aged by solute clouds. However this model and the McCormick's model provided similar results in the presented simulations.

Graff et al. (Graff et al., 2004; Graff et al., 2005) used the macroscopic model suggested by Zhang and McCormick (Zhang et al., 2000) to account for both dynamic and static strain ageing. Their FE analysis showed that complex strain localization phenomena take place at notches and crack tips in several strain ageing materials. They suggested that these localization phenomena can play a significant role in early fracture process.

In this paper, plastic instabilities in $Al-3\%Mg$ alloys reinforced with Al_2O_3 dispersion particles are studied both experimentally and by FE simulations using the model of Graff et al. (Graff et al., 2004; Graff et al., 2005). The conventional macroscopic properties such as the critical strain for serrations and the types of serrations observed on the stress–strain curve are analysed for various applied strain rates and volume fractions of particles. The mesh size sensitivity and the influence of particles distribution are discussed in this work.

The section VI.2 is dedicated to the identification of the material parameters of the model in the case of the bulk parent $Al-3\%Mg$ alloy. This model is then used in section VI.3 to predict the behavior of the composite material based on periodic homogenization methods. The simulation results are compared with the corresponding experimental tests. The discussion of section VI.4 addresses the sensitivity to mesh size in the FE model and the influence of randomness of particle distribution on the behavior of the composite.

VI.2 Simulations for the parent $Al-3\%Mg$ alloy

VI.2.1 Salient experimental features and experimental method

The PLC effect is classified according to the type of serrations observed on the macroscopic stress–strain curves, usually labeled types A, B and C (Chihab et al., 1987). For an $Al-3\%Mg$ alloy at room temperature, type A, B and C bands are associated with an applied strain rate approximatively equal to $\dot{\varepsilon} = 10^{-3}s^{-1}$, $\dot{\varepsilon} = 10^{-4}s^{-1}$, $\dot{\varepsilon} = 10^{-5}s^{-1}$ respectively (Lebyodkin et al., 1996). Type A appears as a continuous propagation of PLC bands which are usually nucleated near one grip of the specimen. The bands propagate with nearly constant velocity and band width to the other end of the specimen. Type B bands propagate discontinuously along the specimen. More precisely, small strain bands nucleate in the nearest surroundings of the former band. Type C deformation is characterized by spatially random bursts of bands without significant propagation accompanied by strong and high frequency load drops.
For an $Al-3\%Mg$ alloy, the dependence of the critical strain ε_c corresponding to the onset of serrations, on the applied strain rate exhibits various types of behavior: (i) "normal" (ε_c increases with $\dot{\varepsilon}$), (ii) "inverse" (ε_c decreases with $\dot{\varepsilon}$) and (iii) "inverse then normal" (Chihab et al., 2002).

Experiments were performed on flat specimens with a gauge part of 54 mm × 4 mm × 1.5 mm in size prepared from polycrystalline cold–rolled sheets of $Al-3\%Mg$ alloy. The first type of samples studied in this work is the bulk parent $Al-3\%Mg$ alloy. All specimens were heat treated for recovery after rolling (5h at 673K) and quenched in water. The average grain size obtained after heat treatments is estimated at about 70 μm. The uniaxial tensile tests were performed at constant strain rate using a screw–driven tensile machine Instron 1185 at room temperature.

VI.2.2 Constitutive equations and finite element identification of the macroscopic strain ageing model

The macroscopic model presented in (Zhang et al., 2000) is available to simulate instabilities in materials containing interstitial or substitutional elements that can segregate to dislocations and lock them. It incorporates in a set of phenomenological constitutive equations several features of the intrinsic behavior of strain ageing materials and can be used to simulate both the PLC effect and the Lüders behavior as shown in (Graff et al., 2004; Graff et al., 2005). The evolution equations try to mimic the mechanisms of repeated breakaway of mobile dislocations temporarily arrested at forest dislocations and by solute atoms. The equations are cast into the following form in order to comply with the thermodynamics of thermally

activated processes.
The total deformation is the sum of elastic and plastic strain tensors:

$$\underset{\sim}{\varepsilon} = \underset{\sim}{\varepsilon}^{\mathrm{e}} + \underset{\sim}{\varepsilon}^{\mathrm{p}} \qquad , \qquad \underset{\sim}{\sigma} = \underset{\sim}{\underset{\sim}{\mathbf{C}}} : \underset{\sim}{\varepsilon}^{\mathrm{e}} \tag{VI.1}$$

The tensor $\underset{\sim}{\underset{\sim}{\mathbf{C}}}$ is the fourth–rank tensor of elastic moduli and $\underset{\sim}{\sigma}$ is the stress tensor. The yield criterion is defined by:

$$f(\underset{\sim}{\sigma}) = J_2(\underset{\sim}{\sigma}) - R \tag{VI.2}$$

J_2 is the second invariant of the stress tensor. The plastic flow rule is deduced from the normality law:

$$\dot{\underset{\sim}{\varepsilon}}^{\mathrm{p}} = \dot{p}\,\frac{\partial f}{\partial \underset{\sim}{\sigma}} = \frac{3}{2}\dot{p}\frac{\underset{\sim}{\mathbf{s}}}{J_2(\underset{\sim}{\sigma})} \qquad , \qquad \dot{p} = \dot{\varepsilon}_0 \exp\left(\frac{< f(\underset{\sim}{\sigma}) > V_{\mathrm{a}}}{k_{\mathrm{B}} T}\right) \tag{VI.3}$$

$\dot{p}$ is the viscoplastic multiplier (in s^{-1}). The deviatoric part of the stress tensor is $\underset{\sim}{\mathbf{s}}$. $\dot{\varepsilon}_0$ depends on temperature. $< f(\underset{\sim}{\sigma}) >$ means the maximum of $(f(\underset{\sim}{\sigma}),\, 0)$. T is the absolute temperature. V_a is the activation volume for plastic flow and k_B is Boltzmann's constant. At each instant, the yield stress R is given by

$$R = R_0 + Q[1 - \exp(-bp)] + P_1 C_{\mathrm{s}} \qquad , \qquad C_{\mathrm{s}} = C_{\mathrm{m}}\ [1 - \exp(-\mathrm{P}_2 \mathrm{p}^{\alpha} \mathrm{t}_{\mathrm{a}}^{\mathrm{n}})] \tag{VI.4}$$

where $R_0 + Q[1 - \exp(-bp)]$ is the isotropic strain hardening. The isotropic strain ageing term $P_1 C_s$ corresponds to the stress associated with strain ageing. It depends on the local plastic strain rate through the time t_{a} (called the ageing time) that a dislocation spends at localized obstacles when it gets additionally pinned by solute atoms diffusing to its core. C_{s} is the concentration of solute atoms segregating around the dislocation lines which are temporarily immobilized by extrinsic obstacles. C_{m} is the saturated concentration around the dislocations. R_0, Q, b, P_1, P_2, α and n are material parameters in equation (VI.4). An exponent n equal to 1/3 instead of the Cottrell Bilby exponent 2/3 is adopted and attributed to pipe diffusion of solute atoms along dislocation lines (Friedel, 1964). Along the macroscopic curve, the switch between low and high C_{s} during the segregation process is achieved through the "relaxation–saturation" kinetics of Avrami for t_{a} according to McCormick (Estrin and McCormick, 1991):

$$\dot{t}_{\mathrm{a}} = \frac{t_{\mathrm{w}} - t_{\mathrm{a}}}{t_{\mathrm{w}}}, \quad t_{\mathrm{w}} = \frac{\omega}{\dot{p}} \tag{VI.5}$$

This simple approximation is used here for easier handling in the computer code. The time t_{w} is the average waiting time for dislocations which are temporarily stopped by extrinsic obstacles. It depends on the plastic strain rate. The parameter ω represents the elementary strain that all mobile dislocations can produce collectively upon unpinning.

The previous model was implemented in the FE program Z–set (Z-set package, 1996). The differential equations were integrated at each Gauss point of each element using a Runge–Kutta method of fourth order with automatic time–stepping. The resolution method for global balance was based on an implicit Newton algorithm.
A 2–dimensional FE analysis was carried out for straight specimens. The mesh of the plate is shown in figure VI.1 (a). The elements used in the simulations were been 8–nodes quadratic elements with reduced integration under plane stress conditions.

Figure VI.1 (a) shows also the boundary conditions for the straight plate specimen geometry. The total length is equal to 12.5 mm and the width is 2.5 mm. The vertical displacement at the bottom is fixed to zero. The vertical displacement at the top is prescribed at a constant displacement rate. An initial defect is introduced in a single element into the specimen (lower yield stress) in order to trigger the first plastic strain rate bands. The

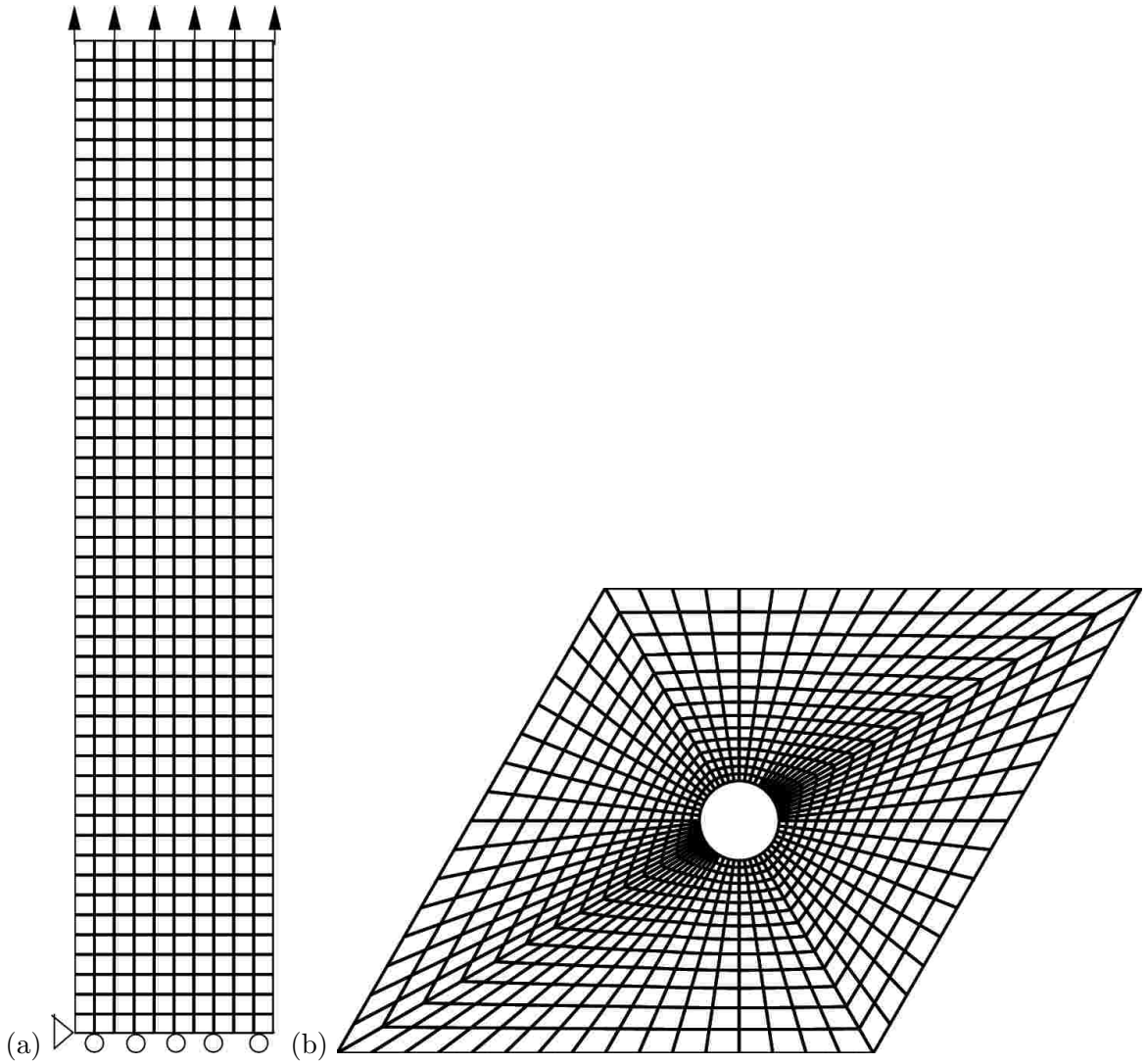

Figure VI.1 : Finite element mesh for two specimen geometries: (a) straight plate specimen, (b) 1–inclusion unit cell for periodic homogenization with $f = 2\%$.

position and the value of this defect do not disturbed significantly the simulation results.
The identification of the material parameters describing the scenario of the initiation and propagation of the plastic strain rate bands was performed on uniaxial tensile tests depending on various strain rates applied at room temperature. The found material parameters are listed in table VI.1 for the parent $Al-3\%Mg$ alloy.

Table VI.1 : Parameters of the strain ageing model for the parent $Al-3\%Mg$ alloy at room temperature.

Parameters	Units	$Al-3\%Mg$ alloy
Young's modulus	MPa	37000
Poisson's ratio	-	0.3
R_0	MPa	73
Q	MPa	165
b	-	16
P_1	MPa (atom %)$^{-1}$	17
P_2	s^{-n}	3.91
ω	-	10^{-4}
α	-	0.44
n	-	0.33
V_{a}	nm^3 atom^{-1}	6.58
C_{m}	atom %	2
$\dot{\varepsilon}_0$	s^{-1}	2.510^{-5}
Initial t_{a}	s	0

VI.2.3 Simulation results

The first purpose of this subsection is to show that the strain ageing model with the set of parameters of table VI.1 is able to reproduce the typical PLC curves and the various types of serrations depending on the applied strain rate. Three constant strain rates are selected for the simulations of the uniaxial tensile tests using straight specimens: $6.2\ 10^{-3}s^{-1}$, $1.1\ 10^{-4}s^{-1}$ and $1.1\ 10^{-5}s^{-1}$. Figure VI.2 compares the overall calculated macroscopic stress–strain curves obtained for the various applied strain rates. Several types of PLC serrations can be observed depending on the strain rates.

At $\dot{\varepsilon} = 6.2\ 10^{-3}s^{-1}$, the macroscopic curve exhibits type A serrations. Each macro–step on the stress-strain curve corresponds to the reflection of one plastic strain rate band at one end of the specimen. At $\dot{\varepsilon} = 1.1\ 10^{-4}s^{-1}$, type B serrations are observed. The propagation of the plastic strain rate bands is not continuous: no single band is observed but only a few elements of the mesh are affected at any one time by repeated plastic localization phenomena. The amplitude of PLC serrations are less pronounced than those at $\dot{\varepsilon} = 6.2\ 10^{-3}s^{-1}$. Then at $\dot{\varepsilon} = 1.1\ 10^{-5}s^{-1}$, the mixed type A+B serrations are characterized by a well defined alternate between irregular serrations and successive stress drops. Only hopping bands of some elements of the mesh are observed during the tensile test. All simulations are stopped after a strain amplitude equal to 0.02.
It is found also that the amplitude of PLC serrations on the macroscopic curve increases with

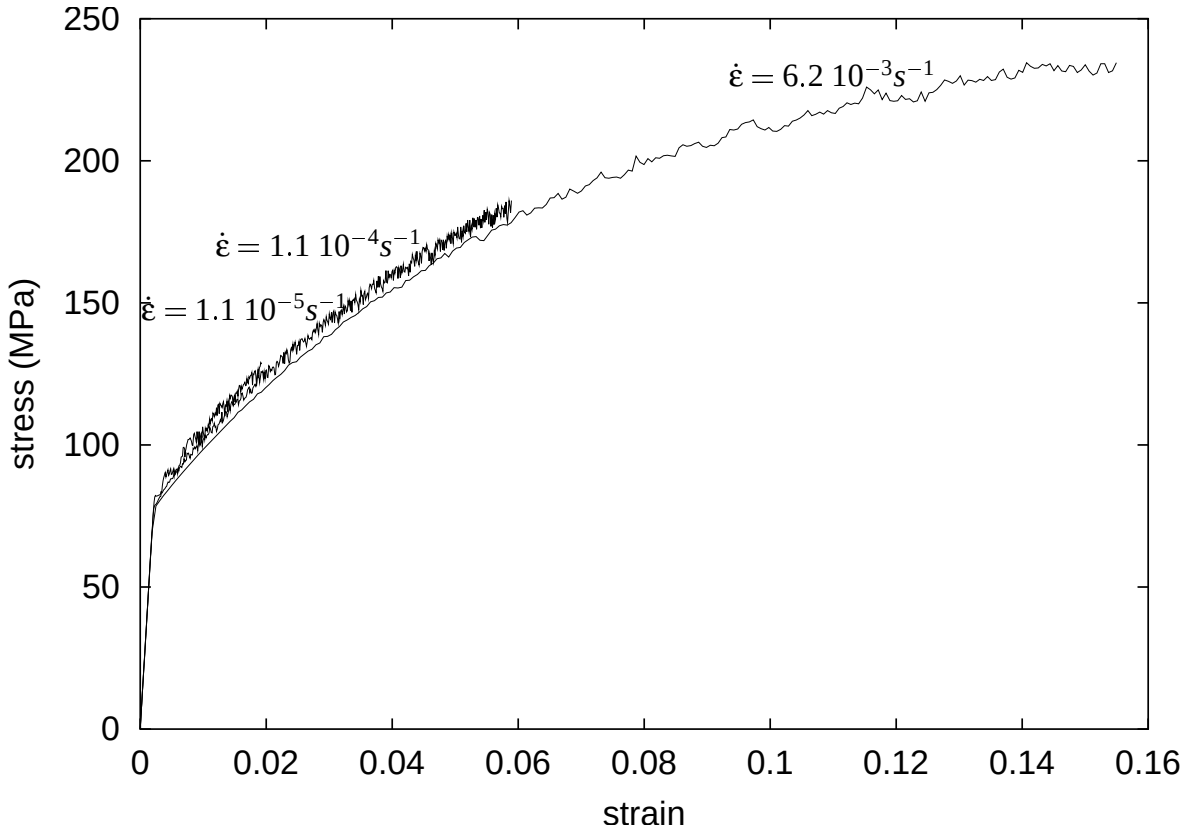

Figure VI.2 : Influence of the applied strain rate on the computed PLC stress–strain curves for the parent $Al - 3\%Mg$ alloy at room temperature.

increasing applied strain rate. This result is also suggested in (Lasko et al., 2005; Saraev and Schmauder, 2003).

Then the influence of the critical strain for serrations ε_c as a function of the applied strain rate is studied. The obtained values are given in table VI.2. The main conclusions are the following:

- the critical strain for serrations decreases when the applied strain rate decreases,
- the type of serrations observed on the macroscopic curve can be identified. It is correlated with the plastic strain rate localized in the band that can determined from the simulation. Type A serrations are associated with the higher strain rates inside the band than type B band as shown in table VI.2,
- the bands propagate at an angle of about 53° with respect to the tensile axis. A detailed description of the band formation and propagation can be found in (Lasko et al., 2005).

Table VI.2 : Critical conditions for the occurrence of PLC instabilities of the simulation results according to different applied strain rates for the parent $Al-3\%Mg$ alloy at room temperature.

Influence of applied strain rate $\dot{\varepsilon}$ (s^{-1})	Critical strain of serrations ε_c (-) simulations / experiments	Plastic strain rate localized in the band (s^{-1})	Type of serrations
$6.2\ 10^{-3}$	0.018 / 0.017	0.03	A
$1.1\ 10^{-4}$	0.006 / 0.007	0.0018	B
$1.1\ 10^{-5}$	0.005 / 0.051	0.0018	A+B

The second objective of this part is to confront experiments and simulation results. The experimental and simulated stress–strain curves are compared in figure VI.3 (a), (b), (c) under similar tensile conditions at room temperature for $\dot{\varepsilon} = 6.2\ 10^{-3}s^{-1}$, $\dot{\varepsilon} = 1.1\ 10^{-4}s^{-1}$ and $\dot{\varepsilon} = 1.1\ 10^{-5}s^{-1}$ respectively.

Regarding the types of PLC serrations, simulations and experiments are in good agreement.
The values of the critical strain for serrations are comparable between experiments and simulations except at $\dot{\varepsilon} = 1.1\ 10^{-5}s^{-1}$. The experimental results show that the "normal behavior" is observed between $\dot{\varepsilon} = 6.2\ 10^{-3}s^{-1}$ and $\dot{\varepsilon} = 1.1\ 10^{-4}s^{-1}$ when the critical strain for serrations increases with the applied strain rate (see figure VI.3 (a)). However the "inverse behavior" is observed between $\dot{\varepsilon} = 1.1\ 10^{-4}s^{-1}$ and $\dot{\varepsilon} = 1.1\ 10^{-5}s^{-1}$ for which the critical strain for serrations decreases with applied strain rate (see figure VI.3 (c)).

As a conclusion, the identified strain ageing model is a good candidate for simulating the influence of particles in AA5754 MMC, even though the "inverse" behavior is not yet accounted for.

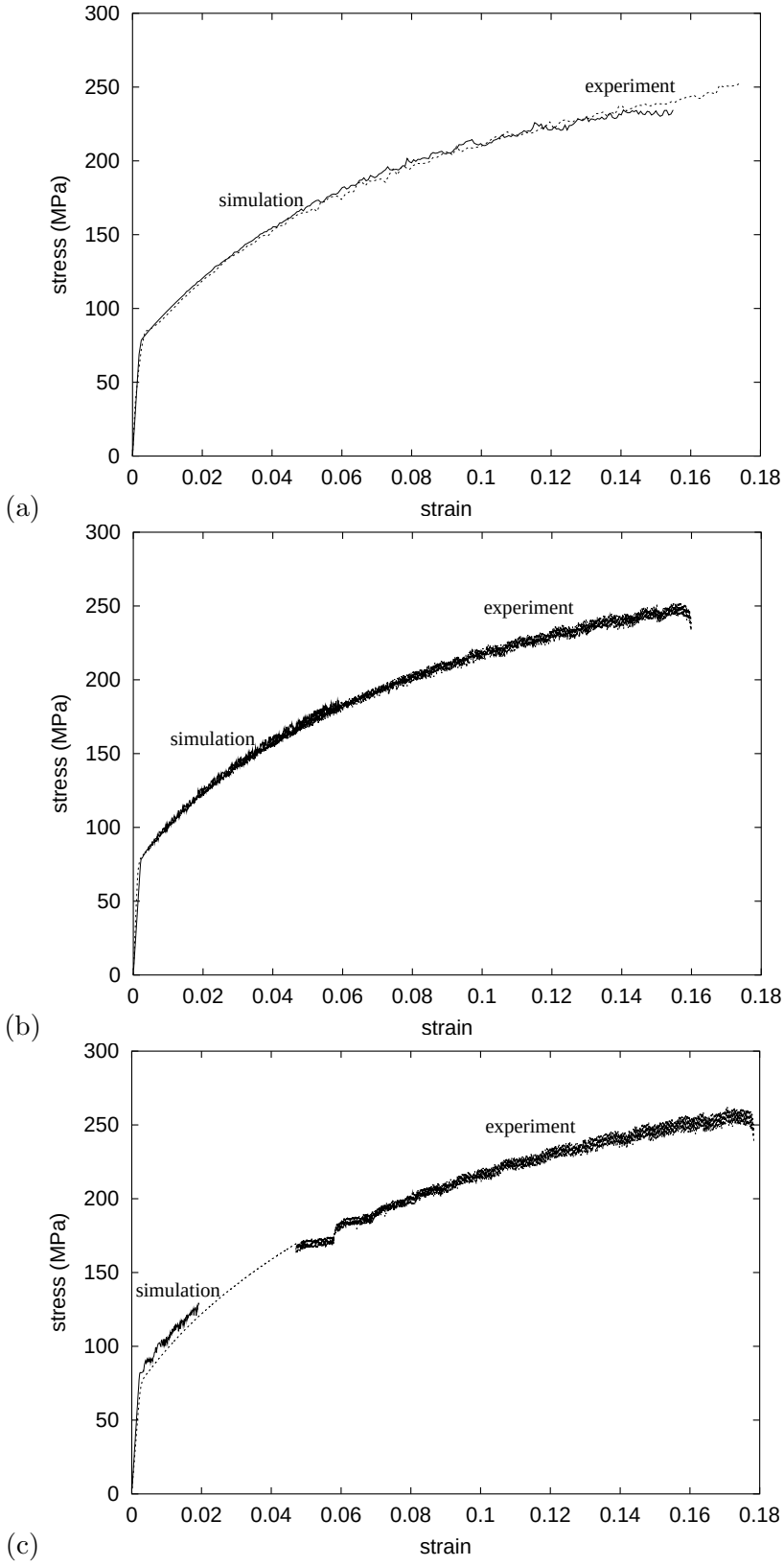

Figure VI.3 : Comparison of the experimental and simulated PLC stress–strain curves for the parent $Al - 3\%Mg$ alloy at room temperature at different applied strain rates: (a) $\dot{\varepsilon} = 6.2\ 10^{-3}s^{-1}$, (b) $\dot{\varepsilon} = 1.1\ 10^{-4}s^{-1}$, (c) $\dot{\varepsilon} = 1.1\ 10^{-5}s^{-1}$. The experimental curves are in dotted lines.

VI.3 Application to the AA5754 MMC

VI.3.1 Periodic homogenization method

Standard homogenization procedures used for composite materials (Sanchez-Palencia and Zaoui, 1987) were applied now to the AA5754 MMC. Periodic homogenization is the most straightforward approach to handle particle composites. It usually provides a correct approximation of the overall behavior at least for small volume fractions of particles, even though the actual materials are not periodic (Ohno et al., 2000). A 2–dimensional unit cell corresponding to an hexagonal distribution of circular inclusions was adopted for the sake of simplicity. Comparisons between 2D and 3D models can be found in (Saraev and Schmauder, 2003). Figure VI.1 (b) shows a 1–inclusion unit cell for a particle volume fraction $f = 2\%$. Plane stress conditions were enforced in the simulations. The influence of randomness is investigated in section VI.4.

The constitutive model of the parent $Al - Mg$ alloy identified in the previous section is used to describe the behavior of the matrix (see table VI.1). The Al_2O_3 particles are regarded as elastic with Young's modulus equal to 370000 MPa and Poisson ratio equal to 0.22.

Periodic boundary conditions were applied to the unit cell. The displacement vector u_i at each node of the mesh took the form:

$$u_i = E_{ij} x_j + v_i \tag{VI.6}$$

The node coordinates are x_i. The components E_{ij} denoted the mean applied strain. The fluctuation v_i is assumed to be periodic, meaning that it took the same value at homologous points on opposite sides of the unit cell. The forces are anti–periodic at homologous points on opposite sides of the unit cell. A classical result of periodic homogenization is that the mean strain over the unit cell V is:

$$E_{ij} = \frac{1}{V} \int_V \varepsilon_{ij}^{local} \, dV = \frac{1}{V} \int_V \frac{1}{2} (u_{i,j} + u_{j,i}) \, dV \tag{VI.7}$$

The resulting stress is computed as the mean value of the local stresses over the unit cell. The components E_{ij} are additional degrees of freedom in the FE program. The associated reaction forces are the components of the mean stress. As a result, it is possible to impose mixed loading conditions (a prescribed axial mean strain E_{22}) and vanishing remaining components of the mean stress tensor. These periodic overall tensile conditions were used in the next section. The mean tensile strain E_{22} is simply called ε in the following.

VI.3.2 Simulation results and comparison with the parent $Al-3\%Mg$ alloy

The first objective of this part is to describe the effect of particles on the simulated macroscopic stress–strain curves, in particular the type of serrations and the critical strain for serrations ε_c. These results are compared with the simulations of the parent $Al - 3\%Mg$ alloy. The main findings are summarized in table VI.3.

In figure VI.4, the computed stress–strain curves at $\dot{\varepsilon} = 6.2\ 10^{-3} s^{-1}$ for various volume fractions of particles are compared with the simulation results of the parent $Al-3\%Mg$ alloy. Classically, in composite theory, the addition of Al_2O_3 particles in the matrix strengthens the macroscopic behavior.

The addition of particles modifies the type of serrations: the amplitude of serrations is smaller for the MMC than for the bulk alloy. However we are not able to define the type of serrations observed on the macroscopic curve for the various MMCs.

The values of the critical strain for serrations ε_c, defined as the onset of serrations on the

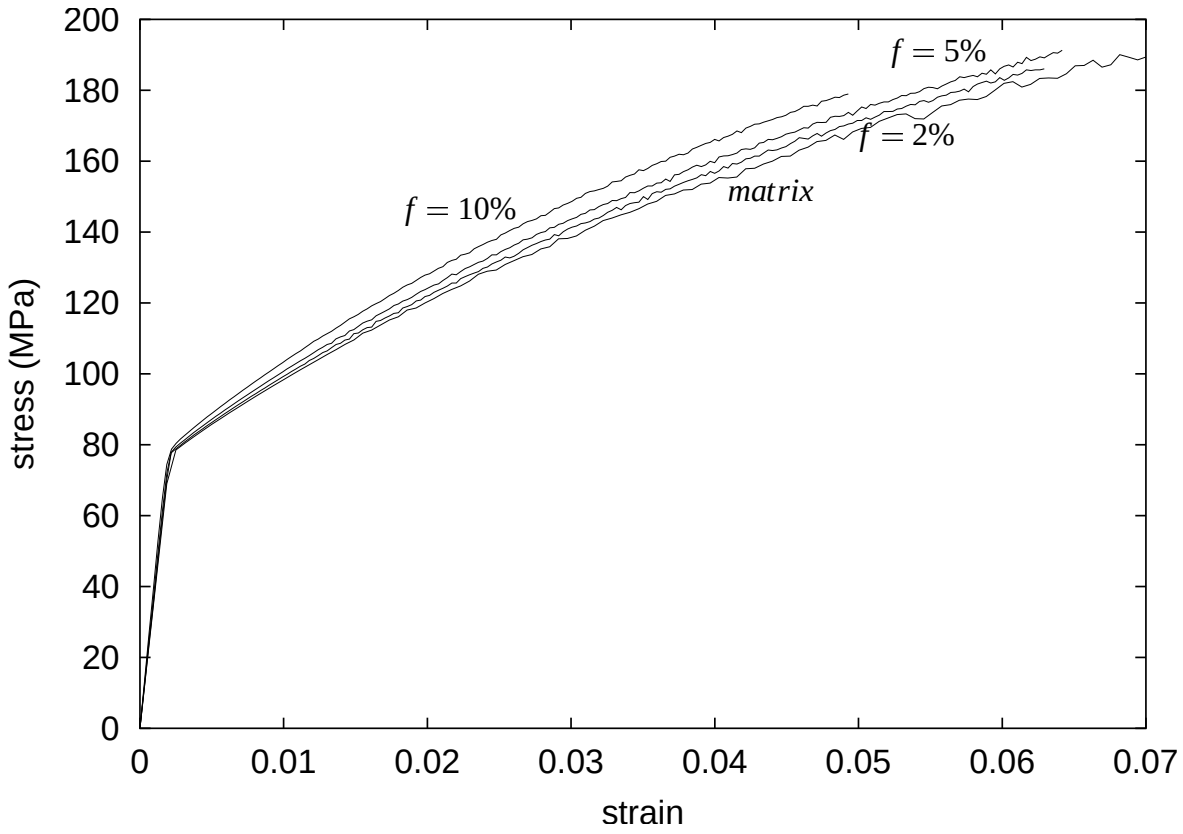

Figure VI.4 : Influence of the volume fraction of particles on the computed PLC stress–strain curves at $\dot{\varepsilon} = 6.2\ 10^{-3} s^{-1}$ for the AA5754 MMC at room temperature. From the lower to the upper curves we have successively: the parent $Al - 3\%Mg$ alloy, the AA5754 MMC with $f = 2\%$, the AA5754 MMC with $f = 5\%$, the AA5754 MMC with $f = 10\%$.

Table VI.3 : Critical strain of serrations for the simulation results at $\dot{\varepsilon} = 6.2\ 10^{-3} s^{-1}$ according to the volume fraction of particles for the AA5754 MMC at room temperature and comparison with the parent $Al - 3\%Mg$ alloy.

Influence of the volume fraction of particles f	Critical strain of serrations ε_c (-) simulations / experiments	Plastic strain rate localized in the band (s^{-1})	Type of serrations
parent $Al - 3\%Mg$ alloy	0.018 / 0.017	0.03	A
$f = 2\%$	0.014 / 0.015	0.09	indeterminate
$f = 5\%$	0.015 / 0.015	0.14	indeterminate
$f = 10\%$	0.017 / 0.008	0.19	indeterminate

overall stress–strain curves, are smaller for the different MMCs than for the parent $Al-3\%Mg$ alloy (see table VI.3). The critical strain ε_c is found to increase with increasing volume fraction f of particles. The apparent yield stress on the overall curves of figure VI.4 turns out to be almost independent of the volume fraction. It is close to the yield stress of the matrix. In contrast, the work hardening of the composite is higher than that of the bulk material. It is found to increase with increasing volume fraction (see figure VI.4). The effect of the applied strain rate on the computed stress–strain curve for $f = 2\%$ is shown in figure VI.5. A negative SRS is observed. This effect is also shown in figure VI.2 for the parent $Al - 3\%Mg$ alloy but it is more pronounced in the MMC.
Figure VI.5 also shows that the work–hardening of the MMC increases with increasing strain rate.

The second objective of this part is to study the strain rate fields inside the unit cell. These observations will provide the explanation for several of the macroscopic effects described previously. The presence of the inclusion induces stress concentrations around the particle. As a result, the first strain rate localization bands start in the close neighbourhood of the inclusion. These bands can be seen on the maps of figure VI.8(b). The formation of the first plastic band is found to coincide with the first serration on the macroscopic curve, i.e. for $\varepsilon = \varepsilon_c$. This explains why the critical strain for serrations is generally smaller for the MMC than in the bulk alloy. Two competing effects are responsible for the dependence of ε_c with respect to volume fraction f. On the one hand, the stress concentration effect leads to smaller values of ε_c. On the other hand, for a given mean strain rate $\dot{\varepsilon}$, in the composite higher volume fractions of particles lead to higher mean strain rates in the matrix since the deforming volume is reduced. This will postpone the occurrence of strain rate bands in the matrix. As a result of both effects, the values of ε_c for the bulk alloy and for the MMC with $f = 10\%$ turn out to be very close. The stress concentration effect is responsible for the fact that the initial yield stress is almost unaffected by the volume fraction of particles. The increase in work hardening rate with decreasing applied strain rate is due to DSA: lower strain rates with longer waiting times at obstacles lead to an increase in the breakaway stress of dislocations.

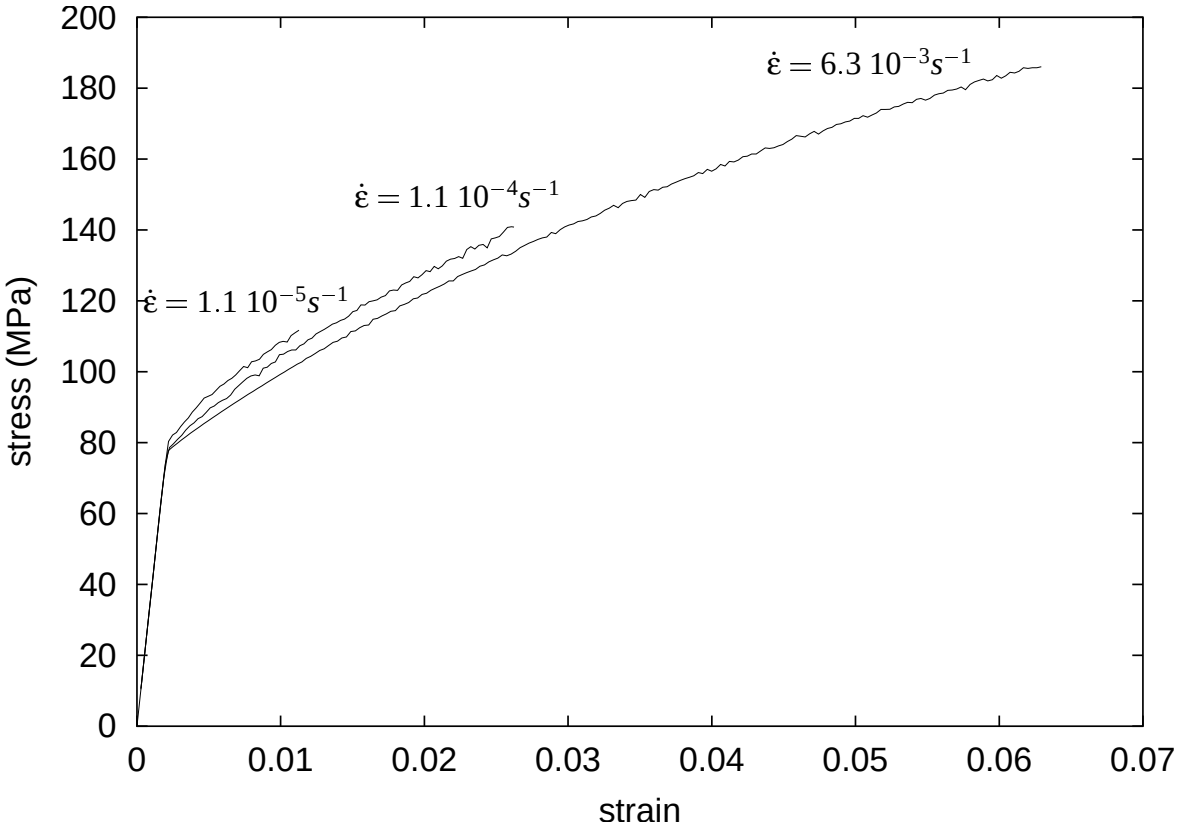

Figure VI.5 : Influence of the applied strain rate on the computed PLC stress–strain curves for the AA5754 MMC with $f = 2\%$ at room temperature.

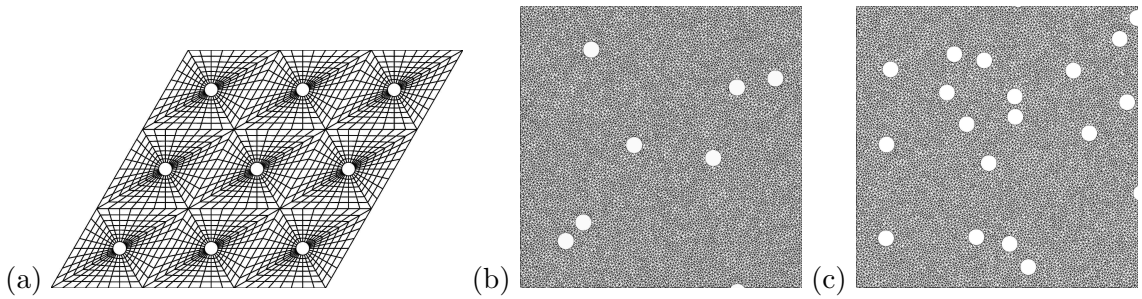

Figure VI.6 : FE meshes for periodic and random distributions of particles: (a) periodic mesh with 9–inclusion unit cell with $f = 2\%$, (b) mesh with a random distribution of particles with $f = 2\%$, (c) mesh with a random distribution of particles with $f = 5\%$.

VI.3.3 Experiment versus simulation results

Experiments were performed on flat specimens with a gauge length of 54 mm × 4 mm × 1.5 mm in size prepared from polycrystalline cold–rolled sheets of $Al-3\%Mg$ alloy and reinforced with Al_2O_3 particles. The average diameter of particles is about 3 μm. All specimens were heat treated for recovery after rolling (5h at 673K) and water quenched. Two types of samples are studied and compared with the parent $Al-3\%Mg$ alloy. Three different volume fractions of particles are tested: $f = 2\%$, $f = 5\%$ and $f = 10\%$. The uniaxial tensile tests were performed at constant strain rate at room temperature.

The experimental study shows that the addition of dispersed particles to the $Al-3\%Mg$ alloy affects the type of serrations as compared with the matrix material (Dierke, 2005). This effect is shown in figure VI.7 (a) and figure VI.7 (b) for $f = 2\%$ and $f = 5\%$ respectively at $\dot{\varepsilon} = 6.2\ 10^{-3}s^{-1}$. The simulation results reproduce correctly the type of serrations and the decrease in amplitude of the stress drops. It can be noted however that the strengthening effect of the particles predicted by the homogenization model is not observed experimentally. The type of serrations does not depend on the strain rate nor volume fraction, contrary to the case of the bulk alloy (see figure VI.5 and VI.4).

The general trend observed in the experimental results is a reduction of the critical strain ε_c in the MMC as compared with the matrix. The values of the critical strain for serrations are quite close for samples with $f = 2\%$ and $f = 5\%$. This observation is also made by Estrin et al. (Estrin and Lebyodkin, 2004) for an $Al-3\%Mg$ alloy reinforced with Al_2O_3 particles at $\dot{\varepsilon} = 2.10^{-5}s^{-1}$ at room temperature. These authors showed also that ε_c is smallest for specimens with $f = 10\%$. They correlated this effect with the clustering of particles. Indeed an increase in the volume fraction of particles favors clustering. The specimens with a small volume fraction of particles exhibit a more homogeneous distribution of particles. As a consequence, larger volumes free of particles exist inside a specimen with high volume fraction of particles so that the mechanical behavior of the specimen on the whole is determined by the matrix material to a higher degree. It is consistent with the hypothesis that the particles mainly limit the mean free path of the plastic bands. Moreover a lower yield stress is observed on the experimental macroscopic curve for the specimens with $f = 5\%$ contrary to the bulk alloy as it is shown in figure VI.7 (b).

VI.4 Discussion

VI.4.1 Mesh sensitivity and impact of periodicity constraint

In the simulation of strain localization phenomena, the analysis of the mesh size sensitivity of the results is an important issue. For that purpose, two mesh sizes of the considered unit cell are considered: (i) 1–inclusion unit cell with one mesh size of figure VI.1(b), (ii) 1–inclusion unit cell with a twice finer mesh size. The macroscopic curves of figure VI.8(a) result from the simulations of tensile tests at $\dot{\varepsilon} = 6.2\ 10^{-3}s^{-1}$ using either mesh sizes. They show that:

- for both mesh sizes, the time spans necessary for the localization phenomena to appear are: 1.9 s,
- the tensile curves are almost identical. In particular, the critical strains for serrations are equal ($\varepsilon_c = 0.014$),
- the width of the plastic strain rate band is always equal to about one element. Consequently the band width is mesh dependent. However it does not affect the mean response,

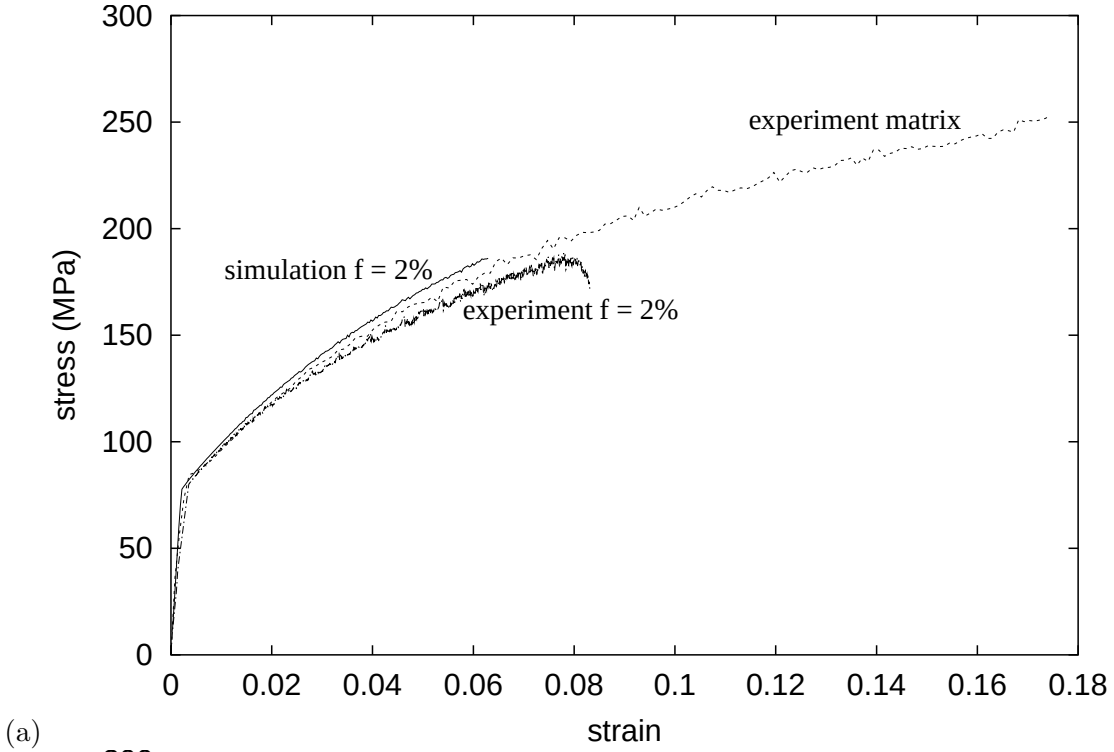

(a)

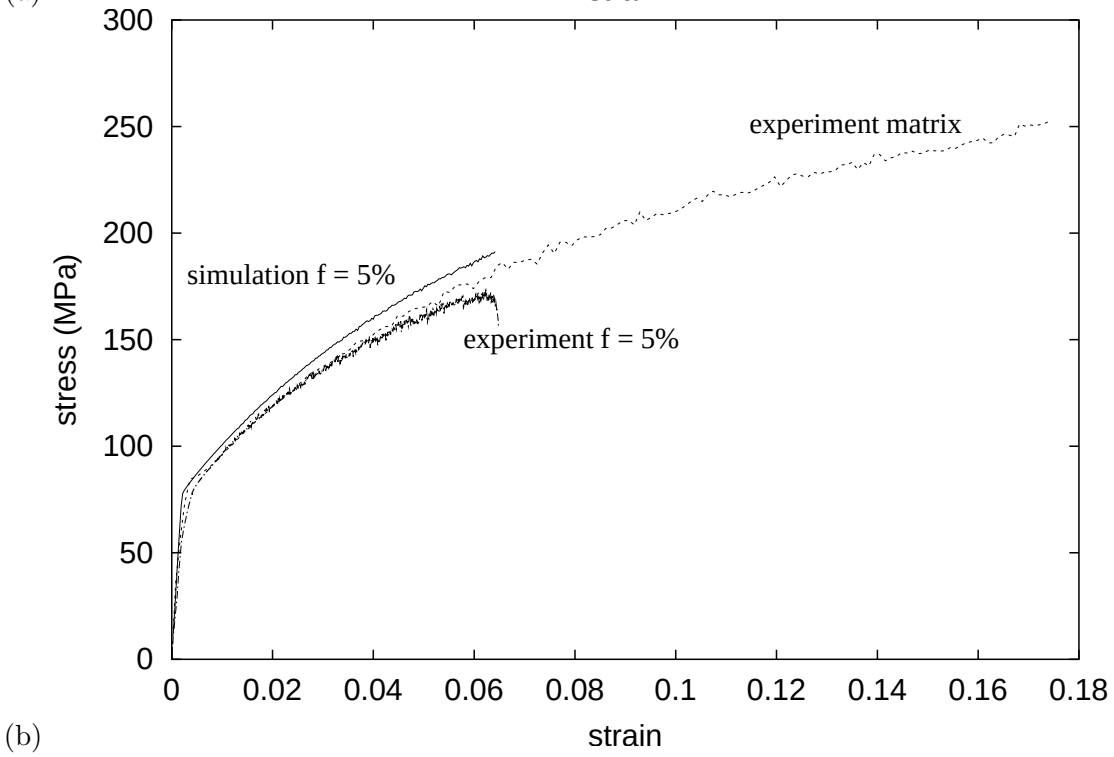

(b)

Figure VI.7 : Comparison of the experimental and simulated PLC stress–strain curves between the parent $Al-3\%Mg$ alloy and the AA5754 MMC at room temperature at $\dot{\varepsilon} = 6.2\ 10^{-3}s^{-1}$ with: (a) $f = 2\%$, (b) $f = 5\%$.

- the orientation of the band with respect to the tensile axis is mesh–independent (it is about 53°).

In the presence of strain localization phenomena, the spatial periodicity of the particles distribution is not necessary reflected in the strain field. That is why we investigated also the influence of the content of the simulated unit cell on the predicted response of the MMC. Two different unit cells are investigated: (i) a 1–inclusion unit cell (see figure VI.1(b)), (ii) a 9–inclusion unit cell (see figure VI.6(a)). Periodic conditions were applied to the outer boundaries in both cases. The results of the simulations clearly indicate that the number of cells has no influence on the macroscopic curves as shown in figure VI.8(a). However PLC serrations are slightly less pronounced using the 9–inclusion unit cell than for the 1–inclusion unit cell.
In figures VI.8(b),(c), the simulated plastic strain rate patterns in samples with 1–inclusion unit cell and 9–inclusion unit cell are shown at four different strain levels pointed out on the macroscopic curves in figure VI.8 (a). The regions with high plastic strain rates are always located directly close to particles, where local stress concentrations develop, in the first step of figures VI.8 (b), (c) in 1–inclusion unit cell and 9–inclusion unit cell respectively. Figure VI.8 (b), (c) shows that, at the beginning of straining (at about 0.017), the plastic strain rate fields around particles are almost identical for the 1–inclusion unit cell and the 9–inclusion unit cell. After a mean strain of about 0.019, the strain rate band patterns differ significantly for 1 and for 9 inclusions. The number of bands inside the central inclusion of the 9-inclusion cell is smaller than in the 1-inclusion unit cell. This effect however has no influence on the type of serrations and the critical strain for serrations as shown in figures VI.8 (a).

VI.4.2 Impact of a random distribution of particles

The actual distribution of particles in real materials is not periodic. The influence of a random distribution of particles of one single size on the simulation of PLC effect is investigated in this subsection. Images containing identical circular particles were created following a Poisson distribution. The mesh of the corresponding unit cells was made of linear triangular elements. Two volume fractions of particles are considered: $f = 2\%$ and $f = 5\%$. The meshes are shown in figure VI.6 (b), (c) respectively. Two mechanical tests were performed: a tensile test at $\dot{\varepsilon}_{22} = 6.2\ 10^{-3} s^{-1}$ and a shear test at $\dot{\varepsilon}_{12} = 6.2\ 10^{-3} s^{-1}$. For the tensile test, a vertical displacement was applied at the top of the mesh and the lateral surfaces were free of forces. Homogeneous strain conditions were applied at the boundary for the shear tests: the displacement at the boundary was then given by equation (VI.6) with $v_i = 0$.

The macroscopic equivalent von Mises stress–strain curves for the tensile and shear tests are plotted for both volume fractions in figure VI.9 (a). They are quasi–identical. This proves the isotropic character of the distribution of particles. The plastic strain rate maps for the tensile test are shown in figure VI.9 (b) and for the shear test in figure VI.9 (c), (d) for $f = 2\%$ and $f = 5\%$ respectively for different overall strain levels pointed out on the macroscopic curve in figure VI.9 (a).

The stress levels are found to be similar for a random distribution and for a periodic one. However, in contrast to the periodic case, the tensile curves obtained with a random distribution exhibit almost no serration. Simulations with larger numbers of inclusions and various types of boundary conditions would be necessary to explain this important fact. The scenario for the initiation and the propagation of plastic strain rate bands is similar in both random and periodic cases. In the shear test, horizontal and vertical PLC bands are observed (see figure VI.9 (b), (c)), which is in agreement with the prediction of classical strain localization criteria (Besson, 2004).

(a)

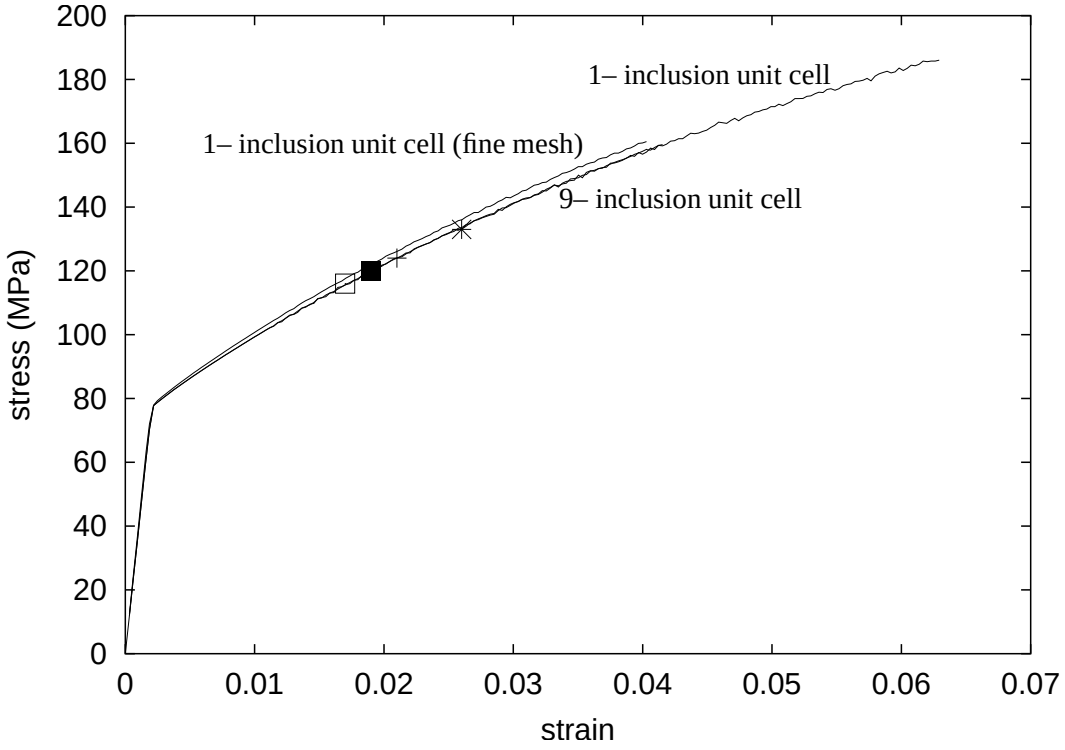

(b)

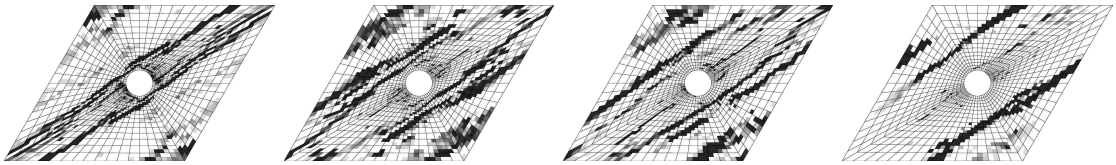

0.017, 0.019, 0.021, 0.026

(c)

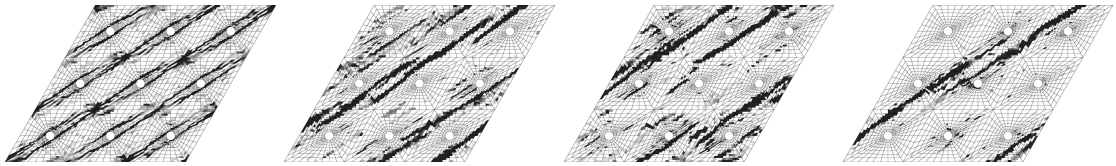

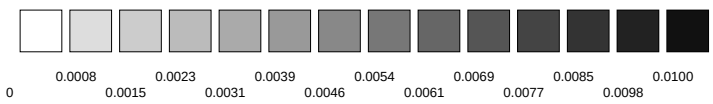

Figure VI.8 : (a) Influence of the type of meshes on the PLC stress–strain curves for the AA5754 MMC with $f = 2\%$ at room temperature at $\dot{\varepsilon} = 6.2\ 10^{-3} s^{-1}$; plastic strain rate maps (in s^{-1}) at different mean strain levels which are pointed out on the macroscopic curve in figure VI.8 (a) using: (b) 1–inclusion unit cell with the periodic distribution of particles for $f = 2\%$, (c) 9–inclusion unit cell with the periodic distribution of particles for $f = 2\%$.

(a)

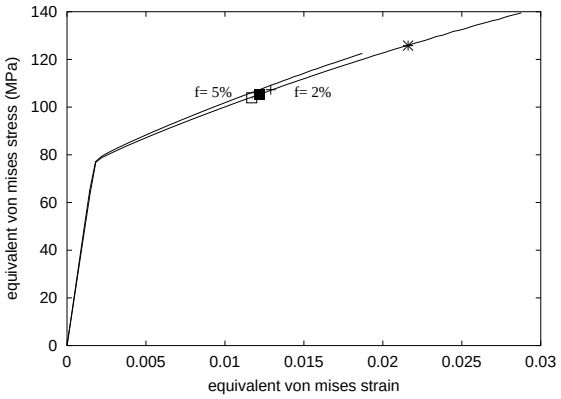

(b)

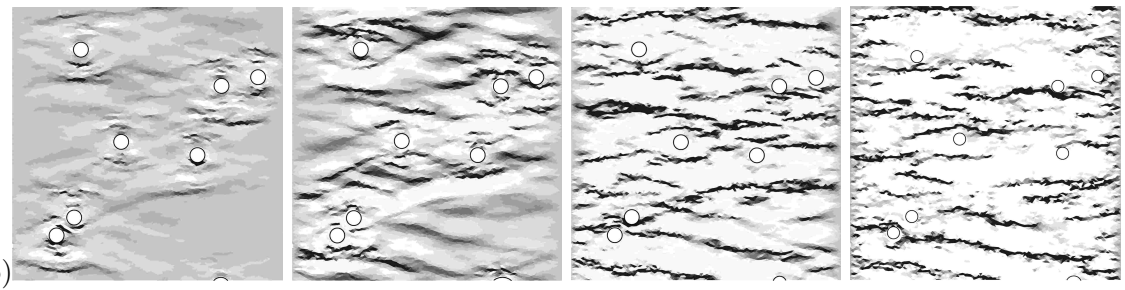

0.0117, 0.0122, 0.0129, 0.0216

(c)

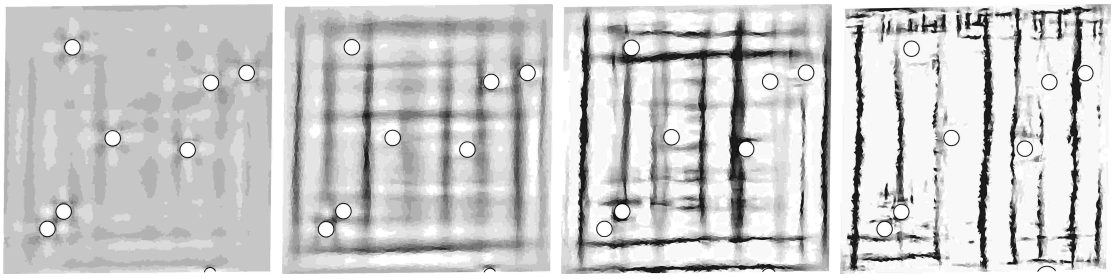

(d)

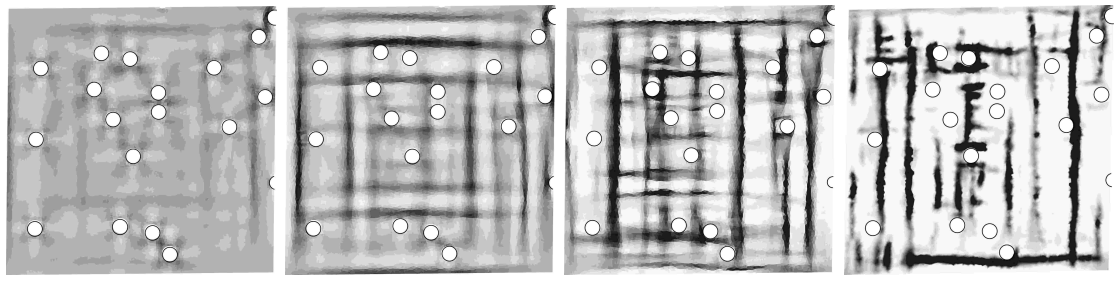

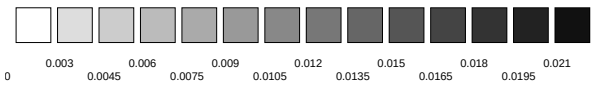

Figure VI.9 : (a) Influence of f on the PLC equivalent von Mises stress–strain curves for the AA5754 MMC at room temperature at $\dot{\varepsilon} = 6.2\ 10^{-3} s^{-1}$; plastic strain rate maps (in s^{-1}) at different strain levels which are pointed out on the macroscopic curve in figure VI.9 (a) using the mesh with a random distribution of particles: (b) for $f = 2\%$ tested in tension, (c) for $f = 2\%$ tested in shear, (d) for $f = 5\%$ tested in shear.

VI.5 Conclusions and prospects

The strain ageing model implemented in a FE code is used to predict the influence of a dispersion of Al_2O_3 particles in a parent $Al-3\%Mg$ alloy. The main features of PLC effect in the bulk alloy and the influence of particles can be summarized as follows.

- The strain ageing model is able to simulate negative SRS in the parent $Al-3\%Mg$ alloy. The experimental observations and simulation results are in good agreement. The critical strain for serrations ε_c decreases with the applied strain rate. Type A serrations (with very fine serrations), type B (intermittent propagation) and types A+B observed on the macroscopic stress–strain curves for the parent $Al-3\%Mg$ alloy are reproduced in a satisfactory manner. The PLC serrations are associated with the initiation and the propagation of the plastic strain rate localization bands.

- The simulations results for MMCs show that introducing a dispersion of particles in the material leads to a decrease of the amplitude of PLC serrations on the macroscopic curve and a reduction of the critical strain for serrations. The critical strain ε_c is found to increase with increasing volume fraction f.

- The simulation results for a periodic distribution of particles and for a random distribution of particles give similar and reliable predictions of the overall stress–strain curves for MMC including PLC effect. The random distribution of particles leads to significantly lower the amplitude of serrations on the macroscopic curve. However plastic strain rate localization bands still develop and propagate but on a finer spatial scale than for the bulk material.

- Although the macroscopic curve is stable for both 1 –inclusion and 9–inclusion unit cells, the simulation results predict differences in the plastic strain rate band patterns in 1–inclusion and 9–inclusion unit cells.

Complex strain localization phenomena take place in strain ageing MMC even if PLC serrations are reduced on the macroscopic curve. Accordingly neglecting them in the design of engineering components is not without consequence regarding fracture processes. In our simulations, the correlation between the critical strain for serrations and the clustering of particles were not investigated systematically. The influence of the distribution of particles size, the clustering of particles and the failure assessment will be the subject of future analysis about MMC.

Acknowledgements

The authors thank F. N'Guyen (Centre des Matériaux / UMR 7633, Ecole des Mines de Paris / CNRS / France) for providing pictures with the random distribution of particles and K. Madi (Centre des Matériaux / UMR 7633, Ecole des Mines de Paris / CNRS / France) for meshing these pictures. The authors thank also for the support given by the European RTN DEFINO network and the DFG (Deutsche Forschungsgemeinschaft).

Bibliography

Ahn, J. and Nam, S. (1990). The effect of dynamic strain ageing on the anomalous strain rate dependent tensile strain of Zircaloy–4. *Materials Letters*, 9(10):413–415.

Ashby, M. (1972). A first report on deformation-mechanism maps. *Acta Met.*, 20:887–897.

Aubrun, P. (1975). L'effet des atomes étrangers mobiles sur une limite d'écoulement. *C.R.A.S.*, Série C, 280:1081–1084.

Azaroff, L. (1960). *Introduction to solids*. Mc Graw–Hill.

Bailly, H., D. Ménessier, and Prunier, C. (1996). *Le combustible nucléaire des réacteurs à eau sous pression et des réacteurs à neutrons rapides*. Eyrolles.

Balik, J. and Lukac, P. (1993). Portevin–Le Chatelier effect in Al–3%Mg conditioned by strain rate and strain. *Acta Metall.*, 41:1447–1454.

Barnby, J. (1965). Effect of strain aging on the high-temperature tensile properties of an AISI 316 austenitic stainless steel. *J. Iron Steel Inst.*, 203:392–397.

Béchade, J. (1995). Le zirconium. *Journées d'études Propriétés Microstructure, INSTN, Saclay 25–26 Avril 1995, EDP*, pages 47–56.

Béchade, J. (2004). Rapport interne de fabrication. *DRT/DTEN/S3M/LMTMEx, CEA*.

Belotteau, J. (2004). *Le vieillissement statique et dynamique des aciers–Influence sur la rupture ductile (in preparation)*. PhD thesis, Ecole Centrale Paris.

Benallal, A., Berstad, T., Borvik, T., Clausen, A., and Hopperstad, O. (2006). Dynamic strain aging and related instabilities: experimental, theoritical and numerical aspects. *European Journal of Mechanics A/Solids*, 25:397–424.

Berry, B. (1965). *IBM Rs. Rep. RC–1350*.

Besson, J. (2004). *Local approach to fracture*. Ecole des Mines de Paris–Les Presses.

Besson, J., Cailletaud, G., Chaboche, J.-L., and Forest, S. (2001). *Mécanique non linéaire des matériaux*. Hermès, France.

Blanc, D. (1987). *Effet de soluté et déformation plastique d'un acier inoxydable austénitique*. PhD thesis, Ecole des Mines de Paris.

Bodner, S. and Baruch, J. (1967a). Determination of dislocation velocities and densities from deformation waves of discontinuous yielding. *J. Appl. Phys.*, 43(5):2092–2101.

Bodner, S. and Baruch, J. (1967b). The influence of strain rate and strain ageing on the flow stress of commercially pure aluminum. *J. Mech. Phys. Solids B*, 63:K29.

Borch, N., Shepard, L., and Dorn, J. (1960). Activation energies for creep of an alpha solid solution of magnesium in aluminum. *Trans. Am. Soc. Met.*, 52:494–513.

Brandes, M. and Mills, M. (2004). Static recovery in titanium alloys at lower temperatures. *Materials Science and Engineering A*, 387–389:570–575.

Brindley, B., Corderoy, D., and Honeycombe, R. (1962). Yield point and Lüders bands in single crystal of copper–base alloys. *Acta Metall.*, 10:1043–1050.

Brindley, B. and Worthington, P. (1970). Yield point phenomena in substitutional alloys. *Metallurgical Reviews*, 145:101–114.

Browne, K. (1971). Stress induced diffusion of oxygen in alpha-zirconium. *Scripta Metallurgica*, 5:519–523.

Browne, K. (1972). Mechanical relaxation and diffusion of interstitial atoms in H.C.P. metals. *Acta Met.*, 20:507–514.

Brzeski, J., Hack, J., Darolia, R., and Field, R. (1993). Strain ageing embrittlement of the ordered intermetallic compound NiAl. *Mater. Sci. Eng. A*, 170:11–18.

Butler, J. (1962). Lüders front propagation in low carbon steels. *J. Mech. Phys. Solids*, 10:313–334.

Béranger, G. and Lacombe, P. (1965). Contribution à l'étude de la cinétique de l'oxydation du zirconium alpha et de la diffusion de l'oxygène dans le métal sous-jacent à l'oxyde. *Journal of Nuclear Materials*, 16:190–207.

Caillard, D. and Couret, A. (1991). *Dislocations in Solids*, volume Dislocation cores and yield stress anomalies, page 139. F.R.N. Nabarro and M.S. Duesbery.

Caillard, D., Couret, A., Clément, N., Farenc, S., and Molénat, G. (1991). *Strength of Metals and Alloys*, page 139. Freund Publish. House, London.

Caillard, D., Couret, A., and Molénat, G. (1993). Mechanisms of yield stress anomalies in beryllium and Ni3Al. *Mater Sci. Eng. A*, 164:69–81.

Caisso, J. (1959). Etude du phénomène Portevin–Le Chatelier à diverses températures dans les alliages aluminium–magnésium. *Revue de Métallurgie*, LVI(3):237–246.

Casarotto, L., Tutsch, R., Ritter, R., Weidenmüller, J., Ziegenbein, A., Klose, F., and Neuhäuser, H. (2003). Propagation of deformation bands investigated by laser scanning extensometry. *Computational Materials Science*, 26:210–218.

Chatelier, F. L. (1909). Influence du temps et de la température sur les essais au choc. *Revue de Métallurgie*, 6:914–917.

Chihab, K. (1987). *Etudes des instabilités de la déformation plastique associées à l'effet Portevin–Le Chatelier dans les alliages aluminium–magnésium.* PhD thesis, Université de Poitiers.

Chihab, K., Ait-Amokhtar, H., and Bouabdellah, K. (2002). Serrated yielding due to Portevin–Le Chatelier effect in commercial Al–Mg alloys. *Ann. Chim. Sci. Mat.*, 27:69–75.

Chihab, K., Estrin, Y., Kubin, L., and J.Vergnol ((1987)). The kinetics of the Portevin–Le Chatelier bands in an Al–5%Mg alloy. *Scripta Metallurgica*, 21:203–208.

Choubey, R. and Jonas, J. (1981). High temperature flow and aging behaviour of oxygen-enriched Zircaloy-2 and Zr-2.5Nb. *Metal. Sci.*, 15:30–38.

Coleman, C., Mills, D., and Kuur, J. V. (1972). Deformation parameters of neutron irradiated Zircaloy-4 at 300°c. *Canadian Metallurgical Quarterly*, 11:91–100.

Conrad, H. (1964). Thermally activated deformation of metals. *J. Met.*, 16:582–588.

Cottrell, A. (1948). Effect of solute atoms on the behaviour of dislocations. pages 30–38. Physical Society, London.

Cottrell, A. (1953). A note on the Portevin–Le Chatelier effect. *Phil. Mag.*, 44:829–832.

Cottrell, A. and Bilby, B. (1949). Dislocation theory of yielding and strain ageing of iron. *Proc. Phys. Soc. Conf. A*, 62:49–62.

Couret, A. and Caillard, D. (1991). Dissociations and friction forces in metals and alloys. *J. Phys. III*, 1:885–907.

Couret, A., Caillard, D., Puschl, W., and Schoeck, G. (1991). Prismatic glide in divalent hcp metals. *Philos. Mag. A*, 63:1045–1057.

Cuddy, L. and Leslie, W. (1972). Some aspects of serrated yielding in substitutional solid solutions of iron. *Acta Met.*, 20:1157–1167.

Delafosse, D., Lapasset, G., and Kubin, L. (1993). Dynamic strain ageing and crack propagation in the 2091 Al–Li alloy. *Scripta Metallurgica Materialia*, 29:1379–1384.

Derep, J., Ibrahim, S., Rouby, R., and Fantozzi, G. (1980). Deformation behavior of Zircaloy 4 between 77K and 900K. *Acta Met.*, 28:607–619.

Dickson, J., Handfield, L., and Boutin, J. (1984). A comparison of two simple methods for measuring cyclic internal and effective stresses. *Materials Science and Engineering A*, 64:7.

Dierke, H. (2005). *PLC Effekt in Al-Mg Legierungen und Verbundwerkstoffen–Experimente, Mikrostrukturuntersuchungen und Modellierung (in preparation).* PhD thesis, TU Braunschweig.

Dierke, H., Krawehl, F., Graff, S., Forest, S., Sachl, J., and Neuhäuser, H. (2006). Portevin–Le Chatelier effect in Al–Mg alloy: influence of obstacle–experiments and modelling. *Computational Materials Science*, In press.

Estrin, Y. and Kubin, L. (1986). Local strain hardening and nonuniformity of plastic deformation. *Acta metall.*, 34:2455–2464.

Estrin, Y. and Kubin, L. (1988). Plastic instabilities: classification and physical mechanisms. *Res. Mechanica*, 23:197.

Estrin, Y. and Kubin, L. (1989). Collective behavior in dilute alloys and the Portevin–Le Chatelier effect. *Journal of mechanical behaviour mater.*, 2:255–292.

Estrin, Y. and Kubin, L. (1995). *H. Mülhaus (Ed.), Continuum Models for Materials with Microstructure*, volume Spatial coupling and propagative plastic instabilites, in:, pages 395–398. John Wiley Sons, Chichester.

Estrin, Y., Kubin, L., and Aifantis, E. (1993). Introductory remarks to the viewpoint set on propagative plastic instabilities. *Scripta Met. Mat.*, 29:1147–1150.

Estrin, Y. and Lebyodkin, M. (2004). The influence of dispersion particles on the Portevin–le Chatelier effect: from average particle characteristics to particle arrangement. *Materials Science and Engineering A*, 387–389:195–198.

Estrin, Y. and McCormick, P. (1991). Modelling the transient behaviour of dynamic strain ageing materials. *Acta Metall.*, 39:2977–2983.

Farenc, S. (1992). *Etude des mécanismes de déformation dans le titane et l'alliage intermétallique TiAl*. PhD thesis, Université de Toulouse.

Farenc, S., Couret, A., and Caillard, D. (1995). A new model for the peak of activation area of alpha-titanium. *Acta Metall. Mater.*, 43:3669–3678.

Ferrer, F. (2000). *Etude des mécanismes de déformation du zirconium entre* $25°C$ *et* $400°C$*– Influence d'une faible teneur en soufre*. PhD thesis, Ecole polytechnique, Palaiseau.

Forest, S. (1997). Strain localization phenomena in generalized single crystal plasticity. *J. Mech. Behav. Mater.*, 11:45–50.

Friedel, J. (1964). *Dislocations*, pages 351–414. Pergamon Press.

Frost, H. and Ashby, M. (1982). Deformation–mechanism maps. *Pergamon Press*.

Gacougnolle, J., Sarrazin, S., and de Fouquet, J. (1970). Pics de frottement intérieur au voisinage de $420°C$ dans les alliages zirconium–hafnium–oxygène. *C.R. Acad. Sc. Paris, t.270*, Série C:158–161.

Garde, A., Aigeltinger, E., Woodruff, B., and Reed-Hill, R. (1975). Concerning the strength of dynamic strain aging in zirconium. *Met. Trans.*, 6A:1183–1188.

Graff, S. (2002). Modélisation des effets viscoplastiques et des phénomènes de localisation de type Portevin–Le Chatelier.

Graff, S. and Béchade, J. (2001). Le comportement en fluage sous pression interne du Zircaloy–4 détendu de $20°C$ à $380°C$ et pour un large domaine de contraintes. *Rapport de stage d'ingénieur*.

Graff, S., Forest, S., Strudel, J.-L., Prioul, C., Pilvin, P., and Béchade, J.-L. (2004). Strain localization phenomena associated with static and dynamic strain ageing in notched specimens : experiments and finite element simulations. *Material Science and Engineering A*, 387-389:181–185.

Graff, S., Forest, S., Strudel, J.-L., Prioul, C., Pilvin, P., and Béchade, J.-L. (2005). Finite element simulations of dynamic strain ageing effects at V–notches and crack tips. *Scripta Materialia*, 52:1181–1186.

Gupta, P. D. and Arunachalam, V. (1968). Thermally activated deformation in dilute zirconium/oxygen alloys. *J. Mat. Sci.*, 3:271–281.

Haasen, P. (1983). *Mechanical properties of solid solutions and intermetallic compounds*, chapter 21. North Holland Physics Publishing, 3^d edition.

Hähner, P. (1993). Modelling the spatio–temporal plastic instabilities. *Material Science and Engineering A*, 164:23–34.

Hähner, P. (1996a). On the foundations of stochastic dislocation dynamics. *Appl. Physics A*, 62:473–481.

Hähner, P. (1996b). On the physics of the Portevin–Le Chatelier effect, Part I.: The statistics of dynamic strain ageing. *Material Science and Engineering A*, 207:208–215.

Hähner, P. (1996c). On the physics of the Portevin–Le Chatelier effect, Part II.: From microscopic to macroscopic behaviour. *Material Science and Engineering A*, 207:216–223.

Hähner, P. (1997). On the critical conditions of the Portevin–Le Chatelier effect. *Acta Met. Mat.*, 45:3695–3707.

Hähner, P., Ziegenbein, A., Rizzi, E., and Neuhäuser, H. (2002). Spatiotemporal analysis of Portevin–Le Chatelier deformation bands : theory, simulation and experiment. *Physical Review B*, 65:134109–1–134109–20.

Hamersky, M. and Trojanova, Z. (1985). An analysis of the stress relaxation curves. *J. Phys. B*, 35:292–297.

Handfield, L., Dickson, J., and G. L'Esperance (1985). A comparison of the cyclic deformation behaviour of two purities of zirconium. volume 1, pages 355–360. Pergamon Press.

Hirth, J. and Lothe, J. (1968). Theory of dislocations. *McGraw–Hill*, ref. 7:613–619.

Hirth, J. and Lothe, J. (1982). *Theory of dislocations*. McGraw–Hill, 2^d edition.

Hollomon, J. (1945). Tensile deformation. *Trans. AIME*, 162:258–272.

Hong, S. (1984). Influence of dynamic strain aging on the apparent activation energy for creep. *Materials Science and Engineering*, 64:L19–L21.

Hong, S., Ryu, W., and Rim, H. (1983). Elongation minimum and strain rate sensitivity minimum of Zircaloy-4. *Journal of Nuclear Materials*, 116:314–316.

Hood, G. (1988). Point defect diffusion in alpha-Zr. *Journal of Nuclear Materials*, 159:149–175.

Hull, D. and Bacon, D. (1984). *Introduction of dislocations*. Pergamon Press, 3^d edition.

Imanaka, T. and Fujimoto, K. (1968). Mechanism of strain age-hardening in low-carbon steels. *Suppl. to Trans. Jap. Inst. Met.*, 9:364–368.

Kapoor, R., Wadekar, S., and Chakravartty, J. (2002). Deformation in Zr–1Nb–1Sn–0.1Fe using stress relaxation technique. *Materials Science and Engineering A*, 328:324–333.

Karimi, A. (1981). *Etude sur machine molle de la déformation plastique hétérogène. Cas d'un acier austénitique*. PhD thesis, Ecole des Mines de Paris.

Kê, T. and Tsien, C. (1956). *Scientia Sin.*, 5:625.

Kearns, J. (1965). Thermal Expansion and Preferred Orientation in Zircaloy. *Rapport WAPD–TM 472, Novembre 1965*.

Keh, A. and Leslie, W. (1963). *Material Science Research*, volume 1, page 208. H.H. Stadelmaier and W.W. Austin, Plenum Press, New York.

Kelly, P. and Smith, P. (1973). Strain ageing in zirconium–oxygen alloys. *Journal of Nuclear Materials*, 46:23–34.

Klose, F. (2004). *Experimental and numerical studies on the Portevin–Le Chatelier effect in Cu-Al and Al-Mg in strain and stress controlled tensile tests.* PhD thesis, Technische Universität Carolo Wilhelmina zu Braunschweig.

Klose, F., Ziegenbein, A., Weidenmüller, J., Neuhäuser, H., and Hähner, P. (2003a). Portevin–Le Châtelier effect in strain and stress controlled tensile tests. *Computational Materials Science*, 26:80–86.

Klose, F., Ziegenbein, A., Weidenmüller, J., Neuhäuser, H., and Hähner, P. (2003b). Portevin–Le Chatelier effect in strain and stress controlled tensile tests. *Computational Materials Science*, 26:80–86.

Knorr, D. and Notis, M. (1975). Deformation mechanism mapping of alpha–Zr and Zircaloy-2. *Journal of Nuclear Materials*, 56:18–24.

Kocks, U., Argon, A., and Ashy, M. (1975). Thermodynamics and kinetics of slip. *Progr. Mater. Sci.*, 19:1–281.

Kok, S., Bharathi, M., Beaudoin, A., Fressengeas, C., Ananthakrishna, G., Kubin, L., and Lebyodkin, M. (2003). Spatial coupling in jerky flow using polycristal plasticity. *Acta Materialia*, 51:3651–3662.

Korbel, A., Blaz, L., Dybiec, H., Gryziecki, J., and Zasadzinski, J. (1979). *Metals Technology*, 6:391–397.

Korbel, A., Zasadzinski, J., and Sieklucka, S. (1976). A new approach to the Portevin–Le Chatelier effect. *Acta Metall.*, 24:919–923.

Kubin, L. and Estrin, Y. (1984). Thermal effects in low temperature deformation: the response to strain rate changes. *Cryst. Res. Technol.*, 19:853–862.

Kubin, L. and Estrin, Y. (1985). The Portevin–Le Chatelier effect in deformation with constant stress rate. *Acta Metall.*, 33:397–407.

Kubin, L. and Estrin, Y. (1989a). Comment on the strain rate sensitivity during serrated yielding. *Scripta Metallurgica*, 23:815–817.

Kubin, L. and Estrin, Y. (1989b). Evolution of dislocation densities and the critical conditions for the Portevin–Le Chatelier effect. *Acta Metall. Mater.*, 38(5):697–708.

Kubin, L. and Estrin, Y. (1991a). Dynamic strain ageing and the mechanical response of alloys. *J. Phys.*, III 1:929–943.

Kubin, L. and Estrin, Y. (1991b). Plastic instabilities: phenomenology and theory. *Material Science and Engineering A*, 137:125–134.

Kubin, L., Estrin, Y., and Perrier, C. (1992). On static strain ageing. *Acta Metall. Mater.*, 40(5):1037–1044.

Kubin, L., Estrin, Y., and Spiesser, P. (1984). Low temperature plastic deformation of metals and the bifurcation theory. *Res. Mechanica*, 10:25.

Lacombe, P. (1985). L'effet Portevin-Le Chatelier, ses caractéristiques et ses conséquences sur les hétérogénéités de déformation plastique. *Matériaux et Techniques*, E:5–15.

Lasko, G., Hähner, P., and Schmauder, S. (2005). Finite element simulation of the Portevin–Le Chatelier effect. *Modelling and simulation in Materials Science and Engineering*, 13:645–656.

Lebyodkin, M., Brechet, Y., Estrin, Y., and Kubin, L. ((1996)). Statistical behaviour and strain localization patterns in the Portevin–Le Chatelier effect. *Acta Mater*, 44:4531–4541.

Lebyodkin, M., Dunin-Barkowskii, L., Brechet, Y., Estrin, Y., and Kubin, L. (2000). Spatio–temporal dynamics of the Portevin–Le Chatelier effect: experiment and modelling. *Acta Materialia*, 48:2529–2541.

Lee, D. (1972). Strain rate dependent hardening in zirconium and zirconium–niobium alloy. *Canadian Metallurgical Quarterly*, 11:113–120.

Lee, K., Kim, S., and Hong, S. (2001). Ductility and strain rate sensitivity of Zircaloy–4 nuclear fuel claddings. *Journal of Nuclear Materials*, 295:21–26.

Legrand, B. (1984). *Influence de la structure électronique sur la facilité relative des glissements dans les métaux de structure hexagonale compacte*. PhD thesis, Université Pierre et Marie Curie.

Lemaignan, C. (2004). *Science des mat ériaux pour le nucléaire*. Génie atomique-INSTN.

Ling, C. and McCormick, P. (1990). Strain rate sensitivity and transient behaviour in Al–Mg–Si alloy. *Acta Metall.*, 38:2631–2635.

Ling, C. and McCormick, P. (1993). The effect of temperature on strain rate sensitivity in an Al–Mg–Si alloy. *Acta Metall. Mater.*, 41:3127–3131.

Lomer, W. (1952). The yield phenomenon in polycrystalline mild steel. *J. Mech. Phys. Solids*, 1:64–73.

Louat, N. (1956). The effect of temperature on Cottrell atmospheres. *Proc. Royal Soc. London*, 69:459–467.

Louat, N. (1981). On the theory of the Portevin–Le Chatelier effect. *Scripta Metallurgica*, 15:1167–1170.

Louche, H. and Chrysochoos, A. (2001). Thermal and dissipative effects accompanying Lüders band propagation. *Materials Science and Engineering A*, 307:15–22.

Lustmann, B. and Kerze, F. (1955). *The metallurgy of zirconium*. Mac Graw–Hill, Book Company inc.

Mahajan, S., Brasen, D., and Haasen, P. (1979). Lüders band in deformed silicon crystals. *Acta Metall.*, 27:1165–1173.

Manning, J. (1968). *Diffusion kinetics for atoms in crystals*. D. van Nostrand.

McCormick, P. (1972). A model for the Portevin–Le Chatelier effect in substitutional alloy. *Acta Met.*, 20:351–354.

McCormick, P. (1986). Dynamic strain ageing. *Acta Metallurgica*, 36:98–106.

McCormick, P. (1988). Theory of flow localisation due to dynamic strain ageing. *Acta Met.*, 36:3061–3067.

McCormick, P. and Ling, C. (1995). Numerical modeling of the Portevin–Le Chatelier effect. *Acta Metall. Mater.*, 43-5:1969–1977.

Mesarovic, S. D. (1995). Dynamic strain aging and plastic instabilities. *J. Mech. Phys. Solids, 43*, 5:671–700.

Miquet, A. (1982). Solid state phase equilibria of Zircaloy–4 in the temperatures range 750-1050°C. *J. Nucl. Mat.*, 105:132–141.

Mishra, S. and Asundi, M. (1971). Comments on stress induced diffusion of oxygen in alpha zirconium. *Scripta Metallurgica*, 5:973–976.

Mishra, S. and Asundi, M. (1972). Internal friction studies in dilute zirconium alloys. *Canadian Metallurgical Quarterly*, 11(1):69–77.

Mulford, R. and Kocks, U. (1979). New observations on the mechansims of dynamic strain aging and of jerky flow. *Acta Met.*, 27:1125–1134.

Nabarro, F. (1947). Dislocations in a simple cubic lattice. *Proc. Phys. Soc.*, 59:256.

Nabarro, F. (2003). One–dimensional models of thermal activation under shear stress. *Philosophical Magazine*, 83-26:3047–3054.

Nadai, A. (1950). *Theory of flow and fracture of solids.* McGraw–Hill.

Naka, S., Lasalmonie, A., Costa, P., and Kubin, L. (1988). The low temperature plastic deformation of alpha-titanium and the core structure of a type screw dislocations. *Philos. Mag. A*, 57:717–740.

Neuhäuser, H. (1983). *Slip line formation and collective dislocation motion*, volume 6, chapter 31, pages 319–440. North Holland.

Nowick, A. and Heller, W. (1963). Anelasticity and stress-induced ordering of. point defects in crystals. *Adv. Phys.*, 12:251.

Ohno, N., Wu, X., and Matsuda, T. (2000). Homogenized properties of elastic–viscoplastic composites with periodic internal structures. *International Journal of Mechanical Sciences*, 42:1519–1536.

Penning, P. (1972). Mathematics of the Portevin–Le Chatelier effect. *Acta Metall.*, 20:1169–1175.

Pink, E. and Grinberg, A. (1982). Stress drops in serrated flow curves of Al5%Mg. *Acta Met.*, 30:2153–2160.

Piobert, G. (1842). Traité d'artillerie théorique et pratique. *Mémorial Artillerie*, V:525.

Portevin, A. and Chatelier, F. L. (1923). Sur un phénomène observé lors de l'essai de traction d'alliages en cours de transformation. *Compt. Rend. Sci.*, 176:507–510.

Povolo, F. and Bisogni, E. (1966). Mechanical relaxation modes of paired point defects in h.c.p. crystals. *Acta Metallurgica*, 14:711–718.

Prioul, C. (1995). *Le zirconium*, volume Le vieillissement dynamique dans les alliages de zirconium. Conséquences sur les propriétés mécaniques, page 25. Les éditions de physique.

Pujol, C. (1994). *Etude des mécanismes de déformation en traction et fluage du zirconium α entre $20°C$ et $300°C$.* PhD thesis, Ecole des Mines de Paris.

Ramachandran, V. and Reed-Hill, R. (1970). Dynamic strain aging and ductility minima in zirconium. *Metal. Trans.*, 1:2105–2109.

Ranc, N. and Wagner, D. (2005). Some aspects of Portevin–Le Chatelier plastic instabilities investigated by infrared pyrometry. *Materials Science and Engineering A*, 394:87–95.

Rauch, E. and G'sell, C. (1989). Flow localization induced by a change in strain path in mild steel. *Materials science and engineering*, 111:71–80.

Rheem, K. and Park, W. (1976). *J. Korean Nucl. Soc.*, 8:19.

Ritchie, I. and Atrens, A. (1977). The diffusion of oxygen in α zirconium. *Journal of Nuclear Materials*, 67:254–264.

Ritchie, I., Rosinger, H., and Atrens, A. (1976). Anelastic relaxation and the diffusion of oxygen in α zirconium. *Journal of Nuclear Materials*, 62:1–8.

Rooyen, G. V. (1970). Basic factors which influence the Lüders strain during discontinuous yielding. *Materials Science and Engineering*, 7:37–48.

Régnier, P. and Dupouy, J. (1970). Prismatic slip in beryllium and the relative ease of glide in h.c.p. metals. *Phys. Status Solidi*, 39:179.

Saitou, K., Otoguro, Y., and Kihara, J. (1988). Effect of the stiffness of the testing system on the discontinuous deformation of 7075–Al alloy. *J. Japan Inst. Metals*, 6:1238–1245.

Sanchez-Palencia, E. and Zaoui, A. (1987). *Homogenization techniques for composite media.* Lecture Notes in Physics No. 272, Springer, Berlin.

Saraev, D. and Schmauder, S. (2003). Finite element modelling of Al/SiC metal matrix composites with particles aligned in stripes: a 2D/3D comparison. *International Journal of Plasticity*, 19:6:733–747.

Schoeck, G. (1956). Moving dislocations and solute atoms. *Phys. Rev.*, 102:1458–1459.

Schoeck, G. (1980). *Thermodynamics and thermal activation of dislocations*, volume 3, chapter 10. North Holland Physics Publishing.

Schoeck, G. and Seeger, A. (1959). The flow stress of iron and its dependence on impurities. *Acta Met.*, 7:469–477.

Schwarz, R. (1974). Dynamic dislocation phenomena in single crystals of Cu–10.5%at.Al at 4.2K. *Phys. rev. B*, 9:3292–3299.

Schwarz, R. (1982). Influence of strain aging on the strain rate sensitivity of the flow stress. *Scripta Metallurgica*, 16:385–390.

Schwarz, R. (1985a). Kinetics of the Portevin–Le Chatelier effect in Al 6061 alloy. *Acta Met.*, 33:295–307.

Schwarz, R. (1985b). The Portevin–Le Chatelier effect: I. model for type B serrations. volume 1, pages 343–348. Pergamon Press.

Shewmon, P. (1963). *Diffusion in solids.* Mc Graw–Hill.

Silva, D. P. E., Com-Nougue, J., Béranger, G., and Lacombe, P. (1971). Relation entre la cinétique de vieillissement après déformation du zirconium α et la diffusion anisotrope de l'oxygène à courte distance. *Scripta Metallurgica*, 5:795–800.

Sinha, T. and Asundi, M. (1977a). Effect of strain rate and temperature on tensile properties of heat–treated zirconium–2.5wt%niobium alloy. *Journal of Nuclear Materials*, 67:311–314.

Sinha, T. and Asundi, M. (1977b). Strain ageing in zirconium–2.5wt%nobium alloy. *Journal of Nuclear Materials*, 67:315–317.

Sleeswyk, A. (1958). Slow strain hardening of lingot iron. *Acta Met.*, 6:598–603.

Snoek, J. (1941). Effect of small quantities of carbon and nitrogen on the elastic and plastic properties of iron. *Physica*, 8:711–733.

Snowden, K. (1970). The effect of temperature on the logarithmic creep of Zircaloy-2. *Journal of Nuclear Materials*, 36:347–349.

Springer, F. (1998). *Quantitative Untersuchungen zur dynamischen Reckalterung an Kupfer–Mangan–Polykristallen.* PhD thesis, Technische Universität Carolo Wilhelmina zu Braunschweig.

Springer, F. and Schwink, C. (1991). Quantitative inverstagations on dynamic strain ageing in polycrystalline cumn alloys. *Scripta Metallurgica*, 25:2739–2744.

Strudel, J. (1969). *Dislocations et déformation plastique*, page 199. Physique–Yravals.

Strudel, J. (1984). Interactions between dislocations and impurities. *Japan-France seminar on fundamental aspects of mechanical properties and microstructure evolution of stainless steels at high temperature, 15-18 Mai 1984, Tokyo*, pages 169–180.

Tabata, T., Fujita, H., and Nakajima, Y. (1980). Behaviour of dislocations in Al–Mg single crystals observed by high voltage electron microscopy. *Acta Met.*, 28:795–8059.

Tenckhoff, E. (1988). Deformation mechanisms, texture and anisotropy in zirconium and Zircaloy. *ASTM STP*, 966.

Thom, R. (1972). *Stabilité structurelle et morphegénèse.* Benjamin.

Thomason, P. (1990). *Ductile fracture of metals.* Pergamon Press.

Thorpe, W. and Smith, I. (1978a). Creep properties of Zr1%Nb alloy. *Journal of Nuclear Materials*, 75:209–219.

Thorpe, W. and Smith, I. (1978b). Tensile properties of Zr1%Nb alloy. *Journal of Nuclear Materials*, 78:49–57.

Thorpe, W. and Smith, I. (1978c). Tensile properties of Zr1%Nb alloy. *Journal of Nuclear Materials*, 78:49–57.

Traub, H. (1974). *Untersuchungen des Fliessbereichs kubisch Flächenzentrierter legierungen.* PhD thesis, Technische Universität Carolo Wilhelmina zu Braunschweig.

Tsukahara, H. and Iung, T. (1998). Finite element simulation of the Piobert–Lüders behavior in an uniaxial tensile test. *Mater. Sci. Eng.*, A:304–308.

Tyson, W. (1967). Strengthening of h.c.p. Zr, Ti and Hf by interstitial solutes. *Canadian Metallurgical Quarterly*, 6(4):301–332.

van den Beukel, A. (1975a). Theory of the effect of dynamic strain aging on mechanical properties. *Acta Met.*, 30:197–206.

van den Beukel, A. (1975b). Theory of the effect of dynamic strain aging on mechanical properties. *Phy.Stat.Sol.*, 30:197–206.

van den Beukel, A. (1980). On the mechanism of serrated yielding and dynamic strain aging. *Acta Met.*, 28:965–969.

van den Brink, S., van den Beukel, A., and McCormick, P. (1975). *Phys. Sta. Sol. (a)*, 30:429.

van den Brink, S., van den Beukel, A., and McCormick, P. (1977). The influence of specimen geometry and machine stiffness on the Portevin–Le Chatelier effect in Al–Cu alloy. *Phys. Sta. Sol. (a)*, 41:513–521.

Veevers, K. (1975). Strain ageing in zirconium alloys. *Journal of Nuclear Materials*, 55:109–110.

Veevers, K. and Rotsey, W. (1968). Effect of irradiation on strain ageing in annealed Zircaloy-2. *Journal of Nuclear Materials*, 27:108–111.

Veevers, K., Rotsey, W., and Snowden, K. (1969). Applications related phenomena in zirconium and its alloys. *ASTM STP*, 458.

Veevers, K. and Snowden, K. (1973). Strain ageing of quenched Zircaloy–2. *Journal of Nuclear Materials*, 47:311–316.

Wijler, A. and van Westrum, J. S. (1971). Strain rate experiments and the Portevin–Le Chatelier effect in Au(14at%Cu). *Scripta Metallurgica*, 5:821–824.

Wu, T. and Wang, C. (1958). *Sci. Sin.*, 7:1029.

Yi, J.-K., Park, H.-B., Park, G.-S., and Lee, B.-W. (1992). Yielding and dynamic strain aging behavior of Zircaloy–4 tube. *Journal of Nuclear Materials*, 189:353–361.

Yoshinaga, H. and Morozumi, S. (1971). The solute atmosphere round a moving dislocation and its dragging stress. *Phil. Mag.*, 23:1367–1385.

Yoshinaga, H., Toma, K., and Morozumi, S. (1976). Internal stresses during high temperature deformation of pure aluminium and an Al-Mg alloy. *Transactions of the Japan Institut of Metals 17*, 2:102–110.

Z-set package (1996). www.nwnumerics.com, www.mat.ensmp.fr.

Zeeman, E. (1977). *Catastrophe theory*. Addison–Wesley.

Zhang, S., McCormick, P., and Estrin, Y. (2000). The morphology of Portevin–Le Chatelier bands : finite element simulation for Al–Mg–Si. *Acta Materialia*, 49:1087–1094.

Ziegenbein, A. (2000). *Laserextensometrische untersuchungen des Portevin–Le Chatelier effektes an einer CuAl legierung*. PhD thesis, Technische Universität Carolo Wilhelmina zu Braunschweig.